INTERNATIONAL DOCTORAL
SCHOOL OF THE USC

Juan Manuel
Ceballos Guzmán

PhD Thesis

Engineering core-shell plasmonic nanoMOFs: synthetic methodologies and applications

Santiago de Compostela, 2024

Doctoral Programme in Materials Science

ESCOLA DE DOUTORAMENTO
INTERNACIONAL DA USC

DOCTORAL THESIS

ENGINEERING CORE-SHELL PLASMONIC NANOMOFs: SYNTHETIC METHODOLOGIES AND APPLICATIONS

Author

Juan Manuel Ceballos Guzmán

Supervisor: Pablo Alfonso del Pino González de la Higuera

Tutor: Pablo Alfonso del Pino González de la Higuera

PHD PROGRAM IN MATERIALS SCIENCE

SANTIAGO DE COMPOSTELA

Acknowledgments

I would like to thank Prof. Pablo del Pino, Prof. Beatriz Pelaz, and Dr. Ester Polo for giving me the opportunity to be part of their group, Bionanotools, and for guiding me in this project with their experience and advice.

I would also like to thank all my lab partners, many of whom have left, while some are still here, for the good relationships and friendships we developed during the working days: Mafer, Aitor, Martina, Enrica, Manuela, Marta, Manolito, Miriam, Lucía, Sara, Giulia, Samuel, Elvira, Antia, Chema, Sajid, André, Espe, Ester, Oleg, Maite, Josef, Brenda, Álvaro, María, Laura, Nikos, Fatima, and also the new members who have joined the group and to Víctor for the Gallego translation.

Special thanks go to the Centro Singular de Investigación en Química Biolóxica e Materiais Moleculares (CiQUS) and the University of Santiago de Compostela for providing the installations and facilities that enabled me to work properly throughout my PhD.

I also want to extend my thanks to the HeatNMOF network and all its members, including the ESRs (Ana and Jon, with whom I worked constantly), and especially to the coordinator, Prof. Patricia Horcajada, as well as all the researchers I had the opportunity to meet during the workshops, particularly Prof. Thomas Devic and Prof. David Fairen-Jiménez, with whom I had the chance to work in their groups at IMN-Nantes, France, and the University of Cambridge, United Kingdom, respectively.

I am also grateful to the European Union's Horizon 2020 research and innovation program under the Marie Sklodowska-Curie grant agreement No. 860942 for supporting my fellowship during the first three years of my PhD.

Special thanks go to Prof. Pablo Taboada Antelo, the coordinator of the PhD program in Materials Science, for the funding in the last year of my PhD through the MOFSiAn project (TED2021-132522D-I00).

I would also like to thank the microscopy unit of the CATUS-USC, especially Ramiro Barreiro Pérez and Raquel Antón Segurado, for allowing me to use the facilities and services. Special thanks to the X-ray unit, particularly Dr. Bruno Dacuña Mariño, for his time spent in many discussions and for always being willing to help and explain my results.

Thanks as well to Dr. Jose Manuel Villa Fungueiriño for his time in conducting TEM analysis and for his valuable input in the discussions and contributions to the publications in this thesis.

My gratitude also goes to Prof. Sara Bals and Timothy Craig, members of HeatNMOF from the University of Antwerp, for their collaboration in HRTEM and tomography studies.

I am deeply grateful to Prof. Carlos Martí-Gastaldo and Prof. Sergio Tatay from ICMol University of Valencia for their time, advice, discussions, and for dedicating significant efforts to certain parts of this research, as well as for their strong collaboration with our group.

USC UNIVERSIDADE DE SANTIAGO

USC
UNIVERSIDADE
DE SANTIAGO
DE COMPOSTELA

List of publications

The following are the publications product of this PhD thesis and the author contribution.

Chapter 3

1. "High-yield halide-assisted synthesis of metal–organic framework UiO-based nanocarriers". (2022). *Nanoscale, 14*(18), 6789-6801. DOI: 10.1039/D1NR08305H

Manuel Ceballos[1], Manuela Cedrún-Morales[1], Manuel Rodríguez-Pérez[1], Samuel Funes-Hernando[1], José Manuel Vila-Fungueiriño[1], Giulia Zampini[1], Maria F. Navarro Poupard[1], Ester Polo[1], Pablo del Pino*[1] and Beatriz Pelaz *[1]

[1]Center for Research in Biological Chemistry and Molecular Materials (CiQUS), University of Santiago de Compostela, 15705 Santiago de Compostela, Spain.

Editorial: Royal Society of Chemistry, ISSN 2040-3372.

Impact Factor: 6.7 in 2022. Q1 in Nanoscience & Nanotechnology.

Contributions:

Experimental: synthesis and characterization of the materials and data analysis.

Manuscript: preparation of the paper, specifically results, discussion, and manuscript writing.

Chapter 6

2. "Seeded-Growth of PCN-224 onto Plasmonic Nanoparticles: Photoactive Microporous Nanocarriers". (2024). *Small Structures, 5*(5), 2300464. DOI: 10.1002/sstr.202300464

Manuel Ceballos[1], Samuel Funes-Hernando[1], Giulia Zampini[1], Manuela Cedrún-Morales[1], José Manuel Vila-Fungueiriño[1], Beatriz Pelaz *[1] and Pablo del Pino*[1]

[1]Center for Research in Biological Chemistry and Molecular Materials (CiQUS), University of Santiago de Compostela, 15705 Santiago de Compostela, Spain.

Editorial: Wiley-VCH, ISSN: 2688-4062.

Impact Factor: 13.9. Q1 in Nanoscience & Nanotechnology.

Contributions:

Experimental: synthesis and characterization of the materials and data analysis.

Manuscript: preparation of the paper, specifically results, discussion, and manuscript writing.

USC UNIVERSIDADE DE SANTIAGO DE COMPOSTELA

USC
UNIVERSIDADE
DE SANTIAGO
DE COMPOSTELA

Table of contents

Acknowledgments i

List of publications iii

Table of contents v

List of figures ix

List of tables xxiii

List of abbreviations xxvii

Resumo xxxi

Resumen xxxvii

Abstract xlv

1. Introduction 1

1.1. RETICULAR CHEMISTRY 3
1.1.1. The design of new inorganic porous materials 3
1.1.2. Metal-organic frameworks (MOFs) 4
1.1.3. Building blocks 5
1.1.4. Topology 9
1.1.5. Isoreticular structures 13
1.1.6. Synthetic approaches of MOFs 14
1.1.7. Applications of MOFs across various fields 18

1.2. Zr-BASED MOFs 21
1.2.1. The $Zr_6(\mu_3\text{-}O)_4(\mu_3\text{-}OH)_4$ secondary building unit 21
1.2.2. Structural defects in UiO-family Zr-based MOFs 22
1.2.3. Compositional and geometrical variants Zr-oxo clusters 24
1.2.4. Porphyrinic Zr-based MOFs 28
1.2.5. Post-synthetic modification of Zr-based MOFs 30

1.3. METAL NANOPARTICLES 34
1.3.1. Optical properties of metal nanoparticles 34
1.3.2. Plasmon 35
1.3.3. Localized Surface Plasmon Resonance (LSPR) 37
1.3.4. Tunning the LSPR 38
1.3.5. Thermoplasmonics 42
1.3.6. Synthetic approaches and surface engineering of plasmonic nanoparticles 44

1.4. INORGANIC NANOPARTICLE@METAL-ORGANIC FRAMEWORKS NANOCOMPOSITES (iNPs@MOFs) 49
1.4.1. Synthetic approaches 49

1.5. OBJECTIVES 52
General Objectives 52
Specific objectives 52

USC UNIVERSIDADE DE SANTIAGO DE COMPOSTELA

1.5.1. Chapter 3 52
1.5.2. Chapter 4 52
1.5.3. Chapter 5 53
1.5.4. Chapter 6 53
1.5.5. Chapter 7 53

2. Materials and methods 55
2.1.1. Scanning electron microscopy (SEM) 57
2.1.2. Transmission electron microscopy (TEM) 57
2.1.3. Powder X-Ray Diffraction (PXRD) 57
2.1.4. Wide-angle X-ray scattering (WAXS) and small-angle X-ray scattering (SAXS). 57
2.1.5. Thermogravimetric analysis (TGA) 57
2.1.6. UV–vis spectroscopy. 58
2.1.7. Fourier-transformed infrared spectroscopy (FTIR) 58
2.1.8. Raman spectroscopy 58
2.1.9. Inductively Coupled Plasma-Optical Emission Spectroscopy (ICP-OES) 58
2.1.10. Dynamic light scattering 58
2.1.11. Nanoparticle tracking analysis (NTA) 58
2.1.12. N_2 adsorption-desorption analysis 58
2.1.13. Differential Scanning calorimetry (DSC) 58
2.1.14. Nuclear magnetic resonance (NMR) spectroscopy 58
2.1.15. Photoluminescence spectroscopy (PL) 59

2.2. Chapter 3 59
2.2.1. Chemicals 59
2.2.2. Synthesis of UiO-66-NH_2 ($ZrOCl_2$), UiO-66-NH_2:X^- (X^-: Cl^-, Br^-, I^-) and UiO-66 nanoMOFs 59
2.2.3. Colloidal stability tests 59
2.2.4. Encapsulation of Rhodamine 6G. 60
2.2.5. Cargo stability tests 60
2.2.6. Cell culture 60
2.2.7. Resazurin test 60
2.2.8. Confocal microscopy imaging 61
2.2.9. Flow cytometry experiments. 61

2.3. Chapter 4 61
2.3.1. Chemicals 61
2.3.2. Synthesis of MOF-525 and PCN-224 61
2.3.3. Synthesis of PCN-222 62
2.3.4. Digestion of Zr-porphyrinic MOFs for ^{1}H-NMR quantification 63
2.3.5. Continuous PCN-224 synthesis procedure 63

2.4. Chapter 5 63
2.4.1. Chemicals 63
2.4.2. Synthesis of Au Nanostars (AuNSs) 64
Synthesis of citrate-stabilized seeds 64
Seed-mediated growth synthesis of AuNSs 64
2.4.3. Synthesis of Au Nanorods (AuNRs) 64
Synthesis of seeds 64
Seed mediated growth synthesis of Au Nanorod (AuNRs) 65
2.4.4. Synthesis of Au Bipyramids (AuBipy) and phase transfer 65
Synthesis of Pentatwinned Seeds 65
Scaled-Up AuBipy Synthesis 65
2.4.5. PEGylation and Phase Transfer of inorganic nanoparticles 65
2.4.6. Synthesis of UiO-family nanocomposistes 66
2.4.7. Laser Irradiation (Heating Experiments) 66

USC UNIVERSIDADE DE SANTIAGO DE COMPOSTELA

2.5. Chapter 6 67
2.5.1. Chemicals 67
2.5.2. Synthesis of mPEG-PO_3 67
2.5.3. Synthesis of Au Bipyramids (AuBipy), functionalization and phase transfer 67
2.5.4. Synthesis of PCN-224 68
Preparation of Zr_6-oxo Cluster 68
MOF Synthesis 68
2.5.5. Cresyl Violet Loading 68
2.5.6. PCN-224 PEGylation 68
2.5.7. Cell Culture 68
2.5.8. Laser Irradiation (Heating Experiments) 69
2.5.9. Microscopy Imaging 69

2.6. Chapter 7 69
2.6.1. Chemicals 69
2.6.2. Synthesis of AuBipy, AuNRs, PEGylation and phase transfer 69
2.6.3. Synthesis of AuNPs@NU-1000 nanocomposites. 70

3. HIGH-YIELD HALIDE-ASSISTED SYNTHESIS OF METAL–ORGANIC FRAMEWORK UiO-BASED NANOCARRIERS 71

3.1. Introduction 75

3.2. Results and discussion 75
3.2.1. Influence of Zirconium precursor 75
3.2.2. Influence of modulator rate 77
3.2.3. Influence of chloride as co-modulator 78
3.2.4. Influence of different halides as co-modulators to produce UiO-66-NH_2 nanoMOFs 78
3.2.5. Chlorine ions as co-modulators for the UiO-66 nanoMOFs synthesis 90
3.2.6. UiO-66 nanoMOFs as DDSs 93
3.2.7. Cell studies 100

3.3. Summary and Conclusions of Chapter 3 104

4. ULTRAFAST SYNTHESIS OF ZIRCONIUM-PORPHYRIN FRAMEWORK NANOCRYSTALS FROM ALKOXIDE PRECURSORS 105

4.1. Introduction 107

4.2. Results and discussion 107
4.2.1. Varying ligand-to-metal ratio at room temperature (MOF-525, PCN-224) 107
4.2.2. Varying temperature and alkoxide precursor (PCN-224) 117
4.2.3. Varying the modulator (PCN-222) 127
4.2.4. Interlaboratory reproducibility study 134
4.2.5. Continuous flow reaction 134

4.3. Summary and Conclusions of Chapter 4 137

5. STRAIGHTFORWARD, UNIVERSAL METHOD FOR SEEDING Zr-BASED MOFS ONTO INORGANIC NANOPARTICLES 139

5.1. Introduction 141

5.2. Results and discussion 141
5.2.1. Nanoparticle reshaping 141
5.2.2. Zr(IV) ethoxide as innovative precursor for MOF synthesis under mild conditions 146
5.2.3. Seeded-growth mechanism and the influence of the shell-thickness in the heating properties. 158

USC UNIVERSIDADE DE SANTIAGO DE COMPOSTELA

5.3. Summary and Conclusions of Chapter 5 ____ 164

6. SEEDED-GROWTH OF PCN-224 ONTO PLASMONIC NANOPARTICLES: PHOTOACTIVE MICROPOROUS NANOCARRIERS ____ 167

6.1. Introduction ____ 171

6.2. Results and discussion ____ 172

6.2.1. Synthesis and Structural Characterization of PCN-224 nanoMOFs and NCs ____ 172
6.2.2. Effect of shell thickness in photoluminescent properties ____ 179
6.2.3. Heating properties of AuB@PCN-224@PEG NCs under 808 nm laser irradiation ____ 183
6.2.4. Photo-stimulation of AuB(10)@PCN-224@PEG inside living cells ____ 188

6.3. Summary and Conclusions of Chapter 6 ____ 193

7. EFFECT OF CORE SHAPE ON THE HEATING AND PHOTOLUMINESCENT PROPERTIES OF CORE-SHELL PLASMONIC NANOMOFs AND THEIR USE AS SERS SUBSTRATES ____ 195

7.1. Introduction ____ 197

7.2. Results and discussion ____ 197

7.2.1. Synthesis and Structural Characterization of NU-1000 nanoMOFs and NCs. ____ 197
7.2.2. Effect of shell thickness and particle shape in photoluminescence properties. ____ 205
7.2.3. Effect of particle shape in heating properties. ____ 208
7.2.4. AuBipy@NU-1000 nanocomposites as SERS substrate in colloidal dispersion ____ 210

7.3. Summary and Conclusions of Chapter 7 ____ 212

8. Conclusions ____ 213

8.1 General conclusions ____ 215

References ____ 217

Appendices – Rights & Permissions ____ 243

Appendix I: Conflict of interest ____ 243

Appendix II: PhD publications and permissions ____ 244

Appendix III: All the other images, tables, and figures ____ 246

USC UNIVERSIDADE DE SANTIAGO DE COMPOSTELA

List of figures

Figure 1-1. Timeline displaying key achievements in MOF research, along with the annual number of MOF publications and the number of MOF structures reported to the CSD. Publications and MOF structure reported data are not cumulative. ____ 3

Figure 1-2. Schematic representation of the MOF structure, illustrating the assembly from metal atoms or clusters and organic linkers to the complete framework and some examples with their building units. _____ 4

Figure 1-3. Timeline of some of the most representative MOFs and their corresponding SBUs. _____ 5

Figure 1-4. Representative polytopic carboxylate linkers used to construct MOFs. _____ 6

Figure 1-5. Schematic representation of secondary building blocks that can be obtained with their corresponding polyhedron. Color scheme: metals (dark blue), carbon (grey), oxygen (red), nitrogen (light blue), halogens (green), anchor points (turquoise). M, metal; L, linker. _____ 8

Figure 1-6. Table of potential bipartite nets created through reticular chemistry. Each topology is presented as its corresponding augmented net. If multiple nets exist, the identifier of the specified net is highlighted in bold._____ 10

Figure 1-7. Differences of pore size and pore aperture in MOFs. _____ 11

Figure 1-8. Schematic representation of different aspect that influence the topology of a MOF. _____ 13

Figure 1-9. Scheme of isoreticular Zr-based MOFs increasing the linker length with the X-ray diffraction patter, showing the relationship between the lattice parameter and the diffracted angle according to Bragg's law. _____ 14

Figure 1-10. Schematic representation illustrating the difficulty of crystallizing a material in relation to the bond energy between the building blocks. _____ 15

Figure 1-11. Overview of conventional MOF synthesis methods organized by temperature, including various alternative approaches. _____ 17

Figure 1-12. Research fields where MOFs are applied. _____ 18

Figure 1-13. $Zr_6(\mu_3\text{-}O)_4(\mu_3\text{-}OH)_4$ SBU and its transformation to the dehydroxylated form. _ 21

Figure 1-14. Co-insertion into. $Zr_6(\mu_3\text{-}O)_4(\mu_3\text{-}OH)_4$ SBU._____ 22

Figure 1-15. Schematic representation of missing linker and missing cluster defects in UiO-66, illustrating the resulting topologies in comparison with pristine UiO-66. _____ 23

Figure 1-16. PXRD pattern of defective reo phase and non-defective fcu phase of UiO-66. 23

Figure 1-17. Schematic illustration of the varying pore sizes in the fcu and reo phases of UiO-66. _____ 24

USC UNIVERSIDADE DE SANTIAGO DE COMPOSTELA

Figure 1-18. Schematic illustration of various spatial and compositional arrangements of Zr-based SBUs. 25

Figure 1-19. Diagram of various Zr-SBUs along with their corresponding connectivities and representative examples. 26

Figure 1-20. Polymorphs derived from $Zr_6(\mu_3\text{-}O)_4(\mu_3\text{-}OH)_4$ cluster and TCPP ligand. 28

Figure 1-21. Zr_8-cluster of the proposed PCN-221 and the actual disordered Zr_6-cluster of dPCN-224, illustrating its four spatial orientations. 29

Figure 1-22. PXRD patterns of the polymorphs of porphyrinic Zr-based MOFs. 30

Figure 1-23. Examples of post-synthetic modification approaches used in Zr-based MOFs. 31

Figure 1-24. Dielectric functions (real and imaginary parts) of Ag, Au and Cu. 34

Figure 1-25. Schematic representation of the collective and coherent oscillation of electrons in a metallic structure known as plasmon. 36

Figure 1-26. Formation of a plasmon by inelastic scattering of an electron on a metal surface. 36

Figure 1-27. Schematic representation of a volume plasmon. 37

Figure 1-28. Schematic representation of a surface plasmon in a dielectric environment. 37

Figure 1-29. Schematic representation of the localized surface plasmon corresponding to the displacement of the electron cloud of a metallic nanosphere and nanorod. 38

Figure 1-30. Light-matter interactions. 38

Figure 1-31. Extinction spectra of spherical nanoparticles. Material = Au, diameter = variable, dielectric environment = water (ε_0 = 1.77). 39

Figure 1-32. Extinction spectra of nanoparticles with different morphology. Material = Au, Length = 100 nm, Aspect Ratio = 3, dielectric environment = water (ε_0 = 1.77). 40

Figure 1-33. Extinction spectra of bipyramids. Material = Au, Length = variable, Aspect Ratio = 4, dielectric environment = water (ε_0 = 1.77). 40

Figure 1-34. Extinction spectra of bipyramids. Material = Au, Length = 100 nm, Aspect Ratio = variable, dielectric environment = water (ε_0 = 1.77). 41

Figure 1-35. Extinction spectra of bipyramids. Material = variable, Length = 100 nm, Aspect Ratio = 3, dielectric environment = water (ε_0 = 1.77). 41

Figure 1-36. Extinction spectra of bipyramids. Material = Au, Length = 100 nm, Aspect Ratio = 3, dielectric environment = variable. 42

Figure 1-37. Soret effect in plasmonic MOF composite, releasing the molecules inside due to a temperature gradient. 44

Figure 1-38. Growth on the {111} facet occurs atom by atom, leading to the gradual extension of the side facets with each gold layer added. The side facets expand through a gradual, continuous process involving galvanic replacement and silver deposition. 47

USC UNIVERSIDADE DE SANTIAGO DE COMPOSTELA

Figure 1-39. Schematic representation of synthetic approaches of composites that integrate MOFs and plasmonic nanoparticles. _____ 49

Figure 3-1. Representative micrographs of the UiO-66-NH_2 particles obtained using (a) $ZrOCl_2$ or (b) $ZrO(NO_3)_2$ as Zr precursor; or using the combination of (c) $ZrO(NO_3)_2$ and HCl; and (d) $ZrO(NO_3)_2$ and NaCl. Scale bars correspond to 500 nm._____ 75

Figure 3-2. Representative SEM images of UiO-66-NH_2 ($ZrOCl_2$) and UiO-66-NH_2 particles obtained using different Zr precursors. Images were taken at different magnifications collected with Everhart-Thornley detector (SE2, secondary electrons) at 3 kV as well as different voltages to get different information. Scale bars from left to right correspond to 500 nm, 400 nm and 200 nm. _____ 76

Figure 3-3. Representative TEM images of the UiO-66-NH_2 ($ZrOCl_2$) and UiO-66-NH_2 particles obtained using different Zr precursors. _____ 76

Figure 3-4.UiO-66-NH_2 particles synthesized with $ZrO(NO_3)_2$ as precursor with different amounts of acetic acid as modulator 1.4, 1.6, 1.8, 2.0 and 2.2 mL (775, 885, 995, 1105, 1215 equivalents). Images were taken at different magnifications collected with Everhart-Thornley detector (SE2, secondary electrons) at 3 kV. _____ 77

Figure 3-5. TEM images of a) UiO-66-NH_2 ($ZrOCl_2$) (black), b) UiO-66-NH_2 (orange), c) UiO-66-NH_2:Cl^- (red), d) UiO-66-NH_2:Br^- (green), and e) UiO-66-NH_2:I^- (blue), HRTEM of f) UiO-66-NH_2:Cl^- and g) UiO-66-NH_2:Br^- and h–j) STEM-EDX images of UiO-66-NH_2:Cl^- h) with Zr i) and Cl^- j) mapping, and k–m) STEM-EDX images of UiO-66-NH_2:Br^- k) STEM, Zr l) and Br^- m) mapping. Scale bars correspond to 200 nm except for the HRTEM images, in which they correspond to 10 nm. _____ 79

Figure 3-6. Representative TEM images of UiO-66-NH_2:X^- (X^-: Cl^-, Br^-, I^-) nanoMOFs. __ 80

Figure 3-7. Representative SEM images of UiO-66-NH_2:X- (X^-: Cl^-, Br^-, I^-) nanoMOFs at different magnifications collected with Everhart-Thornley detector (SE2, secondary electrons) at 3 kV. Scale bars from left to right correspond to 400 nm, 200 nm and 100 nm. _____ 81

Figure 3-8. Photograph of the different UiO-66-NH_2 particles produced dispersed in methanol. _____ 81

Figure 3-9. Histogram of the number distribution N of the edge of the nanoparticles (i.e., vertex-to vertex distance) as determined from SEM images. a) UiO-66-NH_2 ($ZrOCl_2$) 225 ± 37 nm, b) UiO-66-NH_2:Cl^- 94 ± 10 nm, c) UiO-66-NH_2:Br^- 81 ± 9 nm and d) UiO-66-NH_2:I^- 109 ± 14 nm._____ 81

Figure 3-10. UV-Vis absorption spectra of the zirconium precursors $ZrClO_2$ and $ZrO(NO_3)_2$ and the effect of halides with $ZrO(NO_3)_2$ in DMF solution. _____ 82

Figure 3-11. $ZrO(NO_3)_2$ solutions in presence of sodium halide salts in DMF. In the case of F- the formation of a white precipitate was observed (inset). _____ 82

Figure 3-12. Crystallographic characterization of UiO-66-NH_2 nanoMOFs: UiO-66-NH_2 ($ZrOCl_2$) (black), UiO-66-NH_2 (orange), UiO-66-NH_2:Cl^- (red), UiO-66-NH_2:Br^-

USC UNIVERSIDADE DE SANTIAGO DE COMPOSTELA

(green) and UiO-66-NH_2:I^- (blue). A) PXRD pattern, b) WAXS analysis measured at a sample-to-detector distance of 288 mm and c) SAXS analysis measured at a sample-to-detector distance of 1343 mm in capillary mode. 83

Figure 3-13. WAXS experiments measured at a sample to detector distance of 288 mm refined with Pawley's method and with corrected intensities and normalized with the most intense peak and residual. 84

Figure 3-14. a–c) FTIR analysis and d) UV-Vis spectroscopy of UiO-66-NH_2 nanoMOFs: UiO-66-NH_2 ($ZrOCl_2$) (black), UiO-66-NH_2 (orange), UiO-66-NH_2: Cl^- (red), UiO-66-NH_2:Br^- (green) and UiO-66-NH_2:I^- (blue). 85

Figure 3-15. Raman spectra of UiO-66-NH_2 nanoMOFs. 86

Figure 3-16. a) TGA analysis and b) N_2 adsorption isotherms of UiO-66-NH_2 nanoMOFs: UiO-66-NH_2 ($ZrOCl_2$) (black), UiO-66-NH_2 (orange), UiO-66-NH_2:Cl^- (red), UiO-66-NH_2:Br^- (green) and UiO-66-NH_2:I^- (blue). 86

Figure 3-17 Effective diameter (hydrodynamic diameter) of UiO-66-NH_2 nanoMOFs analyzed by a) NTA and b) DLS. c) ζ-Potential measurements. d) Summary of the stability tests in water and lysosomal medium. Black line corresponds to UiO-66-NH2 ($ZrOCl_2$), red to UiO-66-NH_2:Cl^-, green to UiO-66-NH_2:Br^- and blue to UiO-66-NH_2:I^-. 89

Figure 3-18. Representative TEM images of a) UiO-66 ($ZrOCl_2$), b) UiO-66, c) UiO-66:Cl^- and, d) EDX elemental mapping of carbon, zirconium and chloride from a UiO-66:Cl^- nanoMOF. Scale bars correspond to 200 nm for TEM and to 100 nm for STEM-EDX. 90

Figure 3-19. Representative TEM images of the UiO-66 nanoparticles synthesized with different Zr precursors and the effect of Cl^- when the synthesis is performed with $ZrO(NO_3)_2$ precursor at different magnifications. 91

Figure 3-20. Histogram of the number distribution N of the edge of the nanoMOFs (i.e., vertex-to vertex distance) as determined from SEM images. a) UiO-66 ($ZrOCl_2$) 186 ± 13 nm and b) UiO-66:Cl^- 174 ± 13 nm. 91

Figure 3-21. UV-Vis absorption spectra of the UiO-66 samples with different Zr precursors and the effect of Cl^- when the synthesis is performed with $ZrO(NO_3)_2$. 92

Figure 3-22. DLS a) number and b) intensity distributions of the hydrodynamic diameter dh of the UiO-66 samples. 92

Figure 3-23. ζ-potential values for the UiO-66 samples. 93

Figure 3-24. N_2 adsorption isotherm of UiO-66 ($ZrOCl_2$), UiO-66 and UiO-66:Cl^-. 93

Figure 3-25. Rhodamine 6G chemical structure. 94

Figure 3-26. Calibration curve of R6G in water was obtained from fluorescence under excitation at 520 nm (I). Fluorescence intensity (I) at the maximum emission peak as a function of R6G concentration c is plotted and calibration equation is obtained by

USC UNIVERSIDADE DE SANTIAGO DE COMPOSTELA

fitting a linear regression line to the collected data; R^2 is the coefficient of determination. _____ 95

Figure 3-27. UV-Vis absorption spectra normalized to Zr of the UiO-66-NH_2 nanoMOFs after the R6G loading. _____ 95

Figure 3-28. DLS a) intensity and b) number distributions of the hydrodynamic diameter d_h of the UiO-66-NH_2@R6G nanoMOFs. _____ 96

Figure 3-29. ζ- potential distribution for the UiO-66-NH_2 samples after the R6G loading. _ 96

Figure 3-30. UV-Vis absorption spectra normalized to Zr of the UiO-66 samples after the R6G loading. _____ 97

Figure 3-31. DLS a) number and b) intensity distributions of the hydrodynamic diameter dh of the UiO-66@R6G nanoMOFs. _____ 97

Figure 3-32. ζ-potential distribution for the UiO-66 samples after the R6G loading. _____ 97

Figure 3-33. Calibration curves of R6G in DMEM and PSF. _____ 98

Figure 3-34. Cell viability in A549 cell culture after 24 h of UiO-66-NH_2 nanoMOFs exposure, measured by Resazurin assay. Viability values represent the mean ± standard deviation of measurements from three different wells. X axes representing the nanoMOF concentration in terms of Zr, nanoMOF and nanoparticle concentration unless in UiO-66-NH_2 where the lack of a defined structure prevents the calculation of the volume of each particle. _____ 101

Figure 3-35. Cell viability in A549 cell culture after 24 h of UiO-66 nanoMOFs exposure, measured by Resazurin assay. Viability values represent the mean ± standard deviation of measurements from three different wells. _____ 101

Figure 3-36. a) Representative microscopy confocal images of A549 cells incubated for 6 h with 25 pM of different UiO-66-NH_2@R6G and UiO-66-NH_2: X^-@R6G nanoMOFs. Scale bars correspond to 25 μm. b) Flow cytometry analysis of A549 cells exposed to vehicle (PBS) and the different UiO-66-NH_2:X^-@R6G formulations at 25 pM of nanoMOFs or to 2.5 μgZr/mL. Histograms represent experiments done in triplicate. c) Quantification of R6G fluorescence from flow cytometry analysis in (b). Bars represent means ± SD (n =3). _____ 102

Figure 3-37. UiO-66 cell uptake assessment by flow cytometry. Dot plots indicating the cells distribution as function of the rhodamine 6G fluorescence. Each plot represents the measurement of at least 5000 events. _____ 103

Figure 4-1. Top Row: Comparative structures of three different MOFs: PCN-224, PCN-222/MOF-545, and MOF-525, showing varying connectivity and organic linker arrangements. Bottom row: Synthesis approach utilizing Zr alkoxide precursors and TCPP. By adjusting the linker-to-metal (L/M) and modulator-to-metal (Mod/M) ratios, as well as the choice of modulator, we facilitate the formation of single phases of the depicted MOFs. These phases are further delineated in the tertiary diagram (bottom right). _____ 108

USC UNIVERSIDADE DE SANTIAGO DE COMPOSTELA

Figure 4-2. Characterization of nanoMOFs varying the L/M ratio at room temperature. a) PXRD diffractogram with the simulated patterns of PCN-224 and MOF-525, b) normalized first 5 diffraction peaks. HRTEM images of porphyrinic MOF nanoparticles changing the ratio linker/metal (L/M) c) 0.25, d) 0.50, e) 1.00, f) 1.50 and g) 2.00 and their corresponding FFT, indexing some different crystallographic planes (PCN-224 for L/M 0.25 and 0.50 and MOF-525 for L/M 1.00, 1.50 and 2.00). h) Normalized TGA with the theorical mass molar of Zr_6-oxo cluster with different coordination degree with TCPP and acetate molecules (dashed lines are the dehydrated cluster); i) quantification of TCPP molecules by ^{1}H-NMR; j) N_2 adsorption isotherms at 77 K correspond to the expected values for ideal PCN-224 and MOF-525 phases calculated with Zeo++;[308] and k) pore size distribution using NLDFT model. Scale bars are 200 nm for HR-TEM images and 0.5 nm^{-1} for FFT images. 109

Figure 4-3. Small angle diffraction measurements of Zr-porphyrinic MOFs with different L/M ratios. 109

Figure 4-4. Pawley's refinement for PCN-224 of Zr-porphyrinic MOF nanoparticles for a) 0.25, b) 0.50, c) 1.00, d) 1.50 and e) 2.00 L/M ratios. 110

Figure 4-5. SEM images of Zr-porphyrinic MOF nanoparticles at different magnifications (25 kX, 50 kX and 100 kX). Scale bars are 200 nm. 111

Figure 4-6. Particle size distribution histograms of Zr-porphyrinic MOF nanoparticles for a) 0.25, b) 0.50, c) 1.00, d) 1.50 and e) 2.00 L/M ratios. 111

Figure 4-7. TGA without normalization of Zr-porphyrinic MOFs. 112

Figure 4-8. ^{1}H-NMR spectra of the blank (D_2O, $NaHCO_3$, CH_3COOH and $(CH_3)_2SO_2$) and Zr-porphyrinic MOFs. Signals not assigned correspond to remanent DMF and CH_3OH from the washing steps.[310] 113

Figure 4-9. Pore size representation of a) PCN-224, b) MOF-525 and c) PCN-222. 114

Figure 4-10. a) UV-Vis spectra, b) DLS analysis and c) yield of reaction obtained with the amount of Zr by ICP-OES of Zr-porphyrinic MOFs. 115

Figure 4-11. a) FT-IT spectra of Zr-porphyrinic MOFs and b) zoom in carbonyl region. 116

Figure 4-12. Raman spectra of Zr-porphyrinic MOFs. 116

Figure 4-13. DSC analysis of Zr-porphyrinic MOFs for L/M = 0.25 (black), 0.50 (red), 1.00 (blue), 1.50 (gree) and 2.00 (orange). 116

Figure 4-14. a) Normalized absorption spectra and photoluminescence spectra at b) 420nm and c) 515 nm excitation wavelength of Zr-porphyrinic MOFs. 117

Figure 4-15. Representative SEM images for 1 h reaction performed at different temperatures (25 °C, 50 °C, 75 °C, 90 °C and 120 °C). The ratios adopted for the synthesis of the particles are L/M = 0.25, Mod/M = 250; the Zr precursor used is $Zr(OEt)_4$ and the modulator is AA. Scale bars: 200 nm. 118

USC UNIVERSIDADE DE SANTIAGO DE COMPOSTELA

Figure 4-16. a) Graphical representation of the reaction yield evaluated through ICP-OES, b) UV-Vis extinction spectra, c) hydrodynamic diameters (by number) and d) digital images of 1h reaction conducted at different temperatures. _____ 118

Figure 4-17. Characterization of nanosized PCN-224: effect of temperature and alkoxide in the synthesis.a) Representative SEM and b) HRTEM with FTT images of nanoMOFs synthesized starting from $Zr(OEt)_4$ precursor at 75 °C for 1 h in the presence of AA; c) PXRD patterns; d) normalized TGA with the theoretical molar mass of Zr_6-oxo cluster with different coordination degree with TCPP and acetate molecules (dashed lines are the dehydrated cluster); e) N_2 adsorption isotherms at 77 K with the expected uptake values for ideal PCN-224 and MOF-525 phases calculated with Zeo++;[308]; f) NLDFT pore size distribution by using different Zr precursors; g) graphical representation of the reaction yields evaluated through ICP-OES of 1 h reaction conducted at RT and 75 °C; h) UV-Vis extinction spectra and i) hydrodynamic diameters d_h (by number). Scale in FFT represents 0.5 nm^{-1}. __ 120

Figure 4-18. Representative SEM images for 1 h reaction performed at 75 °C by using different Zr precursors and AA as modulator. Scale bars are 200 nm. _____ 121

Figure 4-19. Particle size distribution histogram relative to SEM images of 1 h reaction performed at 75 °C by using different Zr precursors and AA as modulator. __ 121

Figure 4-20. Pawley's refinement of Zr-porphyrinic MOF nanoparticles, synthesized at 75 °C, 1 h reaction, by using different Zr precursors and AA as modulator. _____ 122

Figure 4-21. Representative SEM images for 1 h reaction performed at RT by using different Zr precursors and AA as modulator. Scale bars are 200 nm. _____ 124

Figure 4-22. Particle size distribution histogram relative to SEM images of 1 h reaction performed at RT by using different Zr precursors and AA as modulator. ____ 124

Figure 4-23. a) UV-Vis extinction spectra, b) hydrodynamic diameters (by number), c) TGA, d) PXRD patterns, e) BET analysis and f) NLDFT pore size distribution of 1 h reaction at RT by using different Zr precursors. _____ 125

Figure 4-24. a) UV-Vis extinction spectra, b) PXRD patterns, c) BET analysis and d) NLDFT pore size distribution of 24 h reaction at RT by using different Zr precursors. 126

Figure 4-25. a) HRTEM images of nanoMOFs synthesized starting from $Zr(OEt)_4$, b) graphical representation of the reaction yields evaluated through ICP-OES of 1h-reaction conducted at 75 °C for 24h c) UV-Vis extinction spectra, d) hydrodynamic diameters (by number), e) TGA, f) PXRD patterns, g) N_2 adsorption isotherms at 77K and h) NLDFT pore size distribution. _____ 128

Figure 4-26. Representative SEM images for 24 h reaction performed at 75 °C by using different Zr precursors and formic acid as modulator. Scale bars are 200 nm. _____ 129

Figure 4-27. Particle size distribution histogram relative to SEM images of 24 h reaction performed at 75 °C by using different Zr precursors and formic acid as modulator. _____ 129

USC UNIVERSIDADE DE SANTIAGO DE COMPOSTELA

Figure 4-28. Pawley's refinement of Zr-porphyrinic MOF nanoparticles, synthesized at 75 °C, 24 h reaction, by using different Zr precursors and formic acid as modulator. 130

Figure 4-29. a) Digital images of 1h reaction conducted at 75 °C with FA and $Zr(OEt)_4$, by varying the L/M and Mod/M ratios. UV-Vis extinction spectra of b) Mod/M = 250 and c) Mod/M = 560. 131

Figure 4-30. Representative SEM images of the L/M and Mod/M modulations for Zr-porphyrinic MOF nanoparticles synthesis performed at 75 °C, 1h-reaction, with the use of FA as modulator and $Zr(OEt)_4$ as precursor. Mod/M 250 scale bars: 1 µm. Mod/M 560. Scale bars are 2 µm. 132

Figure 4-31. Characterization of porphyrinic MOF nanoparticles by using $Zr(OEt)_4$ as precursor and FA as modulator (L/M = 1.5 and Mod/M = 560), at 75 °C for 1 h. a) PXRD diffractogram, b) normalized TGA with theorical lines of defects for Zr_6-oxo cluster (dashed lines are the dehydrated cluster), c) N_2 adsorption isotherm at 77 K (with pore size distribution plot inserted using NLDFT model) and SEM images at d) low and e) high magnification of PCN-222 nanoMOFs. Scale bars are 1 µm. 133

Figure 4-32. Pawley's refinement of Zr-porphyrinic MOF nanoparticles, synthesized at 75 °C, 1 h reaction, by using $Zr(OEt)_4$ as precursor and FA as modulator. The ratios adopted were L/M = 1.5 and Mod/M = 560 133

Figure 4-33. Reproducibility test for the synthesis of PCN-224 following synthetic conditions of a) Section 4.2.2 and b) 4.2.1 and for the synthesis of PCN-222 following the synthetic conditions of section 4.2.3, using $Zr(OEt)_4$ as precursor. 134

Figure 4-34. Photo of the reactions using $ZrCl_4$ and $ZrOCl_2$ as metal precursors at room temperature, 1h. 135

Figure 4-35. a) Pump infusion prototype and b) photo of continuous flow setup using an infusion pump with two syringes. 135

Figure 4-36. a) PXRD diffractogram with the simulated pattern of PCN-224; b) representative SEM image of PCN-224 synthesized by continuous flow synthesis; c) UV-Vis extinction spectra; d) d_h (by number); e) normalized TGA showing the theoretical lines for 6-connected Zr_6-oxo cluster (solid line hydrated and dashed line dehydrated cluster); f) N_2 adsorption isotherms at 77K correspond to the expected values for ideal PCN-224 phases calculated with Zeo++;[308], insert - pore size using NLDFT model. Scale bar is 200 nm. 136

Figure 4-37. Pawley's refinement of PCN-224 synthesized by continuous flow reaction. 137

Figure 5-1. a) UV-Vis spectra, b) HR-TEM image with its c) FFT of the dashed region showing the family of planes {111} of Au and d) histogram of particle size distribution of Au pentatwinned seeds used for the synthesis of AuBipy. e) UV-Vis spectra, f) TEM image, g) histogram of length and h) histogram of width of AuBipy. 142

Figure 5-2. a) UV-Vis spectra, b) TEM image, c) histogram of length and d) histogram of width of AuNRs. 142

USC UNIVERSIDADE DE SANTIAGO DE COMPOSTELA

Figure 5-3. a) UV-Vis spectra, b) TEM image and c)histogram of particle size distribution of AuNPs used as seeds for the synthesis of AuNSs. d) UV-Vis spectra, e) TEM image and f) histogram of length tip to tip of AuNSs. 143

Figure 5-4. a) TEM image and b) histogram of edge length of PdNCs. 143

Figure 5-5. a) TEM image and b) histogram of particle diameter of Fe_3O_4 MNPs. 143

Figure 5-6. Absorption spectra of PEGylated AuBipy at heated along the time in DMF at a) 120 °C and b) 90 °C and c) in water at 90 °C. SEM images of PEGylated AuBipy heated at 120 °C for d) 0 h, e) 1 h, f) 6 h and g) 24h. h) Reshaping transformation of PEGylated AuBipy when they are heated at different temperatures and solvents, showing the presence of PEG on the surface after the reshaping corroborated by i) TGA thermogram, j) Raman spectra. Scale bars are 200 nm. 144

Figure 5-7. a) Schematic representation of AuNRs reshaping. UV-Vis spectra of PEGylated AuNRs in DMF heated along the time at b) 90 º C and c) 120 ºC. SEM images d) PEGylated AuNRs and heated at 90 ºC for e) 1 h, f) 6 h and g) 24 h, and heated at 120 ºC for h) 10 min, i) 6h and j) 24 h. Scale bars are 200 nm. 145

Figure 5-8. a) Schematic representation of AuNSs reshaping. UV-Vis spectra of PEGylated AuNSs in DMF heated along the time at b) 90 º C and c) 120 ºC. SEM images d) PEGylated AuNSs and heated at 90 ºC for e) 10 min, f) 6 h and g) 24 h, and heated at 120 ºC for h) 10 min, i) 1h and j) 6 h. Scale bars are 200 nm. 145

Figure 5-9. a) Synthetic approach of AuBipy@nanoMOFs using zirconium ethoxide as precursor, b) yield of reaction determined with the content of Zr by ICP-OES and SEM images for c) AuBipy@UiO-66, d)AuBipy@UiO-66-NH_2, e)AuBipy@DUT-52, f)AuBipy@UiO-67 and g)AuBipy@MOF-867 obtained at 70ºC for 30 min. Absorption spectra of Au@MOF nanocomposites with different synthetic conditions h) 120 ºC – 30 min, i) 90 ºC – 30 min, j) 70 ºC – 30 min and k) RT– 72 h. Scale bars are 200 nm. 147

Figure 5-10. a) TGA analysis of different Zr precursors and b) derivative of TGA thermograms. 147

Figure 5-11. Isoreticular Zr-based MOFs structures with different bidentate carboxylic linkers and $Zr_6(\mu_3\text{-}O)_4(\mu_3\text{-}OH)_4$ as SBU. 148

Figure 5-12. UV-Vis spectra of a) UiO-66, b) UiO-66-NH_2, c) DUT-52, d) UiO-67 and e) MOF-867 using different temperatures and times of reaction. 149

Figure 5-13. FT-IR spectra or a) UiO-66, b) UiO-66-NH_2, c) DUT-52, d) UiO-67 and e) MOF.867 with different synthetic conditions. Gray line corresponds to each MOF linker. 150

Figure 5-14. PXRD patterns of the isoreticular Zr-based MOFs synthesized with $Zr(OEt)_4$ at a) 120 ºC, b) 90 ºC, c) 70 ºC for 30 min and d) RT for 72 h. 150

Figure 5-15. PXRD patterns of a) UiO-66, b) UiO-66-NH_2, c) DUT-52, d) UiO-67 and e) MOF.867 with different synthetic conditions. 151

USC UNIVERSIDADE DE SANTIAGO DE COMPOSTELA

Figure 5-16. SEM images of a, b) UiO-66, c, d) UiO-66-NH_2, e, f) DUT-52, g, h) UiO-67 and i, j) MOF-867 synthesized at RT for 72h. Scale bars are 500 nm left and 200 right side. 151

Figure 5-17. Pawley's refinement for a) UiO-66, b) UiO-66-NH_2, c) DUT-52, d) UiO-67 and e) MOF.867 synthesized at RT for 72 h. 152

Figure 5-18. Normalized TGA thermograms of a) UiO-66, b) UiO-66-NH_2, c) DUT-52, d) UiO-67 and e) MOF.867 at different synthetic conditions, showing the theorical weight of the fully coordinated Zr_6-oxo cluster (solid line) and the dehydrated Zr_6-oxo cluster (dashed line). 153

Figure 5-19. N_2 adsorption isotherms of isoreticular Zr-based MOF a) UiO-66, b) UiO-66-NH_2, c) DUT-52, d) UiO-67 and e) MOF.867 synthesized with $Zr(OEt)_4$ at different synthetic conditions. 154

Figure 5-20. Pore size distribution using NLDFT model with cylindrical pores of isoreticular Zr-based MOF a) UiO-66, b) UiO-66-NH_2, c) DUT-52, d) UiO-67 and e) MOF.867 synthesized with $Zr(OEt)_4$ at different synthetic conditions. 155

Figure 5-21. UV-Vis spectra of a) AuBipy@UiO-66, b) AuBipy@UiO-66NH_2, c) AuBipy@DUT-52, d) AuBipy@UiO-67 and e) AuBipy@MOF-867 with different synthetic conditions. 156

Figure 5-22. SEM images at different magnifications of AuBipy@UiO-66, AuBipy@UiO-66NH_2, AuBipy@DUT-52, AuBipy@UiO-67 and AuBipy@MOF-867 with different synthetic conditions. Scale bars are 200 nm. 157

Figure 5-23. a, b) AuNSs@UiO-66, c, d) PdNCs@UiO-66 and e, f) Fe_3O_4 MNPs@UiO-66 TEM images. All of them synthesized at 120 ºC for 30 min. Scale bars are 200 nm. 157

Figure 5-24. a) PXRD diffractograms, b) TGA analysis, c) N_2 adsorption isotherms and d) NLDFT pore size distribution of AuBipy@UiO-66 using different PEGylated AuBipy as seeds in the synthesis at RT for 72 h. 158

Figure 5-25. a) Absorption spectra of AuBipy@UiO-66 nanocomposites, b) DLS analysis of UiO-66 nanoparticles and its Au@UiO-66 nanocomposites, c) HRTEM image with FFT of UiO-66 nanoparticles, and TEM images of AuBipy@UiO-66 using PEGylated AuBipy d) 0.5 nM, e) 1.0 nM, f) 2.5 nM and g) 5.0 nM, synthesized at 70 °C for 30 min with their corresponding heating curves h-k) at three different concentrations (10, 50 and 100 pM) with 10 W/cm^2 of irradiance, and l) heating curve of 50 pM AuBipy(5.0)@UiO-66 applying three heating and cooling cycles, compared with 50 pM PEGylated AuBipy in water with 10 W/cm^2 of irradiance. Scale bars are 200 nm. 160

Figure 5-26. TEM images of UiO-66 and their AuBipy@UiO-66 nanocomposites with different shell thickness at different magnifications and their corresponding histograms of particle size distribution. 161

USC UNIVERSIDADE DE SANTIAGO DE COMPOSTELA

Figure 5-27. STEM images AuBipy@UiO-66 synthesized at RT for 72h using a) 0.5, b) 1.0, c) 2.5 and d) 5.0 nM of PEGylated AuBipy with their corresponding EDX mapping of C (e-h), Zr (i-l) and Au (m-p) and the deconvolution analysis of Zr and Au (q-t). Scale bars are 200 nm. 162

Figure 5-28. a) Heating curves of PEGylated AuBipy 50 pM in DMF after 5 cyles of 25 s of irradiation with 20 W/cm^2 of irradiance , b) UV-Vis spectra of PEGylated AuBipy before and after 5 cycles of irradiation, and SEM images of PEGylated AuBipy c)before and d) after irradiation. 163

Figure 5-29. UV-Vis spectra of a) AuBipy(0.5)@UiO-66, b) AuBipy(1.0)@UiO-66, c) AuBipy(2.5)@UiO-66 and d) AuBipy(5.0)@UiO-66 nanocomposites synthesized at RT for 72 h, before and after 808nm laser irradiation with 10 W/cm^2 of irradiance. 164

Figure 6-1. Scheme of work representing the use of PEGylated AuBipy as core with PCN-224 as shell loaded with cresyl violet (CV). CV is released under NIR light while the PCN-224 linker is capable of both generate a fluorescence signal and produce reactive oxygen species (ROS) upon NIR irradiation. Also, it is depicted a summary of the effect of AuBipy concentration in size, heating and luminescent properties of the AuB@PCN-224 NCs. 171

Figure 6-2. a) TGA analysis of the cluster as synthesized, lyophilized and washed with MeOH in vacuum for 1 day, b) PXRD diffractogram of Zr_6-oxo cluster and c) image of Zr_6-oxo cluster and the amount of Zr (%) obtained by ICP and TGA compared with the theoretical. 172

Figure 6-3. SEM images of a) AuB(1)@PCN-224, b) AuB(5)@PCN-224 and c) AuB(10)@PCN-224. d) TEM image and e) HR-TEM image with FFT of PCN-224-w. f) TEM image and g) HRTEM image with FFT of AuB(10)@PCN-224. h-l) EDX-STEM analysis of AuB(10)@PCN-224. Scale bars 250 nm except HRTEM images e) and g) are 50 nm. 173

Figure 6-4. AuBipy characterization by a) UV-Vis absorption spectrum, b) representative TEM image and histograms representing c) bipyramids length and d) bipyramids width. 174

Figure 6-5. SEM images at different magnifications and with different detectors for all different nanoMOFs and NCs with their corresponding histograms: a) PCN-224-p (512.5±263.6 nm), b) PCN-224-w (169.1±24.5 nm), c) AuB(1)@PCN-224 (276.4±59.0 nm), d) AuB(5)@PCN-224 (160.5±30.2 nm) and AuB(10)@PCN-224 (138.0±21.3 nm). Scale bars are 250 nm for images at 50 kX and 500 nm for images at 25 kX. 175

Figure 6-6. SEM images of PdNPs@PCN-224 with detectors a) InLens and b) AsB. Scale bar: 200 nm. 176

Figure 6-7. SEM images of PCN-224 decorated with AuBipy with detector SE2. Scale bar: 500 nm. 176

USC UNIVERSIDADE DE SANTIAGO DE COMPOSTELA

Figure 6-8. SEM images of 3 different batches of AuB@PCN-224 using AuBipy concentrations of 1, 5 and 10 nM showing the reproducibility among batches. Right pannel shows the comparison of the final overall NC sizes of 1, 5 and 10 nm represent in red, green and blue, respectively. Scale bars are 200 nm. _____ 176

Figure 6-9. Yield of reaction determined by ICP-OES with the amount of Zr of PCN-224 nanoMOFs and NCs with AuBipy at different concentrations. _____ 177

Figure 6-10. Characterization of PCN-224 NPs and the NCs: a) UV-Vis spectra, b) DLS particle size distribution, c) FTIR analysis, d) PXRD diffractogram, e) TGA analysis, f) N_2 adsorption isotherms and g) porous size distribution._____ 178

Figure 6-11. a-e) SEM Images of AuB@PCN-224 NCs using 1, 2, 3, 5 and 10 nM AuBipy concentration respectively, showing a decrease in the sell thickness. Corrected PL emission spectra of PCN-224 NPs and the NCs by exciting the samples at f) 420 nm; g) 515 nm and h) time-correlated single photon counting decay kinetics (excitation at 375 nm). _____ 180

Figure 6-12. Normalized photoluminescence spectra of PCN-224-w and AuB@PCN-224 NCs at excitation wavelengths of a) 515 nm and b) 420 nm. _____ 180

Figure 6-13. Excitation spectrum of PCN-224 nanoMOFs for 650 and 715 nm emission._ 181

Figure 6-14. mPEG-PO_3 characterization by NMR of a) ^{1}H, b) ^{13}C and c) ^{31}P and d) FT-IR showing the main vibrations. NMR assignment of mPEG-PO_3, 1H NMR (CDCl3, 500 MHz) δ 3.31 (s, 3H, -OCH3), 3.57 (s, 466H, -CH2CH2-O-). 13C NMR (CDCl3, 125 MHz) δ 70.65 (-CH2CH2-O-). 31P NMR (CDCl3, 202 MHz) δ 0.23 (-PO3)._____ 183

Figure 6-15. FTIR spectra of PCN-224-w and AuB@PCN-224 PEGylated and non-PEGylated with the stretching bands of -OH, -CH_2- and -P-O highlighted._____ 184

Figure 6-16. UV-Vis spectra of a) AuB@PCN-224 NCs transferred from MeOH to water, b) before and after PEGylation in water and c) AuB@PCN-224@PEG NCs before and after 808 nm laser irradiation in water._____ 184

Figure 6-17. Hydrodynamic diameter distribution of a) PCN-224-w and AuB@PCN-224 measured by DLS; and PCN-224-w@PEG and AuB@PCN-224@PEG measured by b) DLS and c) NTA._____ 184

Figure 6-18. ζ-potential values of PCN-224-w and AuB@PCN-224 NCs before and after being PEGylated in water. _____ 185

Figure 6-19. Laser irradiation setup used to measure heating curves at different irradiances. _____ 186

Figure 6-20. Heating curves of water at different irradiances. _____ 186

Figure 6-21. a-c) Heating curves of AuB@PCN-224@PEG NCs at different concentrations, d) graph of concentration dependence of the NCs to reach the boiling point of water, e) heating curve of the NCs applying 4 cycles, and f) graph of an inverse temperature dependence with the thickness of the MOF shell in the NCs. ___ 187

USC UNIVERSIDADE DE SANTIAGO DE COMPOSTELA

Figure 6-22. a) Schematic representation of AuBipy reshaping under 808 nm laser irradiation, b) UV-Vis spectra after 3 heating cycles at 10 W cm^{-2}, c) heating curve of AuBipy 50 pM at 10 W cm^{-2} after 3 heating cycles, d) PEGylated AuBipy before laser irradiation and e) PEGylated AuBipy after laser irradiation. _____ 188

Figure 6-23. Colloidal stability of AuB(10)@PCN-224, PEGylated and non-PEGylated in three different media, a) water, b)DMEM and c)PBS. _____ 189

Figure 6-24. a) Cell viability values using MTT viability test, b) corrected cell uptake mean fluorescence intensity (MFI) values of PCN-224-w@PEG and AuB@PCN-224@PEG NCs after 24h of incubation, c) UV-Vis spectra of AuB(10)@PCN-224@PEG loaded with Cresyl Violet (CV). Cell plate mosaic reconstruction of an area of 1 cm^2 before irradiation (d-e) in which a region of interest (inside the red square) after the irradiation with a 405 nm laser (f-g) (dashed yellow line represents the area irradiated with 405 nm laser) for d,f) 2 min and e,g) 5 min. h) Microscopy images before irradiation and i) after irradiation of selected areas. j-k) Specific ROIs before irradiation, and l-m) ROIs before and after irradiation. Scale bars 1 mm for d and e, 200 µm for f and g and 20 µm for h and i _____ 190

Figure 6-25. Cell uptake mean fluorescence intensity (MFI) values of PCN-224-w@PEG and AuB@PCN-224@PEG NCs after 24h of incubation. _____ 191

Figure 6-26. Microscopy images of internalized AuB(10)@PCN-224(CV)@PEG NCs by A549 cells a) CV channel, b) PCN-224 channel, c) merged + BF. Scale bars: 20 µm. 191

Figure 6-27. Cell plate mosaic of control cells after a) 2 min irradiation and b) 5 min irradiation. Scale bar: 1 mm. _____ 192

Figure 6-28. Microscopy images of AuB@PCN-224(CV) NCs before irradiation a) CV channel, b) PCN-224 channel, c) merged; and after laser scanner irradiation d) CV channel, e) PCN-224 channel, c) merged. Scale bar: 20 µm. _____ 193

Figure 7-1. Scheme of reaction of NU-1000. _____ 198

Figure 7-2. SEM images of NU-1000 nanoMOFs at a)50k X and b) 100k X. Scale bars are 200 nm. _____ 198

Figure 7-3. Histograms showing the particle size distribution of NU-1000 nanoMOFs: a) length and b) width. _____ 198

Figure 7-4. SEM images of AuBipy@NU-1000 nanocomposites synthesized with three different concentrations of PEGylated AuBipy (2, 5, and 10 nM) and analyzed using both secondary and backscattered electron imaging. Scale bars are 200 nm. __ 199

Figure 7-5. SEM images of AuNRs@NU-1000 nanocomposites synthesized with three different concentrations of PEGylated AuNRs (10, 20, and 50 nM) and analyzed using both secondary and backscattered electron imaging. Scale bars are 200 nm. _____ 200

Figure 7-6. Characterization of AuBipy@NU-1000 nanocomposites. DLS analysis, UV-Vis spectra, c) PXRD patterns, d) TGA analysis and e) N_2 adsorption isotherms. _ 200

USC UNIVERSIDADE DE SANTIAGO DE COMPOSTELA

Figure 7-7. Characterization of AuNRs@NU-1000 nanocomposites. DLS analysis, UV-Vis spectra, c) PXRD patterns, d) TGA analysis and e) N_2 adsorption isotherms. _ 201

Figure 7-8. SEM images of AuBipy@NU-1000 nanocomposites synthesized with three different concentrations of PEGylated AuBipy (2, 5, and 10 nM) and analyzed using both secondary and backscattered electron imaging at 600k X magnifications. Scale bars are 100 nm. _____ 202

Figure 7-9. 3D tomography with *in situ* heating at 90 ºC at time intervals of a) 0 min, b) 30 min, c) 60 min, and d) 90 min. _____ 203

Figure 7-10. Pawley's refinement of pristine NU-1000. _____ 204

Figure 7-11. HRTEM images with FFT of a) AuB(10)@NU-1000 and b) AuR(50)@NU-1000 _____ 204

Figure 7-12. Pore size distribution of NU-1000 and its nanocomposites a) AuBipy@NU-1000, b) AuNRs@NU-1000 and c) schematic representation of NU-1000 cavities. _ 205

Figure 7-13. a-b) Photoluminescence spectra with an excitation wavelength of 350 nm and c-d) time-correlated single photon counting decay kinetics with an excitation wavelength of 375 nm for AuBipy@NU-1000 and AuNRs@NU-1000 nanocomposites. _____ 206

Figure 7-14. a) Digital photography and b) ICP-OES analysis of NU-1000 and its nanocomposites with AuBipy and Au NRs. _____ 207

Figure 7-15. ζ- potential measurements of NU-1000 and its nanocomposites with and without PEGylation. _____ 208

Figure 7-16. Heating curves of AuB(10)@NU-1000 and AuR(50)@NU-1000 at a) 200 pM, b) 50 pM, and c) NU-1000 at both concentrations with water as a blank, all measured under an irradiance of 10 W/cm^2. _____ 209

Figure 7-17. Simulated extinction spectra of AuNRs and AuBipy, illustrating the contributions from both scattering and absorption components. _____ 209

Figure 7-18. Chemical structure of 4-mercaptobenzonitrile. _____ 210

Figure 7-19. a) Raman spectra of 5 µM 4-mercaptobenzonitrile using AuB(10)@NU-1000 in colloidal dispersion, measured with a 785 nm laser at various dilutions; b) Raman intensities of the vibrational modes at different composite dilutions; and c) the effect of saturated NaCl solution on the SERS spectra. _____ 211

USC UNIVERSIDADE DE SANTIAGO DE COMPOSTELA

List of tables

Table 1-1. Face-transitive nets and their ring size, transitivity and connectivity. 11

Table 1-2. Elementary excitations presented by solids 36

Table 1-3. Summary of Faraday (Fa) and Joule (Jo) numbers for Ag, Au and Cu. 43

Table 1-4. Relevant studies in core-shell approach synthesis for inorganic nanoparticles-MOFs composites. 50

Table 2-1. Adopted quantities for the synthesis of PCN-224 and MOF-525 starting from $Zr(OEt)_4$ precursor. 62

Table 2-2. Adopted quantities for the synthesis of PCN-224 starting from different Zr precursor. 62

Table 2-3. synthetic conditions for the synthesis of UiO-family MOFs and their nanocomposites 66

Table 3-1. Summary table of samples prepared. 79

Table 3-2. Cell parameters obtained with Pawley's method. 83

Table 3-3. BET surface area (SBET) of UiO-66 samples 87

Table 3-4. ICP-OES results of UiO-66-NH_2 samples and yield of reaction 87

Table 3-5. Concentration results, using the size (SEM) and ICP values, expressed in mg Zr/UiO and in nM. 88

Table 3-6. Size values of the UiO-66-NH_2 samples: Edge size (a) of the octahedral nanoparticles calculated using SEM images, hydrodynamic diameters dh (mean value ± SD) as derived from DLS measurements and ζ- potential values (ζ ± SD). SD values correspond to the standard deviation of value as obtained from several repetitions (n=3) of the measurement. The polydispersity index (PdI) for each sample is also given. 88

Table 3-7. Hydrodynamic diameters d_h (mean value ± SD) as derived from DLS measurements of the nanoMOFs in the different media (water, PSF, DMEM and PBS) at different times (0, 1, 5 and 24h) 89

Table 3-8. Yield of reaction determined with ICP-OES results for UiO-66 92

Table 3-9. Size values of the UiO-66 samples: Edge size (a) of the octahedral nanoparticles calculated using SEM images, hydrodynamic diameters dh (mean value ± SD) as derived from DLS measurements and ζ- potential values (ζ ± SD). The polydispersity index (PDI) for each sample is also given. 93

Table 3-10. Rhodamine 6G characteristics 94

Table 3-11 Summary of conditions for the R6G loading. 94

USC UNIVERSIDADE DE SANTIAGO DE COMPOSTELA

Table 3-12. Dye loading for the UiO-66-NH_2 nanoparticles. Percentage of the maximum dye loaded in the nanoparticles calculated via fluorescence measurements of the supernatant, number of dye molecules per UiO nanoparticle and dye molecules/dye mg per mg of zirconium. 95

Table 3-13. Hydrodynamic diameters d_h (mean value ± SD) as derived from DLS measurements of the UiO-66-NH_2 samples as dispersed in water after the dye loading. 96

Table 3-14. Dye loading for the UiO-66 nanoMOFs. Percentage of the maximum dye loaded in the nanoparticles calculated via fluorescence measurements of the supernatant, number of dye molecules per UiO nanoparticle and dye molecules/dye mg per mg of zirconium. 96

Table 3-15. Hydrodynamic diameters dh (mean value ± SD) as derived from DLS measurements of the UiO-66 samples as dispersed in water after the dye loading. 97

Table 3-16. R6G released from the pores of the nanoMOFs. 99

Table 3-17. R6G released from the pores of the nanoMOFs at times 0, 1, 5, 24 and 48h. 99

Table 3-18. Flow cytometry measurements of UiO-66 uptake by A549 cells. Mean fluorescence intensity (MFI) of experiment using an incubation with a constant concentration of Zr (2.5 µg/mL) and the corrected value normalized to the R6G content for each nanoMOF. 104

Table 4-1 Crystallite size of Zr-porphyrinic MOFs with different L/M ratios calculated by Scherrer equation. 110

Table 4-2. Assignation of ^{1}H-NMR spectra from Figure 4-8 and quantification using $(CH_3)_2SO_2$ as internal standard. 113

Table 4-3. Summary of N_2 uptake and BET surface area of Zr-porphyrinic MOFs with different L/M ratios at room temperature. 114

Table 4-4. Summary of different pore sizes of PCN-224, PCN-222 and MOF-525. 114

Table 4-5. Hydrodynamic size of Zr-porphyrinic MOFs with different L/M ratio measure by DLS in MeOH. 115

Table 4-6. Zr quantification through ICP-OES to determine the reaction yield at different temperatures (25 °C, 50 °C, 75 °C, 90 °C and 120 °C) of 1 h reaction. Each measurement is performed in triplicate. 119

Table 4-7. Hydrodynamic diameter by intensity ($d_{h,I}$) and by number ($d_{h,n}$) measured through DLS of the sample synthesized at different temperatures (1 h reaction). 119

Table 4-8. Particle size distribution measured through SEM analysis of the samples synthesized with different Zr precursors. 121

Table 4-9. BET surface area and pore volume of the particles synthesized with different Zr precursors. 122

USC UNIVERSIDADE DE SANTIAGO DE COMPOSTELA

Table 4-10. Zr quantification through ICP-OES to determine the reaction yield of the reaction performed with different Zr precursors. 123

Table 4-11. Hydrodynamic diameter by intensity ($d_{h,I}$) and by number ($d_{h,n}$) and PdI measured through DLS of the samples synthesized with different Zr precursors at 75 ºC foy 1h. 123

Table 4-12. Particle size distribution measured through SEM analysis of the samples synthesized with different Zr precursors. 124

Table 4-13. Zr quantification through ICP-OES to determine the reaction yield of the reaction performed with different Zr precursors after 1h and 24h of reaction. 125

Table 4-14. Hydrodynamic diameter by intensity ($D_{h,I}$) and by number ($D_{h,n}$) and PdI measured through DLS of the samples synthesized with different Zr precursors for 1 h at RT. 126

Table 4-15. BET surface area and pore volume of the particles synthesized with different Zr precursors. 127

Table 4-16. Zr quantification through ICP-OES to determine the reaction yield of the reaction performed with different Zr precursors. 129

Table 4-17. Particle size distribution measured through SEM analysis of the samples synthesized with different Zr precursors. 130

Table 4-18. Hydrodynamic diameter by intensity ($D_{h,I}$) and by number ($D_{h,n}$) and PdI measured through DLS of the samples synthesized with different Zr precursors. 130

Table 4-19. BET surface area and pore volume of the particles synthesized with different Zr precursors. 130

Table 5-1. Cell parameters obtained by Pawley's refinement. 152

Table 5-2. BET surface areas calculated with BETSI analysis of isoreticular Zr-based MOF synthesized with $Zr(OEt)_4$ at different synthetic conditions 154

Table 5-3. BET surface areas calculated with BESTI analysis of AuBipy@UiO-66 nanocomposites synthesized at RT for 72 h and the correction subtraction the amount of Au obtained by TGA. 159

Table 5-4. Hydrodynamic sizes of UiO-66 nanoparticles and its AuBipy@UiO-66 nanocomposites obtained at RT for 72 h. 161

Table 6-1. Diameter values of PCN-224 and AuB@PCN-224 by SEM and DLS in MeOH. 174

Table 6-2. BET surface area and percentage of Au in PCN-224 and NCs. 179

Table 6-3. PL quenching values for NCs at different excitation wavelengths. 181

Table 6-4. Decay times values of PCN-224 and AuB@PCN-224 systems and coefficients values for multiexponential function (Eq. 13). 182

Table 6-5. Diameter values of PCN-224 and AuB@PCN-224 PEGylated and non-PEGylated by NTA and DLS in water. 185

USC UNIVERSIDADE DE SANTIAGO DE COMPOSTELA

Table 6-6. Correction factors calculated via fluorescence values obtained using a plate reader (λ_{exc}=405 nm, λ_{em}=600-660 nm). 191

Table 7-1. Hydrodynamic diameter of AuBipy and AuNRs nanocomposites in intensity and number with PdI. 201

Table 7-2. Amount of Au content determined by TGA and BET surface area of the nanocomposites. 204

Table 7-3. Quantification of photoluminescent quenching for NU-1000 nanocomposites. 207

Table 7-4. Decay times values of NU-1000 and its nanocomposites with AuBipy and Au NRs and coefficients values for multiexponential function (Eq. 13). 207

Table 7-5. Raman modes of 4-mercaptobenzonitrile (MBN). 211

USC UNIVERSIDADE DE SANTIAGO DE COMPOSTELA

List of abbreviations

AA	acetic acid
BET	Brunauer–Emmett–Teller
Bipy	bipyramids
BODIPY	4,4-difluoro-4-bora-3a,4a-diaza-s-indacene
BUT	Beijing University of Technology
COFs	covalent organic frameworks
CSD	Cambridge Structural Database
CTAB	cetyltrimethylammonium bromide
Da	Dalton
DBCO	dibenzocyclooctyne
DDS	drug delivery systems
DLS	dynamic light scattering
DMA	N,N-dimethylacetamide
DMEM	Dulbecco's Modified Eagle Medium
DMF	N,N-dimethylformamide
DNA	deoxyribonucleic acid
DOPA	1,2-dioleoyl-sn-glycero-3-phosphate
DOXO	doxorubicin
DSC	differential scanning calorimetry
DUT	Dresden University of Technology
EDTA	ethylenediaminetetraacetic acid
EDX	energy-dispersive X-ray
EXAFS	extended X-ray absorption fine structure
FA	formic acid
FBS	foetal bovine serum
FDM	Fudan Materials
FFT	fast Fourier transform
FRET	Förster resonance energy transfer
H_2BDC	terephthalic acid
H_2BPDC	biphenyl-4,4′-dicarboxylic acid
H_2Fum	fumaric Acid
H_2NDC	2,6-Naphthalenedicarboxylic acid
H_2TPDC	1,4-bis(4-carboxyphenyl)benzene
H_3BTB	1,3,5-Tris(4-carboxyphenyl)benzene
H_3BTC	trimesic acid
H_3TTCA	triphenylene-2,6,10-tricarboxylic acid

USC UNIVERSIDADE DE SANTIAGO DE COMPOSTELA

H_4ETTC	4',4",4'",4""-(ethene-1,1,2,2-tetrayl)tetrabiphenyl-4-carboxylic acid
H_4TBAPy	4,4',4",4'"-(Pyrene-1,3,6,8-tetrayl)tetrabenzoic acid
H_4TCPP	tetrakis(4-carboxyphenyl)porphyrin
HKUST	Hong Kong University of Science and Technology
HRTEM	high-resolution transmission electron microscopy
ICP-OES	inductively coupled plasma optical emission spectroscopy
IRMOF	isoreticular metal-organic framework
J	Joule
LSPR	localized surface plasmon resonance
MBN	4-mercaptobenzonitrile
MFI	mean fluorescence intensity
MIL	materials institute Lavoisier
MMPF	metal–metalloporphyrin frameworks
MOF	metal-organic framework
MOP	metal-organic polyhedra
MOPs	metal-organic polyhedra
MTV	multivariate
NIR	near infrared
NLDFT	non localized density functional theory
NMR	nuclear magnetic resonance
NPF	Nebraska Porous Framework
NRs	nanorods
NSET	nanosurface energy transfer
NSs	nanostars
NTA	nanoparticle tracking analysis
PBS	phosphate-buffered saline
PBS	phosphate-buffered saline
PCN	porous coordination network
PDDA	poly(diallyldimethylammonium chloride)
PdI	polydispersity index
PDT	photodynamic therapy
PL	photoluminescence
PPA	phenylphosphonic acid
PSF	phagolysosomal simulant fluid
PSS	poly(sodium 4-styrenesulfonate
PVP	polyvinylpyrrolidone
PXRD	powder X-ray diffraction
R6G	rhodamine 6G

USC UNIVERSIDADE DE SANTIAGO DE COMPOSTELA

RCSR	Reticular Chemistry Structure Resource
ROS	reactive oxygen species
SAXS	small-angle X-ray scattering
SBL	supermolecular building layers
SBU	secondary building unit
SERS	surface enhanced Raman spectroscopy
SHE	standard hydrogen electrode
SQA	squaric acid
TCSPC	time-correlated single photon counting
TEA	triethylamine
TEM	transmission electron microscopy
TGA	thermogravimetric analysis
UiO	Universitetet i Oslo
NU	Northwestern University
UV	ultraviolet
WAXS	wide-angle X-ray scattering
WOS	web of science
WSU	Washington State University
ZIF	zeolitic imidazolate framework

USC UNIVERSIDADE DE SANTIAGO DE COMPOSTELA

USC
UNIVERSIDADE
DE SANTIAGO
DE COMPOSTELA

Resumo

A presente tese ten como obxectivo o desenvolvemento de métodos sintéticos para materiais compostos de tipo núcleo-coiraza, onde o núcleo está constituído por nanopartículas plasmónicas de ouro con diversas morfoloxías, e a coraza por materiais híbridos denominados redes metal-orgánicas (MOFs, polas súas siglas en inglés).

Os núcleos plasmónicos destes materiais exhiben propiedades ópticas únicas, debido á presenza de plasmóns de superficie, os cales son xerados pola natureza do enlace metálico. Este enlace pódese definir como un "mar de electrones" libres que percorren a rede condensada de catións metálicos. Cando estes electróns son excitados pola luz, oscilan na superficie do metal. Na nanoescala, o confinamento dos electróns xoga un papel clave na excitación destes plasmóns, permitindo que esta oscilación sexa axustada para ser excitada con luz visible ou infravermella, o que depende de factores como a composición química, o tamaño, a forma, a presenza de axentes estabilizantes na superficie ou o ambiente dieléctrico circundante. Esta oscilación presenta un máximo de absorción coñecido como resonancia de plasmón superficial localizada (LSPR, polas súas siglas en inglés), que xera dipolos eléctricos en rexións específicas da nanopartícula, os cales poden ser aproveitados en diversas aplicacións.

Grazas ás súas propiedades ópticas, gran estabilidade química e a capacidade de modificar estas propiedades, as nanopartículas plasmónicas (principalmente de metais nobres como Au, Ag, Cu, Pt, Pd, Rh, entre outros) teñen numerosas aplicacións en áreas como o sensado químico, a catálise e a terapia fotodinámica mediante a xeración de calor, entre outras.

Por outro lado, os MOFs son un tipo novo de material híbrido composto por unha parte orgánica (ligando) e unha parte inorgánica (nodos metálicos ou unidades de construción secundarias, SBUs polas súas siglas en inglés). Estes compoñentes, unidos por fortes enlaces de coordinación, forman estruturas cristalinas cunha alta porosidade, o cal é a súa característica principal. Esta porosidade permite o almacenamento de grandes cantidades de moléculas, gases ou outras substancias de interese.

As propiedades dos MOFs son o resultado da combinación dos seus dous compoñentes principais, xeran novas propiedades cando se combinan como material híbrido. Estas propiedades poden deseñarse mediante a química reticular, que permite modificar a composición química, o tamaño dos poros, a creación de defectos, a polaridade do poro ou a superficie do material, entre outros aspectos, para satisfacer necesidades específicas.

O desafío de combinar estes dous materiais a nanoescala para crear unha sinerxia das súas propiedades radica nas dificultades sintéticas, especialmente a incompatibilidade das condicións de síntese de ambos materiais e o posible dano que un deles podería sufrir durante o proceso. Este dano pode impactar negativamente en propiedades clave, como a absorción de luz en certas rexións do espectro electromagnético, a xeneración de calor, a cristalinidade do MOF ou a súa porosidade.

Cando estes nanomateriais se combinan correctamente nun sistema núcleo-coiraza, poden ser activados mediante estímulos externos, como a luz, producindo calor no seu interior. Esta calor pode ser aproveitado para realizar reaccións dentro da porosidade do MOF, introducindo

substratos específicos ou producindo unha liberación controlada activada por luz. Isto débese a un incremento local da temperatura entre o interior do MOF e o seu contorno, o que favorece a migración das moléculas aloxadas dentro dos poros cara ao exterior mediante o fenómeno de termodifusión ou efecto Soret.

Esta propiedade de termodifusión ten aplicacións potenciais na xeración de nanotransportadores de fármacos máis eficientes, activados por luz, o que é unha solución á problemática da administración de certos fármacos que, debido á súa alta hidrofobicidade, non poden ser subministrados por vía convencional. Estes fármacos poderían encapsularse no MOF, internalizarse e ser liberados baixo estímulo lumínico en zonas específicas. Para garantir a eficiencia da liberación, é importante que a luz utilizada sexa no rango de infravermello próximo (NIR, polas súas siglas en inglés), que oscila entre 700 e 2500 nm, xa que os tecidos humanos son transparentes nesta rexión do espectro.

A motivación desta tese radica na escaseza de sistemas núcleo-coiraza na literatura que combinen as propiedades das nanopartículas plasmónicas cos MOFs, materiais ideais para sistemas de nanotransporte de fármacos. Desenvolvéronse varias estratexias sintéticas para conservar as propiedades de ambos materiais nun único sistema, e a súa potencial aplicación en biomedicina como nanotransportadores explórase a fondo.

No capítulo 3 de resultados e discusión, abórdase unha nova estratexia sintética para a síntese de nanopartículas dun MOF baseado en zirconio chamado UiO-66. Dito material foi amplamente estudado na comunidade científica debido ás súas excelentes propiedades físicas e químicas, como a súa alta estabilidade química, térmica e estrutural, o que o converte nun candidato ideal para a formación de corazas sobre nanopartículas plasmónicas. Desafortunadamente, os precursores metálicos máis amplamente estudados na literatura para a síntese deste MOF son substancias que conteñen ións halóxenos, como o $ZrCl_4$ ou o $ZrOCl_2$. Reportouse que estes halóxenos poden causar a oxidación das nanopartículas de ouro, destruíndo así a coraza.

Ao substituír os precursores de zirconio que conteñen ións halóxenos por outros que non os conteñen, como o $ZrO(NO_3)_2$, nunha síntese optimizada polo grupo de investigación, descubriuse que non se obtiñan nanopartículas, senón micropartículas compostas por cristais maclados deste MOF. Plantexouse a hipótese de que os ións halóxenos eran un factor primordial para a obtención de nanocristais ben definidos deste MOF. Por conseguinte, engadíronse dúas fontes de ións cloruro, como o HCl e o NaCl, á síntese para descartar o factor pH ou corroborar o seu papel nesta síntese. Os resultados obtidos mostraron a presenza de nanocristais, incluso de menor tamaño que na síntese orixinal, e moito mellor definidos, corroborando o rol dos halóxenos, xa que a síntese tamén funcionou do mesmo xeito cos ións bromuro e iodo.

Posteriormente, unha caracterización extensiva con varias técnicas demostrou a presenza de ións cloruro e bromuro na estrutura do MOF. Estes materiais foron coloidalmente estables e demostraron a súa capacidade para internalizar o colorante rodamina 6G en células vivas, as cales presentaron unha alta viabilidade celular, incluso a altas concentracións de zirconio (> 100 ppm).

USC UNIVERSIDADE DE SANTIAGO DE COMPOSTELA

No capítulo 4, inspirado no uso de distintos precursores de zirconio libres de halóxenos, estudouse o uso de alcóxidos de zirconio, que son precursores incriblemente pouco utilizados na síntese de MOFs baseados en zirconio. Estes precursores son moi utilizados na síntese doutros tipos de materiais, como óxidos metálicos mediante o método sol-gel, debido a que son facilmente hidrolizables, altamente reactivos e de baixo custo.

Os MOFs sintetizados con estes alcóxidos de zirconio denomínanse MOFs porfirínicos e presentan como base un macrociclo porfirínico con grupos quelantes unidos a el, que poden ser bi-, tri-, tetra- ou polidentados, sendo o tetradentado o máis común e utilizado no presente traballo.

Estes MOFs porfirínicos co ligando tetradentado presentan propiedades ópticas moi interesantes, xa que absorben todo o rango visible do espectro electromagnético, emitindo dúas longitudes de onda cuns rendementos cuántico moi elevado. Isto os fai ideais para aplicacións de almacenamento e conversión de enerxía, fotocatálise e bioaplicacións debido á súa capacidade para producir especies de osíxeno reactivas (ROS, polas súas siglas en inglés) que poden ser utilizadas para terapia fotodinámica.

A problemática na síntese destes nanomateriais radica na formación de polimorfos, xa que existen seis deles con distintas conectividades no clúster de seis átomos de Zr con coordinación 6 ligando por clúster, como o PCN-224; oito ligandos por clúster, como o PCN-222, NU-902 e PCN-225; ademais de dous polimorfos con conectividade completa de doce, MOF-525 e PCN-223.

Con tantos polimorfos, a síntese destes MOFs convértese nun reto, xa que a obtención de mesturas de fases é moi común, o que fai extremadamente complicada a súa caracterización. Además, as propiedades mestúranse nun sistema heteroxéneo que pode comportarse de xeito diferente segundo o porcentaxe destes polimorfos na mestura.

Neste estudo, descubriuse que os alcóxidos de zirconio poden lograr a síntese de fases puras de PCN-224, PCN-222 e MOF-525 en tempos de reacción moi curtos comparados coa literatura (1 hora de reacción), a temperatura ambiente ou baixa comparada coa literatura (75 ºC como máximo), e con rendementos de reacción superiores ao 90%.

Además, ao ser reaccións tan rápidas e con rendementos tan altos, realizouse unha síntese en fluxo como proba de concepto, obtendo a fase PCN-224 cun mellor control do tamaño de partícula, altamente cristalina e cunha alta área superficial en só 25 segundos de tempo de residencia a temperatura ambiente.

Este estudo abre a porta ao uso de precursores de zirconio pouco comúns para a síntese de MOFs baseados en zirconio con tempos máis curtos, temperaturas máis baixas e mellores rendementos, permitindo obter fases puras e escalar a súa produción en fluxo a baixo custo.

O capítulo 5 aborda o uso de alcóxidos de zirconio para a síntese de nanocompósitos con núcleos de nanopartículas plasmónicas e magnéticas con coiraza de MOFs. Neste traballo analízase que non só os ións halóxenos na síntese afectan directamente á morfoloxía das nanopartículas plasmónicas de distintas formas, senón tamén a temperatura, o que impacta directamente nas súas propiedades ópticas. Estas nanopartículas plasmónicas foron

USC UNIVERSIDADE DE COMPOSTELA

funcionalizadas con cadeas poliméricas de polietilenglicol (PEG), que conteñen grupos mercapto (-SH) ao inicio das cadeas, os cales se unen químicamente á superficie do ouro, dándolles estabilidade coloidal en distintos medios acuosos ou orgánicos.

As nanopartículas plasmónicas funcionalizadas foron quentadas ás temperaturas habituais para a síntese de MOFs en dimetilformamida (DMF), o disolvente máis utilizado para a síntese de MOFs baseados en zirconio. A cinética de cambio de forma foi seguida por espectroscopía ultravioleta-visible, demostrando que a 120 ºC o LSPR localizado no NIR desprazábase rapidamente cara ao azul, o que indica un cambio de forma ata rematar en morfoloxía esférica, e a súa completa oxidación en dous días. Estas cinéticas tamén se realizaron a 90 ºC en DMF e auga, observando o mesmo efecto, pero máis lento, para morfoloxías bipiramidais, barras e estrelas de ouro.

Tendo en conta o efecto da temperatura, procedeuse a utilizar estas nanopartículas plasmónicas como sementes para unha serie de MOFs isorreticulares baseados en zironio, reducindo a temperatura de 120 ºC a 90 ºC e 70 ºC. Obteuse un mellor rendemento de reacción en só 30 minutos, ademais de que a reducción da temperatura impactaba de menor xeito no corrimento do LSPR cara ao azul, conservando a absorción na zona do NIR.

Coa mesma estratexia sintética, procedeuse a realizar esta síntese a temperatura ambiente, obtendo os mesmos sistemas núcleo-coiraza. Non obstante, esta síntese requiriu tres días de duración, o que é unha desvantaxe. Aínda así, considerando que non se precisou quentamento e que a morfoloxía das nanopartículas non se viu afectada, considérase unha excelente estratexia sintética.

O efecto da concentración de nanopartículas plasmónicas na síntese dos sistemas núcleo-coiraza foi estudado, concluíndo que os núcleos plasmónicos actúan como sementes no crecemento do MOF. Unha baixa concentración de sementes resultaba nunha coiraza máis grosa, mentres que ao aumentar a concentración de sementes, a coiraza diminuía o seu espesor. Este espesor impactaba directamente nas propiedades de xeración de calor, xa que os MOFs son coñecidos por ser illantes térmicos. Cando o sistema era excitado por un láser de 808 nm, o tempo que tardaba en quentar o medio aumentaba co grosor da coiraza.

O capítulo 6 aborda unha nova estratexia sintética de sistemas núcleo-coiraza compostos por nanopartículas plasmónicas e o MOF porfirínico PCN-224. Estes nanocompósitos foron sintetizados a temperatura ambiente, utilizando o clúster de zirconio pre-sintetizado. Para a síntese do clúster, utilizouse como disolvente 1-propanol, que, segundo informes da literatura, era eliminado baixo baleiro durante un día.

Ao utilizar as nanopartículas plasmónicas como sementes no medio de reacción para PCN-224, obtíñanse sistemas núcleo-coiraza moi monodispersos con dito clúster. Non obstante, o MOF sen nanopartículas plasmónicas resultou ser moi polidisperso e cun rendemento de reacción moi baixo. O clúster foi caracterizado mediante análise termogravimétrica, revelando a presenza de 1-propanol, que non se eliminara completamente baixo baleiro debido ao seu alto punto de ebullición (97 ºC) e baixa presión de vapor. Por iso, procedeuse a lavalo con metanol, resultando na completa eliminación do 1-propanol.

USC UNIVERSIDADE DE SANTIAGO DE COMPOSTELA

Ao realizar de novo a síntese do MOF PCN-224 co clúster limpo, as partículas obtidas foron moi monodispersas. Non obstante, no caso dos nanocompósitos, obtivéronse micropartículas cunha gran cantidade de nanopartículas plasmónicas na superficie en vez de sistemas núcleo-coiraza. Isto levou á hipótese de que a presenza de 1-propanol no sistema ten unha influencia notable na cristalización do MOF sobre as nanopartículas plasmónicas PEGyladas. Proponse que o 1-propanol se intercala entre as cadeas de PEG como co-surfactante, facilitando a inserción dos precursores de MOF sobre as partículas plasmónicas.

Estes compostos núcleo-coiraza foron cargados co colorante violeta de cresilo co fin de observar a súa liberación activada por luz en células vivas. A liberación observouse claramente ao facer un escaneo láser localizado de varias células, mostrando mediante microscopía de fluorescencia que o pigmento non estaba presente no citoplasma das células sen estímulo externo, pero liberábase rapidamente ao activalo, corroborando o efecto de termodifusión activado por luz dentro das células vivas.

Ademais da liberación do pigmento como droga modelo, dito MOF presenta a capacidade de xerar ROS, as cales provocaron a morte das células iluminadas con luz visible, combinando así a liberación activada por luz cunha terapia fotodinámica.

No capítulo 7, abórdase outro sistema núcleo-coiraza, nesta ocasión utilizando o MOF de zirconio NU-1000 e un precursor convencional, $ZrOCl_2$. Como se discutiu previamente, o uso de precursores haloxenados comprometía a integridade das nanopartículas plasmónicas. Además, para a formación do clúster de zirconio con estes precursores, é necesario aplicar calor tanto para promover a formación do clúster como para a formación dos enlaces de coordinación entre os ligandos e os núcleos metálicos.

A síntese dos nanoMOFs plasmónicos realizouse utilizando dous tipos de nanopartículas plasmónicas, nanobarras e bipirámides de ouro, que foron funcionalizadas con PEG-SH e transferidas a DMF para logo ser engadidas como sementes no medio de reacción. A razón de seguir utilizando precursores haloxenados e temperaturas (90 ºC) nesta síntese é que presenta a vantaxe de ser moi rápida en comparación con outros MOFs baseados en zirconio, con só 30 minutos de reacción. Isto provoca un desprazamento cara ao azul do LSPR, pero de xeito moi sutil, que pode ser compensada coa síntese de nanopartículas plasmónicas cun LSPR máis desprazado cara ao vermello.

Na síntese corroborouse mediante microscopía electrónica de barrido utilizando electróns retrodispersados e tomografía 3D con quentamento simultáneo de microscopía electrónica de transmisión, que a concentración de sementes afectaba directamente á posición final do LSPR. Non foi debido á formación dunha coiraza de MOF máis grosa, senón que unha menor cantidade de sementes no medio de reacción provocaba un maior dano na forma das nanopartículas plasmónicas, resultando nun maior desprazamento cara ao azul cunha menor cantidade de sementes.

O uso de dúas morfoloxías distintas no sistema núcleo-coiraza, con posicións de LSPR na mesma lonxitude de onda, tiña como obxectivo comprobar o efecto destas nanopartículas nas propiedades de quentamento dos nanocompósitos. Comprobaron que os nanocompósitos con nanobarras de ouro quentaban máis rapidamente o medio circundante que aqueles con

USC DE SANTIAGO DE COMPOSTELA

bipirámides de ouro. Isto atribúese a que a relación de aspecto das nanobarras de ouro é moi alta, o que se traduce nunha absorción total da luz sen xeración significativa de dispersión. Como resultado, a enerxía absorbida transfórmase en calor de xeito máis eficiente en comparación coas bipirámides de ouro, que, debido ás súas dimensións e relación de aspecto menor, absorben só unha parte da luz incidente e dispersan outra, sen transformar toda a enerxía incidente en calor.

Por último, o sistema de bipirámides con coiraza de MOF NU-1000 empregouse como substrato para espectroscopía Raman aumentada en superficies (SERS) debido á posición do seu LSPR e á presenza de puntas afiladas na súa nanoestrutura metálica, que favorecen a formación de puntos quentes ou zonas de alta concentración de campo eléctrico. Estes puntos quentes incrementan os sinais Raman en varios ordes de magnitude. Para esta proba de concepto, empregouse o analito 4-mercaptobenzonitrilo (MBN) a unha concentración de 5 micromolar, o cal foi detectado con dificultade para o nanocompósito sintetizado sen diluir. Cando o analito se puxo en contacto con dilucións de dez, cincuenta e cen veces, o sinal Raman do analito aumentou en catro, cinco e un orde de magnitude, respectivamente. Este aumento atribúese a unha competencia entre a eficiencia de aumento do sinal e a extinción producida polo material.

Finalmente, ás mesmas dilucións engadíuse unha solución saturada de NaCl co obxectivo de observar unha mellora na intensidade dos sinais Raman debido á aglomeración de partículas. Non obstante, observouse o fenómeno oposto: unha redución case total dos sinais Raman. Isto atribúese a que a forza iónica producida polos iones expulsou as moléculas de analito fóra da porosidade do MOF, afastándoas da superficie metálica encargada de producir o aumento na intensidade dos sinais Raman.

A presente tese aborda o desenvolvemento de novas estratexias de síntese, caracterización e aplicación de materiais compostos innovadores para aplicacións biolóxicas, xeración de calor e sensado químico. Este traballo combina materiais orgánicos, inorgánicos e híbridos a nanoescala, o que representa un gran reto, xa que cada un destes materiais presenta comportamentos distintos. A redución de tamaño á escala nanométrica engade complexidade ao control e manipulación da materia.

Resumindo, na presente tese abórdase o uso de precursores haloxenados e temperaturas elevadas na transformación da forma de nanopartículas plasmónicas, o cal impacta directamente nas súas propiedades ópticas. Esta problemática podería ser unha das razóns da escaseza de sistemas núcleo-coiraza que combinen nanopartículas plasmónicas e MOFs baseados en zirconio. Nesta investigación desenvolvéronse tres metodoloxías sintéticas distintas: o uso de alcóxidos de zirconio para a síntese a baixa temperatura ou temperatura ambiente, o uso de clústeres de zirconio pre-sintetizados que permiten reaccións a temperatura ambiente, e a utilización de reaccións con tempos de reacción curtos que, aínda que requiren temperaturas elevadas ou precursores haloxenados, non afectan significativamente ao desprazamento do LSPR cara ao azul. Además, pódese contrarrestar este efecto mediante a síntese de nanopartículas de ouro cun LSPR desprazado ao vermello.

USC UNIVERSIDADE DE SANTIAGO DE COMPOSTELA

Resumen

La presente tesis tiene como objetivo el desarrollo de métodos sintéticos para materiales compuestos de tipo núcleo-coraza, donde el núcleo está constituido por nanopartículas plasmónicas de oro con diversas morfologías, y la coraza por materiales híbridos denominados redes metal-orgánicas (MOFs, por sus siglas en inglés).

Los núcleos plasmónicos de estos materiales exhiben propiedades ópticas únicas, debido a la presencia de plasmones de superficie, los cuales son generados por la naturaleza del enlace metálico. Este enlace puede definirse como un "mar de electrones" libres que recorren la red condensada de cationes metálicos. Cuando estos electrones son excitados por la luz, oscilan en la superficie del metal. En la nanoescala, el confinamiento de los electrones juega un papel clave en la excitación de estos plasmones, permitiendo que dicha oscilación sea ajustada para ser excitada con luz visible o infrarroja, lo que depende de factores como la composición química, el tamaño, la forma, la presencia de agentes estabilizantes en la superficie o el ambiente dieléctrico circundante. Esta oscilación presenta un máximo de absorción conocido como resonancia de plasmón superficial localizada (LSPR, por sus siglas en inglés), que genera dipolos eléctricos en regiones específicas de la nanopartícula, los cuales pueden ser aprovechados en diversas aplicaciones.

Gracias a sus propiedades ópticas, gran estabilidad química y la capacidad de modificar estas propiedades, las nanopartículas plasmónicas (principalmente de metales nobles como Au, Ag, Cu, Pt, Pd, Rh, entre otros) tienen numerosas aplicaciones en áreas como el sensado químico, la catálisis y la terapia fotodinámica mediante la generación de calor, entre otras.

Por otro lado, los MOFs son un tipo novedoso de material híbrido compuesto por una parte orgánica (ligando) y una parte inorgánica (nodos metálicos o unidades de construcción secundarias, SBUs por sus siglas en inglés). Estos componentes, unidos por fuertes enlaces de coordinación, forman estructuras cristalinas con una alta porosidad, lo cual es su característica principal. Esta porosidad permite el almacenamiento de grandes cantidades de moléculas, gases u otras sustancias de interés.

Las propiedades de los MOFs son el resultado de la combinación de sus dos componentes principales, generando nuevas propiedades cuando se combinan como material híbrido. Estas propiedades pueden diseñarse mediante la química reticular, que permite modificar la composición química, el tamaño de los poros, la creación de defectos, la polaridad del poro o la superficie del material, entre otros aspectos, para satisfacer necesidades específicas.

El desafío de combinar estos dos materiales a nanoescala para crear una sinergia de sus propiedades radica en las dificultades sintéticas, especialmente la incompatibilidad de las condiciones de síntesis de ambos materiales y el posible daño que uno de ellos podría sufrir durante el proceso. Este daño puede impactar negativamente en propiedades clave, como la absorción de luz en ciertas regiones del espectro electromagnético, la generación de calor, la cristalinidad del MOF o su porosidad.

USC
UNIVERSIDADE DE SANTIAGO DE COMPOSTELA

Cuando estos nanomateriales se combinan correctamente en un sistema núcleo-coraza, pueden ser activados mediante estímulos externos, como la luz, produciendo calor en su interior. Este calor puede ser aprovechado para llevar a cabo reacciones dentro de la porosidad del MOF, introduciendo sustratos específicos o produciendo una liberación controlada activada por luz. Esto se debe a un incremento local de la temperatura entre el interior del MOF y su entorno, que favorece la migración de las moléculas alojadas dentro de los poros hacia el exterior mediante el fenómeno de termodifusión o efecto Soret.

Esta propiedad de termodifusión tiene aplicaciones potenciales en la generación de nanotransportadores de fármacos más eficientes, activados por luz, lo cual es una solución a la problemática de administración de ciertos fármacos que, debido a su alta hidrofobicidad, no pueden ser suministrados por vía convencional. Estos fármacos podrían encapsularse en el MOF, internalizarse y ser liberados bajo estímulo lumínico en zonas específicas. Para garantizar la eficiencia de la liberación, es importante que la luz utilizada sea en el rango de infrarrojo cercano (NIR, por sus siglas en inglés), que oscila entre 700 y 2500 nm, ya que los tejidos humanos son transparentes en esta región del espectro.

La motivación de esta tesis radica en la escasez de sistemas núcleo-coraza en la literatura que combinen las propiedades de las nanopartículas plasmónicas con los MOFs, materiales ideales para sistemas de nanotransporte de fármacos. Se han desarrollado varias estrategias sintéticas para conservar las propiedades de ambos materiales en un solo sistema, y su potencial aplicación en biomedicina como nanotransportadores se explora a fondo.

En el capítulo 3 de resultados y discusión, se aborda una nueva estrategia sintética para la síntesis de nanopartículas de un MOF basado en zirconio llamado UiO-66. Dicho material ha sido ampliamente estudiado en la comunidad científica debido a sus excelentes propiedades físicas y químicas, como su alta estabilidad química, térmica y estructural, lo que lo convierte en un candidato ideal para la formación de corazas sobre nanopartículas plasmónicas. Desafortunadamente, los precursores metálicos más ampliamente estudiados en la literatura para la síntesis de este MOF son sustancias que contienen iones halógenos, como el $ZrCl_4$ o el $ZrOCl_2$. Se ha reportado que estos halógenos pueden causar la oxidación de las nanopartículas de oro, destruyendo así la coraza.

Al reemplazar los precursores de zirconio que contienen iones halógenos por otros que no los contienen, como el $ZrO(NO_3)_2$, en una síntesis optimizada por el grupo de investigación, se descubrió que no se obtenían nanopartículas, sino micropartículas compuestas por cristales maclados de dicho MOF. Se planteó la hipótesis de que los iones halógenos eran un factor primordial para la obtención de nanocristales bien definidos de este MOF. Por lo tanto, se añadieron dos fuentes de iones cloruro, como el HCl y el NaCl, a la síntesis para descartar el factor pH o corroborar su papel en dicha síntesis. Los resultados obtenidos mostraron la presencia de nanocristales, incluso de menor tamaño que en la síntesis original, y mucho mejor definidos, corroborando el rol de los halógenos, ya que la síntesis también funcionó de igual manera con iones bromuro y yoduro.

Posteriormente, una caracterización extensiva con varias técnicas demostró la presencia de iones cloruro y bromuro en la estructura del MOF. Estos materiales fueron coloidalmente estables y demostraron su capacidad para internalizar el colorante rodamina 6G en células vivas,

las cuales presentaron una alta viabilidad celular, incluso a altas concentraciones de zirconio (> 100 ppm).

En el capítulo 4, inspirado en el uso de distintos precursores de zirconio libres de halógenos, se estudió el uso de alcóxidos de zirconio, que son precursores increíblemente poco utilizados en la síntesis de MOFs basados en zirconio. Estos precursores son muy utilizados en la síntesis de otros tipos de materiales, como óxidos metálicos mediante el método sol-gel, debido a que son fácilmente hidrolizables, altamente reactivos y de bajo costo.

Los MOFs sintetizados con estos alcóxidos de zirconio se denominan MOFs porfirínicos, y presentan como base un macrociclo porfirínico con grupos quelantes unidos a él, que pueden ser bi-, tri-, tetra- o polidentados, siendo el tetradentado el más común y utilizado en el presente trabajo.

Estos MOFs porfirínicos con el ligando tetradentado presentan propiedades ópticas muy interesantes, ya que absorben todo el rango visible del espectro electromagnético, emitiendo dos longitudes de onda con un rendimiento cuántico muy elevado. Esto los hace ideales para aplicaciones de almacenamiento y conversión de energía, fotocatálisis y bioaplicaciones debido a su capacidad para producir especies de oxígeno reactivas (ROS, por sus siglas en inglés) que pueden ser utilizadas para terapia fotodinámica.

La problemática en la síntesis de estos nanomateriales radica en la formación de polimorfos, ya que existen seis de ellos con distintas conectividades en el clúster de seis átomos de Zr con coordinación 6 ligando por clúster, como el PCN-224; ocho ligandos por clúster, como el PCN-222, NU-902 y PCN-225; además de dos polimorfos con conectividad completa de doce, MOF-525 y PCN-223.

Teniendo tantos polimorfos, la síntesis de dichos MOF se convierte en un reto, ya que la obtención de mezclas de fases es muy común, lo que hace extremadamente complicada su caracterización. Además, las propiedades se mezclan en un sistema heterogéneo que puede comportarse de manera diferente según el porcentaje de dichos polimorfos en la mezcla.

En este estudio, se descubrió que los alcóxidos de zirconio pueden lograr la síntesis de fases puras de PCN-224, PCN-222 y MOF-525 en tiempos de reacción muy cortos comparados con la literatura (1 hora de reacción), a temperatura ambiente o baja comparada con la literatura (75 ºC como máximo), y con rendimientos de reacción superiores al 90%.

Además, al ser reacciones tan rápidas y con rendimientos tan altos, se realizó una síntesis en flujo como prueba de concepto, obteniendo la fase PCN-224 con un mejor control del tamaño de partícula, altamente cristalina y con una alta área superficial en solo 25 segundos de tiempo de residencia a temperatura ambiente.

Este estudio abre la puerta al uso de precursores de zirconio poco comunes para la síntesis de MOFs basados en zirconio con tiempos más cortos, temperaturas más bajas y mejores rendimientos, permitiendo obtener fases puras y escalar su producción en flujo a bajo costo.

El capítulo 5 aborda el uso de alcóxidos de zirconio para la síntesis de nanocompósitos con núcleos de nanopartículas plasmónicas y magnéticas con corazas de MOFs. En dicho trabajo se analiza que no solo los iones halógenos en la síntesis afectan directamente la morfología de las

USC UNIVERSIDADE

nanopartículas plasmónicas de distintas formas, sino también la temperatura, lo cual impacta directamente en sus propiedades ópticas. Dichas nanopartículas plasmónicas fueron funcionalizadas con cadenas poliméricas de polietilenglicol (PEG), que contienen grupos mercapto (-SH) al inicio de las cadenas, los cuales se unen químicamente a la superficie del oro, dándoles estabilidad coloidal en distintos medios acuosos u orgánicos.

Las nanopartículas plasmónicas funcionalizadas fueron calentadas a las temperaturas comunes para la síntesis de MOFs en dimetilformamida (DMF), el solvente más utilizado para la síntesis de MOFs basados en zirconio. La cinética de cambio de forma fue seguida por espectroscopía ultravioleta-visible, demostrando que a 120 ºC el LSPR localizado en el NIR se desplazaba rápidamente hacia el azul, lo cual indica un cambio de forma hasta terminar en una morfología esférica, y su posterior completa oxidación en dos días. Dichas cinéticas también se realizaron a 90 ºC en DMF y agua, observando el mismo efecto, pero más lento, para morfologías bipiramidal, barras y estrellas de oro.

Teniendo en cuenta el efecto de la temperatura, se procedió a utilizar dichas nanopartículas plasmónicas como semillas para una serie de MOFs isoreticulares basados en zirconio, reduciendo la temperatura de 120 ºC a 90 ºC y 70 ºC. Se observó un mejor rendimiento de reacción en solo 30 minutos, además de que dicha reducción de temperatura impactaba de menor manera en el corrimiento del LSPR hacia el azul, conservando la absorción en la zona del NIR.

Con la misma estrategia sintética, se procedió a realizar dicha síntesis a temperatura ambiente, obteniendo los mismos sistemas núcleo-coraza. Sin embargo, dicha síntesis requirió tres días de duración, lo cual es una desventaja. No obstante, considerando que no se necesitó calentamiento y que la morfología de las nanopartículas no se vio afectada, se considera una excelente estrategia sintética.

El efecto de la concentración de nanopartículas plasmónicas en la síntesis de los sistemas núcleo-coraza fue estudiado, concluyendo que los núcleos plasmónicos actúan como semillas en el crecimiento del MOF. Una baja concentración de semillas resultaba en una coraza más gruesa, mientras que al aumentar la concentración de semillas, dicha coraza disminuía su espesor. Este espesor impactaba directamente en las propiedades de generación de calor, ya que los MOFs son conocidos por ser aislantes térmicos. Cuando el sistema era excitado por un láser de 808 nm, el tiempo que tardaba en calentar el medio aumentaba con el grosor de la coraza.

El capítulo 6 aborda una nueva estrategia sintética de sistemas núcleo-coraza compuestos por nanopartículas plasmónicas y el MOF porfirínico PCN-224. Dichos nanocompósitos fueron sintetizados a temperatura ambiente, utilizando el clúster de zirconio pre-sintetizado. Para la síntesis del clúster, se utilizó como disolvente 1-propanol, el cual, según reportes de la literatura, era eliminado bajo vacío durante un día.

Al utilizar las nanopartículas plasmónicas como semillas en el medio de reacción para PCN-224, se obtuvieron sistemas núcleo-coraza muy monodispersos con dicho clúster. Sin embargo, el MOF sin nanopartículas plasmónicas resultó ser muy polidisperso y con un rendimiento de reacción muy bajo. Se caracterizó el clúster mediante análisis termogravimétrico, revelando la presencia de 1-propanol, el cual no se había eliminado

USC SANTIAGO DE COMPOSTELA

completamente bajo vacío debido a su alto punto de ebullición (97 ºC) y baja presión de vapor. Por lo tanto, se procedió a lavarlo con metanol, resultando en la completa eliminación del 1-propanol.

Al realizar de nuevo la síntesis del MOF PCN-224 con el clúster limpio, las partículas obtenidas fueron muy monodispersas. Sin embargo, en el caso de los nanocompósitos, se obtuvieron micropartículas con una gran cantidad de nanopartículas plasmónicas en la superficie en lugar de sistemas núcleo-coraza. Esto llevó a la hipótesis de que la presencia de 1-propanol en el sistema tiene una influencia notable en la cristalización del MOF sobre las nanopartículas plasmónicas PEGiladas. Se planteó que el 1-propanol se intercala entre las cadenas de PEG como co-surfactante, facilitando la inserción de los precursores de MOF sobre las partículas plasmónicas.

Estos compuestos núcleo-coraza fueron cargados con el colorante violeta de cresilo con el fin de observar su liberación activada por luz en células vivas. La liberación se observó claramente al hacer un escaneo láser localizado de varias células, mostrando mediante microscopía de fluorescencia que el pigmento no estaba presente en el citoplasma de las células sin un estímulo externo, pero se liberaba rápidamente al activarlo, corroborando el efecto de termodifusión activado por luz dentro de células vivas.

Además de la liberación del pigmento como droga modelo, dicho MOF presenta la capacidad de generar ROS, las cuales provocaron la muerte de las células iluminadas con luz visible, combinando así la liberación activada por luz con terapia fotodinámica.

El capítulo 7 aborda otro sistema núcleo-coraza, esta vez utilizando el MOF de zirconio NU-1000 y un precursor convencional, $ZrOCl_2$. Como se discutió previamente, el uso de precursores halogenados comprometía la integridad de las nanopartículas plasmónicas. Además, para la formación del clúster de zirconio con estos precursores, es necesario aplicar calor tanto para promover la formación del clúster como para la formación de los enlaces de coordinación entre los ligandos y los núcleos metálicos.

La síntesis de los nanoMOFs plasmónicos se realizó utilizando dos tipos de nanopartículas plasmónicas, nanobarras y bipirámides de oro, que fueron funcionalizadas con PEG-SH y transferidas a DMF para luego ser añadidas como semillas en el medio de reacción. La razón de seguir utilizando precursores halogenados y temperaturas (90 ºC) en esta síntesis es que presenta la ventaja de ser muy rápida en comparación con otros MOFs basados en zirconio, con solo 30 minutos de reacción. Esto causa un corrimiento hacia el azul del LSPR, pero de manera muy sutil, la cual puede ser compensada con la síntesis de nanopartículas plasmónicas con un LSPR más desplazado al rojo.

En esta síntesis, se corroboró mediante microscopía electrónica de barrido utilizando electrones retrodispersados y tomografía 3D con calentamiento simultáneo de microscopía electrónica de transmisión, que la concentración de semillas afectaba directamente la posición final del LSPR. No fue debido a la formación de una coraza de MOF más gruesa, sino a que una menor cantidad de semillas en el medio de reacción provocaba un mayor daño en la forma de las nanopartículas plasmónicas, resultando en un mayor corrimiento hacia el azul con una menor cantidad de semillas.

USC DE SANTIAGO DE COMPOSTELA

El uso de dos morfologías distintas en el sistema núcleo-coraza, con posiciones de LSPR en la misma longitud de onda, tenía como objetivo comprobar el efecto de dichas nanopartículas en las propiedades de calentamiento de los nanocompósitos. Se comprobó que los nanocompósitos con nanobarras de oro calentaban más rápidamente el medio circundante que aquellos con bipirámides de oro. Esto se atribuye a que la relación de aspecto de las nanobarras de oro es muy alta, lo que se traduce en una absorción total de la luz sin generación significativa de dispersión. Como resultado, la energía absorbida se transforma en calor de manera más eficiente en comparación con las bipirámides de oro, que, debido a sus dimensiones y relación de aspecto menor, absorben solo una parte de la luz incidente y dispersan otra, no transformando toda la energía incidente en calor.

Por último, el sistema de bipirámides con coraza de MOF NU-1000 se utilizó como sustrato para espectroscopía Raman aumentada en superficies (SERS, por sus siglas en inglés) debido a la posición de su LSPR y a la presencia de puntas afiladas en su nanoestructura metálica, que favorecen la formación de puntos calientes o zonas de alta concentración de campo eléctrico. Estos puntos calientes incrementan las señales Raman en varios órdenes de magnitud. Para esta prueba de concepto, se utilizó el analito 4-mercaptobenzonitrilo (MBN) en una concentración de 5 micromolar, el cual fue detectado con dificultad para el nanocompósito sintetizado sin diluir. Cuando el analito se puso en contacto con diluciones de diez, cincuenta y cien veces, la señal Raman del analito aumentó en cuatro, cinco y un orden de magnitud, respectivamente. Este aumento se atribuye a una competencia entre la eficiencia de aumento de la señal y la extinción producida por el material.

Finalmente, a las mismas diluciones se les añadió una solución saturada de NaCl con el objetivo de observar una mejora en la intensidad de las señales Raman debido a la aglomeración de partículas. Sin embargo, se observó el fenómeno opuesto: una reducción casi total de las señales Raman. Esto se atribuye a que la fuerza iónica producida por los iones expulsó las moléculas de analito fuera de la porosidad del MOF, alejándolas de la superficie metálica encargada de producir el aumento en la intensidad de las señales Raman.

La presente tesis aborda el desarrollo de nuevas estrategias de síntesis, caracterización y aplicación de materiales compuestos innovadores para aplicaciones biológicas, generación de calor y sensado químico. Este trabajo combina materiales orgánicos, inorgánicos e híbridos a nanoescala, lo cual representa un gran reto, ya que cada uno de estos materiales presenta comportamientos distintos. La reducción de tamaño a la escala nanométrica añade complejidad al control y manipulación de la materia.

Resumiendo, en la presente tesis se aborda el uso de precursores halogenados y temperaturas elevadas en la transformación de la forma de nanopartículas plasmónicas, lo cual impacta directamente en sus propiedades ópticas. Esta problemática podría ser una de las razones de la escasez de sistemas núcleo-coraza que combinen nanopartículas plasmónicas y MOFs basados en zirconio. En esta investigación se desarrollan tres metodologías sintéticas distintas: el uso de alcóxidos de zirconio para la síntesis a baja temperatura o temperatura ambiente, el uso de clústeres de zirconio pre-sintetizados que permiten reacciones a temperatura ambiente, y la utilización de reacciones con tiempos de reacción cortos que, aunque requieren temperaturas elevadas o precursores halogenados, no afectan significativamente el

USC DE SANTIAGO DE COMPOSTELA

desplazamiento del LSPR hacia el azul. Además, se puede contrarrestar este efecto mediante la síntesis de nanopartículas de oro con un LSPR desplazado al rojo.

USC
UNIVERSIDADE DE SANTIAGO DE COMPOSTELA

USC
UNIVERSIDADE
DE SANTIAGO
DE COMPOSTELA

Abstract

This thesis aims to develop synthetic methods for core-shell composite materials, where the core consists of gold plasmonic nanoparticles with various morphologies, and the shell is composed of hybrid materials known as metal-organic frameworks (MOFs).

The plasmonic cores of these materials exhibit unique optical properties due to the presence of surface plasmons, which are generated by the nature of the metallic bond. This bond can be defined as a "sea of free electrons" that traverse the condensed lattice of metal cations. When these electrons are excited by light, they oscillate on the surface of the metal. At the nanoscale, the confinement of the electrons plays a key role in the excitation of these plasmons, allowing this oscillation to be tuned for excitation with visible or infrared light, depending on factors such as chemical composition, size, shape, the presence of stabilizing agents on the surface, or the surrounding dielectric environment. This oscillation presents an absorption maximum known as localized surface plasmon resonance (LSPR), which generates electric dipoles in specific regions of the nanoparticle that can be exploited in various applications.

Due to their optical properties, great chemical stability, and the ability to modify these properties, plasmonic nanoparticles (primarily noble metals like Au, Ag, Cu, Pt, Pd, Rh, among others) have numerous applications in areas such as chemical sensing, catalysis, and photothermal therapy, among others.

On the other hand, MOFs are a novel type of hybrid material composed of an organic part (ligand) and an inorganic part (metal nodes or secondary building units, SBUs). These components, linked by strong coordination bonds, form crystalline structures with high porosity, which is their main feature. This porosity allows the storage of large quantities of molecules, gases, or other substances of interest.

The properties of MOFs are the result of the combination of their two main components, generating new properties when combined as a hybrid material. These properties can be designed through reticular chemistry, which allows the modification of chemical composition, pore size, defect creation, pore polarity, or material surface, among other aspects, to meet specific needs.

The challenge of combining these two materials at the nanoscale to create a synergy of their properties lies in the synthetic difficulties, especially the incompatibility of the synthesis conditions of both materials and the potential damage one of them could suffer during the process. This damage can negatively impact key properties, such as light absorption in certain regions of the electromagnetic spectrum, heat generation, MOF crystallinity, or its porosity.

When these nanomaterials are correctly combined in a core-shell system, they can be activated by external stimuli, such as light, generating heat internally. This heat can be harnessed to carry out reactions within the MOF's porosity, by introducing specific substrates or producing controlled light-activated release. This is due to a local increase in temperature between the inside of the MOF and its surroundings, which promotes the migration of

USC
UNIVERSIDADE DE SANTIAGO DE COMPOSTELA

molecules housed within the pores to the exterior through the phenomenon of thermodiffusion or the Soret effect.

This thermodiffusion property has potential applications in the generation of more efficient light-activated drug nanocarriers, providing a solution to the problem of administering certain drugs that, due to their high hydrophobicity, cannot be delivered by conventional means. These drugs could be encapsulated in the MOF, internalized, and released upon light stimulation in specific areas. To ensure the efficiency of the release, it is important that the light used is in the near-infrared (NIR) range, between 700 and 2500 nm, as human tissues are transparent in this spectral region.

The motivation for this thesis lies in the scarcity of core-shell systems in the literature that combine the properties of plasmonic nanoparticles with MOFs, materials ideal for drug nanocarrier systems. Several synthetic strategies have been developed to preserve the properties of both materials in a single system, and their potential application in biomedicine as nanocarriers is explored in depth.

In Chapter 3 of results and discussion, a new synthetic strategy for the synthesis of nanoparticles of a zirconium-based MOF called UiO-66 is addressed. This material has been extensively studied in the scientific community due to its excellent physical and chemical properties, such as high chemical, thermal, and structural stability, making it an ideal candidate for shell formation on plasmonic nanoparticles. Unfortunately, the most widely studied metal precursors in the literature for the synthesis of this MOF are substances containing halogen ions, such as $ZrCl_4$ or $ZrOCl_2$. It has been reported that these halogens can cause the oxidation of gold nanoparticles, thus destroying the shell.

By replacing zirconium precursors containing halogen ions with those that do not, such as $ZrO(NO_3)_2$, in a synthesis optimized by the research group, it was found that nanoparticles were not obtained, but rather microparticles composed of twinned crystals of this MOF. It was hypothesized that halogen ions were a crucial factor for obtaining well-defined nanocrystals of this MOF. Therefore, two sources of chloride ions, such as HCl and NaCl, were added to the synthesis to rule out the pH factor or confirm their role in the synthesis. The results showed the presence of nanocrystals, even smaller than in the original synthesis, and much better defined, confirming the role of halogens, as the synthesis also worked similarly with bromide and iodide ions.

Subsequently, extensive characterization with various techniques demonstrated the presence of chloride and bromide ions in the MOF structure. These materials were colloidally stable and showed their ability to internalize the dye rhodamine 6G in live cells, which exhibited high cell viability, even at high zirconium concentrations (> 100 ppm).

In Chapter 4, inspired by the use of halogen-free zirconium precursors, the use of zirconium alkoxides was studied. These precursors are incredibly underutilized in the synthesis of zirconium-based MOFs. They are, however, widely used in the synthesis of other types of materials, such as metal oxides via the sol-gel method, due to their ease of hydrolysis, high reactivity, and low cost.

USC UNIVERSIDADE DE SANTIAGO DE COMPOSTELA

The MOFs synthesized with these zirconium alkoxides are termed porphyrinic MOFs and are based on a porphyrin macrocycle with chelating groups attached to it, which can be bi-, tri-, tetra-, or polydentate, with tetradentate being the most common and used in this work.

These porphyrinic MOFs with the tetradentate ligand exhibit very interesting optical properties, as they absorb the entire visible range of the electromagnetic spectrum and emit at two wavelengths with a very high quantum yield. This makes them ideal for energy storage and conversion applications, photocatalysis, and bioapplications due to their ability to produce reactive oxygen species (ROS), which can be used for photodynamic therapy.

The challenge in synthesizing these nanomaterials lies in the formation of polymorphs, as there are six of them with different connectivities in the six-atom Zr cluster with 6 ligands per cluster, such as PCN-224; eight ligands per cluster, such as PCN-222, NU-902, and PCN-225; and two polymorphs with complete twelve connectivity, MOF-525 and PCN-223.

With so many polymorphs, synthesizing these MOFs becomes a challenge, as obtaining phase mixtures is very common, making characterization extremely complicated. Additionally, the properties are mixed in a heterogeneous system that can behave differently depending on the percentage of these polymorphs in the mixture.

This study discovered that zirconium alkoxides can achieve the synthesis of pure phases of PCN-224, PCN-222, and MOF-525 in very short reaction times compared to the literature (1 hour of reaction), at room or lower temperatures compared to the literature (75 ºC maximum), and with reaction yields greater than 90%.

Moreover, due to the rapid reactions and high yields, a flow synthesis was performed as a proof of concept, obtaining the PCN-224 phase with better particle size control, high crystallinity, and a high surface area in just 25 seconds of residence time at room temperature.

This study paves the way for the use of less common zirconium precursors for the synthesis of zirconium-based MOFs with shorter times, lower temperatures, and better yields, allowing for the production of pure phases and scaling up flow production at low cost.

Chapter 5 addresses the use of zirconium alkoxides for the synthesis of nanocomposites with magnetic and plasmonic nanoparticle cores and MOF shells. This work analyzes that not only do halogen ions in the synthesis directly affect the morphology of plasmonic nanoparticles of different shapes, but temperature also has a direct impact on their optical properties. These plasmonic nanoparticles were functionalized with polyethylene glycol (PEG) polymer chains, containing thiol (-SH) groups at the chain ends, which chemically bond to the gold surface, providing them with colloidal stability in various aqueous or organic media.

The functionalized plasmonic nanoparticles were heated to common temperatures for MOF synthesis in dimethylformamide (DMF), the most used solvent for zirconium-based MOF synthesis. The shape-changing kinetics were monitored by ultraviolet-visible spectroscopy, showing that at 120 ºC, the LSPR localized in the NIR shifted rapidly to the blue, indicating a shape change ending in a spherical morphology, followed by complete oxidation in two days. These kinetics were also performed at 90 ºC in DMF and water, observing the same effect, but more slowly, for bipyramidal, bar, and star-shaped gold morphologies.

USC
UNIVERSIDADE DE COMPOSTELA

Considering the temperature effect, these plasmonic nanoparticles were used as seeds for a series of isoreticular zirconium-based MOFs, reducing the temperature from 120 ºC to 90 ºC and 70 ºC. A better reaction yield was observed in just 30 minutes, and this temperature reduction had less impact on the blue shift of the LSPR, preserving absorption in the NIR region.

Using the same synthetic strategy, the synthesis was carried out at room temperature, obtaining the same core-shell systems. However, this synthesis required three days, which is a disadvantage. Nevertheless, given that no heating was needed and the nanoparticle morphology was unaffected, it is considered an excellent synthetic strategy.

The effect of plasmonic nanoparticle concentration on the synthesis of core-shell systems was studied, concluding that the plasmonic cores act as seeds in the growth of the MOF. A low seed concentration resulted in a thicker shell, while increasing the seed concentration led to a thinner shell. This thickness directly impacted heat generation properties, as MOFs are known to be thermal insulators. When the system was excited by an 808 nm laser, the time required to heat the medium increased with shell thickness.

Chapter 6 addresses a new synthetic strategy for core-shell systems composed of plasmonic nanoparticles and the porphyrinic MOF PCN-224. These nanocomposites were synthesized at room temperature using the pre-synthesized zirconium cluster. For cluster synthesis, 1-propanol was used as a solvent, which, according to literature reports, was removed under vacuum for one day.

Using plasmonic nanoparticles as seeds in the reaction medium for PCN-224, very monodisperse core-shell systems with this cluster were obtained. However, the MOF without plasmonic nanoparticles turned out to be very polydisperse with a very low reaction yield. The cluster was characterized by thermogravimetric analysis, revealing the presence of 1-propanol, which had not been completely removed under vacuum due to its high boiling point (97 ºC) and low vapor pressure. Therefore, it was washed with methanol, resulting in the complete removal of 1-propanol.

When the synthesis of MOF PCN-224 was repeated with the clean cluster, the obtained particles were highly monodisperse. However, in the case of the nanocomposites, microparticles with a large number of plasmonic nanoparticles on the surface were obtained instead of core-shell systems. This led to the hypothesis that the presence of 1-propanol in the system has a notable influence on the crystallization of the MOF onto the PEGylated plasmonic nanoparticles. It was proposed that 1-propanol intercalates between the PEG chains as a co-surfactant, facilitating the insertion of MOF precursors onto the plasmonic particles.

These core-shell compounds were loaded with the dye cresyl violet to observe its light-activated release in living cells. The release was clearly observed by performing localized laser scanning of various cells, showing through fluorescence microscopy that the pigment was not present in the cytoplasm of cells without an external stimulus, but was rapidly released upon activation, confirming the effect of light-activated thermodiffusion within living cells.

USC UNIVERSIDADE DE SANTIAGO DE COMPOSTELA

In addition to the release of the dye as a model drug, this MOF has the ability to generate ROS, which caused the death of cells illuminated with visible light, thus combining light-activated release with photodynamic therapy.

Chapter 7 addresses another core-shell system, this time using the zirconium MOF NU-1000 and a conventional precursor, $ZrOCl_2$. As discussed previously, the use of halogenated precursors compromised the integrity of the plasmonic nanoparticles. Furthermore, for the formation of the zirconium cluster with these precursors, it is necessary to apply heat both to promote cluster formation and to form coordination bonds between the ligands and the metal cores.

The synthesis of the plasmonic nanoMOFs was performed using two types of plasmonic nanoparticles, gold nanorods and bipyramids, which were functionalized with PEG-SH and transferred to DMF before being added as seeds in the reaction medium. The reason for continuing to use halogenated precursors and temperatures (90 ºC) in this synthesis is that it offers the advantage of being very fast compared to other zirconium-based MOFs, with only 30 minutes of reaction time. This causes a blue shift in the LSPR, but in a very subtle manner, which can be offset by synthesizing plasmonic nanoparticles with an LSPR more shifted to the red.

In this synthesis, it was confirmed by scanning electron microscopy using backscattered electrons and 3D tomography with simultaneous heating of transmission electron microscopy that the concentration of seeds directly affected the final position of the LSPR. This was not due to the formation of a thicker MOF shell, but rather because a lower amount of seeds in the reaction medium caused greater damage to the shape of the plasmonic nanoparticles, resulting in a greater blue shift with fewer seeds.

The use of two different morphologies in the core-shell system, with LSPR positions at the same wavelength, aimed to assess the effect of these nanoparticles on the heating properties of the nanocomposites. It was found that nanocomposites with gold nanorods heated the surrounding medium more rapidly than those with gold bipyramids. This is attributed to the high aspect ratio of the gold nanorods, which results in total light absorption with minimal scattering. Consequently, the absorbed energy is converted into heat more efficiently compared to gold bipyramids, which, due to their dimensions and smaller aspect ratio, absorb only part of the incident light and scatter the rest, not converting all the incident energy into heat.

Lastly, the bipyramid system with MOF NU-1000 shell was used as a substrate for surface-enhanced Raman spectroscopy (SERS) due to its LSPR position and the presence of sharp tips in its metal nanostructure, which favor the formation of hotspots or regions of high electric field concentration. These hotspots increase Raman signals by several orders of magnitude. For this proof of concept, the analyte 4-mercaptobenzonitrile (MBN) was used at a concentration of 5 micromolar, which was detected with difficulty for the undiluted synthesized nanocomposite. When the analyte was exposed to dilutions of ten, fifty, and one hundred times, the Raman signal of the analyte increased by four, five, and one order of magnitude, respectively. This increase is attributed to a competition between signal enhancement efficiency and extinction caused by the material.

USC UNIVERSIDADE DE SANTIAGO DE COMPOSTELA

Finally, a saturated NaCl solution was added to the same dilutions to observe an improvement in Raman signal intensity due to particle agglomeration. However, the opposite phenomenon was observed: an almost total reduction in Raman signals. This is attributed to the ionic strength produced by the ions expelling the analyte molecules from the MOF's porosity, moving them away from the metal surface responsible for producing the Raman signal enhancement.

This thesis addresses the development of new synthesis, characterization, and application strategies for innovative composite materials for biological applications, heat generation, and chemical sensing. This work combines organic, inorganic, and hybrid materials at the nanoscale, which represents a significant challenge, as each of these materials exhibits distinct behaviors. The reduction in size to the nanometer scale adds complexity to the control and manipulation of matter.

In summary, this thesis addresses the use of halogenated precursors and high temperatures in the transformation of plasmonic nanoparticles' shapes, which directly impacts their optical properties. This issue could be one of the reasons for the scarcity of core-shell systems combining plasmonic nanoparticles with zirconium-based MOFs. This research develops three distinct synthetic methodologies: the use of zirconium alkoxides for low-temperature or room-temperature synthesis, the use of pre-synthesized zirconium clusters that allow reactions at room temperature, and the use of reactions with short reaction times that, although requiring high temperatures or halogenated precursors, do not significantly affect the blue shift of the LSPR. Moreover, this effect can be countered by synthesizing gold nanoparticles with a red-shifted LSPR.

USC
UNIVERSIDADE DE SANTIAGO DE COMPOSTELA

1. Introduction

USC
UNIVERSIDADE
DE SANTIAGO
DE COMPOSTELA

USC
UNIVERSIDADE
DE SANTIAGO
DE COMPOSTELA

1.1. RETICULAR CHEMISTRY

1.1.1. The design of new inorganic porous materials

Reticular chemistry refers to the design and construction of new crystalline solid-state materials using molecular building blocks.[1] This approach, called reticular synthesis, involves using secondary building units (SBUs) to guide the assembly of ordered frameworks with a certain connectivity that give a specific net. The resulting materials have predetermined structures, compositions, and properties, characterized by highly porous frameworks held together by strong metal-oxygen-carbon bonds (among others). These materials have exceptionally large surface areas and capacities for gas storage, with systematically varied and functionalized pore metrics.

Over the past three decades, the discovery of new solids with permanent porosity, incorporating a wide variety of organic linkers and their combinations with metals or inorganic clusters, has positioned reticular chemistry as a prominent research area in contemporary scientific studies.[2]

According to web of science (WOS), the number of publications on metal-organic frameworks (MOFs) has increased exponentially over the past three decades. This growth is mirrored by the number of new MOF structures reported in the Cambridge Structural Database (CSD). Since the publication of MOF-1[3] by Yaghi *et al.* in 1995 until 2017, nearly 70,000 structures were registered.[4] Currently, the database contains over 127,000 MOF structures, as illustrated in Figure 1-1, here have also been several key achievements in the field of MOFs since the publication of MOF-1, culminating in the development of highly complex systems such as multivariate (MTV) MOFs.

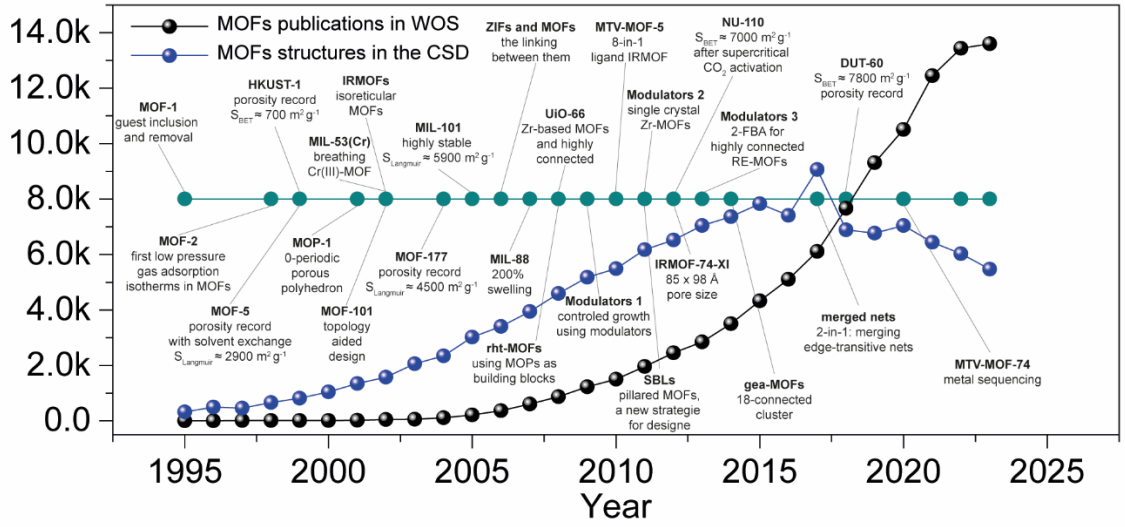

Figure 1-1. Timeline displaying key achievements in MOF research, along with the annual number of MOF publications and the number of MOF structures reported to the CSD. Publications and MOF structure reported data are not cumulative.

USC UNIVERSIDADE DE SANTIAGO DE COMPOSTELA

1.1.2. Metal-organic frameworks (MOFs)

The development of a new class of solid inorganic materials, known as MOFs, involves the assembly of metal atoms or metal clusters (SBUs) linked by strong bonds with organic molecules[5] (Figure 1-2). MOFs represent an emerging category of materials that exhibit remarkable physicochemical properties, including permanent porosity,[6] exceptionally high surface areas,[7–9] and customizable porosity.[10] These properties can be finely tuned through post-synthetic modifications[11] and precise control of particle size.[12,13]

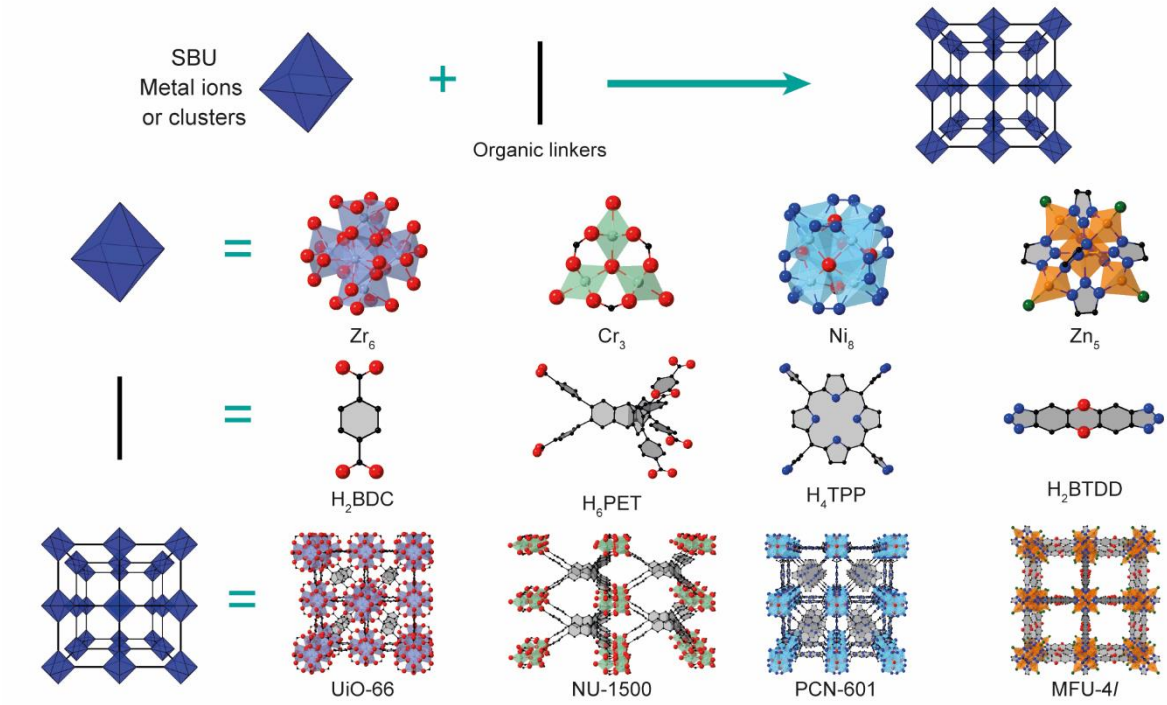

Figure 1-2. Schematic representation of the MOF structure, illustrating the assembly from metal atoms or clusters and organic linkers to the complete framework and some examples with their building units.

Since the discovery of MOF-5[14] and HKUST-1[15] in 1999, two of the most representative structures in the world of MOFs, there has been significant development of new MOF structures with unique properties and diverse applications. This substantial increase is attributed to the combinatorial possibilities of the chemistry of SBUs, involving different metal compositions or combinations of metals, with the organic synthesis of novel ligands featuring varying numbers and arrangements of binding groups, resulting in new topologies.

In addition to MOF-5 and HKUST-1, other notable MOFs include MIL-100[16] and UiO-66,[17] due to their potential for generating diverse new structures with their respective SBUs. It is important to highlight that the SBUs of these MOFs were reported many years before each MOF was fully developed, albeit in isolated forms with monoprotic carboxylic acids. For instance, the SBU of the Cu(II) paddlewheel $Cu_2(CH_3COO)_4$ from HKUST-1 was reported in 1953,[18] and the Zn(II) tetramer $Zn_4O(CH_3COO)_4$ was reported one year later in 1954,[19] both using acetate ligands. Additionally, the Cr(III) trimer with acetate ligands, corresponding to the MIL-100 SBU, was reported in 1965,[20] nearly 40 years before the development of MIL-100 in 2004. Similarly, the $Zr_6O_4(OH)_4$ cluster from UiO-66 was reported in 1997[21] with twelve

USC
UNIVERSIDADE
DE SANTIAGO
DE COMPOSTELA

methacrylate molecules, the same number of terephthalic acid molecules used in UiO-66, paving the way for highly connected MOFs (Figure 1-3).

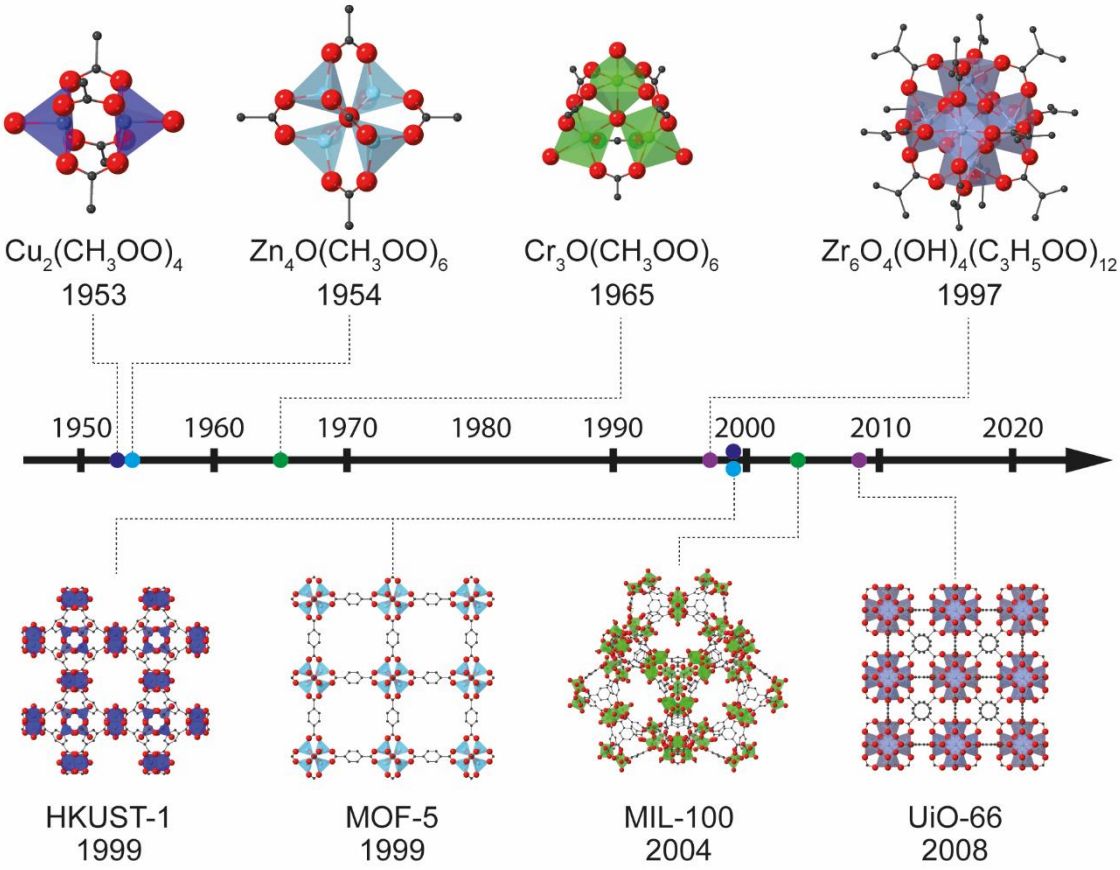

Figure 1-3. Timeline of some of the most representative MOFs and their corresponding SBUs.

1.1.3. Building blocks

Reticular design depends on three fundamental requirements: the use of building blocks, the selection of targeted nets, and the application of isoreticular chemistry. To effectively design and guide the assembly of MOFs, it is fundamental to understand the structural characteristics of their primary components, specifically the building blocks.[22]

The variety of building blocks offers infinite possibilities for emerging applications in reticular chemistry. These building blocks can be classified into two groups: i) molecular and supramolecular building blocks, typically known as linkers, which constitute the organic component of the MOFs, and ii) inorganic building blocks, also known as SBUs, which consist of single metal ions or metallic clusters. The control of the structural characteristics of these building blocks impacts the geometry and topology within the resulting framework.

The nature of the molecular building blocks can be modified by incorporating various functional groups that form strong bonds with metals. The number and position of these functional groups are also crucial in determining the properties of the MOFs. Carboxylate linkers are the most commonly used like (all the previous examples fit in this case),[14–17] yet

USC UNIVERSIDADE DE SANTIAGO DE COMPOSTELA

MOFs can also be constructed with linkers containing phosphates,[23] imidazole rings (as seen in the ZIF family),[24] and unconventional functional groups such as hydroxamates,[25] among others.

Figure 1-4 shows some representative carboxylate linkers. Commonly used ditopic linkers include H_2Fum for the synthesis of MOF-801,[26] H_2BDC for UiO-66,[17] H_2NDC for DUT-52,[27] H_2BPDC for UiO-67,[28] and H_2TPDC for UiO-68,[29] which extend the network by increasing linker length in isoreticular Zr-based MOFs. For tritopic linkers, H_3BTC is utilized in the synthesis of MOF-808,[26] among others. Tetratopic linkers include H_4TCPP, which is used in the synthesis of porphyrinic Zr-based MOFs[30] such as PCN-222 (also known as MOF-545 or MMPF-6),[31–33] PCN-223,[34] PCN-224,[35] PCN-225,[36] NU-902,[37] and MOF-525.[32] Additionally, H_4TBAPy is used in the synthesis of NU-1000[38] and its polymorph NU-901,[39] and H_4ETTC is used in the synthesis of PCN-94[40] and PCN-128.[41]

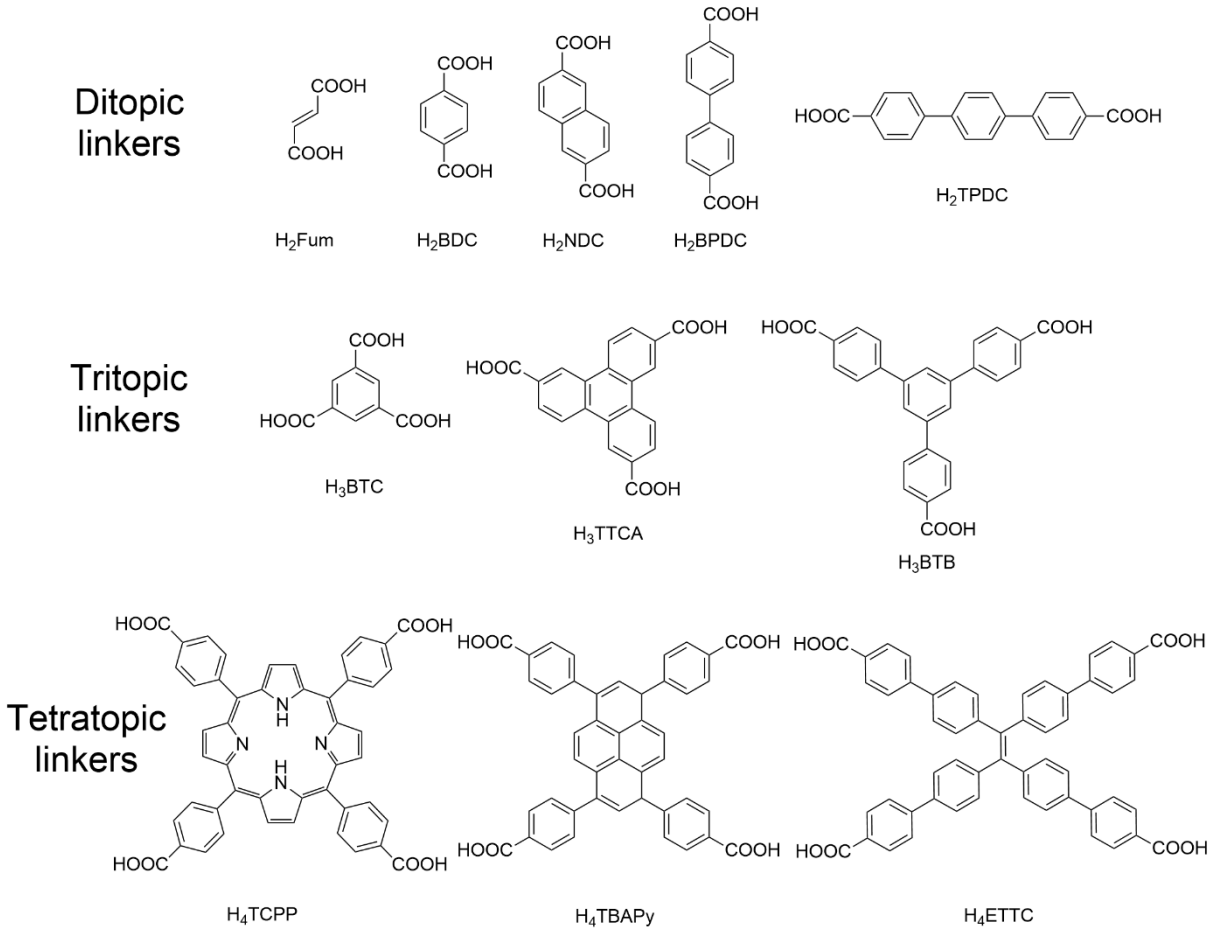

Figure 1-4. Representative polytopic carboxylate linkers used to construct MOFs.

There are some reports of pentatopic linkers being used as building blocks for MOF. However, the lack of symmetry impact directly in their physicochemical properties. For instance, in the case of UMCM-154, where a pentatopic linker is coordinated to a zinc ion, the framework does not exhibit permanent porosity due to the instability of its metal SBU, specifically a three-bladed zinc paddle-wheel cluster.[42] In contrast, various polytopic linkers have been employed as hexatopic linkers, facilitating the formation of rare topologies, as exemplified by PCN-136[43] and NU-1500.[44]

The diversity of SBUs is significantly enhanced by the wide variety of metals, geometries, connectivities, metal combinations, and isomers available. Figure 1-5 illustrates several of the most common SBUs formed with specific metals and linkers, some of which exhibit isomerism due to the various spatial arrangements of the linkers.

The previously mentioned Cu(II) paddlewheel is one of the most extensively studied SBUs, with the formula M_2L_4 (Figure 1-5a). It also exists with Zn(II) and is typically represented as a 4-connected square. The HKUST-1 MOFs incorporate this SBU, linked with four tritopic trimesic acid molecules.[15,18]

In the case of trinuclear clusters, the M_3L_3 units, typically containing Cu(II), Zn(II), or Ag(I), are represented as a 3-connected triangle (Figure 1-5b). In this structure, the metals are positioned in the middle of the edges of the triangle, with three pyrazole derivative linkers at the corners, as seen in FDM-6.[45] Another example of a trinuclear cluster is the M_3L_6, where the metal can be Al(III), Mg(II), Sc(III), Cr(II), Cr(III), Mn(II), Mn(III), Fe(II), Fe(III), Co(II), Ni(II), Ga(III), In(III), among others. This trinuclear cluster accommodates six linkers arranged in a trigonal prism (Figure 1-5c), as observed in MIL-100.[16,20]

The well-known tetranuclear SBU of MOF-5 with the M_4L_6 formula[14] is composed of four Zn(II) metals, but can also include Co(II), Y(III), Ln(III), among others. In the cluster, the metals are bridged by a μ_4-O group in the case of transition metals,[19] whereas in rare-earth clusters, they are linked by four μ_3-OH moieties[46] with six carboxylate linkers arranged in an octahedral disposition (Figure 1-5d).

For tetranuclear clusters, the diversity increases significantly. For example, the planar M_4L_8 cluster, where the metal can be Mn(II), Co(II), Cu(II), Cd(II), Ni(II), Y(III), Ln(III), among others, presents an eight-connected cuboid geometry (Figure 1-5e). In this structure, the ditopic linkers can coordinate two of the metal atoms in the plane, resulting in an 8-connected uninodal 3D structure.[47]

One of the most studied SBUs in the world is the M_6L_{12} cluster in UiO-66, typically composed of Zr(IV) but also possible with Hf(IV) and rare-earth elements. This SBU paved the way for highly connected MOFs, where six Zr atoms are arranged in an octahedral configuration and connected by twelve carboxylate linkers, forming bridges in a cuboctahedron (Figure 1-5f). The metals are connected by four μ_3-O and four μ_3-OH groups, making the resulting MOF very stable and robust.[17,21]

The presence of missing linker defects in the UiO-66 SBU results in alternative spatial dispositions and geometries, such as the 8-connected cuboid M_6L_8 (Figure 1-5g) in MOF-841 and the 6-connected trigonal antiprism M_6L_6 (Figure 1-5h) in MOF-808.[26] The same M_6L_6 Zr-based SBU can acquire different spatial dispositions and orient its linkers in a planar hexagonal arrangement (Figure 1-5i), as seen in PCN-136.[43]

Increasing the number of metal atoms in a cluster directly translates to an increase in connectivity. The M_8L_{12} cluster, where the metal can be Co(II) or Ni(II), exhibits a 12-connected cuboctahedral geometry (Figure 1-5j) using pyrazole-based linkers.[48] With the same number of metals in the cluster but arranged in a snub square antiprism configuration (Figure 1-5k), the planar octanuclear M_8L_{16} cluster, composed of Al(III), Cr(III), or Ti(IV), can

accommodate up to sixteen carboxylate linkers around the planar ring structure, as seen in MOF-520-BPDC.[49]

One of the highly connected and versatile SBUs is the M_9L_{12}, arranged in a hexagonal prism (Figure 1-5l) and composed of Y(III) or Ln(III). During the synthesis of MOFs using this SBU, variations in the angle of the tritopic linker directly influence the resulting MOF structure. When the tritopic linker is symmetric (120º between carboxylate moieties), the outcome is a pek-a net with two different clusters: one M_6L_8 and another M_9L_{12}. However, if the tritopic linker is asymmetric (90º between carboxylate moieties), the resulting structure is an aea-a net with only the M_9L_{12} SBU in a hexagonal prismatic conformation.[50]

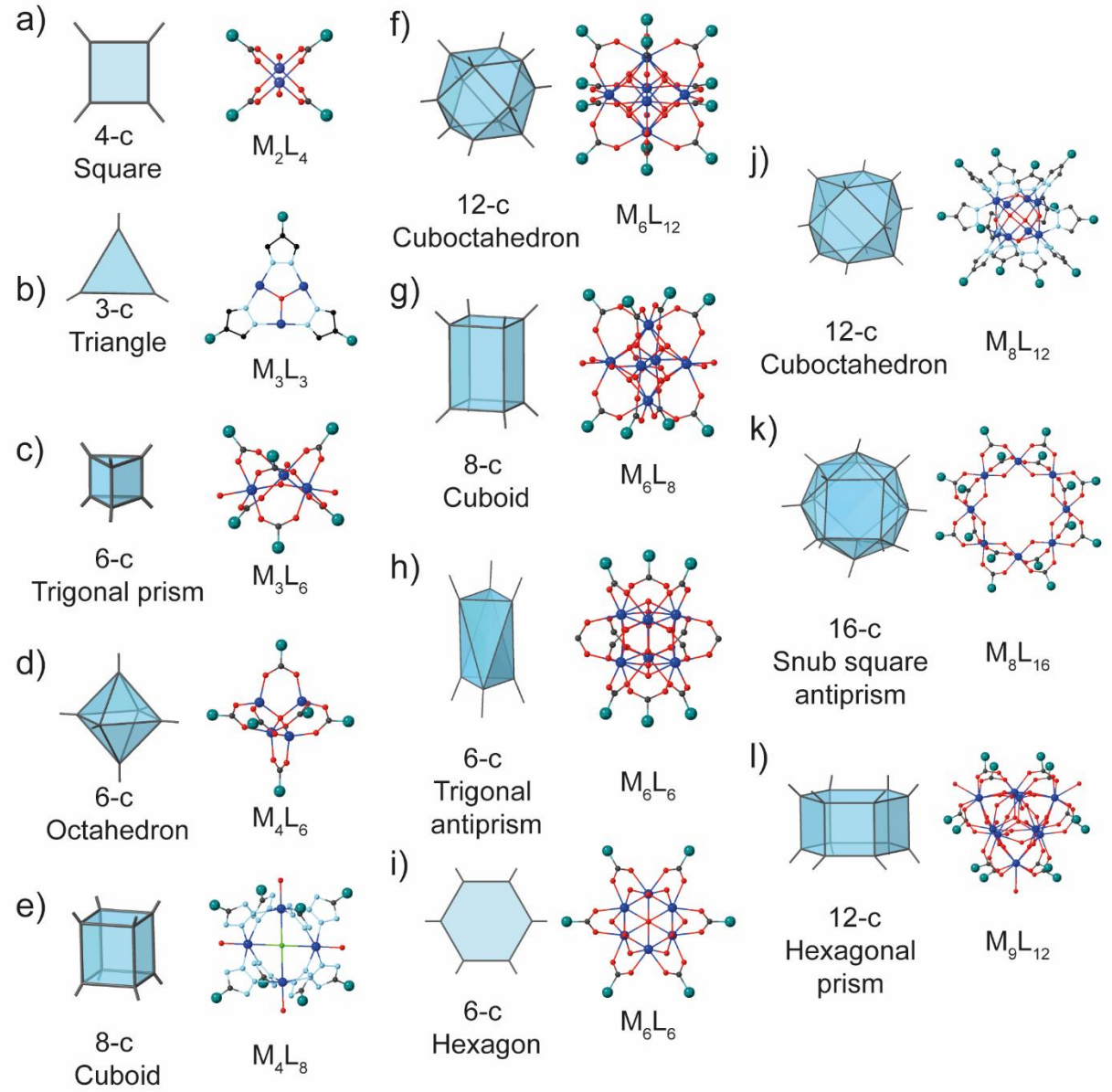

Figure 1-5. Schematic representation of secondary building blocks that can be obtained with their corresponding polyhedron. Color scheme: metals (dark blue), carbon (grey), oxygen (red), nitrogen (light blue), halogens (green), anchor points (turquoise). M, metal; L, linker.

USC UNIVERSIDADE DE SANTIAGO DE COMPOSTELA

1.1.4. Topology

Over the past three decades, reticular chemistry has significantly expanded the variety and complexity of molecular systems, ranging from 0D structures such as metal-organic polyhedra (MOPs) to 2D and 3D MOFs and covalent organic frameworks (COFs). The vast diversity of MOFs, MOPs, and COFs arises from the connectivity of their building blocks, which typically ranges from 4 to 24. When these are combined with organic linkers featuring direct connectivity points, varied functional groups, pendant groups, and differing lengths, it becomes possible to generate over 200 distinct topologies.[51,52]

The aim of reticular chemistry is to develop new crystalline materials with well-defined structures and net topologies based on their building units, taking into account their metal coordination geometries and linker connectivities. However, achieving the desired structure is not straightforward, as using the same metal ions and organic linkers under varying reaction conditions can result in MOFs with completely different structures and, consequently, different net topologies.[53–56]

Given the importance of this field and the exponential growth of reticular chemistry, O'Keeffe *et al.* developed the Reticular Chemistry Structure Resource (RCSR) in 2008.[57] This resource provides a system of symbols for identifying three periodic nets of interest. Figure 1-6 illustrates various net topologies that result from the combination of primary and secondary building units with different connectivities and geometries. These diverse topologies arise from the specific geometry or spatial arrangement of their connecting points in space.

Each topology in the RCSR is classified based on the types of rings formed (attributed to the loops created by the connectivity of vertices and edges), the types of vertices (attributed to metals or clusters), edges (attributed to the linkers), faces (representing the windows in MOFs), and tiles (polyhedral shapes that describe the periodic filling of space and the overall topology).

When applying reticular chemistry to create a new MOF for a specific application, it is fundamental to determine the desired type of faces (size and shape). This is because these faces function as a mesh for the adsorbate entering or exiting the MOF's porosity. It is important to distinguish this from the overall porosity of the MOF, which can be misunderstood, as illustrated in Figure 1-7. Designing a MOF with a single type of face is more straightforward due to the geometry of the SBUs used. Topologies that feature only one kind of face are called face-transitive topologies. There are 53 such topologies, 8 of which are 2D and 45 are 3D, as shown in Table 1-1. Among these 53 net-topologies, 17 also meet the criteria for edge transitivity which means that just present one kind of organic linker.[58]

Another factor to consider in the design of a MOF with a specific topology is the induction of defects. These defects are diverse and are summarized in Figure 1-8. Missing linker defects can promote changes in topology,[59] as can the induction of missing cluster defects. For example, UiO-66-fcu transforms into UiO-66-reo due to these defects, significantly affecting its adsorptive and catalytic properties.[60]

USC UNIVERSIDADE DE SANTIAGO DE COMPOSTELA

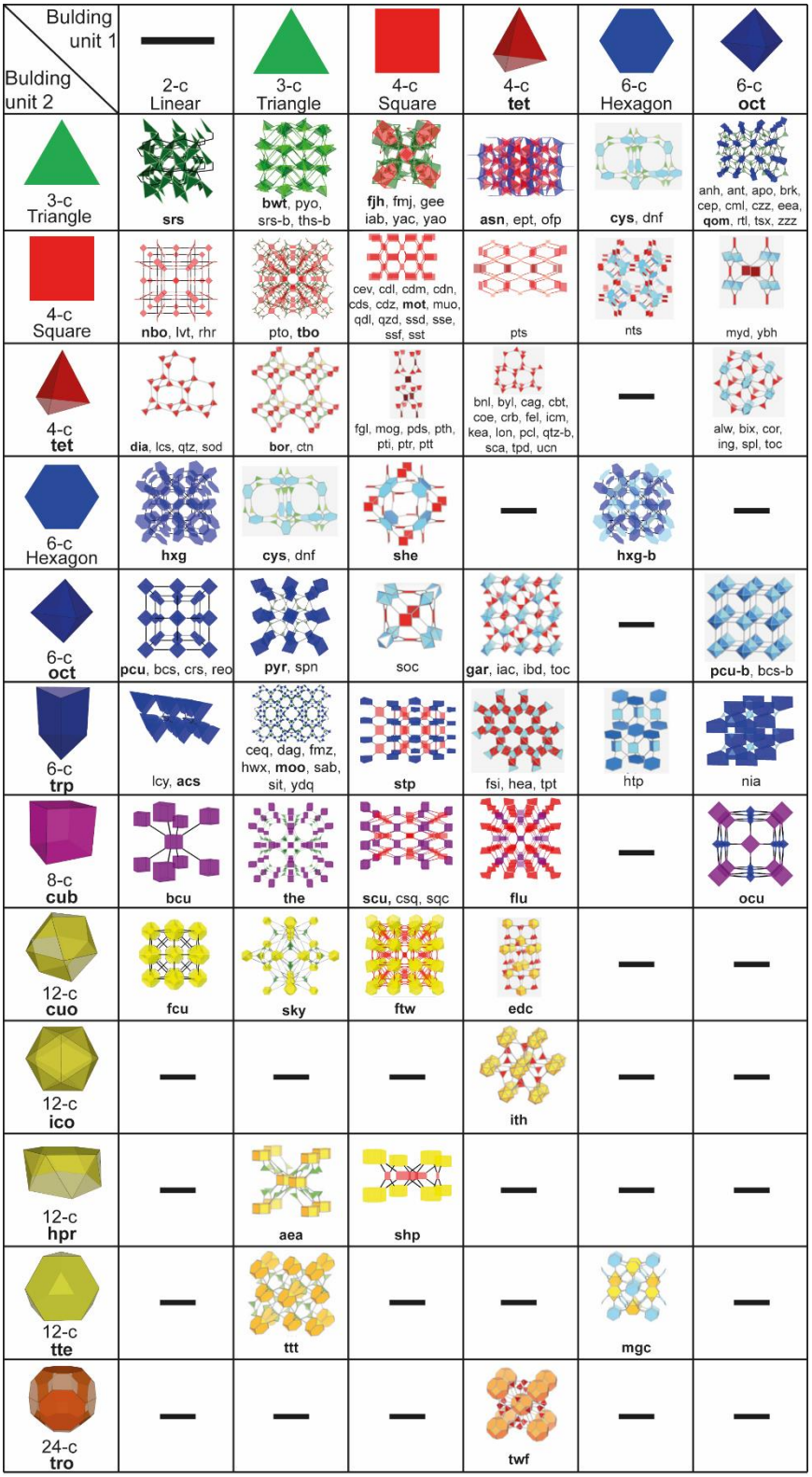

Figure 1-6. Table of potential bipartite nets created through reticular chemistry. Each topology is presented as its corresponding augmented net. If multiple nets exist, the identifier of the specified net is highlighted in bold.

USC UNIVERSIDADE DE SANTIAGO DE COMPOSTELA

The chemical composition of the MOF can also directly affect its topology. The preparation method, whether through one-pot synthesis or with pre-formed clusters, can induce changes in the resulting topology. Additionally, metal exchange in metallic clusters can result in heterometallic clusters, further influencing the topology.[61]

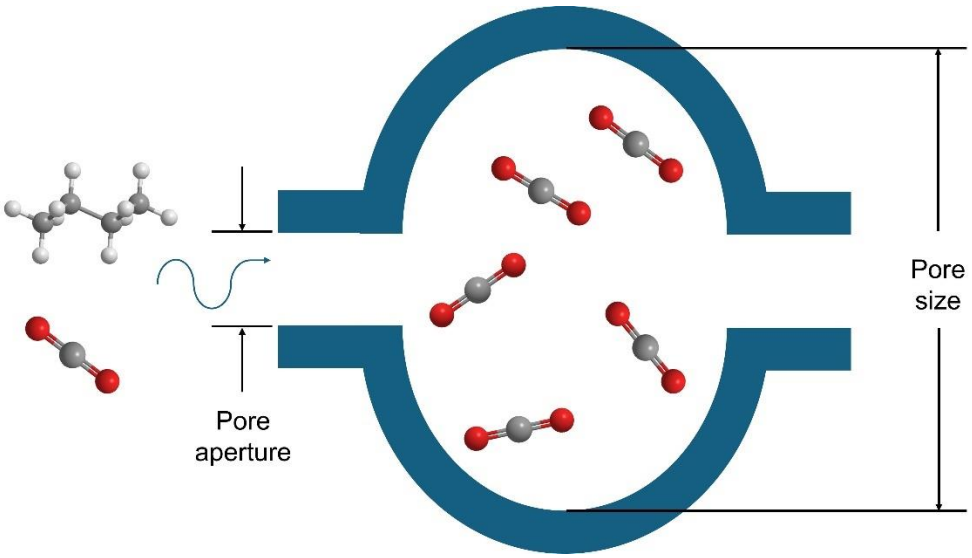

Figure 1-7. Differences of pore size and pore aperture in MOFs.

Table 1-1. Face-transitive nets and their ring size, transitivity and connectivity.

Net	Ring	Transitivity				Connectivity
		Vertices	Edges	Faces	Tiles	
2D						
hxl*	3	1	1	1	-	6-c
kgd*	4	2	1	1	-	3,6-c
sql*	4	1	1	1	-	4-c
cem-d	5	2	3	1	-	3,4-c
fsz-d	5	3	3	1	-	3,3,6-c
mcm	5	2	2	1	-	3,4-c
mta	5	3	2	1	-	3,4,6-c
hcb	6	1	1	1	-	3-c
3D						
fcu*	3	1	1	1	2	12-c
bcu-x	3	1	2	1	1	14-c
ild	3	1	2	1	1	12-c
reo-d	3	2	2	1	1	(8,14)-c
xam	3	2	2	1	1	(6,12)-c
bcu*	4	1	1	1	1	8-c
flu*	4	2	1	1	1	(4,8)-c
ftw*	4	2	1	1	2	(4,12)-c

USC UNIVERSIDADE DE SANTIAGO DE COMPOSTELA

mgc*	4	2	1	1	2	(6,12)-c
ocu*	4	2	1	1	2	(6,8)-c
pcu*	4	1	1	1	1	6-c
twf*	4	2	1	1	2	(4,24)-c
crs-d	4	2	2	1	1	(4,8)-c
epd	4	3	2	1	3	(3,4,6)-c
hxg-d	4	1	2	1	1	10-c
nia-d	4	2	2	1	2	(3,9)-c
she-d	4	2	2	1	2	(6,18)-c
svn	4	1	2	1	1	7-c
urk	4	3	2	1	1	(4,6,6)-c
xbk	4	3	2	1	2	(4,6,12)-c
xbr	4	2	2	1	2	(6,10)-c
nts-d	4	4	4	1	2	(4,10,14,18)-c
cdh	5	2	2	1	1	(4,6)-c
ctn-x	5	2	2	1	1	(4,5)-c
fse	5	2	2	1	1	(4,6)-c
fsn	5	2	2	1	1	(4,6)-c
gan	5	1	2	1	1	5-c
ith-d	5	2	2	1	2	(3,6)-c
fiq	5	2	3	1	1	(4,5)-c
dia*	6	1	1	1	1	4-c
nbo*	6	1	1	1	1	4-c
pyr*	6	2	1	1	2	(3,6)-c
gsi	6	1	2	1	1	4-c
pto-d	6	2	2	1	2	(4,6)-c
twf-d	6	3	2	1	2	(3,4,6)-c
xag	6	3	2	1	2	(3,4,12)-c
alb-d	6	4	3	1	2	(3,4,4,6)-c
fnu	6	1	3	1	1	5-c
qzd	7	1	2	1	1	4-c
tfn	7	2	3	1	1	(3,4)-c
ctn*	8	2	1	1	2	(3,4)-c
tfv	8	2	2	1	2	(3,4)-c
srs*	10	1	1	1	1	3-c
ctn-d	10	2	2	1	2	(3,3)-c
ths	10	1	2	1	1	3-c

*edge transitive nets.

Interpenetration occurs when the pore size is sufficiently large to accommodate another network. This can be prevented by adding bulky functional groups, which, due to steric hindrance, block the growth of an additional network within the porosity. This approach not only reduces the pore size, substantially decreasing adsorption properties, but also alters the symmetry. In cases where the networks interact in a highly symmetrical manner,

USC UNIVERSIDADE DE SANTIAGO DE COMPOSTELA

interpenetration can lead to an increase in the space group symmetry, resulting in a more symmetrical structure. [62,63]

Another aspect that directly impacts topology is the presence of metallo-ligands. Yaghi *et al.* introduced a concept called molecular weaving, where certain COFs have heteroatoms available to chelate metals, inducing an interpenetrated network similar to the process of fabric weaving.[64]

The post-synthetic modification strategy can also induce changes in topology due to linker exchange or linker installation in the incomplete valence sites of the SBUs, resulting in new crystal structures that are non-edge transitive. This not only alters the crystal symmetry but also affects the windows and pore sizes.[65]

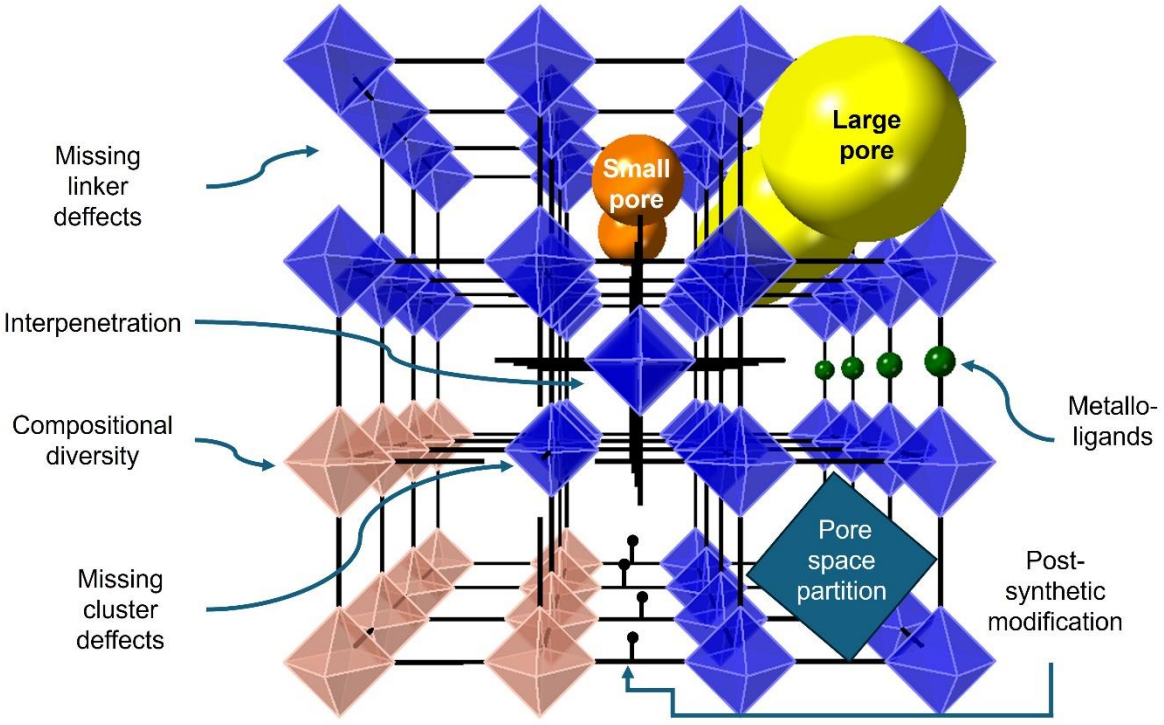

Figure 1-8. Schematic representation of different aspect that influence the topology of a MOF.

1.1.5. Isoreticular structures

The concept of "isoreticular materials" was first proposed by Yaghi *et al.* in 2002, with the aim of developing new materials that share the same topology but differ in the size of the building blocks (linkers), directly impacting the cell parameters of the crystal structure. This expansion in the network is intended to increase pore sizes and surface areas, or to introduce specific affinities by incorporating pending functional groups, while maintaining the synthetic conditions of the original MOF.[66]

Expanding linkers does not always result in increased surface areas; in fact, it can sometimes lead to a reduction in pore size due to the formation of interpenetrated structures.[66] Several synthetic strategies can reduce interpenetration,[67] such as controlling reaction time,[68]

USC UNIVERSIDADE DE SANTIAGO DE COMPOSTELA

the amount of protic solvents in the reaction,[69] using dilute conditions,[70] incorporating bulky substituents,[63] and managing π-stacking interactions.[71]

Figure 1-9 shows the isoreticular series of Zr-based MOFs, starting with UiO-66, one of the first series of MOFs explored using the approach of reticular chemistry.[17] This figure illustrates how the length of the linker increases in the order of UiO-66 < DUT-52 < UiO-67 < BUT-30 < UiO-68, due to the incorporation of longer conjugated systems such as a naphthalene in DUT-52, biphenyl in UiO-67, an alkyne between the biphenyl units in BUT-30, and a triphenyl in UiO-68. All these systems exhibit the same topology and consequently the same space group $Fm\bar{3}m$ (225), which translates to the same diffraction pattern as shown in Figure 1-8. However, there is a slight difference according to Bragg's law: there exists an inverse relationship between the d-spacing (closely related to the lattice parameter) and the diffraction angle. This means that MOFs with longer lattice parameters display diffraction patterns shifted to smaller angles.[72]

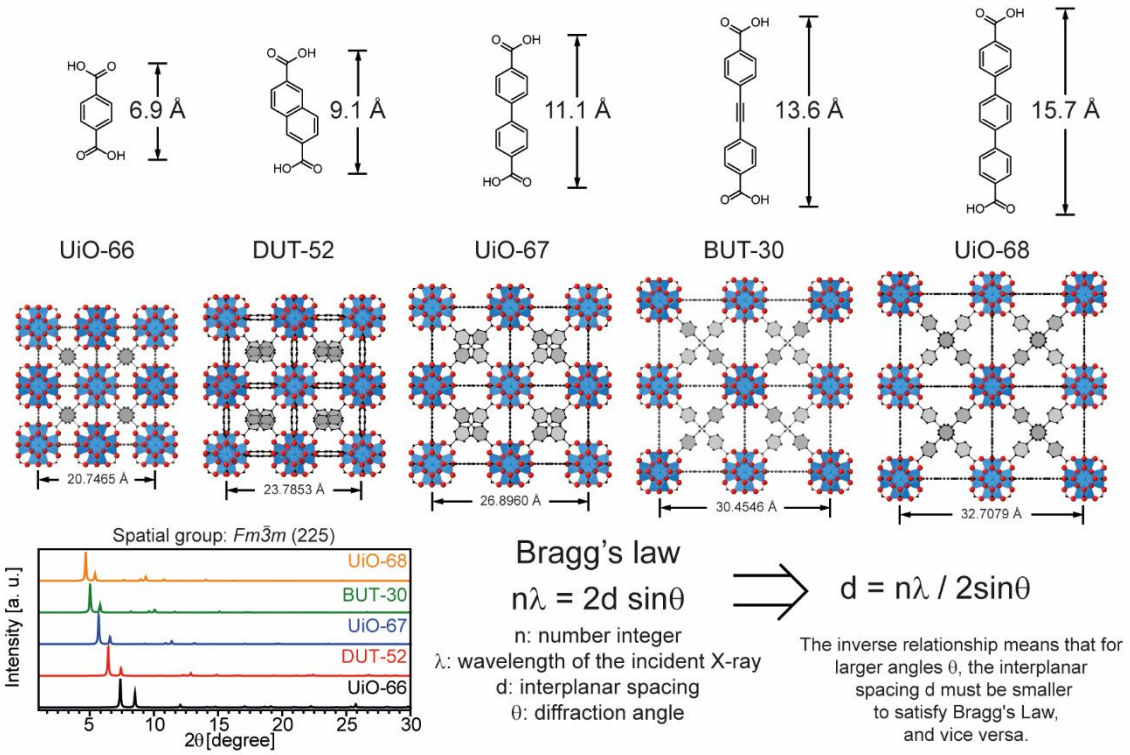

Figure 1-9. Scheme of isoreticular Zr-based MOFs increasing the linker length with the X-ray diffraction patter, showing the relationship between the lattice parameter and the diffracted angle according to Bragg's law.

1.1.6. Synthetic approaches of MOFs

As previously defined, MOFs are crystalline materials synthesized by the coordination of polytopic ligands with metal ions or metal clusters.[73] The resulted materials comes for a crystallization process that requires reversible bond formation in order to correct the defects and prevent the formation of amorphous products.[74]

The challenge of crystallizing materials increases with the bond energy between the building units. Crystal formation is relatively straightforward when weak interactions are involved, such as in solid CO_2, where van der Waals forces with energies between 0.1-10 kJ/mol

predominate, or in the crystallization of ice, where hydrogen bonds with energies between 10 and 50 kJ/mol are involved.[75] Similarly, the crystallization of metal-bipyridine complexes is relatively simple due to the free electron pair on the nitrogen atom, which enables bipyridine to act as a Lewis base[76] (Figure 1-10).

On other hand the crystallization of MOFs and COFs requires the formation of strong covalent bonds where the atoms involved share electrons.[77] Most MOFs are constructed using carboxylate ligands, which form metal-oxygen bonds. The crystallization of MOFs typically begins with the deprotonation of these ligands, where the rate of this deprotonation process plays a crucial role in determining the crystallization kinetics and the quality of the resulting MOF crystals.[78,79]

The use of solvents such as *N*,*N*-dimethylformamide (DMF) or *N*,*N*-dimethylacetamide (DMA), which can release amines under solvothermal conditions due to heating,[80] facilitates the deprotonation of ligands and promotes the formation of strong metal-oxygen bonds.

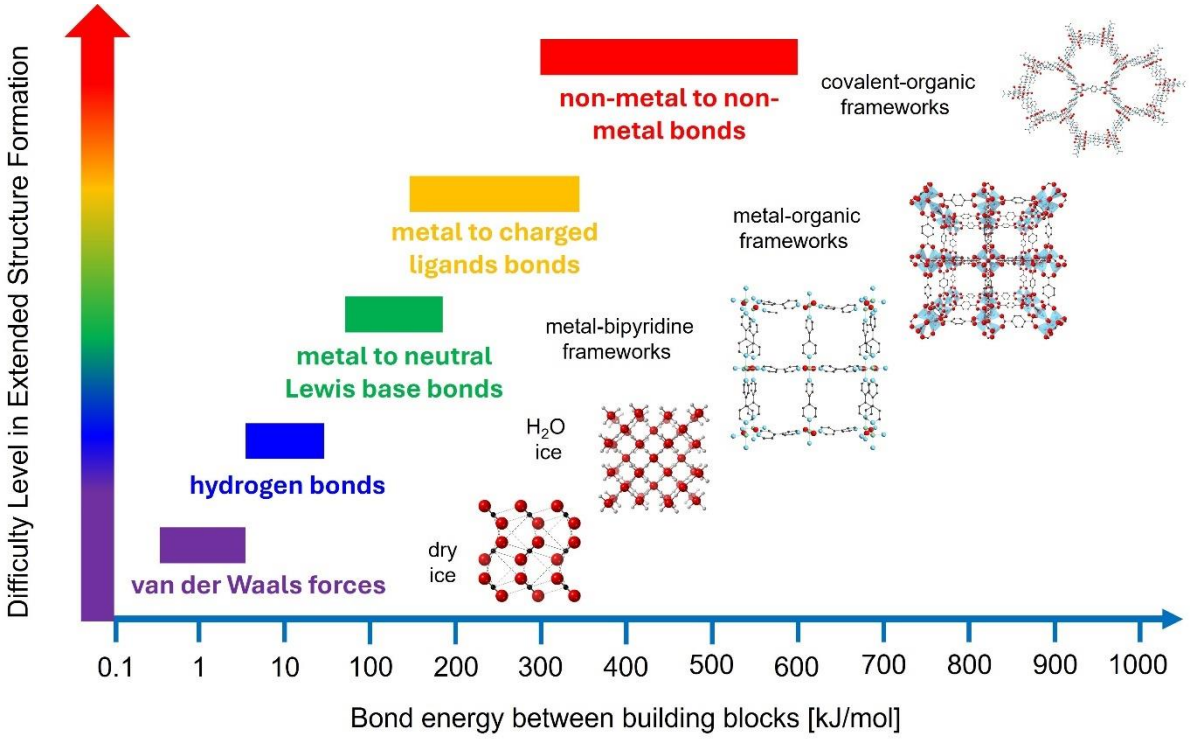

Figure 1-10. Schematic representation illustrating the difficulty of crystallizing a material in relation to the bond energy between the building blocks.

In the literature, numerous synthetic methodologies are described for the synthesis of both established and novel MOFs. Most of these methodologies share a common principle: the reaction between a metal salt and an organic linker, typically involving the addition of a modulating agent and the use of a solvent. An energy source is also applied to help the reactants overcome the activation energy needed to form the desired MOF.

The first well-known MOFs, MOF-5 and HKUST-1,[14,15] were synthesized without the use of any modulators or additional energy sources (both at room temperature); both were formed at room temperature by simply dissolving the metal salts and mixing them with their

corresponding linkers in solution. However, not all MOFs can be synthesized this way. To obtain well-defined or novel MOFs with specific characteristics suited to their intended applications, it is necessary to control various physical and chemical parameters during synthesis.

Physical factors such as the temperature,[81] pressure[82] or even the gravitational forces[83] at which the reaction occurs can directly impact the physicochemical properties of the resulting MOFs, including surface area, crystalline phase, and crystal size.

The primary chemical factors to consider during MOFs synthesis include the choice of metal source,[84] concentration of reagents,[85] solvent,[86] use of modulators,[87] and pH.[88] Each of these factors can significantly influence the outcome of the synthesis, leading to markedly different results.

The effects of each parameter can be explained by various theoretical models. Some effects result from synergistic interactions between multiple parameters. For example, in the context of metal sources, the counter-ion can influence the pH of the reaction medium[89] or form 1D chains by chelating the SBUs.[90]

The concentration of reagents significantly affects crystal size. Higher concentrations lead to the formation of numerous nucleation sites, resulting in a larger number of smaller crystals. Conversely, lower concentrations reduce the nucleation rate, resulting in fewer but larger crystals.[91]

Solvents play roles beyond merely dissolving the precursors for synthesis. They can also deprotonate organic ligands or coordinate with metal ions during the formation of SBUs.[92]

Modulators are crucial not only for controlling crystal size, ranging from nano to microcrystals, but also for competing with ligands to form missing linker defects, enhancing crystallinity, or facilitating the synthesis of different polymorphs.[93]

The pH of the reaction medium is particularly important, especially for high-valence metals (≥3). At higher pH levels, these metal ions can form oxides or hydroxides, which may dominate the reaction environment, sometimes even at acidic pH.[94]

When synthesizing new or known MOFs for a specific application, it is essential to consider not only the physical and chemical parameters but also the precise methodology for mixing reagents and achieving the required synthesis conditions. Typically, the crystallization of MOFs needs heating, which can be conducted using a standard hot plate or within sealed autoclave reactors. The use of solvents with high boiling points, such as DMF, (~153 °C), in these reactors facilitates the crystallization process by generating elevated pressures that promote the formation of the desired crystalline structure.

Figure 1-11 presents some of the most employed synthetic strategies for the preparation of MOFs, in addition to the conventional methods conducted at room temperature, elevated temperatures, or under solvothermal conditions.

Apart from the aforementioned parameters, the method of adding MOF precursors is crucial. The synthesis in fluidic devices is an innovative approach currently under extensive

USC DE COMPOSTELA

study, offering the advantage of producing materials in a continuous flow. This method considers additional parameters such as channel dimensions, precursor addition rates, channel geometries, and even the configuration of the connection points.[95] Typically, due to the dimensions of the channels, the products obtained using this synthetic approach are in the form of micro- or nanocrystals. However, it has been demonstrated that single crystals measuring millimeters can be grown in microchannels, with precise control over the crystal morphology.[96]

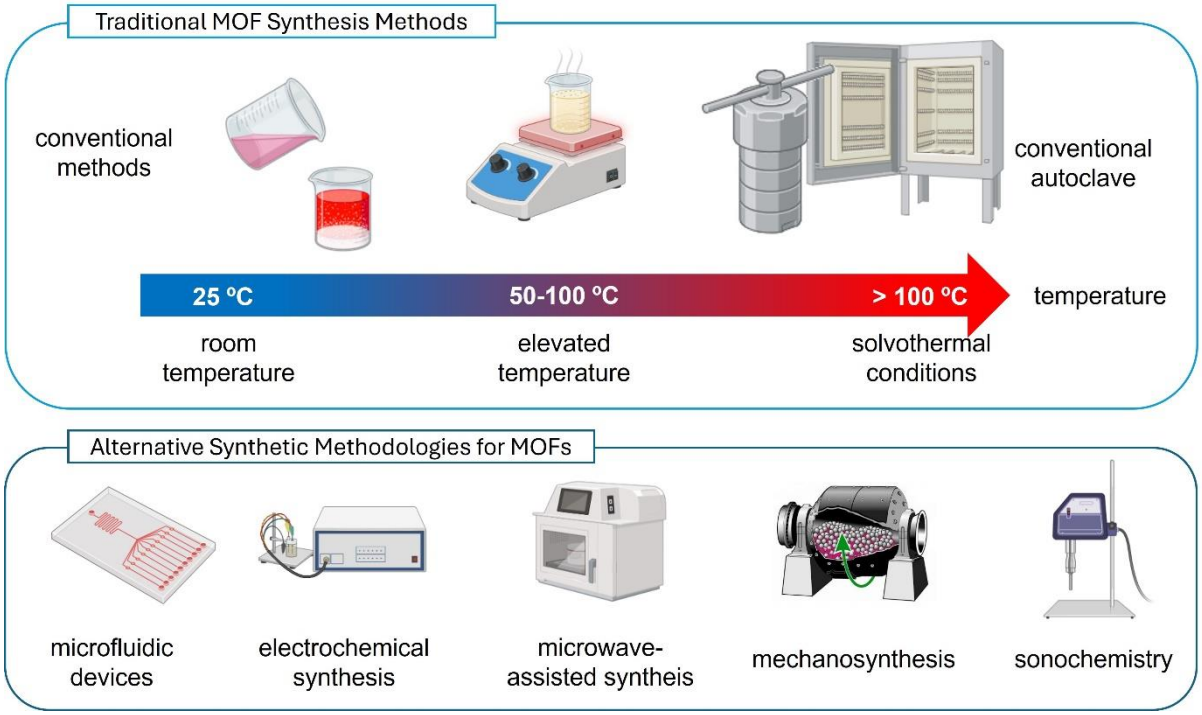

Figure 1-11. Overview of conventional MOF synthesis methods organized by temperature, including various alternative approaches.

The electrochemical synthesis of MOFs encompasses several variants, including electrode surface nucleation, indirect bipolar deposition, and electrophoretic deposition. The first two methods involve the direct formation of MOFs within the system, whereas electrophoretic deposition requires the pre-synthesis of the MOF followed by its deposition. In electrophoretic deposition, the polarization of two electrodes generates electric field lines, which drive the colloidal MOF particles towards the electrode with a surface charge opposite to that of the MOF particles.[97]

Microwave-assisted synthesis has become a widely adopted approach, not only for the fabrication of MOFs but also for a broad range of materials, including nanomaterials and in organic synthesis, among others. This popularity is due to several factors, particularly the significantly reduced reaction times, which contribute to categorizing this technique as a green chemistry approach by minimizing energy consumption. Microwave heating typically occurs through the interaction of electromagnetic radiation with the dipole moments of molecules, causing them to rotate and align with the rapidly oscillating electric field of the microwaves.[98] Additional advantages of the microwave synthesis approach, beyond the faster reaction times and corresponding reduction in energy consumption, include the reduction in crystal size, enhanced control over morphology, and increases in surface area.[99]

Mechanosynthesis is another green approach, particularly in terms of solvent reduction. In this method, the reactants are mixed as powders in a ball mill or directly in an agate mortar until the desired product is formed.[100] Apart from the solvent-free conditions, other variants of mechanosynthesis include liquid-assisted grinding or ion- and liquid-assisted grinding, aimed at addressing some limitations of the technique, such as material amorphization, reduction of potential impurities from the milling reactor, and achieving precise phase control.[101]

Sonochemistry is a synthetic approach that utilizes ultrasound as an energy source, reducing reaction times and enhancing energy efficiency. This method is based on the phenomenon of acoustic cavitation, which involves the sequential formation, growth, and collapse of bubbles in what are known as "hot spots". These hot spots can reach temperatures of 5000 °C, pressures of 1000 atm, and heating/cooling rates exceeding 10^{10} K/s.[102]

1.1.7. Applications of MOFs across various fields

The broad range of applications of MOFs across various fields is largely due to their diverse chemical composition. This compositional diversity allows for the fine-tuning of MOF structures to meet specific needs. Additionally, their intrinsic properties, such as crystallinity, ordered frameworks, and porous structures, further enhance their suitability for a wide array of research areas.[103] Figure 1-12 shows a schematic representation of the diverse fields where MOFs are employed.

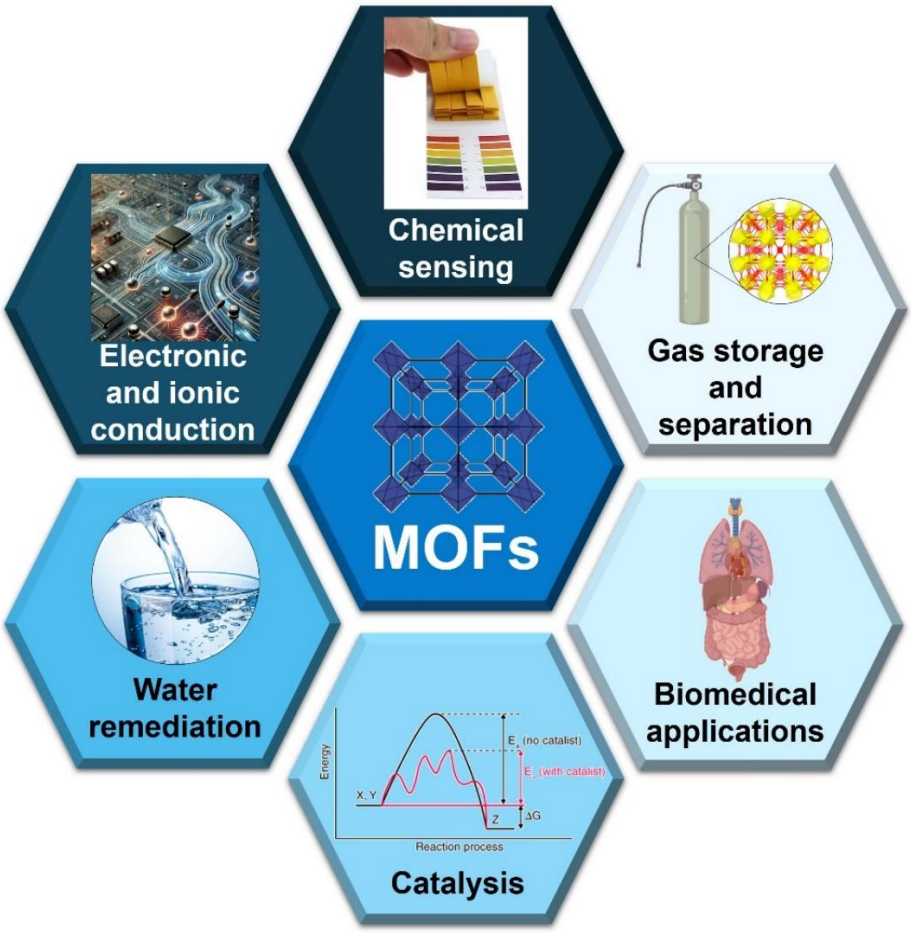

Figure 1-12. Research fields where MOFs are applied.

Gas adsorption represents a primary application of MOFs, attributed to their exceptionally high surface area. The synergistic adsorption capacities of the SBUs and organic linkers, as demonstrated by Yaghi *et al.* in 2005,[104] further enhance this capability. The adsorption properties of MOFs can be precisely tailored by modifying the topology with face-transitive nets, enabling selective permeability to specific gases. This selective permeability allows MOFs to be effectively employed for the separation and storage of targeted gases.[58]

Gas adsorption is a broad field encompassing applications such as CO_2 capture, aimed at reducing carbon footprints by sequestering CO_2 within MOFs and subsequently revalorizing the captured CO_2.[105] Additionally, MOFs are utilized in energy storage, particularly for storing challenging and highly compressible gases like H_2, which is regarded as a potential fuel of the future[106] being possible to separate it from its isotope deuterium gas.[107] Furthermore, MOFs can selectively capture, and separate various hydrocarbon gases present in natural gas.[108]

Chemical sensing is another area where the synergy between the inorganic and organic components of MOFs can be effectively exploited. Chemical sensors encompass a broad range of technologies, with diverse modes of response, including electrochemical, electronic, electromechanical, and optical, among others. These sensors are capable of detecting a variety of substances, such as metals, specific analytes, enzymes, bacteria, temperature changes, chemical reactions, vapors, water, and gases, among others.[109]

Given the current energy challenges, the development of new materials with capabilities for energy storage and conversion has become essential. In this context, MOFs offer significant advantages over other materials, including their high porosity, versatile functionalities, diverse structures, and tunable chemical composition.[110] These properties make MOFs particularly suitable for use in the fabrication of electrodes for batteries, fuel cells, and other energy-related applications. By leveraging the organized structure of MOFs and carefully selecting appropriate linkers and metals to enhance charge transport within spatially confined environments, it is possible to replace traditional oxide or graphite-based materials with MOFs. These materials demonstrate high performance directly attributable to their superior capacity, safety, power density, thermal stability, and cycle life in battery applications. Furthermore, the high surface areas inherent to MOFs provide sufficient Li^+ storage active sites, thereby ensuring a high specific energy for the electrode.[111]

Water remediation is another key area where MOFs have shown significant potential. Their tunable pore sizes make them highly effective for capturing large pollutants, while their adjustable compositions allow for selective adsorption of specific compounds or heavy metals.[112] Various pollutants, including antibiotics,[113] dyes,[114] heavy metals,[115] and pesticides,[116] can be effectively removed from water using MOFs as adsorbents. These MOFs can be reused after multiple cycles, maintaining their efficiency.

In catalysis, MOFs are excellent candidates for heterogeneous catalysis due to their extremely high surface areas (with some exceeding 7000 m^2/g).[6–9] The presence of metal clusters with Lewis acid character makes them highly effective catalysts. Additionally, their tunable properties, such as the ability to induce missing linker defects,[117] further enhance catalytic performance compared to fully coordinated metal nodes.[60]

USC UNIVERSIDADE DE SANTIAGO DE COMPOSTELA

MOFs exhibit diverse applications in biomedicine, including their use as therapeutic agents due to their capacity to target and kill malignant cells under specific stimuli.[118] For instance, Hf-based MOFs can generate reactive oxygen species (ROS) when exposed to X-ray stimuli,[119,120] while porphyrinic systems can produce ROS under visible light stimuli.[121]

Additionally, MOFs can function as drug delivery systems by encapsulating therapeutic agents within their porous structures, thereby overcoming challenges related to cell membrane penetration, as well as solubility or charge issues of the cargo. Their ease of functionalization further enhances compatibility with surface modifications, improving their effectiveness in biomedical applications.[122] Additionally, MOFs have been widely used for drug encapsulation, as they allow for both synthesis-based and post-synthetic loading approaches.[123]

USC
UNIVERSIDADE DE SANTIAGO DE COMPOSTELA

1.2. Zr-BASED MOFs

1.2.1. The $Zr_6(\mu_3\text{-}O)_4(\mu_3\text{-}OH)_4$ secondary building unit

Zirconium-based MOFs are among the most extensively studied MOF families, primarily due to their remarkable chemical, structural, and thermal stability, which distinguishes them from many other MOF families.[124]

As previously mentioned, Zr-based MOFs were first reported in 2008 by Lillerud *et al.*,[17] following the earlier synthesis of their SBU with twelve methacrylate molecules by Schubert and Kickelbick in 1996.[21] The discovery of the UiO-family of MOFs marked the beginning of the synthesis of highly connected MOFs, characterized by twelve dicarboxylate molecules per SBU.

The intrinsic properties of the material are attributed to its SBU, which consists of six Zr atoms arranged in an octahedral configuration, capped by alternating μ_3-O and μ_3-OH groups. When the MOF is heated to approximately 250–300 °C, this Zr_6-oxo cluster undergoes dehydroxylation, losing two water molecules. This thermal treatment induces changes in the local symmetry,[125] resulting in a reduction of the coordination number from eight, where the geometry is square antiprismatic, to seven, leading to a distorted monocapped trigonal prismatic geometry,[126] as illustrated in Figure 1-13.

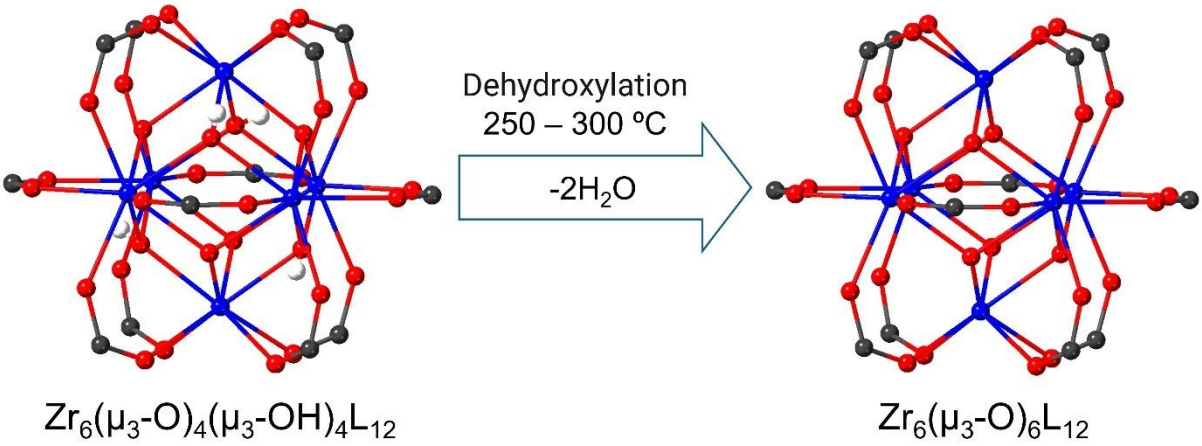

Figure 1-13. $Zr_6(\mu_3\text{-}O)_4(\mu_3\text{-}OH)_4$ SBU and its transformation to the dehydroxylated form.

The $Zr_6(\mu_3\text{-}O)_4(\mu_3\text{-}OH)_4$ SBU might initially be considered inert due to the strong Zr-O bonds; however, it is, in fact, reactive. For instance, Wenbin Lin *et al.* demonstrated the insertion of Co into the Zr_6-oxo cluster in UiO-68 to catalyze hydrogenation and hydroboration reactions.[29] This insertion requires the deprotonation of one of the μ_3-OH bridges using a strong base, nBuLi, as illustrated in Figure 1-14. The formation of the Co-O bond was confirmed using extended X-ray absorption fine structure (EXAFS) and transmission electron microscopy (TEM) with energy-dispersive X-ray (EDX) analysis.

Additionally, other metalations of the cluster have been reported, such as Zr incorporation into MOF-808 for CO_2 hydrogenation.[127]

USC UNIVERSIDADE DE SANTIAGO DE COMPOSTELA

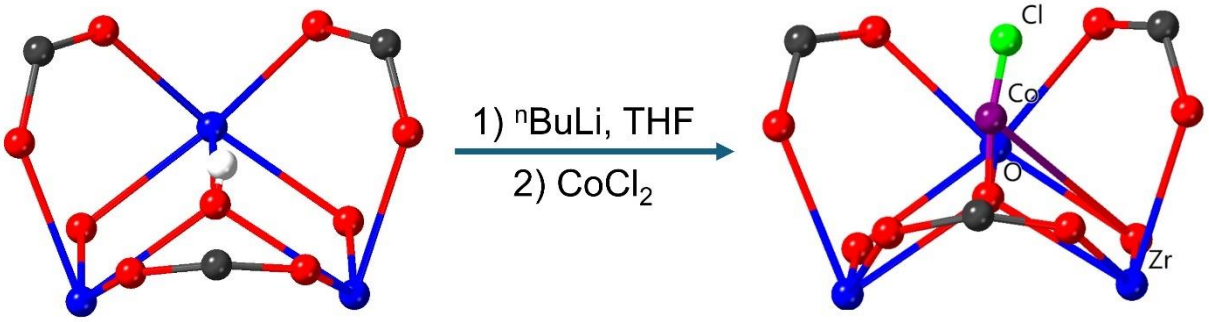

Figure 1-14. Co-insertion into. $Zr_6(\mu_3\text{-}O)_4(\mu_3\text{-}OH)_4$ SBU.

This cluster can also dissolve under highly basic conditions (pH ≥ 12),[128] a property frequently utilized for linker quantification by nuclear magnetic resonance (NMR). Additionally, it can dissolve in the presence of certain anions, such as carbonate, due to the formation of the highly water-soluble anion $[Zr_2(OH)_2(CO_3)_4]^{2-}$, as shown in Equation 1.

$$Zr_6O_4(OH)_4(BDC)_6 + 18HCO_3^- \rightarrow 3[Zr_2(OH)_2(CO_3)_4]^{2-} + 8H_2O + 6CO_2 + 6BDC^{2-}$$

(Eq. 1)

This digestion approach has been demonstrated with UiO-66, which contains terephthalate molecules, as well as derivatives with functional groups on the benzene ring, such as -COOH, naphthalene, and Br. It has also been applied to PCN-224, which contains tetraporphyrin ligands, and to other anions besides carbonate, including bicarbonate and citrate, and the regeneration of the MOFs is possible by simply adding more modulators (such as acetic or benzoic acid) to the dried digestion product, which preserves the original surface area values.[129]

1.2.2. Structural defects in UiO-family Zr-based MOFs

The engineering of defects in MOFs has been extensively studied due to the enhanced properties that these defects can impart compared to the pristine MOFs.[130–132] These defects are characterized as sites where the regular periodic arrangement of atoms or ions in the crystalline parent framework is locally disrupted, either due to the absence of atoms or ions or their incorrect displacement.[133]

There are various types of defects, such as dislocations in polycrystalline systems, atomic vacancies, compositional heterogeneity or vacancies within the crystal, and disorder arising from different orientations of the building units.

In Zr-based MOFs, the most extensively studied defects are missing clusters or linker defects, as these enhance catalytic properties by increasing the accessibility of the metal centers, which are not fully coordinated. This increased accessibility facilitates interactions with substrates, thereby improving the efficiency of the desired reactions.[60]

MOFs are also well-known for their thermal insulating properties.[134–136] The introduction of defects in these materials can lead to either an increase or decrease in thermal conductivity. For instance, in the case of UiO-66 with an fcu topology (fully connected, 12-connected), the introduction of missing linker defects in the SBUs can alter the structure from a 12-connected fcu topology to an 8-connected bcu topology. This structural change significantly increases the

thermal conductivity in the y-axis direction, from 0.32 W/mK to 0.67 W/mK, while reducing it in the x and z-axis directions to 0.27 and 0.21 W/mK, respectively. This indicates that the missing linker defects induce the formation of an anisotropic UiO-66 structure.[137] In the case of missing cluster defects, both reo and scu topologies (Figure 1-15) exhibit a reduction in thermal conductivity, decreasing to 0.17 and 0.10 W/mK, respectively. This reduction is attributed to the removal of linkers, which decreases phonon scattering and thereby invalidates half of the heat transfer pathways.

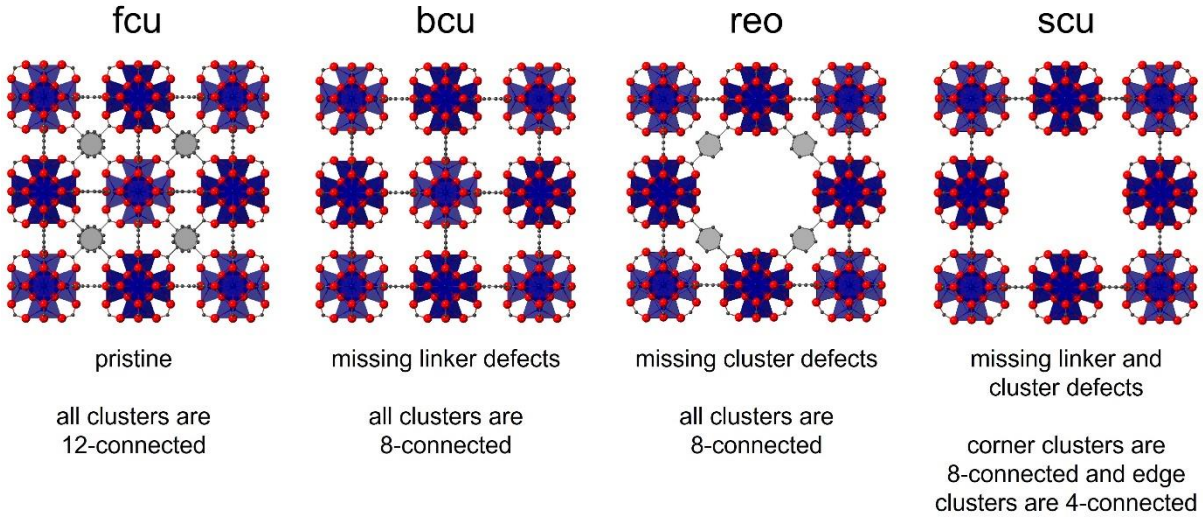

Figure 1-15. Schematic representation of missing linker and missing cluster defects in UiO-66, illustrating the resulting topologies in comparison with pristine UiO-66.

The presence of these defects can be observed in powder X-ray diffraction (PXRD) as a very broad reflection between 2° and 7° two-theta,[138] attributed to the formation of reo nanoregions. The formation of a long-range-ordered reo phase is evidenced by two superlattice reflections (100) and (110) at 4.4° and 6.0° two-theta,[139] as shown in Figure 1-16.

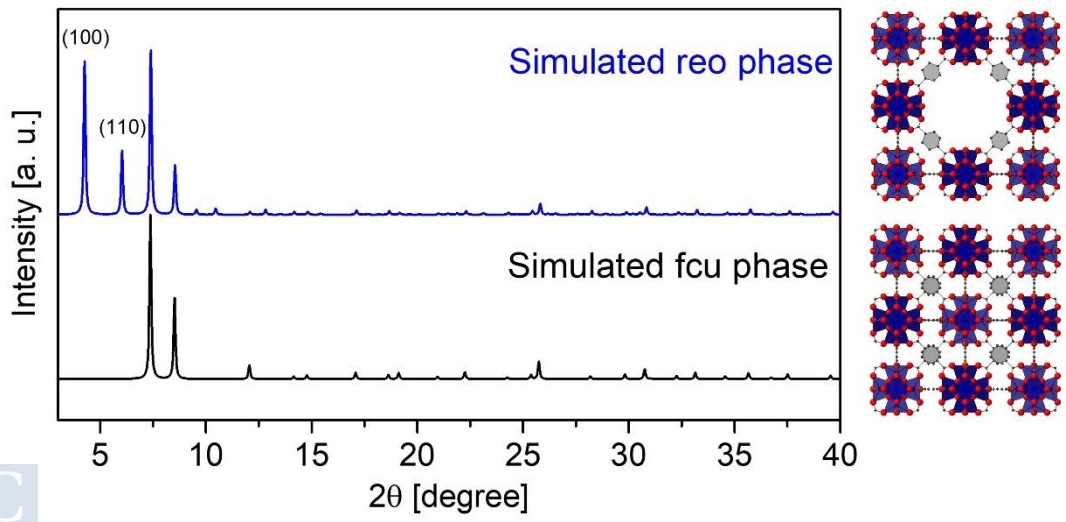

USC UNIVERSIDADE DE SANTIAGO DE COMPOSTELA

Figure 1-16. PXRD pattern of defective reo phase and non-defective fcu phase of UiO-66.

The presence of these defects can also be observed by normalizing the thermogravimetric analysis (TGA) to 100% using the inorganic residue (6 formula units of ZrO_2) and calculating the theoretical mass of the highly connected cluster $Zr_6(\mu_3\text{-}O)_4(\mu_3\text{-}OH)_4(BDC)_6$, as calculated by Valenzano *et al.* If the plateau at the beginning of the thermogram is below the theoretical line, it indicates that the MOF contains missing linker defects.[125]

In addition to PXRD and TGA, structural defects have a direct impact on the adsorption properties of MOFs. For instance, the fcu-phase of UiO-66 exhibits a theoretical N_2 uptake of approximately 150 cm^3/g, whereas the reo-phase shows a significantly higher N_2 uptake of around 300 cm^3/g. This difference is attributed to the presence of larger pores, measuring 1.6 nm in diameter in the reo-phase, compared to the bimodal pore size distribution of the fcu-phase, which features pores of 0.85 and 1.1 nm,[60] as illustrated in Figure 1-17.

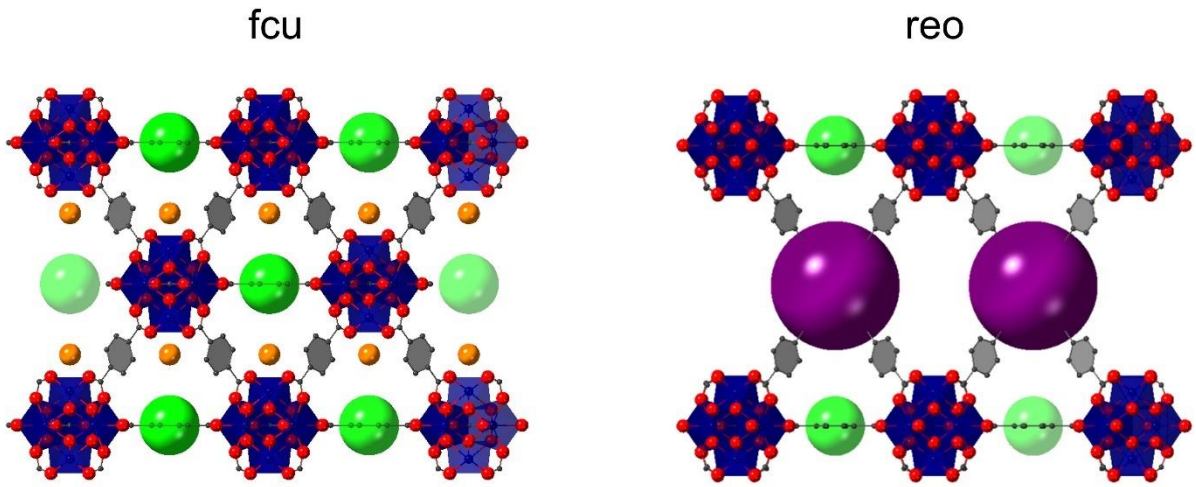

Figure 1-17. Schematic illustration of the varying pore sizes in the fcu and reo phases of UiO-66.

Induction of these defects can be achieved by altering synthetic parameters during the synthesis process, such as temperature,[117] linker/metal or metal/modulator ratios,[60] and the acidity of the modulator.[138] However, the manipulation of this periodic disorder has been refined to enable systematic control over the chemical composition and the growth of correlated defect domains.[140–143]

1.2.3. Compositional and geometrical variants Zr-oxo clusters

The typical Zr hexanuclear SBU $Zr_6(\mu_3\text{-}O)_4(\mu_3\text{-}OH)_4$ has evolved significantly over time in MOFs.[144] This Zr SBU, characterized by six Zr atoms arranged in an octahedral geometry, exhibits a wide range of connectivities, including 4-connected, 5-connected, 6-connected, 8-connected, 9-connected, 10-connected, 11-connected, 12-connected, and even 14-connected SBUs, surpassing the previously assumed maximum of twelve coordination sites that an SBU can accommodate.

Another important consideration is that certain connectivities, due to the spatial arrangement of their linkers, can exhibit isomerism, as observed in the 4-connected, 6-connected, 8-connected, and 9-connected SBUs, as illustrated in Figure 1-18.

USC UNIVERSIDADE DE SANTIAGO DE COMPOSTELA

Compositional changes involve variations in the number of metallic atoms within the SBU. This is achievable in Zr-based nodes, including configurations such as Zr_6, Zr_9 in two distinct arrangements, Zr_{12} in three different configurations, and Zr_{16}, as illustrated in Figure 1-18.

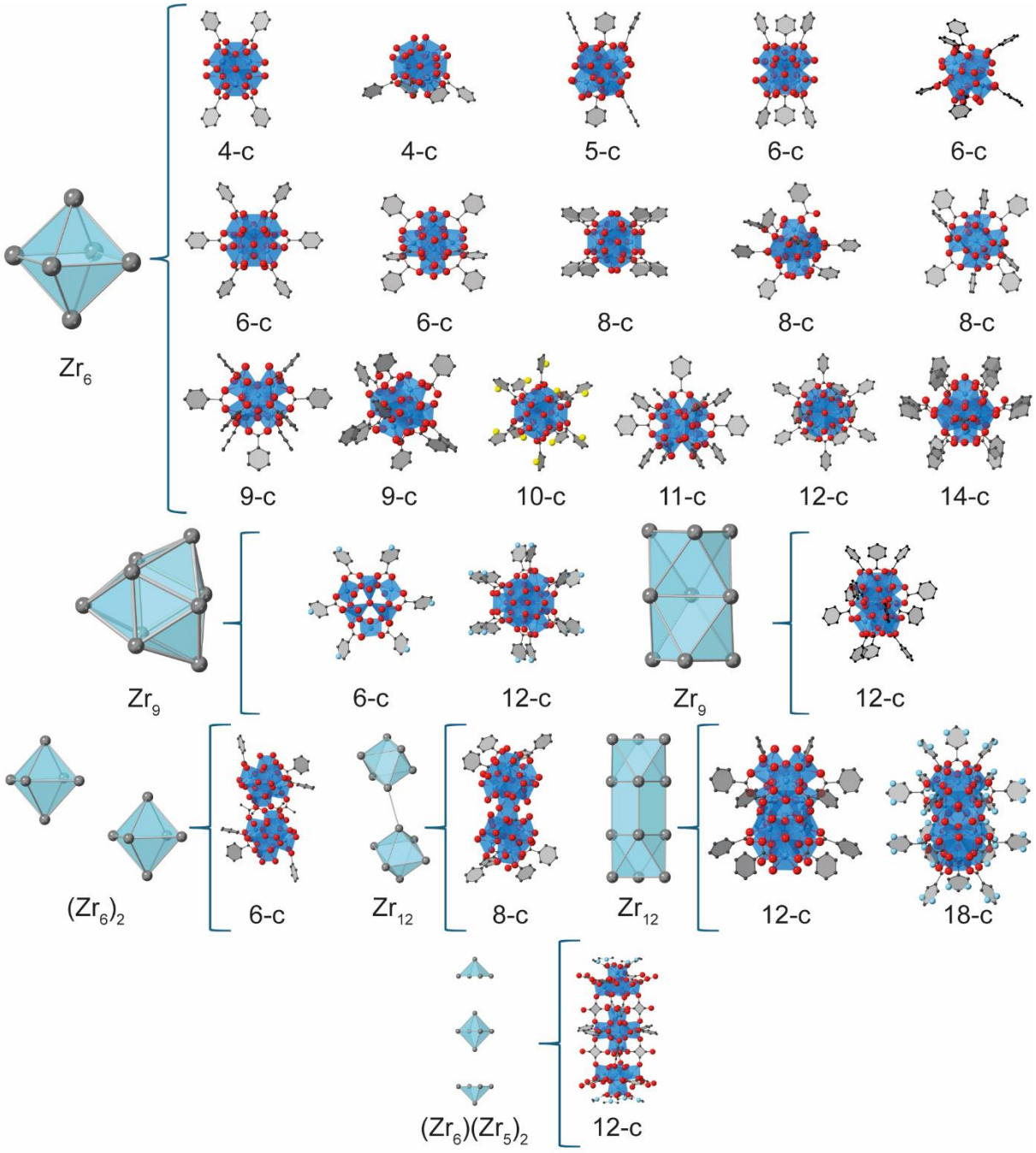

Figure 1-18. Schematic illustration of various spatial and compositional arrangements of Zr-based SBUs.

Figure 1-19 presents examples of Zr-SBUs with various reported connectivities. Notably, the hexanuclear Zr-SBU exhibits a wide range of connectivities, whereas the nonanuclear Zr cluster has been reported with only two types of connectivities: 6-connected and 12-connected. For the twelve-nuclear Zr-SBUs, the reported connectivities include 6-connected, 8-connected,

12-connected, and a less common 18-connected configuration. Additionally, the non-standard Zr_{16} SBU has been observed with a twelve-connected configuration.

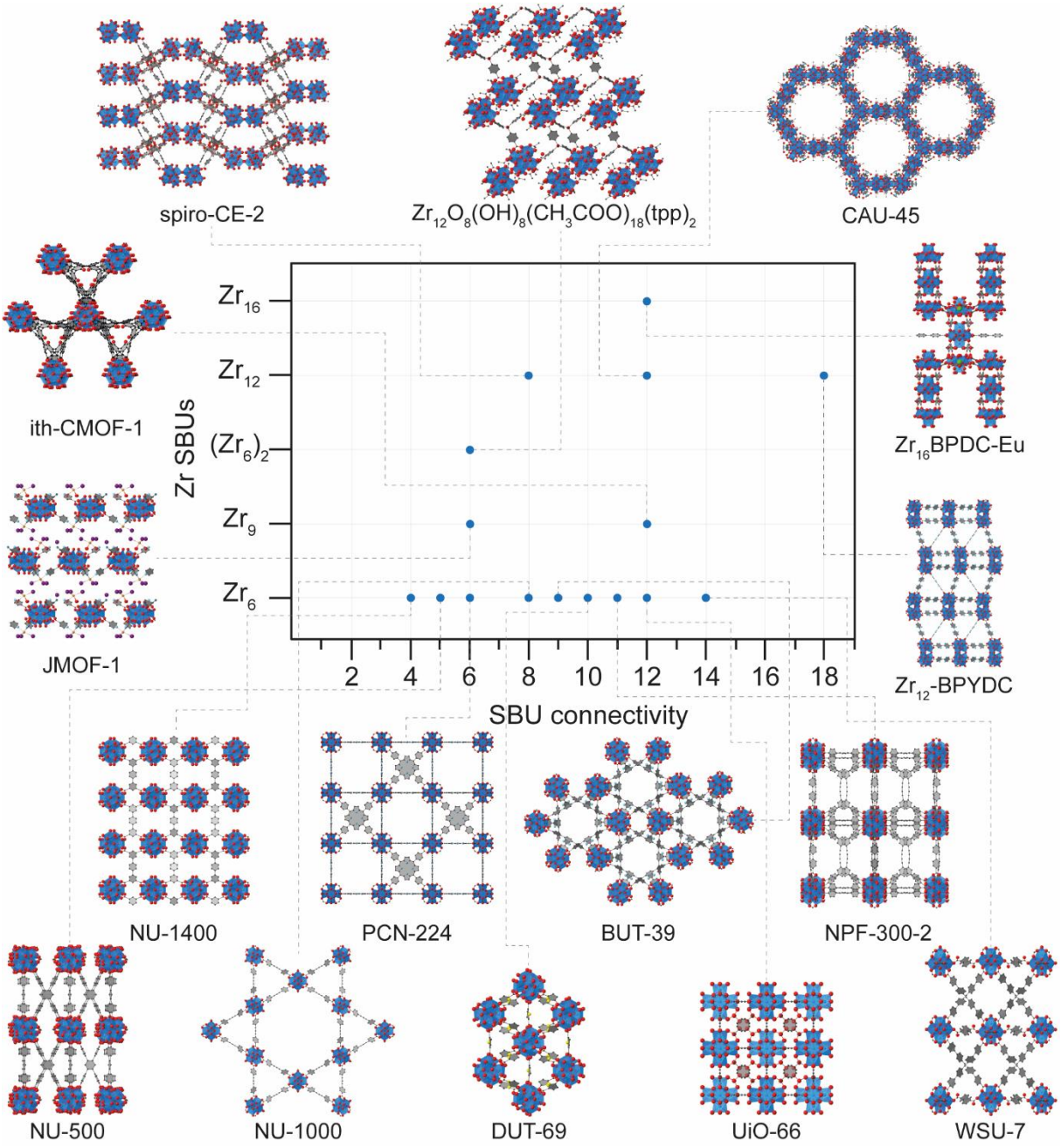

Figure 1-19. Diagram of various Zr-SBUs along with their corresponding connectivities and representative examples.

The low-connectivity Zr_6-node, which is 4-connected, exhibits two distinct spatial orientations as is illustrated in Figure 1-18. Examples of structures with these orientations include NU-1400[145] and PCN-992[146] with planar and rectangular pyramidal geometries respectively.

The 5-connected Zr_6 node is one of the rarest nodes in the literature, primarily due to the asymmetry introduced by its pentahedral geometry, as exemplified in NU-500.[147]

One of the most common and extensively studied connectivities in Zr-based MOFs is the 6-connected Zr_6-node, largely due to the beneficial properties imparted by missing linker defects. This connectivity manifests in various geometries, such as the trigonal antiprism in MOF-808,[26] the distorted trigonal prism in MOF-892 (featuring three bridging bidentate and three monodentate carboxylates),[148] the hexagonal geometry in PCN-224,[35] and the trigonal prism in DUT-84.[27]

The 8-connected Zr_6 node also exhibits various geometries, including the cuboid shape in NU-1000,[38] the distorted cube-like geometry in MOF-893 with five bridging bidentate and three monodentate carboxylates,[148] and a rare distorted gyrobifastigium-like geometry in CZMOF-2.[149]

Another Zr_6-node with low symmetry is the 9-connected cluster, found in BUT-39 with elongated square pyramidal geometry, which is formed by tritopic T-shaped ligands.[150] A different arrangement with this connectivity is observed in BUT-46A with tricapped trigonal prismatic geometry, which is composed of hexatopic ligands.[151]

The 10-connected and 11-connected topologies are relatively uncommon. For the 10-connected topology, DUT-69 is the only documented example with elongated octahedral geometry, utilizing thiophenedicarboxylate ligands.[152] The 11-connected topology was achieved in the NPF-300-2 MOF, with a nido cuboctaheral geometry formed by a combination of eight tetratopic ligands, two ditopic triphenyl ligands, and one ditopic biphenyl ligand.[153]

The most well-known Zr_6-node is the 12-connected variant, which was the first to be discovered in UiO-66 and its isoreticular family, characterized by a cuboctahedral geometry.[17] Other examples of this node include MOF-525[32] and PCN-223,[34] both of which utilize tetratopic porphyrinic ligands.

For many years, it was believed that the Zr_6-node could coordinate a maximum of twelve ligands. However, in 2021, Zhang *et al.* successfully accommodated 14 ligands within this cluster, transforming WSU-5 into WSU-7. The original WSU-5 structure consisted of an 8-connected Zr_6-node with H_4ETTC tetratopic ligands. By adding six H_2NDC ditopic ligands, the researchers achieved an elongated hexagonal bipyramidal geometry in the resulting WSU-7.[154]

Transitioning from the Zr_6-node to the Zr_9-node, with the formula $Zr_9(\mu_3\text{-}O)_8(\mu_3\text{-}OH)_6$ (charge balanced by OH^- and coordination sites completed with H_2O), we observe a triaugmented triangular prism geometry that exhibits two different connectivities: 6-connected and 12-connected, corresponding to JMOF-1 and JMOF-2, which feature octahedral and hexagonal prismatic arrangements, respectively. The synthesis of these MOFs involves the preparation of an intermediate Zr_3-node, derived from the Cp_2ZrCl_2 precursor. This Zr_3-node is coordinated by isonicotinic acid and subsequently reacts with PbI_2 and $Pb(NO_3)_2$ to form JMOF-1 and JMOF-2, respectively.[155] With the same number of Zr atoms but featuring a double triangular antiprismatic geometry, the ith-CMOF-1 is able to form a 12-connected cluster.[156]

The Zr_{12}-node exhibits various structural variations. In some instances, two independent Zr_6-nodes are bridged by carboxylate groups from the modulator, as seen in the 6-connected $Zr_{12}O_8(OH)_8(CH_3COO)_{18}(tpp)_2$ MOF.[157] In other cases, the nodes share an oxygen atom between both clusters, such as in the 8-connected spiro-CE-2.[158] Additionally, all twelve Zr

atoms can be integrated into a single cluster, as observed in the 12-connected CAU-45[159] or the 18-connected Zr_{12}-BPYDC.[160]

One of the rarest Zr nodes reported in the literature is the Zr_{16} or $(Zr_5)_2$ Zr_6 node, with the formula $Zr_6(\mu_3\text{-}OH)_4(\mu_3\text{-}O)_4(COO)_4[Zr_5(\mu_3\text{-}OH)_4(\mu_2\text{-}O)_4(HSQA)_4)(DMF)_4]_2$ (SQA = squaric acid). In this structure, the Zr_6-node is bridged to two Zr_5-nodes, positioned above and below, by four SQA ligands on each side. While this cluster is 12-connected, it possesses 24 potential coordination sites.[161]

1.2.4. Porphyrinic Zr-based MOFs

The porphyrinic Zr-based MOFs are composed of the characteristic $Zr_6(\mu_3\text{-}O)_4(\mu_3\text{-}OH)_4$ cluster and a ligand featuring a porphyrinic macrocycle as the backbone, with chelating groups such as pyridine, imidazole, or carboxylic acids, which can be di-, tri-, tetra-, or octatopic.[162] These MOFs have been extensively studied due to the additional functionalities provided by the porphyrinic systems, such as the ability to generate ROS under visible light, making them suitable for biomedical applications, including photodynamic therapy (PDT).[163] Furthermore, the porphyrinic ring can be metallated with transition metals, enabling its use in catalytic applications, as well as in photoluminescence, sensing, and other related applications.[164]

One of the most commonly used porphyrinic ligands is tetrakis(4-carboxyphenyl)porphyrin, also known as TCPP, which, in combination with the hexanuclear Zr cluster, can form six distinct polymorphs with varying connectivities, as illustrated in Figure 1-20.

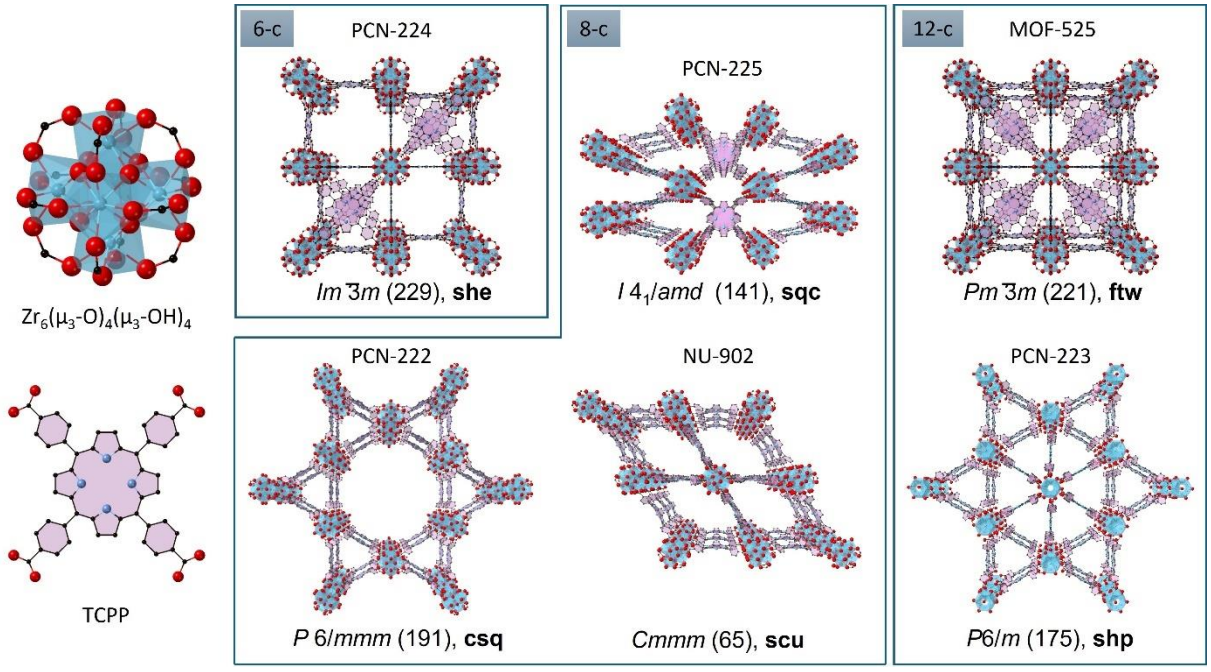

Figure 1-20. Polymorphs derived from $Zr_6(\mu_3\text{-}O)_4(\mu_3\text{-}OH)_4$ cluster and TCPP ligand.

The polymorphs of porphyrinic Zr-based MOFs can be classified based on the connectivity of their Zr_6-clusters. The 6-connected polymorph is known as PCN-224,[35] which exhibits a cubic structure with a she topology.

For the 8-connected structures, there are three polymorphs: PCN-222 (also known as MOF-545 or MMPF-6),[31–33] which has a hexagonal structure with csq topology; PCN-225,[36] which features a tetragonal structure with sqc topology; and NU-902,[37] which has an orthorhombic structure with scu topology.

The fully connected Zr_6-cluster is found in two polymorphs: MOF-525,[32] with a cubic structure and ftw topology, and PCN-223,[34] with a hexagonal structure and shp topology, where the cluster appears to consist of eighteen Zr atoms. However, this is due to the presence of three different orientations of the hexanuclear cluster. In each individual Zr_6-cluster, only eight carboxylate groups bridge adjacent Zr atoms, while the remaining four carboxylates chelate individual Zr atoms.

There are other porphyrinic Zr-based MOFs, but they are not classified as polymorphs due to the nature of their SBUs. For example, PCN-226 features infinite zigzag zirconium chains,[165] while PCN-228, PCN-229, and PCN-230 represent extended lattices similar to MOF-525.[166]

One "polymorph" in this group was PCN-221, which consisted of a $Zr_8O_6(CO_2)_{12}$ cluster arranged in a cubic configuration and coordinated by twelve TCPP ligands.[167] However, due to the unrealistic Zr-Zr distance of 2.69 Å, Lotsch *et al.* determined that this cluster actually comprised a Zr_6-oxo cluster arranged in four spatial orientations, which gives the appearance of an octanuclear cluster,[168] as illustrated in Figure 1-21.

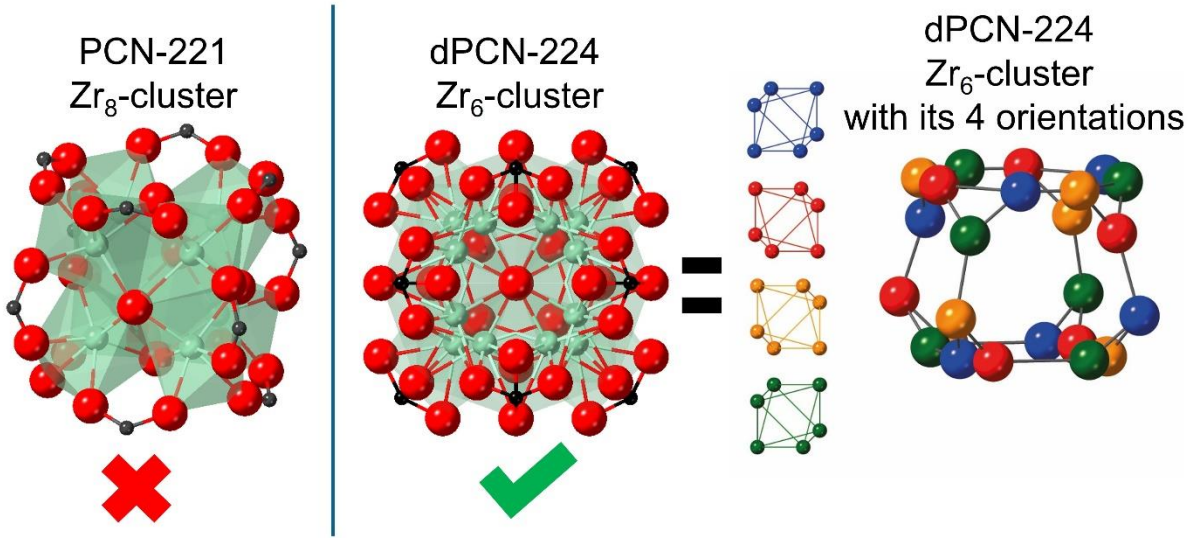

Figure 1-21. Zr_8-cluster of the proposed PCN-221 and the actual disordered Zr_6-cluster of dPCN-224, illustrating its four spatial orientations.

This new polymorph was designated as dPCN-224, a disordered variant of PCN-224. It exhibited a diffraction pattern identical to that of MOF-525, as both share the same space group and cell parameters, as shown in Figure 1-22. The differentiation between dPCN-224, PCN-224, and MOF-525 cannot be fully achieved through PXRD alone. It is essential to employ complementary characterization techniques such as TGA, solid state NMR, HRTEM, gas adsorption, and NMR to quantify the ligand content, detect structural defects, and evaluate their intrinsic properties.

USC
UNIVERSIDADE DE SANTIAGO DE COMPOSTELA

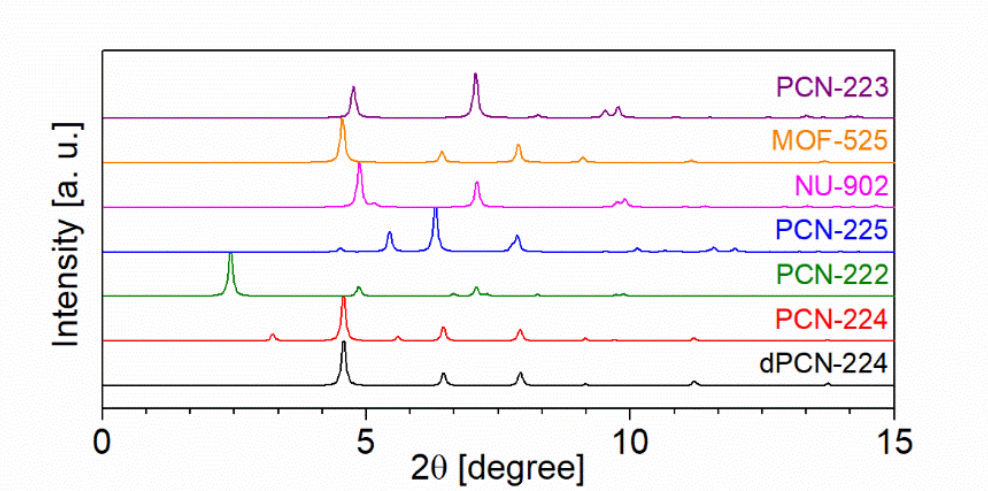

Figure 1-22. PXRD patterns of the polymorphs of porphyrinic Zr-based MOFs.

The synthesis of porphyrinic Zr-based MOFs typically involves solvothermal conditions using zirconium precursors such as $ZrCl_4$ or $ZrOCl_2$. However, this approach often leads to mixtures of polymorphs. To address this issue, the use of a preformed $Zr_6(\mu_3\text{-}O)_4(\mu_3\text{-}OH)_4(benzoate)_{12}$ cluster has been employed, which facilitates the formation of single phases. Depending on the modulator and synthetic conditions, either PCN-224[169] or PCN-222[170] can be obtained. PCN-224 is often referred to as the kinetic product, while PCN-222 is considered the thermodynamic product.[171]

A study conducted by Lotsch *et al.* demonstrated the influence of water during the synthesis of PCN-224. They found that when $ZrCl_4$ was kept in a glove box under anhydrous conditions, the reaction yielded very low amounts of product and resulted in mixtures of phases with minimal porosity. In contrast, allowing the dry precursor to equilibrate under laboratory conditions or adding controlled amounts of water facilitated the formation of single phases.[172]

In another study conducted by the same group, specific conditions for the preparation, purification, and activation of pure phases of PCN-222 and PCN-224 were distributed to ten different laboratories for an interlaboratory comparison. The results revealed significant variability: only one laboratory was able to obtain a pure phase of PCN-222, and three laboratories achieved a pure phase of PCN-224. Most laboratories, however, produced mixtures of PCN-222 and PCN-224, often including intermediates or PCN-225.[173]

1.2.5. Post-synthetic modification of Zr-based MOFs

One of the advantages of Zr-based MOFs is their high resistance to pH changes, corrosion, and temperature, making them suitable for post-synthetic modification. These modifications can enhance their compatibility and impart additional properties and functionalities, thereby improving their overall performance for specific applications compared to the bare MOF.[174]

In Zr-based MOFs, surface defects within the SBUs, such as missing linker defects, can be exploited to covalently attach molecules of interest, thereby enhancing or improving certain properties of the MOF. Additionally, the organic linkers can be chemically modified with specific functional groups that enable further reactions. Examples of post-synthetic modifications in Zr-based MOFs are illustrated in Figure 1-23.

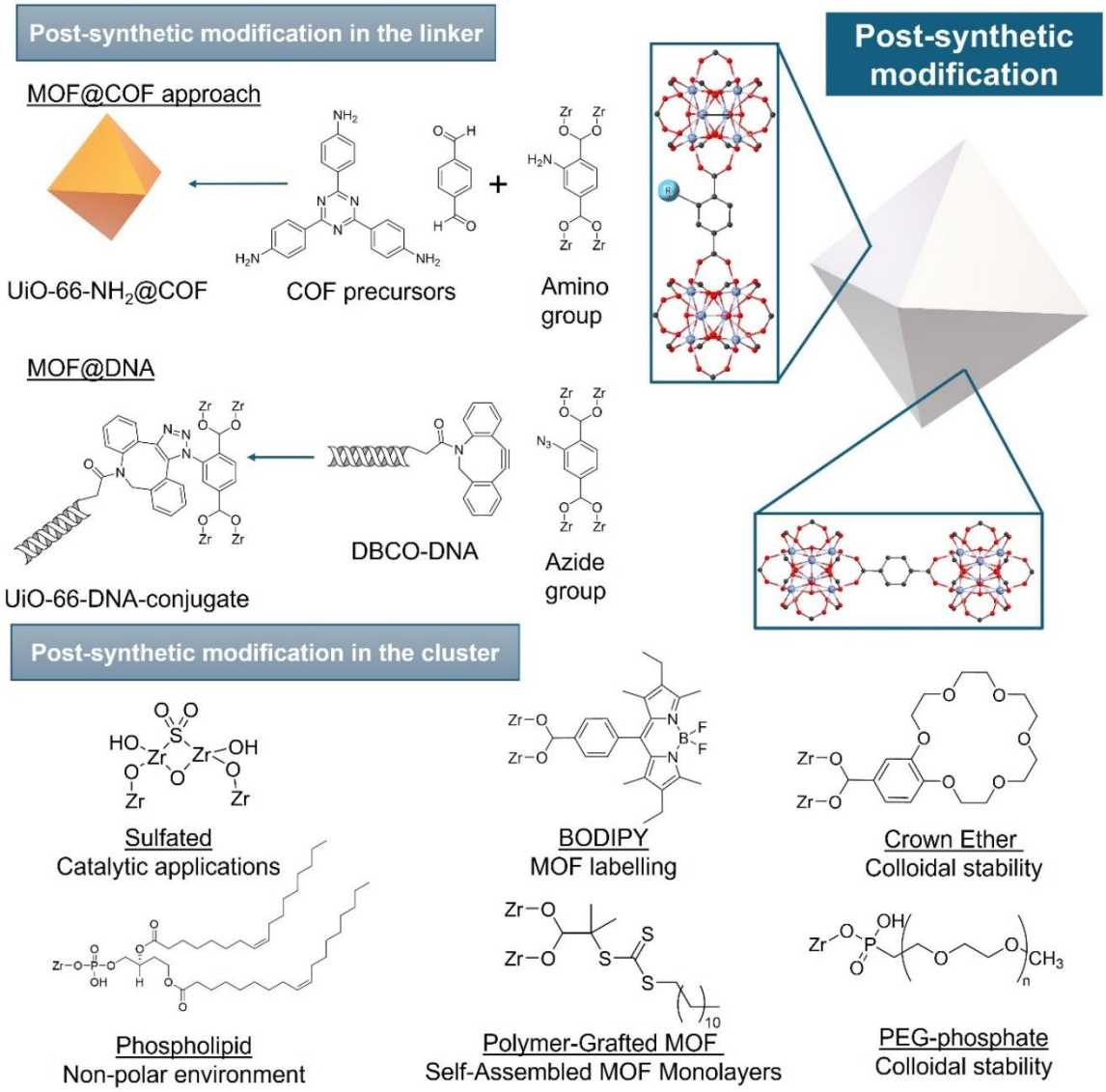

Figure 1-23. Examples of post-synthetic modification approaches used in Zr-based MOFs.

In post-synthetic modifications involving the linker, it is easy to leverage functional groups with high reactivity, such as amino groups (-NH_2), thiol groups (-SH), azide groups (-N_3), among others.

Amino groups, for instance, can readily react with carbonyl groups from aldehydes or ketones to form imine groups (-N=CH-), also known as Schiff bases. The formation of imine groups is common in COF chemistry and has been employed in the synthesis of COFs using UiO-66-NH_2 as a seed template.[175] This template can be dissolved by digesting the metallic SBU, resulting in a hollow COF structure.[176]

Another strategy to selectively functionalize the surface of Zr-based MOFs involves the use of linkers containing azide groups. These linkers can spontaneously react with alkyne groups (-C≡C-) to form triazole rings via click-chemistry reaction. The click-chemistry reaction, first described by Sharpless *et al.* in 2001,[177] led to Sharpless, Bertozzi, and Meldal being awarded the Nobel Prize in 2022 for this contribution. Utilizing this reaction with a ligand

containing an azide group, followed by reaction with dibenzocyclooctyne (DBCO) functionalized with deoxyribonucleic acid (DNA), resulted in increased stability and enhanced cellular uptake compared to unfunctionalized MOF particles.[178]

Regarding the functionalization of the Zr-cluster, it exhibits a special affinity for certain inorganic functional groups such as sulfates[179] (SO_4^{2-}) and phosphates[180] (PO_3^{4-}), which can be easily incorporated into organic molecules. Additionally, the Zr-cluster shows affinity for carboxylic groups (-COOH), which can effectively fill the missing linker defects on the surface of the MOF.

The incorporation of sulfate groups into the cluster can offer advantages, such as improved catalytic performance, but it also has potential drawbacks, like a reduction in surface area due to the small size of these molecules, which can easily infiltrate any porosity. However, in the case of NU-1000, its surface area is large enough that this decrease was considered negligible in the study conducted by Farha *et al.*[181] This research demonstrated that sulfate incorporation enhanced the proton donor ability, and the efficacy of this supported catalyst was proven in the stoichiometric and catalytic activation of benzene-d_6 and toluene.

The colloidal stability is sometimes one of the weaknesses of MOF, due to the lack of surface charge and the presence of non-fully connected metals and likers on the surface that tends to form agglomerates. To improve the colloidal stability in water, or organic solvents with different affinities the use of several capping agents has been studied.

One example of using molecules with phosphate groups was investigated by Mirkin *et al.*, who employed 1,2-dioleoyl-sn-glycero-3-phosphate (DOPA) with UiO-66 and its isoreticular analogues UiO-67 and BUT-30, enabling the transfer of these MOFs into chloroform, a non-polar solvent.[182] Another example of phosphate group functionalization was studied by Fairen-Jimenez *et al.*, where they used 5 kDa polyethylene glycol (PEG) chains with phosphate groups to directly modify a series of Zr-based MOFs, including UiO-66, MOF-808, NU-901, PCN-128, and PCN-222. This modification provided colloidal stability in water and phosphate-buffered saline (PBS) solutions, improved the dispersibility of lyophilized powders in water, and prevented the burst release of the loaded cargo, doxorubicin (DOXO), thereby reducing cytotoxicity.[170]

Regarding the enhancement of colloidal stability, Xing *et al.* developed a universal strategy to redisperse MOFs from powders into various solvents of differing polarities. They achieved this by coordinating carboxylate crown ether to the SBUs of different MOFs, including MIL-101-Cr, MIL-53-Fe, UiO-67, PCN-223, and HKUST-1. This modification enabled their redispersion in water, MeOH, DMF, CH_3CN, EtOH, $CHCl_3$, iPrOH, EtOAc, CH_2Cl_2, Et_2O, and toluene. Moreover, these functionalized MOFs demonstrated potential as effective phase-transfer catalysts and could be recycled for use in different solvents.[183]

In some cases, the fluorescence of the ligand can be advantageous, as seen with NU-1000[38] or PCN-224.[169] However, ligands such as terephthalic acid do not exhibit fluorescence, necessitating the use of dyes to enhance their functionality. Nevertheless, loading dyes into the pores of MOFs can present challenges, such as the window size limiting the incorporation of larger molecules and the potential for dye leakage in solution. Post-synthetic modification can

USC DE SANTIAGO DE COMPOSTELA

address these issues by functionalizing the Zr-clusters with fluorescent molecules, such as 4,4-difluoro-4-bora-3a,4a-diaza-s-indacene (BODIPY), which has an absorption peak at 524 nm. This dye can be modified with -COOH groups to covalently attach to the Zr-clusters, as demonstrated in the study by Cohen *et al.* They showed that UiO-66, MIL-88B-NH_2, and ZIF-8 could be labeled with BODIPY, and they measured the apparent binding constants for different ligands that detached BODIPY. Their findings indicated that HF completely digested the MOF, while citric acid and phenylphosphonic acid (PPA) had higher affinities for detaching BODIPY compared to other ligands, with phenylboronic acid showing the least affinity for removing BODIPY from the Zr-cluster.[184]

The functionalization of Zr-based MOFs with catechol-appended chain-transfer agents for the polymerization of methyl methacrylate has been investigated by Cohen *et al.* This approach enables the production of UiO-66 with grafted polymers on the surface, enhancing its dispersibility at very high concentrations. Notably, this method also yields highly ordered self-assembled structures that, upon drying, form centimeter-scale monolayers of particles.[185,186]

USC
UNIVERSIDADE DE SANTIAGO DE COMPOSTELA

1.3. METAL NANOPARTICLES

1.3.1. Optical properties of metal nanoparticles

The theoretical foundations for understanding the optical properties of metallic nanoparticles have been established since the early 1900s. However, these concepts have gained significant attention in the last two decades due to the wide range of potential applications, including sensing,[187] surface enhanced Raman spectroscopy (SERS),[188], signal modulation,[189] energy harvesting,[190] photocatalysis,[191] and more. The unique optical properties of metallic nanoparticles can be primarily tuned by altering their shape, size, dielectric environment and nature of the metal, making the design of anisotropic nanoparticles a powerful strategy for manipulating localized surface plasmon resonance (LSPR).[192]

The distinctive optical properties of metals, particularly noble metals such as Au, Ag, Pt, Pd, and Cu, arise from their dielectric function $\varepsilon(\omega)$. This function is closely related to the more familiar concept of the refractive index $n(\omega)$, which is expressed as $n(\omega) = \sqrt{\varepsilon(\omega)}$. Both properties are dependent on the natural frequency (ω) of light, defined as $\omega = \frac{2\pi c}{\lambda}$, where c represents the speed of light and λ is the wavelength. Consequently, the dielectric function is inherently wavelength-dependent, $\varepsilon(\lambda)$.

When a material is not transparent, as is the case with metals, its dielectric function is not a positive number like the refractive index, but rather a complex number, meaning it has both real and imaginary components.

Figure 1-24 illustrates the dielectric functions of Au, Ag and Cu spanning from the near UV (~250 nm) to the NIR (~950 nm), based on experimental data from Palik's *Handbook of Optical Constants of Solids*.[193] These graphs show that the real part of the dielectric function for both metals remains negative throughout the visible spectrum. This is a key characteristic of their optical properties and a primary reason for their use as plasmonic materials. The three metals Au, Ag and Cu exhibit similar electron densities, as reflected by the close proximity of the real parts of their dielectric functions.[194]

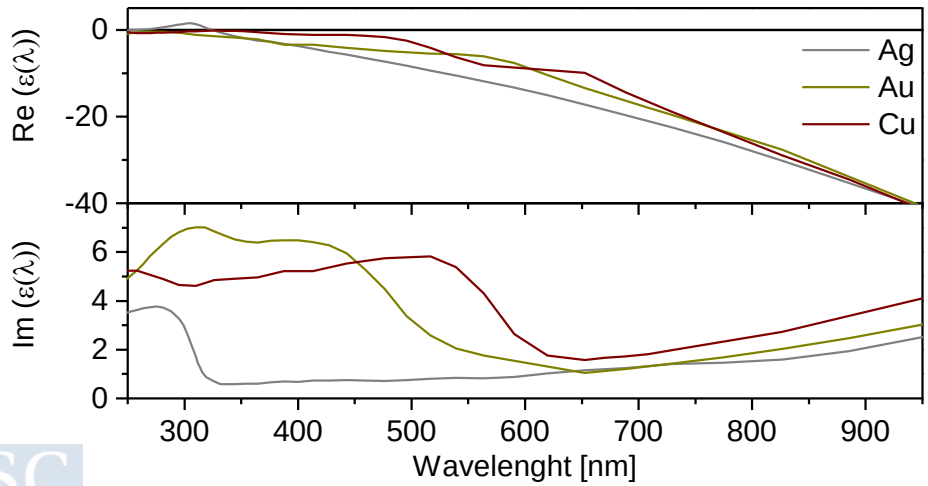

Figure 1-24. Dielectric functions (real and imaginary parts) of Ag, Au and Cu.

The imaginary part of the dielectric function tells us that bulk metals are not lossless, and is crucial for understanding their absorption properties. Although the imaginary part of $\varepsilon(\lambda)$ is smaller than the real part in the visible range for Ag, Au and Au, it still plays a significant role. The imaginary part is linked to the absorption of the material, with a value of zero indicating no absorption. For Ag, the imaginary part can be explained by the lossless Drude model, but Au or Cu have additional contributions from electronic transitions in its band structure. This results in higher absorption for Au at wavelengths below 600 nm, with a noticeable "double hump" around 400 nm due to interband transitions.

To understand the concept of LSPR, it is essential to understand the meaning of the dielectric function, which describes how a material behaves when subjected to an electric field and is therefore related to its polarizability. The complex dielectric function is expressed as $\varepsilon = \varepsilon_1 + i\varepsilon_2$, where the real part, ε_1, is given by $\varepsilon_1 = n^2 - \kappa^2$ (with n as the refractive index and κ as the absorption coefficient), and the imaginary part is $\varepsilon_2 = 2n\kappa$. The real and imaginary components of the dielectric function can be modeled using the Drude-Lorentz model.[195]

$$\varepsilon_1 = 1 - \frac{\omega_p^2}{\omega^2 + \gamma^2}$$

Eq. 2

$$\varepsilon_2 = \frac{\omega_p^2 \gamma}{\omega(\omega^2 + \gamma^2)}$$

Eq. 3

Where γ is the collision frequency and ω_p represents the plasma frequency, which is given by:

$$\omega_p^2 = \frac{Ne^2}{m\varepsilon_0}$$

Eq. 4

Where m is the electron mass, e is the electron charge, N is the free electron density, and $\varepsilon_0$is the permittivity of free space. Equation 4 indicates that the square of the plasma frequency is proportional to the electron density. Consequently, metals have a negative real dielectric constant due to their high free electron density, which results in a high plasma frequency. The negative real dielectric constant is responsible for Rayleigh resonance scattering, while the imaginary part of the dielectric constant accounts for absorption.

1.3.2. Plasmon

A plasmon is one of the seven fundamental excitations that a solid can undergo.[196] Table 1-2 lists these seven types of excitations that solids can exhibit.

A plasma is defined as a system with equal concentrations of positive and negative charges, with at least one type being mobile charges.[197] It is sometimes referred to as "the fourth state of matter".

USC DE SANTIAGO DE COMPOSTELA

In a metallic solid, the negative charge of the conduction electrons is balanced by the positive charge of the cationic lattice. These valence electrons, quantum-confined within the three-dimensional lattice of cations, behave like a plasma.

A plasmon can be described as a quantum of plasma oscillation in a metal.[198] Figure 1-25 provides a schematic representation of the collective oscillation of valence electrons.

Table 1-2. Elementary excitations presented by solids

Symbol	Name	Field
	Electron	-
	Photon	Electromagnetic wave
	Phonon	Elastic wave
	Plasmon	Collective electronic wave
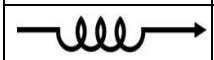	Magnon	Magnetization wave
-	Polaron	Electron + elastic deformation
-	Exciton	Polarization wave

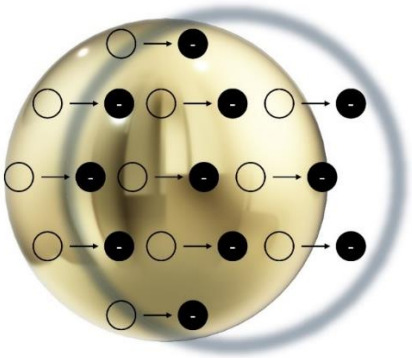

Figure 1-25. Schematic representation of the collective and coherent oscillation of electrons in a metallic structure known as plasmon.

A plasmon can be excited by the interaction of an electron or a photon with the surface of a metal. Figure 1-26 illustrates the formation of a plasmon through the inelastic scattering of an electron on a metallic surface.

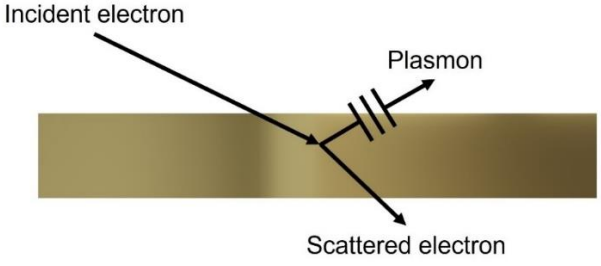

USC UNIVERSIDADE DE SANTIAGO DE COMPOSTELA

Figure 1-26. Formation of a plasmon by inelastic scattering of an electron on a metal surface.

1.3.3. Localized Surface Plasmon Resonance (LSPR)

Resonance occurs when the frequency of the incident photon matches the oscillation frequency of the surface electrons. The collective and coherent oscillation of free electrons in a metal induced by a photon is known as volume plasmon resonance, as shown in Figure 1.27. Similarly, oscillations that occur at the interface between two materials are referred to as surface plasmons, as depicted in Figure 1-28.

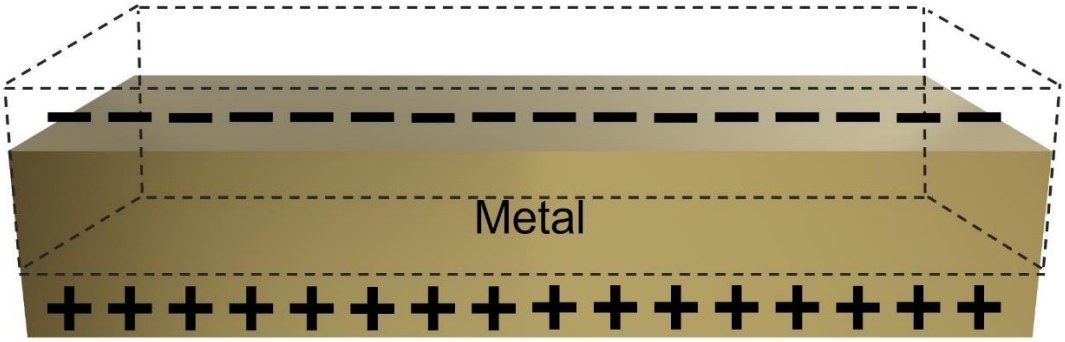

Figure 1-27. Schematic representation of a volume plasmon.

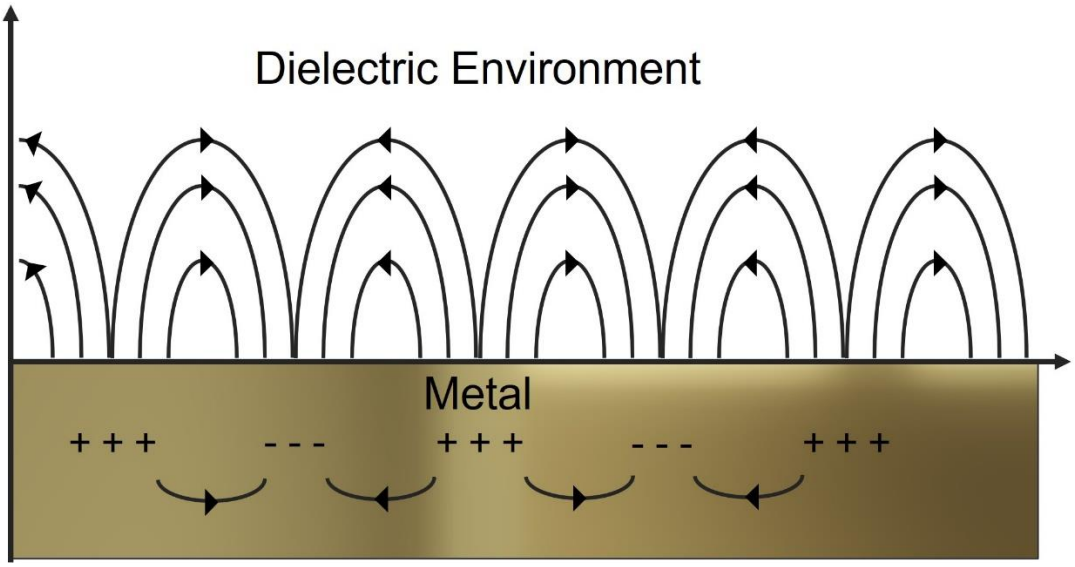

Figure 1-28. Schematic representation of a surface plasmon in a dielectric environment.

For a metallic nanostructure, the electromagnetic wave associated with surface plasmon resonance cannot propagate due to confinement within the space defined by the nanocrystal. Consequently, this resonance is localized in a defined region and is referred to as LSPR. Figure 1-29 shows a representation of the localized surface plasmon corresponding to the displacement of the electron cloud in a metallic nanosphere.

The frequency of the LSPR is determined by the dielectric function, which depends on the frequency of the metal and the dielectric constant of the surrounding medium and is also significantly influenced by the size and shape of the nanostructure.

USC DE SANTIAGO

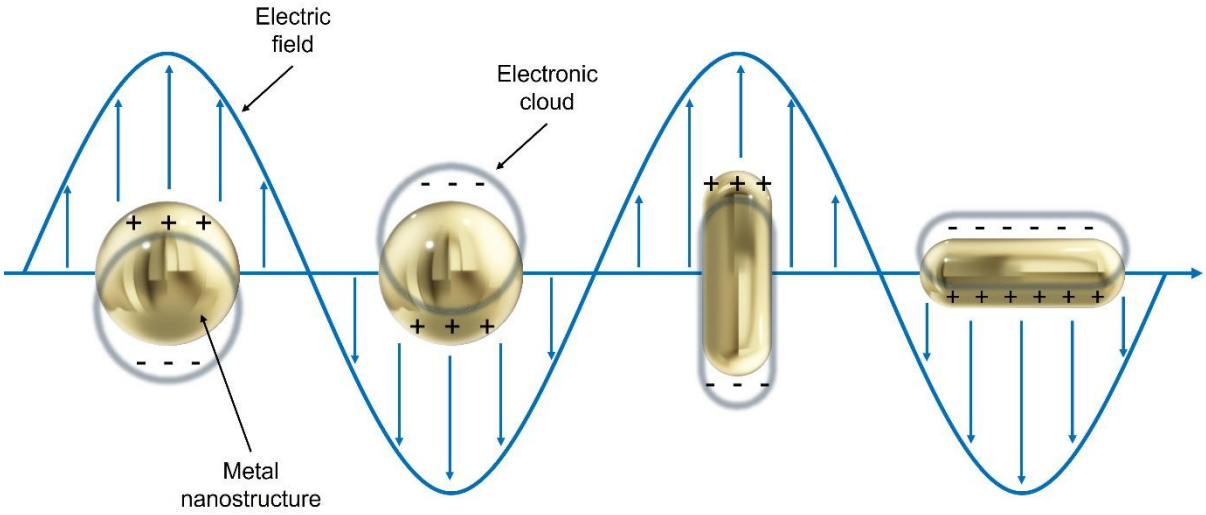

Figure 1-29. Schematic representation of the localized surface plasmon corresponding to the displacement of the electron cloud of a metallic nanosphere and nanorod.

1.3.4. Tunning the LSPR

Plasmonic nanoparticles exhibit unique optical properties, which arise from the dielectric function of the metals, as previously discussed. This behavior is a consequence of the high electron density inherent to the nature of metallic bonding, often described as an “electron sea”.

When light interacts with plasmonic nanoparticles, it induces distinct optical phenomena, such as color variations compared to the bulk material. These color changes result from the selective absorption of light, which is one of the primary mechanisms of light-matter interaction, alongside transmission, refraction, reflection, and scattering as is shown in Figure 1-30. Scattering, in particular, is a notable feature in plasmonic nanoparticles and is primarily influenced by the nanoparticle size.

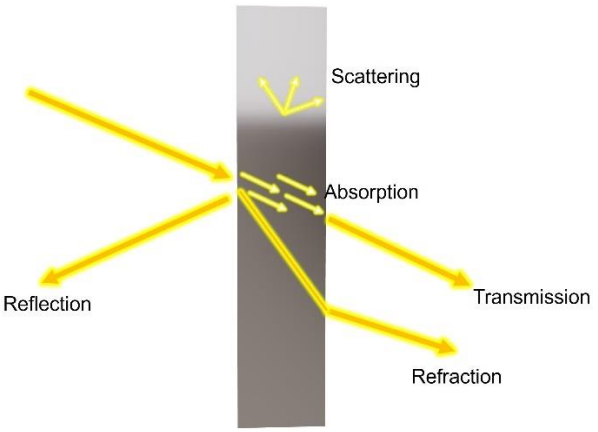

Figure 1-30. Light-matter interactions.

One of the main advantages of plasmonic nanoparticles is the ability to tune the LSPR across the electromagnetic spectrum, particularly within the visible and NIR regions. Several factors influence this absorption: i) the nature of the metal, which determines the dielectric

function; ii) the particle shape, which, in the case of anisotropic particles, can result in multiple LSPR modes; iii) the size, which not only dictates the specific region of the spectrum where light is absorbed and scattered but also how the aspect ratio impacts these interactions; and iv) the dielectric environment, which alters the dielectric function of the surrounding medium (proportional to the square of the refractive index).

Considering the aforementioned factors, the extinction spectra of gold nanospheres, defined as the sum of absorbed and scattered light, was simulated using the universal analytical model for plasmonic nanoparticles developed by García de Abajo *et al.*,[199] accessible via his website (widgets.nanophotonics.es).

According to Mie's theory, isotropic nanoparticles (such as spheres) exhibit a single LSPR mode.[200] The peak absorption wavelength of this mode shifts toward the red end of the spectrum as the particle size increases, as illustrated in Figure 1-31. The figure demonstrates that as the nanoparticle size significantly increases (greater than 50 nm), there is a substantial increase in scattering, particularly around 700–800 nm. Furthermore, when the size becomes bigger (>100 nm), additional LSPR modes emerge due to the diminished electron confinement. At these larger sizes, higher-order moments, such as quadrupolar and octupolar, also contribute to the optical response, in addition to the dipolar moment.[201]

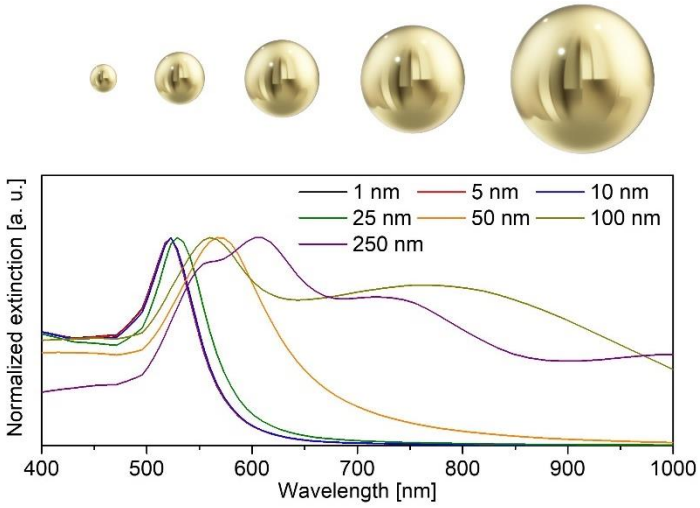

Figure 1-31. Extinction spectra of spherical nanoparticles. Material = Au, diameter = variable, dielectric environment = water (ε_0 = 1.77).

Anisotropy is a crucial factor in plasmonics, as variations in particle morphology allow for tuning of the LSPR, even when the particles are composed of the same material, share identical dimensions and aspect ratios, or are surrounded in the same medium, as shown in Figure 1-32. Since these particles are anisotropic, the modes of electron oscillation differ, leading to variations in absorption within the same particle. This tunability across the electromagnetic spectrum explains why certain morphologies are more suitable for specific applications than others. For instance, nanorods or bipyramids are preferred for applications requiring NIR

USC UNIVERSIDADE DE SANTIAGO DE COMPOSTELA

absorption, whereas spheres typically absorb around 520 nm, making them less ideal for such purposes.

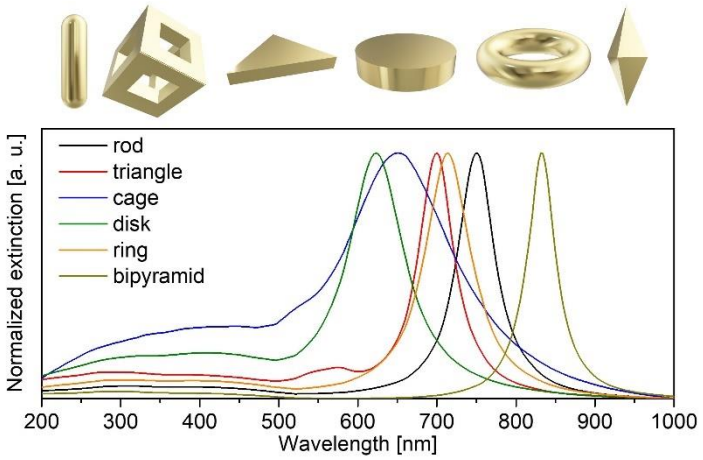

Figure 1-32. Extinction spectra of nanoparticles with different morphology. Material = Au, Length = 100 nm, Aspect Ratio = 3, dielectric environment = water (ε_0 = 1.77).

The impact of particle size is evident in the shift of the absorption wavelength, as illustrated in Figure 1-33. As the particle dimensions increase, the absorption wavelength shifts toward the red end of the spectrum. Additionally, the amount of absorbed light increases, with a significant contribution from scattering (represented by dotted lines). However, when the particle dimensions decrease while maintaining the aspect ratio between length and width, the scattering becomes negligible, resulting in absorption being the predominant contribution.

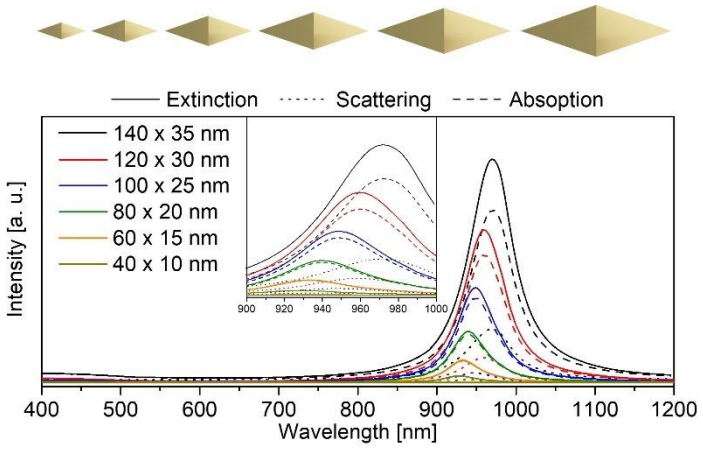

Figure 1-33. Extinction spectra of bipyramids. Material = Au, Length = variable, Aspect Ratio = 4, dielectric environment = water (ε_0 = 1.77).

The impact of the length-to-width ratio (aspect ratio) effectively alters the particle size in just one dimension. By fixing the length at 100 nm and varying the width, it is possible to tune

USC
UNIVERSIDADE DE SANTIAGO DE COMPOSTELA

the LSPR across the entire visible spectrum and into the NIR region. Additionally, as the aspect ratio increases, there is a greater contribution from scattering, as demonstrated in Figure 1-34.

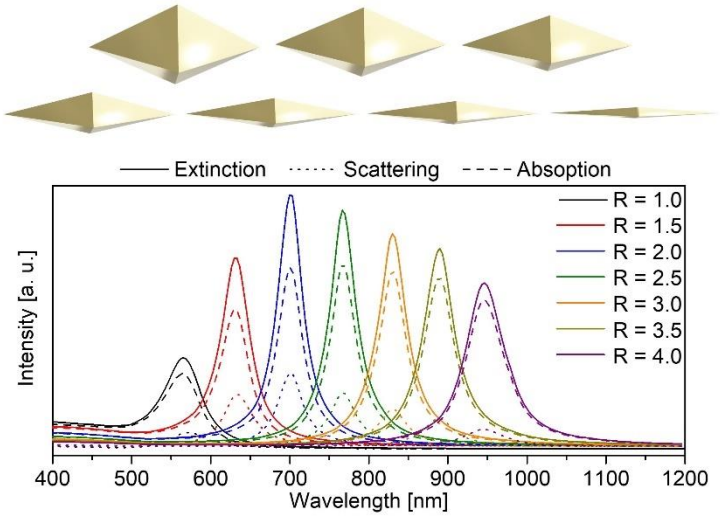

Figure 1-34. Extinction spectra of bipyramids. Material = Au, Length = 100 nm, Aspect Ratio = variable, dielectric environment = water (ε_0 = 1.77).

The choice of metal significantly influences the position, shape, and number of LSPR modes. Figure 1-35 illustrates bipyramidal nanoparticles with identical characteristics, differing only in the metal used. The electron density of each metal affects the real part of the dielectric function, which is why metal nanoparticles exhibit plasmonic behavior. However, each metal will exhibit distinct behavior in the electromagnetic spectrum, as well as in the intensity of electron oscillations when they resonate with incident light.

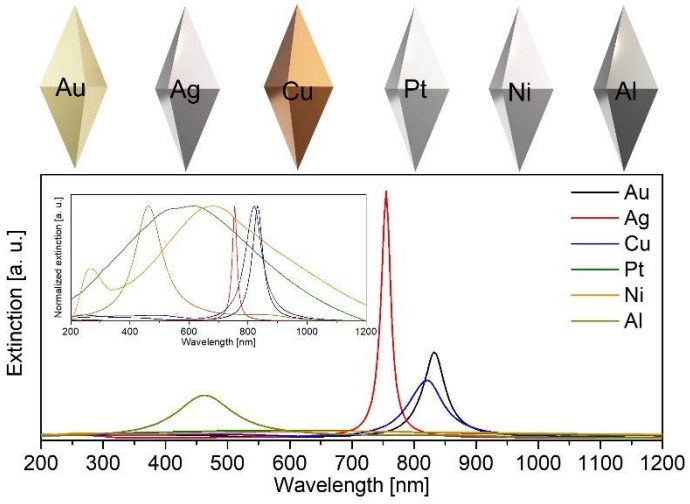

Figure 1-35. Extinction spectra of bipyramids. Material = variable, Length = 100 nm, Aspect Ratio = 3, dielectric environment = water (ε_0 = 1.77).

The final factor that primarily influences the position of the LSPR in the electromagnetic spectrum is the surrounding medium. Typically, metal nanoparticles are suspended in colloidal

USC UNIVERSIDADE DE COMPOSTELA

solutions with water or other solvents, stabilized by capping agents or stabilizers. Water has a refractive index of 1.33 (with no imaginary part, as it is transparent), which, when squared to obtain the dielectric function, yields a value of 1.77. Compared to air, which has a refractive index of 1.00, water induces a red shift in the LSPR as is shown in Figure 1-36. This red shift is similarly observed with other solvents, with short-chain alcohols (e.g., methanol, ethanol) exhibiting refractive indices closest to that of water. There exists a gap between the dielectric functions of air (1.00) and water (1.77), within which few substances, such as certain gases (e.g., CO_2, He) or specific silicone oils and aerogels, fit, however, these are not commonly used as dispersing agents for nanoparticles.

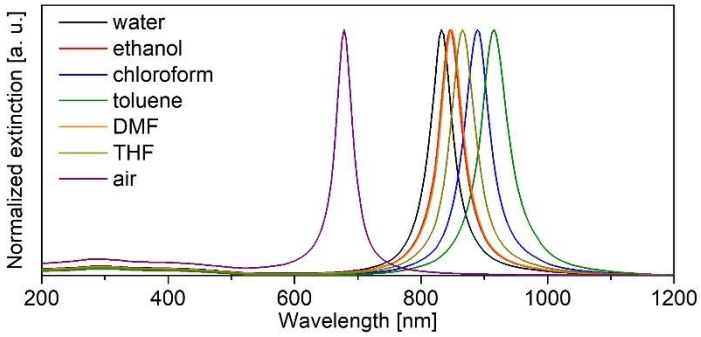

Figure 1-36. Extinction spectra of bipyramids. Material = Au, Length = 100 nm, Aspect Ratio = 3, dielectric environment = variable.

1.3.5. Thermoplasmonics

Plasmonic nanoparticles are employed in various applications due to their unique optical properties. Additionally, they are extensively studied for their ability to generate heat, a property whose efficiency is influenced by factors such as their composition, morphology, surrounding environment, and the wavelength of the illuminating light.[202]

Two key figures of merit are used to assess plasmonic nanoparticles: the Faraday number (Equation 5), which evaluates the ability of a nanoparticle to enhance its internal electric field in the surrounding medium, and the Joule number (Equation 6), which quantifies the efficiency of heat generation under optical excitation.

$$\mathrm{Fa}(\lambda) = \frac{3\varepsilon_1(\lambda)}{3\varepsilon_1(\lambda) + 2\varepsilon_s} \qquad \text{(Eq. 5)}$$

$$\mathrm{Jo}(\lambda) = \frac{\varepsilon_1(\lambda)}{\varepsilon_2(\lambda) + 2\varepsilon_s} \qquad \text{(Eq. 6)}$$

Table 1-3 summarizes the previous figures of merit for Ag, Au and Cu, with their corresponding wavelengths in resonance and the melting temperature at atmospheric pressure.

USC
DE SANTIAGO
DE COMPOSTELA

Table 1-3. Summary of Faraday (Fa) and Joule (Jo) numbers for Ag, Au and Cu.

Metal	λ_{res}^{in}	Fa	Jo	T_s (ºC)
Ag	357	118	52.0	961
Au	528	19.6	6.32	1064
Cu	585	15.2	2.65	1085

According to Tables 1-3, Ag is identified as the most effective material for enhancing the electric field and excels in heat generation. However, it is less favored for thermal applications due to its activation near the UV region and its susceptibility to chemical degradation, such as oxide or sulfide formation on its surface, similar to copper. Consequently, Au emerges as the most suitable material for thermoplasmonics, owing to its tunable LSPR across the visible and near-infrared (NIR) regions and its high chemical stability.

The heating mechanism of the plasmonic nanoparticles are diverse, but the main is due to the electronic nature of the nanoparticles, which experience significant energy loss when they are excited with light. The excited electrons relax though electron-phonon coupling on a picosecond timescale, after this, their energy is transferred from electrons to lattice phonons of the nanoparticle, and the heated lattice exchange energy with the surrounding medium through phonon-phonon coupling leading to an increase in the temperature of the medium until the thermal equilibrium is reached.[203]

Heat dissipates from the nanostructure through the three heat transfer mechanisms: i) conduction into the surrounding medium, ii) convection (natural and forced), and iii) radiation. A stable state is reached when the rate of heat deposition ($\dot{q}$) equals the rate of heat removal. This equilibrium is maintained by the temperature difference between the irradiated nanoparticles and the bulk medium.

$$\dot{q} = \kappa A \frac{dT}{dx} + hA(T_s - T_{bulk})$$

(Eq. 7)

Where κ is the thermal conductivity of the medium; $\frac{dT}{dx}$ is the temperature gradient; h is the heat transfer coefficient for convection ; A is the area normal to the direction of the heat transfer.

From Equation 7, it is evident that a medium with higher thermal conductivity (κ) will exhibit a smaller temperature difference (ΔT) between the surface of the nanoparticle and the bulk medium. This principle underlies the use of liquid media, such as water, which has a thermal conductivity value of approximately 0.6 W/m·K.

The heat generated by plasmonic nanoparticles for light-triggered release applications can be utilized in an isotropic fluid system within an enclosed medium. In the absence of external forces, a concentration gradient develops in response to the applied temperature gradient until the system reaches a steady state. This phenomenon is referred to as the Soret effect, Ludwig–Soret effect, thermodiffusion, or thermal diffusion.[204]

USC UNIVERSIDADE DE SANTIAGO DE COMPOSTELA

$$\vec{J_i} = -\rho_0 \sum_{k=1}^{p-1} D_{ik} \vec{\nabla} c_i - \rho_0 D_{Ti} c_{i0} (1 - c_{i0}) \vec{\nabla} T$$

(Eq. 8)

In Equation 8, the mass flux $\vec{J_i}$ is expressed under the assumption of negligible pressure gradient. In this context, ρ_0 represents the density, c_i is the mass fraction of the component, c_{i0} is the initial mass fraction, D_{ik} is the isothermal molecular diffusion coefficient, D_{Ti} is the thermodiffusion coefficient, and $\vec{\nabla} c_i$ is the gradient of the mass fraction induced by the temperature gradient $\vec{\nabla} T$.

Figure 1-37 illustrates the Soret effect in action. A plasmonic nanoparticle embedded within a MOF composite, loaded with specific molecules, is activated by light-triggered release. This activation generates heat due to the excitation of the plasmonic nanoparticle, creating a temperature gradient that drives the movement of molecules from within the MOF to the surrounding medium.

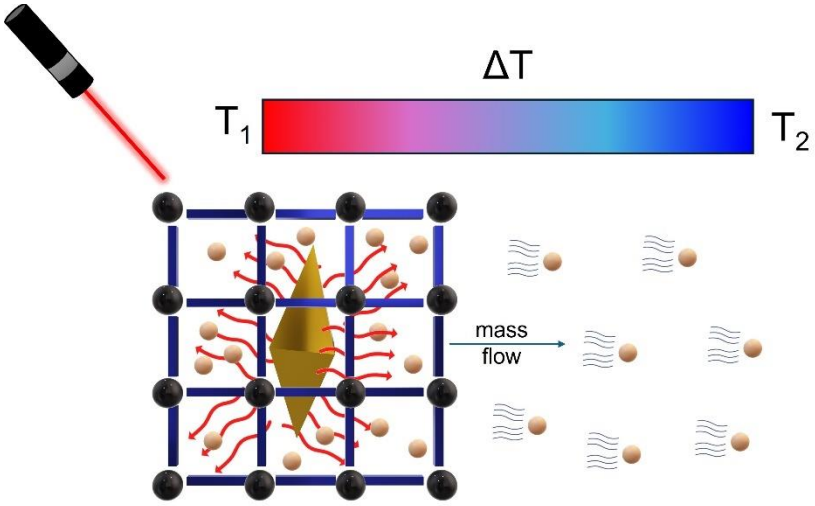

Figure 1-37. Soret effect in plasmonic MOF composite, releasing the molecules inside due to a temperature gradient.

1.3.6. Synthetic approaches and surface engineering of plasmonic nanoparticles

The synthetic approaches for plasmonic nanoparticles are diverse and, like other nanomaterials, can be broadly categorized into two families. The bottom-up approach involves the chemical reduction of metal salts in solution, using stabilizing agents to achieve colloidal stability and control the nanoparticle shape. In contrast, the top-down methodologies rely on physical processes, where atoms are detached from bulk materials or targets to form nanoscale arrangements.[205]

Bottom-up approaches offer superior control over material properties, allowing precise manipulation of size, shape, and composition. These methods encompass a wide variety of techniques, including chemical reduction combined with stabilizers such as citrate ions, surfactants like cetyltrimethylammonium bromide (CTAB), and polyvinylpyrrolidone (PVP). Additional methodologies include shape modification using light, the use of plant extracts as

USC
UNIVERSIDADE DE SANTIAGO DE COMPOSTELA

both reducing and stabilizing agents, galvanic replacement and seed-mediated growth, where pre-synthesized nanoseeds are introduced into a growth medium to promote anisotropic nanoparticle formation in specific directions.[206]

The use of sodium citrate for the reduction and stabilization of gold nanoparticles was first proposed by Turkevich *et al.* in 1951.[207] The method, now known as the Turkevich method, involves adding a sodium citrate solution to a boiling solution of $HAuCl_4$. This process produces highly monodispersed spherical gold nanoparticles, with their size controllable by adjusting the concentration of citrate. To avoid the formation of anisotropic nanoparticles, such as small triangles that may arise from impurities in the gold precursors (traces of Cu, Ni, Cr, and other metals), modifications to the method can be made, including the addition of ethylenediaminetetraacetic acid (EDTA) as a chelating agent. This significantly improves the monodispersity of the nanoparticles.[208] Remarkably, the nanoparticles produced by this method are similar to those synthesized by Faraday over 150 years ago,[209] which remain stable to this day in the Faraday Museum in London.

Photosynthetic methods have been increasingly employed for the synthesis of Ag nanoparticles, as light can induce the reduction of Ag^+ ions. However, these approaches are often more focused on shape transformation, such as converting citrate-capped Ag nanospheres into Ag triangular nanoprisms using light.[210,211] Unfortunately, this method lacks precise control over size polydispersity. To achieve this specific morphology, alternative synthetic strategies have been developed, involving the addition of H_2O_2 and PVP. This study highlights the critical role of the number and spatial arrangement of carboxylate groups, which exhibit a strong affinity for adsorption onto the (111) crystallographic plane. citrate ions, therefore, act as a crucial reagent in the synthesis of Ag and Au nanoparticles.[212]

The use of plant extracts is classified as a "green method" due to the reduction in the use of toxic reagents like $NaBH_4$ and the valorization of natural waste materials such as nutshells, rice husk, and certain teas. These extracts are rich in polyphenols, which exhibit antioxidant properties, enabling them to reduce Ag^+ and $AuCl_4^-$ ions into nanoparticles while simultaneously stabilizing them. However, a significant drawback of this approach is the limited control over the size and shape of the resulting nanoparticles.[213]

A "galvanic" electrochemical reaction refers to a spontaneous process, whereas an electrochemical reaction that requires an externally applied potential difference is termed "electrolytic". By leveraging certain spontaneous reactions, it is possible to oxidize nanoparticles in the presence of other ions, which are subsequently reduced on the nanoparticle surface, leading to the formation of hollow structures or frames. This process is known as "galvanic replacement" and it is crucial to understand the underlying spontaneity, as described by Equation 9.

$$\Delta G° = -nFE^{\circ}_{cell} \qquad \text{(Eq. 9)}$$

Where $\Delta G°$ represents the standard Gibbs free energy change, n is the number of electrons transferred in the reaction, F is the Faraday constant (approximately 96,500 C/mol), and E°_{cell} is the standard cell potential.

USC UNIVERSIDADE DE SANTIAGO DE COMPOSTELA

For the gold reduction reaction described in Equation 10, the standard reduction potential is $E°_{AuCl_4^-/Au} = 0.99$ V vs SHE. For the silver oxidation reaction described in Equation 11, the standard reduction potential is $E°_{Ag^+/Ag} = -0.80$ V vs SHE.

$$AuCl_{4(aq)}^- + 3e^- \rightarrow Au_{(s)} + 4Cl_{(aq)}^- \quad \text{(Eq. 10)}$$

$$Ag_{(s)} \rightarrow Ag_{(aq)}^+ + e^- \quad \text{(Eq. 11)}$$

The calculus of the E_{cell}° is determined by convention as the difference between the $E_{cathode}^{\circ} - E_{anode}^{\circ}$, obtaining for this reaction a $E_{cell}^{\circ} = 1.79$ V, which in Equation 9 gives a result of a $\Delta G° < 0$, what means a spontaneous reaction.

The standard cell potential, E_{cell}°, is conventionally calculated as the difference between the standard reduction potentials of the cathode and anode, i.e., $E_{cell}^{\circ} = E_{cathode}^{\circ} - E_{anode}^{\circ}$ For this reaction, E_{cell}° is determined to be 1.79 V. According to Equation 9, this results in a $\Delta G° < 0$, indicating that the reaction is spontaneous.

The group led by Xia has been a pioneer in developing this synthetic approach, effectively utilizing nanoparticles primarily of Ag, Pd, Cu, or Co as sacrificial templates due to their low reduction potentials. These sacrificial nanoparticles can be replaced by Rh, Pd, Ir, or Au in strategic positions through the use of blocking agents, as well as by controlling parameters such as temperature and concentration.[214–216]

The most recent synthetic approaches for plasmonic nanoparticles focus on the synthesis of anisotropic nanoparticles, such as nanorods (NRs), nanostars (NSs), and bipyramids (Bipy). This method involves the use of presynthesized nanoseeds with specific characteristics that enable the controlled growth of these anisotropic nanoparticles. The seeds used in the synthesis can be categorized into three types: very small seeds approximately 2 nm in size, which do not exhibit LSPR; citrate-capped nanoparticles around 10-12 nm in size; and seeds with pentatwinned defects approximately 15 nm in size.

The seed growth solution for these nanoparticles is quite similar across different syntheses and typically consists of an aqueous mixture of $HAuCl_4$, CTAB, ascorbic acid, HCl, and $AgNO_3$.[217] $HAuCl_4$ serves as the gold source, while CTAB forms a soft micellar template with a tubular morphology.[218] Upon the addition of ascorbic acid, which reduces Au(III) to Au(I), strong CTA-Au complexes are formed. This complexation prevents the instantaneous reduction of Au(I) to metallic gold, given the inherent instability of Au(I). HCl is used to maintain an acidic pH, and $AgNO_3$ acts as a facet-blocking agent, directing gold reduction in a specific orientation,[219,220] as illustrated in Figure 1-38.

USC UNIVERSIDADE DE SANTIAGO DE COMPOSTELA

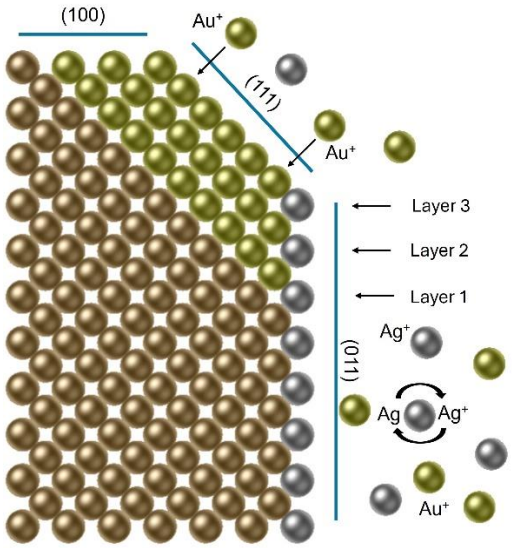

Figure 1-38. Growth on the {111} facet occurs atom by atom, leading to the gradual extension of the side facets with each gold layer added. The side facets expand through a gradual, continuous process involving galvanic replacement and silver deposition.

The seeds are introduced into the growth solution, where Au(I) is reduced on their surface, facilitated by electron transfer to the gold particle. Very small seeds are used to produce monocrystalline AuNRs,[218] citrate-capped Au nanoparticles are utilized for the growth of AuNSs,[221] and pentatwinned seeds, prepared by aging in the presence of agents such as citric acid that induce these pentatwinned defects, are employed in the synthesis of AuBipy as well as polycrystalline AuNRs, and the amount of seed control the aspect ratio of the final nanoparticles.[222]

Plasmonic nanoparticles can be functionalized to impart additional properties or enhance their affinity for specific environments. When comparing Au and Ag for surface engineering, Au offers significant advantages due to its exceptional chemical stability. In contrast, Ag is prone to oxidation and the formation of sulfide layers, which can reduce its reactivity compared to Au. Both metals exhibit a high affinity for sulfur-containing molecules, which can be chemisorbed through an oxidative addition reaction,[223] as shown in Equation 12 (this is also possible with Ag).

$$\mathrm{R-S-H\ + Au_n^0\ \rightarrow R-S-\ Au^+ - Au_{n-1}^0 + \frac{1}{2}H_2} \qquad \text{(Eq. 12)}$$

By leveraging the sulfur-containing thiol groups, various molecules can be conjugated to plasmonic nanoparticles. These include aliphatic chains, which confer affinity for non-polar solvents;[224] thiol-functionalized DNA;[225] or amphiphilic polymers that exhibit affinities for both polar and non-polar media. This functionalization allows the transfer of plasmonic nanoparticles with these molecules on the surface, such as PEG-SH, which can include additional functional groups at the end of the chain, enabling further chemical modifications.[226,227]

Another surface engineering strategy for plasmonic nanoparticles is the use of polyelectrolytes through a layer-by-layer approach, which exploits the surface charge induced by stabilizing agents. For instance, citrate-capped gold nanoparticles exhibit a negative zeta

potential due to the carboxylate groups on their surface. In this case, a positively charged polyelectrolyte, such as poly(diallyldimethylammonium chloride) (PDDA), can be used to reverse the surface charge to positive. Subsequently, a second layer can be added using a negatively charged polyelectrolyte, such as poly(sodium 4-styrenesulfonate) (PSS). This process can be repeated to create multiple bilayers of polyelectrolytes, allowing for diverse surface modifications.[228,229]

USC
UNIVERSIDADE DE SANTIAGO DE COMPOSTELA

1.4. INORGANIC NANOPARTICLE@METAL-ORGANIC FRAMEWORKS NANOCOMPOSITES (iNPs@MOFs)

1.4.1. Synthetic approaches

Integrating MOFs, which offer high surface area, pore tunability, recyclability, and thermal insulation, with plasmonic nanoparticles, known for their unique optical properties, catalytic activity, and heat generation, presents a significant challenge due to the inherent incompatibility between these two types of materials.[230–233] This incompatibility arises primarily from the differing synthetic conditions required: MOFs are typically synthesized under solvothermal conditions in organic solvents like DMF at elevated temperatures, whereas plasmonic nanoparticles are generally synthesized in aqueous environments at room temperature, often involving stabilizers that are physically adsorbed onto their surfaces.

There are two main approaches for the synthesis of these nanocomposites. The first approach involves the synthesis of plasmonic nanoparticles with a specific morphology and composition, followed by functionalization with a coating or capping agent that enables redispersion in the reaction medium. These nanoparticles are then used as seeds in a mixture of the desired metal and linker for the growth of the MOF on the nanoparticle surface. The second strategy involves the synthesis of the desired MOF, followed by a subsequent step where the metal is impregnated into the MOF structure. This metal is then reduced into plasmonic nanoparticles (e.g., Ag, Au, Cu, Pd, Pt), with the addition of a reducing agent to facilitate nanoparticle growth. Figure 1-39 provides a schematic representation of these two approaches.

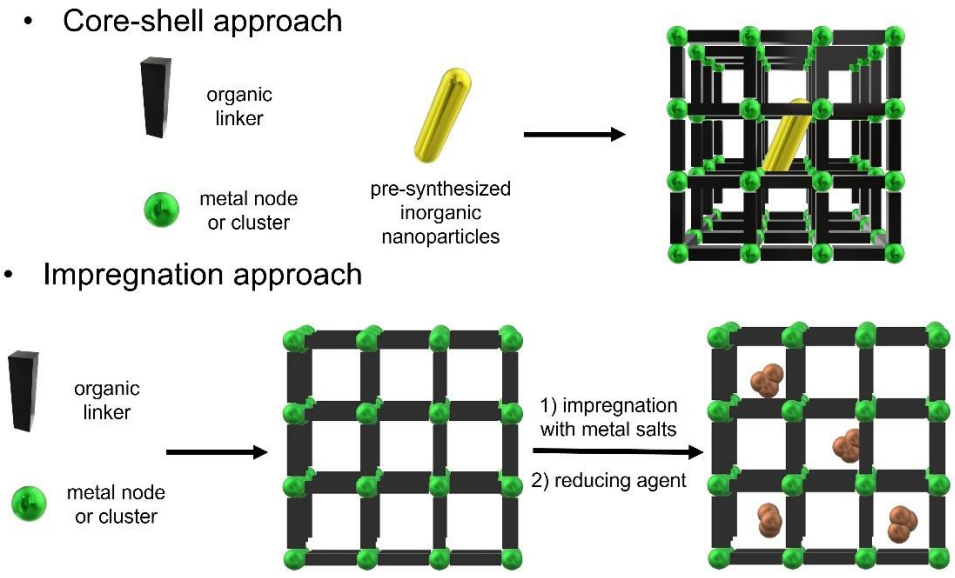

Figure 1-39. Schematic representation of synthetic approaches of composites that integrate MOFs and plasmonic nanoparticles.

Among these two strategies, the core-shell approach is particularly challenging, not only due to the compatibility issues between the nanoparticles and the synthetic conditions but also because the capping agent may hinder the crystallization of the MOF on its surface. In contrast, the impregnation approach faces limitations in controlling particle size, which is constrained

by the pore size and pore polarity of the MOF. As a result, the process often yields very small clusters of atoms or nanoparticles in the 1-2 nm range, which lack plasmonic activity but can be useful for catalytic applications.[234] Another drawback of the impregnation approach is the uneven distribution of particles within and on the surface of MOF structures.[235] However, it is possible to utilize the pore channels of the MOF as templates to form aligned metallic nanowires.[236]

Significant research has been conducted on the synthesis of core@shell nanocomposites incorporating inorganic nanoparticles with ZIF-8, such as plasmonic[237,238] or catalytic nanoparticles,[239] due to their stability in aqueous solutions facilitated by CTAB. This surfactant not only stabilizes the nanoparticles but also serves as a size-controlling agent during the crystallization of ZIF-8. The growth mechanism of these nanocomposites is well understood, demonstrating that the concentration of CTAB in the solution containing inorganic nanoparticles plays a critical role in determining whether the resulting nanoparticles are monocrystalline, polycrystalline, or highly twinned. Furthermore, the sequence of reactant addition significantly influences the final product, as 2-methylimidazole has the ability to displace CTAB from the nanoparticle surface.[240]

Table 1-4 provides a summary of some relevant studies that have employed the core-shell approach in the synthesis of nanocomposites.

Table 1-4. Relevant studies in core-shell approach synthesis for inorganic nanoparticles-MOFs composites.

Inorganic nanoparticle	**MOF**	**Application**	**Reference**
Au nanostar	ZIF-8	Reactions inside living cells	This group [237]
Au nanostar	ZIF-8	Light-triggered release	This group [238]
Pd nanocube	ZIF-8	Uncaging reactions inside living cells	This group [239]
Pd nanocube / Au nanosphere	ZIF-8 / UiO-66-F_4	Selective hydrogenation	[240]
Au nanorods	ZIF-8	Neurotransmitters detection	[241]
Au different morphologies	ZIF-8	Shape control for ZIF-8	[242]
Au bipyramid	ZIF-8	SERS detection of thiols	[243]
Au bipyramid	ZIF-8	SERS and antibodies immobilization	[244]
PS@Ag beads	ZIF-8	SERS detection of Cu	[245]
Au@Ag nanorods	ZIF-8	SERS detection of biomarkers in cells cultures	[246]
Au bipyramid	PCN-224	Light-triggered release of cresyl violet combined with PDT	This group[169]
Au bipyramid	ZIF-8 / NU-1000	Drug delivery of cancer drugs in 2D and 3D cell cultures	This group[247]
Au nanorod	NU-901	SERS with pore exclusion	[248]
Au@Al_2O_3 nanorod	Al(OH)(1,4-ndc)	Light-triggered release of anthracene	[249]

Au nanorod	NU-901	Improved SERS performance compared with Au arrays	250
Cu nanoparticles	UiO-66	Hydrogenation of MeOH	251
Au@Pd nanoparticles	UiO-66	CO_2 hydrogenation	252
Pd nanoparticles	IRMOF-3	Catalysts for Cascade Reactions	253
Au nanoparticles	MOF-5	SERS detection of CO_2	254
Fe_3O_4 nanoparticles	MIL-100(Fe)	pH-triggered drug release of DOXO	255
$NaYF_4$:Yb,Er	MIL-101-NH_2(Fe)	Nanoprobes for targeted luminescence/MR	256
$NaYF_4$:Yb,Er	MIL-100(Fe)	Drug Delivery and Cell Imaging	257
$NaYF_4$:Yb,Er	ZIF-8	Targeting, imaging and pH responsive drug release	258
MnO_2	PCN-224	Triggered and enhanced PDT	259

USC UNIVERSIDADE DE SANTIAGO DE COMPOSTELA

1.5. OBJECTIVES

General Objectives

The integration of plasmonic nanoparticles with metal-organic frameworks (MOFs) gives rise to a novel class of composite materials exhibiting distinctive properties. These composites not only retain the characteristics of their constituent materials but also exhibit emergent properties that can be leveraged across various fields of nanotechnology. This PhD. thesis focuses on the development of synthetic methodologies for creating core-shell systems that combine these two nanomaterials, specifically gold cores and Zr-based MOF shells. Additionally, it aims to elucidate the synthetic and environmental factors influencing the formation of these systems. The resulting nanocomposites are intended for use as drug delivery systems activated by external stimuli within living cells.

Chapter 3 examines the use of non-traditional Zr precursors in the synthesis of MOFs and investigates the role of counterions in the formation of nanoMOFs. Chapter 4 explores the application of Zr-alkoxides as precursors for the synthesis of porphyrinic Zr-based nanoMOFs under mild conditions. Chapter 5 investigates the use of Zr-alkoxides for the fabrication of core-shell systems incorporating plasmonic nanoparticles, and evaluates the effects of temperature on the optical properties, reaction yields, and structural characteristics of these systems. Chapter 6 explores the utilization of preformed Zr_6-oxo clusters for the synthesis of room-temperature plasmonic nanoMOFs and their application as light-triggered drug delivery systems combined with photodynamic therapy in living cells. Finally, Chapter 7 examines the influence of the morphology and concentration of plasmonic nanoparticles on the thermal properties of core-shell systems and their application as surface-enhanced Raman scattering (SERS) substrates in colloidal dispersions.

Specific objectives

1.5.1. Chapter 3

The objectives of this chapter are summarized as follows:

i) To develop a novel synthetic approach employing non-halogenated zirconium precursors.
ii) To investigate the role of halides in the formation of nanoMOFs and to characterize these materials chemically, thermally, and structurally.
iii) To evaluate the influence of functional groups on the structure of the linker.
iv) To assess cell viability to determine the maximum concentration of metal that can be used in in vitro experiments.
v) To utilize these nanoMOFs, loaded with rhodamine 6G, for tracking via confocal microscopy, assessing their potential as drug delivery systems.

1.5.2. Chapter 4

USC DE COMPOSTELA

The objectives of this chapter are:

i) To utilize Zr-alkoxides in the synthesis of porphyrinic Zr-based MOFs, aiming to produce nanoMOFs under mild conditions.
ii) To identify the optimal synthetic conditions for the generation of pure phases at the nanoscale.
iii) To characterize these nanoMOFs to delineate the boundary between missing linker defects and polymorphs.
iv) To adapt this synthetic approach for flow chemistry to assess the feasibility and scalability of the method.

1.5.3. Chapter 5

This chapter addresses the following objectives:

i) To understand the impact of temperature on the reshaping of plasmonic nanoparticles with various morphologies and evaluate the influence of PEG both before and after thermal treatment.
ii) To utilize Zr-ethoxide in the synthesis of plasmonic nanoMOFs with a series of isoreticular MOFs, investigating the effect of temperature on reaction yield, crystallinity, and defect formation.
iii) To explore the synthesis of plasmonic nanoMOFs at room temperature and assess the impact of seed concentration on shell thickness.
iv) To evaluate how shell thickness affects the heating properties of the nanocomposites.

1.5.4. Chapter 6

The objectives of Chapter 6 are summarized as follows:

i) To employ pre-synthesized Zr_6-oxo clusters in the synthesis of core-shell plasmonic nanoMOFs using the porphyrinic MOF PCN-224.
ii) To investigate the impact of 1-propanol, a contaminant in the preparation of Zr_6-oxo clusters, on the attainment of monodisperse nanosystems.
iii) To evaluate the effect of seed concentration on shell thickness and its subsequent impact on the photoluminescence and heating properties of the plasmonic nanoMOFs.
iv) To explore the application of these plasmonic nanoMOFs as drug delivery systems activated by external stimuli, combined with photodynamic therapy, within living cells.

1.5.5. Chapter 7

The objectives of Chapter 7 are as follows:

i) To investigate the effect of plasmonic nanoparticle concentration on the reshaping process within the MOF synthesis medium and its impact on the final optical properties of the nanoparticles.

USC UNIVERSIDADE DE SANTIAGO DE COMPOSTELA

ii) To characterize the nanocomposites chemically, optically, structurally, and thermally to elucidate the differences in plasmonic nanoparticle morphology within the core-shell system.
iii) To evaluate the influence of nanoparticle shape on the photoluminescent and heating properties of the plasmonic nanoMOFs.
iv) To utilize the plasmonic nanoMOFs as proof-of-concept substrates for surface-enhanced Raman scattering (SERS) in colloidal dispersion.

USC UNIVERSIDADE DE SANTIAGO DE COMPOSTELA

2. Materials and methods

USC
UNIVERSIDADE
DE SANTIAGO
DE COMPOSTELA

USC
UNIVERSIDADE
DE SANTIAGO
DE COMPOSTELA

GENERAL CONSIDERATIONS: All glassware was initially cleaned with detergent, followed by treatment with aqua regia to oxidize and dissolve any remaining organic and inorganic impurities. The glassware was then thoroughly rinsed with Milli-Q water and acetone to ensure an exceptionally clean surface. Aqua regia was freshly prepared by mixing three parts hydrochloric acid (HCl) with one part nitric acid (HNO_3) and must be handled with caution. As a highly corrosive and strong oxidizing agent, aqua regia should be prepared in a well-ventilated fume hood while wearing appropriate protective gear, including clothing, goggles, and gloves. All reagents were used as received without further purification or modification unless otherwise specified.

2.1. Characterization techniques

2.1.1. Scanning electron microscopy (SEM)

SEM micrographs were obtained using a ZEISS FE-SEM ULTRA Plus after the deposition of a drop of diluted sample onto a piece of clean silicon wafer.

2.1.2. Transmission electron microscopy (TEM)

TEM measurements were carried out on a JEOL JEM F200 microscope equipped with a cold-field emission gun operated at 80 kV. TEM images were acquired using a Gatan OneView Camera. EDX analyses were performed with a Centurio Detector. Samples were prepared by adding a drop of diluted samples to a 400 mesh Cu grid and letting them dry.

2.1.3. Powder X-Ray Diffraction (PXRD)

Crystalline powder underwent Powder X-Ray diffraction (PXRD) analysis at room temperature using a Bragg-Brentano geometry on a "Bruker D8 Advance" X-ray diffractometer (40 kV, 40 mA, θ/θ configuration). The diffractometer was equipped with a sealed Cu X-ray tube ($\lambda_{CuK\alpha1}$ = 1.5406 Å) and a LYNXEYE detector. Diffractograms were generated within the angular range of $3<2\theta<40$, with a step size of 0.02° (2θ) at 2 seconds per step. Throughout the measurement, sample rotation optimized peak profiles for analysis and minimized the impact of preferred orientation. To prevent background noise from a glass support, samples were positioned on a Si(511) oriented crystal base.

2.1.4. Wide-angle X-ray scattering (WAXS) and small-angle X-ray scattering (SAXS).

WAXS and SAXS measurements were carried out using an Anton Paar SAXSpoint 5.0 equipped with a micro X-ray source of Cu (λ = 0.154 nm) with a 2D Pilatus3 R 1 M detector at 2 different distances, 288 mm for WAXS and 1343 mm for SAXS in a Hilgenberg brand capillary tube of 1 mm external diameter.

2.1.5. Thermogravimetric analysis (TGA)

TGA measurements were carried out using a TA Instruments Inc. SDT Q-600 thermobalance with a general heating profile from 25 to 800 °C and a heating rate of 5 °C/min under air using a flux of 25 mL/min.

USC UNIVERSIDADE DE SANTIAGO DE COMPOSTELA

2.1.6. UV–vis spectroscopy.

UV-visible extinction spectra ranging from 200 to 1000 nm were recorded using an Agilent Cary 3500 Multicell UV-Vis Spectrophotometer with the nanoparticles dispersed in MeOH. The measurements were performed using a 1 cm quartz cell, using pure MeOH as a blank.

2.1.7. Fourier-transformed infrared spectroscopy (FTIR)

FTIR measurements were carried out using a PerkinElmer Spectrum Two spectrometer with ATR. The dried powders were placed in the ATR window and analyzed from 700 to 4000 cm^{-1}.

2.1.8. Raman spectroscopy

The Raman measurements were performed with a Renishaw inVia Reflex on a glass substrate with a laser beam at 785 nm, with a 50× objective. The samples were irradiated with a power of 10 mW with an acquisition time of 10 s and 3 accumulations.

2.1.9. Inductively Coupled Plasma-Optical Emission Spectroscopy (ICP-OES)

20 µL of the samples were digested overnight with 480 µL of aqua regia and then diluted to 5 mL with 2% v/v HCl. The measurements were performed using an Agilent 5800 ICP-OES, calibrated against 1 ppm and 10 ppm standards.

2.1.10. Dynamic light scattering

The hydrodynamic diameter (d_h) and polydispersity index (PDI) of the nanoparticles were determined via DLS using a Malvern Zetasizer Nano ZSP equipped with a 10 mW He-Ne laser operating at a wavelength of 633 nm and a fixed scattering angle of 173°.

2.1.11. Nanoparticle tracking analysis (NTA)

All the samples were analysed in water using a NanoSight NS300 (Malvern Instrument Ktd) equipped with a 405 nm laser. All measurements were carried out at 24 °C.

2.1.12. N_2 adsorption-desorption analysis

N_2 sorption isotherms at 77 K were measured on a Micromeritics 3Flex Adsorption Analyzer. The samples (about 20-30 mg) were activated overnight under a high vacuum at 90 °C prior to analysis. The specific surface area was extrapolated within the relative pressure (P/P_0, where P_0 is the saturation pressure) interval of 0.05–0.3 by applying the Brunauer, Emmett & Teller (BET) equation.

2.1.13. Differential Scanning calorimetry (DSC)

DSC measurements were performed using a TA Instruments Q200 calorimeter with a flow nitrogen flow rate of 50 mL/min. Around 0.5-1.0 mg of samples were place in aluminum crucibles hermetically closed and an empty aluminum crucible also hermetically closed were please as reference.

2.1.14. Nuclear magnetic resonance (NMR) spectroscopy

^{1}H NMR spectra were obtained at room temperature employing a BRUKER AVIII 500 MHz spectrometer, with a frequency of 500 MHz. d_1 = 20 s and 64 scans. The spectra were

referenced to the residual solvent peak (D_2O, singlet, 4.80 ppm). Analysis of the spectra was performed using MestreNova© NMR data processing software. Chemical shifts (δ) are reported in ppm.

2.1.15. Photoluminescence spectroscopy (PL)

Photoluminescence (PL) emission spectra were performed using an Edinburgh-FS5-Spectrofluorometer from Edinburgh Instruments Ltd. Steady-state measurements involved the use of a Xenon lamp as the excitation source, and the recorded spectra were corrected for the instrument's response characteristics.

2.2. Chapter 3

2.2.1. Chemicals

Zirconyl chloride octahydrate ($ZrOCl_2 \cdot 8H_2O$ 98%), zirconyl nitrate trihydrate ($ZrO(NO_3)_2 \cdot 3H_2O$ 99%) and 2-aminoterephthalic ($H_2NC_6H_3$-1,4-$(CO_2H)_2$ 99%, NH_2–BDC) were purchased from Sigma Aldrich. Rhodamine 6G (R6G) was purchased from Alpha Aesar (~95%). All the reagents were used as received.

2.2.2. Synthesis of UiO-66-NH_2 ($ZrOCl_2$), UiO-66-NH_2:X^- (X^-: Cl^-, Br^-, I^-) and UiO-66 nanoMOFs

25 mL of a DMF solution containing 51 mg of $ZrOCl_2 \cdot 8H_2O$ (Sigma Aldrich #224316) or 45 mg of $ZrO(NO_3)_2 \cdot 3H_2O$ (Sigma Aldrich #243493) for UiO-66-NH_2 ($ZrOCl_2$) or UiO-66-NH_2:X^- (X^-: Cl^-, Br^-, I^-), respectively, was taken. Then, 25 mL of DMF containing 72.5 mg of 2-aminoterephthalic acid (NH_2–BDC, Sigma Aldrich #381071) were prepared. Later, a heating plate and the adaptor for the 50 mL vial was prepared at 120 °C. When the temperature had been reached, 5 mL of $ZrOCl_2 \cdot 8H_2O$ (or $ZrO(NO_3)_2 \cdot 3H_2O$) and 5 mL of NH_2–BDC were added to a 50 mL round flask and the mixture was sonicated for 30 seconds. In the case of halide-modulated synthesis, the 50 mL flask contained the corresponding sodium halide salt (32 mg of NaCl (Fisher Scientific #S/3161/60), 56 mg of NaBr (Sigma Aldrich #71329) or 81 mg of NaI (Sigma Aldrich #383112)). Then, 1.8 mL of acetic acid (AA) was added to the solution. After sonication for another 30 seconds, the round flask was placed in the heating plate, and was left at 120 °C overnight.

The sample was collected by centrifugation (10 min, 7100 rcf). Then it is washed 3 times in DMF and 3 times in methanol. Finally, the UiO-66-NH_2 ($ZrOCl_2$) was left in 1 mL of MeOH in an Eppendorf tube.

The same reaction protocol was used but replacing the NH_2–BDC with 66.5 mg (Sigma Aldrich #185361) of BDC to produce UiO-66 and UiO-66:Cl^- nanoMOFs.

2.2.3. Colloidal stability tests

DLS measurements at different times (up to 24 h) were carried out in different media: MilliQ water, cell culture medium (Dulbecco's Modified Eagle Medium with phenol red, 4.5 g/L D-glucose, L-glutamine and pyruvate (DMEM Gibco, Thermo Fisher Scientific, Massachusetts, USA) supplemented with 10% fetal bovine serum (Gibco, Thermo Fisher, Massachusetts, USA) and 1% penicillin/streptomycin (P/S, Gibco, Thermo Fisher Scientific,

USC DE COMPOSTELA

Massachusetts, USA)), phosphate-buffered saline (PBS, 1×, pH = 7.4) and lysosomal medium (phagolysosomal simulant fluid (PSF), pH = 5; PSF (100 mL): 114 mM sodium phosphate dibasic anhydrous, 114 mM sodium chloride, 0.5 mM sodium sulfate anhydrous, 0.2 mM calcium chloride dihydrate, 6 mM glycine and 20 mM potassium hydrogen phthalate).

2.2.4. Encapsulation of Rhodamine 6G.

UiO-66-NH_2 was loaded with Rhodamine 6G (R6G, a fluorescent dye widely used to stain cell mitochondria; Rhodamine 6G J62315; Alfa Aesar) just by mixing the UiO-66-NH_2 as dispersed in water (100 µL, 1 mg/mL Zr) with a solution of R6G in water (100 µL, 2 mg/mL). The mixture was incubated for 5 days at 80 °C to ensure that the maximum loading was reached regardless of the diffusion kinetics of the dye molecules through the UiO-66-NH_2 pores. Then the excess dye was removed by centrifugation and the UiO-66-NH_2@R6G was washed three times with water in order to remove the R6G that was weakly adsorbed onto the UiO-66-NH_2 surface.

2.2.5. Cargo stability tests

Cargo stability tests were performed at different times (t = 0, 1, 5 and 24 h) in different media: MilliQ water, PSF and DMEM. For the analysis, 100 µL of the samples of UiO-66-NH_2 (1 mg/mL of Zr) were centrifuged, and the pellets was redispersed in 500 µL of the corresponding media for the analysis. At each time point, 100 µL of each sample were centrifuged to remove the supernatant and measure its fluorescence using the same procedure that was used previously to calculate the dye/MOF.

2.2.6. Cell culture

The A549 (human lung carcinoma) cell line was maintained in culture in Dulbecco's Modified Eagle Medium with phenol red, 4.5 g/L D-glucose, L-glutamine and pyruvate (DMEM Gibco, Thermo Fisher Scientific, Massachusetts, USA) supplemented with 10% fetal bovine serum (Gibco, Thermo Fisher, Massachusetts, USA) and 1% penicillin/streptomycin (P/S, Gibco, Thermo Fisher Scientific, Massachusetts, USA). Cells were cultured at 37 °C under a 5% CO_2 atmosphere and kept under humid conditions. After reaching 80% confluency, the cells were washed three times with Dulbecco's phosphate buffered saline (PBS, Biowest, France) and passaged after incubation with 0.25% Trypsin–EDTA (Gibco, Thermo Fisher Scientific, Massachusetts, USA).

2.2.7. Resazurin test

A549 cells were seeded (5×10^3 cells per well) in 96-well microplates 24 h prior to their exposure to different nanoMOFs in a concentration range from 0 to 100 µg/mL for 24 hours. After that, cells were washed three times with PBS and a freshly prepared solution of 10% v/v resazurin (from a 0.2 mg/mL stock solution; Sigma Aldrich, USA, #199303-1G) in complete culture medium was added and incubated for 4 h at 37 °C. The fluorescence at 610/20 nm was measured in a microplate reader (Infinite® 200 PRO, Tecan, Switzerland). Viability values represent the mean ± standard deviation of measurements from three wells.

USC UNIVERSIDADE DE SANTIAGO DE COMPOSTELA

2.2.8. Confocal microscopy imaging

100 μL containing 5×10^3 A549 cells were seeded in each well of an 18 well-ibiTreat chamber slide (0.34 cm^2 per well, Ibidi, Germany, #81816). Cells were exposed for 6 hours to 50 pM of nanoMOFs. Cells were washed with PBS and fixed with a 3.7% *p*-formaldehyde solution (Sigma, USA # 47608) for 20 min at RT and imaged in an Andor Dragonfly spinning disk confocal system mounted on a Nikon TiE microscope equipped with a Zyla 4.2 PLUS camera (Andor, Oxford Instruments) and an OKO-lab incubator. The emission filter used for imaging was 561/620 nm under a 561 nm laser excitation. After acquisition, images were analyzed with FIJI software A549.

2.2.9. Flow cytometry experiments.

1×10^4 cells per well were seeded in a 48 well plate (Corning, New York, USA), 24 h prior to their exposure to 25 pM or 2.5 μg/mL of nanoMOFs (300 μL) in DMEM for 6 hours. Then, cells were washed three times with PBS and detached by incubating them for 5 minutes with 75 μL of 0.25% trypsin-EDTA which was later neutralized with complete DMEM without phenol red. After that, cell suspensions were transferred to a 96 well plate and analyzed in a Guava easyCyte BG HT flow cytometer (Merck Millipore, Massachusetts, USA) with a forward scatter signal threshold value of 20 000. UiOs-66-NH_2@R6G nanoMOF uptake was measured *via* fluorescence in the RED-B channel (695/50 nm) and a total of 5000 cells per group (in triplicate) were analyzed (including a control cell group with no nanoMOF exposure). After acquisition, data were analyzed with Flowjo software.

2.3. Chapter 4

2.3.1. Chemicals

Zirconium ethoxide ($Zr(OEt)_4$, 97%), Zirconium(IV) isopropoxide isopropanol complex ($Zr(OiPr)_4$, 99.9% trace metals basis), Zirconium(IV) butoxide solution ($Zr(OBut)_4$, 80 wt. % in 1-butanol), formic acid (FA, ≥96%), Methylsulfonylmethane ($(CH3)_2SO_2$, Pharmaceutical secondary standard) from Sigma-Aldrich. 5,10,15,20-(Tetra-4-carboxyphenyl)porphyrin (TCPP, 98%) from PorphyChem. N,N-dimethylformamide (DMF ≥99.8%), methanol (MeOH, LC/MS Grade), acetic acid glacial (AA, 99.7%), Sodium hydrogen carbonate ($NaHCO_3$) were purchased from Fischer Scientific. Deuterium oxide (D_2O, 99.8% D atoms, Acros Organics. All the chemical reagents were used without further purification.

2.3.2. Synthesis of MOF-525 and PCN-224

In 2 mL-vials, two solutions (A and B) are separately prepared and then mixed to start the reaction. In one solution it is dissolved the metal precursor (solution A – Zr alkoxide) together with the modulator (acetic acid), and in the other one the linker (solution B – TCPP or Tetrakis(4-carboxyphenyl) porphyrin). The two solutions are prepared in DMF.

The quantities are specified below, depending on the ratio L/M, the Zr precursor and Mod/M adopted.

In a vial, equipped with a magnetic stirrer, the solution B is added and put under magnetic stirring at 500 rpm; then, the solution A is quickly added, the vial is sealed, and the reaction is stirred at 75 °C (or room temperature) for 1 hour in dark condition.

USC DE COMPOSTELA

The reaction is then centrifuged at 10000 g for 10 min; the recovered pellet is washed by centrifugation (10000 g, 10 min) 3-times with 1 mL of DMF and 2-times with 1 mL of MeOH. The final sample is resuspended in 1 mL of MeOH.

Table 2-1. Adopted quantities for the synthesis of PCN-224 and MOF-525 starting from $Zr(OEt)_4$ precursor.

	Entry	**Ratio Mod/M 560**
Sol. A	$Zr(OEt)_4$	6.8 mg
	AA	0.800 mL
	DMF	0.200 mL

	Entry	**Ratio L/M 0.25**	**Ratio L/M 0.5**	**Ratio L/M 1.0**	**Ratio L/M 1.5**	**Ratio L/M 2.0**
Sol. B	TCPP	5.0 mg	10.0 mg	20.0 mg	30.0 mg	40.0 mg
	DMF	1.000 mL	1.000 mL	1.000 mL	1.000 mL	1.000 mL

Table 2-2. Adopted quantities for the synthesis of PCN-224 starting from different Zr precursor.

	Entry	**Ratio Mod/M 250**	**Entry**	**Ratio Mod/M 250**	**Entry**	**Ratio Mod/M 250**
Sol. A	$Zr(OEt)_4$	6.8 mg	$Zr(OiPr)_4$	9.7 mg	$Zr(OBut)_4$	11.5 µL
	AA	0.358 mL				
	DMF	0.642 mL				

	Entry	**Ratio L/M 0.25**
Sol. B	TCPP	5.0 mg
	DMF	1.000 mL

2.3.3. Synthesis of PCN-222

In 2 mL-eppendorfs, the two solutions A (containing the modulator and the metal precursor) and B (with TCPP linker) are separately prepared and then mixed together to start the reaction.

In this case, the modulator is formic acid and the temperature is fixed at 75 °C.

The quantities specified below are relative to:

ratio L/M = 0.33 and Mod/M = 100: 24 h reaction.

USC UNIVERSIDADE DE SANTIAGO DE COMPOSTELA

ratio L/M = 0.35-1.5 and Mod/M = 250 or 560: 1 h reaction.

In a vial, equipped with a magnetic stirrer, the solution B is added and put at 75 °C under magnetic stirring at 500 rpm for 10 minutes; then, the solution A is quickly added, the vial is sealed, and the reaction is stirred in dark condition for the proper time.

The reaction is then centrifuged at 10000 g for 10 min; the recovered pellet is washed by centrifugation (10000 g, 10 min) 3-times with 1 mL of DMF and 2-times with 1 mL of MeOH.

The final sample is resuspended in 1 mL of MeOH.

2.3.4. Digestion of Zr-porphyrinic MOFs for ^{1}H-NMR quantification

Quantification of TCPP/OAc^- was conducted by digesting approximately 2 mg of each sample (L/M ratios 0.25, 0.50, 1.00, 1.50, and 2.00) using a tip of a spatula in a 2 mL Eppendorf tube. Subsequently, 980 µL of a 1M $NaHCO_3$ solution prepared in D_2O were added, and the mixture was sonicated for 20 minutes to achieve complete digestion of Zr-porphyrinic nanoMOFs, as per the following reaction:[129]

$$Zr_6O_4(OH)_4(TCPP)_x(OAc)_y + 18HCO_3^- \rightarrow 3[Zr_2(OH)_2(CO_3)_4]^{2-} + 8H_2O + 6CO_2 + x\,TCPP + y\,OAc$$

Following digestion, 20 µL 50 mM of methylsulfonylmethane ($(CH_3)_2SO_2$) were introduced into the solution as an internal standard, featuring a singlet peak for 6 protons at a chemical shift of 3.18 ppm.[240]

2.3.5. Continuous PCN-224 synthesis procedure

Stock solutions of ligand and metal precursor were prepared separately: TCPP (0.032mmol, 25mg) was dissolved in 5 mL of DMF and $Zr(OEt)_4$ (0.125 mmol, 34 mg) in a mixture of DMF (1 mL) and acetic acid (4 mL). Then both solutions $Zr(OEt)_4$ and TCPP were loaded in two discrete injection channels and were pumped using a syringe pump at room temperature with an individual flow rate 0.5 mL/min into PP Y-micromixer (I.D= 2.3mm) connected to 146 mm long silicone tube (1.8 I.D mm) giving a residence time of 25 s. The obtained purple powder was washed twice with DMF (1mL) and three times with MeOH (1 mL). The final sample is resuspended in 1 mL of MeOH.

2.4. Chapter 5

2.4.1. Chemicals

hydrogen tetrachloroaurate (III) hydrate ($HAuCl_4$, Au≥49%, Thermo Scientific); hydrochloric acid (HCl, 37%); N,N-dimethylformamide (DMF, ≥99.8%, Fisher Scientific); chloroform ($CHCl_3$, ≥99.8%, Fisher Scientific); silver nitrate ($AgNO_3$, ≥99.0%, Sigma-Aldrich); L-Ascorbic acid ($C_6H_8O_6$, ≥99%, Sigma-Aldrich); sodium borohydride ($NaBH_4$, ≥98.0%, Sigma-Aldrich); citric acid (≥ 99.5%, Sigma-Aldrich); cetyltrimethylammonium chloride (CTAC, 25 wt% in H_2O, Sigma-Aldrich); hexadecyltrimethylammonium bromide (CTAB, ≥98%, Sigma-Aldrich); poly(ethylene glycol) methyl ether thiol (MeO-PEG-SH, 2 kDa, Sigma Aldrich), Zirconium ethoxide ($Zr(OEt)_4$, 97%, Sigma-Aldrich), 2-aminoterephthalic acid (NH_2–BDC, 99% Sigma-Aldrich), terephthalic acid (BDC, 98% Sigma-Aldrich), 2,6-naphthalenedicarboxylic acid (NDC, 99%, Sigma-Aldrich), biphenyl-4,4′-

USC
DE SANTIAGO
DE COMPOSTELA

dicarboxylic acid (97%, Sigma-Aldrich), 2,2′-bipyridine-5,5′-dicarboxylic acid (97% Sigma-Aldrich) and acetic acid glacial (AA, 99.7%, Fisher Scientific)

2.4.2. Synthesis of Au Nanostars (AuNSs)

Synthesis of citrate-stabilized seeds

Citrate-stabilized gold nanoparticles (Cit-Au NPs) with an average core diameter of approximately 15 nm were synthesized following the established protocol. Initially, 144 mL of Milli-Q water was added to a 250 mL three-necked round-bottom flask equipped with a condenser, and the system was heated on a hot plate set to 120ºC. Once the water reached boiling, a mixture of sodium citrate (3.75 mL, 60 mM) and citric acid (1.25 mL, 60 mM) was introduced under vigorous stirring at 450 rpm for 15 minutes. EDTA (0.1 mL, 30 mM) was then rapidly injected into the solution, followed by the quick addition of $HAuCl_4$ (1 mL, 25 mM). After approximately 60 seconds, the solution color transitioned from pale yellow to dull blue, and subsequently to wine-red, indicating the formation of Cit-Au NPs. Heating was then discontinued, although magnetic stirring was maintained. When the temperature of the mixture dropped to 95ºC, the reaction was quenched by immersing the flask in an ice bath.

Seed-mediated growth synthesis of AuNSs

A solution of $HauCl_4$ (100 mL, 0.25 mM) was prepared and placed in a 250 mL beaker under magnetic stirring at 350 rpm. To this solution, HCl (150 µL, 1 M) was added, followed by the addition of 1.7 mL of gold nanoparticles citrate-stabilized (AuNPs) with a diameter of 11 nm at a concentration of 37.2 nM after a few seconds. Subsequently, a solution of $AgNO_3$ (1.5 mL, 1 mM) and freshly prepared ascorbic acid (0.75 mL, 66.67 mM) were added simultaneously, and the mixture was left to stir for 5 minutes. Finally, a pre-heated solution of CTAB (25 mL, 0.2 M) was added to prevent crystallization and the mixture was stirred for an additional 2–5 minutes.

To isolate the gold nanostars (AuNSs), the solution was centrifuged twice (10 minutes, 7000 rcf). After the final centrifugation, the sediments were redispersed in a 0.16 mg/mL CTAB solution with a gold concentration of 0.2 M to ensure the stability of the AuNSs and prevent aggregation during storage.

The color of the solution transitioned from a clear yellow ($HauCl_4$ solution) to a dark blue-gray following the addition of $AgNO_3$ and ascorbic acid. The final sample exhibited a darker blue-gray color.

2.4.3. Synthesis of Au Nanorods (AuNRs)

Synthesis of seeds

CTAB stock 0.2 M solution was prepared and warmed to 40°C prior to each reaction to ensure complete transparency. A solution of $HauCl_4$ (0.25 mL, 0.01 M) was then added to 7.5 mL of the 0.2 M CTAB solution, and the mixture was equilibrated to the temperature of a water bath set at 26°C. A freshly prepared $NaBH_4$ solution (600 µL, 0.01 M) was rapidly added to the stirring solution (350 rpm), and the mixture was stirred for 2 minutes. To ensure complete removal of any unreacted $NaBH_4$, the seed solution was left for 1 hour before use in the growth solution.

The seed solution typically exhibits a yellow-brown color, which should appear clear. If the solution is too dark, gold nanorods (AuNRs) may not form correctly, leading to the formation of spherical nanoparticles instead.

Seed mediated growth synthesis of Au Nanorod (AuNRs)

A solution of CTAB (0.2 M, 100 mL) was placed in a glass vessel (250 mL capacity) and equilibrated to 26°C. $HauCl_4$ (0.01 M, 4.25 mL) was then added to the CTAB solution. Once the mixture had stabilized at 26°C under stirring (350 rpm), a solution of $AgNO_3$ (1.23 mL, 0.01 M) was introduced. After 2 minutes of stirring, a freshly prepared ascorbic acid solution (0.1 M, 680 µL) was added. Following an additional 10 minutes of stirring, 1.1 mL of the pre-prepared seed solution (maintained at 26°C to prevent CTAB crystallization) was added, and stirring was continued for another 2 minutes. The reaction mixture was then left to stand overnight in a 26°C water bath.

The resulting sample was collected by centrifugation at 10000 rcf for 30 minutes at 28°C, a process that must be carried out as quickly as possible to prevent CTAB crystallization. The sample was then washed twice with water under the same conditions and redispersed in a 0.16 mg/mL CTAB solution.

2.4.4. Synthesis of Au Bipyramids (AuBipy) and phase transfer

Synthesis of Pentatwinned Seeds

In a glass vial of 20 mL, initial seeds were prepared adding 8.639 mL of water together with 0.661 mL of the CTAC solution and 0.100 mL of $HAuCl_4$ 25 mM (in water) under vigorous magnetic stirring (1000 rpm) for 5 min. After that, 0.1 mL of citric acid 0.5 M (in water) was added to the mixture of reaction, and immediately two doses nonstop of 0.25 mL of freshly prepared $NaBH_4$ 25 mM (in water). The solution turned from pale yellow to brownish solution indicating the formation of gold seeds. After 2 min of stirring, the vial was closed, and these seeds were heated in a heating block at 80 °C for 90 min under gentle stirring (300 rpm). Finally, the color of the solution changed from brown to red indicating that the aging process was successful in creating the pentatwinned defects. The solution was stored at room temperature.

Scaled-Up AuBipy Synthesis

In a glass bottle of 1 L, the growth solution of AuBipy was prepared by adding under magnetic stirring (500 rpm) 275 mL of water, 250 mL of CTAB 0.2 M, 10 mL of $HAuCl_4$ 25 mM, 5 mL of $AgNO_3$ 10 mM, 0.833 mL of HCl 12 M, and 4 mL of ascorbic acid 0.1 M (all in water). After the change of color from orange-yellow to colorless with the addition of the ascorbic acid, 12 mL of pentatwinned seeds were added. The mixture of reaction was kept at 30 °C for 2 h. After this, the AuBipy were washed with water three times to remove CTAB excess and left in a final volume of 10 mL of water.

2.4.5. PEGylation and Phase Transfer of inorganic nanoparticles

AuBipy without the CTAB excess presents a LSPR around 808 nm. At this wavelength, the absorption molar coefficient is $3.63 \times 10^{10}\ M^{-1}\ cm^{-1}$. The number of chains of MeO-PEG-SH used for the PEGylation was 500 000 chains per particle. A 1% of this total amount (5000 chains) was added to the colloidal dispersion of AuBipy, which means that 75 µL of MeO-PEG-

SH and 20 mg/mL solution were added to 10 mL of 15 nM AuBipy in water. In a separate tube, 150 mg of MeO-PEG-SH, which would correspond to 500000 chains per particle, were dissolved in chloroform. The NPs in water and the PEG solution in chloroform were mixed in a separation funnel and strongly shaken followed by the addition of 10 mL of methanol for beginning the phase transfer from aqueous to organic phase. The emulsion formed was destroyed with the addition of more water. Once the AuBipy was in the organic phase, they were collected and dried under rotatory evaporation and redispersed in the same volume of DMF as they were in the beginning.

The phase transfer of AuNRs was following the same protocol than AuBipy but using a absorption molar coefficient of $4.90 \times 10^9\ M^{-1}\ cm^{-1}$, and in case of AuNSs, the concentration of particle is determined with the amount of citrate stabilized seeds added into the synthesis.

2.4.6. Synthesis of UiO-family nanocomposistes

For the synthesis of UiO-family nanocomposites, 1 mL of 10 nM (or a lower concentration depending on the desired shell thickness) was added to 5 mL of $Zr(OEt)_4$ and 5 mL of the linker solution in DMF, as outlined in Table 2-3. The reaction mixture was maintained at the desired temperature for 30 minutes, or for 72 hours if conducted at room temperature. The samples were washed three times with DMF, followed by three washes with MeOH, and subsequently suspended in 1 mL of MeOH. For the MOF-867 samples, three additional washing steps with DMSO at 45°C were required after the DMF washes and before the MeOH washes to remove excess insoluble linker.

Table 2-3. synthetic conditions for the synthesis of UiO-family MOFs and their nanocomposites

MOF	$Zr(OEt)_4$ equivalents	$Zr(OEt)_4$ concentration (mg/mL)	Linker equivalents	Linker concentration (mg/mL)	HOAc equivalents	HOAc added (mL)
UiO-66	1.00	1.72	2.5	2.66	995	1.8
UiO-66-NH2			2.5	2.90	995	1.8
DUT-52			2.5	3.44	552	1.0
UiO-67			2.0	3.06	221	0.4
MOF-867			2.0	3.10	387	0.7

2.4.7. Laser Irradiation (Heating Experiments)

For the laser irradiation experiments, 200 µL of the samples were placed in the wells of a 96-well plate. Depending on the specific experiment described in each section, the samples either contained cells or did not. Irradiation was performed using an 808 nm laser (Lasing, #FC-W-808A) coupled to a zoom fiber collimator (Thorlabs, #ZC618SMA-B). This collimator was utilized to control the spot size and ensure homogeneous irradiation of the cells.

USC DE SANTIAGO DE COMPOSTELA

To determine the intensity of the laser irradiation received by the cells, a power energy meter (Thorlabs, #PM100D) equipped with a thermal power head (10 W, 25 mm, Thorlabs, #S425C) was employed to measure the output power. The spot size was determined by using a viewing card (Thorlabs, #VRC4) to visualize the spot, and ImageJ software was utilized to measure its dimensions. Since the beam was collimated, a uniform spot distribution was assumed, allowing the intensity to be calculated by dividing the power (7.85 W) by the surface area (0.785 cm^2) of the spot giving an irradiance of 10 W/cm^2. Various experimental conditions involving different time intervals and power densities were investigated, as specified in each individual experiment.

2.5. Chapter 6

2.5.1. Chemicals

All the reagents including phosphorus oxychloride ($POCl_3$, 99%, Sigma-Aldrich); poly(ethylene glycol) methyl ether (mPEG, Mn 5000, Sigma-Aldrich); triethylamine (≥99.5%, Sigma-Aldrich); dichloromethane (DCM, ≥99.8%, Fisher Scientific);hydrogen tetrachloroaurate (III) hydrate ($HAuCl_4$, Au≥49%, Thermo Scientific); hydrochloric acid (HCl, 37%); N,N-dimethylformamide (DMF, ≥99.8%, Fisher Scientific); chloroform ($CHCl_3$, ≥99.8%, Fisher Scientific); silver nitrate ($AgNO_3$, ≥99.0%, Sigma-Aldrich); L-Ascorbic acid ($C_6H_8O_6$, ≥99%, Sigma-Aldrich); sodium borohydride ($NaBH_4$, ≥98.0%, Sigma-Aldrich); citric acid (≥ 99.5%, Sigma-Aldrich); cetyltrimethylammonium chloride (CTAC, 25 wt% in H_2O, Sigma-Aldrich); hexadecyltrimethylammonium bromide (CTAB, ≥98%, Sigma-Aldrich); poly(ethylene glycol) methyl ether thiol (MeO-PEG-SH, 2 kDa, Sigma Aldrich);zirconium (IV) n-butoxide (80 wt% in 1-butanol, Sigma-Aldrich); 5,10,15,20-(tetra-4-carboxyphenyl)porphyrin (TCPP, 98%, PorphyChem); 1-propanol (99.7%, Sigma-Aldrich); acetic acid glacial (CH_3COOH, 99.7%, Fisher Scientific); N,N-dimethylformamide (DMF, ≥99.8%, Fisher Scientific); benzoic acid (≥99.5%, Sigma-Aldrich); and methanol (MeOH) were used as purchased without any purification.

2.5.2. Synthesis of mPEG-PO_3

mPEG-PO_3 was synthesized using a slightly modified version of a previously reported method.[170] The synthesis was conducted in a two-neck flask, where 50 mmol of $POCl_3$ dissolved in 5 mL of DCM were initially added. Subsequently, 150 mmol of triethylamine was introduced at 0 °C. After 30 min, 15 mmol of mPEG 5 kDa was added to the mixture in 50 mL of DCM. The resulting solution was stirred at room temperature for a period of 10 h. Following the stirring process, 20 mL of water was added to the reaction mixture and allowed to react for an additional 3 h. Subsequently, the DCM solvent was removed under vacuum using a rotavapor, and the crude product was subjected to purification by dialysis, utilizing a dialysis membrane with a molecular weight cutoff of 3500. Finally, the residual water was eliminated through lyophilization, resulting in the formation of mPEG-PO_3 as a white solid.

2.5.3. Synthesis of Au Bipyramids (AuBipy), functionalization and phase transfer

The synthesis, functionalization and phaser transfer of the AuBipy, was following the same protocol than in the chapter number 5.

USC UNIVERSIDADE DE SANTIAGO DE COMPOSTELA

2.5.4. Synthesis of PCN-224

Preparation of Zr_6-oxo Cluster

100 mL of 1-propanol and 5 mL of Zr (IV) n-butoxide (80 wt %) were mixed and stirred for 10 min. Then, 33 g of benzoic acid was added, and the mixture was ultrasonicated for 20 more minutes. After that, it was heated at reflux and stirred overnight. The next day, it was rotavapored and the solid product was washed 3 times with 1-propanol and 10 min of centrifugation at 7000 rcf. The final product was dried under a vacuum at RT. This cluster was used for the synthesis of PCN-224-p and AuB@PCN-224. For PCN-224-w, the nonvolatile remnants of 1-propanol were washed and removed with MeOH, and the solid was dried under vacuum at room temperature.

MOF Synthesis

20 mg of Zr_6-oxo cluster was added together with 0.8 mL of acetic acid and 0.2 mL of DMF in a glass vial. In an Eppendorf tube, 10 mg of TCPP linker were weighed and dissolved in 1 mL of DMF or in 1 mL of AuBipy DMF solution using ultrasonication. The mixture in the vial was stirred with a magnetic bar at 300 rpm and then the solution of the Eppendorf tube was added. The reaction was carried out at RT for 1 h. The resulting solution was sonicated and collected in a 2 mL Eppendorf tube and centrifugated at 10000 rcf for 10 min. It was washed 3 times with 1 mL of DMF and 3 more with 1 mL of MeOH and centrifugated each of them (10 min, 10000 rcf). It was left in 1 mL of MeOH.

2.5.5. Cresyl Violet Loading

PCN-224 or AuB@PCN-224 NCs, 200 µL dispersions at a concentration of 1 mg/mL of solid in methanol (MeOH) were combined with a solution of CV in water (200 µL, 2 mg/mL). The resulting mixture was incubated overnight at RT under continuous shaking. After incubation, the nanoMOFs or NCs were separated from the solution by centrifugation at 10000 rpm for 10 min.

2.5.6. PCN-224 PEGylation

The surface modification of PCN-224 was carried out using the mPEG-PO_3 polymer. To accomplish this, the product of one synthesis of PCN-224-w or AuB@PCN-224 in water was combined with 2.5 mL of a 25 mg/mL aqueous solution of mPEG-PO_3. The resulting mixture was stirred using a magnetic bar at a speed of 500 rpm for 3 h. Subsequently, the coated material underwent a washing procedure consisting of three water washes. Each wash involved centrifugation at 10000 rcf for 10 min.

2.5.7. Cell Culture

The A549 cell line, derived from human lung carcinoma, was maintained in a culture of DMEM with phenol red, containing 4.5 g/L of D-glucose, L-glutamine, and pyruvate. This culture medium (DMEM Gibco, Thermo Fisher Scientific, Massachusetts, USA) was further supplemented with 10% fetal bovine serum (Gibco, Thermo Fisher, Massachusetts, USA) and 1% penicillin/streptomycin (P/S, Gibco, Thermo Fisher Scientific, Massachusetts, USA) to create complete DMEM (cDMEM). Cell culture was conducted at a constant temperature of 37 °C, within a 5% CO_2 atmosphere, and maintained under humid conditions. Subsequently,

when the cells reached 80% confluency, they were subjected to a washing step using Dulbecco's PBS (Thermo Fisher #14 190 169) before being passaged. The passaging process involved incubating the cells with 0.25% trypsin-ethylenediaminetetraacetic acid (Gibco, Thermo Fisher Scientific, Massachusetts, USA) to facilitate detachment and subsequent subculture.

2.5.8. Laser Irradiation (Heating Experiments)

The experiments were conducted using the same methodology as described in Chapter 5.

2.5.9. Microscopy Imaging

A549 cells were initially seeded onto µ-slide 8 well-ibiTreat chambers, with each well having a surface area of 1 cm^2 (Ibidi, Germany, #80 826). The seeding density used was 20 000 cells per well, and they were cultured in cDMEM for 24 h.

After the 24 h incubation period, the cDMEM was replaced with freshly prepared solutions of PCN-224 and AuBipy@PCN-224 with and without CV at a concentration of 100 pM, diluted in cDMEM. Following a 3 h exposure to these particles, the cells underwent a single rinse with 1X PBS. This step aimed to eliminate any noninternalized particles that might have remained dispersed in the cDMEM prior to the subsequent image acquisition.

Fluorescence images of the cells were captured using a Leica Microscope type DMI8, equipped with a Leica DFC9000 camera, and maintained in an incubator at a temperature of 37 °C under a 5% CO_2 atmosphere. To analyze the images, ImageJ software was utilized for image processing and data extraction.

NIR irradiation of the samples was performed using Leica infinity scanner installed in the microscope that allows the scanning of the selected ROIs with a NIR laser using LAS X software.

To study the PDT effect of the particles, AuBipy@PCN-224 was excited with a 405 nm laser in a confocal microscope. The experiments were performed using an Andor Dragonfly spinning disk confocal system mounted on a Nikon TiE microscope equipped with a Zyla 4.2 PLUS camera (Andor, Oxford Instruments) and an OKO-lab incubator to keep cells at 37 °C under a 5% CO_2 atmosphere during the whole experiment. Samples were irradiated for 2 and 5 min. To study the viability, a live-dead assay employing calcein-AM and propidium iodide was employed as reporters for viable and apoptotic cells, respectively. All the images were processed with ImageJ.

2.6. Chapter 7

2.6.1. Chemicals

Zirconyl chloride octahydrate ($ZrOCl_2$ $8H_2O$, 98%), was provided by Sigma-Aldrich. acetic acid glacial (CH_3COOH, 99.7%); DMF (≥99.8%) were provided by Thermo Scientific, and H_4TBAPy ($C_{44}H_{26}O_8$, 97%) was provided by Alfa Chemical.

2.6.2. Synthesis of AuBipy, AuNRs, PEGylation and phase transfer

The synthesis of the plasmonic nanoparticles, PEGylation process and phase transfer, were carried out according to the protocols described in Chapter 5.

USC DE COMPOSTELA

2.6.3. Synthesis of AuNPs@NU-1000 nanocomposites.

In a 20 mL glass vial, a mixture was prepared by dissolving 64 mg of $ZrOCl_2 \cdot 8H_2O$ and 10 mg of H_4TBAPy in 9 mL of DMF. Subsequently, 1 mL of PEGylated AuNPs (bipyramids or nanorods) with the desired concentration was added, followed by the addition of 2 mL of acetic acid and 1 mL of water. The vial was sealed and heated at 90°C for 30 minutes. After the reaction, the product was collected by centrifugation at 7200 rcf for 10 minutes, followed by three washes with DMF and three washes with acetone. The final product was dried under vacuum for further characterization.

USC UNIVERSIDADE DE SANTIAGO DE COMPOSTELA

3. HIGH-YIELD HALIDE-ASSISTED SYNTHESIS OF METAL–ORGANIC FRAMEWORK UiO-BASED NANOCARRIERS

USC
UNIVERSIDADE DE SANTIAGO DE COMPOSTELA

USC
UNIVERSIDADE
DE SANTIAGO
DE COMPOSTELA

The results presented in the following chapter are published in:

"High-yield halide-assisted synthesis of metal–organic framework UiO-based nanocarriers". (**2022**). Nanoscale, *14*(18), 6789-6801.

Manuel Ceballos[1], Manuela Cedrún-Morales[1], Manuel Rodríguez-Pérez[1], Samuel Funes-Hernando[1], José Manuel Vila-Fungueiriño[1], Giulia Zampini[1], Maria F. Navarro Poupard[1], Ester Polo[1], Pablo del Pino*[1] and Beatriz Pelaz *[1]

[1]Center for Research in Biological Chemistry and Molecular Materials (CiQUS), University of Santiago de Compostela, 15705 Santiago de Compostela, Spain.

Contributions: Preparation, optimization, and characterization of the materials; writing – original draft.

Impact Factor: 6.7 in 2022. Q1 in Nanoscience & Nanotechnology.

USC UNIVERSIDADE DE SANTIAGO DE COMPOSTELA

USC
UNIVERSIDADE
DE SANTIAGO
DE COMPOSTELA

3.1. Introduction

The synthesis of nanosized metal-organic frameworks (nanoMOFs) is requisite for their application as injectable drug delivery systems (DDS) and other biorelevant purposes. Herein, we have critically examined the role of different synthetic parameters leading to the production of UiO-66 crystals smaller than 100 nm. Of note, we demonstrate the co-modulator role conferred by halide ions, not only to produce nanoMOFs with precise morphology and size, but to significantly improve the reaction yield. The resulting nanoMOFs are highly crystalline, and exhibit sustained colloidal stability in different biologically relevant media. As a proof of concept, these nanoMOFs were loaded with Rhodamine 6G (R6G), which remained trapped in most common biologically relevant media. When incubated with living mammalian cells, the R6G-loaded nanoMOFs were efficiently internalized and did not impair cell viability even at relatively high doses.

3.2. Results and discussion

3.2.1. Influence of Zirconium precursor

In order to produce UiO-66-NH_2 nanoMOFs, as starting point, $ZrOCl_2$, NH_2-BDC and AA were used as Zr source, ligand and modulator, respectively, using a molar ratio of 1:2.5:995, herein kept constant unless otherwise specified (see experimental section). The first parameter that we varied was the Zr source, i.e., $ZrO(NO_3)_2$ instead of $ZrOCl_2$. While the Zr cluster (i.e. tetramer) produced by $ZrOCl_2$ favors the kinetic growth of the MOF, the impact of $ZrO(NO_3)_2$ (which forms as cluster the extended oligomer $Zr_8O_{28}(NO_3)_8$)[260] has been previously studied in terms of the product crystallinity, regardless of how it influences the size and shape of the MOFs.[261,262]

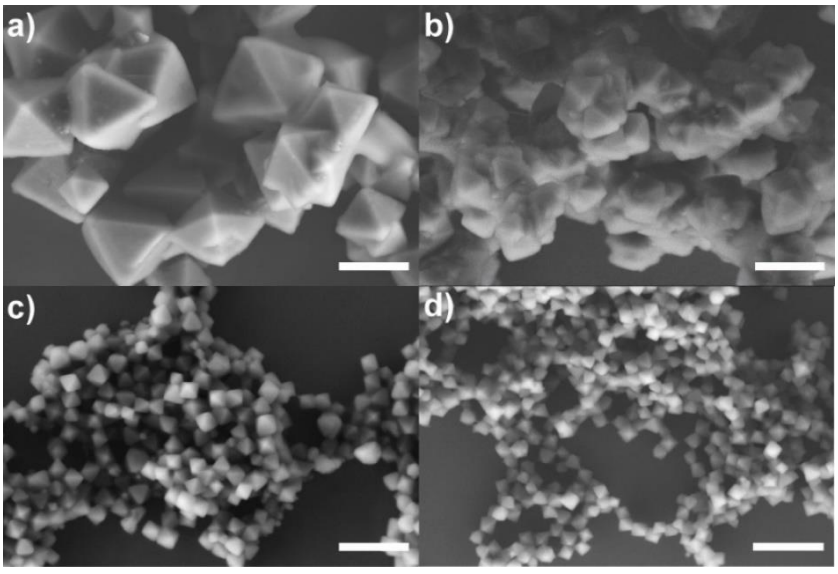

Figure 3-1. Representative micrographs of the UiO-66-NH_2 particles obtained using (a) $ZrOCl_2$ or (b) $ZrO(NO_3)_2$ as Zr precursor; or using the combination of (c) $ZrO(NO_3)_2$ and HCl; and (d) $ZrO(NO_3)_2$ and NaCl. Scale bars correspond to 500 nm.

It was observed that using $ZrOCl_2$ leads to octahedral crystals with a well-defined shape and facets but a broad size distribution, ranging from 200 to 400 nm (see Figures 3-1a 3-2 and 3-3). In the case of $ZrO(NO_3)_2$, the formation of twinned particles can be related with the cluster

USC UNIVERSIDADE DE SANTIAGO DE COMPOSTELA

formed, as shown in Figure 1b (see Figures 3-2 and 3-3). As the Zr stoichiometry for the cluster formed with oxynitrate precursor is double than in the case of the oxychloride one, we hypothesized that during MOF crystal growth several facets grow simultaneously leading to the formation of octahedral particles.

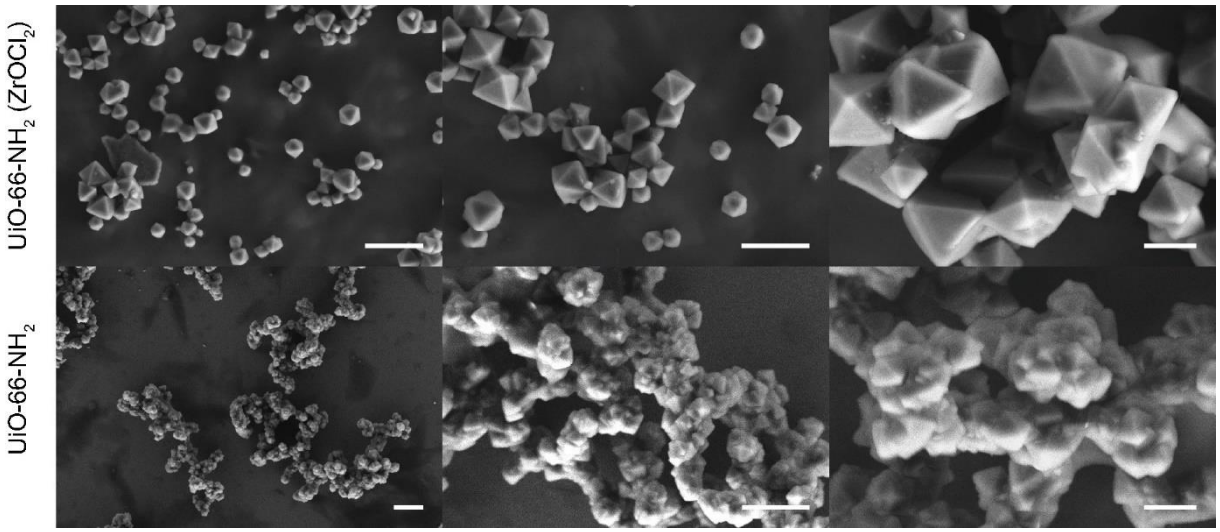

Figure 3-2. Representative SEM images of UiO-66-NH_2 ($ZrOCl_2$) and UiO-66-NH_2 particles obtained using different Zr precursors. Images were taken at different magnifications collected with Everhart-Thornley detector (SE2, secondary electrons) at 3 kV as well as different voltages to get different information. Scale bars from left to right correspond to 500 nm, 400 nm and 200 nm.

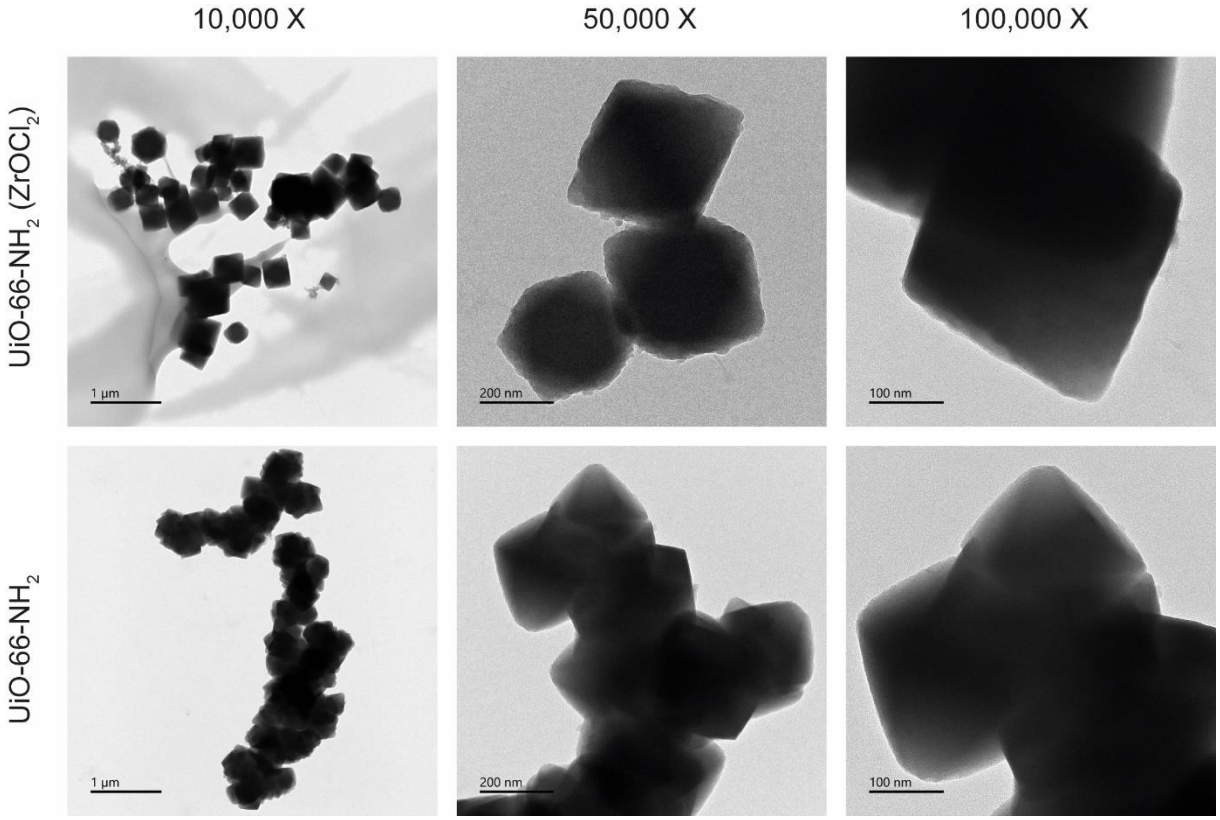

Figure 3-3. Representative TEM images of the UiO-66-NH_2 ($ZrOCl_2$) and UiO-66-NH_2 particles obtained using different Zr precursors.

USC UNIVERSIDADE DE SANTIAGO DE COMPOSTELA

3.2.2. Influence of modulator rate

Aiming to prevent the formation of twinned particles, while using the $ZrO(NO_3)_2$ precursor, the modulator equivalents were varied around our standard conditions (i.e., 995 equivalents of AA, 1.8 mL), using the following volumes (equivalents) of AA: 1.4, 1.6, 1.8, 2.0 and 2.2 mL (775, 885, 995, 1105, 1215 equivalents of AA, respectively). As shown in Figure 3-4, the variation of modulator equivalents in this range appears uninfluential with respect to the size or morphology of the nanoMOFs formed. In particular, it was observed that this parameter appears uninfluential with regards to the morphology of the MOFs formed as in all cases it was obtained twinned particles.

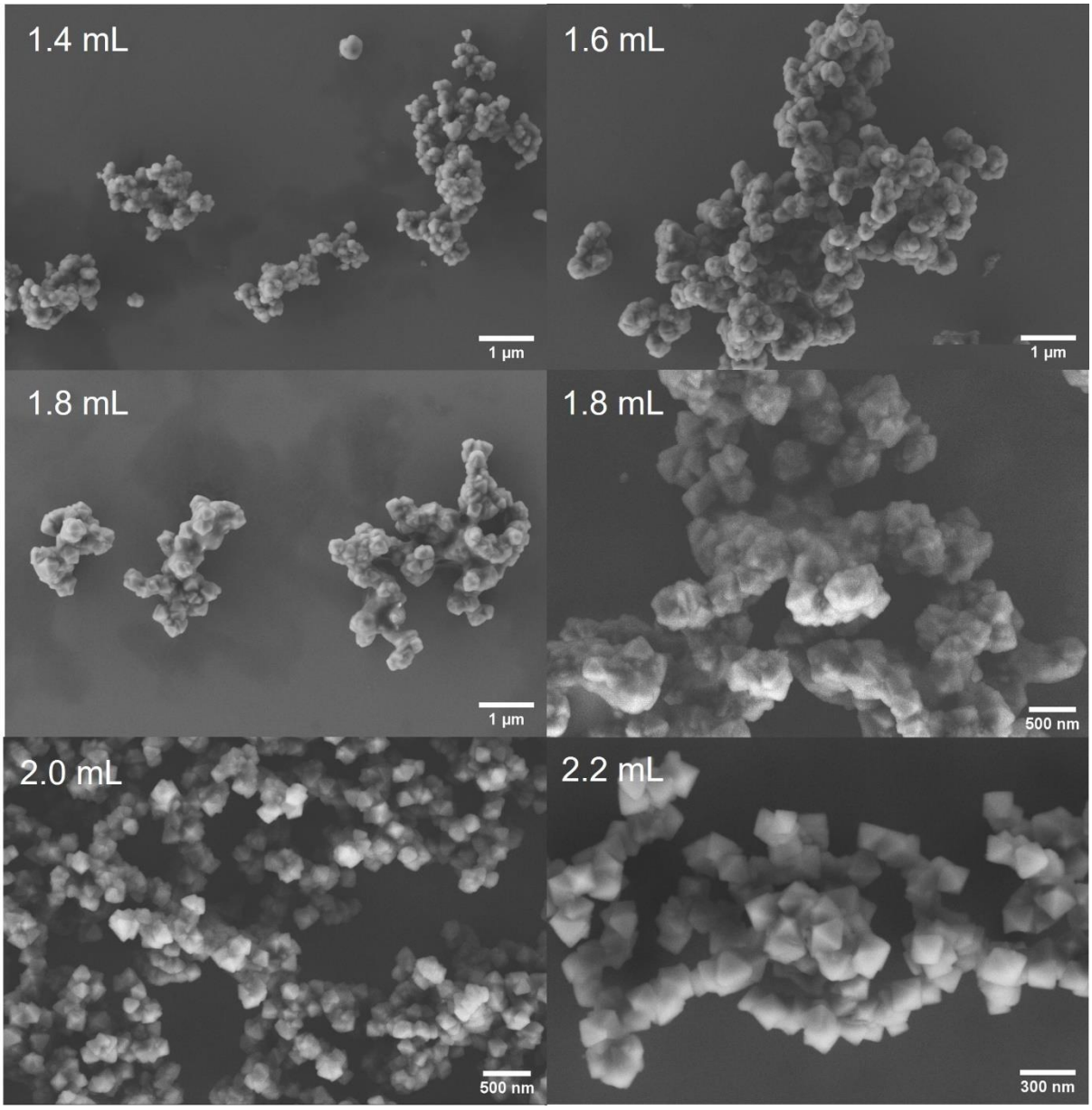

Figure 3-4.UiO-66-NH_2 particles synthesized with $ZrO(NO_3)_2$ as precursor with different amounts of acetic acid as modulator 1.4, 1.6, 1.8, 2.0 and 2.2 mL (775, 885, 995, 1105, 1215 equivalents). Images were taken at different magnifications collected with Everhart-Thornley detector (SE2, secondary electrons) at 3 kV.

USC UNIVERSIDADE DE SANTIAGO DE COMPOSTELA

3.2.3. Influence of chloride as co-modulator

The results from the influence of the two first parameters conclude that the chlorine ions present in the $ZrOCl_2$ precursor were involved on the crystal growth of the particles. Thus, the effect of chloride as co-modulator was investigated by adding it externally, during the synthesis while using the precursor $ZrO(NO_3)_2$. We expected to produce particles with a defined morphology (i.e., octahedral) as it occurred when using $ZrOCl_2$. To confirm this hypothesis, were selected two different chlorine sources, i.e., hydrochloric acid (Figure 3-1c) and sodium chloride (Figure 3-1d) at a fixed ratio of 1:17 $Zr:Cl^-$, leading to discrete nanocrystals with size less than 100 nm.

HCl has been previously identified as responsible for improving the reaction yield and reducing reaction times for the synthesis of UiO-66 and UiO-67.[92,263] Goesten *et al.*[264] argued that this fact was surprising when $ZrCl_4$ was used as precursor, considering that upon the precursor hydrolysis more HCl is produced in the media during the MOF growth. One might think that HCl neutralization would have been a parameter to improve the speed and the synthesis yield instead of the opposite.[264] In this direction, Mu *et al.*[78] related the typically small UiO-66 crystals size (around 200 nm) with the partial ligand deprotonation as a result of the increment of protons in the solution during the synthesis. They used formic acid (FA), hypothesizing that it was responsible for the partial protonation of BDC on the MOF surface, leading to the generation of discrete particles. When a deprotonating agent as triethylamine (TEA) was added, twinned particles were formed instead of octahedral ones.[78] As discussed, in this case, the use of the same amount of Cl^- ions from different sources gives the same result; that are octahedral nanoMOFs of less than 100 nm. This result demonstrates that the pH effect is not a critical factor here, confirming that chlorine ions play an active role, preventing the generation of twinned particles, and more importantly, to get discrete particles with sizes below 100 nm.

3.2.4. Influence of different halides as co-modulators to produce UiO-66-NH_2 nanoMOFs

Some reports have investigated the role of different dihalides or halides such as iodine and fluoride.[265,266] In the case of iodine, its reaction with thiol ligands to form UiO-66-SH has been studied. Iodine can form an RS–I bond. However, this reaction prevents the MOF oxidation, thereby increasing its stability.[265] For fluoride ions, it has been reported that it is capable of strongly interacting with the metal site,[266] acting as blocking agents for carboxylate ligands and breaking the $Zr_8O_{28}(NO_3)_8$ oligomer formed by the oxynitrate precursor.[260]

The anion effect in Zr-based MOF has already been investigated by Reinsch *et al.*[267] They reported that sulphate and dichromate anions coordinate to the metal positions in the Zr cluster, leaving available just eight of the twelve positions for the linker coordination. This led to the formation of UiO-66 with an incomplete number of ligands, which is very frequent.

Therefore, we decided to study systematically the role of the different halides (X^-) in the synthesis of UiO-66-NH_2 nanoMOFs. For that, it was established a common synthetic condition using $ZrO(NO_3)_2$ as a Zr source and the corresponding sodium halide (NaX) salts, which are, sodium fluoride, sodium chloride, sodium bromide, and sodium iodide, while fixing the ratio $Zr:X^-$. As previously discussed, the Zr oxychloride (Figure 3-5a) and the oxynitrate precursors

(Figure 3-5b) led to octahedra with broad size distribution (200–400 nm) and large twinned microparticles, respectively; these samples will be referred to as UiO-66-NH_2 ($ZrOCl_2$) and UiO-66-NH_2, respectively (see Table 3-1).

Table 3-1. Summary table of samples prepared.

Name	Zr precursor	Ligand	Co-modulator	Size (nm)
UiO-66-NH_2($ZrOCl_2$)	$ZrOCl_2$	NH_2-BDC	-	225±37
UiO-66-NH_2	$ZrO(NO_3)_2$	NH_2-BDC	-	>1000
UiO-66-NH_2:Cl^-	$ZrO(NO_3)_2$	NH_2-BDC	Cl^-	94±10
UiO-66-NH_2:Br^-	$ZrO(NO_3)_2$	NH_2-BDC	Br^-	81±9
UiO-66-NH_2:I^-	$ZrO(NO_3)_2$	NH_2-BDC	I^-	109±14
UiO-66($ZrOCl_2$)	$ZrOCl_2$	BDC	-	186±13
UiO-66	$ZrO(NO_3)_2$	BDC	-	>1000
UiO-66:Cl^-	$ZrO(NO_3)_2$	BDC	Cl^-	174±13

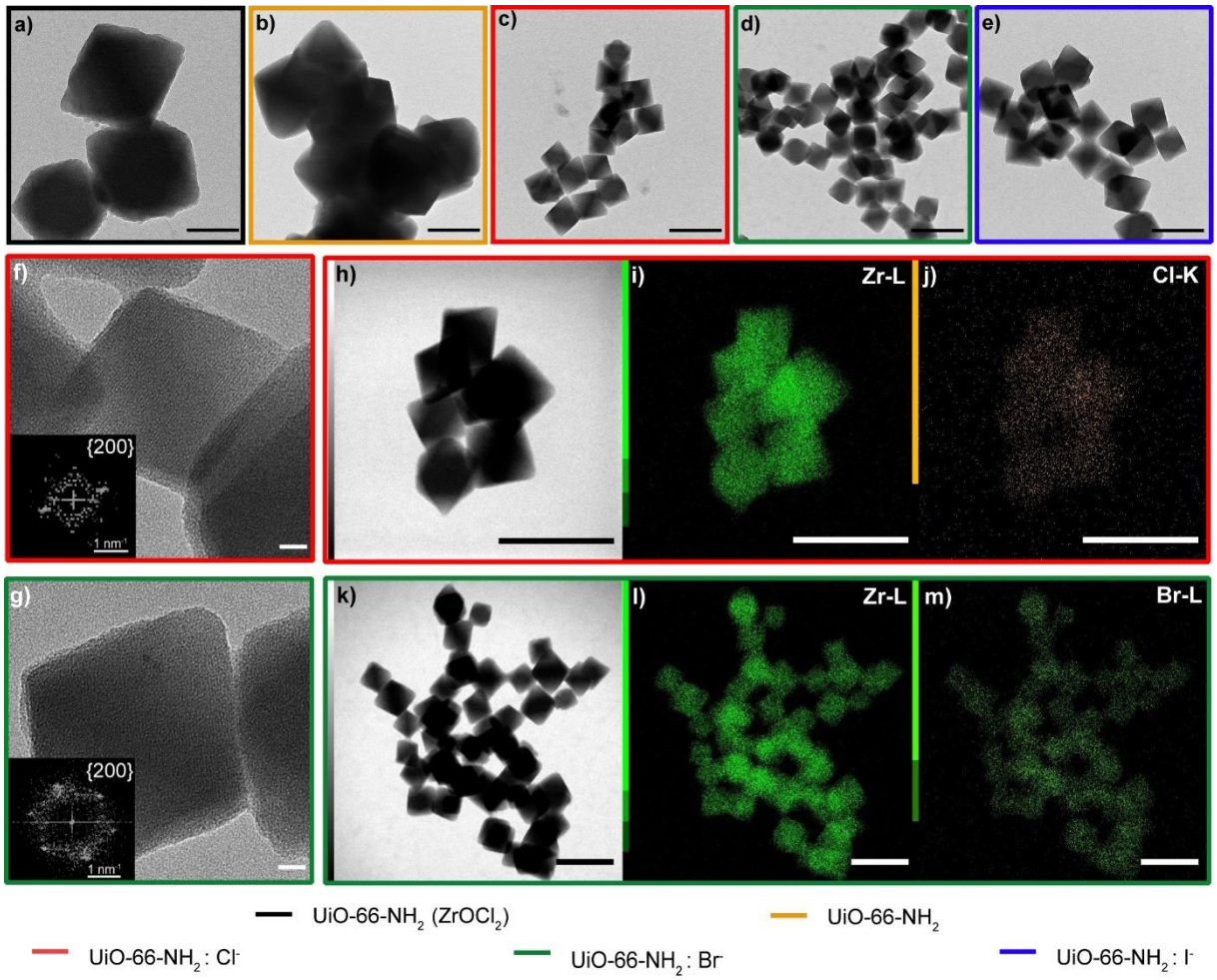

Figure 3-5. TEM images of a) UiO-66-NH_2 ($ZrOCl_2$) (black), b) UiO-66-NH_2 (orange), c) UiO-66-NH_2:Cl^- (red), d) UiO-66-NH_2:Br^- (green), and e) UiO-66-NH_2:I^- (blue), HRTEM of f) UiO-66-NH_2:Cl^- and g) UiO-66-NH_2:Br^- and h–j) STEM-EDX images of UiO-66-NH_2:Cl^- h) with Zr i) and Cl^- j) mapping, and k–m) STEM-EDX images of UiO-66-NH_2:Br^- k) STEM, Zr l) and Br^- m) mapping. Scale bars correspond to 200 nm except for the HRTEM images, in which they correspond to 10 nm.

USC UNIVERSIDADE DE SANTIAGO DE COMPOSTELA

Keeping constant the molar ratio of halide used during the UiO-66-NH_2 nanoMOF synthesis, the previously observed morphology (octahedral and not-twinned particles) and size range (i.e., 80-90 nm) observed using different chloride sources (Figure 3-1c and Figure 3-1d) were maintained in the case of chloride, bromide, and iodide ions (Figure 3-5c, d and e, respectively; Figures 3-6 and 3-7 for additional TEM and SEM images; Figure 3-8 shows the aspect of the solutions in methanol). The halide-assisted nanoMOFs will be denoted as UiO-66-NH_2:Cl^-; UiO-66-NH_2:Br^- and UiO-66-NH_2:I^- for the samples assisted by chlorine, bromine and iodine, respectively; they showed average sizes of 94 ± 10 nm, 81 ± 9 nm, and 109 ± 14 nm (Table 1 and Figure 3-9), respectively, as measured from SEM micrographs. The slightly larger size of UiO-66-NH_2:I^- is attributed to the partial oxidation of iodide in the presence of NO_3^- ions (E° Cl_2/Cl^- = 1:396V, E° Br_2/Br^- = 1:098V, E° I_2/I^- = 0:0620V, and E° NO_3^-/NO_2^- = 0:0940V), decreasing the amount of this co-modulator and increasing the size of the nanoMOFs.

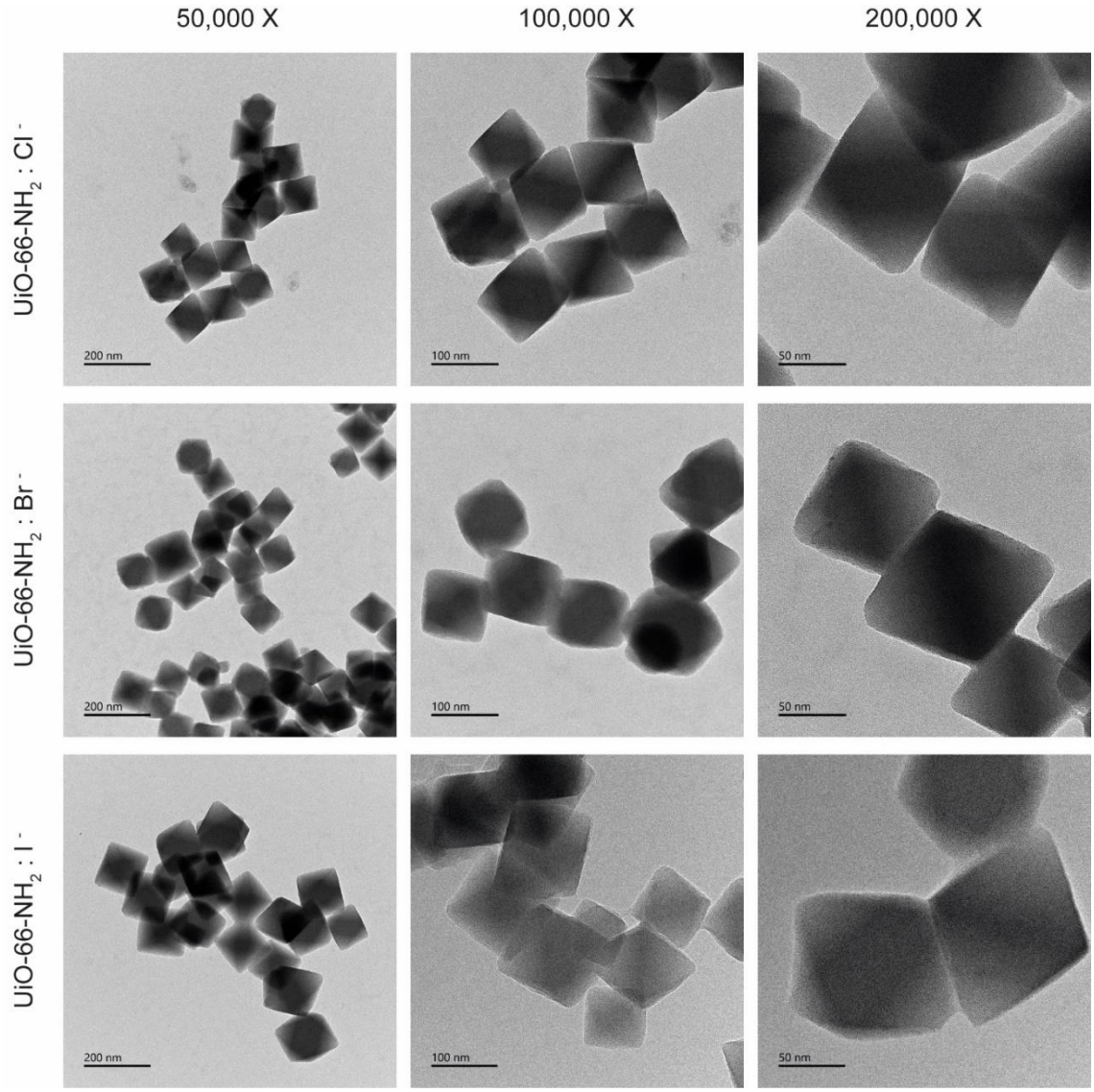

Figure 3-6. Representative TEM images of UiO-66-NH_2:X^- (X^-: Cl^-, Br^-, I^-) nanoMOFs.

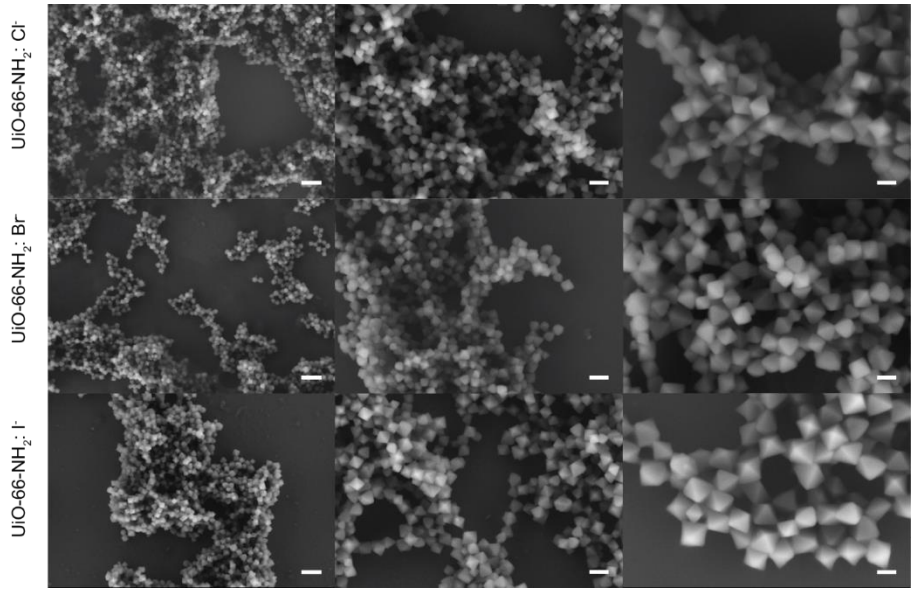

Figure 3-7. Representative SEM images of UiO-66-NH_2:X- (X^-: Cl^-, Br^-, I^-) nanoMOFs at different magnifications collected with Everhart-Thornley detector (SE2, secondary electrons) at 3 kV. Scale bars from left to right correspond to 400 nm, 200 nm and 100 nm.

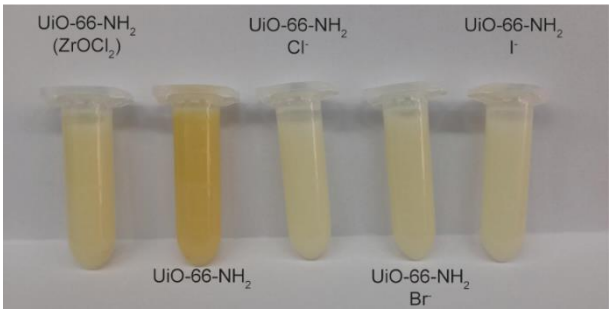

Figure 3-8. Photograph of the different UiO-66-NH_2 particles produced dispersed in methanol.

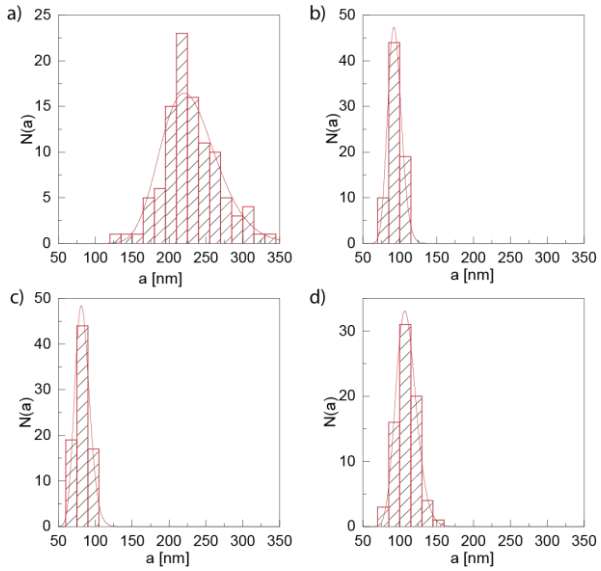

Figure 3-9. Histogram of the number distribution N of the edge of the nanoparticles (i.e., vertex-to vertex distance) as determined from SEM images. a) UiO-66-NH_2 ($ZrOCl_2$) 225 ± 37 nm, b) UiO-66-NH_2:Cl^- 94 ± 10 nm, c) UiO-66-NH_2:Br^- 81 ± 9 nm and d) UiO-66-NH_2:I^- 109 ± 14 nm.

For completeness, we also tried NaF as a co-modulator, which however prevented the formation of particles. The hypothesis that fluorine ions coordinate to the zirconium cluster, preventing further crystal growth was confirmed by measuring the UV-Vis spectra of the formed clusters using all the halides (Figure 3-10). Moreover, the formation of a precipitate was observed in the case of the fluoride ions, leading to high scattering in a broad spectral range as a result of the poor solubility of ZrF_4 formed in the solution (Figure 3-11). The results obtained with iodide and bromide confirm the hypothesis about the critical role of halide ions in the growth of the UiO-66-NH_2 nanoMOFs.

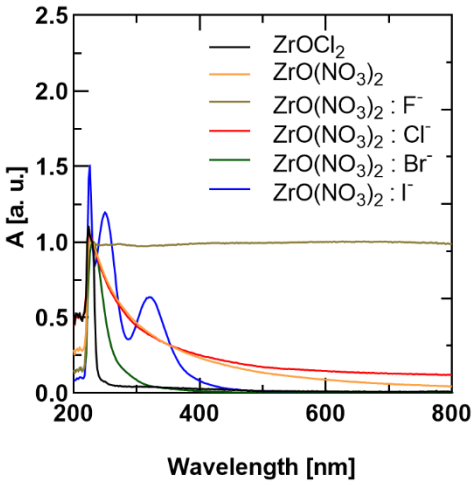

Figure 3-10. UV-Vis absorption spectra of the zirconium precursors $ZrClO_2$ and $ZrO(NO_3)_2$ and the effect of halides with $ZrO(NO_3)_2$ in DMF solution.

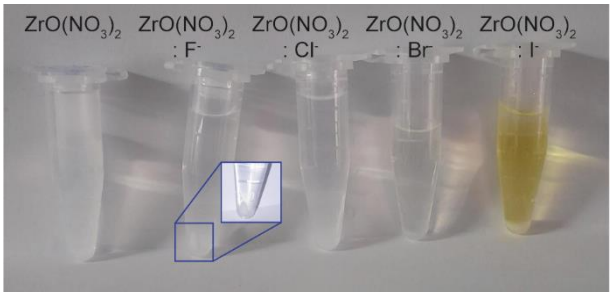

Figure 3-11. $ZrO(NO_3)_2$ solutions in presence of sodium halide salts in DMF. In the case of F- the formation of a white precipitate was observed (inset).

High-resolution transmission electron microscopy (HRTEM) showed highly crystalline nanoMOFs; in the case of UiO-66-NH_2:Cl^- and UiO-66-NH_2:Br^-, the fast Fourier transform (FFT) analysis of the corresponding TEM images of single nanoMOFs showed the characteristic {200} index of the a face-centered-cubic structure of the $Fm\bar{3}m$ space group (insets in Figure 3-5f and g). The d-spacing, in this case, corresponds to ca. 10.780 Å and ca. 10.000 Å nm, respectively. These d-spacings are in good agreement with the theoretical d-spacing (200) for UiO-66, 10.373 Å, and as a consequence with one half of the lattice parameter of the UiO-66 unit cell (20.746. Å) EDX experiments confirmed, in all the nanoMOFs, a homogeneous Zr and N distribution. In the case of the halides, Cl^- and Br^- ions were detected (Figure 3-5j and m, respectively) distributed in all the crystals. However, the I^- was not present

in a detectable amount, probably due to that they were washed out during the washing steps of the nanoMOFs as their coordination ability was reduced compared with that of Cl^- or Br^-.

PXRD and wide-angle X-ray scattering (WAXS) measurements were performed in capillary mode in order to discard the preferential orientation (Figure 3-12a), the main reflections of which were in agreement with previously reported powder X-ray diffraction patterns,[268] and which revealed the presence of broad peaks at low 2θ values, in both the samples containing halides and the sample synthesized with $ZrOCl_2$ (Figure 3-12b). To corroborate this broad peak around 4° 2θ, small-angle X-ray scattering (SAXS) measurements were performed (Figure 3-12c); these broad peaks have been attributed to the presence of ordered missing cluster defects.[261,269] The diffraction pattern were corroborated performing a unit-cell refinement with Pawley's method on the diffractogram in Figure 3-13, comparing each sample with Pawley's model and the residual, which was less than 1% in all the samples. With this method, the intensities and background were corrected and the cell parameters of each nanoMOF were calculated and compared with those of a UiO-66-NH_2 cubic cell (Table 3-2). The refined cell parameters are in agreement with the reference used to fix the peak position.[139,269]

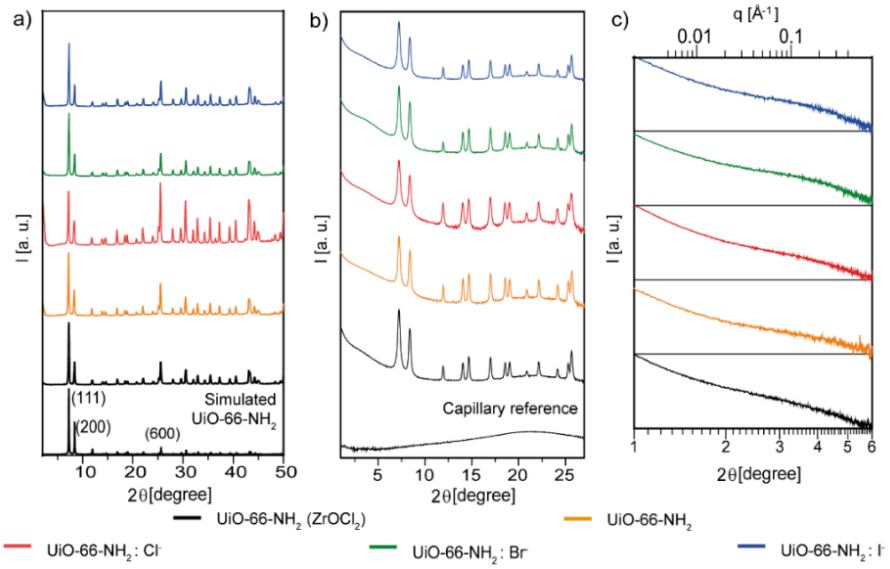

Figure 3-12. Crystallographic characterization of UiO-66-NH_2 nanoMOFs: UiO-66-NH_2 ($ZrOCl_2$) (black), UiO-66-NH_2 (orange), UiO-66-NH_2:Cl^- (red), UiO-66-NH_2:Br^- (green) and UiO-66-NH_2:I^- (blue). A) PXRD pattern, b) WAXS analysis measured at a sample-to-detector distance of 288 mm and c) SAXS analysis measured at a sample-to-detector distance of 1343 mm in capillary mode.

Table 3-2. Cell parameters obtained with Pawley's method.

Sample	a (Å)	V (Å^3)
Reference[269]	20.7680	8957.44
UiO-66-NH_2	20.8123	9014.89
UiO-66-NH_2 ($ZrOCl_2$)	20.8292	9036.86
UiO-66-NH_2:Cl^-	20.8347	9044.03
UiO-66-NH_2:Br^-	20.8208	9025.94
UiO-66-NH_2:I^-	20.8239	9029.97

USC UNIVERSIDADE DE SANTIAGO DE COMPOSTELA

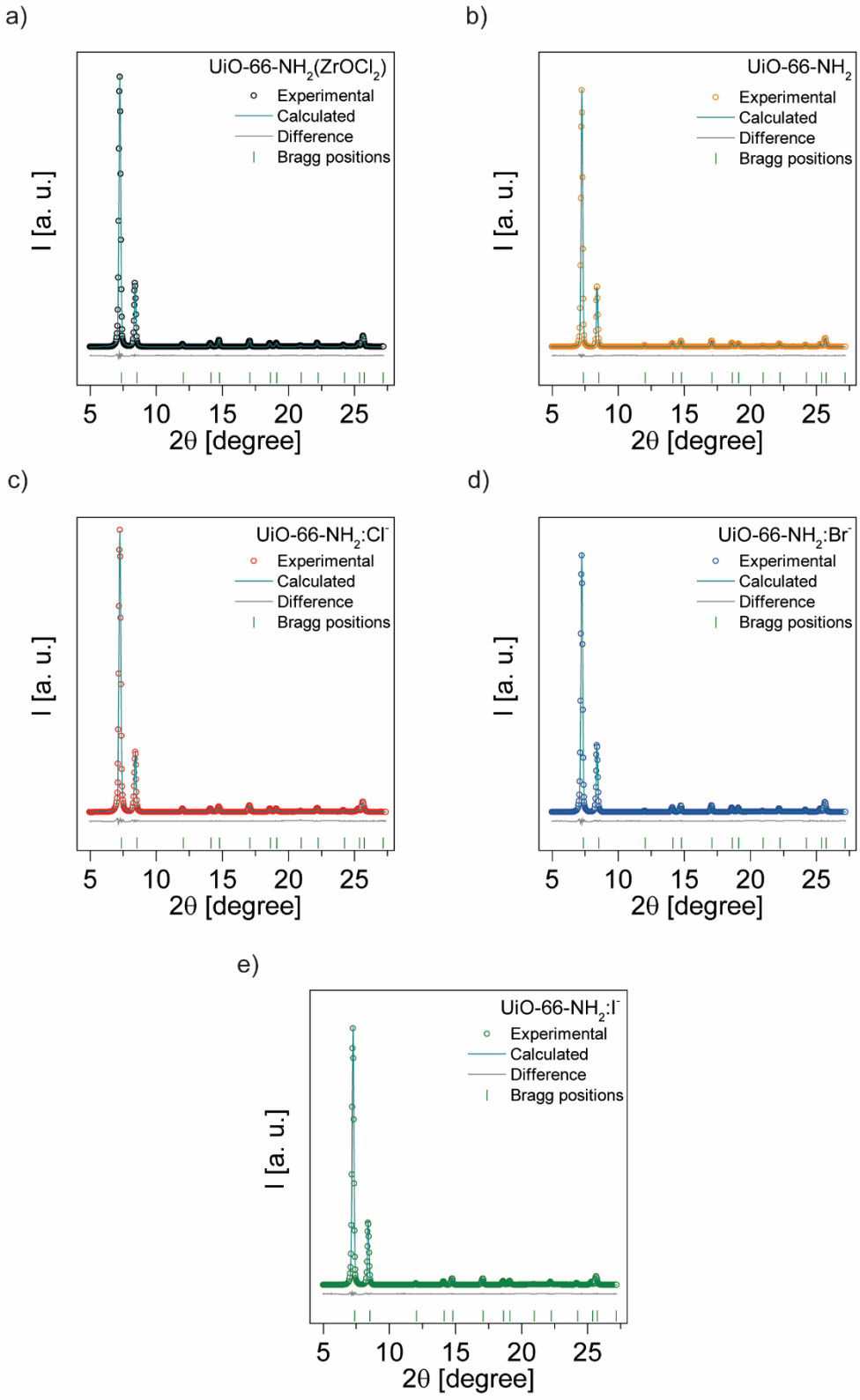

Figure 3-13. WAXS experiments measured at a sample to detector distance of 288 mm refined with Pawley's method and with corrected intensities and normalized with the most intense peak and residual.

USC
UNIVERSIDADE DE SANTIAGO DE COMPOSTELA

Fourier-transformed infrared spectra (FTIR) of the samples were compared with that of pure NH_2–BDC as a reference (Figure 3-14a–c). The C=O vibration at 1671 cm^{-1} was shifted for all the experiments to 1558 cm^{-1} for the samples synthesized with $ZrO(NO_3)_2$, and to 1555 cm^{-1} for UiO-66-NH_2($ZrOCl_2$). It is well known that the vibrations of the bands for UiO-66-NH_2($ZrOCl_2$) are less intense than those for UiO-66-NH_2:X^- (X^-:Cl^-,Br^- and I^-), in particular compared with UiO-66-NH_2:Cl^-; this evidence corroborates the better complexation of the ligand with the Zr cluster in this sample compared with the others, due to the carboxylate anion having two strongly coupled C–O bonds with a Zr cluster.[270,271] The vibrations at 3505 cm^{-1} and 3390 cm^{-1} corresponding to the asymmetric and symmetric stretching of N–H bond were shifted to 3465 cm^{-1} and 3350 cm^{-1} because the complexation changed the chemical environment in the MOF formation.[272,273]

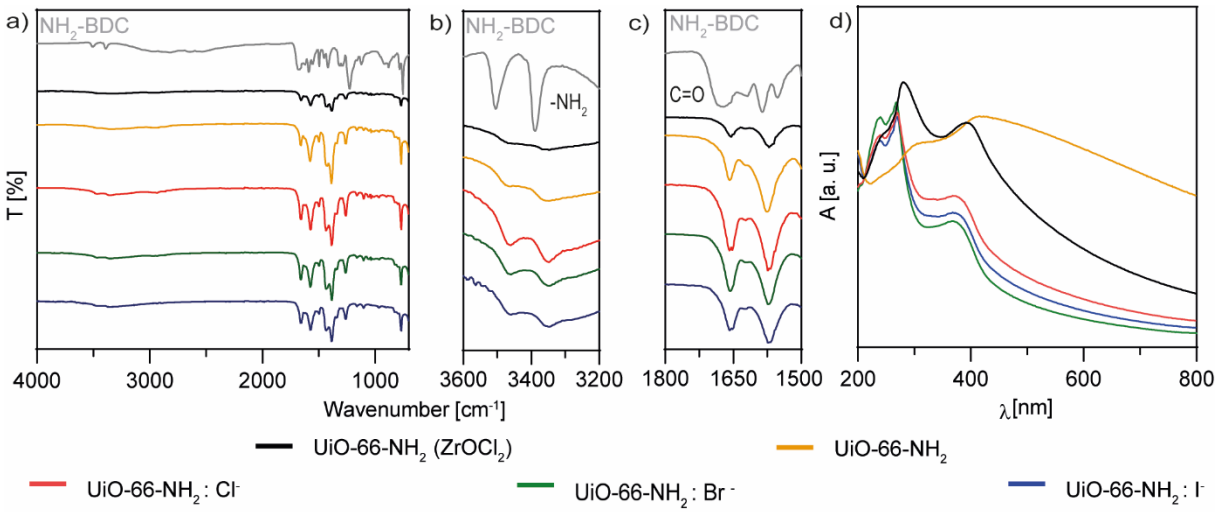

Figure 3-14. a–c) FTIR analysis and d) UV-Vis spectroscopy of UiO-66-NH_2 nanoMOFs: UiO-66-NH_2 ($ZrOCl_2$) (black), UiO-66-NH_2 (orange), UiO-66-NH_2: Cl^- (red), UiO-66-NH_2:Br^- (green) and UiO-66-NH_2:I^- (blue).

The UV-Vis spectra of UiO-66-NH_2:X^- (X^-:Cl^-,Br^- and I^-) (Figure 3-14d) show three sharp bands, one at 240 nm, a transition that can be attributed to an electronic transition between the halide and the Zr–O cluster,[274] and two at 270 and 370 nm corresponding to the n–π* transition of the amine group and the π–π* transition of the NH_2–BDC and Zr–O clusters,[275] respectively. For UiO-66-NH_2($ZrOCl_2$) the bands shifted slightly to 246, 281 and 392 nm, respectively, due to the bigger particle size. Interestingly, in the case of UiO-66-NH_2, without halide just two bands appeared at 306 and 415 nm, red shifted due to the size of the particles. In this case, the band attributed to the halide at shorter wavelengths was not present.

Raman spectra (Figure 3-15) of the different UiO-66-NH_2 nanoMOFs samples showed, in all cases, C=C stretching of aromatic rings centered at 1627 cm^{-1},O–C–O symmetric stretching in-phase at 1425–1447 cm^{-1} and C–O stretching at 1270 cm^{-1} related to the organic linker;[276] and for the metalligand coordination signatures, peaks related to Zr–O were observed at 247, 365 and 620 cm^{-1}.[277]

USC UNIVERSIDADE DE SANTIAGO DE COMPOSTELA

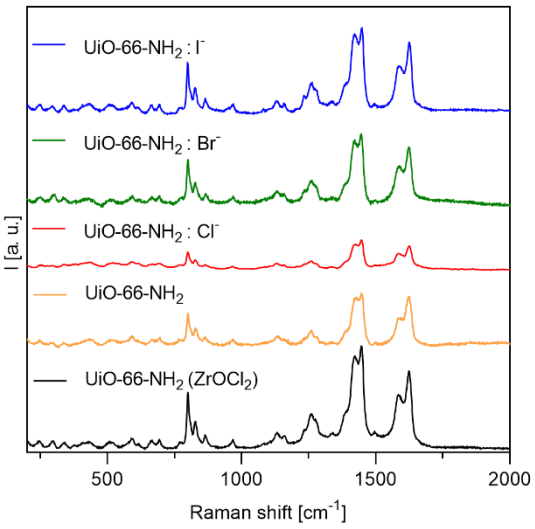

Figure 3-15. Raman spectra of UiO-66-NH_2 nanoMOFs.

Thermogravimetric analysis (TGA) of the samples (Figure 3-16a) shows the thermal stability of the MOFs. All of them were stable up to 350 °C, and only UiO-66-NH_2 started to decom pose before that temperature. Also, it is interesting to observe that the samples that might be ligand defective are UiO-66-NH_2 and UiO-66-NH_2:I^-, as indicated by their lower rate compared with the Zr cluster.[138] This is sustained by our observations of an active role of chloride and bromide ions as a part of the crystalline structure of the nanoMOFs, as iodide ions were not observed in our TEM studies. N_2 sorption measurements at 77 K show type I isotherms (Figure 3-16b), characteristic of microporous materials. The Brunauer–Emmett–Teller-specific surface area (S_{BET}) of UiO-66-NH_2 ($ZrOCl_2$) is 865.8 m^2/g, whereas the areas of UiO-66-NH_2 1020.6 and UiO-66-NH_2: X^- (X^-: Cl^-, Br^-, I^-) are virtually the same, with values of 1017.7, 1027.9 and 1040.0 m^2/g, respectively (Table 3-3). These findings are in good agreement with results reported elsewhere.[92,278,279]

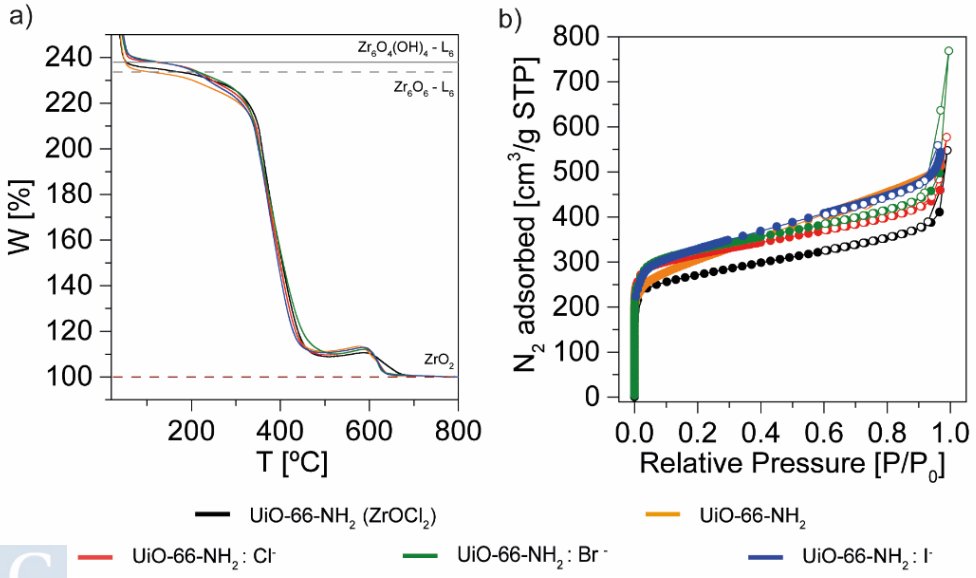

Figure 3-16. a) TGA analysis and b) N_2 adsorption isotherms of UiO-66-NH_2 nanoMOFs: UiO-66-NH_2 ($ZrOCl_2$) (black), UiO-66-NH_2 (orange), UiO-66-NH_2:Cl^- (red), UiO-66-NH_2:Br^- (green) and UiO-66-NH_2:I^- (blue).

The lower BET surface area of UiO-66-NH_2 ($ZrOCl_2$) can be ascribed to the higher dimension of the particles with respect to that of UiO-66-NH_2:X^- (X^-:Cl^-,Br^-, I^-). Furthermore, the halide samples present very similar values of S_{BET}, indicating the high reproducibility of the synthetic strategy in terms of the precise morphology and size, despite the change in the halide ion.

Table 3-3. BET surface area (SBET) of UiO-66 samples

Sample	S_{BET} (m^2/g)
UiO-66-NH_2 ($ZrOCl_2$)	865.8
UiO-66-NH_2	1020.6
UiO-66-NH_2:Cl^-	1017.7
UiO-66-NH_2:Br^-	1027.9
UiO-66-NH_2:I^-	1040.0
UiO-66 ($ZrOCl_2$)	1459.6
UiO-66	1416.9
UiO-66:Cl^-	1493.1

Inductively coupled plasma optical emission spectroscopy (ICP-OES) measurements were performed for all the samples (Table 3-4). These measurements helped to determine both the molar concentration and the number of nanoMOFs particles per milliliter. This last calculation was done considering their dimensions as obtained by SEM measurements (Table 3-5),[224] and on the other hand to determine the zirconium concentration (mg/mL). Additionally, with these measurements the reaction yields were calculated (Table 3-4). An increase in the reaction yield was observed for all the syntheses in which a halide was added. In particular, the yield of the reaction increased from 10% and 34% for UiO-66-NH_2 ($ZrOCl_2$) and UiO-66-NH_2, respectively, to ca. 77%, 52% and 45% for UiO-66-NH_2:Cl^-, UiO-66-NH_2:Br^- and UiO-66-NH_2:I^-, respectively. The yield increment was especially significant in the case of the chloride ions, leading to more than twice the amount of MOF than in the equivalent synthesis performed without this halide.

Table 3-4. ICP-OES results of UiO-66-NH_2 samples and yield of reaction

Sample	mg/mL Zr ICP	Yield of reaction (%)
UiO-66-NH_2 ($ZrOCl_2$)	0.21 ± 0.02	10.3 ± 0.98
UiO-66-NH_2	0.92 ± 0.03	34.1 ± 1.11
UiO-66-NH_2: Cl^-	2.08 ± 0.07	77.2 ± 2.60
UiO-66-NH_2: I^-	1.40 ± 0.34	44.9 ± 10.9
UiO-66-NH_2: Br^-	1.21 ± 0.27	51.9 ± 11.6

Nanoparticle tracking analysis (NTA) and dynamic light scattering (DLS) experiments were carried out to evaluate the effective hydrodynamic diameter of the nanoMOFs (Figure 3-17a and b). NTA showed that UiO-66-NH_2 ($ZrOCl_2$) has an effective diameter of ca. 200 nm, while for UiO-66-NH_2:X^- (X^-:Cl^-,Br^-,I^-) the effective diameters were below 140 nm (Figure 3-17a and Table 3-6). These data were in good agreement with the DLS measurements carried out where the hydrodynamic diameter was above 200 nm for UiO-66-NH_2($ZrOCl_2$) and around

150 nm for the samples synthesized with halides (Figure 3-17b, and Table 3-6). For UiO-66-NH_2 the NTA measurements could not be carried out due to its poor colloidal stability and DLS showed hydrodynamic diameters above 700 nm.

Table 3-5. Concentration results, using the size (SEM) and ICP values, expressed in mg Zr/UiO and in nM.

Sample	V SEM (nm^3)	unit cells / UiO	Zr / part UiO	mg Zr / UiO	UiO NPs / mL	nM UiO
UiO-66-NH_2 ($ZrOCl_2$)	1.04 x 10^6	1.16 x 10^5	2.78 x 10^6	4.22 x 10^{-13}	4.93 x 10^{11}	0.82
UiO-66-NH_2: Cl^-	3.92 x 10^5	4.38 x 10^4	1.05 x 10^6	1.59 x 10^{-13}	1.30 x 10^{13}	21.64
UiO-66-NH_2: Br^-	6.10 x 10^5	6.84 x 10^4	1.64 x 10^6	2.48 x 10^{-13}	5.63 x 10^{12}	9.34
UiO-66-NH_2: I^-	2.51 x 10^5	2.81 x 10^4	6.73 x 10^5	1.02 x 10^{-13}	1.19 x 10^{13}	19.70

To complete the characterization of the UiO-66-NH_2 nanoMOFs, the colloidal stability in different media at different times was studied. The selected media were MilliQ water, lysosomal medium (phagolysosomal simulant fluid (PSF), 0.02 M and pH 5), complete cell media (Dulbecco's Modified Eagle Medium (DMEM) supplemented with 10% foetal bovine serum (FBS)) and phosphate-buffered saline (PBS, 0.1 M, pH 7.4) (Figure 3-17d, and Table 3-7). UiO-66-NH_2($ZrOCl_2$) nanoMOFs showed good stability in water, PSF and DMEM, while in PBS an increment in the effective diameter was observed after 1 h, indicating that the nanoMOFs were aggregating. In the case of UiO-66-NH_2:X^- (X^-:Cl^-,Br^-, I^-), in PFS an increment in size was observed with respect to the samples in water; however, they remained stable along the measured time. For DMEM all samples showed an increment in size consistent with the protein corona formation;[226] finally in PBS the samples showed a similar tendency to UiO-66-NH_2($ZrOCl_2$) but with much lower aggregation rates.

ζ-Potential measurement showed values above 5 mV for all the nanoMOFs (Figure 3-17c, and Table 3-6). This is explained by the presence of the amine group from NH_2–BDC as a pendant group.

Table 3-6. Size values of the UiO-66-NH_2 samples: Edge size (a) of the octahedral nanoparticles calculated using SEM images, hydrodynamic diameters dh (mean value ± SD) as derived from DLS measurements and ζ- potential values (ζ ± SD). SD values correspond to the standard deviation of value as obtained from several repetitions (n=3) of the measurement. The polydispersity index (PdI) for each sample is also given.

Sample	d_{SEM} (nm)	$d_{h,NTA}$ (nm)	$d_{h,N(DLS)}$(nm)	PdI	ζ (mV)
UiO-66-NH_2 ($ZrOCl_2$)	225 ± 36	200 ± 3	202 ± 3	0.170	5.40 ± 0.1
UiO-66-NH_2	-	-	756 ± 74	0.483	-
UiO-66-NH_2: Cl^-	94 ± 10	140 ± 2	163 ± 5	0.040	8.70 ± 0.3
UiO-66-NH_2: Br^-	109 ± 14	136 ± 2	153 ± 5	0.030	16.0 ± 1.0
UiO-66-NH_2: I^-	81 ± 9	123 ± 1	167 ± 1	0.004	16.1 ± 0.4

USC UNIVERSIDADE DE SANTIAGO DE COMPOSTELA

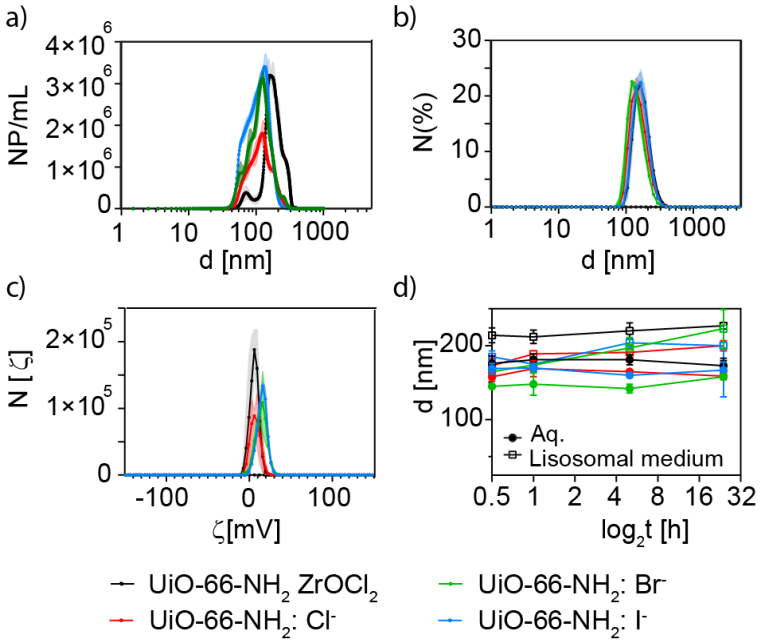

Figure 3-17 Effective diameter (hydrodynamic diameter) of UiO-66-NH_2 nanoMOFs analyzed by a) NTA and b) DLS. c) ζ-Potential measurements. d) Summary of the stability tests in water and lysosomal medium. Black line corresponds to UiO-66-NH2 ($ZrOCl_2$), red to UiO-66-NH_2:Cl^-, green to UiO-66-NH_2:Br^- and blue to UiO-66-NH_2:I^-.

Table 3-7. Hydrodynamic diameters d_h (mean value ± SD) as derived from DLS measurements of the nanoMOFs in the different media (water, PSF, DMEM and PBS) at different times (0, 1, 5 and 24h)

Water				
t (h)	UiO-66-NH_2 ($ZrOCl_2$)	UiO-66-NH_2: Cl^-	UiO-66-NH_2: Br^-	Ui-66-NH_2: I^-
0	176 ± 10	158 ± 6	145 ± 4	169 ± 7
1	181 ± 8	169 ± 11	148 ± 15	170 ± 6
5	181 ± 7	165 ± 4	142 ± 6	160 ± 4
24	173 ± 10	159 ± 5	158 ± 4	167 ± 11
Lysosomal medium (PSF)				
t (h)	UiO-66-NH_2 ($ZrOCl_2$)	UiO-66-NH_2: Cl^-	UiO-66-NH_2: Br^-	UiO-66-NH_2: I^-
0	214 ± 10	173 ± 10	165 ± 10	185 ± 8
1	212 ± 9	189 ± 4	174 ± 2	175 ± 10
5	220 ± 11	191 ± 10	197 ± 14	204 ± 7
24	227 ± 47	200 ± 7	223 ± 26	200 ± 69
DMEM (complete)				
t (h)	UiO-66-NH_2 ($ZrOCl_2$)	UiO-66-NH_2: Cl^-	UiO-66-NH_2: Br^-	UiO-66-NH_2: I^-
0	196 ± 6	253 ± 10	201 ± 10	236 ± 8
1	247 ± 116	222 ± 21	220 ± 5	224 ± 2
5	251 ± 160	271 ± 10	221 ± 13	236 ± 20
24	245 ± 173	251 ± 100	201 ± 10	237 ± 9

USC UNIVERSIDADE DE SANTIAGO DE COMPOSTELA

PBS				
t (h)	UiO-66-NH_2 ($ZrOCl_2$)	UiO-66-NH_2: Cl^-	UiO-66-NH_2: Br^-	UiO-66-NH_2: I^-
0	212 ± 65	170 ± 10	180 ± 1	177 ± 11
1	292 ± 10	180 ± 13	212 ± 16	183 ± 4
5	312 ± 88	207 ± 14	183 ± 15	223 ± 14
24	668 ± 173	256 ± 42	250 ± 40	239 ± 20

These data show that our nanoMOFs have consistent colloidal stability despite lacking induced defects by the use of a defect-inducer modulator during the synthesis[280,281] or being modified with an additional external surface coating.

3.2.5. Chlorine ions as co-modulators for the UiO-66 nanoMOFs synthesis

For completeness, it was studied the synthesis of UiO-66 nanoMOFs using the same optimized conditions as used for the synthesis of UiO-66-NH_2 nanoMOF. That is, using both Zr precursors ($ZrOCl_2$ and $Zr(NO_3)_2$) and chlorine ions (NaCl) in the same optimized ratio (Table 3-1).

Interestingly, individual octahedral particles smaller than 200 nm were obtained when chloride ions were present on the synthesis, as part of the precursor or added as a salt (UiO-66 $ZrOCl_2$ and UiO-66:Cl^-, Figure 3-18a and b). In the absence of chloride ions, the particles obtained were bigger than 800 nm, forming multitwinned particles (Figure 3-18c). This result confirms the role of the chloride ions in the generation of small UiO-66 particles. TEM microscopy was performed (Figures 3-19 and 3-20) and STEM-EDX experiments for UiO-66:Cl^- nanoMOFs, and chloride ions were detected, showing the same homogeneous distribution in the MOFs (Figure 3-18d) as observed for the UiO-66-NH_2:X^- (X^-: Cl^-, Br^-) nanoMOFs.

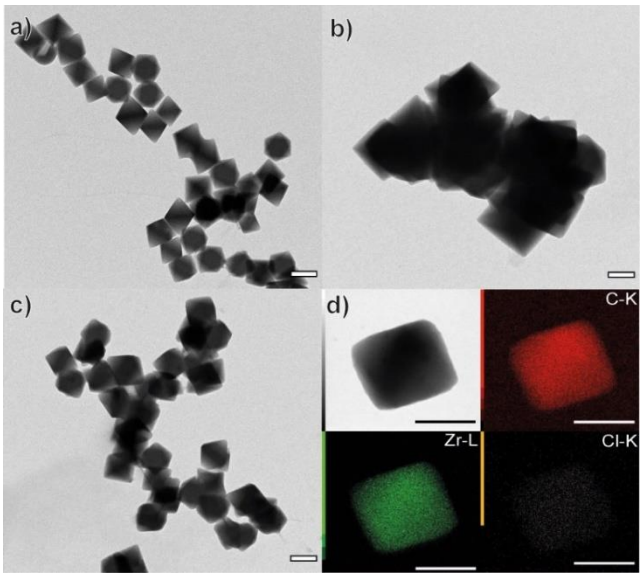

Figure 3-18. Representative TEM images of a) UiO-66 ($ZrOCl_2$), b) UiO-66, c) UiO-66:Cl^- and, d) EDX elemental mapping of carbon, zirconium and chloride from a UiO-66:Cl^- nanoMOF. Scale bars correspond to 200 nm for TEM and to 100 nm for STEM-EDX.

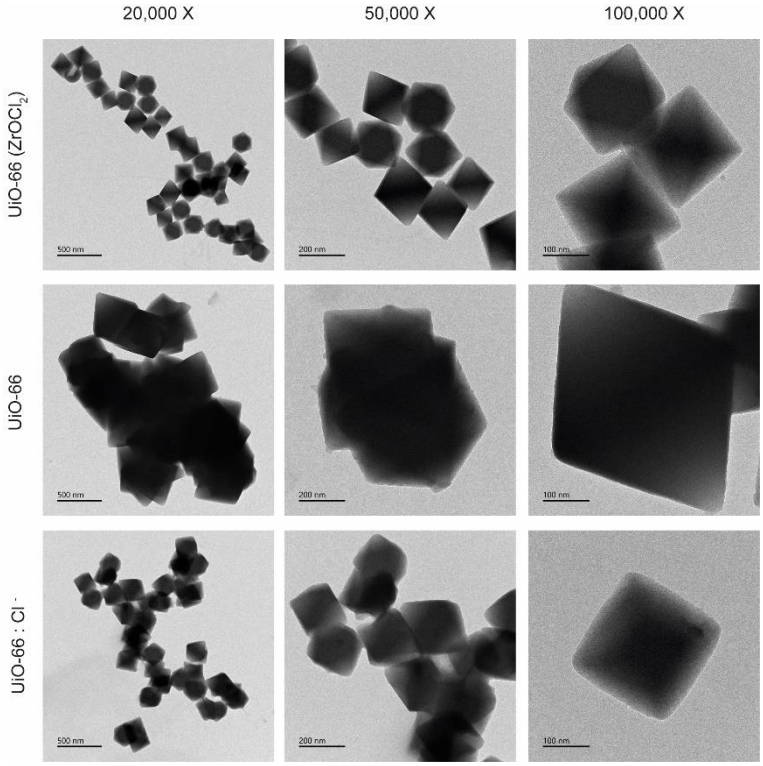

Figure 3-19. Representative TEM images of the UiO-66 nanoparticles synthesized with different Zr precursors and the effect of Cl^- when the synthesis is performed with $ZrO(NO_3)_2$ precursor at different magnifications.

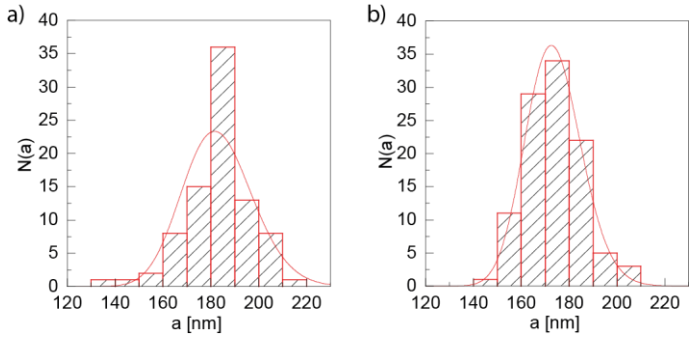

Figure 3-20. Histogram of the number distribution N of the edge of the nanoMOFs (i.e., vertex-to vertex distance) as determined from SEM images. a) UiO-66 ($ZrOCl_2$) 186 ± 13 nm and b) UiO-66:Cl^- 174 ± 13 nm.

As previously done with UiO-66-NH_2, we characterized the UiO-66 produced using ICP-OES, UV-Vis spectroscopy, DLS, ζ-potential and N_2 adsorption (Figures 3-21, 3-22, 3-23, 3-24 and Tables 3-8 and 3-9). UiO-66-NH_2 yielded bigger hydrodynamic diameters and a ζ-potential closer to neutrality. In the case of UiO-66 ($ZrOCl_2$) and UiO-66:Cl^- they showed positive potential values. As expected, the samples presented higher values of S_{BET} with respect to the relative aminated samples, with values of 1459.6, 1416.9 and 1493.1 m^2/g for UiO-66 ($ZrOCl_2$), UiO-66 and UiO-66:Cl^-, respectively (Table 3-3 and Figure 3-24).

USC
UNIVERSIDADE DE SANTIAGO DE COMPOSTELA

Table 3-8. Yield of reaction determined with ICP-OES results for UiO-66

Sample	mg/mL Zr ICP	Yield of reaction (%)
UiO-66 ($ZrOCl_2$)	1.15	39.83
UiO-66	0.24	11.13
UiO-66: Cl^-	0.42	19.71

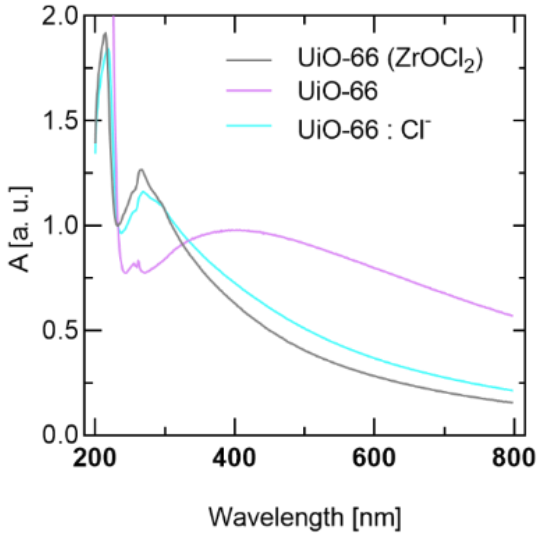

Figure 3-21. UV-Vis absorption spectra of the UiO-66 samples with different Zr precursors and the effect of Cl^- when the synthesis is performed with $ZrO(NO_3)_2$.

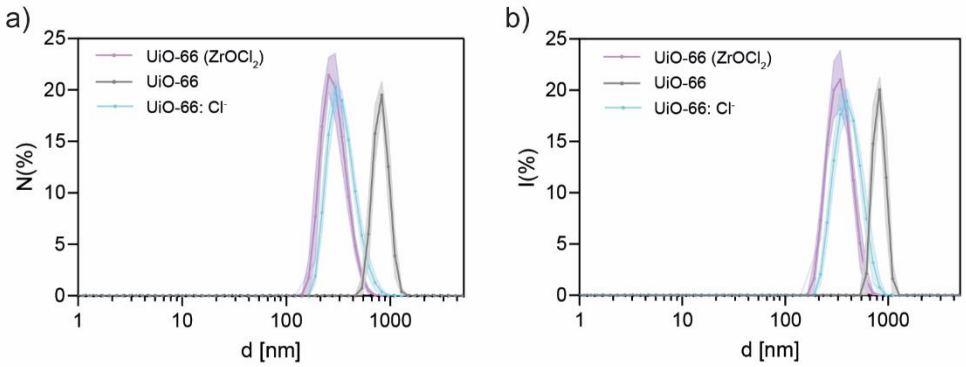

Figure 3-22. DLS a) number and b) intensity distributions of the hydrodynamic diameter dh of the UiO-66 samples.

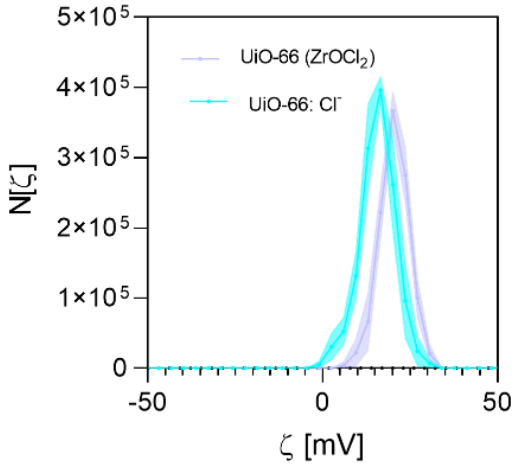

Figure 3-23. ζ-potential values for the UiO-66 samples.

Table 3-9. Size values of the UiO-66 samples: Edge size (a) of the octahedral nanoparticles calculated using SEM images, hydrodynamic diameters dh (mean value ± SD) as derived from DLS measurements and ζ- potential values (ζ ± SD). The polydispersity index (PDI) for each sample is also given.

Sample	d_{SEM} (nm)	$d_{h,N(DLS)}$ (nm)	PdI	ζ (mV)
UiO-66 ($ZrOCl_2$)	186 ± 13	273 ± 82	0.072	26.4 ± 0.3
UiO-66	-	821 ± 42	0.414	4.8 ± 0.6
UiO-66: Cl^-	174 ± 13	376 ± 120	0.142	16.0 ± 0.3

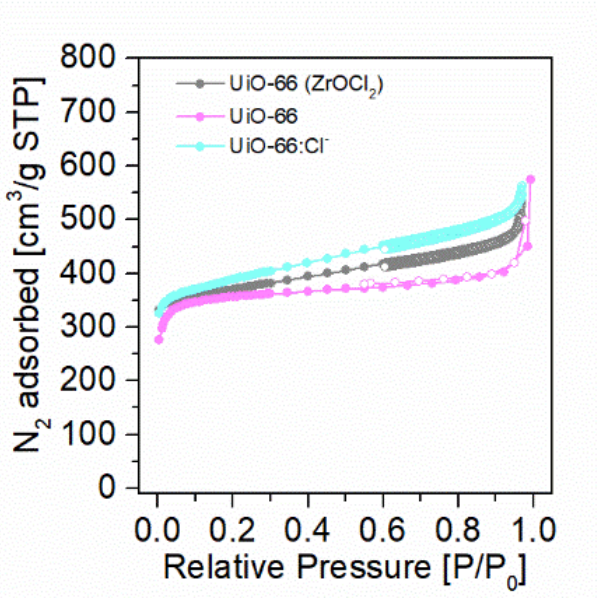

Figure 3-24. N_2 adsorption isotherm of UiO-66 ($ZrOCl_2$), UiO-66 and UiO-66:Cl^-.

3.2.6. UiO-66 nanoMOFs as DDSs

The UiO-66 MOF family has been extensively used as DDSs because of their good stability, the low toxicity of their components, and their large porosity. According to its crystal data, UiO-66 has a cage size of 0.75 and 1.2 nm with a pore aperture of 0.6 nm, and different

molecules have been encapsulated, such as calcein,[282] dichloroacetate,[283,284] 5-fluorouracil,[283] doxorubicin,[285,286] 5-aminolevulinic acid,[287] etc.

As a model molecule, we selected Rhodamine 6G (R6G, Table 3-10 and Figure 3-25) to evaluate the loading abilities of the synthesized nanoMOFs. To load the nanoMOFs, a post-loading strategy was applied by simply mixing the nanoMOFs with a solution of R6G in a ratio of 1:2 Zr:R6G (w:w) (Table 3-11). After thorough washing of the nanoMOFs, we evaluated the loading rate for UiO-66-NH_2 nanoMOFs, finding loading rates from 27 to 31%, corresponding to a ratio of ca. 0.6 mg R6G per mg Zr and a loading rate of R6G per nanoMOF on the order of 105 per nanoMOF (Figure 3-26 and Table 3-12). The loading of R6G increased the hydrodynamic size of the nanoMOFs while their ζ-potentials were kept positive except for UiO-66-NH_2 ($ZrOCl_2$)@R6G, the potential of which was nearly 0 mV (Figures 3-27, 3-28, 3-29 and Table 3-13). Interestingly, similar results were found for UiO-loading rates for UiO-66 nanoMOFs (ca. 30% of loading), with a ratio of ca. 0.6 mg R6G per mg Zr, corresponding to $6–7\times10^5$ molecules of R6G per nanoMOF (Tables 3-14, 3-15 and Figures 3-30, 3-31 and 3-32). The observed loading ratio corresponds to ca.17–20% w/w for all the synthesized nanoMOFs, UiO-66-NH_2 and UiO-66.

Table 3-10. Rhodamine 6G characteristics

Dye	MW (g/mol)	λ_{exc} (nm)	λ_{em} (nm)	Size (nm)
R6G	479.02	520	550/560	1.61

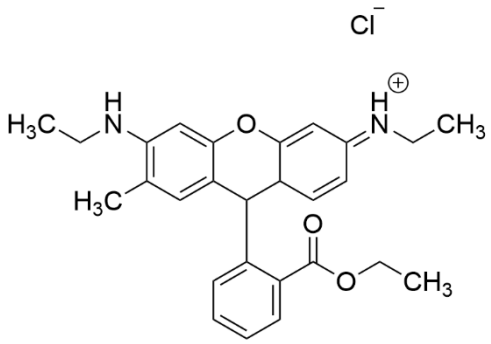

Figure 3-25. Rhodamine 6G chemical structure.

Table 3-11 Summary of conditions for the R6G loading.

Dye	[dye] (mg/mL)	[UiO] (mg/mL)	V_{R6G} (µL)	V_{UIO} (µL)	solvent
R6G	2	1	100	100	water

USC UNIVERSIDADE DE SANTIAGO DE COMPOSTELA

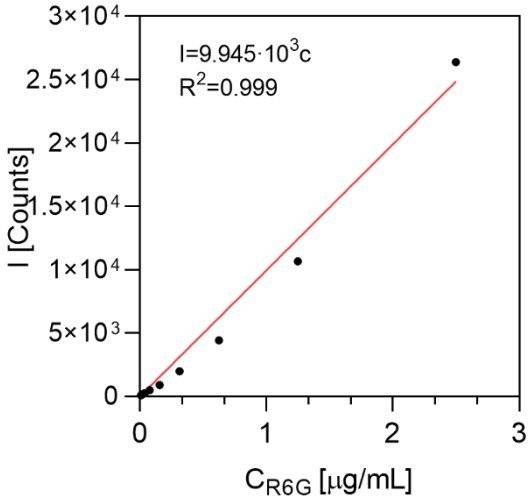

Figure 3-26. Calibration curve of R6G in water was obtained from fluorescence under excitation at 520 nm (I). Fluorescence intensity (I) at the maximum emission peak as a function of R6G concentration c is plotted and calibration equation is obtained by fitting a linear regression line to the collected data; R^2 is the coefficient of determination.

Table 3-12. Dye loading for the UiO-66-NH_2 nanoparticles. Percentage of the maximum dye loaded in the nanoparticles calculated via fluorescence measurements of the supernatant, number of dye molecules per UiO nanoparticle and dye molecules/dye mg per mg of zirconium.

Sample	% R6G IN	R6G / MOF	Mg R6G / mgZr	mol R6G / mgZr	w/w (%)
UiO-66-NH_2 ($ZrOCl_2$) @R6G	28%	2.97 x 10^5	0.56	2.34 x 10^{-7}	17.5
UiO-66-NH_2@R6G	21%	-	0.42	1.75 x 10^{-7}	-
UiO-66-NH_2: Cl^- @R6G	28%	1.12 x 10^5	0.56	2.34 x 10^{-7}	17.5
UiO-66-NH_2: Br^- @R6G	31%	1.94 x 10^5	0.62	2.59 x 10^{-7}	19.4
UiO-66-NH_2: I^- @R6G	27%	6.92 x 10^5	0.54	2.25 x 10^{-7}	16.9

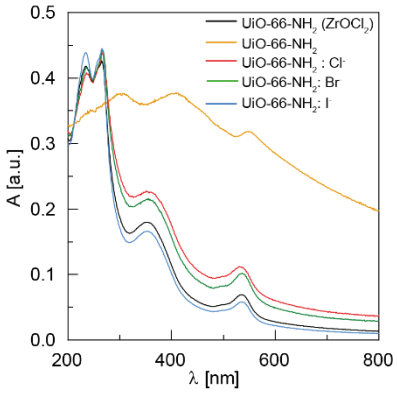

Figure 3-27. UV-Vis absorption spectra normalized to Zr of the UiO-66-NH_2 nanoMOFs after the R6G loading.

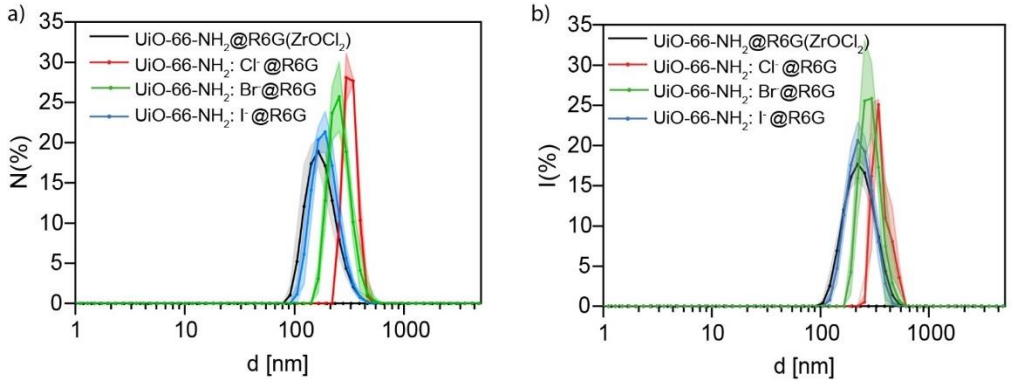

Figure 3-28. DLS a) intensity and b) number distributions of the hydrodynamic diameter d_h of the UiO-66-NH_2@R6G nanoMOFs.

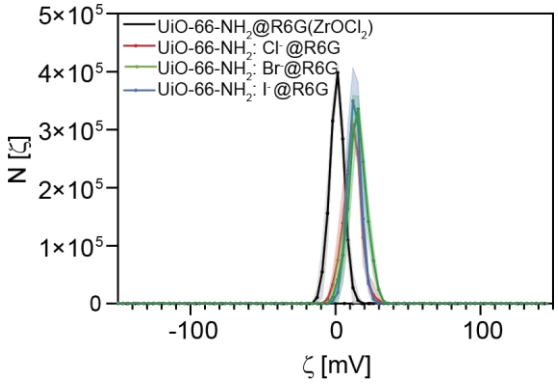

Figure 3-29. ζ- potential distribution for the UiO-66-NH_2 samples after the R6G loading.

Table 3-13. Hydrodynamic diameters d_h (mean value ± SD) as derived from DLS measurements of the UiO-66-NH_2 samples as dispersed in water after the dye loading.

Sample	$d_{h,N}$ (nm)	$d_{h,I}$ (nm)	PdI	ζ (mV)
UiO-66-NH_2 ($ZrOCl_2$)@R6G	182 ± 12	238 ± 7	0.12	-0.3 ± 0.1
UiO-66-NH_2: Cl^- @R6G	271 ± 80	319 ± 76	0.86	13.4 ± 0.5
UiO-66-NH_2: Br^- @R6G	254 ± 11	290 ± 25	0.32	15.8 ± 0.1
UiO-66-NH_2: I^- @R6G	192 ± 5	237 ± 10	0.23	15.7 ± 0.3

Table 3-14. Dye loading for the UiO-66 nanoMOFs. Percentage of the maximum dye loaded in the nanoparticles calculated via fluorescence measurements of the supernatant, number of dye molecules per UiO nanoparticle and dye molecules/dye mg per mg of zirconium.

Sample	% R6G IN	R6G / MOF	mg R6G / mgZr	mol R6G / mgZr	w / w (%)
UiO-66 ($ZrOCl_2$)@R6G	30%	6.15×10^5	0.60	2.51×10^{-7}	18.7
UiO-66@R6G	20%	-	0.40	1.67×10^{-7}	-
UiO-66 Cl^- @R6G	29%	7.50×10^5	0.58	2.42×10^{-7}	18.1

USC UNIVERSIDADE DE SANTIAGO DE COMPOSTELA

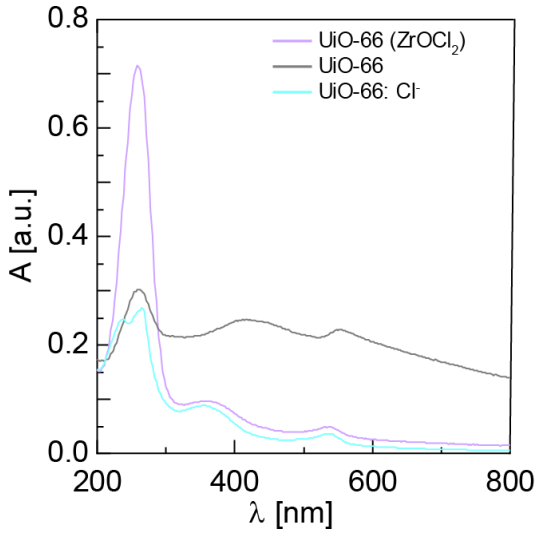

Figure 3-30. UV-Vis absorption spectra normalized to Zr of the UiO-66 samples after the R6G loading.

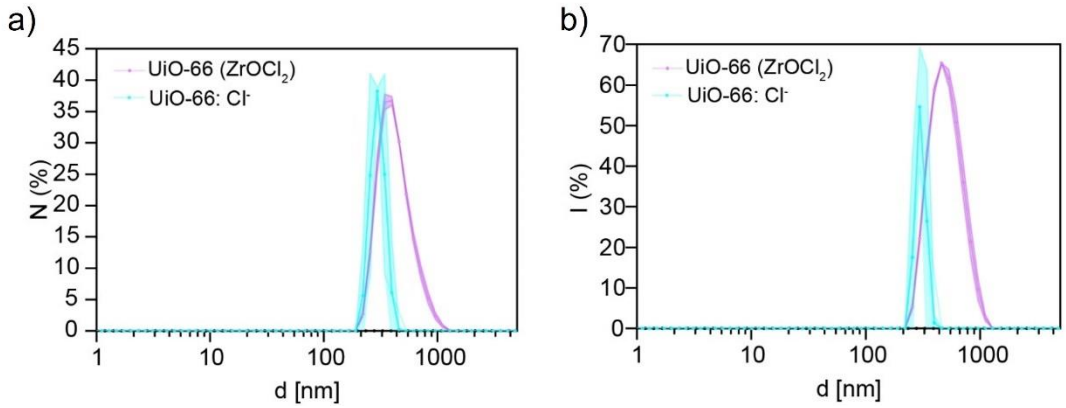

Figure 3-31. DLS a) number and b) intensity distributions of the hydrodynamic diameter dh of the UiO-66@R6G nanoMOFs.

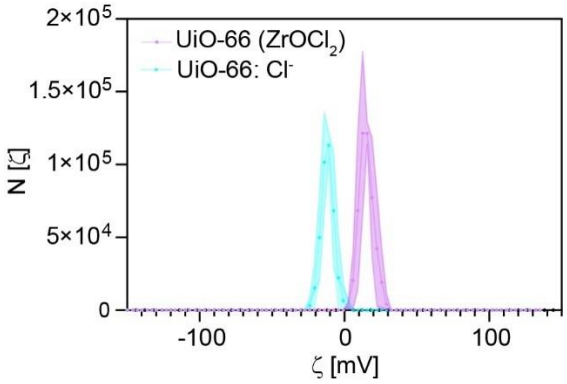

Figure 3-32. ζ-potential distribution for the UiO-66 samples after the R6G loading.

Table 3-15. Hydrodynamic diameters dh (mean value ± SD) as derived from DLS measurements of the UiO-66 samples as dispersed in water after the dye loading.

Sample	$d_{h,N}$ (nm)	$d_{h,I}$ (nm)	PdI	ζ (mV)
UiO-66 ($ZrOCl_2$)@R6G	438 ± 20	790 ± 140	0.51	-15.1 ± 0.3
UiO-66: Cl^- @R6G	299 ± 29	302 ± 29	0.32	-7.7 ± 0.4

USC UNIVERSIDADE DE SANTIAGO DE COMPOSTELA

Despite working with highly crystalline structures, this post-loading efficiency is higher than that previously reported with 5-fluorouracil, in which loadings of about 2%[288] or 5%[283] w/w (in the case of UiO-66-NO_2) were achieved using different synthetic approaches and working with highly defective UiO-66. An extremely high loading of 1 mg doxorubicin per mg MOF was reported by Chen *et al.*[286] and another high loading ratio higher than 25% w/w has been reported, but as a consequence of the incorporation of the drugs as a part of the UiO-66 structure.[288] On the other hand, the number of molecules per nanoMOF was of the same order of magnitude as the encapsulation of Hoechst or pro-fluorophores in ZIF-8-based nanocomposites previously reported by the group.[237,238]

The aim was to use these nanoMOFs as DDSs to transport the R6G to the intracellular domain of cells. It is well known that most nanomaterials are trapped in lysosomal compartments where they are further degraded.[289,290] nanoMOFs are not an exception.[238,239,291] The stability of the loading of R6G in different media was studied for different times up to 24 h. We used the same media as previously selected for colloidal stability studies except for PBS, that is, water, complete DMEM, and PSF. The results proved that for UiO-66-NH_2 nanoMOFs, the R6G encapsulated was stable in MilliQ water with no significant release in any of the samples (Figure 3-33 and Table 3-16). However, the time-dependent release of R6G showed a clear increase in the cases of UiO-66-NH_2:Cl^- and UiO-66-NH_2:Br^-, with 1 and 1.8% release at 24 h, respectively, while for the rest the R6G release remained below 0.7%. The same trend was observed in both PSF and DMEM. For PSF, both samples showed a release of ca. 3% at 24 h, while for DMEM a higher release was observed close to 4% and 4.5% for UiO-66-NH_2:Cl^- and UiO-66-NH_2:Br^-, respectively.

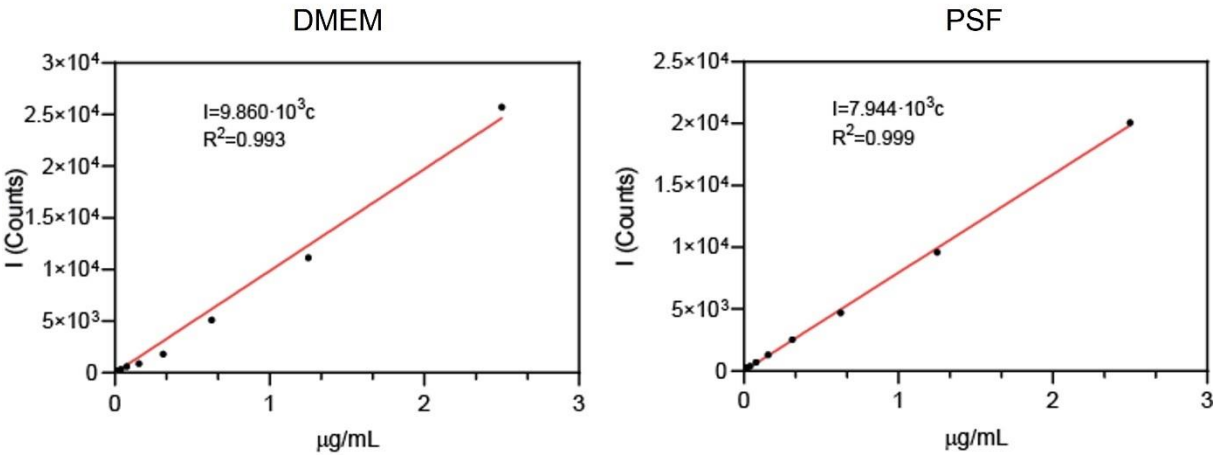

Figure 3-33. Calibration curves of R6G in DMEM and PSF.

USC UNIVERSIDADE DE SANTIAGO DE COMPOSTELA

Table 3-16. R6G released from the pores of the nanoMOFs.

WATER (% SN)					
t (h)	UiO-66-NH_2 ($ZrOCl_2$)	UiO-66-NH_2	UiO-66-NH_2: Cl^-	UiO-66-NH_2: Br^-	UiO-66-NH_2: I^-
0	0.08%	0.20%	0.22%	0.31%	0.03%
1	0.34%	0.28%	0.57%	0.75%	0.09%
5	0.50%	0.23%	0.81%	1.35%	0.17%
24	0.65%	0.35%	1.07%	1.77%	0.26%
PSF (% SN)					
t (h)	UiO-66-NH_2 ($ZrOCl_2$)	UiO-66-NH_2	UiO-66-NH_2: Cl^-	UiO-66-NH_2: Br^-	UiO-66-NH_2: I^-
0	0.39%	0.22%	0.78%	0.94%	0.18%
1	0.37%	0.33%	1.19%	1.74%	0.25%
5	0.92%	0.49%	1.80%	2.30%	0.49%
24	1.47%	0.88%	2.94%	3.14%	1.19%
DMEM (% SN)					
t (h)	UiO-66-NH_2 ($ZrOCl_2$)	UiO-66-NH_2	UiO-66-NH_2: Cl^-	UiO-66-NH_2: Br^-	UiO-66-NH_2: I^-
0	0.79%	0.47%	1.37%	1.39%	0.27%
1	0.31%	0.52%	1.74%	2.17%	0.54%
5	2.14%	0.84%	2.69%	1.40%	1.06%
24	1.33%	1.16%	3.84%	4.48%	2.72%

In the case of UiO-66 the released R6G was higher in all the cases and in all the media, in particular for UiO-66:Cl^- in PSF and DMEM at 24 h releases of ca. 14% and 4% were observed (Table 3-17). These results show that the presence of the amine group is uninfluential concerning the loading rate of the nanoMOFs, yet it stabilizes RG6 within the nanoMOFs. Additionally, it demonstrates that the encapsulation stability in these nanoMOFs is very high.

Table 3-17. R6G released from the pores of the nanoMOFs at times 0, 1, 5, 24 and 48h.

WATER (% SN)			
t (h)	UiO-66 ($ZrOCl_2$)	UiO-66	UiO-66: Cl^-
0	0.11%	0.28%	0.51%
1	0.17%	0.35%	1.00%
5	0.18%	0.55%	1.69%
24	0.67%	0.77%	1.82%

USC UNIVERSIDADE DE SANTIAGO DE COMPOSTELA

PSF (% SN)			
t (h)	UiO-66 ($ZrOCl_2$)	UiO-66	UiO-66: Cl^-
0	0.48%	1.00%	1.27%
1	0.94%	1.42%	2.04%
5	4.89%	6.64%	6.87%
24	6.69%	7.85%	10.75%
DMEM (% SN)			
t (h)	UiO-66 ($ZrOCl_2$)	UiO-66	UiO-66: Cl^-
0	1.00%	1.58%	2.76%
1	1.57%	2.00%	3.66%
5	2.99%	1.01%	4.17%
24	4.01%	2.63%	7.25%

Comparing the cargo release from other UiO-66 nanosystems (please note that this is referring to UiO-66 not to UiO-66-NH_2 nanoMOFs as, for the latter, literature examples are scarce), it was found that the release of doxorubicin after 24 h at 37 ℃ was higher than 20% at pH 5, 6.8 and 7.4, being very close to the 25% at pH 5,54 while the release of encapsulated calcein from UiO-66 MOFs has been reported to occur at approximately 80% mass release after 5 h in solution.[282]

3.2.7. Cell studies

Next, the interaction of UiO-66-NH_2 nanoMOFs with cells in 2D cell cultures of A549 adenocarcinoma cells was evaluated. The biocompatibility was assessed using the resazurin test, which confirmed the correct metabolic rate of mitochondria in cell cultures. The concentrations used were up to 100 μgZr/mL (which corresponds to ca. 320 μg/mL or 0.82, 2.1, 0.93 and 1.97 nM of UiO-66-NH_2, UiO-66-NH_2:Cl^-, UiO-66-NH_2:Br^-, and UiO-66-NH_2:I^-, respectively), which showed no significant toxicity for any sample after 24 h of incubation (Figure 3-34). The same result was obtained when testing the UiO-66 nanoMOFs (Figure 3-35) in the same concentration range. These results are in good agreement with previous toxicity tests reported with the UiO-66 family particles.[287] As mentioned above, the biocompatibility of this MOF family is very high, being one of the reasons the reduced toxicity of its components, for example, Zr is one of the rare transition metals that are naturally present in the human body (ca. 300 mg of Zr).[282]

After confirming the low toxicity of our nanoMOFs, the uptake of UiO-66-NH_2 nanoMOFs was studied using fluorescence microscopy and flow cytometry (Figures 3-36, 3-37 and Table 3-18). To do this, the R6G-loaded nanoMOFs were used. R6G was selected as cargo for two reasons, i) to provide the nanoMOFs with fluorescence to track them intracellularly and ii) due to its ability to target functional mitochondria.[292,293]

USC UNIVERSIDADE DE SANTIAGO DE COMPOSTELA

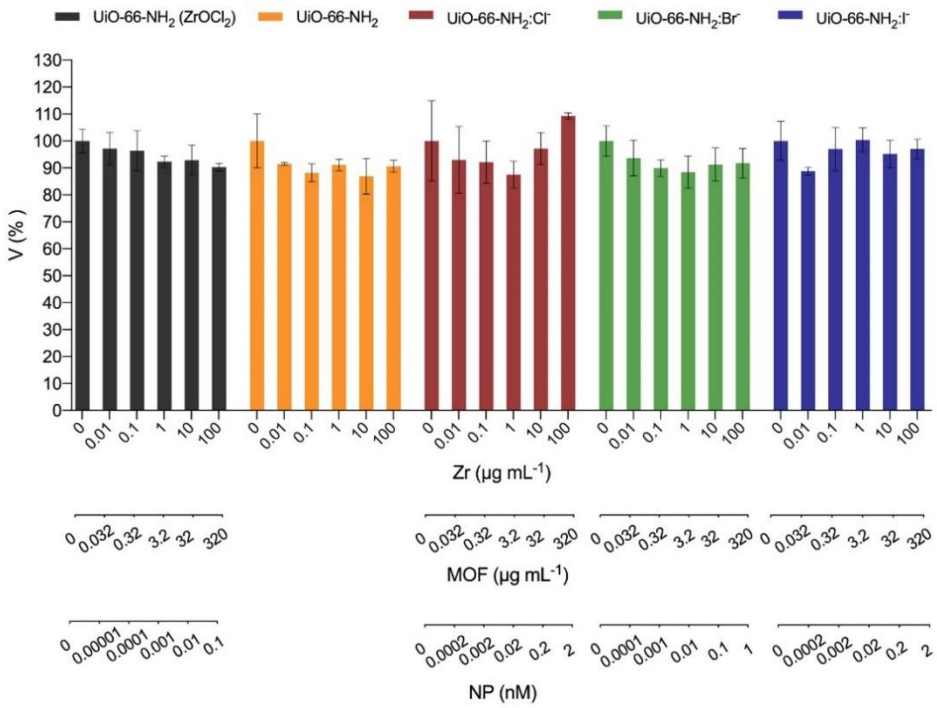

Figure 3-34. Cell viability in A549 cell culture after 24 h of UiO-66-NH_2 nanoMOFs exposure, measured by Resazurin assay. Viability values represent the mean ± standard deviation of measurements from three different wells. X axes representing the nanoMOF concentration in terms of Zr, nanoMOF and nanoparticle concentration unless in UiO-66-NH_2 where the lack of a defined structure prevents the calculation of the volume of each particle.

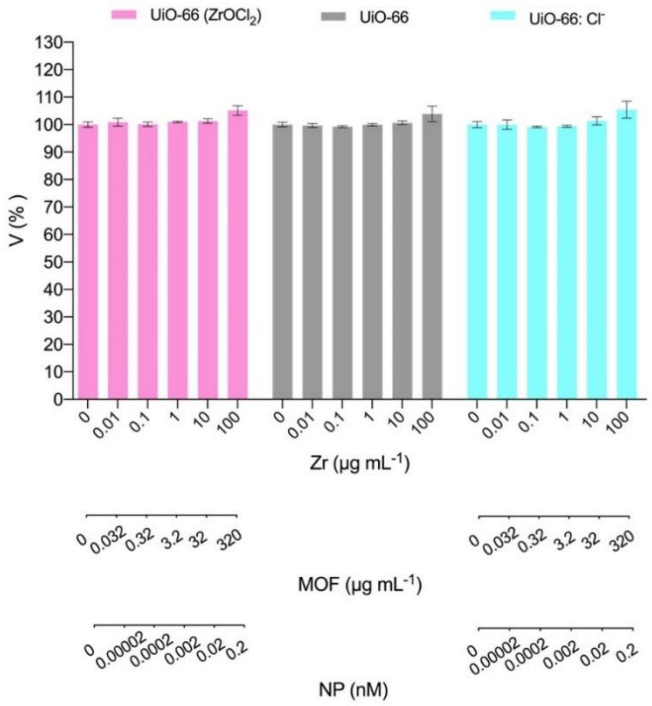

Figure 3-35. Cell viability in A549 cell culture after 24 h of UiO-66 nanoMOFs exposure, measured by Resazurin assay. Viability values represent the mean ± standard deviation of measurements from three different wells.

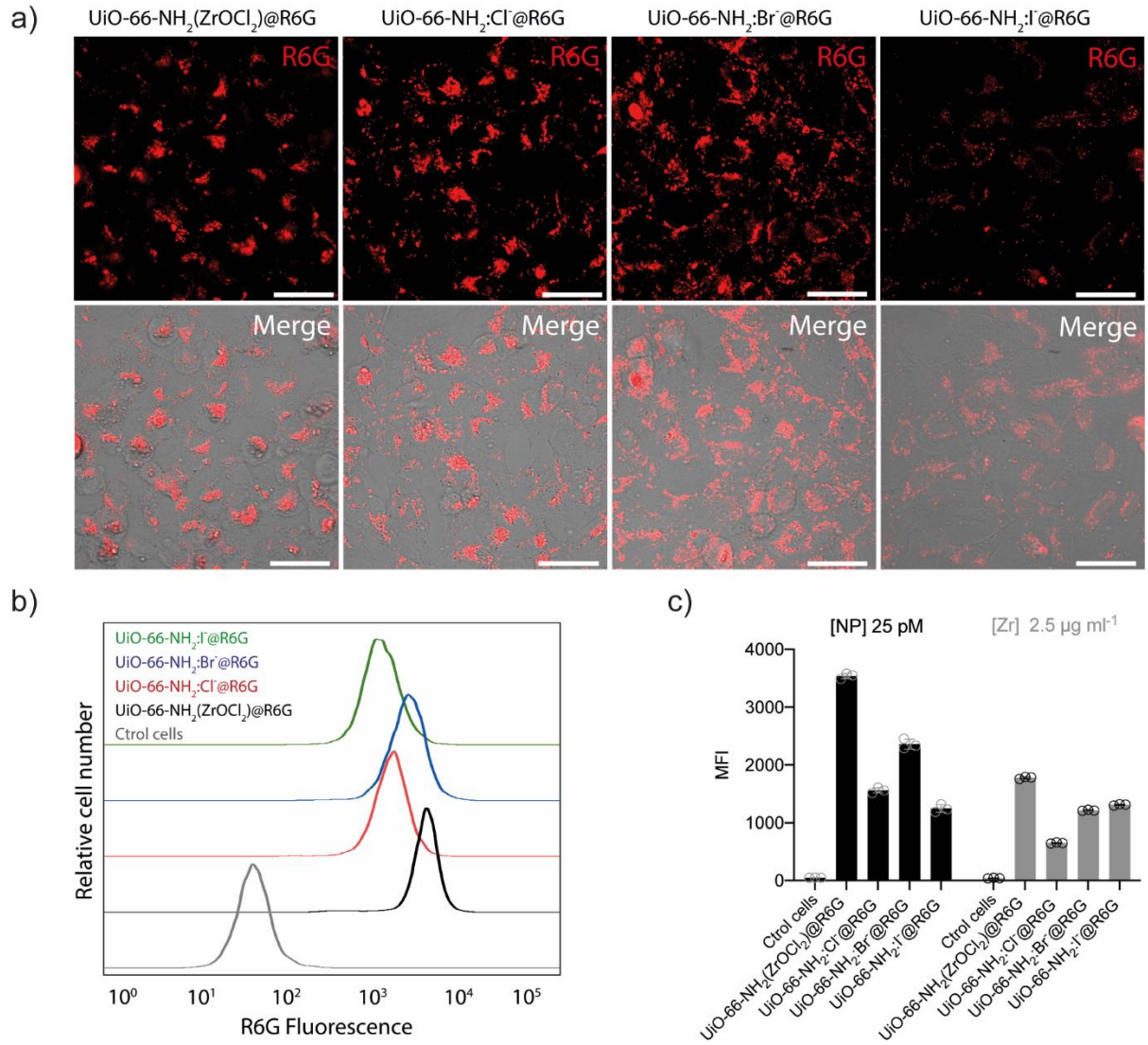

Figure 3-36. a) Representative microscopy confocal images of A549 cells incubated for 6 h with 25 pM of different UiO-66-NH_2@R6G and UiO-66-NH_2: X^-@R6G nanoMOFs. Scale bars correspond to 25 µm. b) Flow cytometry analysis of A549 cells exposed to vehicle (PBS) and the different UiO-66-NH_2:X^-@R6G formulations at 25 pM of nanoMOFs or to 2.5 µgZr/mL. Histograms represent experiments done in triplicate. c) Quantification of R6G fluorescence from flow cytometry analysis in (b). Bars represent means ± SD (n =3).

Confocal microscopy imaging experiments showed the intracellular location of the nanoMOF in the perinuclear region, as expected (Figure 3-36a).[238,239] This intracellular localization indicates that R6G remains inside the nanoMOFs, as mitochondria staining is not visible as a result of intracellular R6G leakage. Also, despite presenting a positive ζ-potential, the loaded R6G is not capable of vectorizing the nanoMOFs to the mitochondria either.

To study the cellular uptake by flow cytometry, 25 pM of UiO-66-NH_2($ZrOCl_2$) and UiO-66-NH_2:X^- (X^-: Cl^-, Br^-, I^-) were incubated for 6h in complete cell media at 37°C, 5% CO_2. It was found that the cellular uptake was higher for UiO-66-NH_2 ($ZrOCl_2$) compared with UiO-66-NH_2:X^- (X^-:Cl^-, Br^-, I^-), which presented similar internalization rates (Figure 3-36b,c). This difference might be related to the conversion of the concentration of nanoMOF from mass to molar concentration, as UiO-66-NH_2 ($ZrOCl_2$) is the sample with a less defined morphology and broader size distribution. However, this difference in the uptake was significantly reduced

when the experiment was performed using a constant amount of Zr (2.5 µg/mL, which corresponds to 8 µg/mL of nanoMOF). In this case, the internalization rate was very similar in all cases. Reduced uptake was only observed for UiO-66-NH_2 nanoMOFs (Figure 3-36c).These uptake rates are expected based on the physicochemical parameters studied during the characterization of the nanoMOFs, i.e. their hydrodynamic diameters and their ζ-potential values.[294] These results are in good agreement with the results obtained by fluorescence microscopy analysis and evidence the critical impact of per forming the experiments using a particular metric or another one.[295]

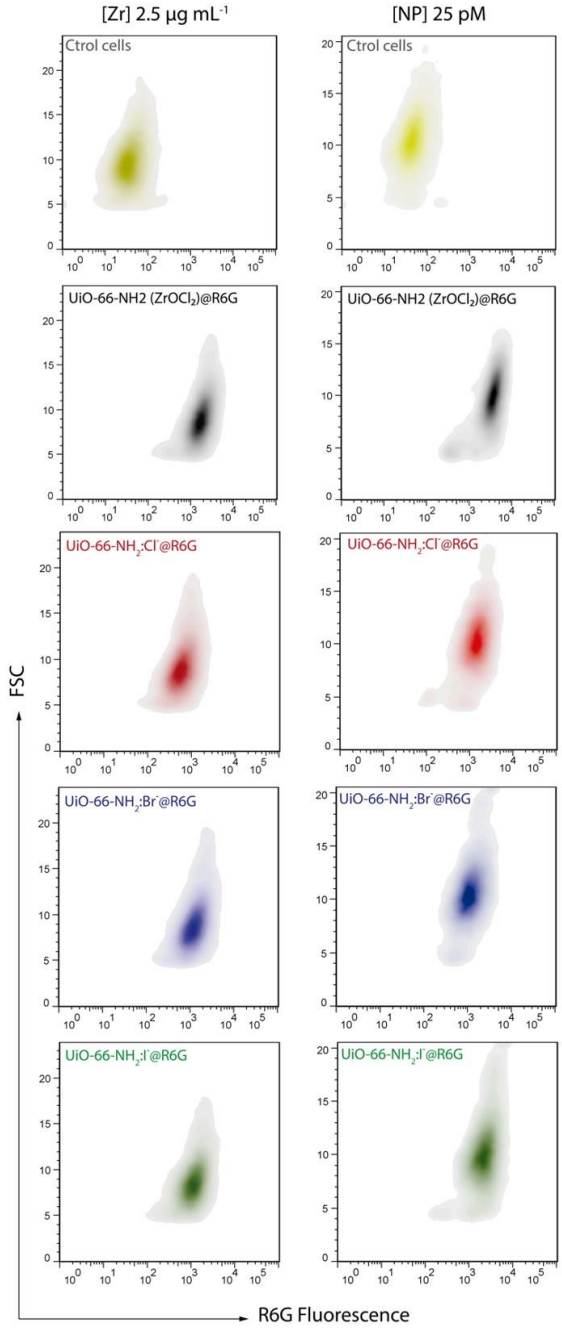

Figure 3-37. UiO-66 cell uptake assessment by flow cytometry. Dot plots indicating the cells distribution as function of the rhodamine 6G fluorescence. Each plot represents the measurement of at least 5000 events.

USC DE SANTIAGO DE COMPOSTELA

Table 3-18. Flow cytometry measurements of UiO-66 uptake by A549 cells. Mean fluorescence intensity (MFI) of experiment using an incubation with a constant concentration of Zr (2.5 µg/mL) and the corrected value normalized to the R6G content for each nanoMOF.

Sample	[Zr] (µg/mL)	MFI	[R6G] (µg/mL)	corrected MFI
UiO-66-NH_2 ($ZrOCl_2$)@R6G	2.5	1778.66± 17.61	1.65	1778.66 ± 17.61
UiO-66-NH_2:Cl^-@R6G	2.5	649.66 ± 9.29	1.10	864.05 ± 12.35
UiO-66-NH_2:Br^-@R6G	2.5	1214.33 ± 9.45	1.10	1615.06 ± 12.57
UiO-66-NH_2:I^-@R6G	2.5	1311.33 ± 11.23	1.25	1639.16 14.04

3.3. Summary and Conclusions of Chapter 3

In this chapter, the role of halides was studied as co-modulators to produce UiO-66-NH_2 nanoMOFs with a size below 100 nm using a new synthetic method. Interestingly, all halides except fluoride ions yielded highly crystalline nanoMOFs, and their addition improved greatly the reaction yield. In the case of chlorine and bromine, the halide ions were present in the crystalline structure, as confirmed by STEM-EDX experiments. The critical role of halides, in particular of chlorine, in controlling the final particle size was further corroborated by extending the synthetic method to produce UiO-66 nanoMOFs.

The nanoMOFs synthesized exhibited great colloidal stability against different pHs, with the presence of proteins or ionic strength maintaining a constant effective diameter. These nanoMOFs could be post-loaded with ca. 17–20% w/w of R6G. The leaking of R6G was negligible up to 24 h in different media with different values of pH (i.e. MilliQ water, complete DMEM and PSF).

These nanoMOFs are highly biocompatible as observed by resazurin assay up to 100 µg/mL of Zr. The intracellular distribution of the nanoMOFs was the expected one. The nanoMOFs were located in the perinuclear region, most likely trapped in lysosomes, as normally happens with nanomaterials having equivalent features. The uptake was evaluated and despite observing a different uptake of UiO-66-NH_2 ($ZrOCl_2$)@R6G when molar concentrations were considered, when the uptake was compared using the mass of Zr per volume, this difference was minimized, as expected considering their physicochemical features.

USC UNIVERSIDADE DE SANTIAGO DE COMPOSTELA

4. ULTRAFAST SYNTHESIS OF ZIRCONIUM-PORPHYRIN FRAMEWORK NANOCRYSTALS FROM ALKOXIDE PRECURSORS

USC
UNIVERSIDADE DE SANTIAGO DE COMPOSTELA

USC
UNIVERSIDADE
DE SANTIAGO
DE COMPOSTELA

4.1. Introduction

Porphyrinic MOFs feature exceptional attributes, such as high surface area, and tunable catalytic and optoelectronic properties. These properties render them highly promising and versatile candidates for numerous applications, including phototherapy, drug delivery, photocatalysis, electronics or energy storage. However, a significant challenge hindering their integration into diverse industries is the rapid, cost-effective production in sizes amenable to their processing. In this study, Zr(IV) alkoxides were used as metal precursors to enable ultrafast (~ min) and high yield (> 90%) synthesis of the three well established Zr-based porphyrinic MOF nanocrystals with varying topologies: MOF-525, PCN-224 and PCN-222. By modulating linker-to-metal and modulator-to-metal ratios, a precise control over the formation of single phases was achieved.

While metal alkoxides have been extensively utilized in sol-gel synthesis due to their rapid hydrolysis, enabling the synthesis of catalytically active metal oxides such as Al_2O_3, Y_2O_3, ZrO_2, or TiO_2,[296] their use as metal sources in Zr-MOFs synthesis is more limited. They have been employed in the early synthesis of molecular oxo-clusters like $[Zr_6(\mu_3\text{-}O)_4(\mu_3\text{-}OH)_4]^{12+}$ stabilized with various carboxylic acids.[297–299] These clusters were next used as precursors to isolate Zr_6-oxo MOFs, that because of cluster facile hydrolysis, could be prepared in mild conditions,[300] and short reaction times while avoiding the formation of ordered defects and impurities,[301] and preventing the formation of polymorphs.[169]

The benefits of using alkoxides as metal sources also include high reaction yields, and the production of alcohols as byproducts rather than hydrochloric acid or chlorides that may impact the reaction pathway and the structure of the resulting MOFs.[302] Moreover, their use helps to control the amount of water used during synthesis that has been shown to directly affect the speciation and phase formation of Zr-porphyrinic MOFs.[172] Nonetheless, Zr alkoxides have scarcely been used for the direct synthesis of Zr-based MOFs.[303–306] On top of that, alkoxide rapid hydrolysis makes them well-suited for the synthesis of MOFs nanocrystals (nanoMOFs) because it favors seeding during the crystallization process. These nanoMOFs often possess a larger outer surface area, which imparts distinct properties such as higher surface energy and a greater number of defects. These properties can significantly affect the flexibility, processability and catalytic performance of the MOFs.[307]

To demonstrate the potential of alkoxides, the synthesis of nanosized PCN-224 was successfully performed at room temperature in just a few seconds using a continuous multifluidic method. This advancement represents a significant leap forward in simplifying the production of porphyrinic MOFs, paving the way for their broader application across various industrial and scientific fields.

4.2. Results and discussion

4.2.1. Varying ligand-to-metal ratio at room temperature (MOF-525, PCN-224)

This initial section explores the influence of the L/M ratio on the crystal phase of the attempted solids, while keeping other potential reaction variables constant. With constant reaction time of 1 h at room temperature (RT), and used $Zr(OEt)_4$ as the metal precursor and AA as the modulator. The Mod/M ratio was set to 560, inspired in previous work.[169] To

synthetize the porphyrinic framework with the lowest coordination connectivity, specifically the 6-c PCN-224, initially the L/M ratio was set to 0.25. This value aligns with the ideal formula of this MOF, $Zr_6O_4(OH)_4(TCPP)_{1.5}(AA)_6$, with the anticipation that higher values would favor the formation of phases of higher connectivity such as the 8-c PCN-222 or the 12-c MOF-525. Then, the L/M ratio was gradually increased up to 2.00, four times the amount necessary for maximal connectivity within the Zr_6-oxo cluster of the canonical 12-c MOF-525 as is shown in Figure 4-1. A comprehensive physicochemical characterization was conducted on the five purified solids, examined both as dried solids, to assess the coordination degree of the Zr_6-oxo cluster and the potential presence of defects, and as colloidal dispersions.

The crystalline nature of the purified solids was confirmed through PXRD analysis. Figure 4-2a-b display the PXRD diffractogram and its detailed magnification for the five solids studied, along with the simulated patterns for PCN-224 and MOF-525. Figure 4-2b present close-up views of the initial five diffraction reflections. Notably, the absence of the (110) and (211) crystallographic planes occurring at 3.2° and 5.6° two-theta angles characteristic of PCN-224 is evident for L/M ratios of 1.00, 1.50, and 2.00 and points to the presence of MOF-525. To corroborate the absence of this reflection (110) for the higher L/M ratios, small angle diffraction was performed (Figure 4-3). Overall, summarizing the PXRD data in Figure 4-2a-b, the L/M ratio in the stoichiometric condition for PCN-224 (L/M = 0.25) and the double (L/M = 0.50) suggest the formation of PCN-224 solids, while overpassing this L/M ratio, i.e. 1.00, 1.50 and 2.00, suggest the formation of MOF-525, compatible with Pawley's refinement (Figure 4-4).

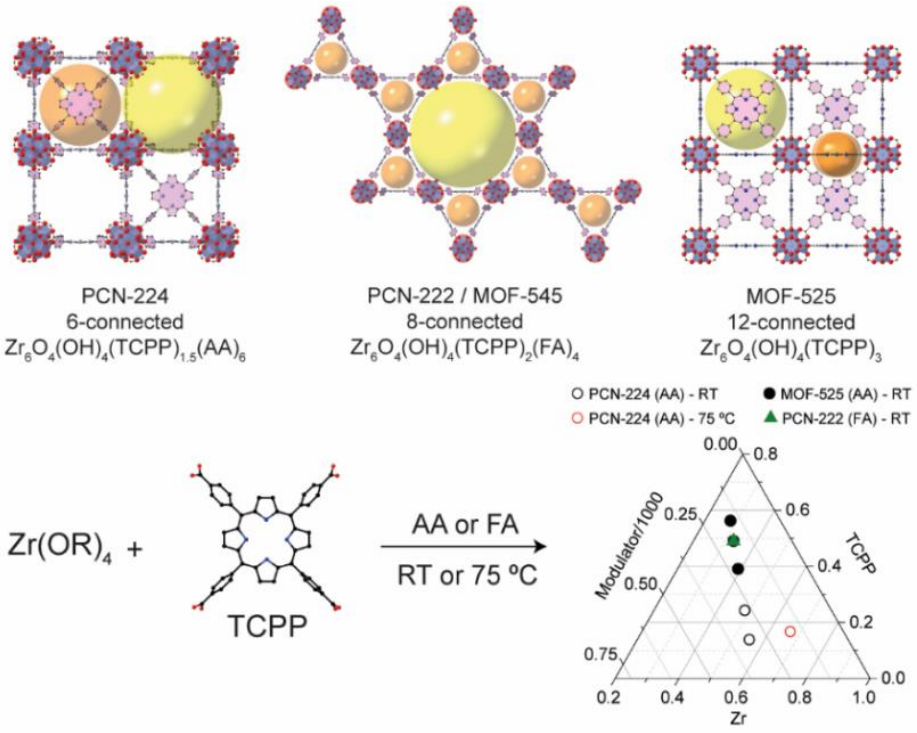

Figure 4-1. Top Row: Comparative structures of three different MOFs: PCN-224, PCN-222/MOF-545, and MOF-525, showing varying connectivity and organic linker arrangements. Bottom row: Synthesis approach utilizing Zr alkoxide precursors and TCPP. By adjusting the linker-to-metal (L/M) and modulator-to-metal (Mod/M) ratios, as well as the choice of modulator, we facilitate the formation of single phases of the depicted MOFs. These phases are further delineated in the tertiary diagram (bottom right).

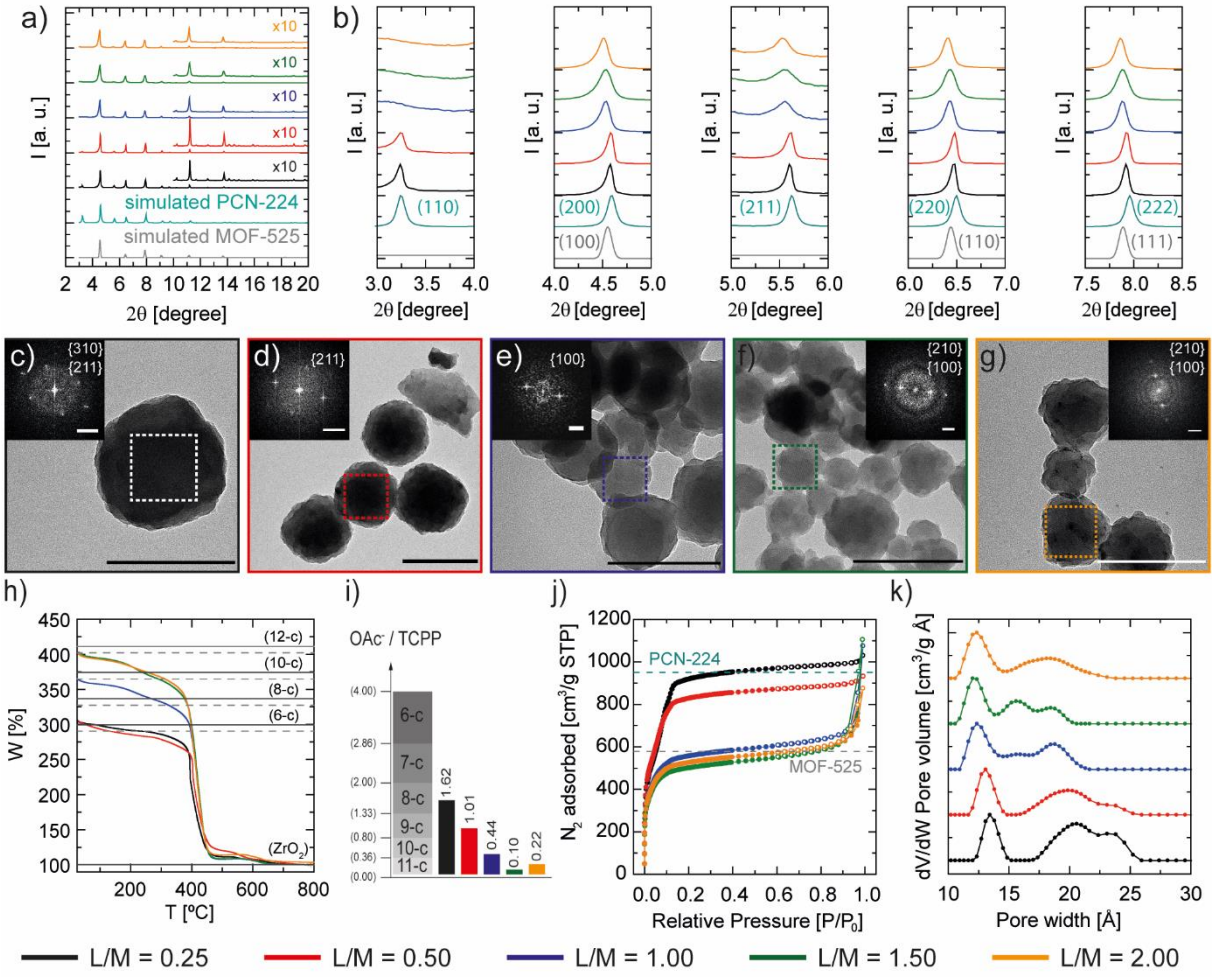

Figure 4-2. Characterization of nanoMOFs varying the L/M ratio at room temperature. a) PXRD diffractogram with the simulated patterns of PCN-224 and MOF-525, b) normalized first 5 diffraction peaks. HRTEM images of porphyrinic MOF nanoparticles changing the ratio linker/metal (L/M) c) 0.25, d) 0.50, e) 1.00, f) 1.50 and g) 2.00 and their corresponding FFT, indexing some different crystallographic planes (PCN-224 for L/M 0.25 and 0.50 and MOF-525 for L/M 1.00, 1.50 and 2.00). h) Normalized TGA with the theorical mass molar of Zr_6-oxo cluster with different coordination degree with TCPP and acetate molecules (dashed lines are the dehydrated cluster); i) quantification of TCPP molecules by ^{1}H-NMR; j) N_2 adsorption isotherms at 77 K correspond to the expected values for ideal PCN-224 and MOF-525 phases calculated with Zeo++;[308] and k) pore size distribution using NLDFT model. Scale bars are 200 nm for HR-TEM images and 0.5 nm^{-1} for FFT images.

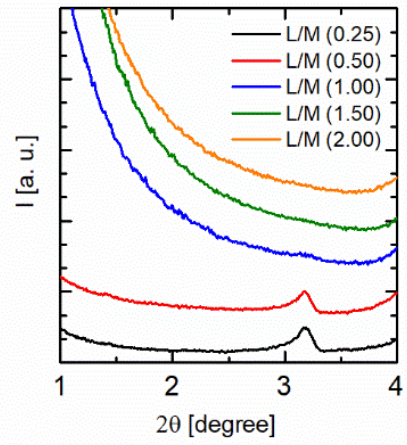

Figure 4-3. Small angle diffraction measurements of Zr-porphyrinic MOFs with different L/M ratios.

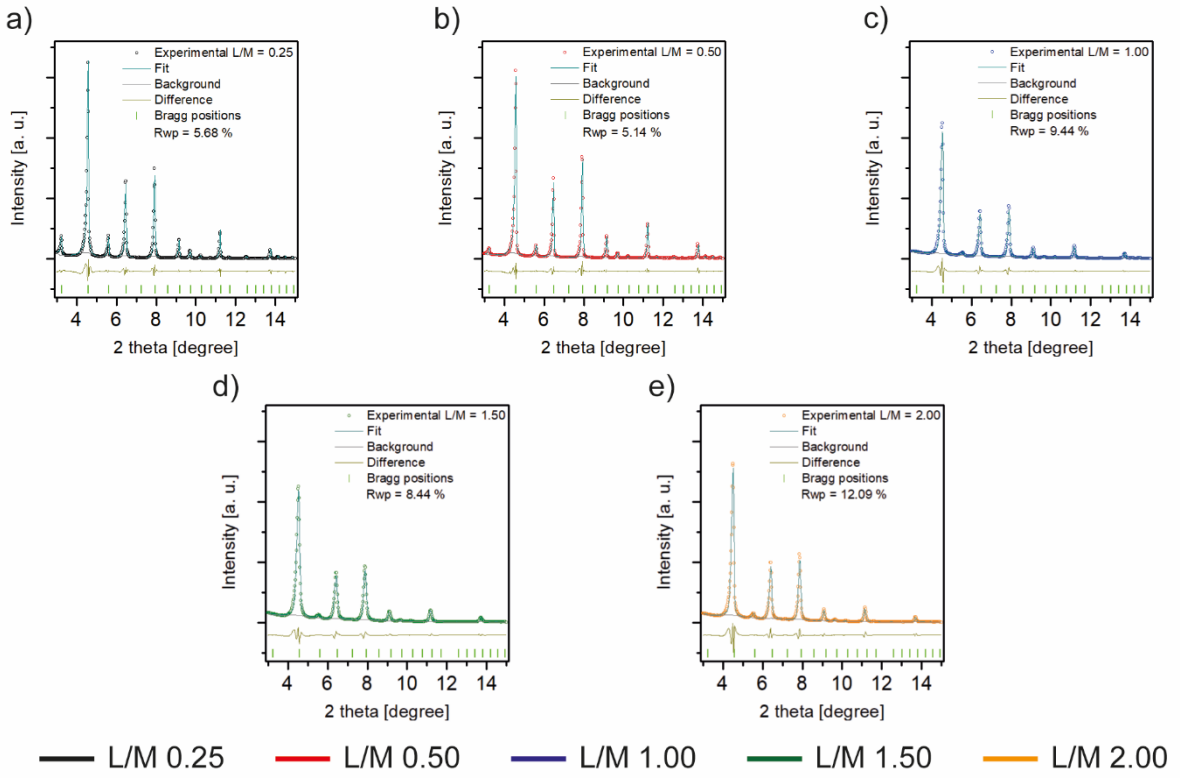

Figure 4-4. Pawley's refinement for PCN-224 of Zr-porphyrinic MOF nanoparticles for a) 0.25, b) 0.50, c) 1.00, d) 1.50 and e) 2.00 L/M ratios.

Figure 1c-g display TEM images of the five solids at L/M ratios ranging from 0.25 to 2.00. Average particle sizes for these ratios were measured as 527.7 ± 251.7, 193.0 ± 61.4, 105.0 ± 22.9, 97.1 ± 17.5, and 102.8 ± 16.3 nm, respectively (Figures 4-5 and 4-6) A trend is observed where an increase in L/M ratio leads to a decrease in both particle size and polydispersity, as well as a decrease in crystallite size calculated using the Scherrer equation (Equation12, Table 4-1).

$$D = \frac{K\lambda}{\beta \cos\theta} \qquad \text{(Eq. 12)}$$

$D =$ Average crystallite size (nm)

$K =$ Shape factor (0.94 for spherical crystallites with cubic symmetry)

$\lambda =$ X − ray wavelength. Cu K_α average $= 1.54178$ Å

$\beta =$ FWHM (Full Width at Half Maximum)

$\theta =$ XRD peak position, one half of 2θ

Table 4-1 Crystallite size of Zr-porphyrinic MOFs with different L/M ratios calculated by Scherrer equation.

L/M	Crystallite size (nm)
0.25	96.50
0.50	63.48
1.00	39.29
1.50	34.38
2.00	37.15

USC UNIVERSIDADE DE SANTIAGO DE COMPOSTELA

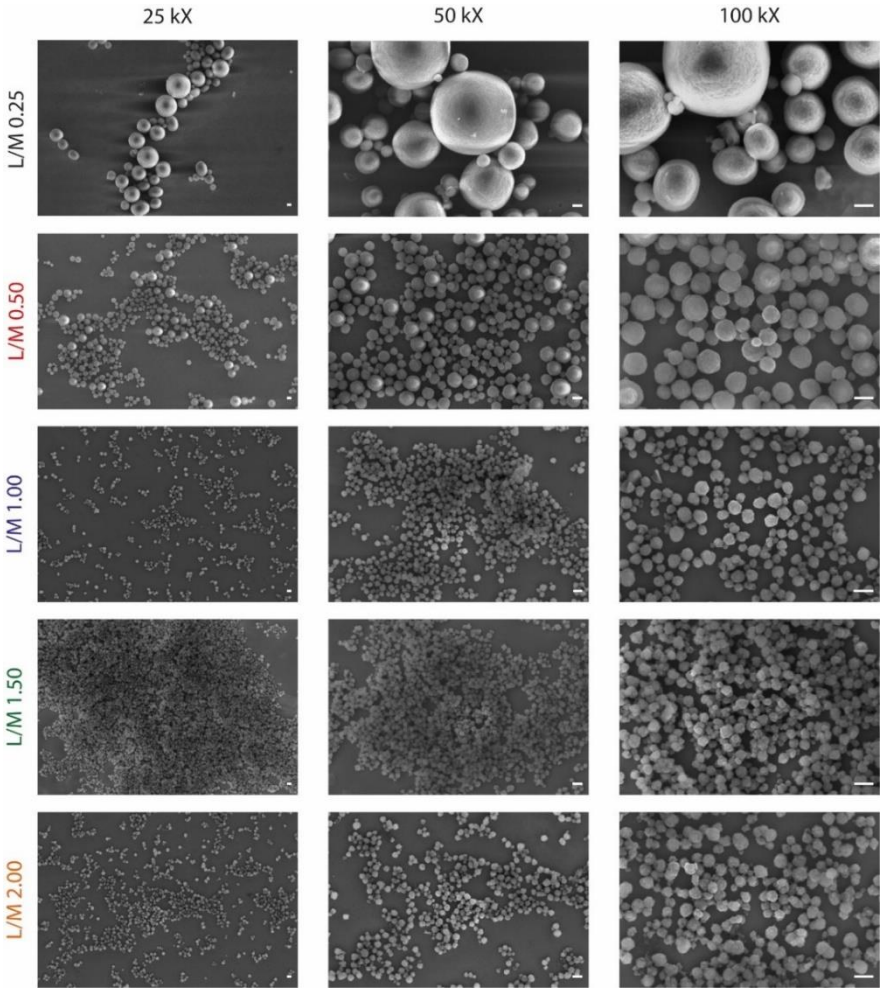

Figure 4-5. SEM images of Zr-porphyrinic MOF nanoparticles at different magnifications (25 kX, 50 kX and 100 kX). Scale bars are 200 nm.

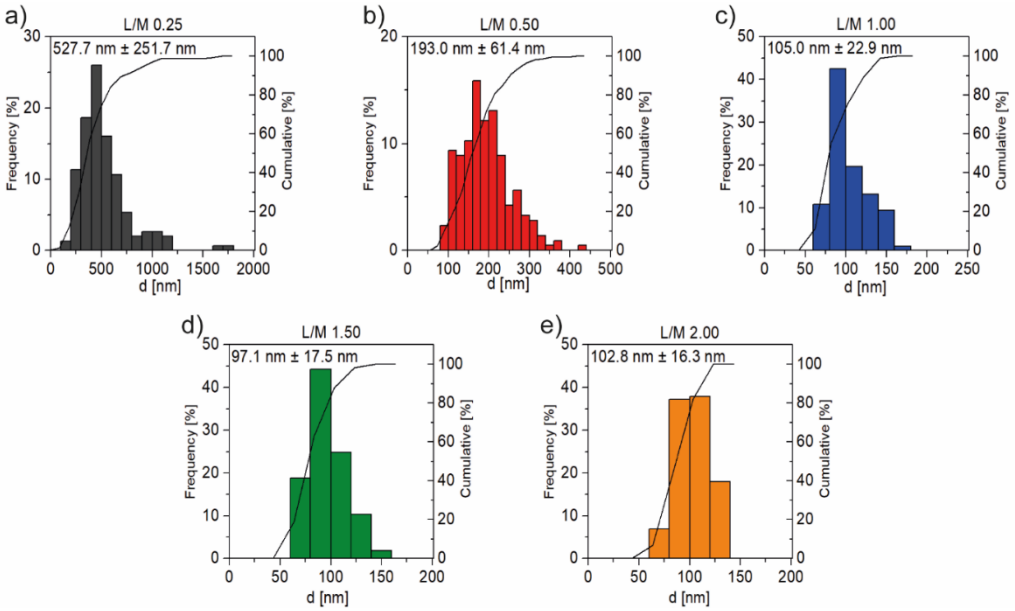

Figure 4-6. Particle size distribution histograms of Zr-porphyrinic MOF nanoparticles for a) 0.25, b) 0.50, c) 1.00, d) 1.50 and e) 2.00 L/M ratios.

Furthermore, HRTEM images (Figure 4-2c-g) confirm the stability of MOF structures under an 80 kV electron beam, FFT analyses on designated regions of interest (dashed ROIs) providing critical d-spacing measurements that illustrate a transition to the MOF-525 phase at higher L/M ratios in agreement with the PXRD analysis results depicted in Figures 1a-b.

The TGA analysis of the dried crystalline solids clearly demonstrated the high thermal stability of the samples, enduring temperatures up to 400 °C (Figure 4-2h), as expected for such Zr frameworks (Figure 4-7).[34] For lower L/M ratios (0.25 and 0.50), the analysis revealed an inorganic residue constituting approximately 33% of the overall weight, attributable to residual ZrO_2 which strongly agrees with the theoretical residue of the 6-c $Zr_6O_4(OH)_4(TCPP)_{1.5}(OAc)_6$ of 33.4 %, following thermal decomposition. For intermediate L/M ratio (1.00) and higher (1.50 and 2.00), inorganic residues of around 27% and 25% were obtained, respectively. The latter being in fully agreement with the theoretical value of the 12-c MOF-525 ($Zr_6O_4(OH)_4(TCPP)_3$), i.e., 24.3 %.

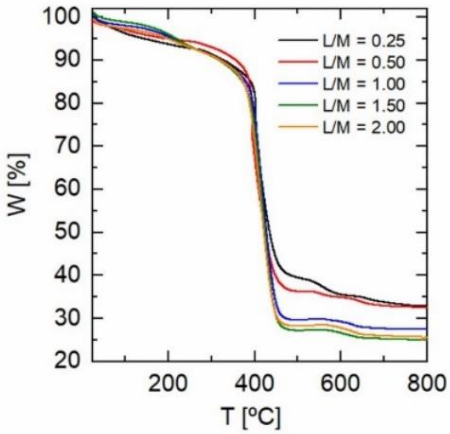

Figure 4-7. TGA without normalization of Zr-porphyrinic MOFs.

The normalized TGA results illustrate that the two solids with the lower L/M reflect the stoichiometric ratio expected for 6-c PCN-224 with the theoretical formula $Zr_6O_4(OH)_4(TCPP)_{1.5}(OAc)_6$ indicating full coordination with modulator AA (Figure 4-2h). At a moderate L/M ratio (1.00), the degree of coordination involved fewer than 10 TCPP molecules. This finding suggests a slightly defective variant of the canonical 12-c MOF-525, characterized by few missing linker defects (12.8%). Finally, for the two higher L/M ratios (1.50 and 2.00) the 12-c expected for MOF-525 is attained. As far as we are aware, there appears to be limited literature providing TGA evidence for a nearly saturated 12-c porphyrinic MOF.[309]

To further validate the TCPP coordination extent of the Zr porphyrinic MOFs, quantification was carried out using ^{1}H-NMR. This process involved dissolving the solids in a deuterated aqueous solution of $NaHCO_3$,[129] and incorporating an internal standard (methylsulfonylmethane),[240] to establish a correlation between the proton signal areas and the quantities of TCPP molecules and acetate ions (OAc). This correlation facilitated the determination of the OAc/TCPP ratio (Figure 4-2i).

In cases of lower L/M ratios with coordination index of 6, the OAc/TCPP ratios were lower than 4.00 (1.62 and 1.01 for L/M 0.25 and 0.50, respectively). This is compatible with an excess of TCPP molecules or a coordination degree slightly over 8 or the loss of OAc ions in the cluster. At an L/M ratio of 1, the ^{1}H-NMR quantification yielded a ratio of 0.44, closely approximating a coordination of 10. This implies the presence of 10 TCPP molecules for every 2 OAc molecule within a cluster. Furthermore, the two higher L/M ratios (1.50 and 2.00)

yielded ratios of 0.10 and 0.22, respectively being lower than the ratio of 0.36 within the range of 11-12 TCPP molecules per cluster. These results imply that the L/M ratio of 1.50 accommodates more than 11 TCPP molecules per cluster. Similarly, the L/M ratio of 2.00 exhibits an alignment with nearly 12 TCPP molecules per Zr_6-oxo cluster. NMR spectra and quantification are shown in Figure 4-8 and Table 4-2.

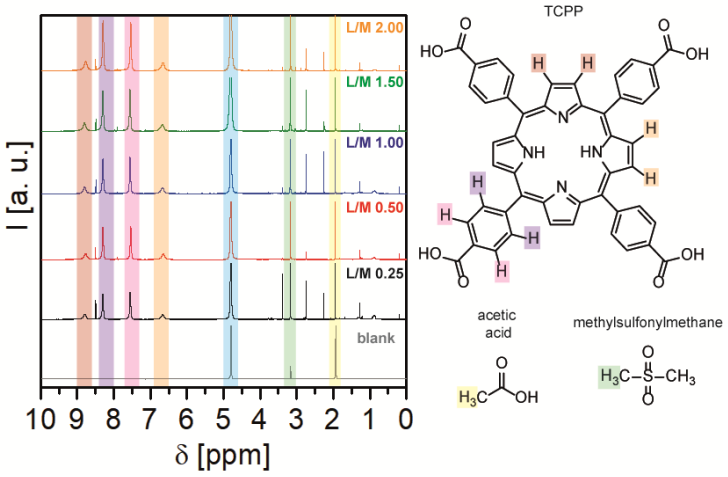

Figure 4-8. ^{1}H-NMR spectra of the blank (D_2O, $NaHCO_3$, CH_3COOH and $(CH_3)_2SO_2$) and Zr-porphyrinic MOFs. Signals not assigned correspond to remanent DMF and CH_3OH from the washing steps.[310]

Table 4-2. Assignation of ^{1}H-NMR spectra from Figure 4-8 and quantification using $(CH_3)_2SO_2$ as internal standard.

Sample	6H	3H	4H	4H	8H	8H	$(CH3)_2SO_2$ molecules	CH_3COO^- molecules	TCPP molecules	CH_3COO^- / TCPP
	$(CH_3)_2SO_2$	CH_3COO^-	pyrrol(1)	pyrrol (2)	benzene-o-porphyrin	benzene-m-porphyrin				
	(3.18ppm)	(1.95 ppm)	(8.79 ppm)	(6.66 ppm)	(8.30 ppm)	(7.55 ppm)				
L/M 0.25	1,95E+04	8,03E+04	-	-	1,37E+05	1,27E+05	6.0E+17	4,96E+18	3,06E+18	1,62
L/M 0.50	8,27E+04	7,89E+04			2,09E+05	2,08E+05		1,15E+18	1,14E+18	1,01
L/M 1.00	8,49E+04	2,46E+04			1,85E+05	1,82E+05		4,29E+17	9,76E+17	0,44
L/M 1.50	8,20E+04	2,33E+04			2,08E+05	1,98E+05		4,29E+17	4,46E+18	0,10
L/M 2.00	8,41E+04	3,01E+04			3,59E+05	3,63E+05		4,31E+17	2,00E+18	0,22

N_2 adsorption isotherms, measured at 77 K as shown in Figure 4-2j and detailed in Table 4-3, reveal the expected differences in N_2 uptake among samples with varying L/M ratios impacting directly in Brunauer–Emmett–Teller (BET) surface areas, which were calculated with BETSI analysis.[311] Lower L/M ratios (0.50 and 0.25) result in adsorption isotherms and pore width distributions that align with those expected for PCN-224,[35] while higher L/M ratios (1.00, 1.50, and 2.00) lead to a decreased N_2 uptake, a reduction in BET surface areas and a narrowing of pore size distribution that align with that expected for MOF-525,[171] as depicted in Figure 4-2k and elaborated in Table 4-4 and Figure 4-9. Higher ratios feature a primary pore size centered around 12 Å (Figure 4-9). The N_2 adsorption data thus supports and complements

USC UNIVERSIDADE DE SANTIAGO DE COMPOSTELA

the structural characterization previously discussed, underlining the impact of L/M ratio variations on the physicochemical properties of the MOFs.

Table 4-3. Summary of N_2 uptake and BET surface area of Zr-porphyrinic MOFs with different L/M ratios at room temperature.

L/M	N_2 uptake (cm^3/g)	BET surface area (m^2/g)
0.25	991	2532
0.50	895	2428
1.00	670	2154
1.50	628	1987
2.00	631	2097

Table 4-4. Summary of different pore sizes of PCN-224, PCN-222 and MOF-525.

Zr-porphyrinic MOF	Partial group	Cell parameter (Å)	Cluster connectivity	Pore width (Å) calculated with Zeo++[308]
PCN-224	$Im\bar{3}m$ (229)	a = 38.452	6-c	P_1 = 13.5 P_2 = 24.2
PCN-222	P6/mmm (191)	a = 41.968 c = 17.143	8-c	P_1 = 11.4 P_2 = 32.1
MOF-525	$Pm\bar{3}m$ (221)	a = 19.393	12-c	P_1 = 7.6 P_2 = 16.6

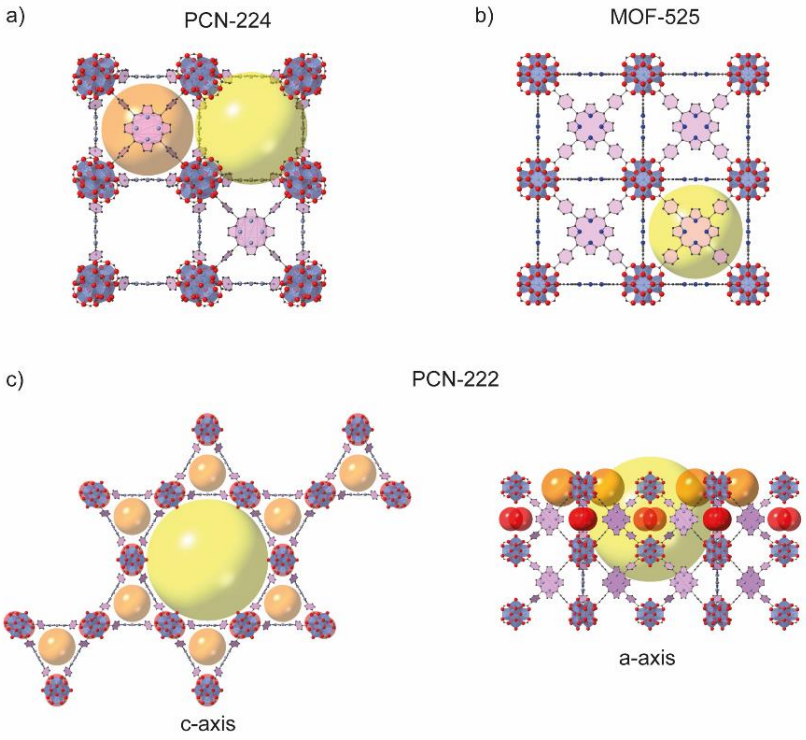

Figure 4-9. Pore size representation of a) PCN-224, b) MOF-525 and c) PCN-222.

The UV-Vis spectra of colloidal dispersions of the purified solids in MeOH reveal that at a L/M ratio of 0.25 (black line), the porphyrinic framework characteristic Soret band undergoes a red shift and notable broadening, with significant scattering observed in the four Q bands beyond 515 nm due to large particle sizes (Figure 4-10a). Increasing the L/M ratio to 0.50 (red line) narrows the Soret band and decreases Q band scattering. Higher L/M ratios (1.00, 1.50, and 2.00) further narrow the Soret band and eliminate scattering in the 700 to 1000 nm range, indicating reduced polydispersity and smaller nanoMOFs sizes. Similarly, DLS data of colloidal dispersions of the purified solids presented in Figure 4-10b, show a decrease in particle size and polydispersity with higher L/M ratios. Initial ratios (0.25 and 0.50) resulted in relatively large, polydisperse nanoMOFs, while higher ratios yielded smaller, highly monodisperse nanoMOFs. Details on hydrodynamic sizes and the corresponding PdI are provided in Table 4-5. Most notably, the chosen synthesis conditions achieved remarkably high reaction yields in terms of Zr consumed, ranging from approximately 80% to nearly 100% for L/M ratios of 0.50 and 1.00, as determined by inductively coupled plasma optical emission spectroscopy (ICP-OES) measurements of Zr content post-purification of the solids (Figure 4-10c).

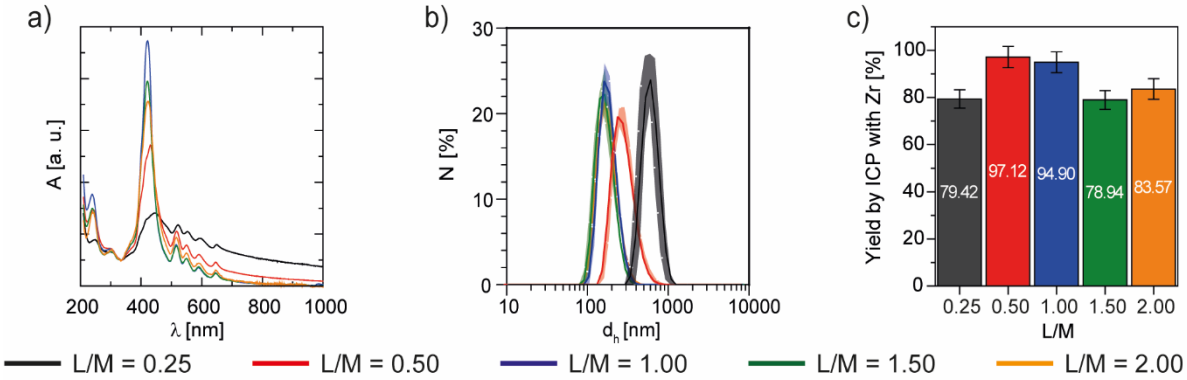

Figure 4-10. a) UV-Vis spectra, b) DLS analysis and c) yield of reaction obtained with the amount of Zr by ICP-OES of Zr-porphyrinic MOFs.

Table 4-5. Hydrodynamic size of Zr-porphyrinic MOFs with different L/M ratio measure by DLS in MeOH.

L/M	$D_{h,I}$ (nm)	$D_{h,V}$ (nm)	$D_{h,N}$ (nm)	PdI
0.25	636.0 ± 66.9	679.2 ± 78.7	618.1 ± 71.1	0.314 ± 0.050
0.50	386.8 ± 33.6	442.5 ± 93.2	307.7 ± 5.4	0.175 ± 0.044
1.00	216.2 ± 8.9	217.5 ± 9.2	186.1 ± 3.7	0.185 ± 0.023
1.50	200.7 ± 4.7	200.5 ± 4.3	168.7 ± 5.2	0.064 ± 0.043
2.00	222.5 ± 2.7	223.9 ± 2.9	180.9 ± 4.8	0.099 ± 0.038

Vibrational spectroscopy techniques, including FTIR and Raman, revealed no significant differences among the samples (Figures 4-11 and 4-12). However, differential scanning calorimetry (DSC) analysis produced two distinct sets of thermograms (Figure 4-13). Specifically, the samples with larger L/M ratios (1.00, 1.50, and 2.00) exhibited a single endothermic peak around 140 °C. In contrast, the samples with lower L/M ratios (0.25 and 0.50) demonstrated three endothermic peaks, with the most intense peaks occurring at 260 °C and 250 °C, respectively. These findings align with results from previous characterization

USC UNIVERSIDADE DE SANTIAGO DE COMPOSTELA

techniques, indicating that the samples with lower L/M ratios (0.25 and 0.50) differ from those with higher L/M ratios (1.00, 1.50, and 2.00).

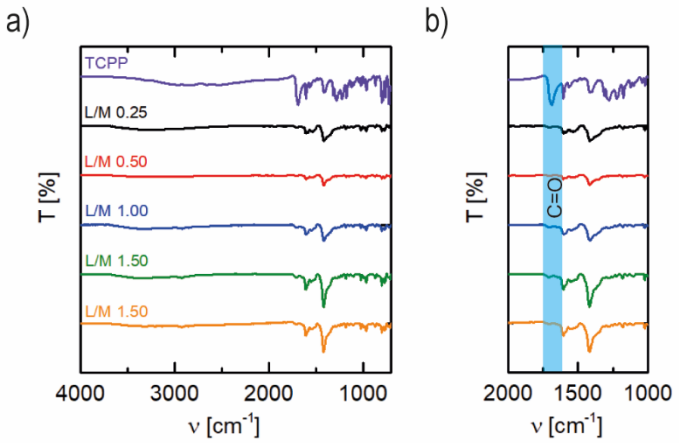

Figure 4-11. a) FT-IT spectra of Zr-porphyrinic MOFs and b) zoom in carbonyl region.

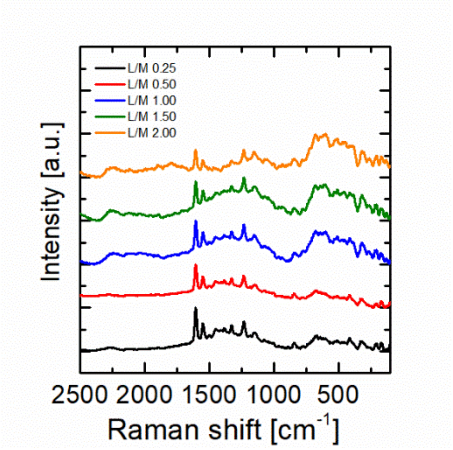

Figure 4-12. Raman spectra of Zr-porphyrinic MOFs.

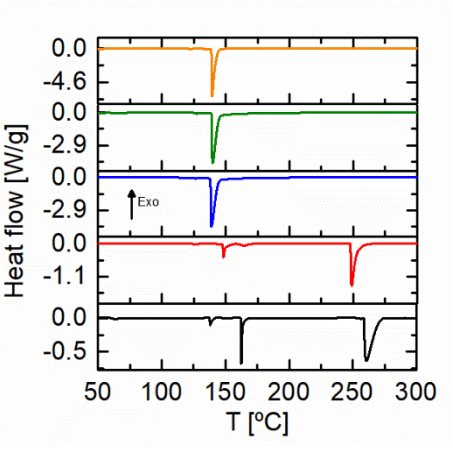

Figure 4-13. DSC analysis of Zr-porphyrinic MOFs for L/M = 0.25 (black), 0.50 (red), 1.00 (blue), 1.50 (gree) and 2.00 (orange).

The emission spectra of all prepared samples exhibit two bands when excited at both their Soret (excitation at 420 nm) and Q-band (excitation at 515 nm) regions: a first band located at

approximately 650 nm and a second band at around 720 nm, assigned to Q_{00} and Q_{01} transitions, respectively. The normalized emission spectra of the porphyrinic MOFs (Figure 4-14) demonstrate consistent emission behavior, regardless of excitation at the Soret or the Q-band. As displayed by TCPP emission, Q_{01} is typically less intense than the Q_{00} band because it involves vibrational excitation in the ground state, making it an overtone transition. However, as the ratio of the components (referring to L/M ratio) increases, the intensity of the Q_{01} emission band (~720 nm) over the Q_{00} emission band (~650 nm) coherently increases. This suggests that higher L/M ratios enhance the electronic environment, favoring changes in oscillator strength due to increased incorporation of coordinated TCPP molecules. This change potentially leads to enhanced electronic coupling, altered vibrational relaxation pathways, and variations in structural rigidity and symmetry, affecting the radiative transitions of the porphyrinic system. Moreover, the increase in TCPP coordination number from 6-c (L/M = 0.25) to 12-c (L/M = 2.00) results in a different spatial arrangement and orientation of the porphyrin units within the MOF framework. Such changes in dihedral angles and increased structural rigidity modify the electronic environment, leading to variations in the emission spectra akin to those observed in simpler porphyrin aggregates.

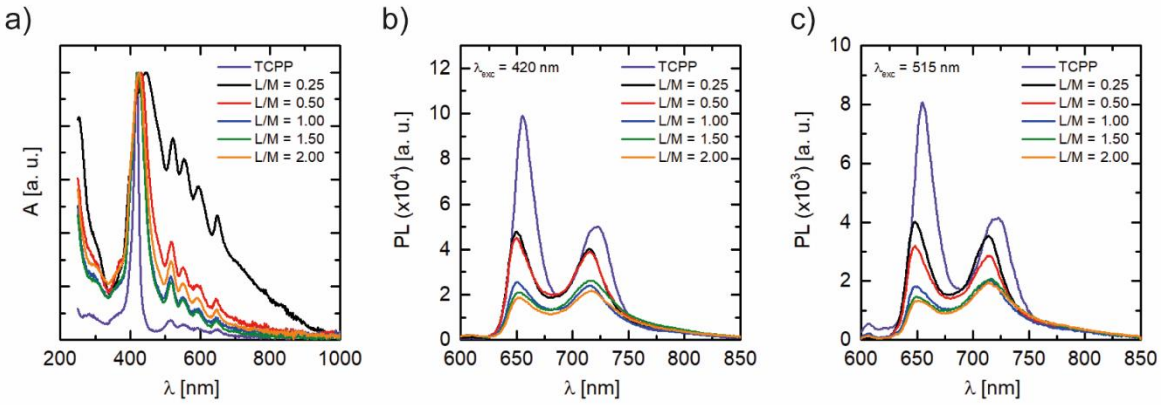

Figure 4-14. a) Normalized absorption spectra and photoluminescence spectra at b) 420nm and c) 515 nm excitation wavelength of Zr-porphyrinic MOFs.

4.2.2. Varying temperature and alkoxide precursor (PCN-224)

Once confirmed that using the $Zr(OEt)_4$ at RT enables the production of single phase polydisperse (PdI > 0.3) PCN-224 and monodisperse (PdI < 0.1) MOF-525 nanocrystals, we decided to explore new synthetic conditions to reduce the polydispersity of nanosized PCN-224. Aiming to PCN-224 nanocrystals with sizes around 100 nm and low polydispersity, as in the previous section, we set the L/M ratio to 0.25, fixed the reaction time at 1 h and used AA as modulator. However, we substantially decreased the Mod/M ratio to 250, aiming to reduce the nanocrystal size, and varied the temperature (Figures 4-15 and 4-16). To this end, five temperature settings ranging from RT to 120 °C were explored, the latter being widely used to produce MOFs based on the Zr_6-oxo cluster. As anticipated from Figure 4-15, relatively monodisperse nanoparticles are obtained across the entire temperature range, with their size increasing as the temperature rises, with particle size ranging from 50 to 200 nm.

USC UNIVERSIDADE DE SANTIAGO DE COMPOSTELA

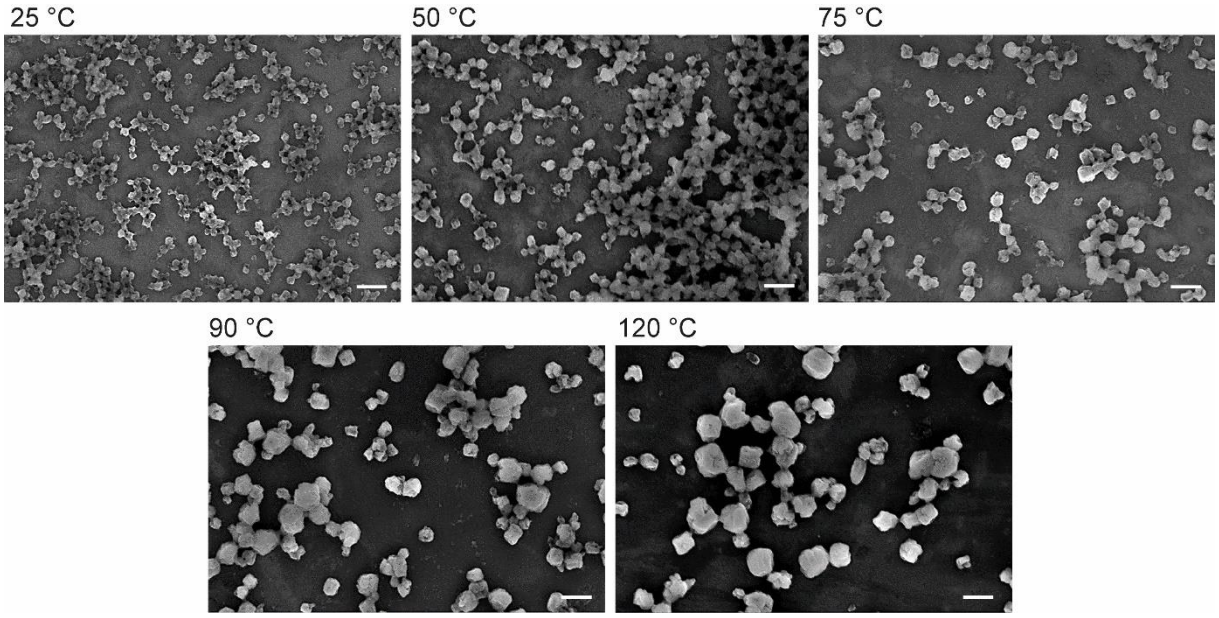

Figure 4-15. Representative SEM images for 1 h reaction performed at different temperatures (25 °C, 50 °C, 75 °C, 90 °C and 120 °C). The ratios adopted for the synthesis of the particles are L/M = 0.25, Mod/M = 250; the Zr precursor used is $Zr(OEt)_4$ and the modulator is AA. Scale bars: 200 nm.

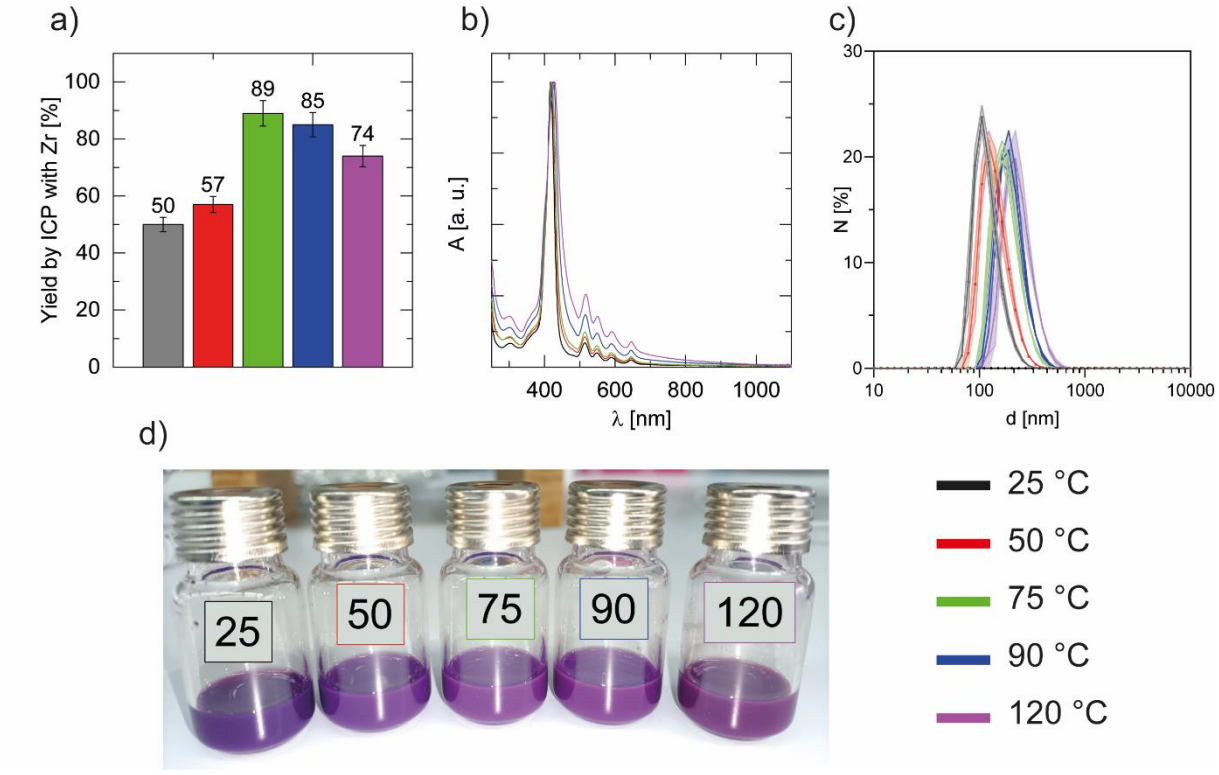

Figure 4-16. a) Graphical representation of the reaction yield evaluated through ICP-OES, b) UV-Vis extinction spectra, c) hydrodynamic diameters (by number) and d) digital images of 1h reaction conducted at different temperatures.

By examining at the reaction yields in terms of Zr consumed (Figure 4-16a), it was observed that when moving from RT to 75 °C the reaction yield moved from 50% to 85% of added Zr, as quantified by ICP-OES (Table 4-6). Additionally, we noted that increasing the temperature led to subtle changes in the optical properties. Specifically, there was a progressive broadening of the Soret band, and an enhancement of the scattering baseline observed (Figure

4-16b). These changes are attributed to an increase in particle size and polydispersity, as qualitatively confirmed through SEM (Figure 4-15), and DLS in Figure 4-16c and Table 4-7.

Table 4-6. Zr quantification through ICP-OES to determine the reaction yield at different temperatures (25 °C, 50 °C, 75 °C, 90 °C and 120 °C) of 1 h reaction. Each measurement is performed in triplicate.

Entry	Zr average	Yield%
Zr (precursor)	2.05 ± 0.10	-
25 °C	1.02 ± 0.05	49.9 ± 2.5
50 °C	1.17 ± 0,06	57.1 ± 2.8
75 °C	1.83 ± 0.09	88.9 ± 4.4
90 °C	1.74 ± 0.09	85.0 ± 4.2
120 °C	1.52 ± 0.08	74.2 ± 3.7

Table 4-7. Hydrodynamic diameter by intensity ($d_{h,I}$) and by number ($d_{h,n}$) measured through DLS of the sample synthesized at different temperatures (1 h reaction).

Entry	$d_{h,I}$ (nm)	$d_{h,n}$ (nm)	PdI
25 °C	163.4 ± 3.6	121.3 ± 5.2	0.190 ± 0.028
50 °C	195.6 ± 3.7	144.9 ± 5.9	0.137 ± 0.013
75 °C	233.0 ± 5.4	184.4 ± 2.2	0.221 ± 0.009
90 °C	250.9 ± 6.5	200.8 ± 4.7	0.093 ± 0.022
120 °C	302.1 ± 12.8	237.5 ± 5.5	0.089 ± 0.027

To go one step further, and to analyze the impact of different alkoxide precursors in the reaction that allows to produce nanoMOFs (Figure 4-17a-b), the temperature was fixed at 75 °C, keep the rest of the parameters unchanged, and employ other Zr-precursors besides the ethoxy, such as $Zr(OiPr)_4$ and $Zr(OBut)_4$ (Figures 4-18, 4-19 and Table 4-8). The crystalline structure of these solids was confirmed through PXRD analysis, which revealed that the use of different Zr precursors led to the formation of virtually the same crystalline phase (Figure 4-17c). Moreover, HRTEM confirmed the crystallinity of all the MOF nanocrystals (Figure 4-17b) obtained, as can be seen with FFT analysis on designated region of interest (dashed ROI), providing critical d-spacing of 16.528 Å compatible with {211} family of planes for PCN-224, which are not present in MOF-525.

USC UNIVERSIDADE DE SANTIAGO DE COMPOSTELA

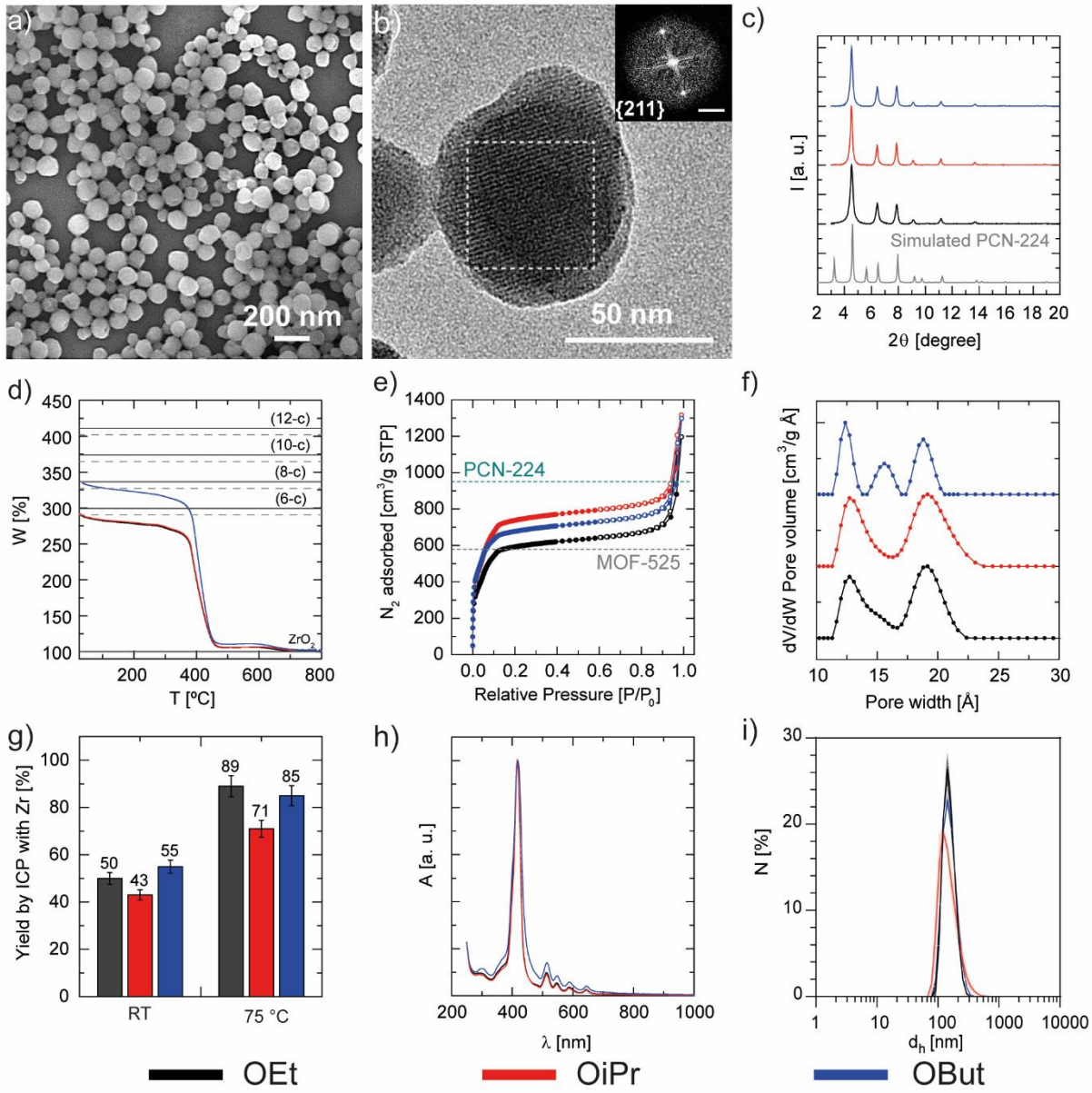

Figure 4-17. Characterization of nanosized PCN-224: effect of temperature and alkoxide in the synthesis.a) Representative SEM and b) HRTEM with FTT images of nanoMOFs synthesized starting from $Zr(OEt)_4$ precursor at 75 °C for 1 h in the presence of AA; c) PXRD patterns; d) normalized TGA with the theoretical molar mass of Zr_6-oxo cluster with different coordination degree with TCPP and acetate molecules (dashed lines are the dehydrated cluster); e) N_2 adsorption isotherms at 77 K with the expected uptake values for ideal PCN-224 and MOF-525 phases calculated with Zeo++;[308] f) NLDFT pore size distribution by using different Zr precursors; g) graphical representation of the reaction yields evaluated through ICP-OES of 1 h reaction conducted at RT and 75 °C; h) UV-Vis extinction spectra and i) hydrodynamic diameters d_h (by number). Scale in FFT represents 0.5 nm^{-1}.

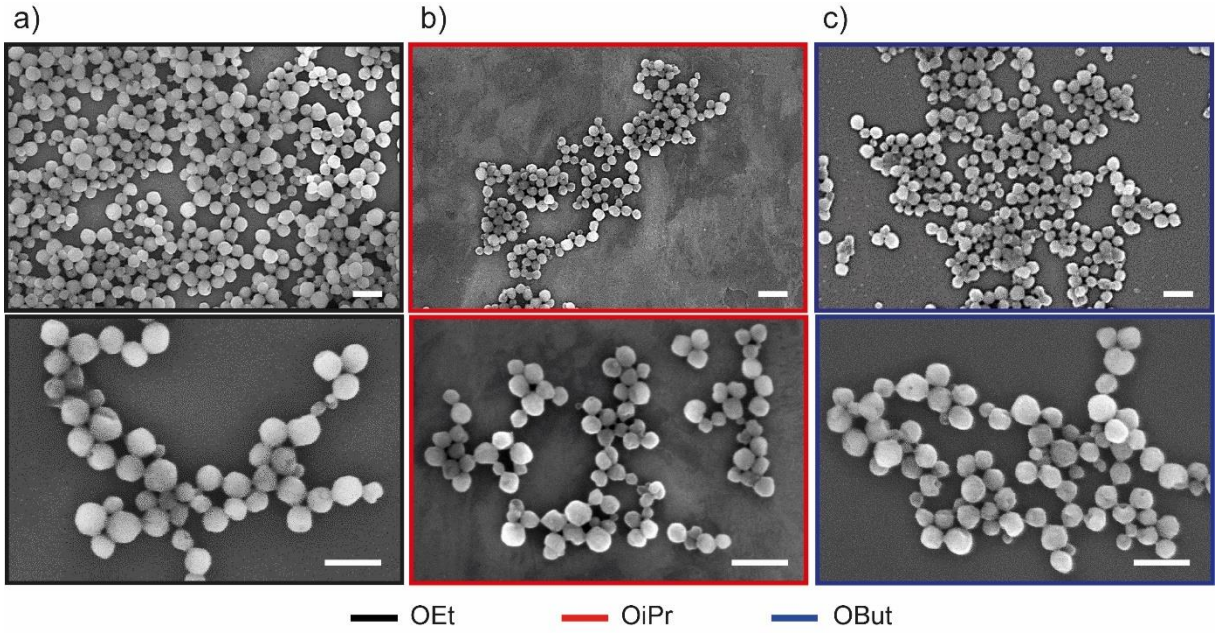

Figure 4-18. Representative SEM images for 1 h reaction performed at 75 °C by using different Zr precursors and AA as modulator. Scale bars are 200 nm.

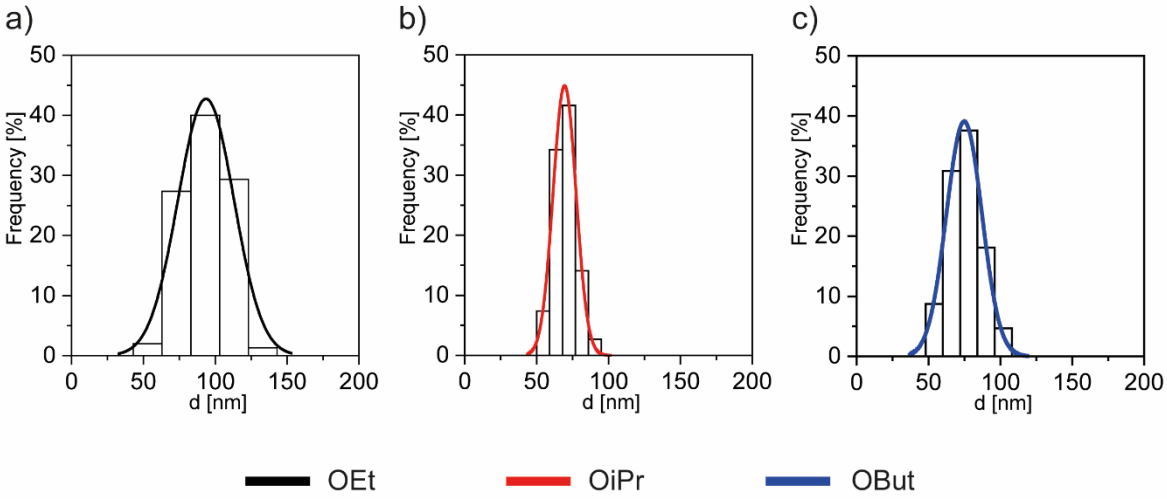

Figure 4-19. Particle size distribution histogram relative to SEM images of 1 h reaction performed at 75 °C by using different Zr precursors and AA as modulator.

Table 4-8. Particle size distribution measured through SEM analysis of the samples synthesized with different Zr precursors.

Precursor	Modulator	Time	Temperature	d_{SEM} (nm)
$Zr(OEt)_4$	AA	1 h	75 °C	92.7 ± 17.3
$Zr(OiPr)_4$				69.8 ± 7.6
$Zr(OBut)_4$				75.5 ± 11.5

USC UNIVERSIDADE DE SANTIAGO DE COMPOSTELA

Although PXRD analysis does not unequivocally differentiate between PCN-224, MOF-525 and dPCN-224,[168] our results align with initial expectations of using a L/M ratio of 0.25

(Figure 4-20). Pawley's refinement supports the presence of the PCN-224 phase, reinforcing the interpretation of the normalized TGA thermograms (Figure 4-17d). This is further evidenced by the exclusive presence of the {211} family of planes in PCN-224. Additionally, the absence of supercell peaks at 3.2º and 5.6º two-theta can be attributed to disorder in defects and/or variations in cluster orientation compared to the ordered structure of PCN-224.[168]

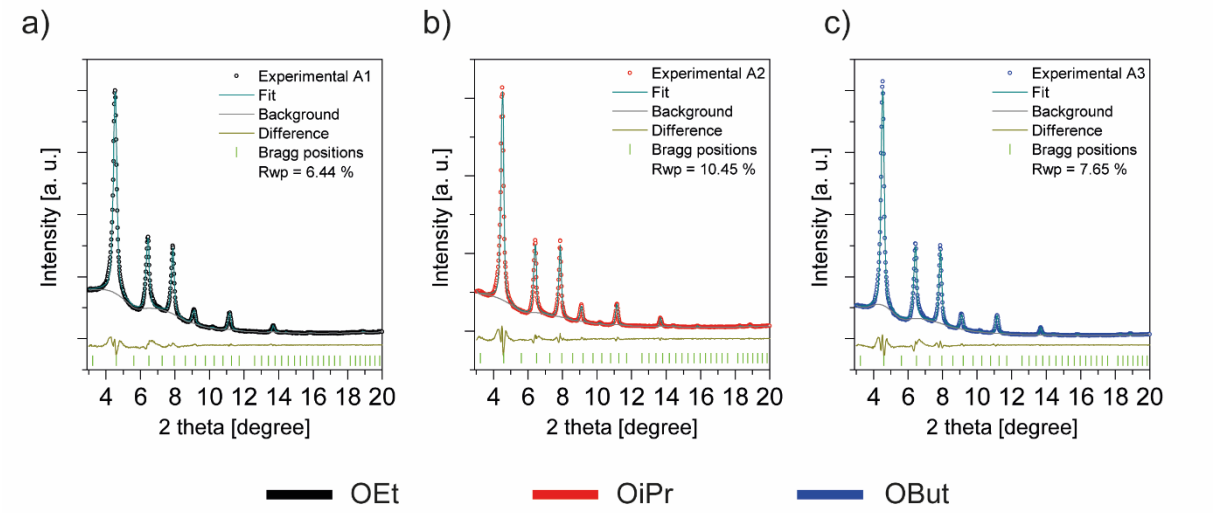

Figure 4-20. Pawley's refinement of Zr-porphyrinic MOF nanoparticles, synthesized at 75 °C, 1 h reaction, by using different Zr precursors and AA as modulator.

N_2 adsorption isotherms of the materials revealed the microporosity of the nanoMOFs, with BET surface areas reaching values between 2600-3000 m²/g, closely aligning with expectations for PCN-224 (Figure 4-17e, Table 4-9).[35] The pore size distribution analysis (Figure 2f), regardless of the alkoxy precursor used, revealed the presence of two primary pore sizes, centered approximately at 13 Å and 19 Å (Figure 4-9 and Table 4-4) with an extra pore size around 15 Å. This distribution is more closely aligned with the characteristics of PCN-224, rather than with those of MOF-525. The presence of some degree of defectivity in our samples was confirmed by TGA analysis, which nevertheless showed cluster connectivity indexes compatible with PCN-224 (6-c) but far from that of MOF-525 (12-c) (Figure 2d).

Table 4-9. BET surface area and pore volume of the particles synthesized with different Zr precursors.

Precursor	**BET surface area (m^2/g)**	**t-plot micropore volume (cm^3/g)**
$Zr(OEt)_4$	2467	0.718
$Zr(OiPr)_4$	3083	0.904
$Zr(OBut)_4$	2629	0.845

The 1h-reaction conducted at 75 °C displayed high reaction yields (> 70%) with all the alkoxide precursors (Figure 4-17g and Table 4-10).

In all cases, the characteristic optical signature of porphyrin nanoMOFs could be clearly observed (Figure 4-17h), with a very narrow Soret band (approx. at 420 nm) and with a high ratio whether compared to the Q-bands (500-630 nm), imparting to the colloidal solution a

purple/violet color (Figure 4-16d) easily distinguishable with respect to the starting red TCPP solution. All the produced nanoMOFs presented superimposable extinction spectra, suggesting similar outcomes despite the different Zr precursors. The average d_h (hydrodynamic diameter by number distribution) was about 150 nm, with relatively low PdI (<0.15), demonstrating the uniformity in particle d_h (Figure 4-17i and Table 4-11).

Table 4-10. Zr quantification through ICP-OES to determine the reaction yield of the reaction performed with different Zr precursors.

Precursor	**Modulator**	**Time**	**Temperature**	**Yield (%)**
$Zr(OEt)_4$	AA	1 h	75 °C	88.9 ± 4.4
$Zr(OiPr)_4$				71.2 ± 3.6
$Zr(OBut)_4$				85.2 ± 4.2

Table 4-11. Hydrodynamic diameter by intensity ($d_{h,I}$) and by number ($d_{h,n}$) and PdI measured through DLS of the samples synthesized with different Zr precursors at 75 ºC foy 1h.

Precursor	**$d_{h,I}$ (nm)**	**$d_{h,n}$ (nm)**	**PdI**
$Zr(OEt)_4$	176.6 ± 3.4	153.9 ± 1.8	0.026 ± 0.005
$Zr(OiPr)_4$	241.2 ± 17.0	158.1 ± 13.6	0.155 ± 0.041
$Zr(OBut)_4$	189.2 ± 2.2	158.2 ± 1.1	0.021 ± 0.018

For completeness, we assessed the impact of temperature on the crystallinity and particle size of the nanoMOFs and conducted the reactions with the three different alkoxy precursors at RT (Figures 4-21, 4-22 and Table 4-12). Under these conditions, the 1 h reaction reached a yield of 50%, regardless of the alkoxide used (Figure 4-17g and Table 4-13). While the optical properties were comparable to those of particles synthesized at 75 °C (Figure 4-23a), a notable reduction in d_h to approximately 100 nm was observed (Figure 4-23b and Table 4-14). Most notably, the TGA thermograms closely resemble those obtained at 75°C, even in the case of using $Zr(OBut)_4$ (Figure 4-23c), which we tentatively associate with the presence of missing cluster defects. Moreover, the crystalline phase of the systems synthesized at RT was similar to that of the solids obtained at 75°C (Figure 4-17c), consistent with PCN-224 (Figure 4-23d). However, a pronounced decrease in BET surface areas was observed (Figure 4-23e-f).

Aiming to improve the reaction yield, the RT reaction was extended to 24 h. As anticipated, this adjustment led to an increase in reaction yields up to 70% (Table 4-13), without compromising the optical properties and crystalline phase of the synthesis conducted at 75 °C (Figure 4-24a-b). Despite these adjustments, there was no significant enhancement in the BET surface areas, which remained indicative of a semi-condensed phase (Figure 4-24c-d and Table 4-15), echoing the outcomes observed with the 1 h of reaction.

USC UNIVERSIDADE DE SANTIAGO DE COMPOSTELA

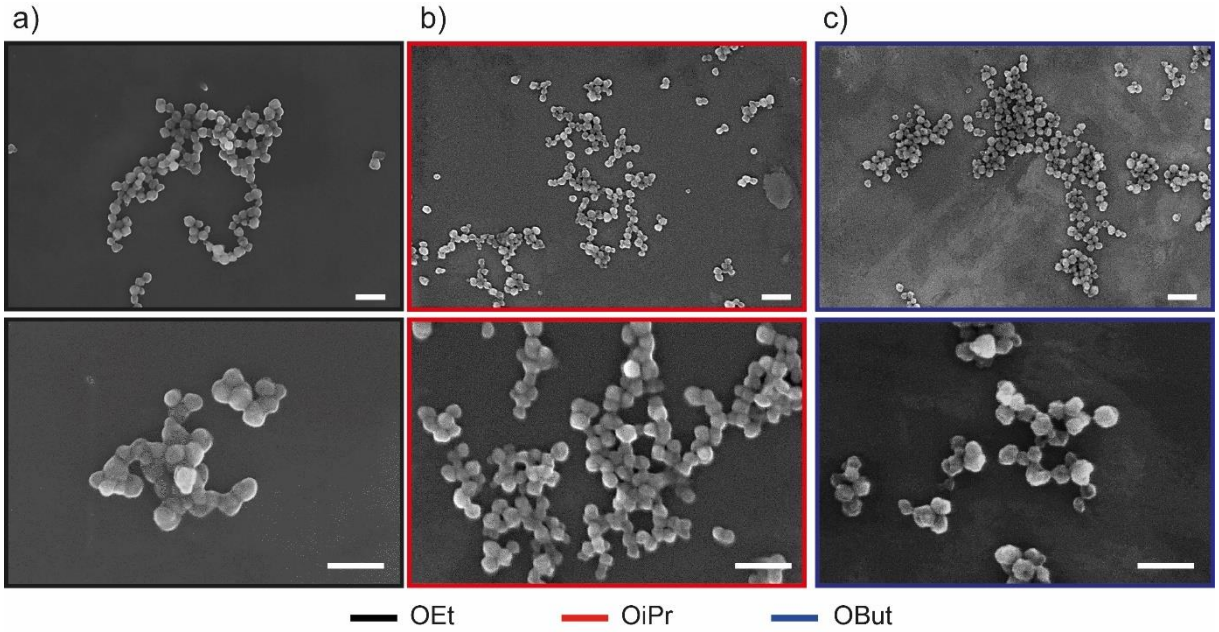

Figure 4-21. Representative SEM images for 1 h reaction performed at RT by using different Zr precursors and AA as modulator. Scale bars are 200 nm.

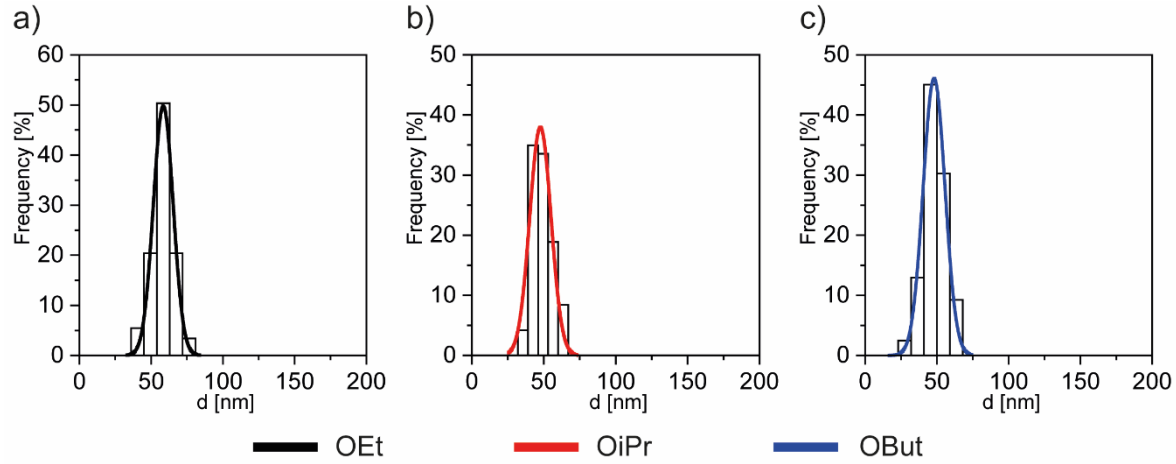

Figure 4-22. Particle size distribution histogram relative to SEM images of 1 h reaction performed at RT by using different Zr precursors and AA as modulator.

Table 4-12. Particle size distribution measured through SEM analysis of the samples synthesized with different Zr precursors.

Precursor	**Modulator**	**Time**	**Temperature**	**d_{SEM} (nm)**
$Zr(OEt)_4$	AA	1 h	25 °C	58.2 ± 7.7
$Zr(OiPr)_4$				49.1 ± 6.8
$Zr(OBut)_4$				48.2 ± 8.3

USC UNIVERSIDADE DE SANTIAGO DE COMPOSTELA

Table 4-13. Zr quantification through ICP-OES to determine the reaction yield of the reaction performed with different Zr precursors after 1h and 24h of reaction.

Precursor	Modulator	Temperature	Time	Yield%
$Zr(OEt)_4$	AA	25 °C	1 h	49.9 ± 2.5
$Zr(OiPr)_4$				43.0 ± 2.2
$Zr(OBut)_4$				55.3 ± 2.8
$Zr(OEt)_4$			24 h	68.5 ± 3.4
$Zr(OiPr)_4$				69.8 ± 3.5
$Zr(OBut)_4$				78.1 ± 3.9

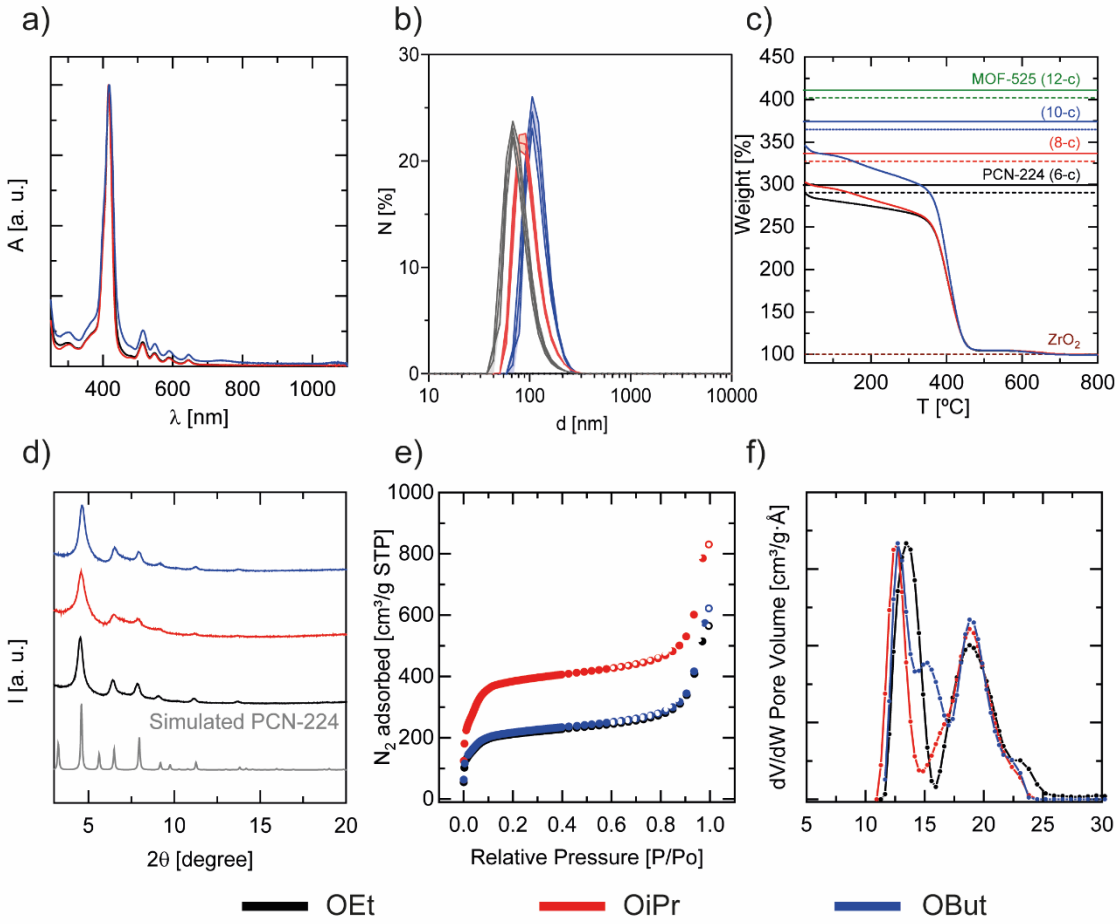

Figure 4-23. a) UV-Vis extinction spectra, b) hydrodynamic diameters (by number), c) TGA, d) PXRD patterns, e) BET analysis and f) NLDFT pore size distribution of 1 h reaction at RT by using different Zr precursors.

USC UNIVERSIDADE DE SANTIAGO DE COMPOSTELA

Table 4-14. Hydrodynamic diameter by intensity ($D_{h,I}$) and by number ($D_{h,n}$) and PdI measured through DLS of the samples synthesized with different Zr precursors for 1 h at RT.

Precursor	Time	$D_{h,I}$ (nm)	$D_{h,n}$ (nm)	PdI
$Zr(OEt)_4$	1 h	141.6 ± 1.8	79.5 ± 3.0	0.206 ± 0.003
$Zr(OiPr)_4$		156.6 ± 1.5	99.2 ± 1.8	0.102 ± 0.018
$Zr(OBut)_4$		153.5 ± 4.3	119.8 ± 39.3	0.060 ± 0.011

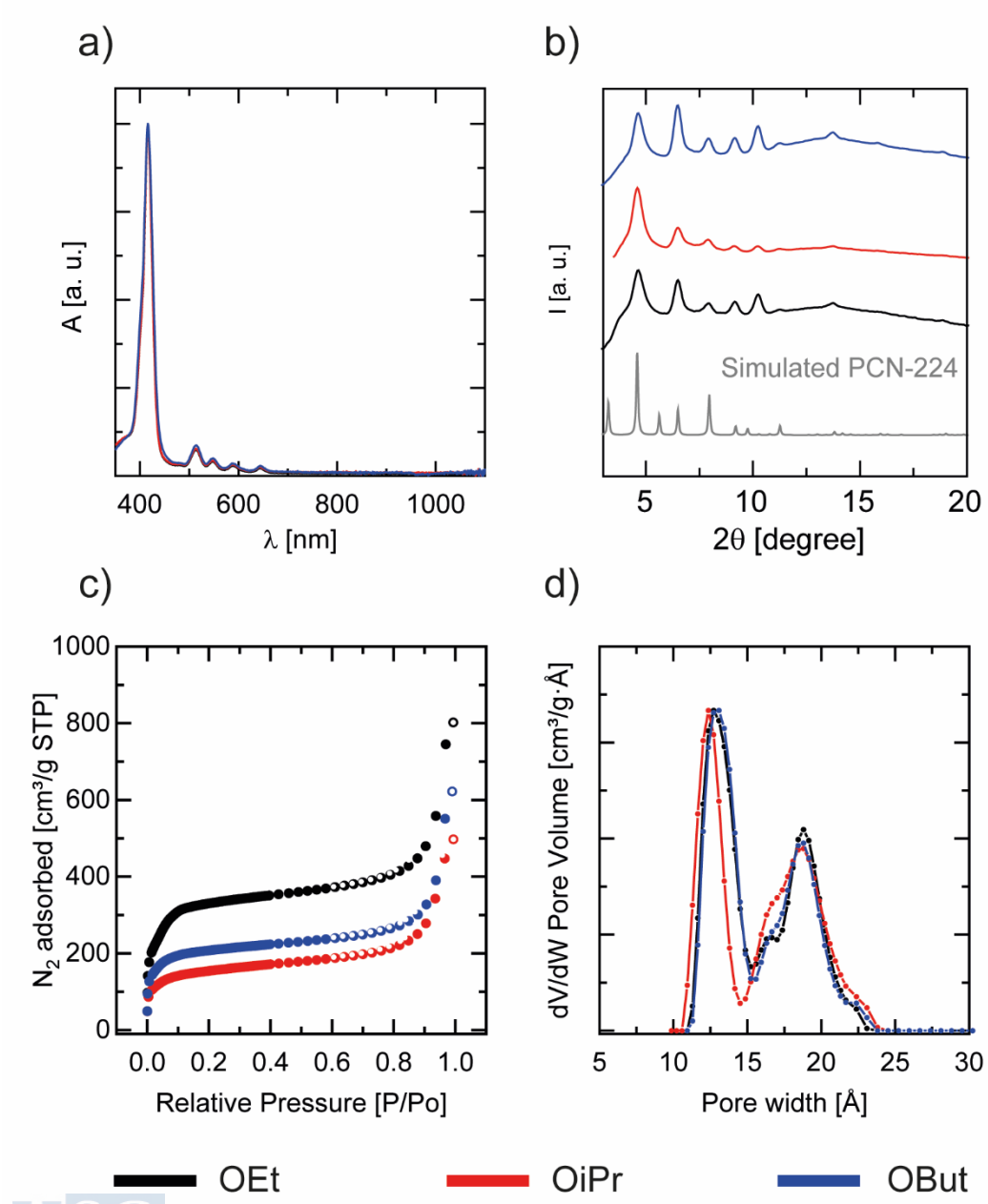

Figure 4-24. a) UV-Vis extinction spectra, b) PXRD patterns, c) BET analysis and d) NLDFT pore size distribution of 24 h reaction at RT by using different Zr precursors.

Table 4-15. BET surface area and pore volume of the particles synthesized with different Zr precursors.

Precursor	Time	BET surface area (m^2/g)	t-plot micropore volume (cm^3/g)
$Zr(OEt)_4$	1 h	816	0.218
$Zr(OiPr)_4$		1561	0.444
$Zr(OBut)_4$		833	0.206
$Zr(OEt)_4$	24 h	1347	0.363
$Zr(OiPr)_4$		580	0.132
$Zr(OBut)_4$		792	0.223

4.2.3. Varying the modulator (PCN-222)

Despite PCN-222 is sometimes found during zirconium halide synthesis of Zr-oxo MOFs, this phase was systematically absent during all our previous experiments. It has been previously reported, that subtle changes not only in reaction conditions but also in the modulator used, can lead to substantially different phase proportion in Zr-oxo MOFs.[30] To demonstrate the capability of introducing an additional phase through minor modifications in the experimental setup, we substituted the AA modulator with FA and systematically varied L/M (0.35 – 1.5) and Mod/L (100, 250 and 560) ratios, the temperature (25 - 75ºC) and the Zr precursor (OEt, O^{i}Pr or OBut).

Conducting the reaction at RT for 24 h with any of the Zr precursors at L/M=0.35, the ideal L/M ratio for PCN-222, and Mod/M = 100 did not yield a solid product. However, at 75 °C, solid particles were formed after 24 h (Figure 4-25a), with almost quantitative yields observed thereafter (Figure 4-25b and Table 4-16). The particles exhibited an elongated morphology (Figures 4-26, 4-27 and Table 4-17), suggesting a crystalline phase distinct from those observed in previous sections. Figure 4-25f presents PXRD diffractograms of Zr-porphyrinic nanocrystals synthesized with different Zr-alkoxides and shows that the three samples comprise a phase mixture of MOF-525 and PCN-222, as corroborated by Pawley's refinement (Figure 4-28), which agrees with TGA analysis showing a plateau slightly above the 8-c line (Figure 4-25e). Although this refinement does not allow for the quantification of each phase, it is clear that $Zr(OEt)_4$ predominantly favors the formation of PCN-222, evident from the intensity of its reflections (Figure 4-28a) and the predominantly elongated particle morphology (Figure 4-26a). This contrasts with $Zr(OiPr)_4$ and $Zr(OBu)_4$, where PXRD patterns indicate a greater presence of the MOF-525 phase (Figures 4-28b-c), aligning with SEM images that show more pseudospherical particles (Figures 4-26b-c) all of them with sizes around 150 nm (Table 4-18) and with BET surface areas bellow the canonical PCN-222 phase (Table 4-19). In the case of $Zr(OEt)_4$, with an increase in the L/M ratio, there was a gradual transition towards predominantly pseudospherical particles, indicating a loss of the elongated shape characteristic of PCN-222. Conversely, with a Mod/M ratio of 560 (Figure 4-29), an increase in the L/M ratio noticeably favored the formation of rod-like shaped particles. Particularly at an L/M ratio of 1.5, there was a marked shift towards the exclusive presence of elongated nanocrystals, highlighting a clear correlation between the Mod/M ratio, the L/M ratio, and the resulting particle morphology (Figure 4-30).

USC
UNIVERSIDADE DE SANTIAGO DE COMPOSTELA

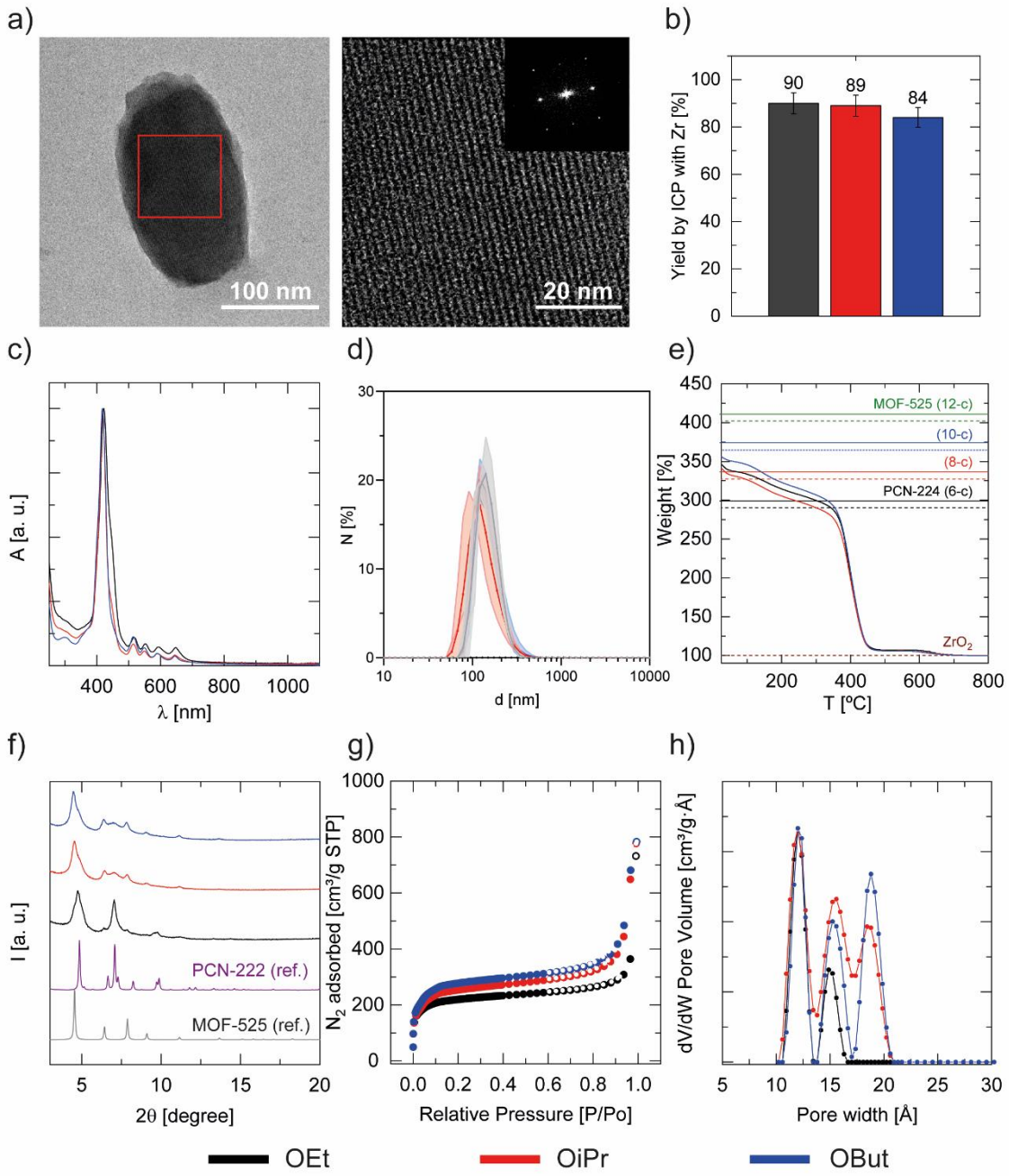

Figure 4-25. a) HRTEM images of nanoMOFs synthesized starting from $Zr(OEt)_4$, b) graphical representation of the reaction yields evaluated through ICP-OES of 1h-reaction conducted at 75 °C for 24h c) UV-Vis extinction spectra, d) hydrodynamic diameters (by number), e) TGA, f) PXRD patterns, g) N_2 adsorption isotherms at 77K and h) NLDFT pore size distribution.

Table 4-16. Zr quantification through ICP-OES to determine the reaction yield of the reaction performed with different Zr precursors.

Precursor	Modulator	Time	Temperature	Yield%
$Zr(OEt)_4$	FA	24 h	75 °C	89.7 ± 4.5
$Zr(OiPr)_4$				88.6 ± 4.4
$Zr(OBut)_4$				84.5 ± 4.2

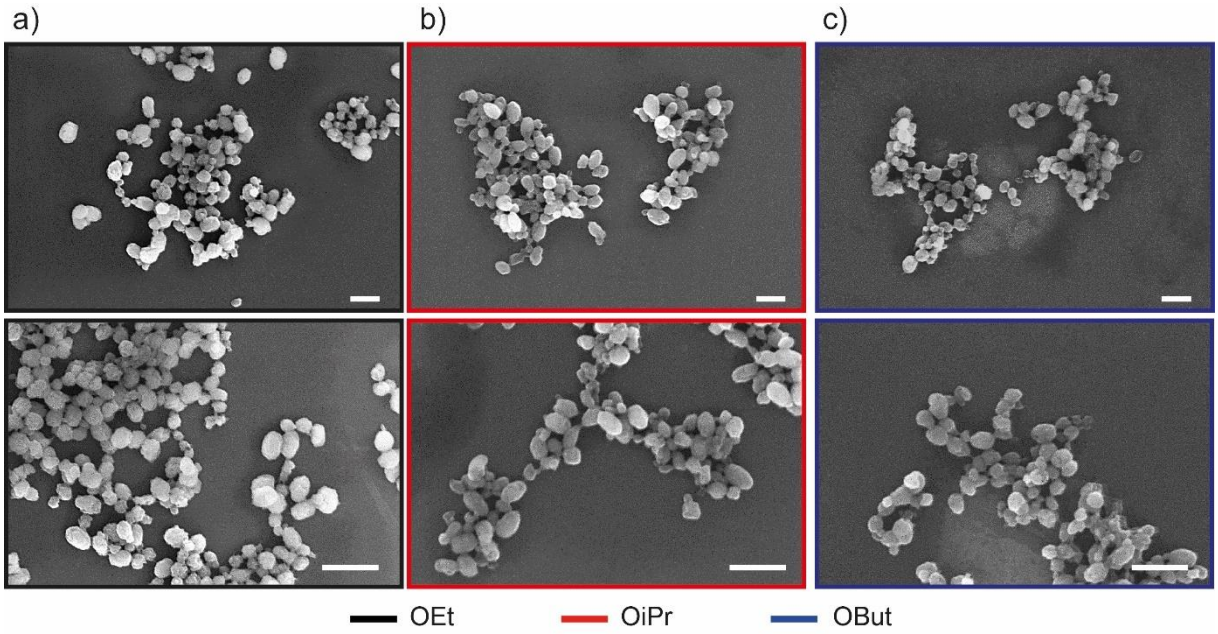

Figure 4-26. Representative SEM images for 24 h reaction performed at 75 °C by using different Zr precursors and formic acid as modulator. Scale bars are 200 nm.

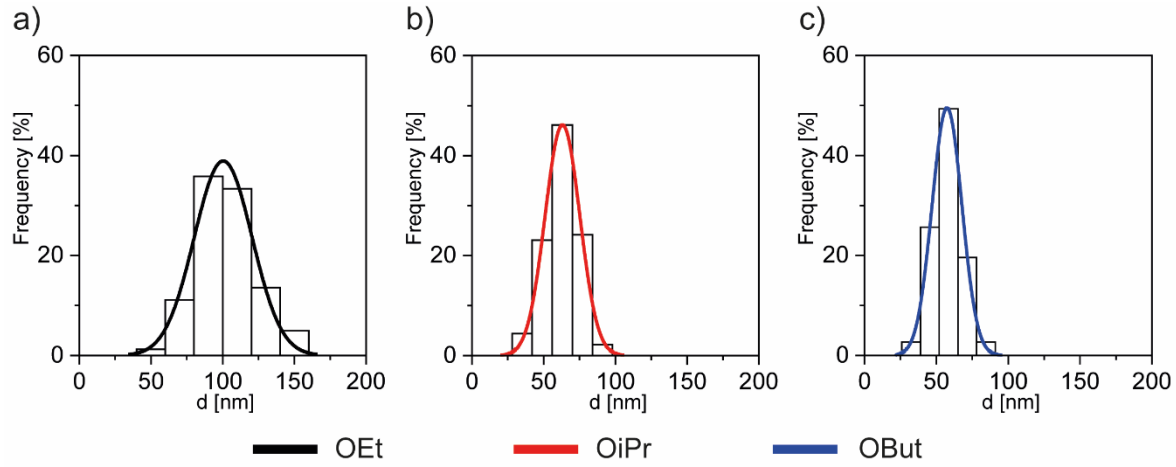

Figure 4-27. Particle size distribution histogram relative to SEM images of 24 h reaction performed at 75 °C by using different Zr precursors and formic acid as modulator.

USC UNIVERSIDADE DE SANTIAGO DE COMPOSTELA

Table 4-17. Particle size distribution measured through SEM analysis of the samples synthesized with different Zr precursors.

Precursor	Modulator	Time	Temperature	d_{SEM} (nm)
$Zr(OEt)_4$	FA	24 h	75 °C	102.8 ± 20.1
$Zr(OiPr)_4$				62.8 ± 12.1
$Zr(OBut)_4$				57.2 ± 10.0

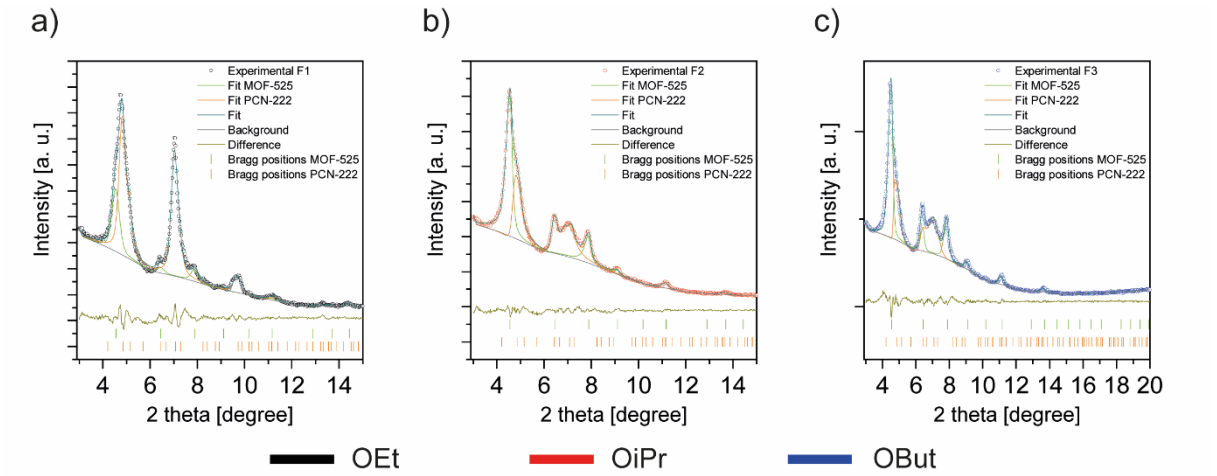

Figure 4-28. Pawley's refinement of Zr-porphyrinic MOF nanoparticles, synthesized at 75 °C, 24 h reaction, by using different Zr precursors and formic acid as modulator.

Table 4-18. Hydrodynamic diameter by intensity ($D_{h,I}$) and by number ($D_{h,n}$) and PdI measured through DLS of the samples synthesized with different Zr precursors.

Precursor	Time	$D_{h,I}$ (nm)	$D_{h,n}$ (nm)	PdI
$Zr(OEt)_4$	24 h	191.5 ± 4.4	151.7 ± 11.3	0.038 ± 0.032
$Zr(OiPr)_4$		214.2 ± 5.1	136.1 ± 19.1	0.174 ± 0.053
$Zr(OBut)_4$		215.6 ± 34.6	154.0 ± 11.9	0.135 ± 0.065

Table 4-19. BET surface area and pore volume of the particles synthesized with different Zr precursors.

Precursor	BET surface area (m^2/g)	t-plot micropore volume (cm^3/g)
$Zr(OEt)_4$	840	0.250
$Zr(OiPr)_4$	981	0.275
$Zr(OBut)_4$	1068	0.315

USC UNIVERSIDADE DE SANTIAGO DE COMPOSTELA

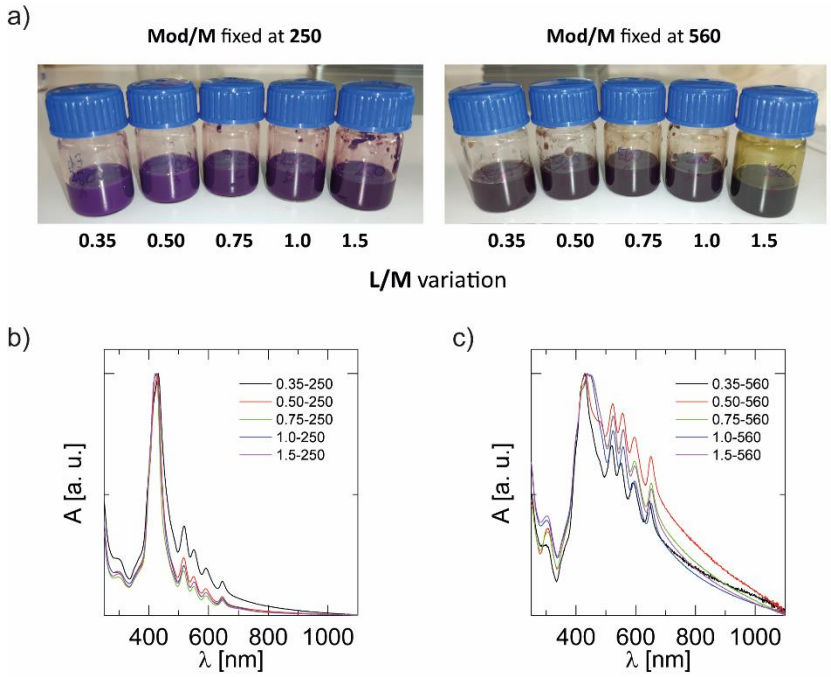

Figure 4-29. a) Digital images of 1h reaction conducted at 75 °C with FA and $Zr(OEt)_4$, by varying the L/M and Mod/M ratios. UV-Vis extinction spectra of b) Mod/M = 250 and c) Mod/M = 560.

Encouraged by the promising outcomes, a comprehensive characterization study of the system with L/M = 1.5 and Mod/M = 560 was performed, detailed in Figure 4-31. Further structural insights were obtained from PXRD analysis (Figure 4-31a), wherein the sample diffractogram was compared against simulated patterns for PCN-222. Pawley's refinement (Figure 4-32) facilitated the determination of lattice parameters as a = b = 41.905 Å and c = 17.206 Å. These measurements align closely with the established cell parameters for PCN-222, a = b = 41.968 Å and c = 17.143 Å, within the P6/mmm space group, underscoring the precision of our synthetic approach. This was further confirmed by HRTEM analysis, after applying the FFT to the selected region (indicated by a dashed line), the d-spacings corresponding to the crystalline planes were determined (Figure 4-25a). Specifically, d-spacings for the {002} family of planes were found to be 8.620 Å, and for the {300} family of planes, 11.600 Å. These measurements are indicative of the hexagonal phase of PCN-222.

TGA analysis (Figure 4-31b) indicated a coordination of approximately 8 TCPP molecules per Zr_6-oxo cluster, which agrees with the connectivity of the canonical PCN-222 phase. Moreover, the BET surface area measurement presented in Figure 4-31c, 2142 m^2/g, along with a pore size distribution featuring diameters of 1.2 nm and 3.3 nm (Table 4-4 and Figure 4-9), closely mirrors reported values for PCN-222.[312] These figures closely match the reported values for canonical PCN-222, validating the successful synthesis and characterization of the material and its compliance with the anticipated structural and physicochemical properties of PCN-222.

The SEM images (Figure 4-31d-e) consistently revealed the presence of elongated nanoparticles across the sample, with the particles displaying characteristic optical properties of nanoMOFs (Figure 4-25c) and a d_h of approximately 150 nm (Figure 4-25d and Tables 4-17, 4-18), highlighting the unique morphology achieved under these conditions.

USC
DE SANTIAGO
DE COMPOSTELA

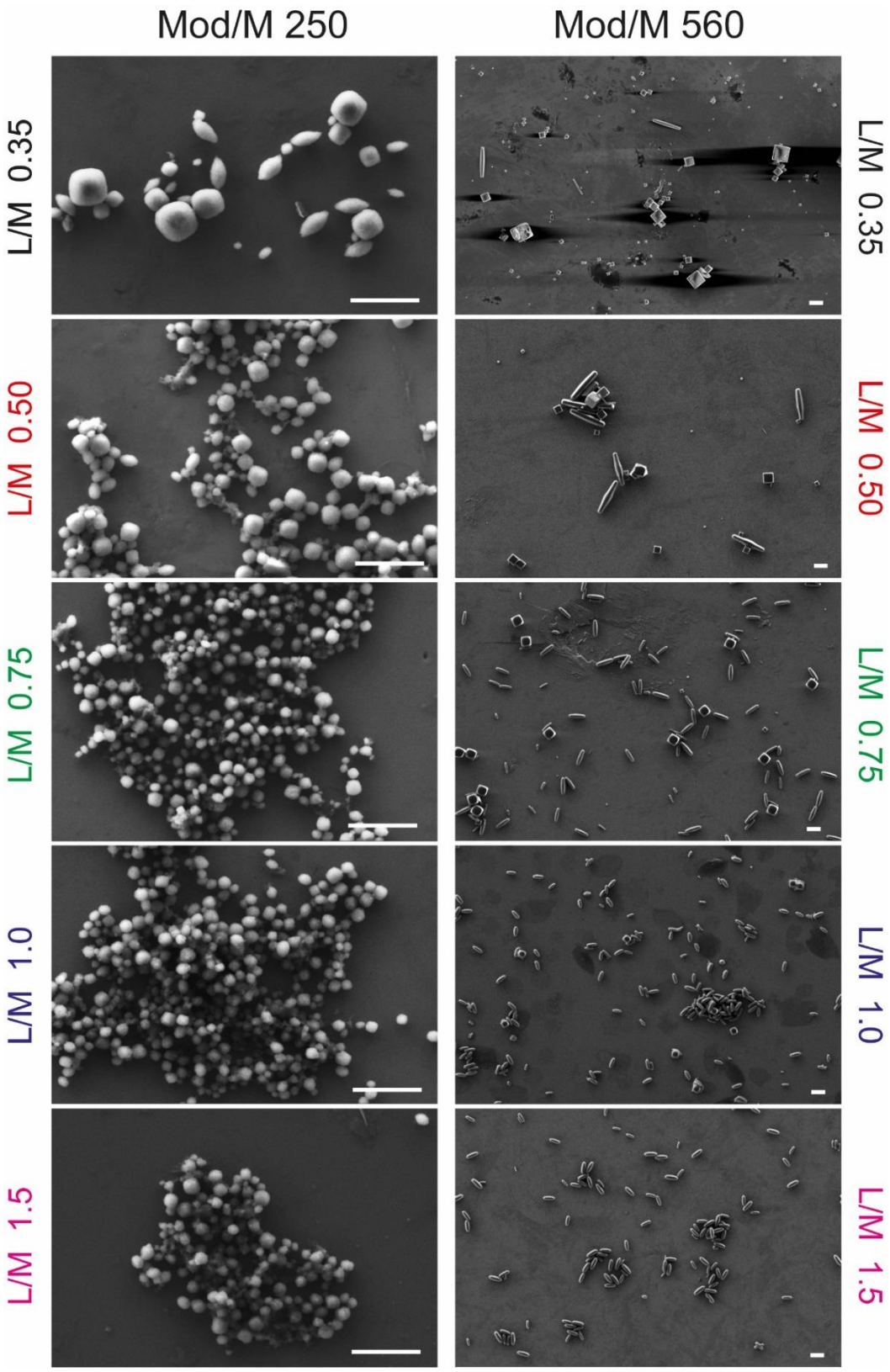

Figure 4-30. Representative SEM images of the L/M and Mod/M modulations for Zr-porphyrinic MOF nanoparticles synthesis performed at 75 °C, 1h-reaction, with the use of FA as modulator and $Zr(OEt)_4$ as precursor. Mod/M 250 scale bars: 1 µm. Mod/M 560. Scale bars are 2 µm.

USC UNIVERSIDADE DE SANTIAGO DE COMPOSTELA

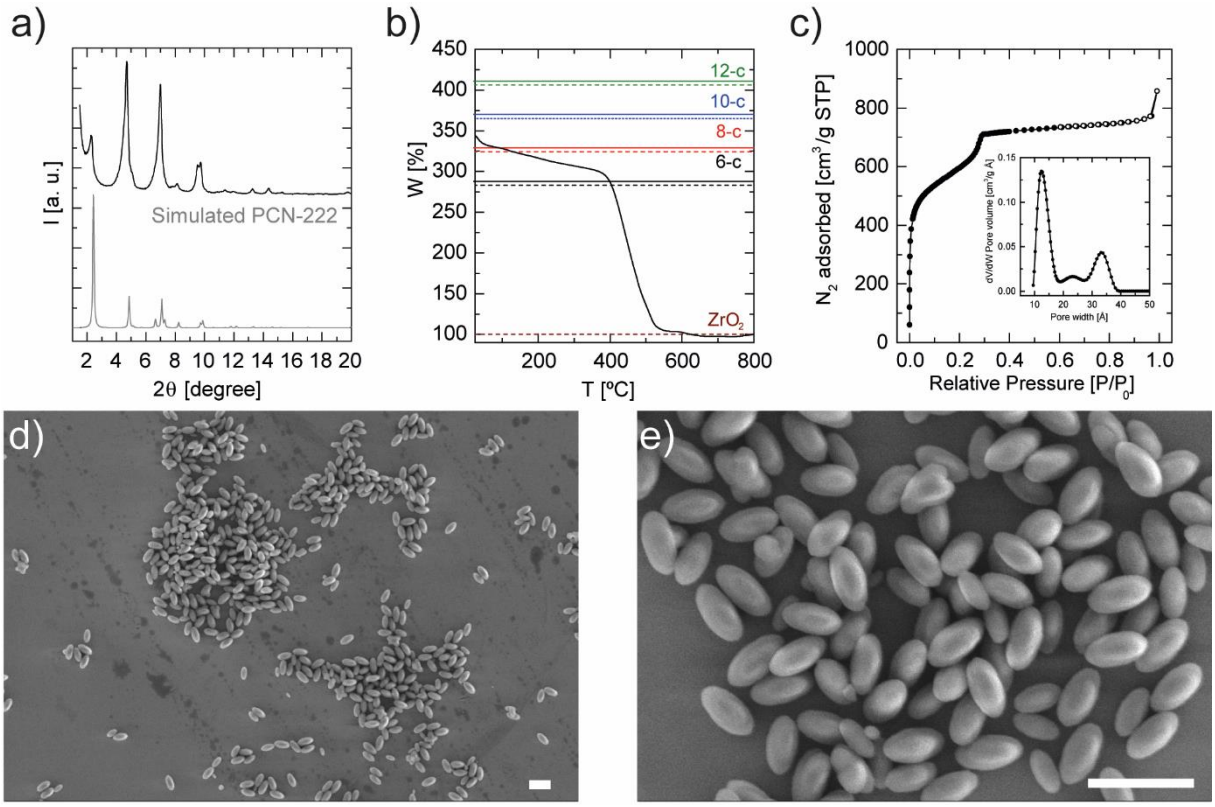

Figure 4-31. Characterization of porphyrinic MOF nanoparticles by using $Zr(OEt)_4$ as precursor and FA as modulator (L/M = 1.5 and Mod/M = 560), at 75 °C for 1 h. a) PXRD diffractogram, b) normalized TGA with theorical lines of defects for Zr_6-oxo cluster (dashed lines are the dehydrated cluster), c) N_2 adsorption isotherm at 77 K (with pore size distribution plot inserted using NLDFT model) and SEM images at d) low and e) high magnification of PCN-222 nanoMOFs. Scale bars are 1 µm.

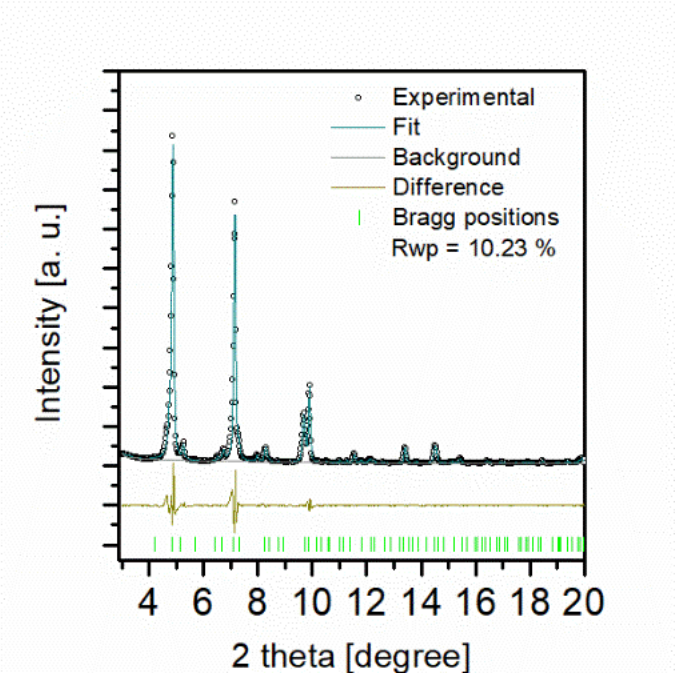

Figure 4-32. Pawley's refinement of Zr-porphyrinic MOF nanoparticles, synthesized at 75 °C, 1 h reaction, by using $Zr(OEt)_4$ as precursor and FA as modulator. The ratios adopted were L/M = 1.5 and Mod/M = 560

USC UNIVERSIDADE DE SANTIAGO DE COMPOSTELA

4.2.4. Interlaboratory reproducibility study

As previously discussed, achieving reproducibility in the synthesis of porphyrinic Zr-based MOFs has posed significant challenges.[173] To validate the reproducibility of the synthesis method, the specific conditions from each experimental section was replicated by another research group using $Zr(OEt)_4$ as the precursor. The porphyrinic Zr-MOF structure, as outlined in section 4.2.2, was confirmed through Powder X-ray Diffraction (PXRD) analysis of PCN-224, which showed no supercell peaks (Figure 4-33a), consistent with the findings in Figure 4-17c. Similarly, the structure in section 4.2.1, which used a L/M of 0.25, exhibited distinct supercell peaks of PCN-224 (Figure 4-33b) in alignment with the data shown in Figure 4-2a-b. Moreover, the PCN-222 structure from section 4.2.3 using FA/Zr ratio of 560 were analyzed and confirmed (Figure 4-33c), validating the results in Figure 4-31a. These interlaboratory findings further strengthen the reproducibility of our synthesis method using Zr-alkoxide precursors.

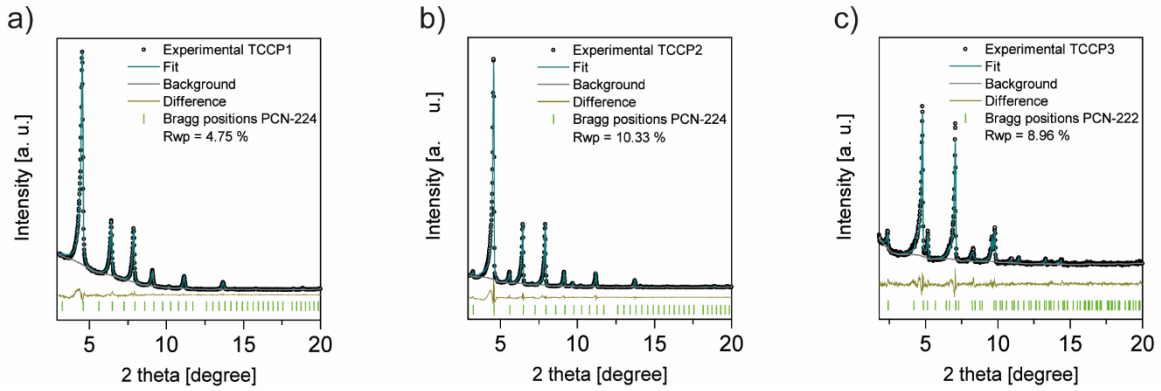

Figure 4-33. Reproducibility test for the synthesis of PCN-224 following synthetic conditions of a) Section 4.2.2 and b) 4.2.1 and for the synthesis of PCN-222 following the synthetic conditions of section 4.2.3, using $Zr(OEt)_4$ as precursor.

4.2.5. Continuous flow reaction

Batch processes have traditionally been the mainstay for producing MOFs.[313–315] These conventional methods are noted for their high costs, limited scalability, and prolonged durations, which can range from several hours to days.[316–319] Despite progress in scaling up MOF synthesis, industrial production still faces significant challenges.[320] Consequently, there is a pressing need for more efficient MOF preparation methods. Continuous processing has been recognized for significantly improving space-time yields (STY) under analogous reaction parameters.[321,322] Recent advancements in continuous synthesis include techniques such as spray-drying,[323–325] mechanochemical,[326,327] flow methods,[328–334] and microwave[321,335] and sonication-assisted methods,[336] along with the use of supercritical fluids,[334] among others.[337,338] Notably, microfluidic and millifluidic technologies offer rapid mixing, enhanced heat transfer and energy efficiency, precise control over reaction parameters, and the capability to produce various configurations of MOF composites.[330,339,340]

A few studies have explored continuous flow synthesis for Zr-MOFs, utilizing high temperatures that incur elevated operating costs.[341,342] In contrast, as demonstrated in this work, using alkoxide precursors enables the ultrafast (second scale) production of nanosized Zr-based

USC UNIVERSIDADE DE SANTIAGO DE COMPOSTELA

porphyrinic MOFs at RT. Notably, traditional precursors like $ZrCl_4$ and $ZrOCl_2$ remained unreacted after 1 h at RT, as shown in Figure 4-34.

To showcase this method's potential due to the high surfaces areas and catalytic activities of Zr-porphyrinic MOFs,[31–33,35] continuous synthesis was carried out using a homemade flow reactor with two syringes, one with $Zr(OEt)_4$ dissolved in a mixture of HOAc and DMF and the other with TCPP ligand dissolved in DMF. Both reagents were infused thought hoses with internal diameter of 1.8 mm until they mixed in a Y-shape tube with resilience time of 25 s, as detailed in Figure 4-35.

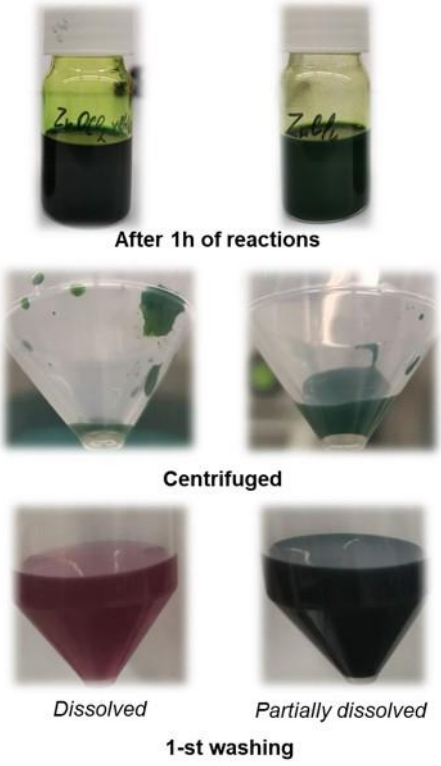

Figure 4-34. Photo of the reactions using $ZrCl_4$ and $ZrOCl_2$ as metal precursors at room temperature, 1h.

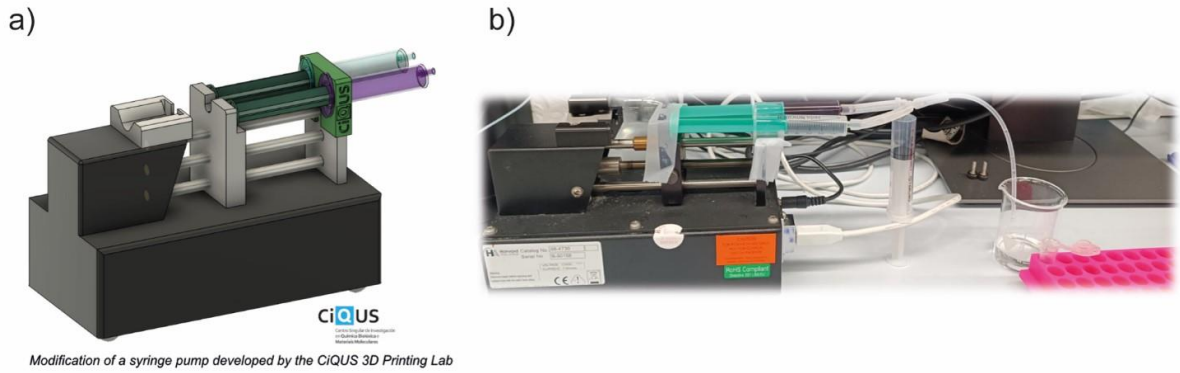

Figure 4-35. a) Pump infusion prototype and b) photo of continuous flow setup using an infusion pump with two syringes.

USC UNIVERSIDADE DE SANTIAGO DE COMPOSTELA

Satisfyingly, PXRD analysis of the resulting sample confirmed that the RT, twenty-second residence time reaction successfully produces a pure and highly crystalline phase of PCN-224, with a cell parameter a = 38.4084 Å following Pawley refinement (Figures 4-36a and Figure 4-37). SEM images showed pseudospherical nanoparticles of 100-200 nm (Figure 4-36b). These findings align with the UV-Vis spectra, which display the characteristic optical fingerprint of porphyrin MOFs, including a broad Soret band (Figure 4-36c). The d_h determined by DLS was approximately 200 nm (Figure 4-36d). TGA analysis, normalized to the inorganic residue (ZrO_2) set at 100%, is presented in Figure 4-36e, and confirms the 6-c expected for PCN-224. Notably, the microporosity of PCN-224 remained high under rapid flow synthesis, with a BET surface area of 2387 m^2/g and a pore size distribution (Figure 4-36f and inset graph) reminiscent of that of nanosized PCN-224 crystals.

This proof-of-concept experiment underscores the feasibility of synthesizing PCN-224 at RT within seconds, highlighting the process's efficiency. To evaluate the synthesis efficiency in the continuous flow regime, the STY and the surface area production rate (SAPR), based on the Zr ICP-OES yield (7.8±0.4%; 9.2 mg), were calculated. The results, 78122 $kg \cdot m^{-3} \cdot day^{-1}$ for STY and 1.9×10^{11} $m^2 \cdot m^{-3} \cdot day^{-1}$ for SAPR, demonstrate a high-quality and rate of production of PCN-224 by the continuous multifluidic method, showing substantial potential for industrial application.

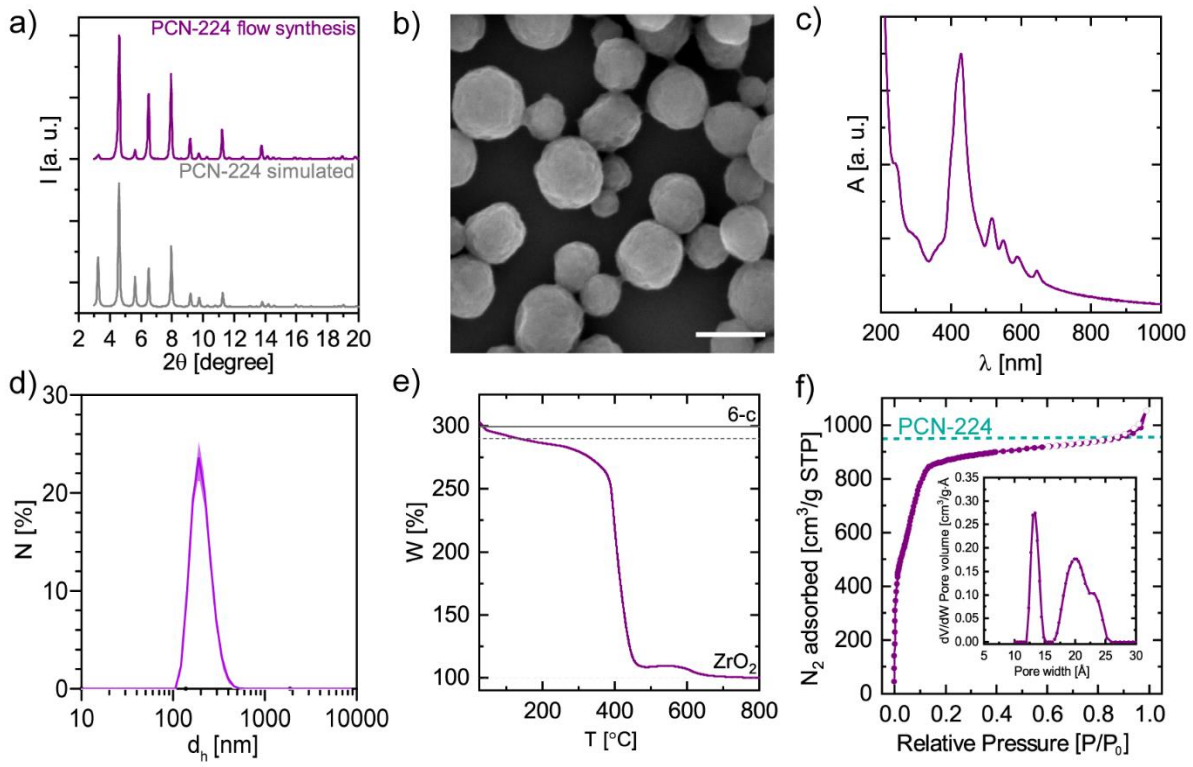

Figure 4-36. a) PXRD diffractogram with the simulated pattern of PCN-224; b) representative SEM image of PCN-224 synthesized by continuous flow synthesis; c) UV-Vis extinction spectra; d) d_h (by number); e) normalized TGA showing the theoretical lines for 6-connected Zr_6-oxo cluster (solid line hydrated and dashed line dehydrated cluster); f) N_2 adsorption isotherms at 77K correspond to the expected values for ideal PCN-224 phases calculated with Zeo++;[308], insert - pore size using NLDFT model. Scale bar is 200 nm.

USC UNIVERSIDADE DE SANTIAGO DE COMPOSTELA

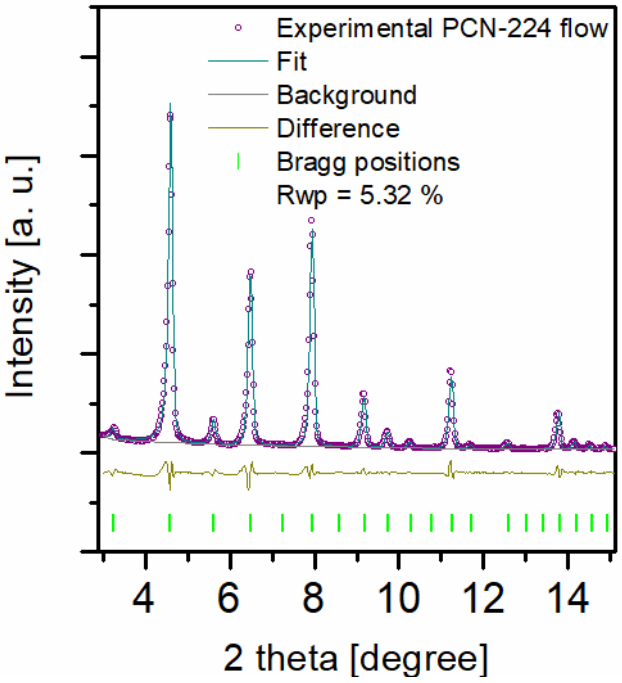

Figure 4-37. Pawley's refinement of PCN-224 synthesized by continuous flow reaction.

4.3. Summary and Conclusions of Chapter 4

In this chapter an innovative approach using Zr(IV) alkoxides was introduced, in order to facilitate the synthesis of porphyrinic MOF nanocrystals with remarkably high efficiency and speed. By utilizing Zr alkoxide precursors, it was demonstrated the capability to rapidly produce nanosized MOF-525, PCN-224, and PCN-222 within minutes, achieving high yields and controlled phase purity under mild conditions. This method significantly surpasses traditional Zr precursors, which typically require longer reaction times, higher temperatures, and yield less favourable outcomes, thereby addressing a major bottleneck in the large-scale production of MOFs.

By tuning the linker-to-metal and modulator-to-metal ratios, as well as the modulator, it is possible to have precise control over the crystal phases. This advancement is crucial for understanding the factors that facilitate the production of specific phases, which has recently been a subject of controversy.

Furthermore, the successful synthesis of nanosized PCN-224 using a continuous multifluidic method at RT represents a significant leap forward. This approach not only simplifies the MOF production process but also paves the way for the integration of MOFs into various applications, offering a scalable and economically viable option. The high surface areas and biocompatibility of these materials underscore their immense potential across a broad spectrum of technological and medical applications, promising to overcome previous limitations in MOF production. This work sets a new benchmark for the synthesis of porphyrinic MOFs and opens the door to their widespread industrial and scientific use.

USC UNIVERSIDADE DE SANTIAGO DE COMPOSTELA

USC
UNIVERSIDADE
DE SANTIAGO
DE COMPOSTELA

5. STRAIGHTFORWARD, UNIVERSAL METHOD FOR SEEDING Zr-BASED MOFS ONTO INORGANIC NANOPARTICLES

USC
UNIVERSIDADE DE SANTIAGO DE COMPOSTELA

USC
UNIVERSIDADE
DE SANTIAGO
DE COMPOSTELA

5.1. Introduction

Creating advanced nanocomposites of the core@shell type, particularly through the controlled growth of MOFs on nanoparticles (NPs), continues to present synthetic limitations. This study introduces a simple, rapid synthetic pathway using a Zr(IV) ethoxide precursor to grow UiO-type MOF nanocoatings on various gold NPs, akin to the classical seeded growth approach for epitaxial inorganic coatings.

Recent advances in the synthetic methodologies for nanocomposites combining NPs and MOFs have attracted significant attention. This interest is driven by the unique physical and chemical properties these composites exhibit, which result from the synergistic effects of integrating these materials. Such integration is made possible by the versatile chemistries of NPs and MOFs, along with the substantial internal space MOFs provide for accommodating guest molecules.[230,233] These methods generally fall into three categories: i) metallic impregnation of MOFs, followed by the introduction of a reductive agent; ii) one-pot synthesis, which involves mixing metal precursors for the core, metal ions for the MOF shell, and organic linkers to form the composites;[122,231] and iii) the core@shell method, where the inorganic NPs acts as the core with a MOF shell grown directly onto its surface.

The impregnation technique frequently leads to the formation of nanoclusters or NPs with poorly controlled sizes upon the reduction of metallic salts,[235] although it has been successful in producing well-defined nanowires in specific cases.[236] In contrast, the core@shell method stands out as particularly significant due to the homogeneous properties it imparts. This method facilitates a synergistic combination of the two nanomaterials, enhancing their inherent characteristics.

The method presented here enables precise control over MOF-shell thickness and bypasses the need for pre-synthesizing the Zr cluster, achieving near-quantitative efficiency within less than one hour at 70 °C. The resultant plasmonic nanocomposites demonstrate resilience to reshaping phenomena under mild irradiance conditions common in thermoplasmonics. This approach not only expands the possibilities for creating user-defined NP@MOF composites but also deepens our understanding of how NPs integrate with MOF-centric applications, setting the stage for groundbreaking advancements in nanotechnology.

5.2. Results and discussion

5.2.1. Nanoparticle reshaping

In the context of fabricating plasmonic core-MOF nanocomposites, the sensitivity of localized surface plasmon resonance (LSPR) in anisotropic nanocores can be harnessed to detect minimal changes in the surrounding dielectric environment, whether these changes arise from coatings or dispersion media.[343–346] This sensitivity is not only useful for confirming the formation of the MOF-type shell but also for detecting any potential reshaping or metal corrosion induced during MOF growth.

The synthetic procedures for Zr-based MOFs typically involve a limited range of components: metallic salts (typically $ZrCl_4$, $ZrOCl_2$, or $ZrO(NO_3)_2$), organic linkers (comprising bi-, tri-, tetra-, or more carboxylate molecules), and modulators (frequently acetic,

USC DE COMPOSTELA

formic, or benzoic acid). These constituents are commonly dissolved in DMF and subjected to heating at temperatures around 120 ºC for periods ranging from several hours to days. Adapting plasmonic NPs to the synthetic conditions of MOFs presents challenges, necessitating the identification of suitable capping agents capable of chemical or physical attachment, as well as the development of a robust method for transferring significant quantities of plasmonic NPs, typically synthesized in aqueous solutions, to organic solvents. polyethylene glycol (PEG) polymers were selected featuring mercapto groups (-SH) as anchoring moieties for the functionalization of anisotropic gold NPs such as AuBipy (Figure 5-1), AuNRs (Figure 5-2), and AuNSs (Figure5-3), as well as catalytic NPs such as PdNCs (Figure 5-4). Additionally, PEG polymers containing organosilane groups (-Si(OCH_2CH_3)$_3$) were utilized to functionalize Fe_3O_4 magnetic NPs (Figure 5-5). This selection was based on the amphiphilic nature of PEG, which renders it soluble in both polar and non-polar solvents.

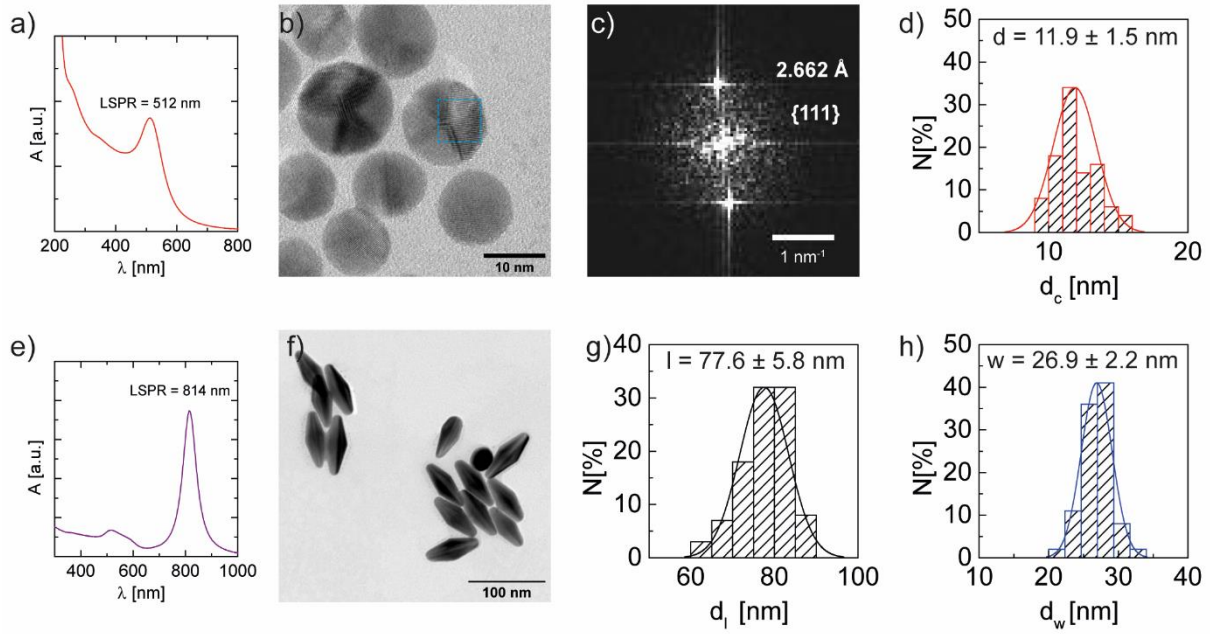

Figure 5-1. a) UV-Vis spectra, b) HR-TEM image with its c) FFT of the dashed region showing the family of planes {111} of Au and d) histogram of particle size distribution of Au pentatwinned seeds used for the synthesis of AuBipy. e) UV-Vis spectra, f) TEM image, g) histogram of length and h) histogram of width of AuBipy.

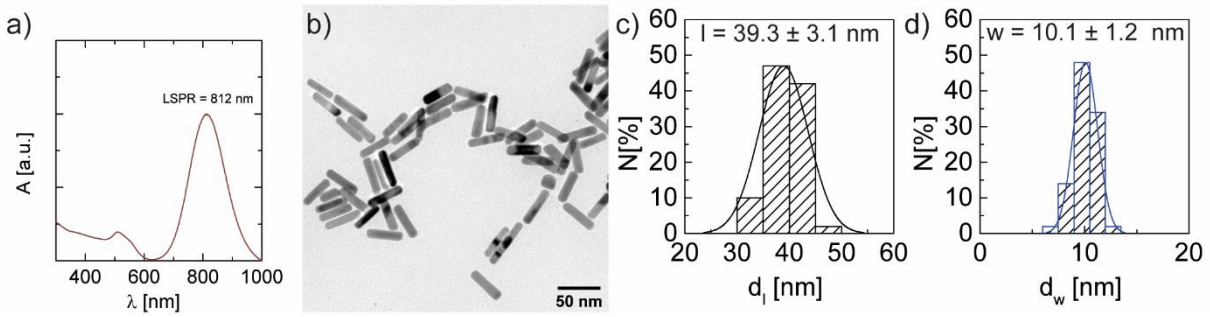

Figure 5-2. a) UV-Vis spectra, b) TEM image, c) histogram of length and d) histogram of width of AuNRs.

USC UNIVERSIDADE DE SANTIAGO DE COMPOSTELA

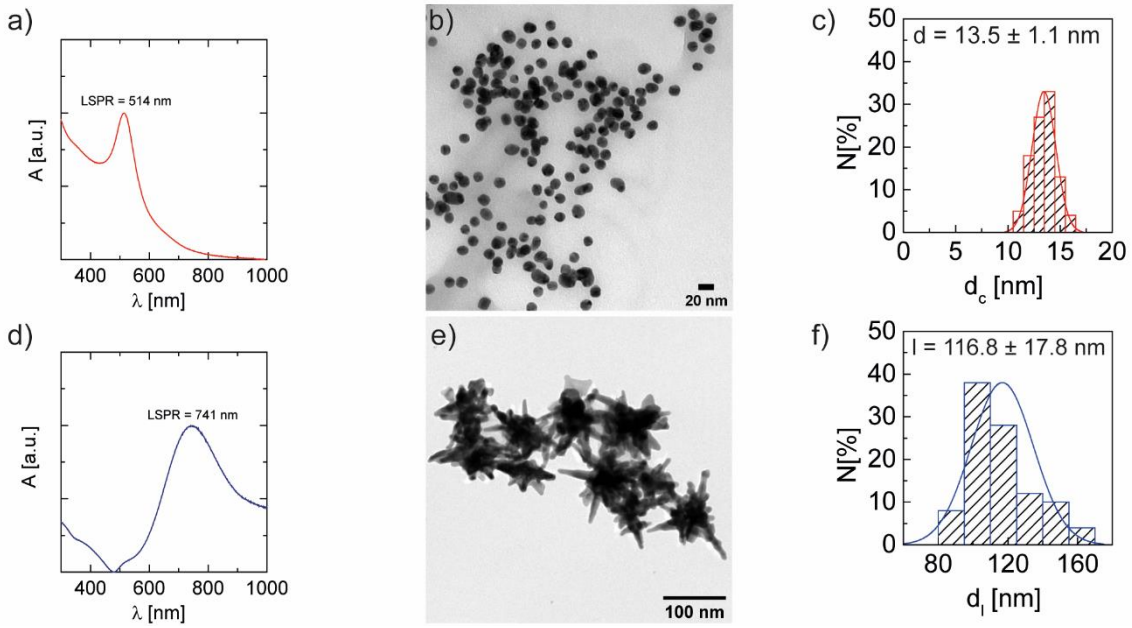

Figure 5-3. a) UV-Vis spectra, b) TEM image and c)histogram of particle size distribution of AuNPs used as seeds for the synthesis of AuNSs. d) UV-Vis spectra, e) TEM image and f) histogram of length tip to tip of AuNSs.

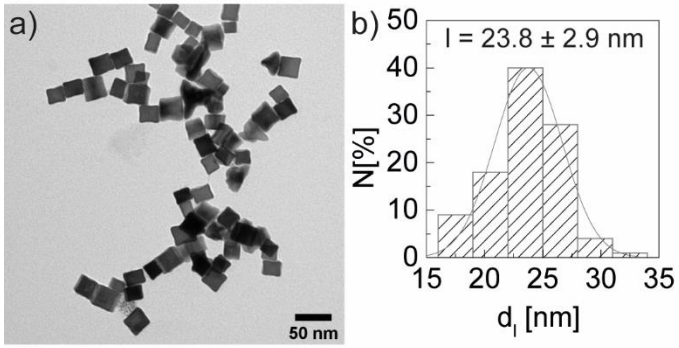

Figure 5-4. a) TEM image and b) histogram of edge length of PdNCs.

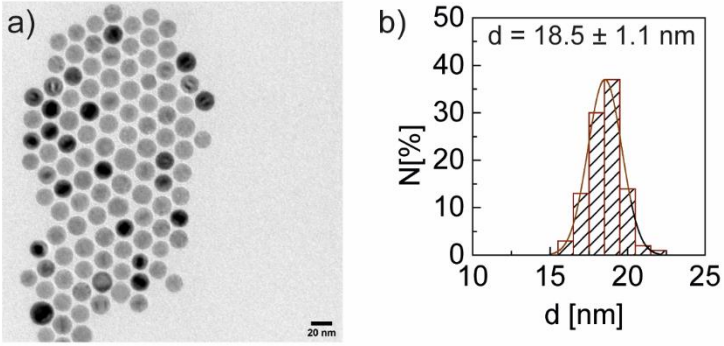

Figure 5-5. a) TEM image and b) histogram of particle diameter of Fe_3O_4 MNPs.

USC UNIVERSIDADE DE SANTIAGO DE COMPOSTELA

To gain insight into the behavior of anisotropic gold NPs under the synthetic conditions employed in Zr-based MOF synthesis, gold NPs with various morphologies were synthesized. These NPs were functionalized with HS-PEG-OMe with a molecular weight of 2 kDa and transferred to DMF, as outlined in the experimental section. Following functionalization and phase transfer, the AuBipy (Figure 5-6), additionally for AuNRs and AuNSs, as depicted in Figures 5-7 and 5-8 respectively were heated at 120 ºC (Figure 5-6a) and 90 ºC (Figure 5-6b). Their absorption spectra were monitored over 2 days. Within less than one hour, a significant blue shift was observed in the original LSPR longitudinal absorption band at 816 nm, which continued to blue shift homogeneously at both temperatures until the last recording. In addition, the influence of the solvent was evaluated by substituting DMF with water. Due to boiling point of water, PEGylated AuBipy were only heated to 90 ºC (Figure 5-6c), observing a similar blue shifting trend.

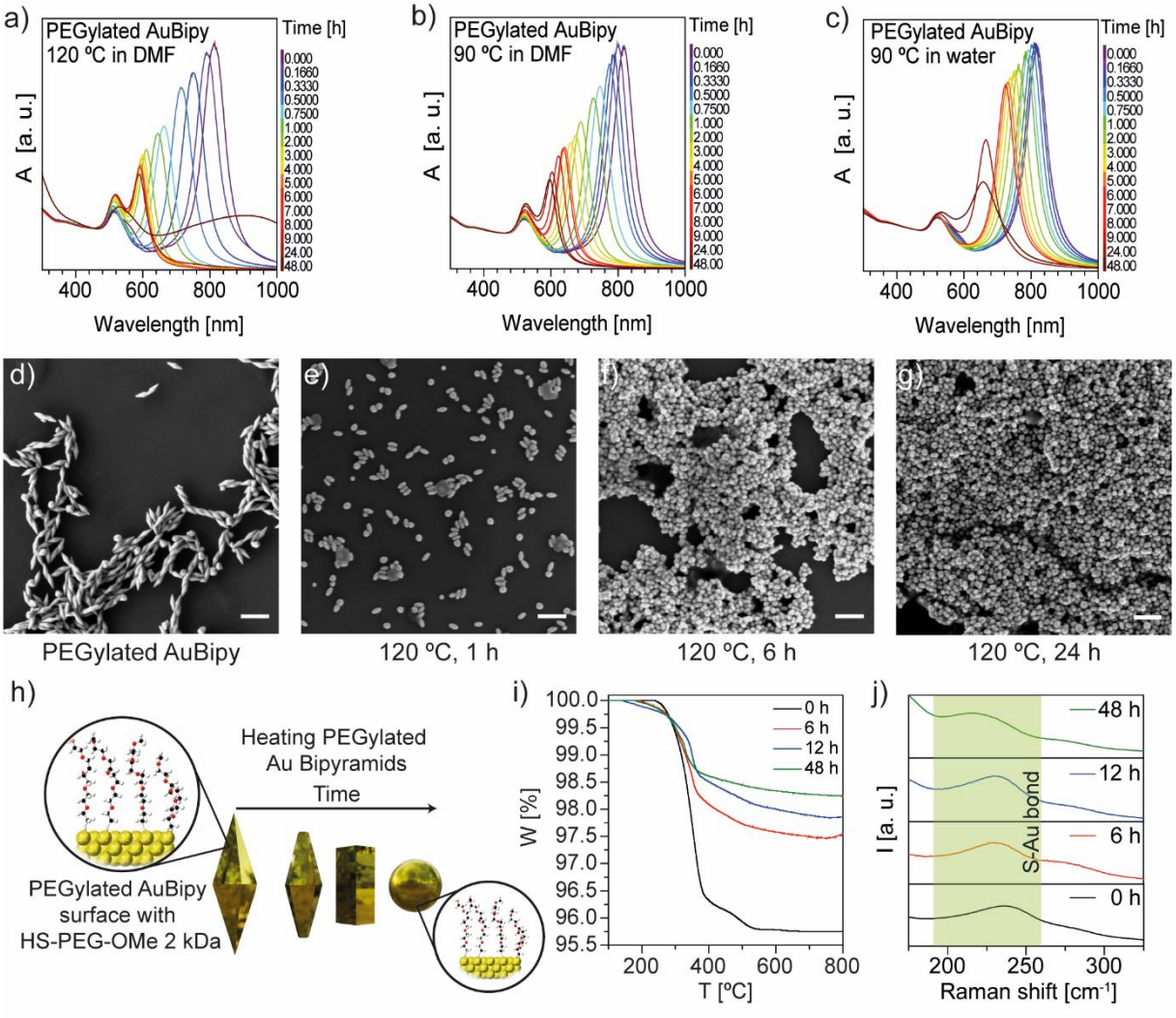

Figure 5-6. Absorption spectra of PEGylated AuBipy at heated along the time in DMF at a) 120 °C and b) 90 °C and c) in water at 90 °C. SEM images of PEGylated AuBipy heated at 120 °C for d) 0 h, e) 1 h, f) 6 h and g) 24h. h) Reshaping transformation of PEGylated AuBipy when they are heated at different temperatures and solvents, showing the presence of PEG on the surface after the reshaping corroborated by i) TGA thermogram, j) Raman spectra. Scale bars are 200 nm.

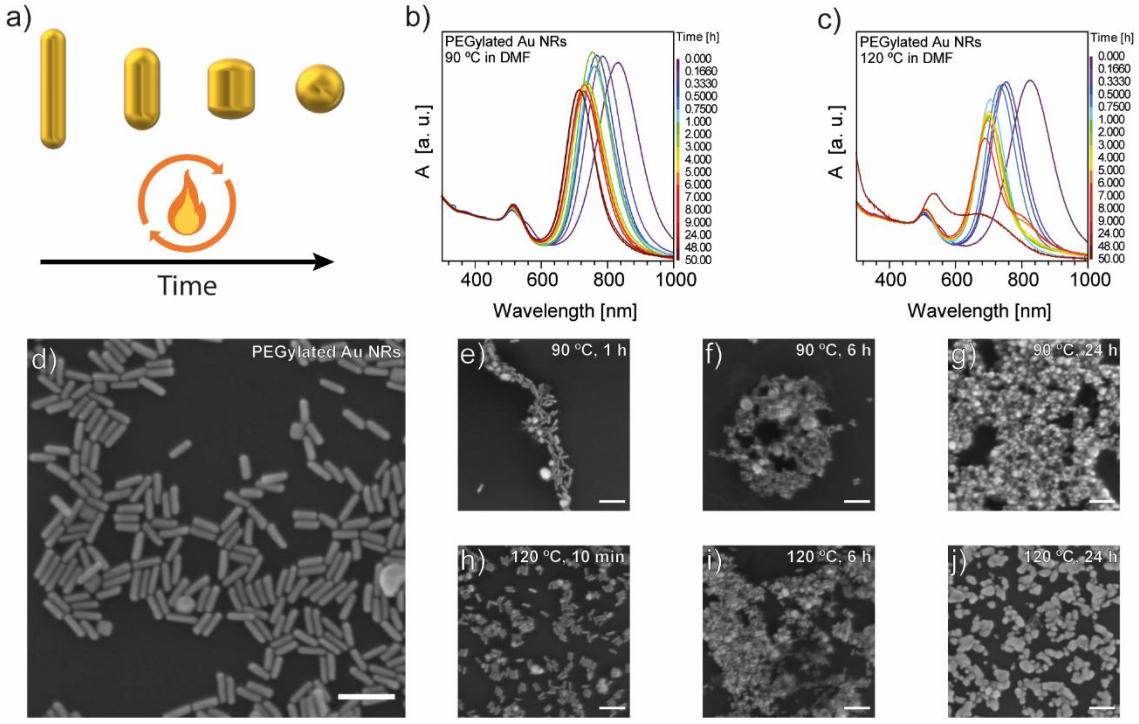

Figure 5-7. a) Schematic representation of AuNRs reshaping. UV-Vis spectra of PEGylated AuNRs in DMF heated along the time at b) 90 º C and c) 120 ºC. SEM images d) PEGylated AuNRs and heated at 90 ºC for e) 1 h, f) 6 h and g) 24 h, and heated at 120 ºC for h) 10 min, i) 6h and j) 24 h. Scale bars are 200 nm.

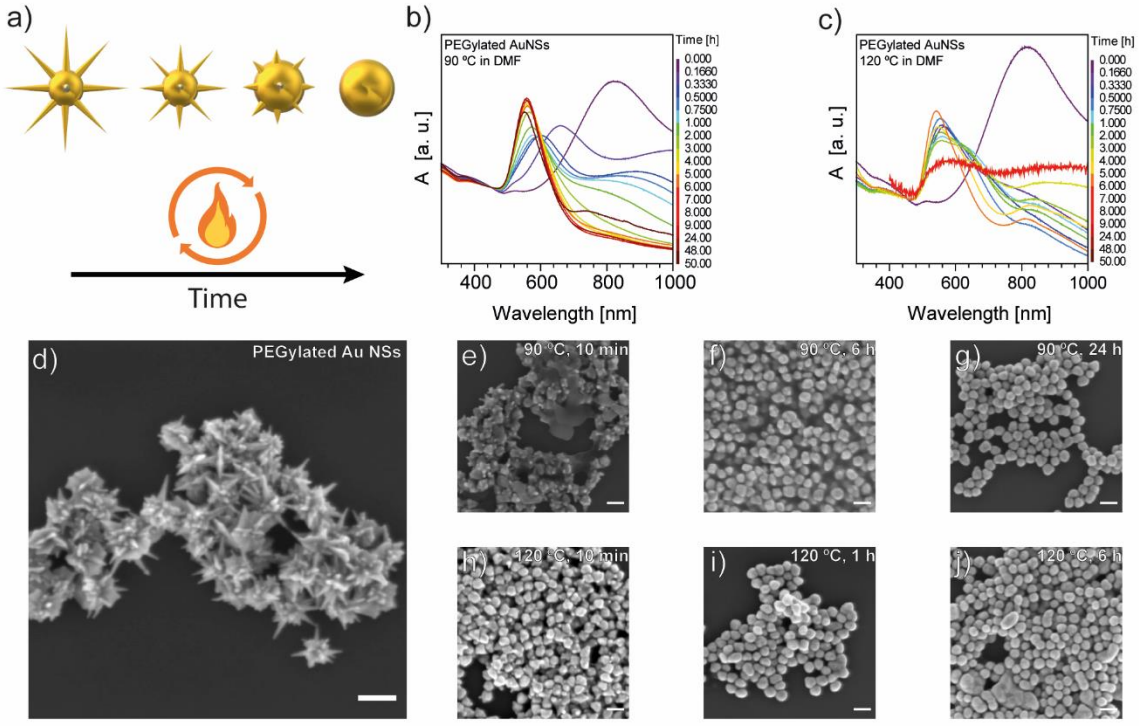

Figure 5-8. a) Schematic representation of AuNSs reshaping. UV-Vis spectra of PEGylated AuNSs in DMF heated along the time at b) 90 º C and c) 120 ºC. SEM images d) PEGylated AuNSs and heated at 90 ºC for e) 10 min, f) 6 h and g) 24 h, and heated at 120 ºC for h) 10 min, i) 1h and j) 6 h. Scale bars are 200 nm.

USC
DE SANTIAGO
DE COMPOSTELA

After 2 days at 90 ºC or 120 ºC, the original AuBipy (Figure 5-6d-g), AuNRs (Figure 5-7d-j) and AuNSs (Figure 5-8d-j) experienced a near-complete loss of their characteristic shape anisotropy (Figures 5-6h, 5-7a and 5-8a), as expected from the extreme blue shift of their longitudinal LSPRs (Figures 5-6a-c, 5-7b-c and 5-8b-c). Interestingly, however, NPs remained colloidally stable in the solution, indicating that they were likely still PEGylated. Figure 5-6i presents the TGA analysis of purified PEGylated AuBipy. Samples were subjected to heating at 120 ºC for 6, 12, and 48 h. It is evident that initially, PEGylated AuBipy contained 4.25 wt% of HS-PEG-OMe (2 kDa) on the surface. With heating, the PEG content decreased to 2.55 wt% after 6 h, 2.15 wt% after 12 h, and 1.75 wt% after 48 h. This reduction in PEG content correlates with the reshaping process observed, indicating a transition from elongated NPs to quasinanospheres after 48 h (Figure 5-6a). This suggests a decrease in surface area, leading to the detachment of HS-PEG-OMe molecules from the surface.

To confirm the presence of HS-PEG-OMe after heating at 120 ºC in DMF, Raman spectra were recorded for the PEGylated AuBipy samples heated for 6, 12, and 48 hours. The characteristic Au-S stretching vibration at 235 cm^{-1} exhibited a slight shift to 229 cm^{-1} for the samples heated for 6 and 12 h, and to 217 cm^{-1} for the sample heated for 48 h (Figure 5-6j). This shift is attributed to the movement of thiol groups, indicating radial and tangential vibrations against the metal surface.[347]

All the characterizations mentioned above and the initial conclusions regarding the reshaping process were validated through electron microscopy analysis. PEGylated AuBipy, initially measuring 77.6 nm in length and 26.9 nm in width (Figure 5-1f and Figure 5-6d), began to lose their tips, transitioning into ovoidal NPs after 1 hour at 120 ºC (Figure 1e). This reshaping process continued, yielding irregular but still elongated NPs after 6 hours (Figure 1f), culminating in nearly complete spherical formation after 24 hours of heating at 120 ºC in DMF (Figure 1g).

5.2.2. Zr(IV) ethoxide as innovative precursor for MOF synthesis under mild conditions

There is limited literature regarding core@shell nanocomposites comprised of a plasmonic NP as the core, enveloped MOF shell. However, these nanocomposites typically share common synthetic conditions, such as short reaction times,[249] mild temperatures,[247] or even RT conditions.[169,248,250]

Excluding composites with ZIF-8, the synthesis of NPs@MOF nanocomposites, particularly those based on Zr-based MOFs like the UiO-family MOFs, presents significant challenges. In this study, we present a novel and straightforward approach to synthesizing such nanocomposites without compromising the plasmonic properties of the core. This method involves utilizing Zr(IV) ethoxide as a precursor (Figure 5-9a). Alkoxides, such as Zr(IV) ethoxide, are known for their ease of hydrolysis and decomposition at low temperatures (approximately 70 ºC), compared to other Zr precursors (Figure 5-10). This characteristic accelerates the reaction kinetics and permits the reduction of reaction temperature, thereby mitigating potential damage to the plasmonic NPs.

USC UNIVERSIDADE DE SANTIAGO DE COMPOSTELA

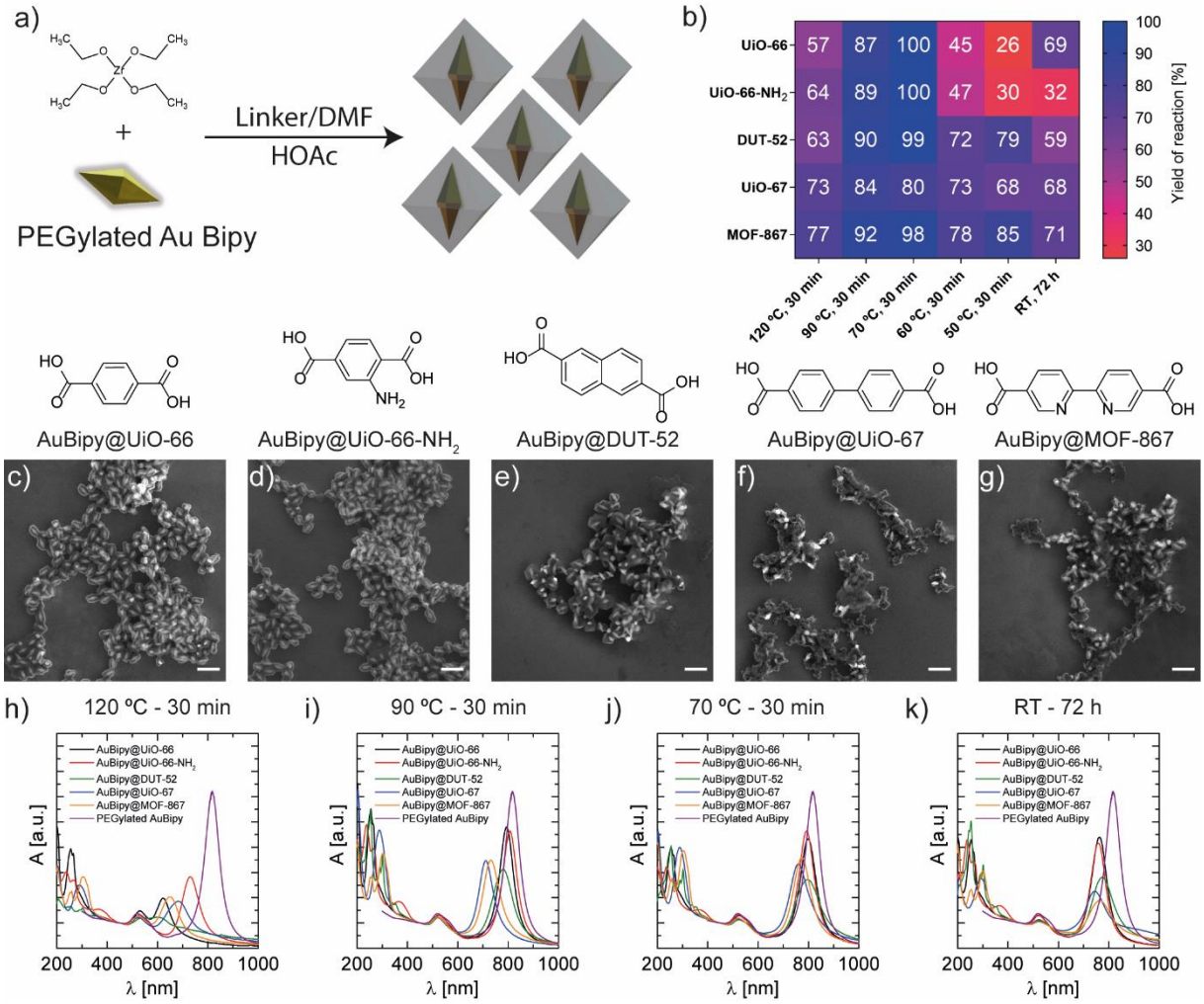

Figure 5-9. a) Synthetic approach of AuBipy@nanoMOFs using zirconium ethoxide as precursor, b) yield of reaction determined with the content of Zr by ICP-OES and SEM images for c) AuBipy@UiO-66, d)AuBipy@UiO-66-NH_2, e)AuBipy@DUT-52, f)AuBipy@UiO-67 and g)AuBipy@MOF-867 obtained at 70ºC for 30 min. Absorption spectra of Au@MOF nanocomposites with different synthetic conditions h) 120 ºC – 30 min, i) 90 ºC – 30 min, j) 70 ºC – 30 min and k) RT– 72 h. Scale bars are 200 nm.

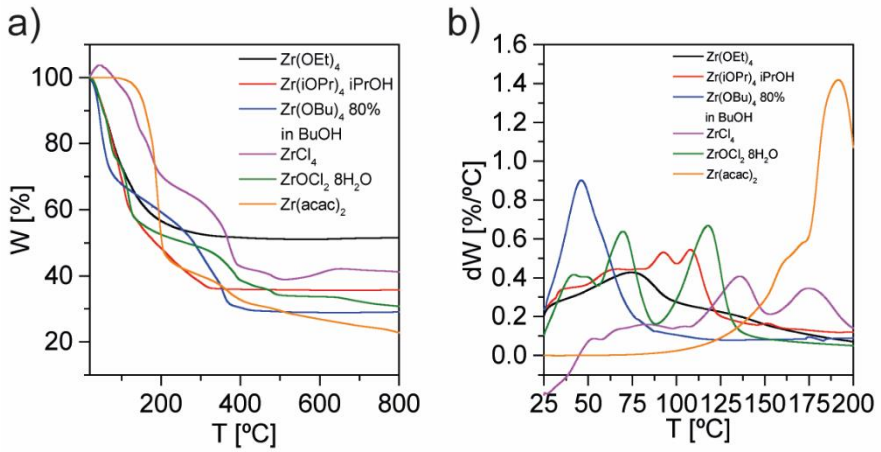

Figure 5-10. a) TGA analysis of different Zr precursors and b) derivative of TGA thermograms.

USC UNIVERSIDADE DE SANTIAGO DE COMPOSTELA

Figure 5-9b illustrates the reaction yield (considering the total Zr content after purification of the solid) of five distinct Zr-based MOFs belonging to the UiO family (UiO-66, UiO-66-NH2, DUT-52, UiO-67, and MOF-867). These MOFs (Figure 5-11) were chosen due to the ease of obtaining NPs and to investigate the influence of linker length (UiO-66 < DUT-52 < UiO-67) and the presence of pendant groups or heteroatoms moieties (UiO-66-NH_2 and MOF-867) on the linker.

The Figure 5-9b demonstrates that quantitative yields of all MOFs can be achieved at 120 ºC (standard condition for UiO family MOFs) within just 30 min, a notably rapid reaction compared to much of the literature. Additionally, it was observed that the reaction yield decreased with decreasing temperature to 90 ºC over the same time period for all studied Zr-based MOFs. Remarkably, nearly 100% yield was achieved for almost all MOFs at 70 ºC, a phenomenon attributed to Le Châtelier's principle. This principle suggests that for an exothermic reaction, heating will shift the equilibrium towards reactants due to heat acting as a product. The high yield at 70 ºC can be explained by the decomposition of Zr(IV) ethoxide (Figure 5-10). Furthermore, a decrease in reaction yield was anticipated at 50 ºC and 60 ºC for 30 min due to insufficient reaction time to complete precursor hydrolysis, but still the MOF were formed according to UV-Vis spectra (Figure 5-12). The reactions conducted at RT for 30 min did not proceed to the same extent as those conducted at 120 ºC for 30 min. However, when the reactions were carried out at RT for 3 days, the yields became comparable to those achieved at 120 ºC for 30 min (Figure 5-9b).

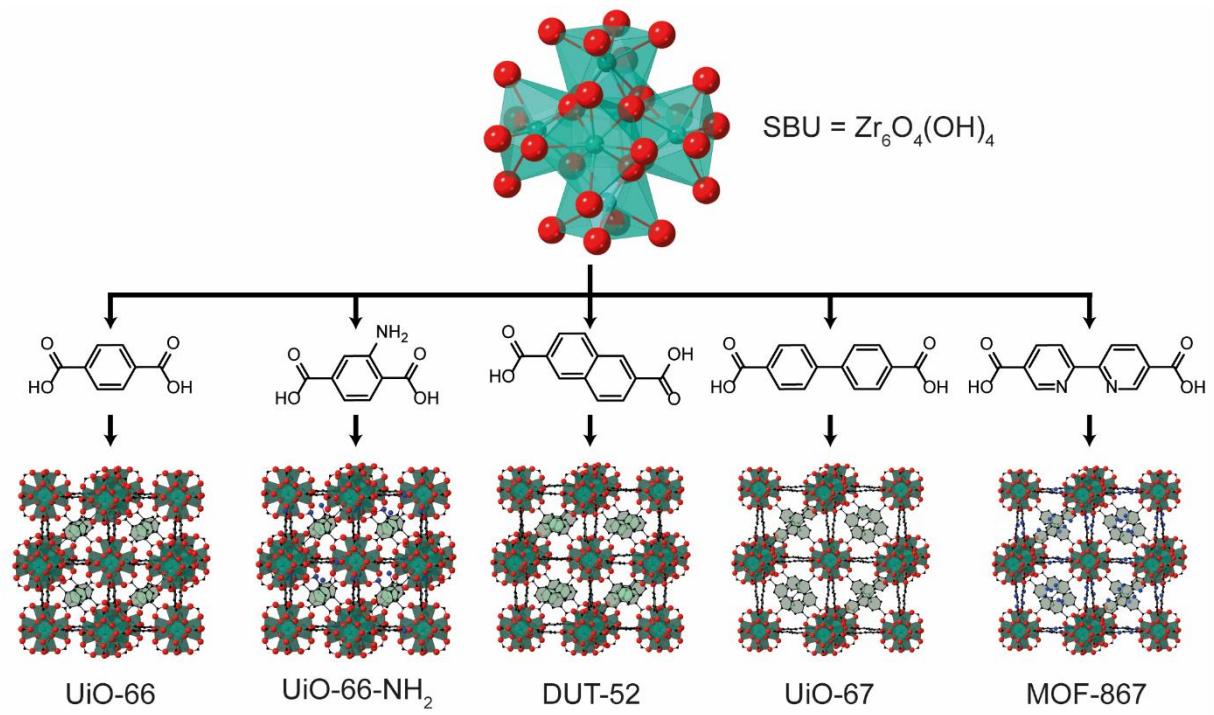

Figure 5-11. Isoreticular Zr-based MOFs structures with different bidentate carboxylic linkers and $Zr_6(\mu_3\text{-}O)_4(\mu_3\text{-}OH)_4$ as SBU.

USC UNIVERSIDADE DE SANTIAGO DE COMPOSTELA

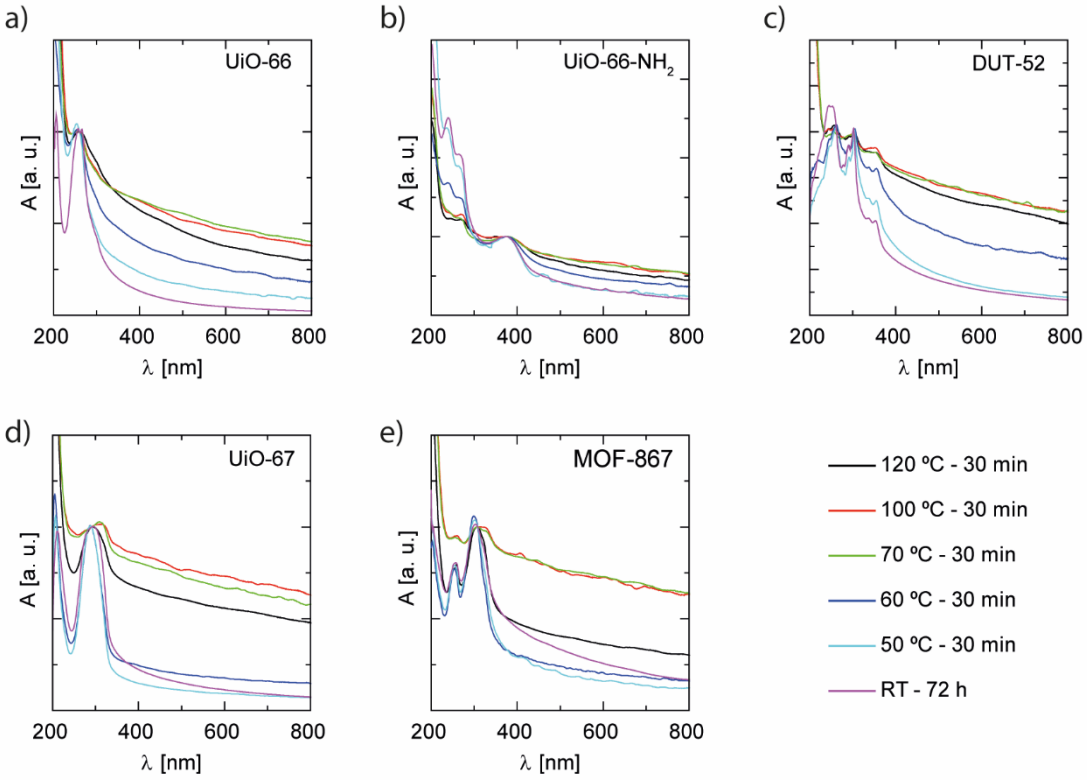

Figure 5-12. UV-Vis spectra of a) UiO-66, b) UiO-66-NH_2, c) DUT-52, d) UiO-67 and e) MOF-867 using different temperatures and times of reaction.

The specified synthetic conditions facilitated the formation of Zr-based MOFs, as confirmed by FTIR analysis (Figure 5-13), which demonstrated the absence of carbonyl bands characteristic of each linker around 1690 cm^{-1}. These conditions yielded both advantages and disadvantages. For instance, synthesis at 120°C resulted in excellent crystallinity (Figure 5-14) for the Zr-based MOFs investigated but incurred significant damage to plasmonic properties due to core reshaping (Figure 5-9h).

Lowering the temperature to 90 °C or 70 °C noticeably affected the crystallinity of the Zr-based MOFs (Figure 5-14b-c). Surprisingly, synthesis at RT was expected to yield poor crystallinity. However, after three days, this condition exhibited the best crystallinity among all the studied synthetic conditions (Figure 5-14d and Figure 5-15) and with very well defined octahedral morphology (Figure 5-16) with the exception of MOF-867 which presented some elongated particles, which belongs to the organic linker which has very poor solubility in DMF, and for removing it was necessary to wash it three times with dimethylsulfoxide (DMSO) at 50 ºC.

The previous observation was supported by Pawley's refinement analysis (Figure 5-17 and Table 5-1), indicating the successful synthesis of the five isoreticular Zr-based MOFs.

USC UNIVERSIDADE DE SANTIAGO DE COMPOSTELA

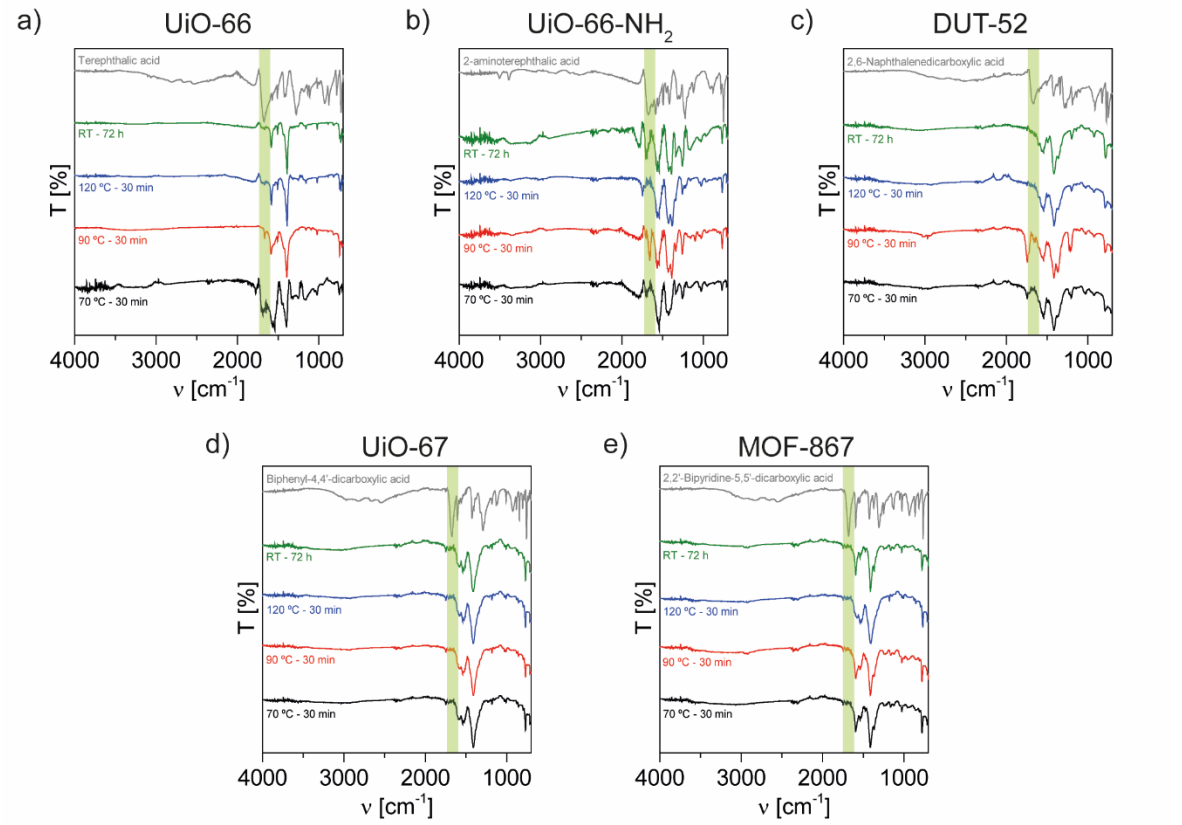

Figure 5-13. FT-IR spectra or a) UiO-66, b) UiO-66-NH_2, c) DUT-52, d) UiO-67 and e) MOF.867 with different synthetic conditions. Gray line corresponds to each MOF linker.

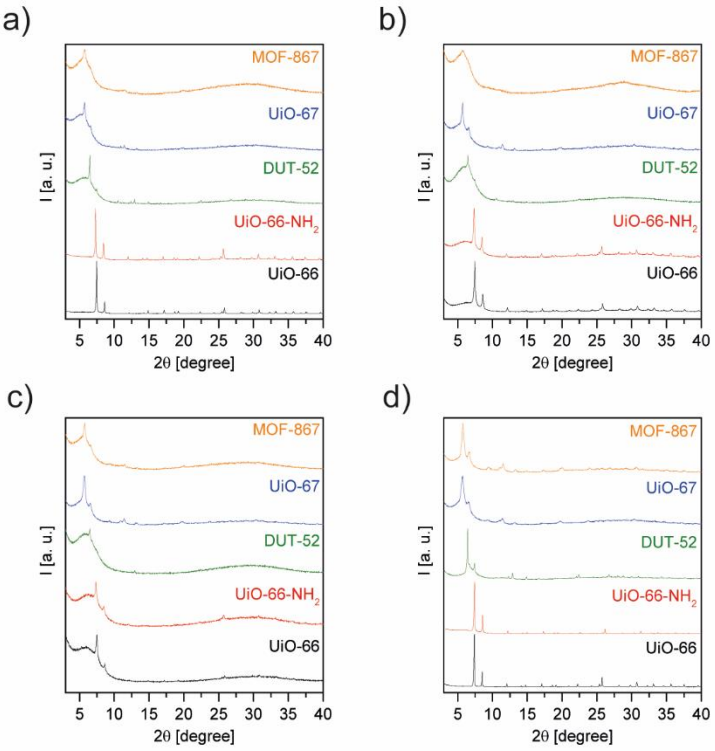

Figure 5-14. PXRD patterns of the isoreticular Zr-based MOFs synthesized with $Zr(OEt)_4$ at a) 120 ºC, b) 90 ºC, c) 70 ºC for 30 min and d) RT for 72 h.

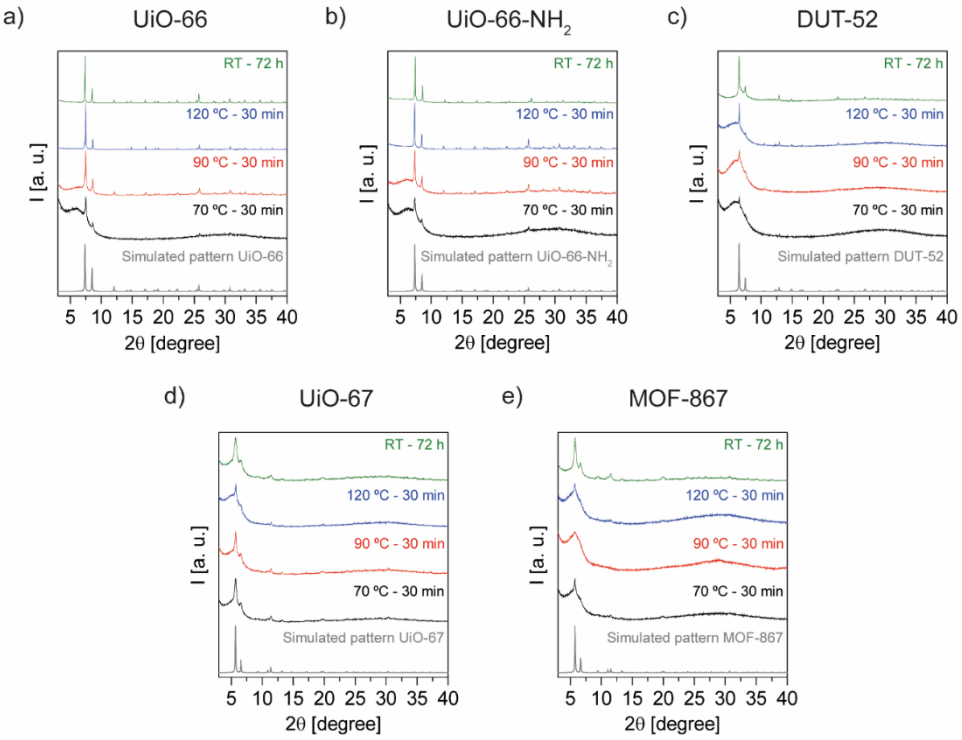

Figure 5-15. PXRD patterns of a) UiO-66, b) UiO-66-NH_2, c) DUT-52, d) UiO-67 and e) MOF.867 with different synthetic conditions.

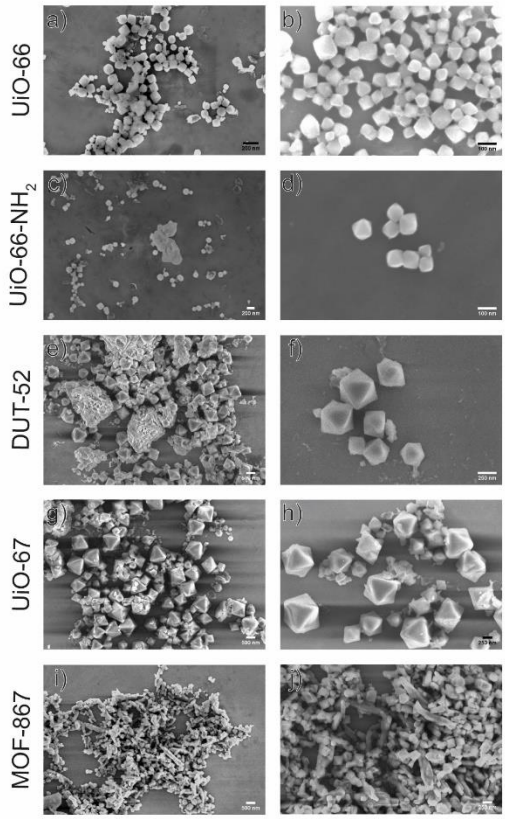

Figure 5-16. SEM images of a, b) UiO-66, c, d) UiO-66-NH_2, e, f) DUT-52, g, h) UiO-67 and i, j) MOF-867 synthesized at RT for 72h. Scale bars are 500 nm left and 200 right side.

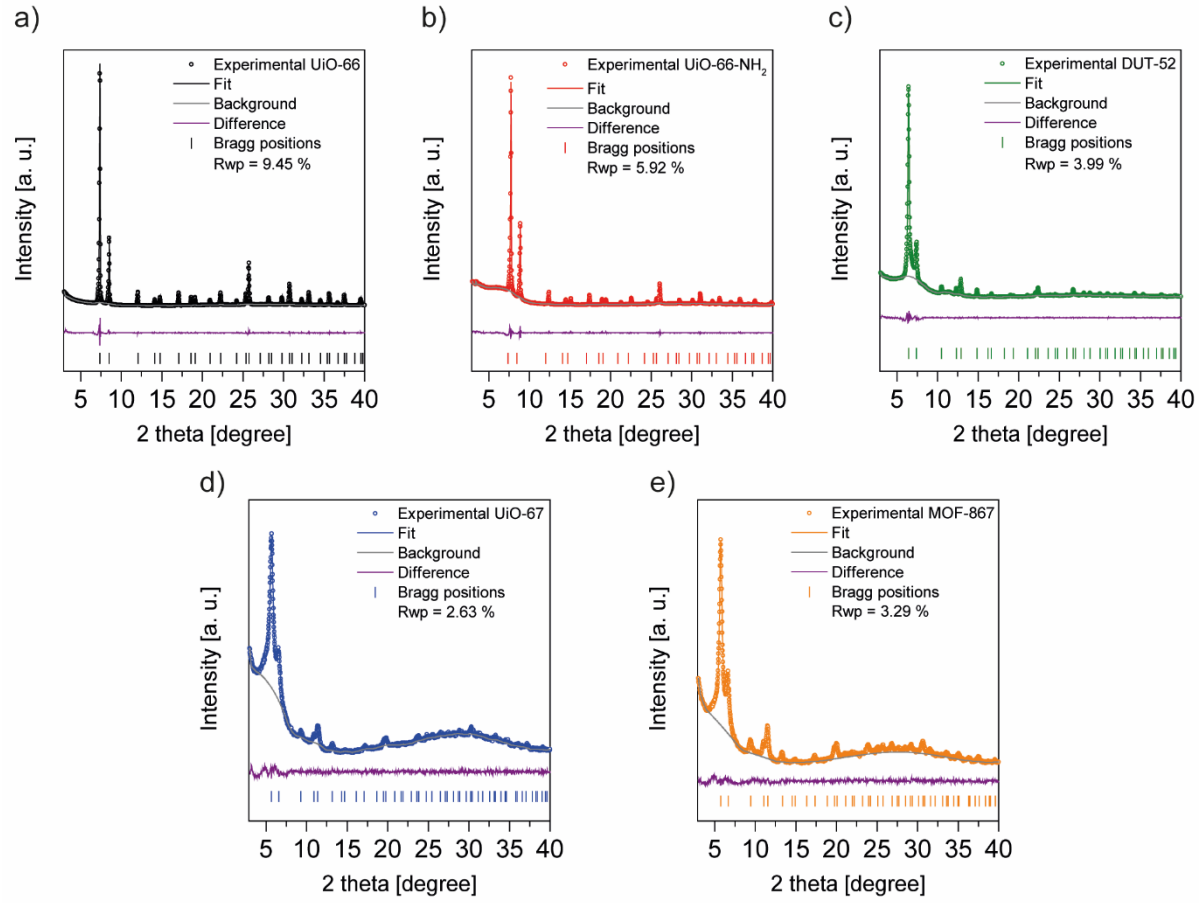

Figure 5-17. Pawley's refinement for a) UiO-66, b) UiO-66-NH_2, c) DUT-52, d) UiO-67 and e) MOF.867 synthesized at RT for 72 h.

Table 5-1. Cell parameters obtained by Pawley's refinement.

MOF	Connectivity	Spatial group	Reported cell parameter (Å)	Refined cell parameter (Å)	R_p (%)	R_{exp} (%)	R_{wp} (%)
UiO-66	12-c	$Fm\bar{3}m$ (225)	20.7465[28]	20.7132	6.03	1.61	9.45
UiO-66-NH_2			20.7988[348]	20.8868	4.39	0.77	5.92
DUT-52			23.7853[27]	23.7776	3.07	0.99	3.99
UiO-67			26.8960[349]	26.6819	2.03	2.62	2.63
MOF-867			26.5200[350]	26.5695	2.48	1.59	3.29

USC UNIVERSIDADE DE SANTIAGO DE COMPOSTELA

The observed poor crystallinity in these samples can be attributed to the presence of missing linker defects, which are often evident in the PXRD patterns (Figures 5-14 and 5-15) as a broad peak at low angles.[138] This observation is further supported by normalized TGA thermograms (Figure 5-18), where it is evident that the RT condition for 3 days produced the fewest missing linker defects across all cases, with UiO-66 and UiO-67 MOFs nearly achieving complete 12-connectivity. Across all Zr-based MOFs studied, a trend in missing linker defects was observed, with RT < 120°C < 90°C < 70°C, which impacts their adsorption properties. Notably, the RT condition for 3 days resulted in the highest Brunauer-Emmett-Teller (BET) surface area calculated with BETSI analysis[311] for each Zr-based MOF (Table 5-2 and Figure 5-19). Pore size distribution analysis using the non-local density functional theory (NLDFT) model with cylindrical pores (Figure 5-20) revealed that the condition of 70°C for 3 days exhibited high disorder in the pores, with multiple pores ranging from 10 to 30 Å. Conversely, at RT for 3 days, the pores were ordered according to the corresponding pore size for each MOF. In the case of UiO-66 and UiO-66-NH_2, a larger pore of 16 Å was observed, likely due to the presence of reo-domains known to possess such pore size.[60]

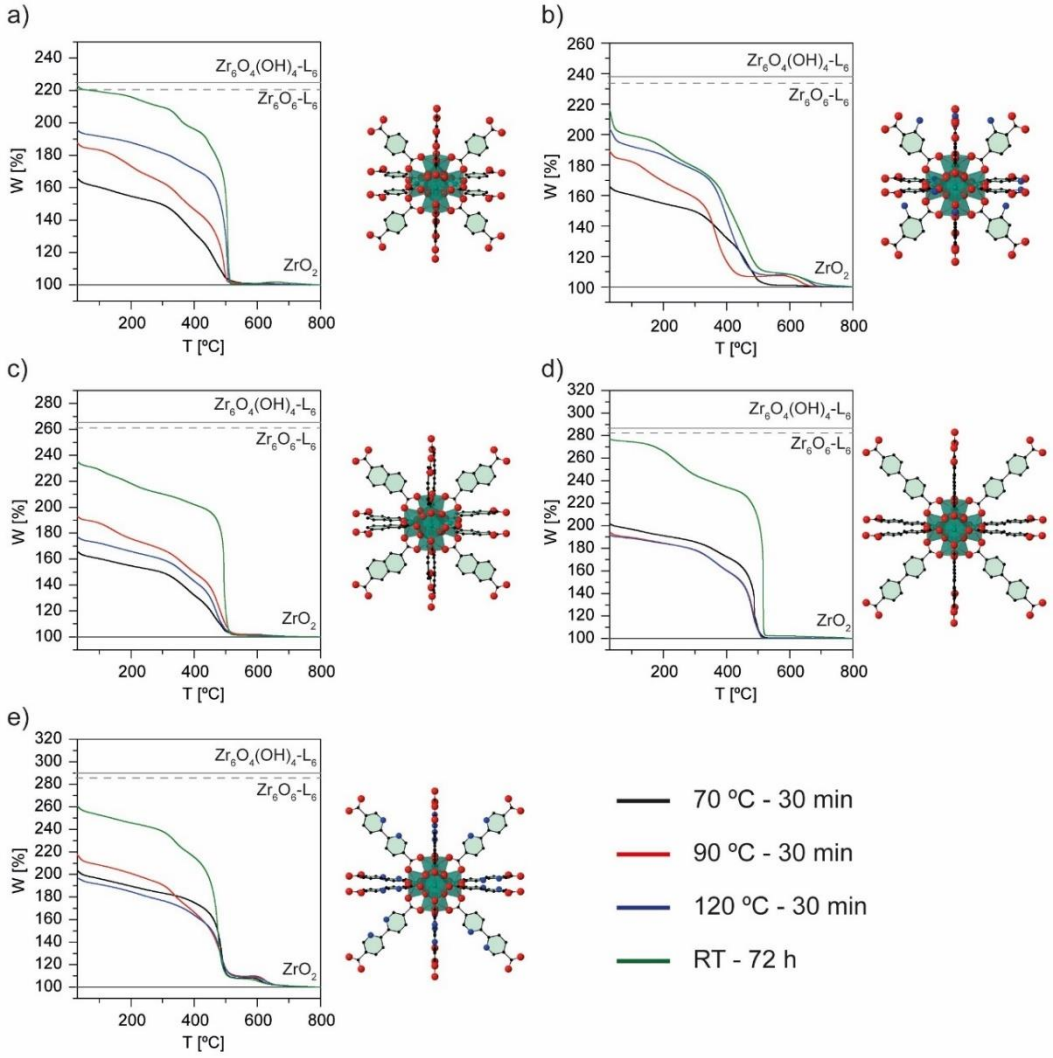

Figure 5-18. Normalized TGA thermograms of a) UiO-66, b) UiO-66-NH_2, c) DUT-52, d) UiO-67 and e) MOF.867 at different synthetic conditions, showing the theorical weight of the fully coordinated Zr_6-oxo cluster (solid line) and the dehydrated Zr_6-oxo cluster (dashed line).

Table 5-2. BET surface areas calculated with BETSI analysis of isoreticular Zr-based MOF synthesized with $Zr(OEt)_4$ at different synthetic conditions

	Synthetic conditions			
MOF	**70 ºC – 30 min (m^2/g)**	**90 ºC – 30 min (m^2/g)**	**120 ºC – 30 min (m^2/g)**	**RT – 72 h (m^2/g)**
UiO-66	415	571	871	1249
UiO-66-NH_2	454	442	708	993
DUT-52	488	386	427	1216
UiO-67	680	613	542	1243
MOF-867	501	306	431	1001

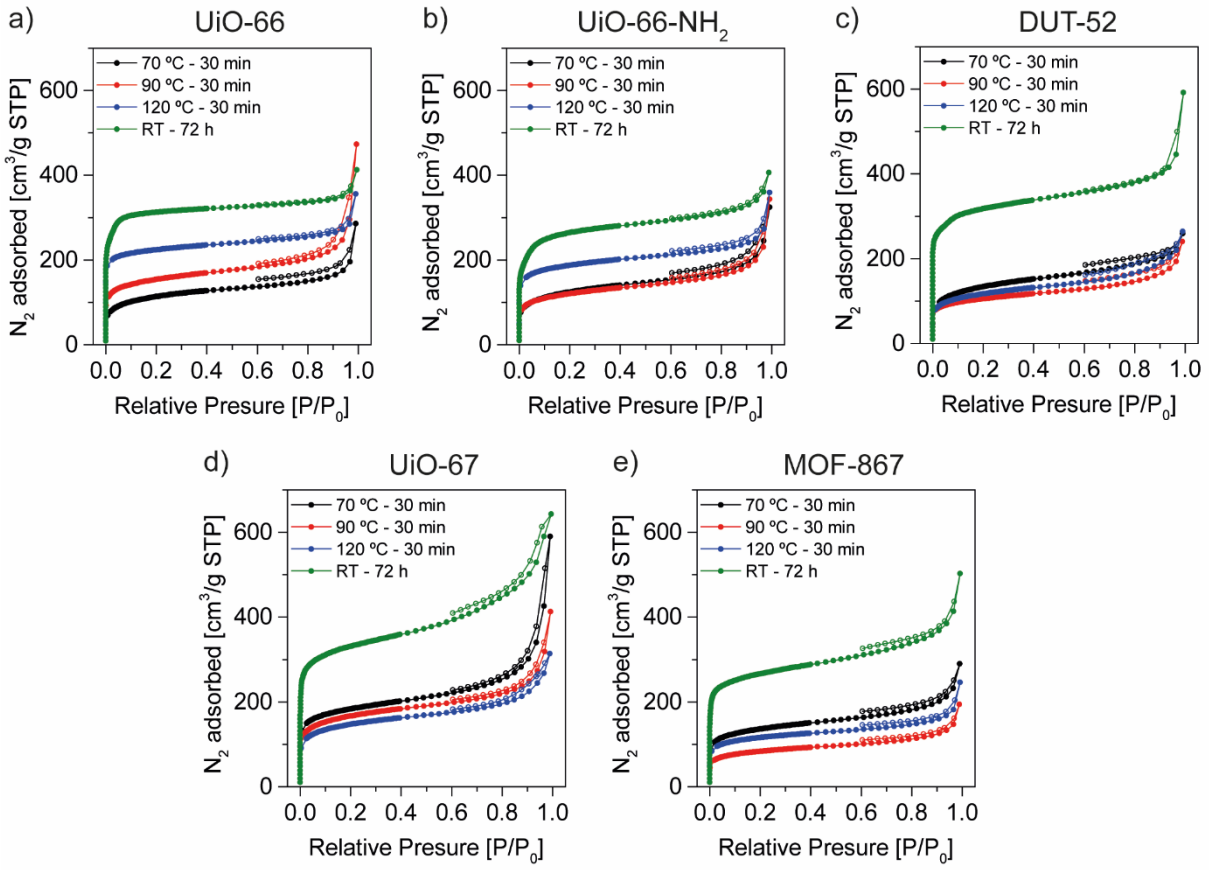

Figure 5-19. N_2 adsorption isotherms of isoreticular Zr-based MOF a) UiO-66, b) UiO-66-NH_2, c) DUT-52, d) UiO-67 and e) MOF.867 synthesized with $Zr(OEt)_4$ at different synthetic conditions.

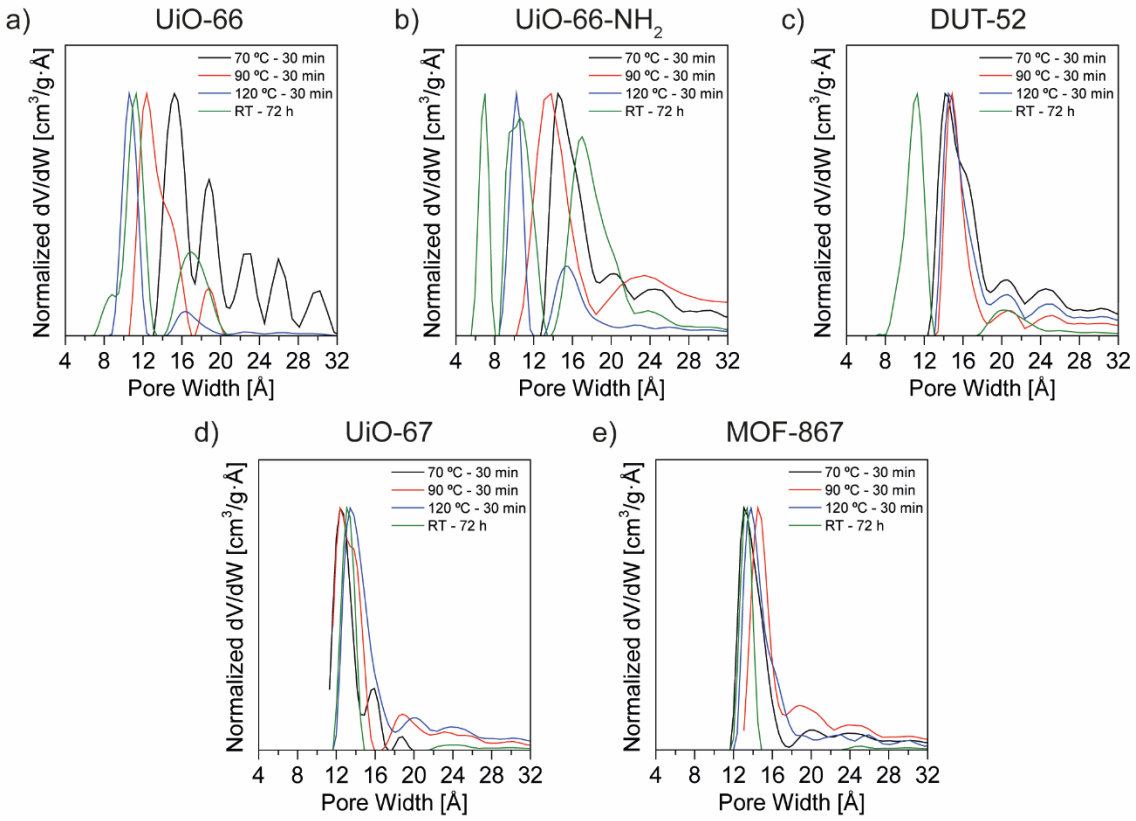

Figure 5-20. Pore size distribution using NLDFT model with cylindrical pores of isoreticular Zr-based MOF a) UiO-66, b) UiO-66-NH_2, c) DUT-52, d) UiO-67 and e) MOF.867 synthesized with $Zr(OEt)_4$ at different synthetic conditions.

Figure 5-9c-g display SEM images of AuBipy@UiO-66, AuBipy@UiO-66-NH_2, AuBipy@DUT-52, AuBipy@UiO-67, and AuBipy@MOF-867, respectively. These images depict nanocomposites prepared at 70 ºC for 30 min, conditions which yielded high conversion rates for most of the MOFs. In the first three cases, distinct core@shell nanocomposites are evident. However, in the case of AuBipy@UiO-67, AuBipy particles are observed with the MOF shell less defined, likely due to synthetic conditions described in the experimental section, where despite lowering the linker-to-metal (L/M) ratio compared to UiO-66, UiO-66-NH_2, and DUT-52, the linker solubility was insufficient, potentially affecting nucleation onto the AuBipy surface. This situation is analogous to MOF-867, where the MOF shell was more defined than UiO-67 despite having a similarly insoluble linker. This difference can be attributed to an increase in the modulator amount, promoting the formation of larger particles capable of growing onto the AuBipy surface.

Figures 5-9h-k show the absorption spectra of AuBipy@MOFs under four distinct conditions: 120°C for 30 min (Figure 5-9h), 90°C for 30 min (Figure 5-9i), 70°C for 30 min (Figure 5-9j), and at RT for 72 h (Figure 5-9k). In Figure 5-9h, it is observed that the localized LSPR peak around 816 nm experienced a blue shift across all AuBipy@MOF nanocomposites due to AuBipy reshaping, resulting in diminished absorption in the near-infrared (NIR) region, rendering them promising for biological applications. Nanocomposites synthesized at 90°C for 30 min exhibited less deterioration in plasmonic properties (Figures 5-9i, 5-21 and 5-22). For

USC DE COMPOSTELA

UiO-66, UiO-66-NH2, and DUT-52, the LSPR peaks were slightly blue-shifted at this condition but remained within the NIR region (approximately 800 nm). The optimal condition for synthesizing nanocomposites without significant alteration in absorption wavelength was found to be at 70°C for 30 min (Figure 5-9j), which yielded the best results. However, synthesis at RT for 72 hours also exhibited favorable LSPR absorption (Figure 5-9k) with a greater blue shift compared to the 70 °C condition, attributed not to reshaping but rather to the quality of shell crystallinity and thickness.

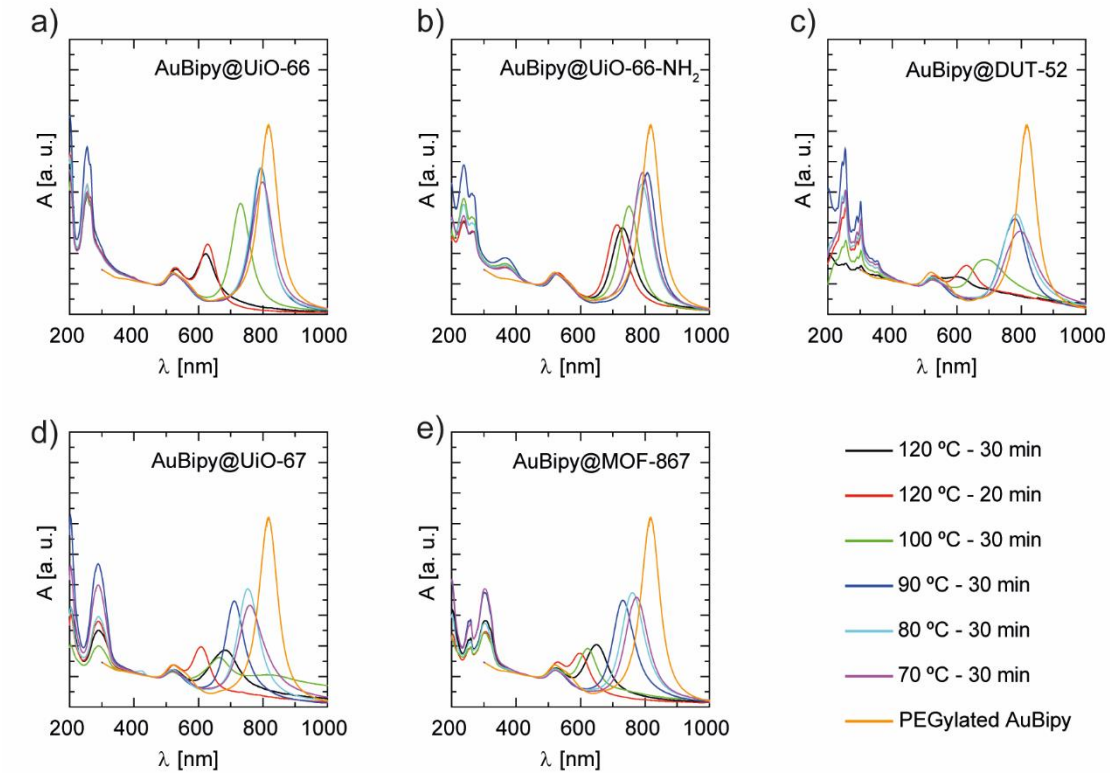

Figure 5-21. UV-Vis spectra of a) AuBipy@UiO-66, b) AuBipy@UiO-66NH$_2$, c) AuBipy@DUT-52, d) AuBipy@UiO-67 and e) AuBipy@MOF-867 with different synthetic conditions.

To explore the universality of our method, we attempted the growth of UiO-66 on other PEGylated NPs, including AuNSs, PdNCs, and Fe_3O_4 NPs. As previously noted, these NPs share a common 2 kDa PEGylated surface, which facilitates the transfer of the NPs into DMF and is crucial for using the NPs as nanoseeds to promote MOF growth. The successful growth of UiO-66 on various NPs was confirmed and TEM (Figure 5-23). The use of PEGylated gold nanorods to promote MOF growth (NU-901) was initially demonstrated by the group led by Fairen-Jimenez, which employed a 5 kDa carboxylated PEG.[248] They suggested that the carboxylic pendant group is crucial for coordinating the Zr-oxo cluster. However, in our current and previous work, we have found that neither the carboxylic pendant group nor the higher molecular weight of PEG are useful. Instead, we attribute the promotion of MOF growth to the amphiphilic nature of PEG.

USC UNIVERSIDADE DE SANTIAGO DE COMPOSTELA

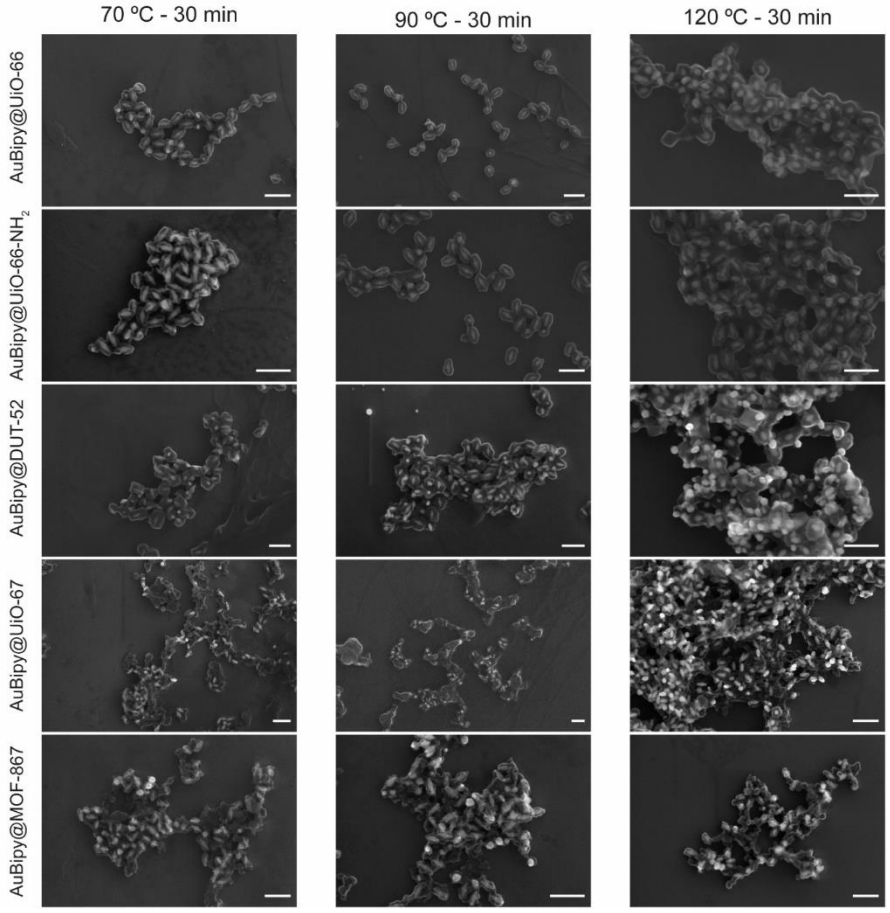

Figure 5-22. SEM images at different magnifications of AuBipy@UiO-66, AuBipy@UiO-66NH_2, AuBipy@DUT-52, AuBipy@UiO-67 and AuBipy@MOF-867 with different synthetic conditions. Scale bars are 200 nm.

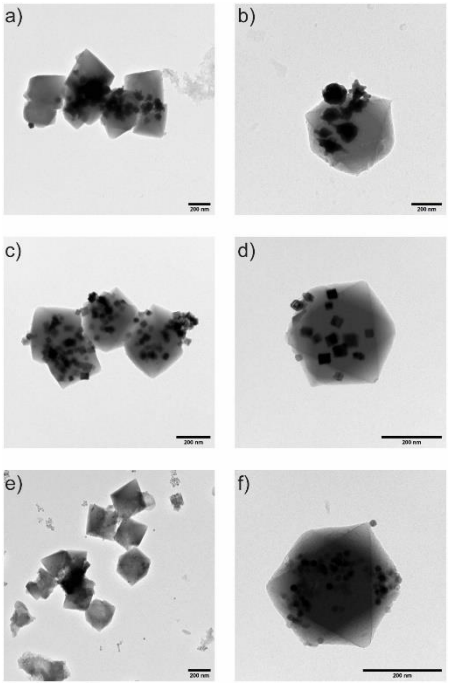

Figure 5-23. a, b) AuNSs@UiO-66, c, d) PdNCs@UiO-66 and e, f) Fe_3O_4 MNPs@UiO-66 TEM images. All of them synthesized at 120 ºC for 30 min. Scale bars are 200 nm.

5.2.3. Seeded-growth mechanism and the influence of the shell-thickness in the heating properties.

To elucidate the role of PEGylated AuBipy as seeds in the synthesis of AuBipy@Zr-based MOFs nanocomposites, UiO-66 was chosen due to its superior crystallinity, minimal defects, and anticipated BET surface area when synthesized at RT for 3 days. To this end, four concentrations of seeds (PEGylated AuBipy) were employed: 0.5, 1.0, 2.5, and 5.0 nM (see experimental section). The synthesized nanocomposites characterized, confirming the formation of the UiO-66 crystallographic phase (Figure 5-24a). Additionally, there was a progressive increase in the intensity of the (111) crystallographic plane of Au at 38.3° two-theta degrees, indicating elevated Au concentration alongside a decrease in shell thickness.

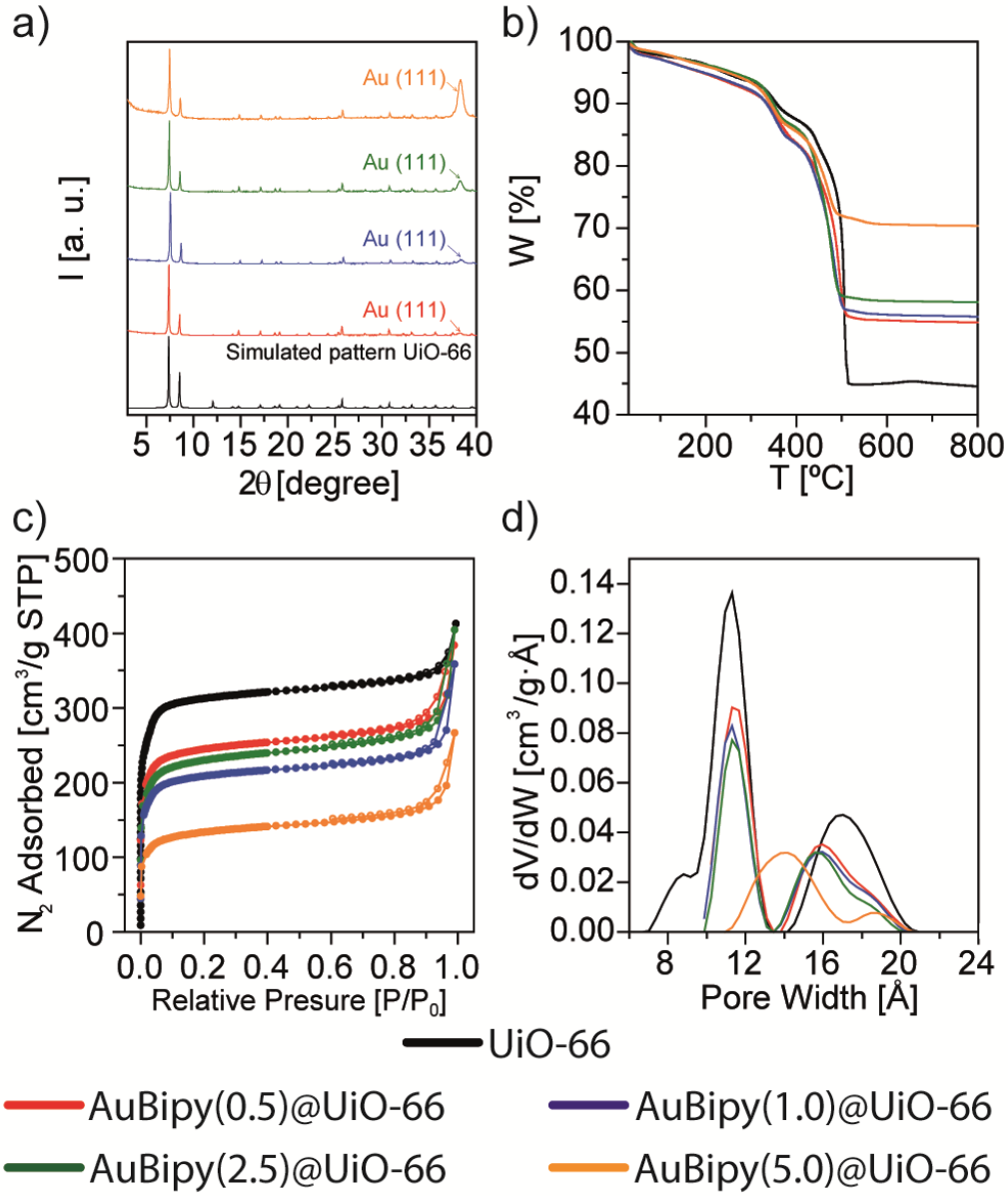

Figure 5-24. a) PXRD diffractograms, b) TGA analysis, c) N_2 adsorption isotherms and d) NLDFT pore size distribution of AuBipy@UiO-66 using different PEGylated AuBipy as seeds in the synthesis at RT for 72 h.

TGA analysis of AuBipy@UiO-66 synthesized at RT for 3 days was conducted (Figure 5-24b), affirming an augmentation in Au content with increasing seed concentrations during synthesis. The differences in inorganic residue of ZrO_2 between pristine UiO-66 synthesized at RT for 3 days and the composites with seed concentrations of 0.5, 1.0, 2.5, and 5.0 nM were measured at 10.24, 11.19, 13.49, and 25.77 wt%, respectively.

N_2 adsorption measurements were performed on the aforementioned samples in comparison with pristine UiO-66 synthesized at RT for 3 days (Figure 5-24c). A progressive reduction in N_2 uptake was observed due to the non-porous nature of AuBipy present in the samples. However, after subtracting the amount of non-porous material (AuBipy), the BET surface area remained progressively lower than that of pristine UiO-66 (Table 5-3). This decrease in BET surface area is attributed to a decline in microporosity in each sample, corroborated by measurements of pore size distribution (Figure 5-24d), which resulted from the reduction in shell thickness and the intercalation of PEG chains at the Au-PEG-UiO-66 interface, particularly pronounced as shell thickness decreases.

Table 5-3. BET surface areas calculated with BESTI analysis of AuBipy@UiO-66 nanocomposites synthesized at RT for 72 h and the correction subtraction the amount of Au obtained by TGA.

Sample	**N_2 uptake (cm^3/g)**	**BET surface area (m^2/g)**	**% Au by TGA**	**BET surface area corrected (m^2/g)**
UiO-66-RT-72	337.0	1249	-	1249
AuBipy(0.5)@UiO-66	273.7	962	10.24	1072
AuBipy(1.0)@UiO-66	260.3	897	11.19	1010
AuBipy(2.5)@UiO-66	233.1	818	13.49	946
AuBipy(5.0)@UiO-66	157.3	513	25.77	691

The influence of seed concentration on shell thickness was validated through DLS measurements (Figure 5-25a and Table 5-4). Interestingly, the sample with a lower seed concentration (0.5 nM) exhibited a larger size than pristine UiO-66 nanoparticles, indicating that the presence of nucleation sites (PEGylated AuBipy seeds) promotes the crystallization process. This assertion was supported by the observation of progressively smaller shell thicknesses with increasing seed concentration.

Shell thickness plays a crucial role in the LSPR absorption, as evidenced by blue-shifting LSPR when the shell thickness was reduced (Figure 5-25b). This phenomenon can be attributed to increased isolation of the MOF from the surrounding media when the shell is thicker, directly impacting the dielectric environment.

Figure 4c presents a HRTEM image of pristine UiO-66 synthesized at RT for 3 days, with its FFT indexing to the {200} family of planes for UiO-66, indicating a d-spacing of 10.07 Å. In this image, polydisperse octahedral nanoparticles with a size of 122.2 ± 18.6 nm are observed (Figure 5-26). However, the addition of seeds resulted in a significant reduction in polydispersity (Table 5-4 and Figure 5-27).

USC UNIVERSIDADE DE SANTIAGO DE COMPOSTELA

Figures 5-25d-g shows AuBipy@UiO-66 synthesized at RT for 3 days with a progressive increase in seed concentration (0.5, 1.0, 2.5, and 5.0 nM, respectively), exhibiting a gradual decrease in UiO-66 shell thickness. This reduction in shell thickness was corroborated by energy dispersive X-ray analysis (Figure 5-27), which revealed a decrease in the Zr/Au ratio as particle size decreased.

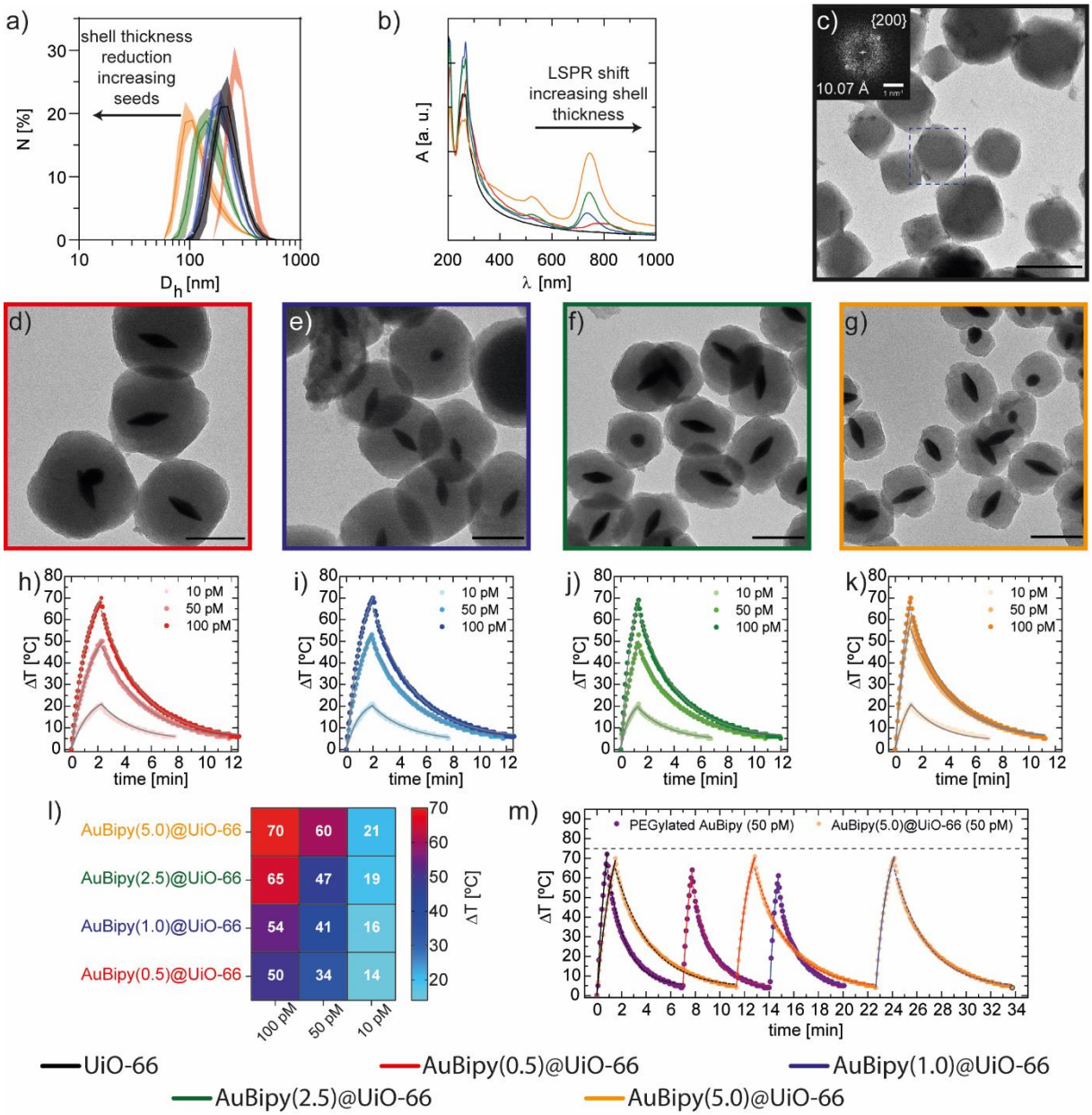

Figure 5-25. a) Absorption spectra of AuBipy@UiO-66 nanocomposites, b) DLS analysis of UiO-66 nanoparticles and its Au@UiO-66 nanocomposites, c) HRTEM image with FFT of UiO-66 nanoparticles, and TEM images of AuBipy@UiO-66 using PEGylated AuBipy d) 0.5 nM, e) 1.0 nM, f) 2.5 nM and g) 5.0 nM, synthesized at 70 °C for 30 min with their corresponding heating curves h-k) at three different concentrations (10, 50 and 100 pM) with 10 W/cm^2 of irradiance, and l) heating curve of 50 pM AuBipy(5.0)@UiO-66 applying three heating and cooling cycles, compared with 50 pM PEGylated AuBipy in water with 10 W/cm^2 of irradiance. Scale bars are 200 nm.

USC UNIVERSIDADE DE SANTIAGO DE COMPOSTELA

Table 5-4. Hydrodynamic sizes of UiO-66 nanoparticles and its AuBipy@UiO-66 nanocomposites obtained at RT for 72 h.

Sample	PdI	N (%)	V (%)	I (%)
UiO-66	0.307 ± 0.036	222.3 ± 8.3	568.7 ± 319.8	348.4 ± 97.3
AuBipy(0.5)@UiO-66	0.127 ± 0.059	279.8 ± 11.9	306.8 ± 17.45	301.4 ± 15.9
AuBipy(1.0)@UiO-66	0.229 ± 0.020	196.6 ± 8.8	310.8 ± 163.7	253.0 ± 40.76
AuBipy(2.5)@UiO-66	0.263 ± 0.029	162.7 ± 8.6	362.2 ± 223.2	263.7 ± 81.3
AuBipy(5.0)@UiO-66	0.298 ± 0.041	131.1 ± 8.9	544.7 ± 278.9	376.2 ± 122.2

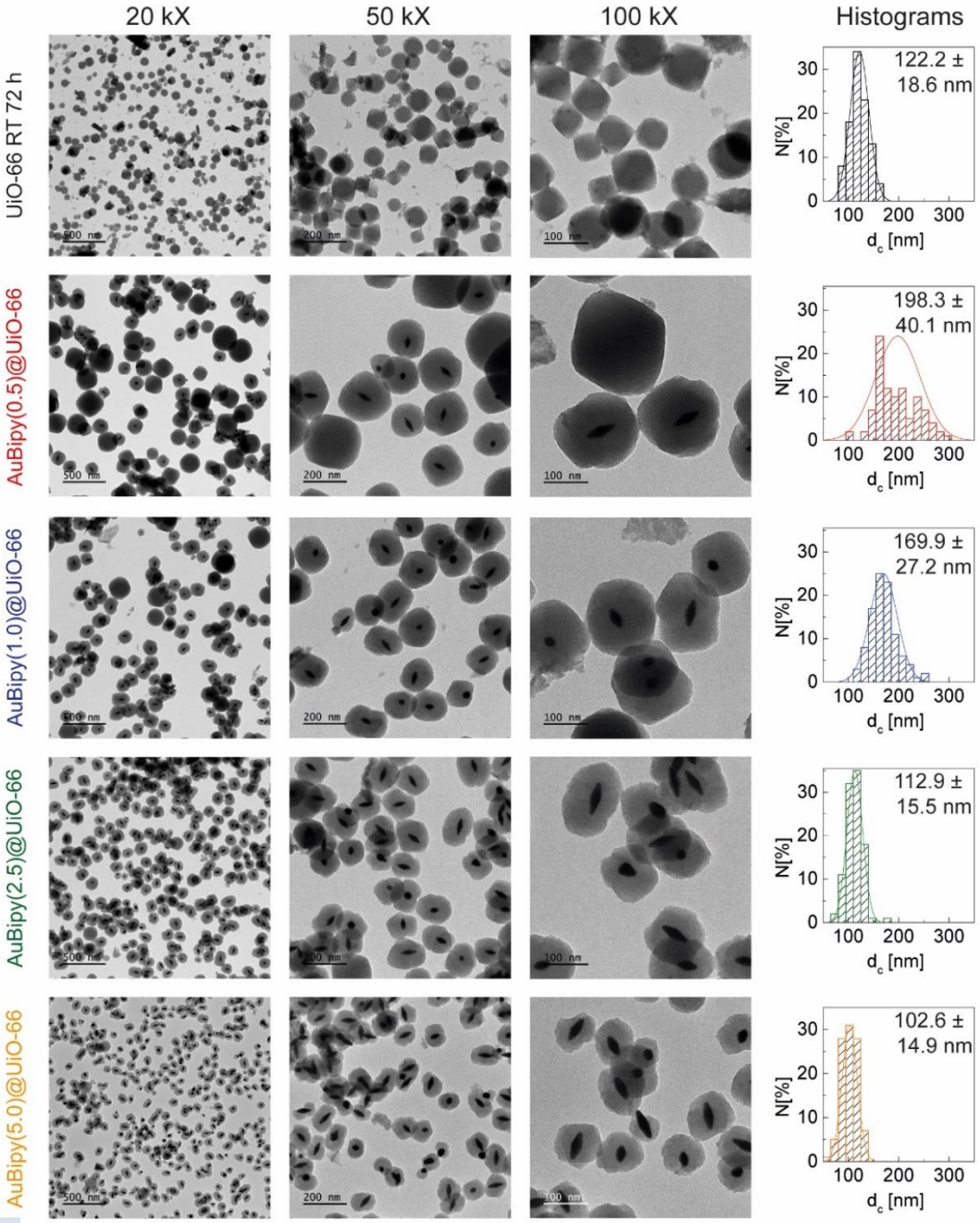

Figure 5-26. TEM images of UiO-66 and their AuBipy@UiO-66 nanocomposites with different shell thickness at different magnifications and their corresponding histograms of particle size distribution.

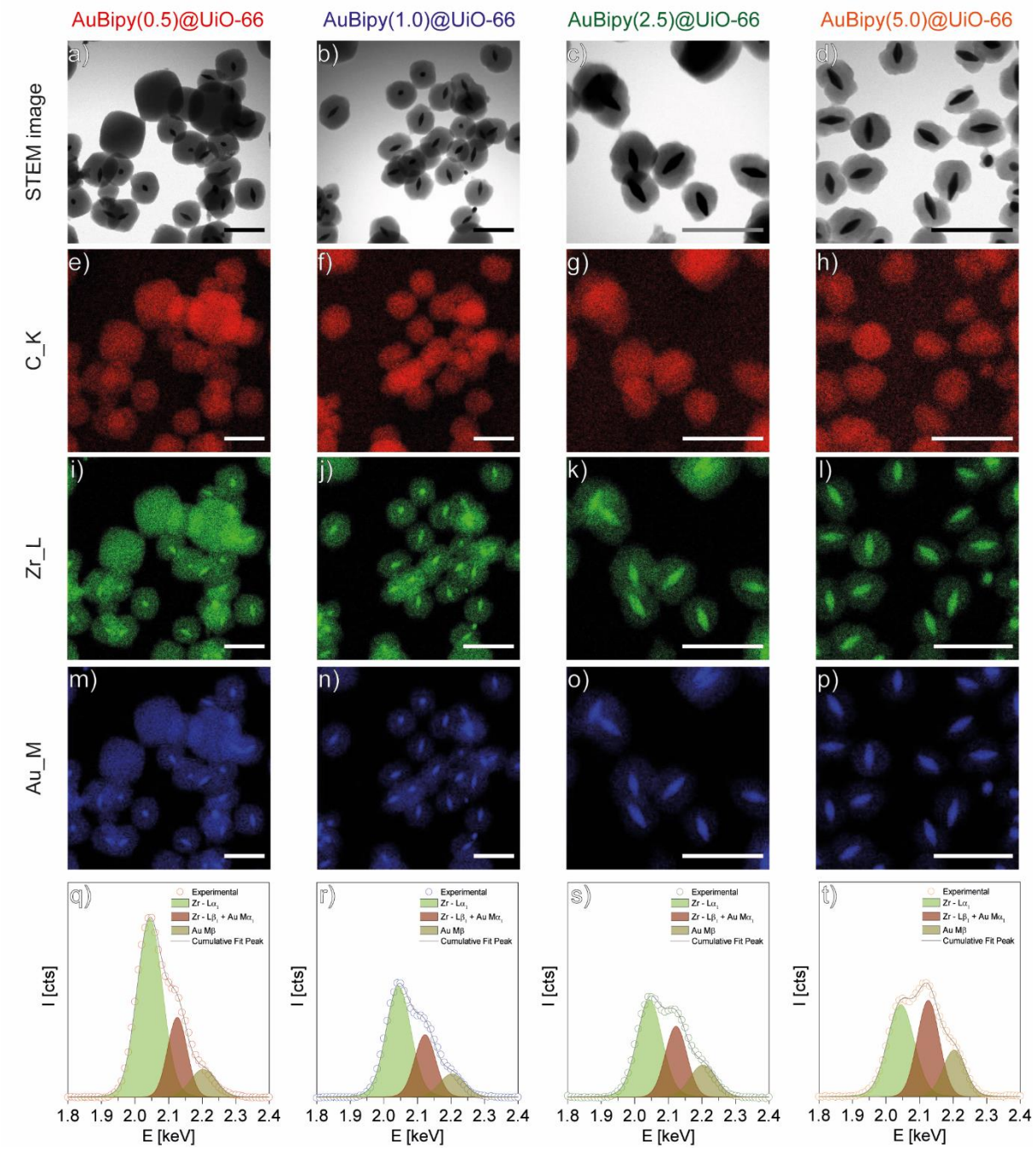

Figure 5-27. STEM images AuBipy@UiO-66 synthesized at RT for 72h using a) 0.5, b) 1.0, c) 2.5 and d) 5.0 nM of PEGylated AuBipy with their corresponding EDX mapping of C (e-h), Zr (i-l) and Au (m-p) and the deconvolution analysis of Zr and Au (q-t). Scale bars are 200 nm.

The effect of shell thickness on the heating properties of these nanocomposites was investigated. Figures 5-25h-k present heating curves of AuBipy@UiO-66 synthesized at RT for 3 days, with an increase in seed concentration (0.5, 1.0, 2.5, and 5.0 nm respectively), irradiated with an 808 nm laser at three different concentrations: 10, 50, and 100 pM. In all cases, a similar behavior was observed, characterized by a Box-Lucas function for heating and an exponential function for cooling. A concentration dependence was evident, as higher concentrations led to faster heating, with the nanocomposites reaching the boiling point of water (~95°C) more

rapidly than at lower concentrations. Additionally, a dependency on shell thickness was observed.

The AuBipy(5.0)@UiO-66 sample reached the boiling point of water fastest, taking only 70 seconds of irradiation (Figure 5-25k), followed by AuBipy(2.5)@UiO-66 at 80 seconds, AuBipy(1.0)@UiO-66 at 120 seconds, and finally AuBipy(0.5)@UiO-66 at 135 seconds. This trend corroborates the dependence of shell thickness on the heating properties of the composites, attributed to the increased thermal insulation provided by thicker shells, which slows down the distribution of heat to the surrounding medium upon irradiation.

A summary of the temperatures reached after 70 seconds of irradiation (time to reach the boiling point of water faster at higher concentration of AuBipy(5.0)@UiO-66) is presented in Figure 5-25l, illustrating both the concentration and shell thickness dependencies.

A comparison between bare PEGylated AuBipy and AuBipy(5.0)@UiO-66, both at a concentration of 50 pM, is depicted in Figure 5-25m. The bare PEGylated AuBipy rapidly reached a temperature increase of $\Delta T = 70°C$, making accurate data acquisition challenging. In contrast, the AuBipy(5.0)@UiO-66 sample achieved the same ΔT in 90 seconds, nearly twice the time taken by the bare PEGylated AuBipy. This difference is attributed to the very low thermal conductivity of UiO-66 (0.32 W/mK in fcu topology),[137] which slows down heat transfer within the composite material.

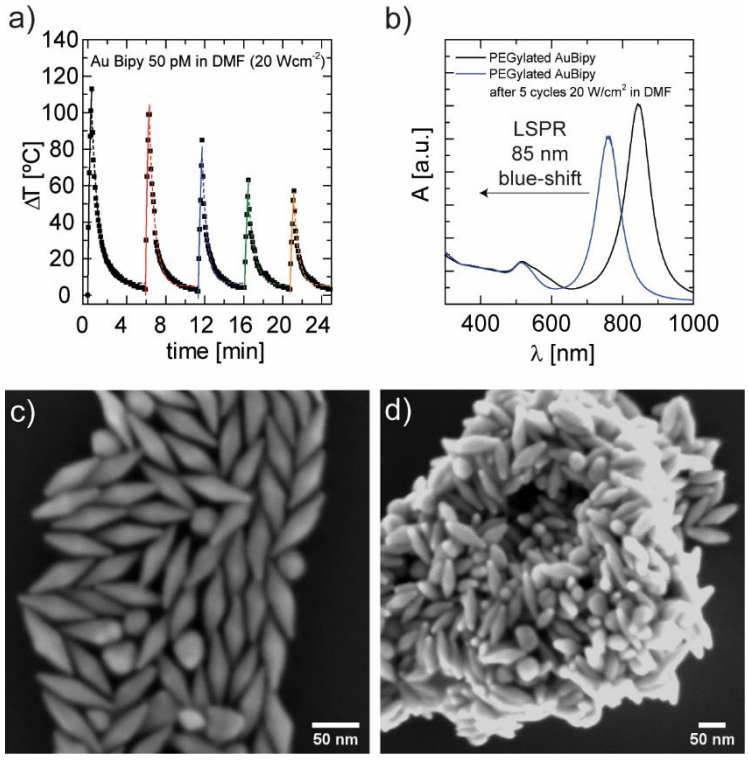

Figure 5-28. a) Heating curves of PEGylated AuBipy 50 pM in DMF after 5 cyles of 25 s of irradiation with 20 W/cm^2 of irradiance , b) UV-Vis spectra of PEGylated AuBipy before and after 5 cycles of irradiation, and SEM images of PEGylated AuBipy c)before and d) after irradiation.

When the PEGylated AuBipy are subjected to higher irradiance levels in a different solvent such as DMF, which permits an increase in temperature beyond 100 ºC, more significant

changes in the LSPR are observed, typically manifested as a blue shift. However, it is noteworthy that repeated on-off cycles under the same on-time conditions result in a decrease in the maximum temperature attained (Figure 5-28). The alterations in morphology resultant from reshaping are avoided when the PEGylated AuBipy are encapsulated with a UiO-66 shell This was examining UV-Vis spectra pre- and post-irradiation, demonstrating no discernible modifications in LSPR (Figure 5-29).

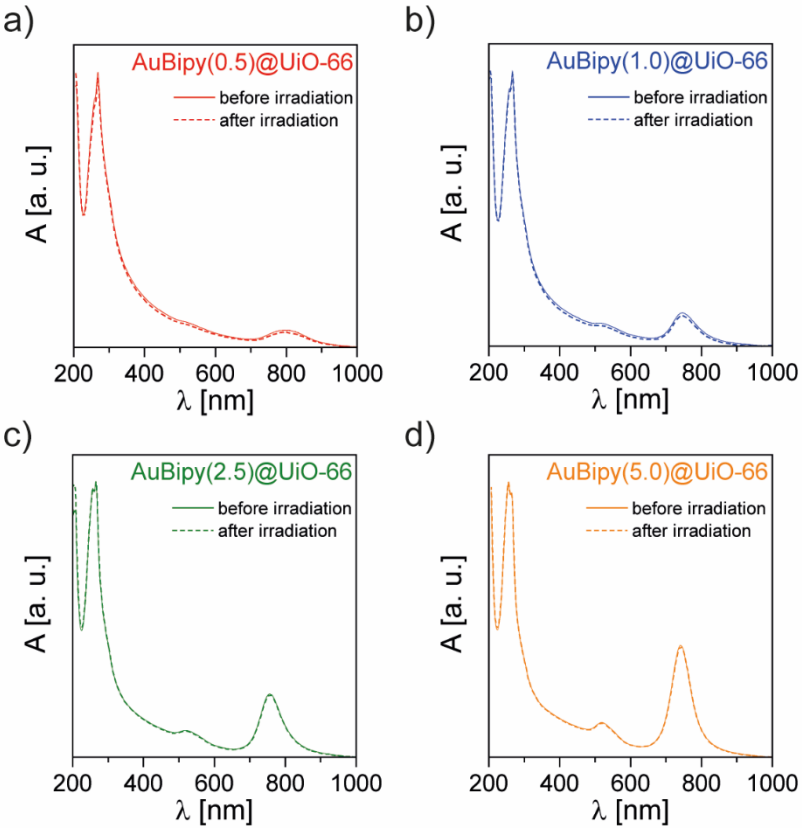

Figure 5-29. UV-Vis spectra of a) AuBipy(0.5)@UiO-66, b) AuBipy(1.0)@UiO-66, c) AuBipy(2.5)@UiO-66 and d) AuBipy(5.0)@UiO-66 nanocomposites synthesized at RT for 72 h, before and after 808nm laser irradiation with 10 W/cm^2 of irradiance.

5.3. Summary and Conclusions of Chapter 5

In this chapter, the use of Zr(IV) alkoxides was explored to mitigate damage to the cores of plasmonic nanoparticles caused by reshaping during heating. This synthetic method reduces the reaction temperature from the typical 120 ºC required for the synthesis of UiO-family MOFs to 70 ºC, achieving a reaction yield greater than 90% within just 30 minutes. Although the reaction can also proceed at room temperature, requiring 72 hours, the MOFs produced under these conditions exhibit excellent crystallinity and adsorption properties. Importantly, performing the synthesis without elevated temperatures prevents damage to the plasmonic cores.

This synthetic approach is applicable to various morphologies of gold nanoparticles as well as catalytic nanoparticles such as palladium (Pd) and magnetic nanoparticles functionalized with polyethylene glycol (PEG) chains, which enhance their compatibility with the organic solvents used in MOF synthesis.

The effect of shell thickness on the heating properties was also investigated. It was demonstrated that the thermal insulating properties of the MOF shell influence the heating and cooling rates of the nanocomposites. Specifically, a thicker shell requires longer irradiation times to heat the surrounding media effectively. Additionally, it was shown that increasing the shell thickness prevents reshaping caused by heat from laser excitation, this allows the application of multiple cycles of heating and cooling while maintaining the heating properties of the plasmonic core.

USC
UNIVERSIDADE DE SANTIAGO DE COMPOSTELA

USC
UNIVERSIDADE
DE SANTIAGO
DE COMPOSTELA

6. SEEDED-GROWTH OF PCN-224 ONTO PLASMONIC NANOPARTICLES: PHOTOACTIVE MICROPOROUS NANOCARRIERS

USC
UNIVERSIDADE DE SANTIAGO DE COMPOSTELA

USC
UNIVERSIDADE
DE SANTIAGO
DE COMPOSTELA

The results presented in the following chapter are published in:

"Seeded-Growth of PCN-224 onto Plasmonic Nanoparticles: Photoactive Microporous Nanocarriers". (2024). Small Structures, 5(5), 2300464.

Manuel Ceballos[1], Samuel Funes-Hernando[1], Giulia Zampini[1], Manuela Cedrún-Morales[1], José Manuel Vila-Fungueiriño[1], Beatriz Pelaz *[1] and Pablo del Pino*[1]

[1]Center for Research in Biological Chemistry and Molecular Materials (CiQUS), University of Santiago de Compostela, 15705 Santiago de Compostela, Spain.

Contributions: Preparation, optimization, and characterization of the materials; writing – original draft.

Impact Factor: 13.9. Q1 in Nanoscience & Nanotechnology.

USC UNIVERSIDADE DE SANTIAGO DE COMPOSTELA

USC
UNIVERSIDADE
DE SANTIAGO
DE COMPOSTELA

6.1. Introduction

Combining the characteristics of metal-organic frameworks at the nanoscale (nanoMOFs) and plasmonic nanoparticles (NPs) has led to a novel class of nanocomposites (NCs) characterized by exceptional properties.[230] Unfortunately, the development of core@shell systems, such as incorporating plasmonic NPs within MOFs (NPs@NMOF), poses considerable challenges. This difficulty primarily arises from the rigorous synthetic conditions typically associated with MOF production, involving elevated temperatures (>100 ºC), extended reaction times (typically 24 hours), and the use of organic solvents, most commonly dimethylformamide (DMF). These conditions are often incompatible with the stability of plasmonic NPs or others.

The advancement of core@shell systems, wherein inorganic NPs are employed as the core while nanoMOFs serve as the outer shell, has recently been established as an exciting new research area. For example, when the core is a plasmonic NP, these systems present the remarkable storage capabilities of nanoMOFs, capable of encapsulating a wide range of molecules, including drugs and dyes, in tandem with the potent heating capabilities of plasmonic NPs. This synergy has paved the way for the development of remotely-controlled nanomaterials capable of selectively releasing cargo through thermodiffusion process, commonly referred to as the Soret effect.[204]

Here, a simple, fast, and efficient synthesis of core@shell NCs that occurs at mild conditions, i.e., room temperature and short reaction time (1 h) was developed. These NCs comprises a gold bipyramid (AuBipy) nanoparticle as core and PCN-224 Zr-porphyrinic nanoMOF as shell. AuBipy are functionalized with thiol-polyethylene glycol (HS-PEG), which provides them with stability in DMF. The PCN-224 shell has been loaded with cresyl violet (CV), as model cargo, to demonstrate its light-triggered induced-release under NIR laser irradiation within living cells and proving the photodynamic properties of the MOF (Figure 6-1).

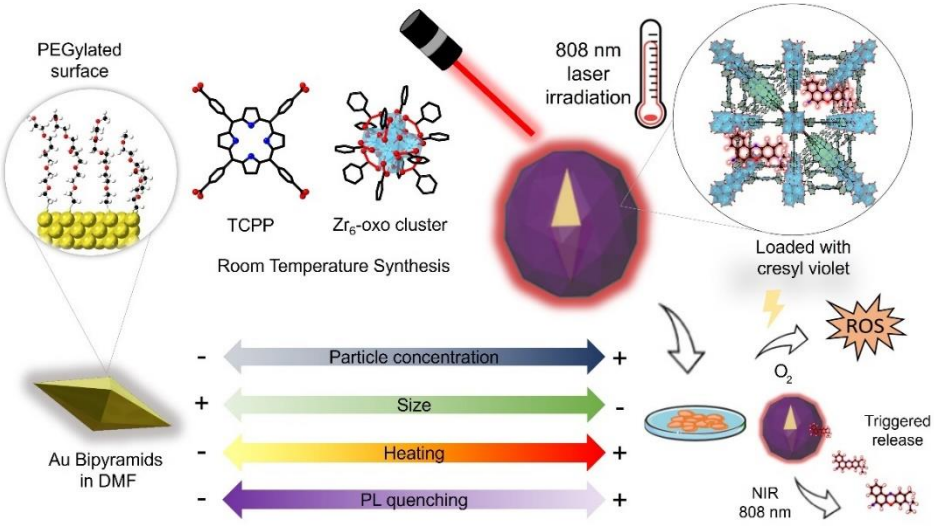

Figure 6-1. Scheme of work representing the use of PEGylated AuBipy as core with PCN-224 as shell loaded with cresyl violet (CV). CV is released under NIR light while the PCN-224 linker is capable of both generate a fluorescence signal and produce reactive oxygen species (ROS) upon NIR irradiation. Also, it is depicted a summary of the effect of AuBipy concentration in size, heating and luminescent properties of the AuB@PCN-224 NCs.

6.2. Results and discussion

6.2.1. Synthesis and Structural Characterization of PCN-224 nanoMOFs and NCs

The use of preformed Zr_6-oxo cluster has been described in some syntheses of Zr-based MOFs such as PCN-222,[170] and NU-901.[248] This synthetic approach offers the benefit of preventing the formation of secondary phases or mixed-phases. In this study, PCN-224 in its pure phase (Figure 6-2), without the presence of other polymorphs, was synthesized using the mentioned cluster, with acetic acid as modulator. The preformed cluster was characterized by TGA and PXRD. The synthesis of the cluster was conducted in 1-propanol, followed by washing with the same solvent to remove any excess of benzoic acid. Subsequently, the sample was dried under vacuum. TGA results confirmed the presence of 1-propanol even after dry-freezing. Therefore, an additional washing step with MeOH, followed by vacuum drying was required (Figure 6-2a). Approximately 50% of the initial amount of 1-propanol used in the synthesis, remained after drying in vacuum for a day. The cluster exhibited a good crystallinity after the removal of 1-propanol washing it with MeOH and drying in vacuum (Figure 6-2b). The cluster was analyzed by ICP-OES, which yielded a Zr content of 22.67%, in good agreement with the 22.18% obtained via TGA. These values closely align with the theoretically expected Zr content of 25.66% (Figure 6-2c), taking into consideration the coordination of twelve benzoate molecules to the cluster.

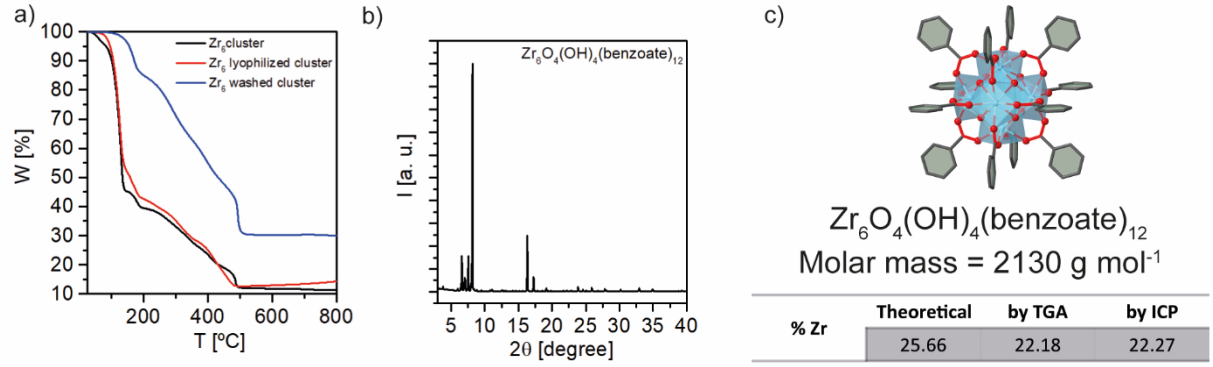

% Zr	Theoretical	by TGA	by ICP
	25.66	22.18	22.27

Figure 6-2. a) TGA analysis of the cluster as synthesized, lyophilized and washed with MeOH in vacuum for 1 day, b) PXRD diffractogram of Zr_6-oxo cluster and c) image of Zr_6-oxo cluster and the amount of Zr (%) obtained by ICP and TGA compared with the theoretical.

The synthesis of PCN-224 at room temperature was conducted using two types of clusters: i) the non-washed cluster containing 1-propanol (PCN-224-p) in which the ratio linker (TCPP) / metal (Zr) was 1.3 while the ratio modulator (HOAc) / metal (Zr) was 1450; and ii) the washed cluster that was thoroughly cleaned with MeOH to remove completely the 1-propanol (PCN-224-w) in which the ratios were TCPP / Zr 0.25 and HOAc / Zr 290 . Figure 6-3a-c shows SEM images of PCN-224 NCs with AuBipy core (Figure 6-4). The particles obtained in each case showed distinct sizes and polydispersity degree. Figure 6-5 shows a SEM image of PCN-224-p, PCN-224-w here is possible to appreciate the difference in polydispersity using their cluster with 1-propanol or the washed cluster PCN-224-p rendered highly polydisperse particles ranging from 150 to 900 nm, whereas PCN-224-w produced highly monodisperse nanoMOFs of about 150 nm (Figure 6-5 and Table 6-1). Figure 1d-e shows TEM and HRTEM images of PCN-224-w corroborating the monodispersity and crystallinity of the nanoMOFs. The reaction

time, temperature, and modulator amount were kept identical for both experiments. However, the ratio of linker to modulator differs due to the presence or absence of 1-propanol in the cluster. Compared with the highly monodisperse sample PCN-224-w, the polydispersity of PCN-224-p can be attributed to both the presence of 1-propanol and the difference in the linker-modulator ratio. Interestingly, when the synthesis of MOF using the cluster PCN-224-p was carried out with the presence of PEGylated AuBipy (83 nm length per 28 nm width, Figure 6-4), we obtained extraordinarily monodisperse core@shell NCs (Figure 6-3f-g and Figure 6-5). Moreover, NCs using PEGylated Pd nanocubes (PdNCs) instead of AuBipy were also equivalently produced, proving that our method is suitable for other inorganic NPs (Figure 6-6).

Results confirmed that the presence of 1-propanol appears crucial to obtain these NCs, as we were unable to obtain core@shell nanosystems using the 1-propanol free cluster used for PCN-224-w (Figure 6-7). The hypothesis is that 1-propanol likely acts as a co-surfactant in the presence of AuBipy and interacts with the PEG chains promoting an enhanced local accumulation of Zr_6-oxo clusters in the oxygen moieties of the PEG monomers. EDX-STEM analysis of AuB(10)@PCN-224 (Figure 6-3h-l) corroborated the presence and distribution of C and O due to the linker (TCPP), Zr due to the Zr_6-oxo cluster, and Au in the core for the bipyramids.

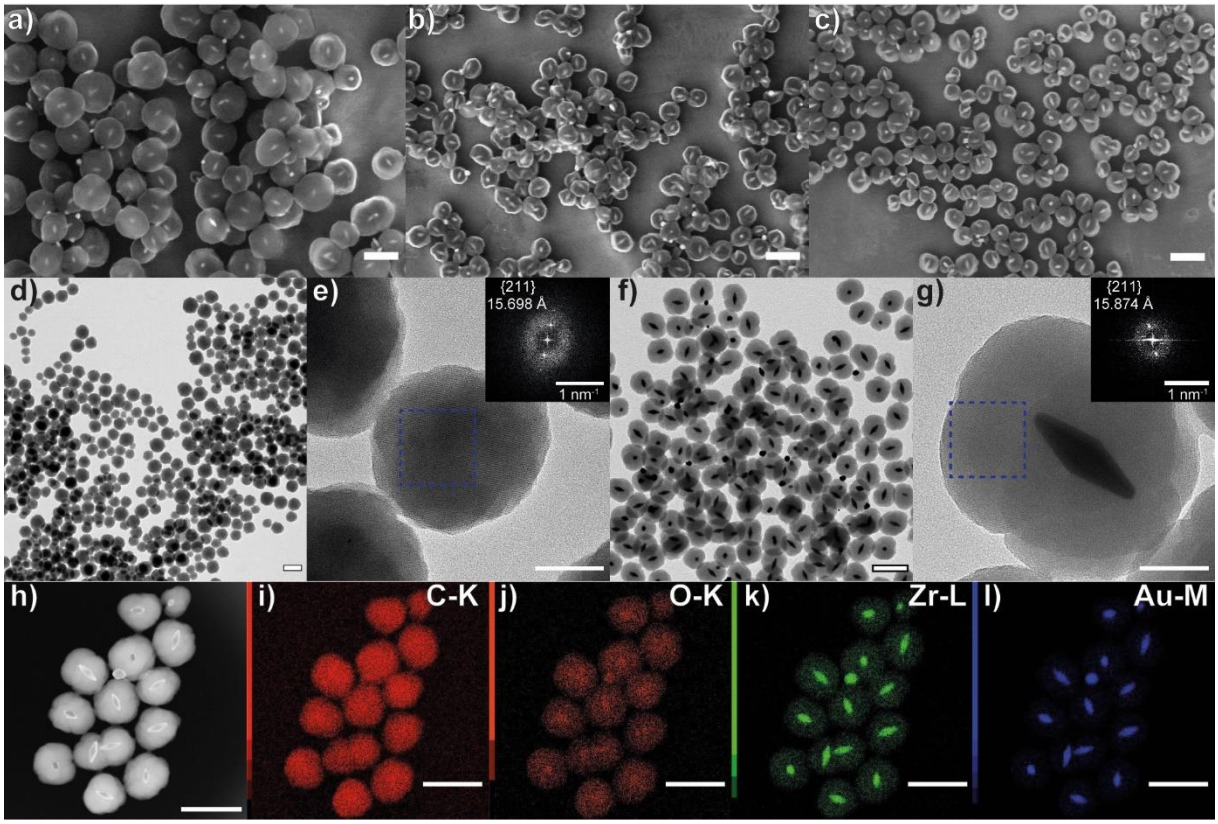

Figure 6-3. SEM images of a) AuB(1)@PCN-224, b) AuB(5)@PCN-224 and c) AuB(10)@PCN-224. d) TEM image and e) HR-TEM image with FFT of PCN-224-w. f) TEM image and g) HRTEM image with FFT of AuB(10)@PCN-224. h-l) EDX-STEM analysis of AuB(10)@PCN-224. Scale bars 250 nm except HRTEM images e) and g) are 50 nm.

Figure 6-3a-c illustrates the AuB@PCN-224 NCs obtained by introducing increasing amounts of PEGylated AuBipy (1, 5, and 10 nM) in the reaction mixture, while keeping

precisely the same reaction conditions as to produce PCN-224-p. Using a concentration of 1 nM, the NCs exhibit a thicker MOF shell (AuB(1)@PCN-224), and as the concentration increases (AuB(5)@PCN-224 and AuB(10)@PCN-224), the thickness of the shell decreases progressively with very good reproducibility among batches (Figure 6-8). We also observed that the presence of seeds increased the yield (Zr) of reaction as determined by ICP-OES with respect to both PCN-224 systems (Figure 6-9). Figure 6-3h presents a STEM image of AuB(10)@PCN-224, revealing a distinctive core-shell structure where a single AuBipy is encapsulated within the center of the MOF shell.

Figure 6-3e and Figure 6-3g display HRTEM images accompanied by FFT analysis of PCN-224-w and AuB(10)@PCN-224, respectively. The FFT measurement reveals a d-spacing value of 15.689 Å for PCN-224-w and 15.874 Å for AuB(10)@PCN-224 , which corresponds to the {211} family of crystallographic planes. In a cubic system with a lattice parameter of 38.4520 Å and space group $Im\bar{3}m$, the expected d-spacing for the {211} planes is 15.698 Å.[35]

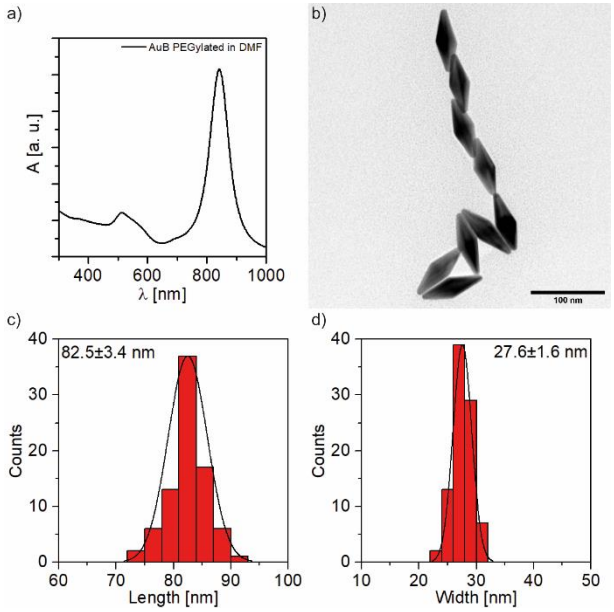

Figure 6-4. AuBipy characterization by a) UV-Vis absorption spectrum, b) representative TEM image and histograms representing c) bipyramids length and d) bipyramids width.

Table 6-1. Diameter values of PCN-224 and AuB@PCN-224 by SEM and DLS in MeOH.

Sample	SEM size (nm)	DLS size (nm)	PdI
PCN-224-p	512.5±263.6	873.2±28.8	0.47±0.03
PCN-224-w	169.1±24.5	268.3±6.7	0.16±0.02
AuB(1)@PCN-224	276.4±59.0	330.9±2.9	0.05±0.03
AuB(2)@PCN-224	224.4±31.5	238.3±3.0	0.07±0.03
AuB(3)@PCN-224	217.6±25.1	230.6±4.3	0.06±0.02
AuB(5)@PCN-224	160.5±30.2	203.5±6.7	0.09±0.05
AuB(10)@PCN-224	138.0±21.3	178.5±5.9	0.07±0.02

USC UNIVERSIDADE DE SANTIAGO DE COMPOSTELA

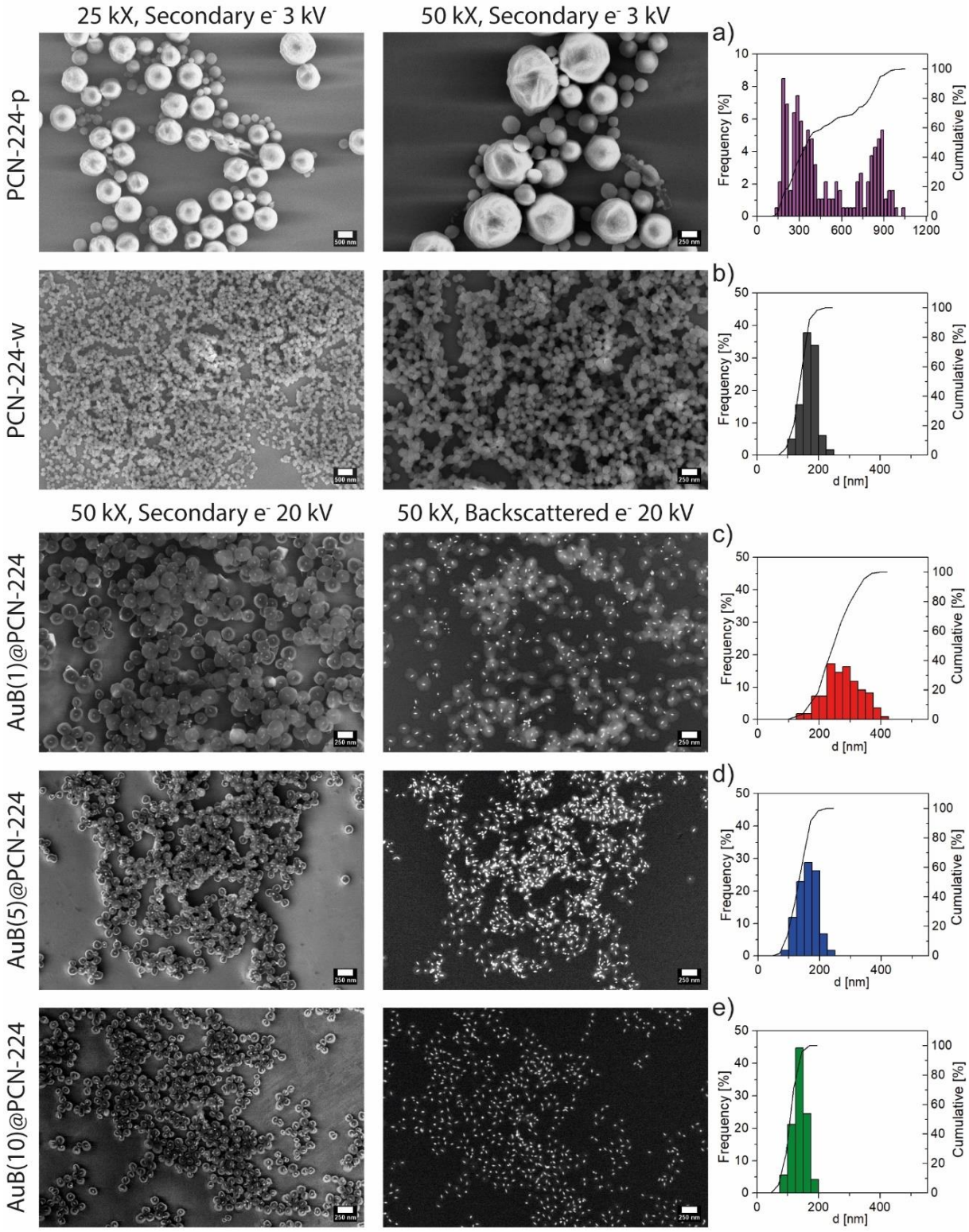

Figure 6-5. SEM images at different magnifications and with different detectors for all different nanoMOFs and NCs with their corresponding histograms: a) PCN-224-p (512.5±263.6 nm), b) PCN-224-w (169.1±24.5 nm), c) AuB(1)@PCN-224 (276.4±59.0 nm), d) AuB(5)@PCN-224 (160.5±30.2 nm) and AuB(10)@PCN-224 (138.0±21.3 nm). Scale bars are 250 nm for images at 50 kX and 500 nm for images at 25 kX.

USC
UNIVERSIDADE DE SANTIAGO DE COMPOSTELA

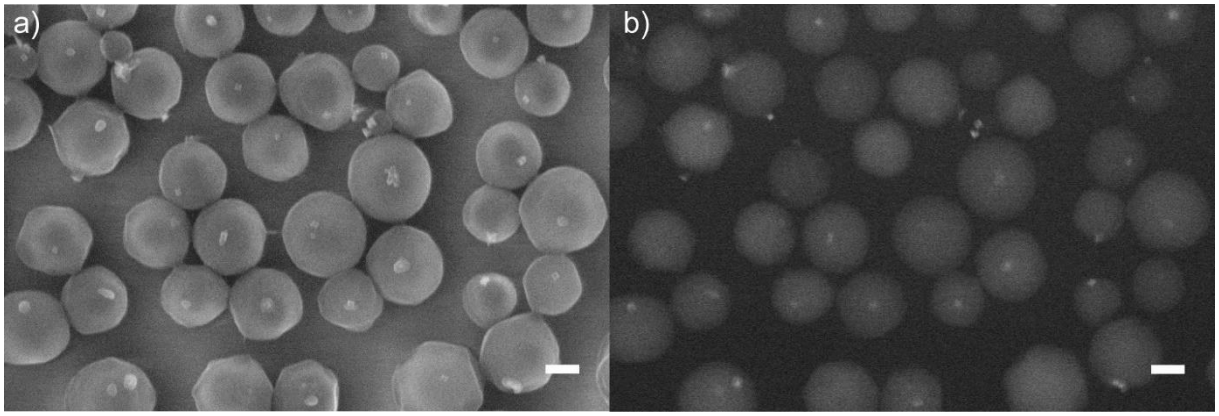

Figure 6-6. SEM images of PdNPs@PCN-224 with detectors a) InLens and b) AsB. Scale bar: 200 nm.

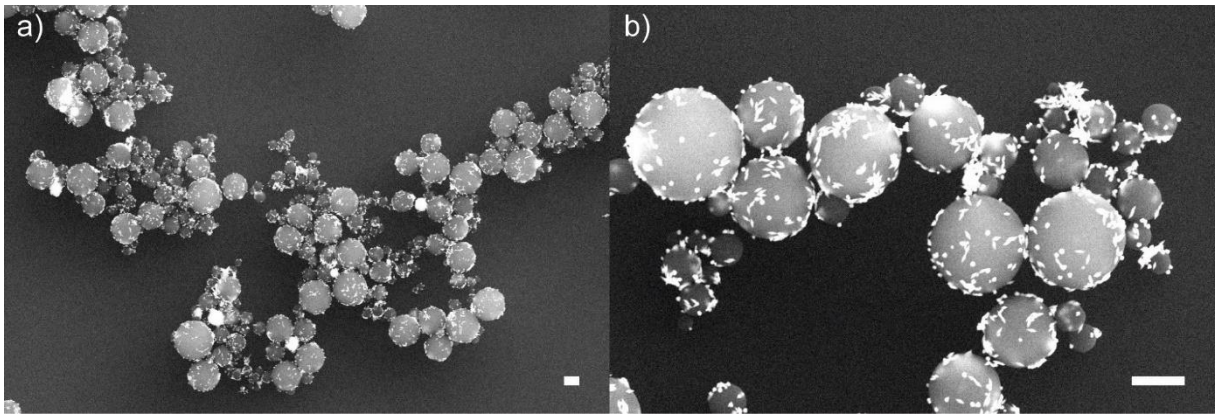

Figure 6-7. SEM images of PCN-224 decorated with AuBipy with detector SE2. Scale bar: 500 nm.

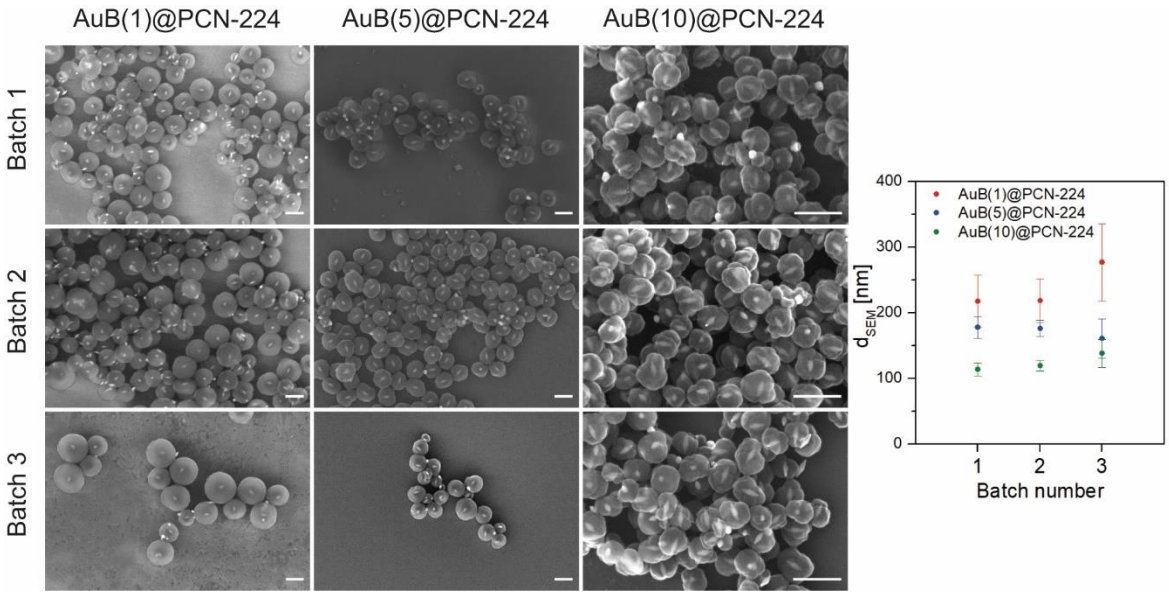

Figure 6-8. SEM images of 3 different batches of AuB@PCN-224 using AuBipy concentrations of 1, 5 and 10 nM showing the reproducibility among batches. Right pannel shows the comparison of the final overall NC sizes of 1, 5 and 10 nm represent in red, green and blue, respectively. Scale bars are 200 nm.

USC
UNIVERSIDADE DE SANTIAGO DE COMPOSTELA

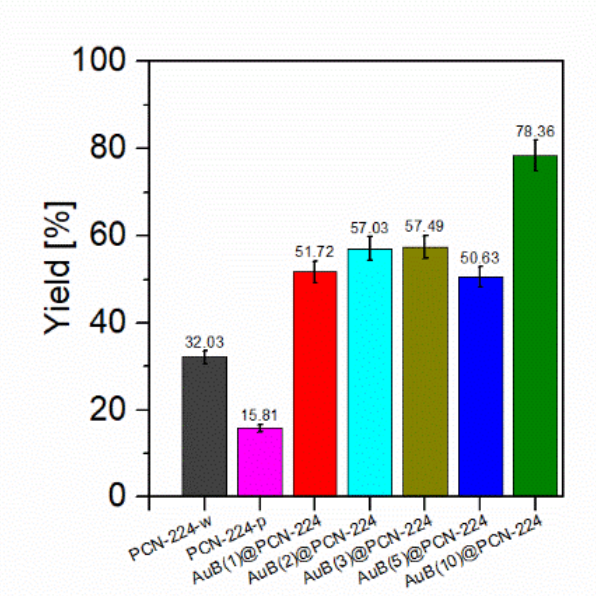

Figure 6-9. Yield of reaction determined by ICP-OES with the amount of Zr of PCN-224 nanoMOFs and NCs with AuBipy at different concentrations.

Figure 6-0a presents the UV-Vis absorption spectra of the prepared samples. In the case of PCN-224-p (pink line), a considerably broad Soret band is observed, with a maximum absorbance at around 420 nm, owing to the polydispersity on this sample. Additionally, four Q bands exhibit scattering, which can be attributed to the presence of larger particles (> 1µm). Conversely, PCN-224-w (black line) displays a distinct and narrow Soret band, accompanied by the absence of scattering in the Q bands, in agreement with a smaller particle size. The large difference in polydispersity between the PCN-224-p and PCN-224-w was also confirmed by DLS analysis (Figure 6-10b). Moreover, in the UV-Vis spectra of the NCs (AuB@PCN-224) analogous absorption bands to PCN-224-w were identified, while the characteristic longitudinal LSPR centered at 810 nm from the AuBipy was also present. The plasmonic-to-Soret peak ratios increased as more seeds were used. These spectra agree with the formation of core@shell NCs. Furthermore, a slight blue shift in the LSPR peak is observed in Figure 6-10a, which can be attributed to the influence of the PCN-224 shell thickness on the surrounding dielectric environment. DLS analysis showed monodispersed colloidally stable samples (Figure 6-10b). Increasing AuBipy concentrations led to smaller hydrodynamic diameters, in line with the formation of NCs with thinner PCN-224 shells. Figure 6-10c shows FTIR spectra of the systems, showing the characteristic C=O vibration in TCPP linker at 1690 cm^{-1}, which is absent in PCN-224 samples due to the formation of coordination bond between Zr-O and the vibration of O-C-O ant 1609 and 1417 cm^{-1}.

The crystalline nature of all the particles was confirmed by PXRD analysis (Figure 6-10d). The obtained diffraction patterns indicated the presence of the pure-phase PCN-224. The main diffraction peaks were observed at 3.204°, 4.616°, 5.553°, 6.433°, 7.893°, and 9.113° two-theta degree, corresponding to the crystallographic planes (110), (200), (211), (220), (222), and (400), respectively. These findings indicate that the crystallinity of the PCN-224 material was unaffected by the presence of 1-propanol or AuBipy during the synthesis. Notably, the presence

USC UNIVERSIDADE DE SANTIAGO DE COMPOSTELA

of Au was observed in the corresponding NCs. The diffraction pattern exhibited a peak at 38.200° two-theta degree, corresponding to the Au (111) crystallographic plane.

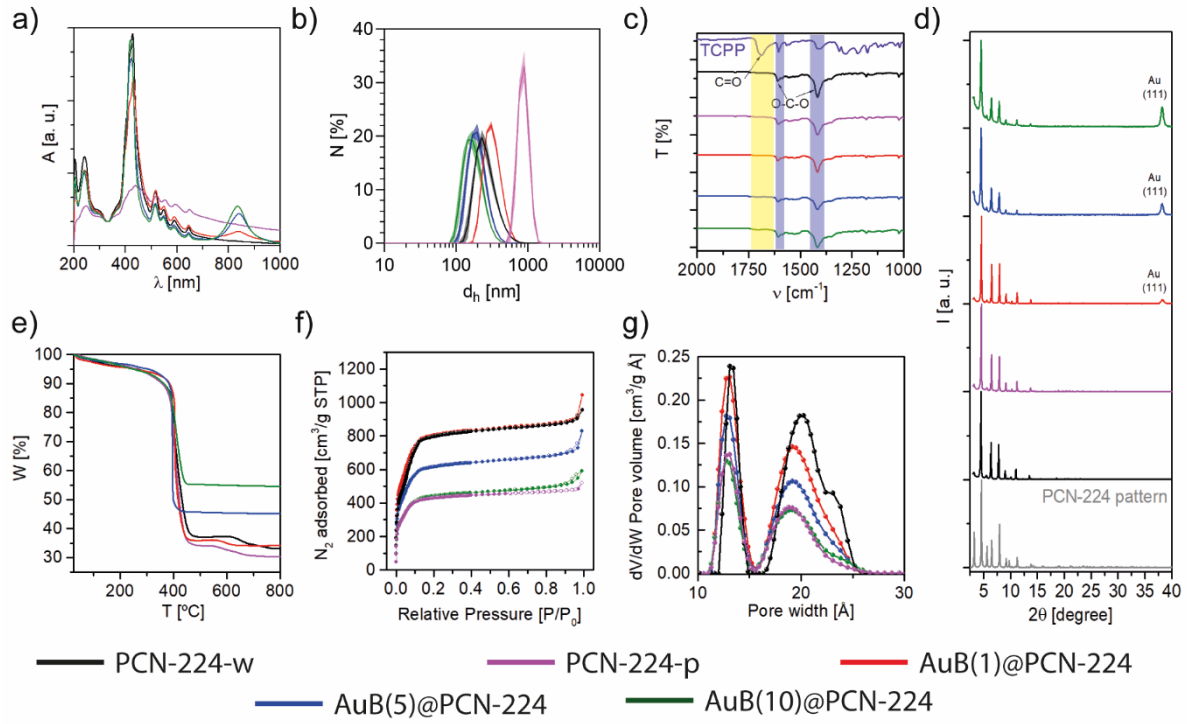

Figure 6-10. Characterization of PCN-224 NPs and the NCs: a) UV-Vis spectra, b) DLS particle size distribution, c) FTIR analysis, d) PXRD diffractogram, e) TGA analysis, f) N_2 adsorption isotherms and g) porous size distribution.

TGA reveals the stability of the samples up to a temperature of 400 °C (Figure 6-10e). Comparative analysis between PCN-224-p and PCN-224-w shows that PCN-224-p exhibited a lower presence of inorganic residue (ZrO_2) than PCN-224-w. This disparity can be attributed to the existence of missing linker defects in PCN-224-w caused by a low linker/metal (L/M) ratio. Specifically, PCN-224-p possessed a L/M ratio of 1.45, while PCN-224-w had a L/M ratio of 0.30. Additionally, an increase in the concentration of AuBipy resulted in a gradual increase in the quantity of inorganic residue. The estimation of the gold amount (Au) was performed by subtracting the plateau value of PCN-224-w from the plateau value of samples with gold (Table 6-2).

The porosity of PCN-224 samples was assessed through N_2 adsorption measurements conducted at 77 K (Figure 6-10f). The N_2 uptake for PCN-224-w was determined to be 910 cm^3/g (STP), accompanied by a BET surface area of 2624 m^2/g. In comparison, PCN-224-p exhibited a N_2 uptake of 480 cm^3/g (STP) and a BET surface area of 1377 m^2/g. These findings indicate that PCN-224-w possesses superior crystallinity when compared to PCN-224-p, which can be corroborated with a decrease in the pore volume in the porous size distribution (Figure 6-10g). The N_2 uptake of the composites exhibited a gradual decrease while increasing the gold content. This decrease can be attributed to the presence of non-porous Au mass, which reduces the available porous space for N_2 adsorption. Furthermore, the BET surface areas were corrected by subtracting the percentage of Au obtained through TGA analysis (Figure 6-10e). Interestingly, the sample with the lower amount of Au (1 wt%, AuB(1)@PCN-224) showed nearly the same BET surface area as PCN-224-w, indicating minimal impact on porosity.

However, as the amount of Au increased decreasing the thickness of the shell, the BET surface areas decreased. We speculatively correlate this reduction to the presence of PEG molecules which can fill the pores in the Au-PCN-224 interface (i.e., Au-S-PEG-PCN-224),[248] thereby increasingly affecting the accessible surface area for gas adsorption as the MOF thickness decreases (Table 6-2).

Table 6-2. BET surface area and percentage of Au in PCN-224 and NCs.

Sample	BET surface area (cm^3/g)	% Au	Corrected BET surface area (cm^3/g)
PCN-224-w	2647	-	-
PCN-224-p	1377	-	-
AuB(1)@PCN-224	2598	1.00	2625
AuB(5)@PCN-224	1989	12.02	2261
AuB(10)@PCN-224	1425	21.26	1810

6.2.2. Effect of shell thickness in photoluminescent properties

Aiming to systematically evaluate the influence of varying MOF shell thickness on the optical properties of our systems, two additional NCs were prepared, AuB(2)@PCN-224 and AuB(3)@PCN-224, to complete a comprehensive library (Figure 6-11a-e for AuBipy 1, 2 ,3, 5 and 10 nM respectively). For these two new samples, the amount of starting PEGylated AuBipy during the synthesis process was fixed at 2 nM and 3 nM, respectively. The produced NCs present a highly homogeneous core@shell structure in which the AuBipy is centered at the NCs. Therefore, we can assume considering the geometric feature of the NCs that bipyramids are coated with a nanoMOF PCN-224 shell of ca. 138 nm, 112 nm, 108 nm, 80 nm and 69 nm, for AuB(1)@PCN-224, AuB(2)@PCN-224, AuB(3)@PCN-224; AuB(5)@PCN-224 and AuB(1)@PCN-224, respectively, as measured from the SEM images.

To make easier the rationalization of the results (displayed in Figure 6-11f-g), the concentrations of the NCs were systematically adjusted in order to provide the same absorption value at the used excitation wavelength (420 nm or 515 nm, alternatively).

The emission profile of PCN-224-w closely resembles that of the porphyrinic precursor (TCPP), exhibiting two emission bands at 650 nm and 720 nm. The presence of AuBipy within the core of the particles NCs does not alter the emission profile (Figure 6-11f-g and Figure 6-12), which is also supported by the superimposable excitation spectra of PCN-224 (Figure 6-13). However, it significantly affects the photoluminescence (PL) intensity of the samples. Notably, this effect is dependent on the excitation wavelength used. Excitation at 420 nm (Figure 6-11f), which lies outside the main absorption range of the AuBipy core (500-850 nm, Figure 6-4 and Figure 6-14), leads to significant PL quenching in the NCs, albeit with slight variations among them. Conversely, when an excitation wavelength in resonance with the AuBipy plasmon is employed (515 nm, Figure 6-11g), a clear decreasing trend of PL intensity from AuB(1)@PCN-224 to AuB(10)@PCN-224 is observed (Table 6-3).

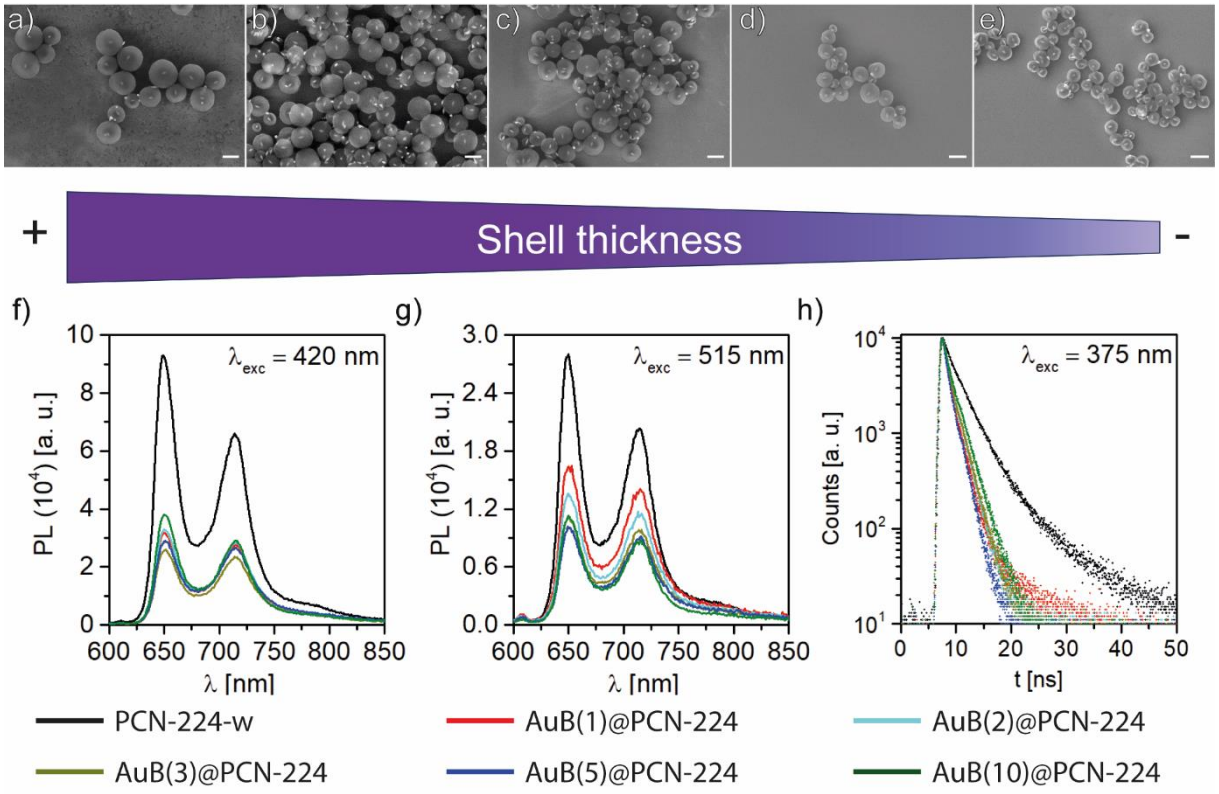

Figure 6-11. a-e) SEM Images of AuB@PCN-224 NCs using 1, 2, 3, 5 and 10 nM AuBipy concentration respectively, showing a decrease in the sell thickness. Corrected PL emission spectra of PCN-224 NPs and the NCs by exciting the samples at f) 420 nm; g) 515 nm and h) time-correlated single photon counting decay kinetics (excitation at 375 nm).

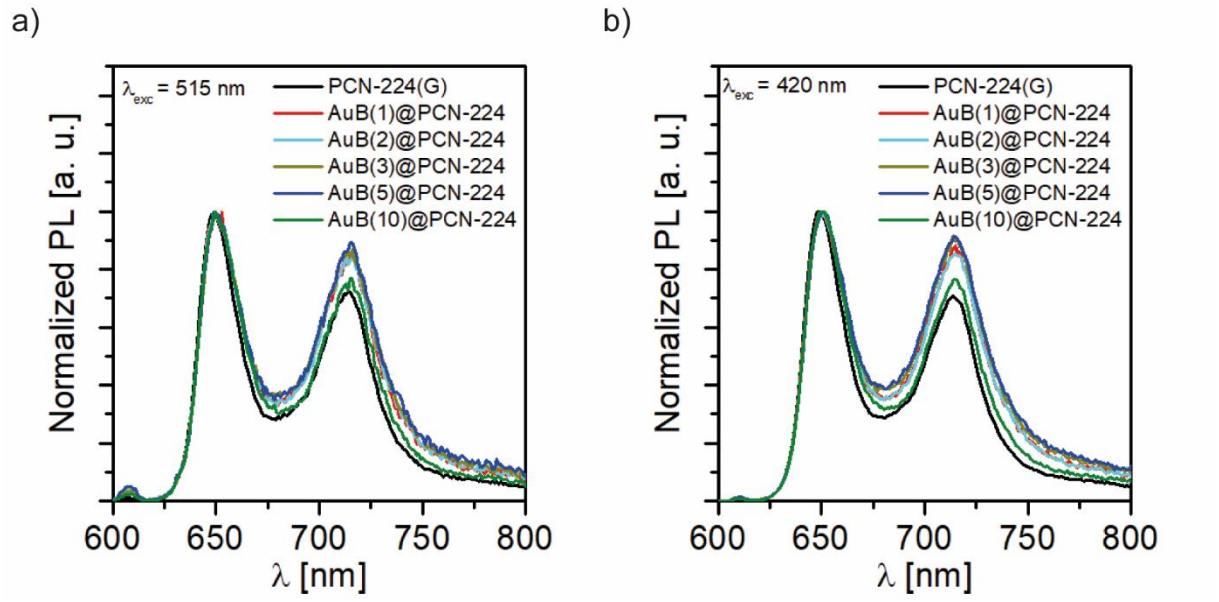

Figure 6-12. Normalized photoluminescence spectra of PCN-224-w and AuB@PCN-224 NCs at excitation wavelengths of a) 515 nm and b) 420 nm.

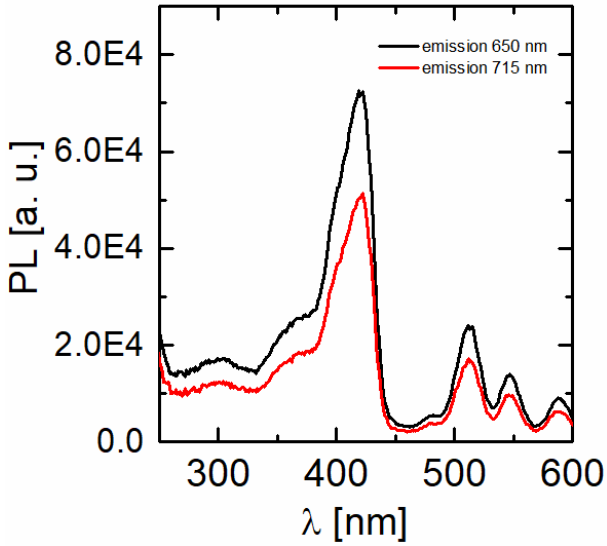

Figure 6-13. Excitation spectrum of PCN-224 nanoMOFs for 650 and 715 nm emission.

Table 6-3. PL quenching values for NCs at different excitation wavelengths.

Sample	**λ_{exc} = 420 nm**	**λ_{exc} = 515 nm**
	PL quenching (%)	**PL quenching (%)**
PCN-224-w	-	-
AuB(1)@PCN-224	57.79	28.78
AuB(2)@PCN-224	56.17	40.53
AuB(3)@PCN-224	63.56	49.44
AuB(5)@PCN-224	58.36	52.79
AuB(10)@PCN-224	54.92	55.40

The pathways affecting the PL of a system can be various, like intersystem transitions, energy transfer, and thermal radiation, among others. Among these mechanisms, Förster resonance energy transfer (FRET) and nanosurface energy transfer (NSET) are recognized as relevant theories explaining fluorescence quenching by gold nanomaterials.[351,352] However, due to the complexity of PCN-224 system, it is important to acknowledge that other energetic radiationless processes can be affected by the presence of gold nanomaterials, such as the intersystem crossing yield or the energy transfer to molecular oxygen to produce photoinduced reactive oxygen species.[353–355]

Nevertheless, to definitively attribute the observed PL quenching to the presence of AuBipy, time-resolved analysis was performed. Through time-correlated single photon

counting (TCSPC) technique, the PL decay kinetics of PCN-224 nanoMOFs and the relative NCs were acquired by exciting the samples at 375 nm (Figure 6-11h). Based on the data depicted in Figure 3h, it is unlikely to detect a substantial disparity among the NCs by using this excitation wavelength. However, a distinct variation is clearly observed when compared to PCN-224 nanoMOFs.

The recorded decay times were analyzed using a multiexponential function (Equation 13), which indicates the existence of multiple luminescent components within our systems (Table 6-4). The decay times of PCN-224 nanoMOFs align with the literature data.[356–358] However, with the introduction of AuBipy, a notable reduction in the decay times (τ) is observed, with the average decay time halved. Furthermore, when analyzing the luminescent components individually, additional observations can be made. The longer component of PCN-224 (6.9 ns) is in very good agreement with the value reported for PCN-224 in anoxic environment.[357] Considering that the measurements are conducted in an air-saturated condition, this longer component can be assigned to the porphyrin molecules located within the core of PCN-224 particles, which are shielded from external oxygen, resulting in their longer decay times. Nevertheless, the external porphyrin molecules and the ones within the porous channels undergo effective quenching process, causing a reduction in the decay time to approximately 2.6 ns.

$$A + B_1 \exp\left(-t/\tau_1\right) + B_2 \exp\left(-t/\tau_2\right) + B_3 \exp\left(-t/\tau_3\right) \qquad \text{(Eq. 13)}$$

Table 6-4. Decay times values of PCN-224 and AuB@PCN-224 systems and coefficients values for multiexponential function (Eq. 13).

Sample	A	B_1	τ_1(ns)	B_2	τ_2(ns)	B_3	τ_3(ns)	χ^2
PCN-224-w	8.290	0.1015	2.65	0.0130	6.93	-	-	1.25
		74.96 %		25.04%		-		
AuB(1)@PCN-224	3.967	0.0215	0.44	0.0370	1.44	0.0004	7.54	1.18
		14.39 %		80.91 %		4.70 %		
AuB(2)@PCN-224	5.802	0.0247	0.80	0.0279	1.84	-	-	1.02
		27.77 %		72.23 %		-		
AuB(3)@PCN-224	4.134	0.0241	0.69	0.0294	1.88	-	-	1.10
		23.23 %		76.77 %		-		
AuB(5)@PCN-224	4.296	0.0307	0.62	0.0279	1.55	-	-	1.21
		30.68 %		69.32 %		-		
AuB(10)@PCN-224	4.415	0.0184	0.70	0.0324	2.09	-	-	1.09
		16.13 %		83.87 %				

Considering the relative positions of AuBipy and the PCN-224 network, it can be reasonably assumed that the molecules in close proximity to the gold surface, thus within the core, experience a more pronounced quenching effect. In the case of AuB(1)@PCN-224, with a thicker PCN-224 shell, the PCN network directly coordinated to the gold surface undergoes substantial PL quenching, even if the higher shell thickness allows the longer component to still exist, albeit with a significant lower percentage (5%, Table 6-4). Similar observations and

conclusions can be drawn for the other NCs, despite the absence of a longer decay component, which is likely due to the thinner PCN shell in those cases.

These findings collectively illustrate the direct influence of AuBipy on the photophysical behavior of the PCN-224, playing a role in the PL processes; moreover, by manipulating the thickness of the PCN-224 shell (Table 6-1), different outcomes can be achieved in terms of the observed photophysical behavior.

6.2.3. Heating properties of AuB@PCN-224@PEG NCs under 808 nm laser irradiation

Prior to investigating the photothermal characteristics of the plasmonic AuB@PCN-224 NCs, the NCs were functionalized with mPEG-PO_3 (Figure 6-14). This functionalization was verified with FTIR, where characteristic stretching vibrations of -CH_2- at 2869 cm^{-1}, -P-O at 1098 cm^{-1}, and a broad band corresponding to -O-H at 3433 cm^{-1} were observed (Figure 6-15).[170] The purpose of this functionalization was to enhance the colloidal stability of the NCs to prevent nanoparticle aggregation, which could be caused by increased Brownian motion during heating. As an initial step, the samples were transferred from methanol (MeOH) to water, resulting in a blue shift in the LSPR due to the change in the dielectric environment (Figure 6-16a). Furthermore, the hydrodynamic size of the NCs according with DLS and NTA results, increased compared to the unmodified system (Figure 6-17 and Table 6-5), and their ζ-potential shifted from positive to negative values, as expected (Figure 6-18). This shift was attributed to the presence of Zr atoms on the surface that neutralize their positive charge with phosphate groups and, deprotonated phosphate groups contribute to decrease the ζ-potential due to the negative charged O atoms, confirming the successful PEGylation. Notably, the LSPR remained consistent when compared to the samples in water (Figure 6-16b).

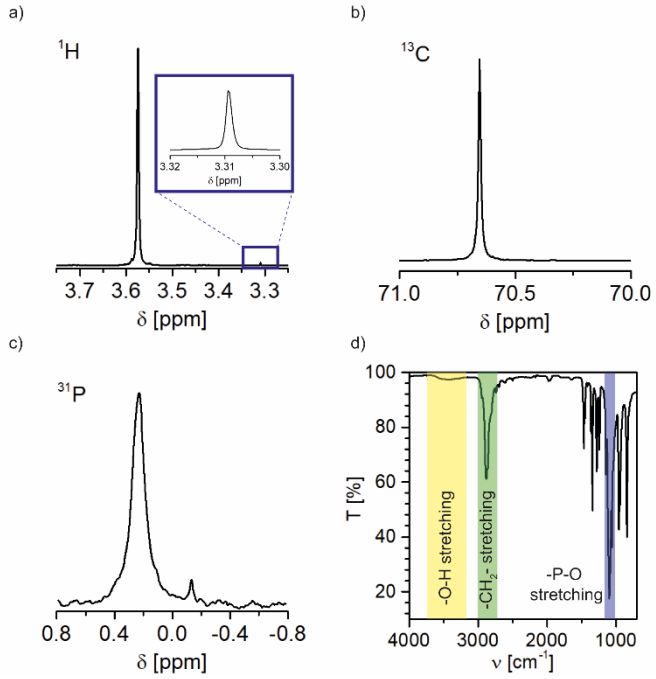

Figure 6-14. mPEG-PO_3 characterization by NMR of a) ^{1}H, b) ^{13}C and c) ^{31}P and d) FT-IR showing the main vibrations. NMR assignment of mPEG-PO_3, 1H NMR (CDCl3, 500 MHz) δ 3.31 (s, 3H, -OCH3), 3.57 (s, 466H, -CH2CH2-O-). 13C NMR (CDCl3, 125 MHz) δ 70.65 (-CH2CH2-O-). 31P NMR (CDCl3, 202 MHz) δ 0.23 (-PO3).

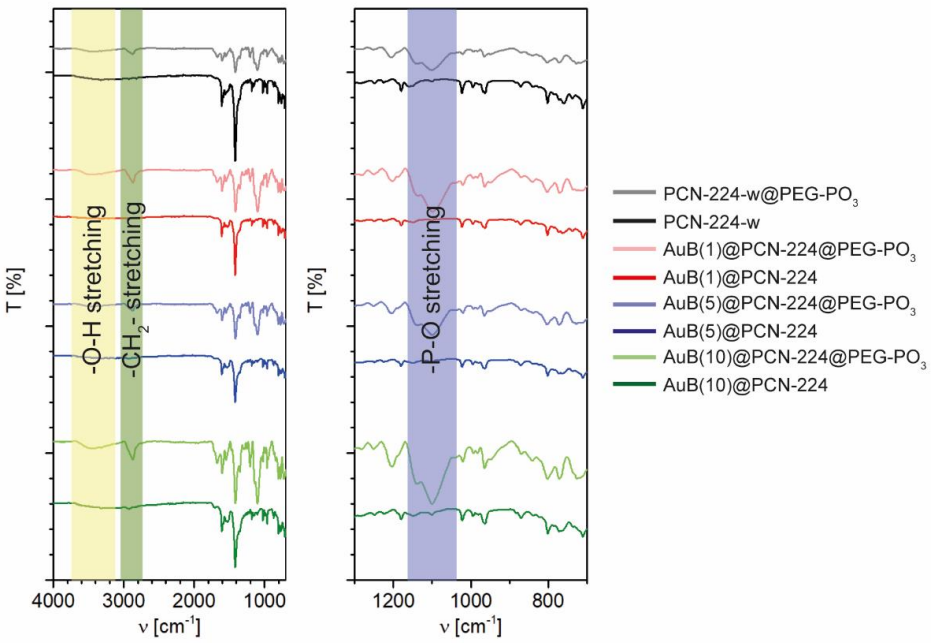

Figure 6-15. FTIR spectra of PCN-224-w and AuB@PCN-224 PEGylated and non-PEGylated with the stretching bands of -OH, -CH_2- and -P-O highlighted.

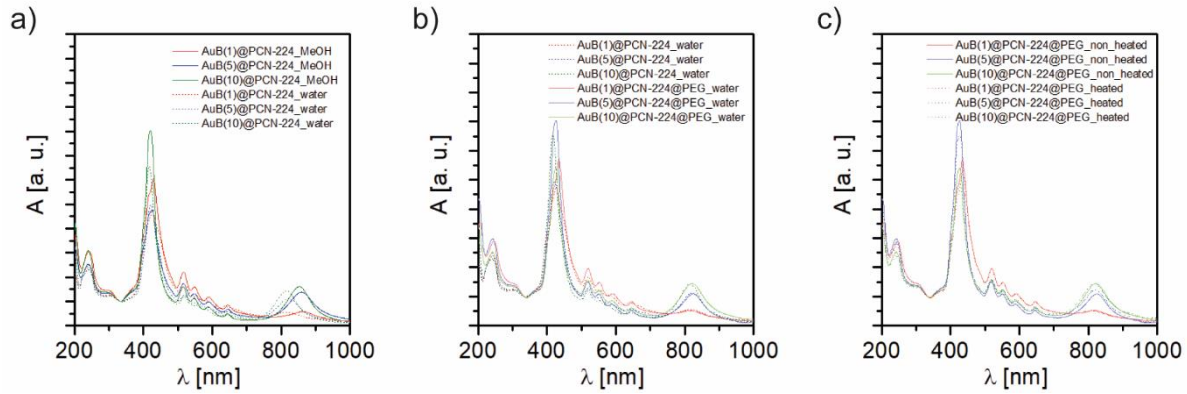

Figure 6-16. UV-Vis spectra of a) AuB@PCN-224 NCs transferred from MeOH to water, b) before and after PEGylation in water and c) AuB@PCN-224@PEG NCs before and after 808 nm laser irradiation in water.

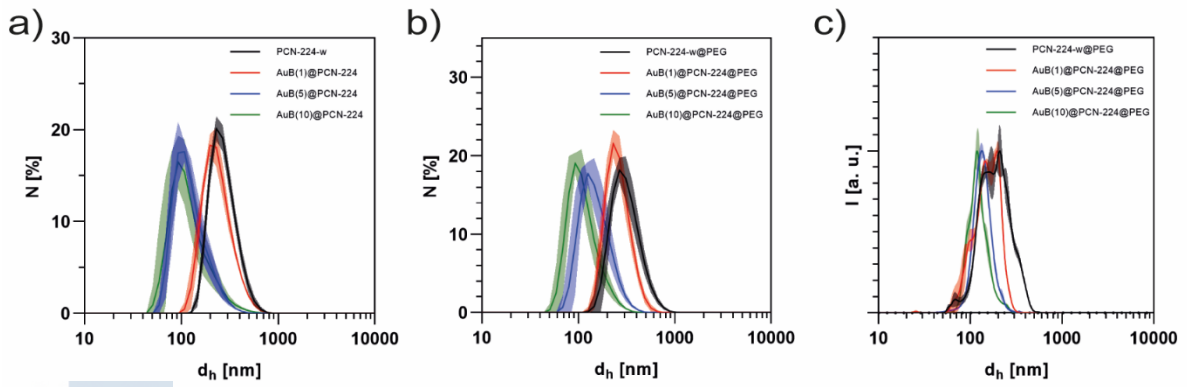

Figure 6-17. Hydrodynamic diameter distribution of a) PCN-224-w and AuB@PCN-224 measured by DLS; and PCN-224-w@PEG and AuB@PCN-224@PEG measured by b) DLS and c) NTA.

Table 6-5. Diameter values of PCN-224 and AuB@PCN-224 PEGylated and non-PEGylated by NTA and DLS in water.

Sample	NTA size (nm)	d_h, N (nm)		PdI	
		w/o PEG	@PEG	w/o PEG	@PEG
PCN-224-w	228.2±83.8	278.7±9.7	321.2±22.9	0.12±0.04	0.11±0.02
AuB(1)@PCN-224	166.9±53.0	245.8±6.8	264.5±10.2	0.16±0.02	0.15±0.06
AuB(5)@PCN-224	148.1±39.4	129.1±11.7	155.0±15.8	0.15±0.02	0.19±0.03
AuB(10)@PCN-224	135.4±42.0	129.3±18.0	116.1±12.1	0.24±0.03	0.28±0.02

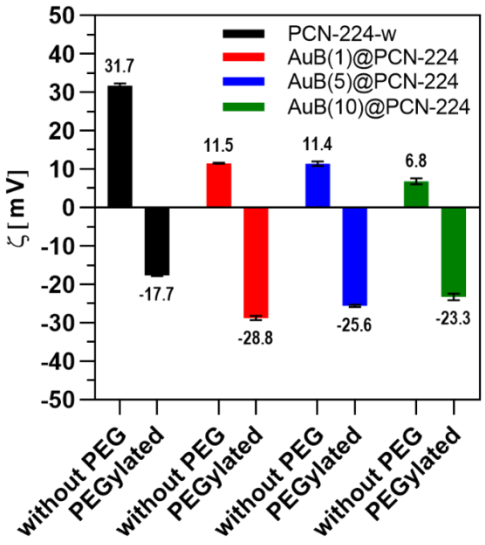

Figure 6-18. ζ-potential values of PCN-224-w and AuB@PCN-224 NCs before and after being PEGylated in water.

Plasmonic NPs are widely known to exhibit photothermal properties. To investigate these properties in the NCs, the samples were exposed to irradiation with an irradiance of 10 W/cm^2 using the irradiation setup shown in Figure 6-19. This irradiance level was chosen because it induces a temperature increase in water of less than 8 °C in the time span of 1 minute (Figure 6-20). The NCs were irradiated until reaching the boiling point (~95 °C) at three different concentrations: 50, 25, and 10 pM (Figure 6-21a-c). The results demonstrated that the time required to reach the boiling point of water (Figure 6-21d) decreased when the thickness of the NCs shell decrease as is schematically depicted in Figure 6-21f. Interestingly, the differences between AuB(10)@PCN-224@PEG and AuB(5)@PCN-224@PEG are less pronounced at a high concentration of 50 pM, while these differences become more significant as the concentration decreases. This can be attributed to the slight disparity in size between these two NCs, with AuB(10)@PCN-224@PEG and AuB(5)@PCN-224@PEG having sizes of 138 nm and 160 nm, respectively. On the other hand, AuB(1)@PCN-224@PEG is nearly twice as large, measuring 276 nm (Tables 6-1 and 6-5). Differences into the heat generation of each of these NCs is clearly observed in Figure 4d which illustrates the time (s) required for reach water boiling temperature.

USC UNIVERSIDADE DE SANTIAGO DE COMPOSTELA

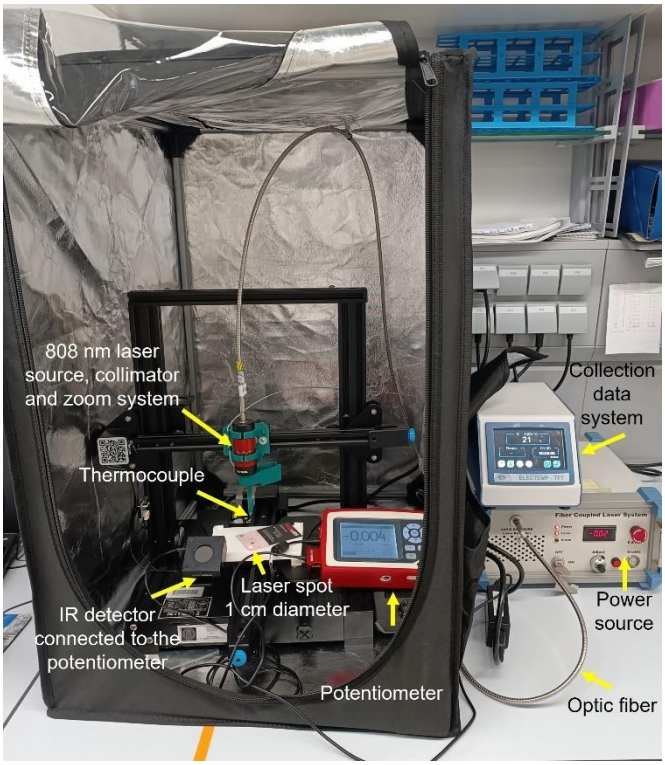

Figure 6-19. Laser irradiation setup used to measure heating curves at different irradiances.

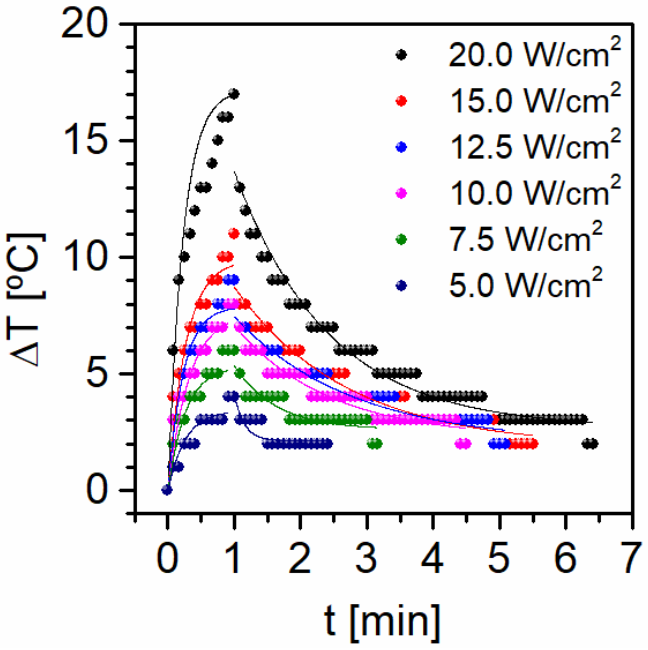

Figure 6-20. Heating curves of water at different irradiances.

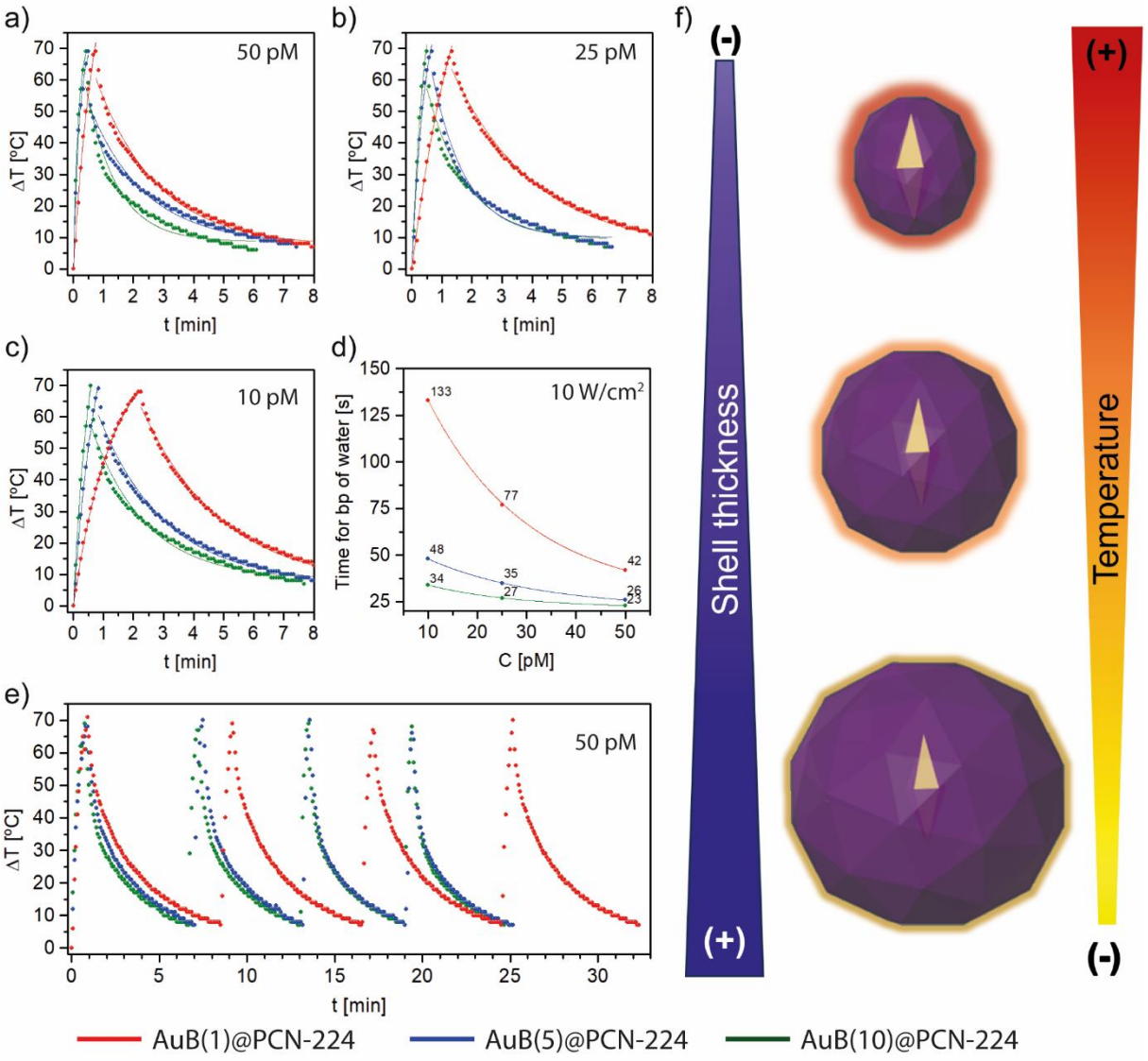

Figure 6-21. a-c) Heating curves of AuB@PCN-224@PEG NCs at different concentrations, d) graph of concentration dependence of the NCs to reach the boiling point of water, e) heating curve of the NCs applying 4 cycles, and f) graph of an inverse temperature dependence with the thickness of the MOF shell in the NCs.

All the NCs at a concentration of 50 pM were exposed to heating cycles, wherein the same behavior of shell-thickness versus the rate of heating the medium was observed. This behavior was consistently replicated in at least four cycles (Figure 6-21e), with each cycle reaching the boiling point of water. Furthermore, the times required to reach the boiling point of water (23, 26, and 42 s for AuB@PCN-224@PEG (10), (5) and (1), respectively) were virtually identical, indicating that the PCN-224 shell prevents the reshaping and/or etching of the AuB@PCN-224@PEG when exposed to high temperatures conserving the characteristic LSPR band around 810 nm confirms that there is no alteration in the plasmonic properties (Figure 6-16c). The confined space within the MOF shell effectively restricts these undesirable structural changes which were clearly observed with the uncoated AuBipy (Figure 6-22).

Finally, cooling cycles were monitored and differences in the time to reach 30 °C were observed Figure 4e), i.e., 5.92, 6.08 and 7.58 min for AuB(10)@PCN-224@PEG, AuB(5)@PCN-224@PEG and AuB(1)@PCN-224@PEG, respectively. These differences are

explained due to the heat transfer pathway through a thermal insulator material (Table 6-1), such as a MOF, requires more time to dissipate this heat into the surrounding medium.

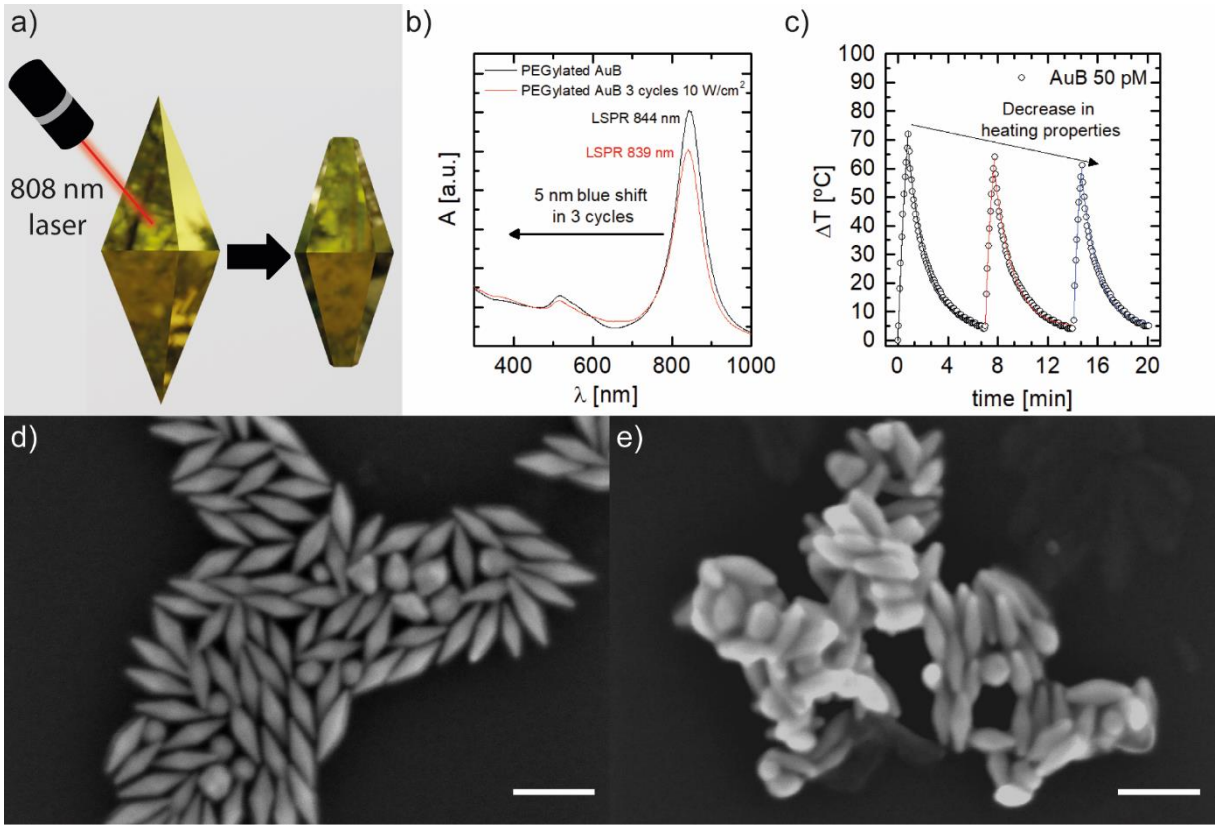

Figure 6-22. a) Schematic representation of AuBipy reshaping under 808 nm laser irradiation, b) UV-Vis spectra after 3 heating cycles at 10 W cm^{-2}, c) heating curve of AuBipy 50 pM at 10 W cm^{-2} after 3 heating cycles, d) PEGylated AuBipy before laser irradiation and e) PEGylated AuBipy after laser irradiation.

6.2.4. Photo-stimulation of AuB(10)@PCN-224@PEG inside living cells

Before the *in vitro* studies, the colloidal stability was studied during 120 hours in different media (water, complete cell media (DMEM) and PBS, Figure 6-23). NCs remained colloidally stable in all cases, being this stability increased upon PEGylation. Then the interaction of the PEGylated nanoMOFs and NCs with cells was analyzed using 2D cell cultures of A549 adenocarcinoma cells. First, cell viability was analyzed by determining the cellular metabolic activity by an MTT assay. This study confirmed the high viability related to the nanoMOFs and the NCs using different concentrations. The concentration used were up to 0.5 nM (corresponding to ca. 50 μg/mL of Zr), which showed no significant toxicity for any sample after 24 h of incubation (Figure 6-24a). These results are in good agreement with previous toxicity tests reported with the PCN family particles. Due to the low cytotoxicity of the Zr, this family of MOFs has a high biocompatibility, as Zr is one of the rare transition metals that are naturally present in the human body (ca. 300 mg of Zr).[359]

USC
UNIVERSIDADE
DE SANTIAGO
DE COMPOSTELA

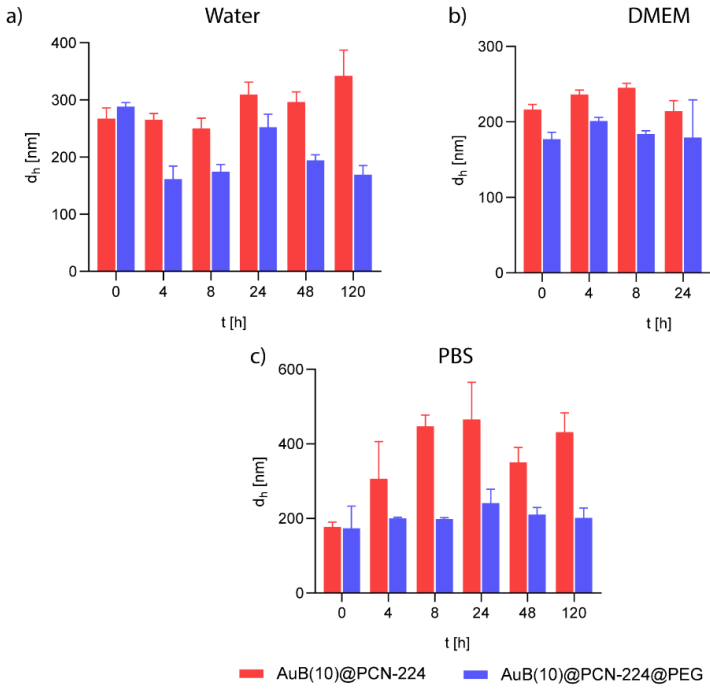

Figure 6-23. Colloidal stability of AuB(10)@PCN-224, PEGylated and non-PEGylated in three different media, a) water, b)DMEM and c)PBS.

In vitro cellular uptake of the samples was also evaluated with flow cytometry using the fluorescence of the PCN-224 porphyrin linker. Particles were exposed to A549 cells at different concentrations for 24 h. Results show an increasing cell uptake with the increment of the concentrations and a clear correlation of the mean fluorescence intensity (MFI) of the different samples related to the thickness of the shell in each case. This way, as the shell for the PCN-224-w@PEG and the AuB(1)@PCN-224@PEG is considerably larger than for the AuB(5)@PCN-224@PEG and AuB(10)@PCN-224@PEG, the MFI resulting from the same particle concentration leads to higher values for the first ones (Figure 6-25). The obtained values were corrected using a correction factor calculated from the fluorescence measurements of each sample in the same conditions employed for the cytometer experiments (Table 6-6). It is possible to appreciate that the tendency changes and the internalization is inversely proportional to the thickness of the shell NCs´ size, indicating that smaller NCs are more efficiently internalized (Figure 6-24b).

Then, the uptake of the AuB(10)@PCN-224@PEG was studied using fluorescence microscopy as this NC was the one with the highest internalization rate. For this, cresyl violet (CV)-loaded NCs were used (Figure 6-24c). CV was selected as cargo for three reasons, (i) to prove the abilities of the NCs as drug nanocarriers, (ii) to provide the nanoMOFs with an additional fluorescence signal and (iii) due to its ability to target functional lysosomes. Epifluorescence microscopy imaging experiments showed the intracellular location of the nanoMOF in the perinuclear region, as expected (Figure 6-26). This intracellular localization indicates a clear colocalization of the CV and the nanoMOFs, confirming that NCs are capable to storage intracellularly the CV. This ability is related with the PEG functionalization which prevents CV unspecific leaking.

USC
UNIVERSIDADE DE SANTIAGO DE COMPOSTELA

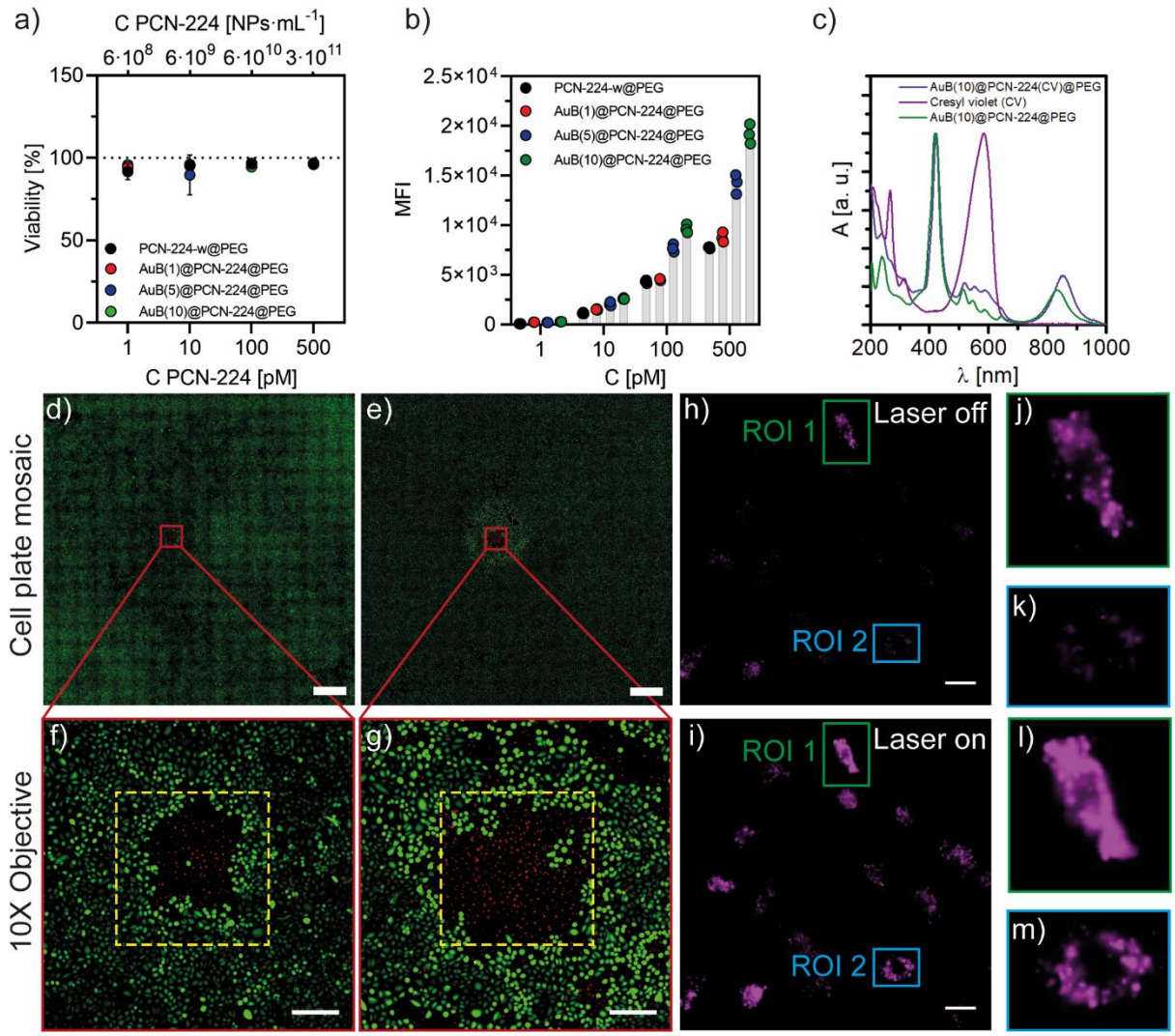

Figure 6-24. a) Cell viability values using MTT viability test, b) corrected cell uptake mean fluorescence intensity (MFI) values of PCN-224-w@PEG and AuB@PCN-224@PEG NCs after 24h of incubation, c) UV-Vis spectra of AuB(10)@PCN-224@PEG loaded with Cresyl Violet (CV). Cell plate mosaic reconstruction of an area of 1 cm^2 before irradiation (d-e) in which a region of interest (inside the red square) after the irradiation with a 405 nm laser (f-g) (dashed yellow line represents the area irradiated with 405 nm laser) for d,f) 2 min and e,g) 5 min. h) Microscopy images before irradiation and i) after irradiation of selected areas. j-k) Specific ROIs before irradiation, and l-m) ROIs before and after irradiation. Scale bars 1 mm for d and e, 200 µm for f and g and 20 µm for h and i

Besides the good internalization and biocompatibility of the PCN-224@PEG NCs, these structures have other interesting characteristics for their use in biomedicine. This is due to two main features: i) the MOF shell can be used for PDT, as the porphyrin linkers of the structure are light-activable photosensitizers (PSs) that can create cytotoxic ROS and cause cell death,[360] and ii) the NCs can serve as a good example of stimuli-responsive DDSs, as the AuBipy cores can get excited by NIR light irradiation generating temperature gradients that lead to the release of an encapsulated cargo in a controlled manner.[122] Here, the abilities of the NCs to explode both behaviors were studied.

First, to study the *in vitro* induced cytotoxicity of the systems acting as PDT agents Figure 5d-g), A549 cells loaded with NCs were irradiated with a 405 nm laser. This excitation

USC UNIVERSIDADE DE SANTIAGO DE COMPOSTELA

wavelength was specifically selected considering the high extinction coefficient of PCN-224 in the range of 400 – 450 nm, where the Soret band is located.

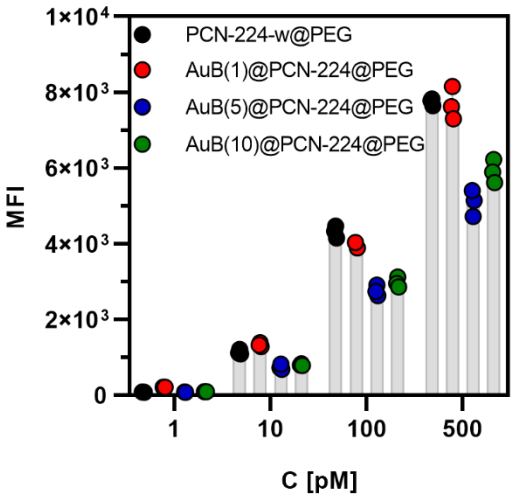

Figure 6-25. Cell uptake mean fluorescence intensity (MFI) values of PCN-224-w@PEG and AuB@PCN-224@PEG NCs after 24h of incubation.

Table 6-6. Correction factors calculated via fluorescence values obtained using a plate reader λ_{exc}=405 nm, λ_{em}=600-660 nm).

Sample	Correction factor
PCN-224-w@PEG	1.00
AuB(1)@PCN-224@PEG	1.14
AuB(5)@PCN-224@PEG	2.79
AuB(10)@PCN-224@PEG	3.25

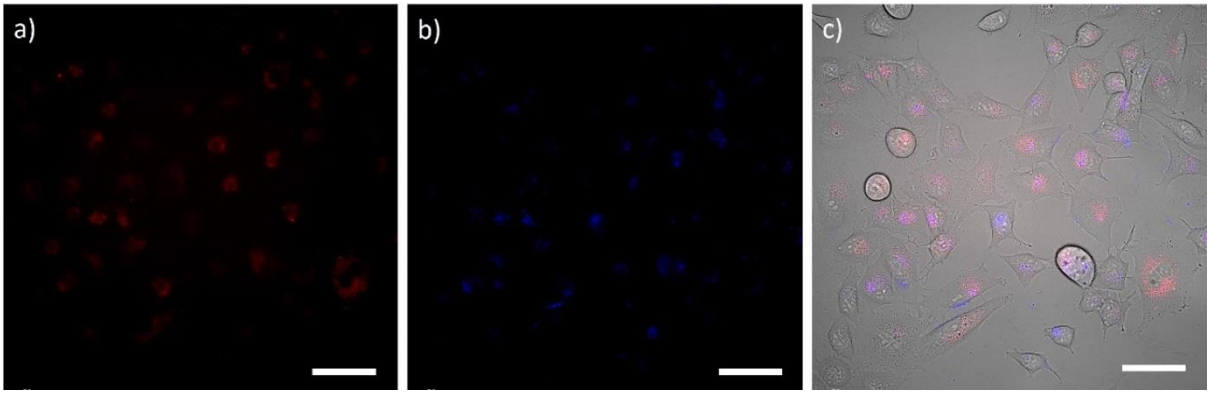

Figure 6-26. Microscopy images of internalized AuB(10)@PCN-224(CV)@PEG NCs by A549 cells a) CV channel, b) PCN-224 channel, c) merged + BF. Scale bars: 20 µm.

Two different irradiation times were tested, i.e., 2 and 5 minutes. Right after the sample irradiation, we performed a live-dead assay employing calcein-AM and propidium iodide as reporters for viable and dead cells, respectively. As shown in Figure 6-24d-e and their

USC DE SANTIAGO DE COMPOSTELA

corresponding magnifications (Figure 6-24f-g), we can clearly see the induced cell death (PI tinction, in red) corresponding to the irradiated area, whereas the rest of the sample presents calcein tinction (green) indicating the viability of the non-irradiated NCs-loaded cells. Furthermore, when control cells without NCs were irradiated using equivalent conditions, the complete sample shows a calcein tinction for both irradiation conditions (Figure 6-27). These results confirm the ability of our porphyrin-based NCs to act as efficient PDT agents when subjected to 405 nm laser irradiation. It is widely recognized that porphyrin molecules have the capacity to generate ROS, including singlet oxygen ($^1O_2$), when exposed to appropriate illumination.[361–363] Specifically, the triplet excited state of porphyrin, achieved through electron promotion from the ground state to the singlet excited state and subsequent intersystem crossing, can transfer its energy to adjacent molecular oxygen, resulting in the formation of $^1O_2$, which induces cell apoptosis.

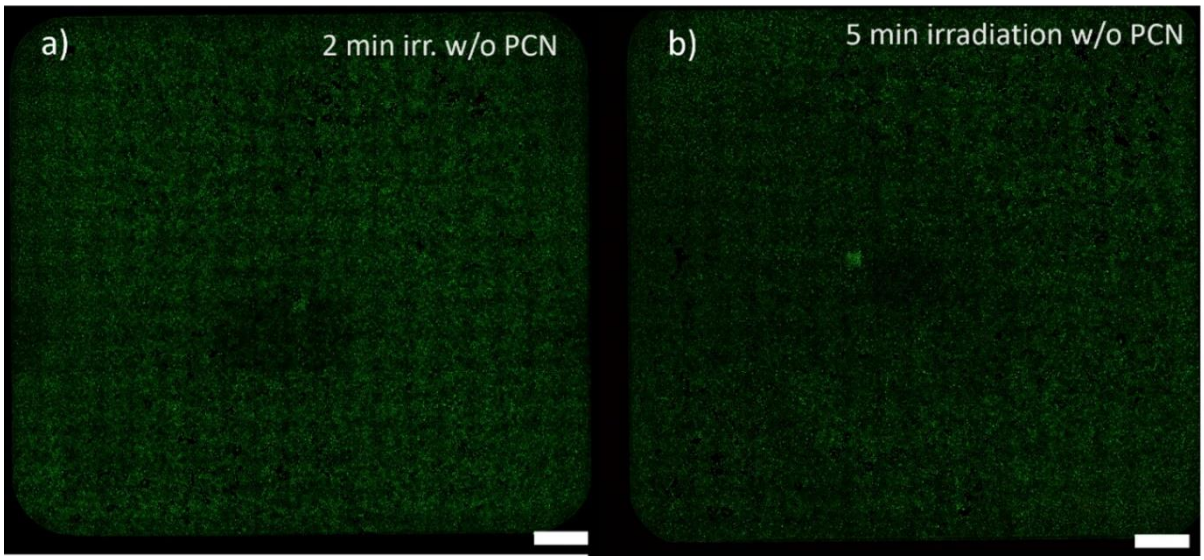

Figure 6-27. Cell plate mosaic of control cells after a) 2 min irradiation and b) 5 min irradiation. Scale bar: 1 mm.

On the other hand, the stimuli-responsive effectivity to release an encapsulated cargo was studied by the excitation with a NIR laser (808 nm) coupled to the fluorescence microscope via a laser scanner, which allow the irradiation with a spatial and temporal control of selected areas (Figure 6-24h-i and Figure 6-28). Like to the previous experiments, A549 cells were incubated with CV-loaded AuB(10)@PCN-224@PEG NCs. As previously mentioned, particles showed accumulation (magenta-colored dots) in the lysosomes. As discussed above, CV remained encapsulated into the NC´s pores even once they are internalized by the cells. After loading the cells with NCs, single cells were selected and irradiated using NIR light to evaluate the induced release of the encapsulated CV, which is evidenced before and after irradiation (Figure 6-24h and 6-24i, respectively). To illustrate this process, two regions of interest containing a single cell (ROI 1 and 2) are shown in magnified images (before and after irradiation in Figure 6-24j-k and 6-24l-m, respectively). These areas were immediately inspected after the irradiation, showing a clear increase in the fluorescence intensity of the CV channel. The CV controlled release is associated by the local increment of the temperature in the surroundings of the AuBipy upon NIR irradiation, leading to a release of the CV encapsulated from the NC´s pores.

USC UNIVERSIDADE DE SANTIAGO DE COMPOSTELA

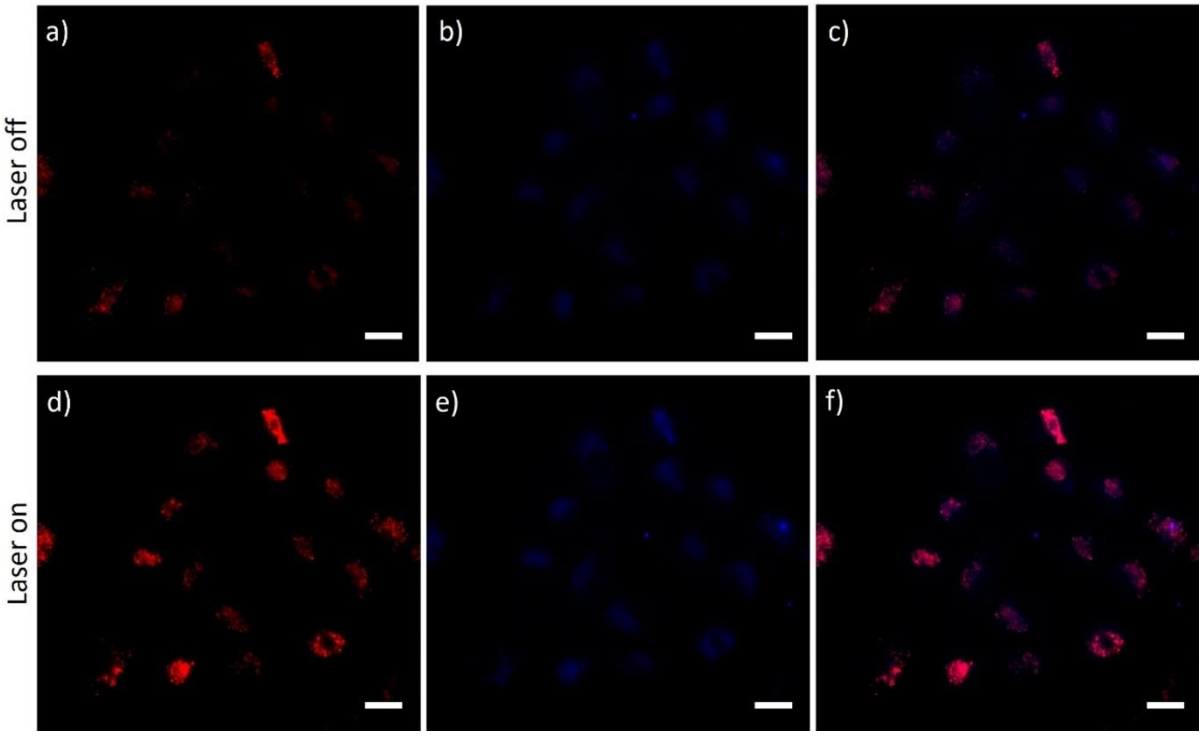

Figure 6-28. Microscopy images of AuB@PCN-224(CV) NCs before irradiation a) CV channel, b) PCN-224 channel, c) merged; and after laser scanner irradiation d) CV channel, e) PCN-224 channel, c) merged. Scale bar: 20 µm.

6.3. Summary and Conclusions of Chapter 6

In this chapter is introduced a facile seed-growth method to produce plasmonic core@shell NCs comprising a single AuBipy core and a PCN-224 shell. This approach enables precise control of the PCN-224 shell thickness by adjusting the AuBipy seed concentration while preserving the AuBipy morphology and properties. The NCs exhibit the photoluminescent features derived from the PCN-224 shell with an influence of the plasmonic core. In general, thinner shells correlate with more pronounced photoluminescent changes. Nevertheless, all the NCs were capable to generate ROS.

Heating dynamics of PEGylated NCs upon NIR light irradiation were analyzed, revealing a direct relationship between shell thickness and their heating/cooling behavior. Specifically, thicker shells result in slower heating and extended cooling.

The good biocompatibility of PEGylated NCs was proven in *in vitro* studies. NCs were readily internalized by cells in a size-manner fashion, i.e., the smaller the NCs (AuB(10)@PCN-224@PEG), the greater the internalization rates. Two applications were explored in vitro. First, they were used as PDT agents. They effectively killed cancer cells exposed to a 405 nm laser, leaving untreated cells unharmed. Second, PEGylated NCs loaded with CV showcased an efficient NIR-induced release of CV through a thermodiffusion mechanism. In conclusion, these NCs stand out as potent tools for integrative therapeutic and imaging applications.

USC
UNIVERSIDADE DE SANTIAGO DE COMPOSTELA

USC
UNIVERSIDADE
DE SANTIAGO
DE COMPOSTELA

7. EFFECT OF CORE SHAPE ON THE HEATING AND PHOTOLUMINESCENT PROPERTIES OF CORE-SHELL PLASMONIC NANOMOFs AND THEIR USE AS SERS SUBSTRATES

USC
UNIVERSIDADE DE SANTIAGO DE COMPOSTELA

USC
UNIVERSIDADE
DE SANTIAGO
DE COMPOSTELA

7.1. Introduction

The synthesis of plasmonic@MOF nanocomposites presents a significant challenge due to the synthetic conditions required for MOF formation,[230–233] as well as the difficulty in modifying the surface of plasmonic nanoparticles to achieve colloidal stability in organic media without compromising their physical and chemical properties. These plasmonic nanoMOFs exhibit unique properties resulting from the combination of the optical characteristics of plasmonic nanoparticles due to their surface plasmons, whose absorption can be tuned across the electromagnetic spectrum and the catalytic properties,[164] high surface areas,[6] defect control,[60,133,138] among others offered by MOFs.

Plasmonic nanoMOFs have a wide range of applications in bionanotechnology, including as drug delivery systems,[238] where they can be loaded with substrates that react internally when stimulated by heat generated from an external source.[237] Additionally, they have been employed in sensing applications, particularly in SERS,[248,364] where the Raman signal is significantly amplified when molecules are adsorbed onto nanostructured metallic surfaces, such as gold or silver nanoparticles.[188] This enhancement occurs through two primary mechanisms: (i) electromagnetic enhancement, in which localized surface plasmons in the metal amplify the electric field near the surface, substantially increasing the Raman scattering; and (ii) chemical enhancement, where direct interactions between the adsorbed molecules and the metallic surface alter the molecular polarizability, further enhancing the Raman signal.

7.2. Results and discussion

7.2.1. Synthesis and Structural Characterization of NU-1000 nanoMOFs and NCs.

Most Zr-based MOFs, whether at the nano, micro, or single-crystal scale, require high temperatures and extended reaction times due to the crystallization process and the formation of strong bonds between ligands and metal centers. However, NU-1000 represents an exception, as it can be synthesized at relatively low temperatures (90 ºC) compared to other MOFs, such as the UiO-family,[17] and within much shorter reaction times (30 minutes).[365] This makes it particularly suitable for the synthesis of plasmonic nanoMOF composites.

Figure 7-1 illustrates the reaction scheme for NU-1000 synthesis, where a typical Zr precursor ($ZrOCl_2$) is used in the presence of the tetratopic linker H_4TBAPy, with AA as a modulator in a water/DMF solvent mixture. NU-1000 exhibits a hexagonal crystal structure featuring both triangular and hexagonal channels.

Figure 7-2 shows SEM images of NU-1000 nanoMOFs, where the morphology of the MOF exhibits a rice-like shape. These particles display polydispersity, with an average length of 378.2 ± 76.1 nm and a width of 145.7 ± 25.8 nm, as further illustrated in Figure 7-3.

The use of PEGylated plasmonic nanoparticles, as described in Chapters 5 and 6, during the synthesis of NU-1000 results in the formation of plasmonic nanoMOFs. Two types of nanoparticles were employed: AuBipy and Au NRs. As previously mentioned, the synthesis of NU-1000 requires a temperature of 90 ºC due to the need for a Zr salt, which provides the energy necessary to form the $Zr_6O_4(OH)_4$ SBU. Additionally, the effect of temperature on the morphology of the plasmonic nanoparticles was investigated, as these changes directly impact

USC DE COMPOSTELA

their physicochemical properties, such as LSPR absorption, heat generation capacity, and reactivity.

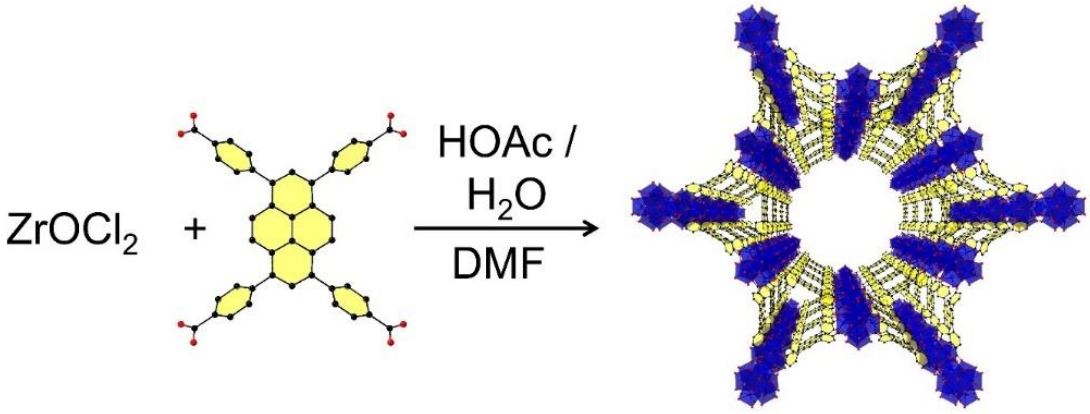

Figure 7-1. Scheme of reaction of NU-1000.

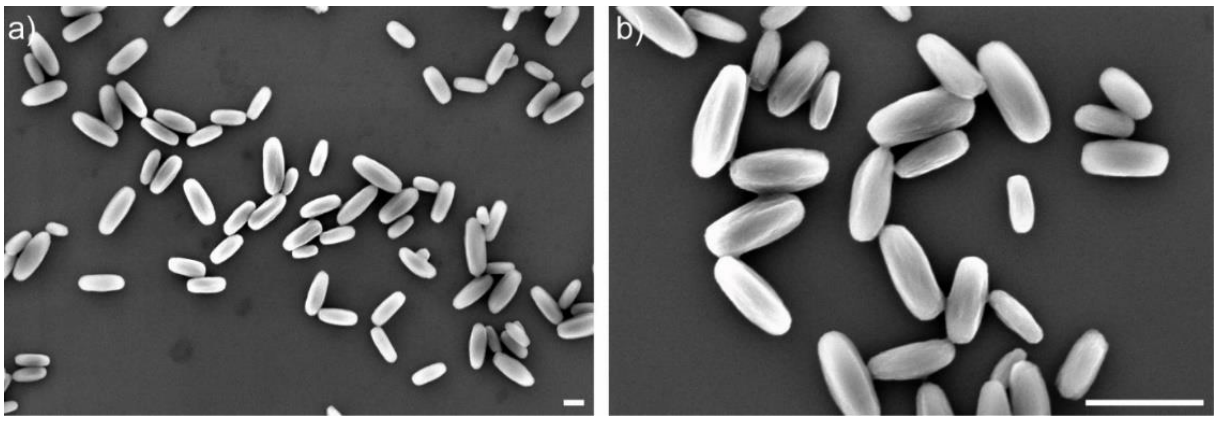

Figure 7-2. SEM images of NU-1000 nanoMOFs at a)50k X and b) 100k X. Scale bars are 200 nm.

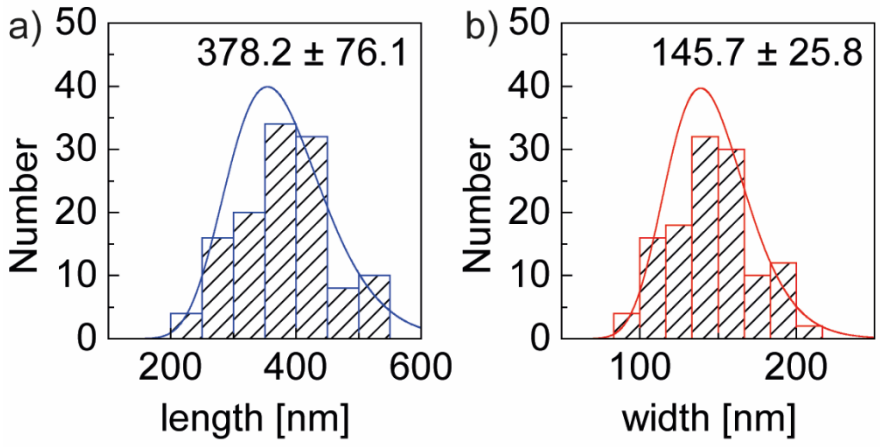

Figure 7-3. Histograms showing the particle size distribution of NU-1000 nanoMOFs: a) length and b) width.

USC UNIVERSIDADE DE SANTIAGO DE COMPOSTELA

Figure 7-4 presents the AuBipy@NU-1000 nanocomposites obtained using different concentrations (2, 5, and 10 nM) of PEGylated AuBipy seeds, while Figure 7-5 shows the nanocomposites synthesized using PEGylated AuNRs (10, 20, and 50 nM). The variation in nanoparticle concentrations is due to the size difference (which is directly proportional to the amount of gold) between AuBipy and Au NRs, as shown in Figures 5-1 and 5-2.

Both figures display SEM images analyzed with different detectors. The top row presents images taken with secondary electrons at an acceleration voltage of 3 kV, and the bottom row shows images captured with backscattered electrons at 20 kV. The secondary electron images reveal the morphology of the particles, which resembles that of pristine NU-1000, but with additional twinned particles attributed to the multiple and different crystallographic orientations of the AuBipy and AuNRs seeds. In contrast, the backscattered electron images highlight the core of the nanocomposites, as these electrons are more sensitive to differences in atomic number (Au > Zr). It is also evident that each nanocomposite has a smaller size compared to pristine NU-1000 (Figures 7-2 and 7-3). Moreover, the seeded growth mechanism is observed here, as in Chapters 5 and 6, where the shell thickness is inversely proportional to the amount of seeds added during synthesis.

Figures 7-6 and 7-7 present the comprehensive characterization of AuBipy@NU-1000 and AuNRs@NU-1000, respectively. Figures 7-6a and 7-7a display the results of DLS analysis, which indicates a reduction in particle size with increasing seed concentration in both cases (Table 7-1). This also leads to a decrease in polydispersity, with values falling below 0.200 in the PdI, compared to the polydispersity observed in pristine NU-1000.

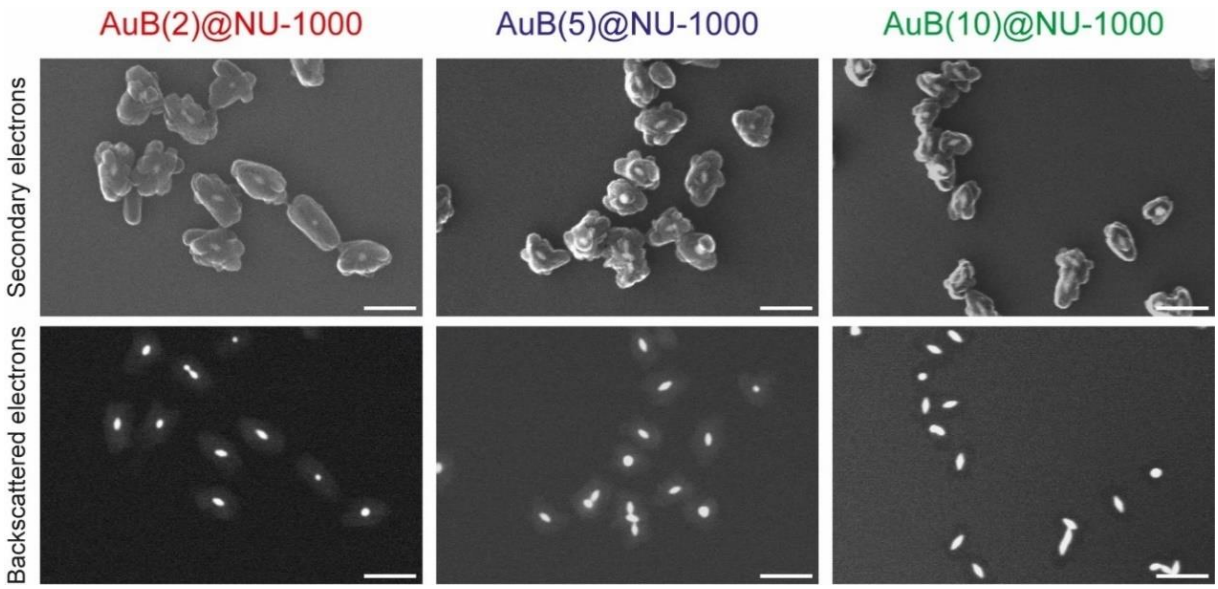

Figure 7-4. SEM images of AuBipy@NU-1000 nanocomposites synthesized with three different concentrations of PEGylated AuBipy (2, 5, and 10 nM) and analyzed using both secondary and backscattered electron imaging. Scale bars are 200 nm.

USC UNIVERSIDADE DE SANTIAGO DE COMPOSTELA

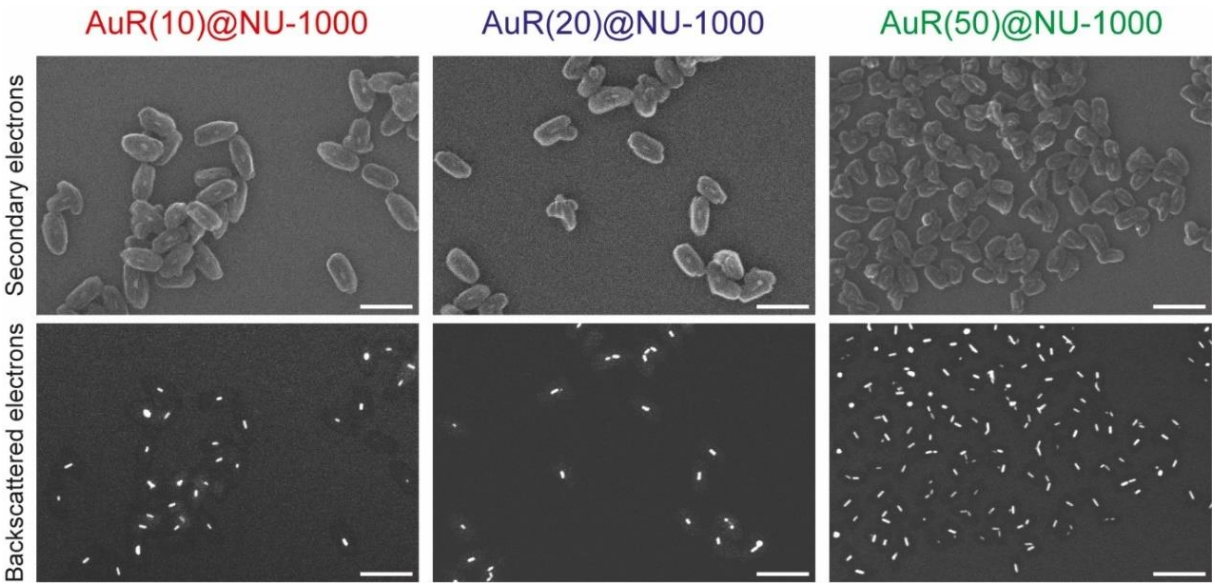

Figure 7-5. SEM images of AuNRs@NU-1000 nanocomposites synthesized with three different concentrations of PEGylated AuNRs (10, 20, and 50 nM) and analyzed using both secondary and backscattered electron imaging. Scale bars are 200 nm.

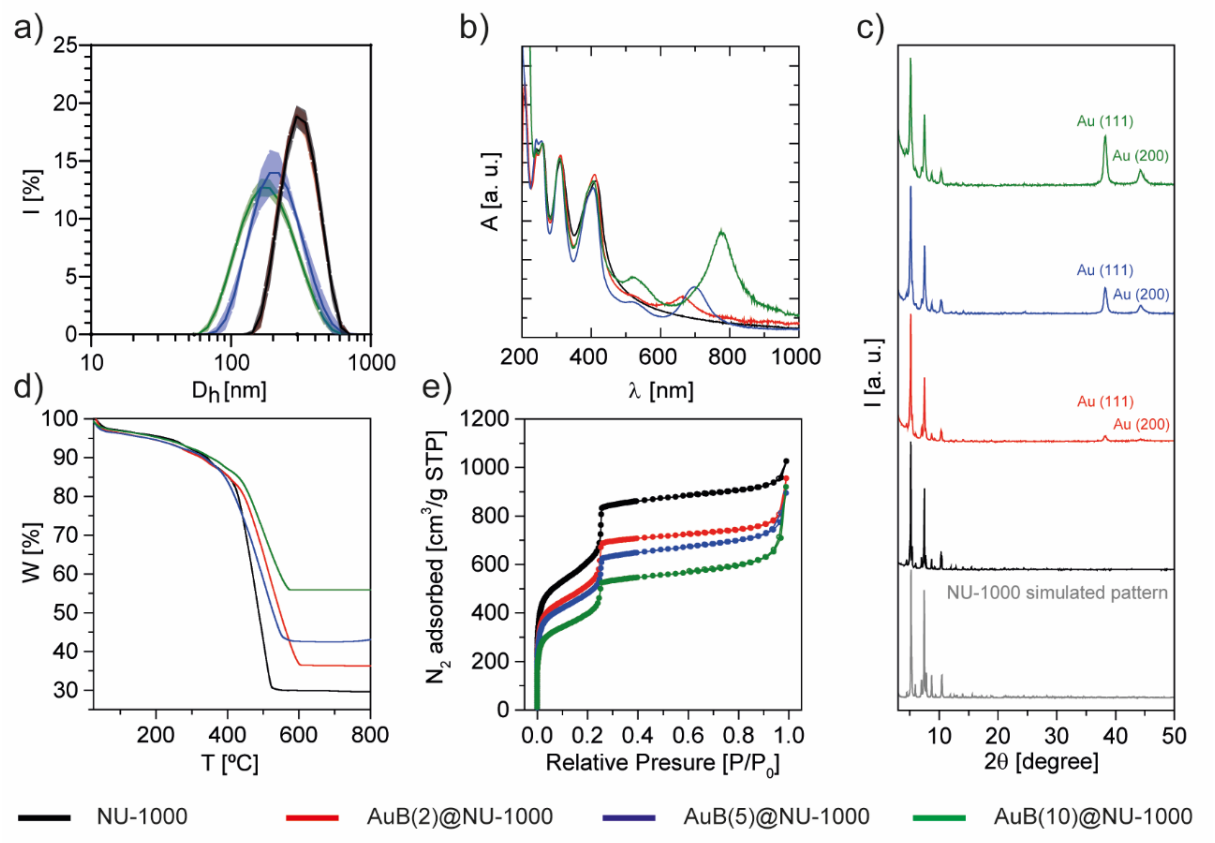

Figure 7-6. Characterization of AuBipy@NU-1000 nanocomposites. DLS analysis, UV-Vis spectra, c) PXRD patterns, d) TGA analysis and e) N_2 adsorption isotherms.

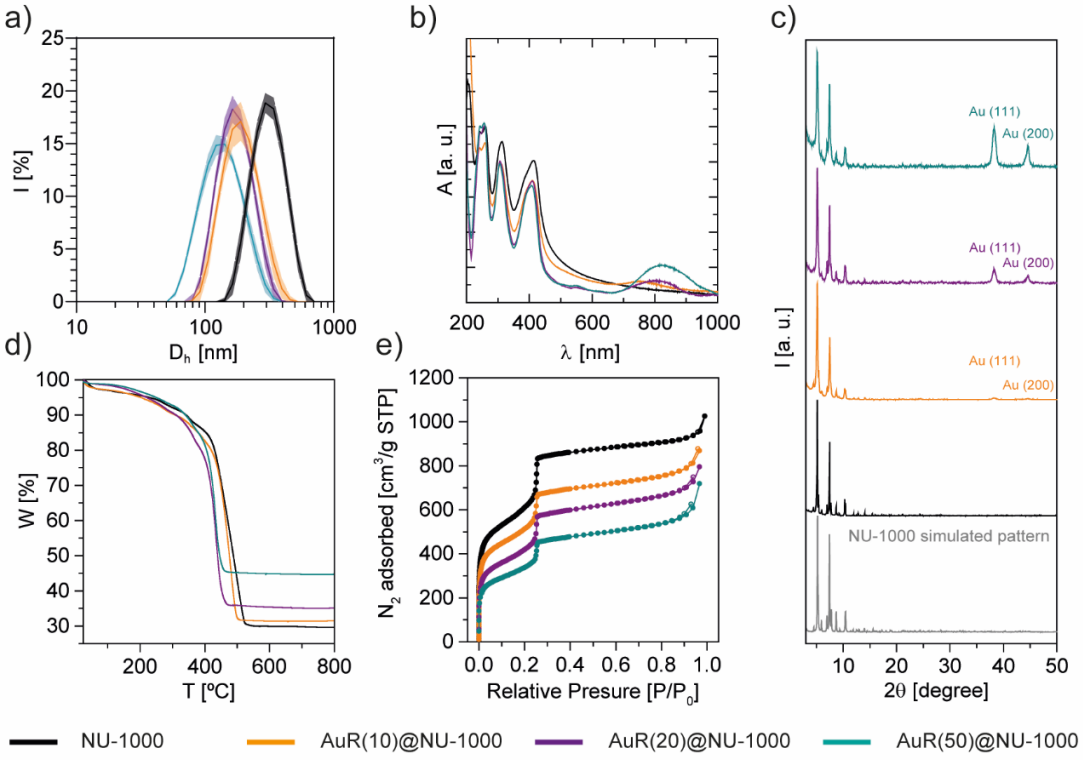

Figure 7-7. Characterization of AuNRs@NU-1000 nanocomposites. DLS analysis, UV-Vis spectra, c) PXRD patterns, d) TGA analysis and e) N_2 adsorption isotherms.

Table 7-1. Hydrodynamic diameter of AuBipy and AuNRs nanocomposites in intensity and number with PdI.

Sample	Intensity size (nm)	Number size (nm)	PdI
NU-1000	335.5 ± 9.9	262.5 ± 11.9	0.329
AuB (2)@NU-1000	320.2 ± 6.0	263.0 ± 9.1	0.245
AuB(5)@NU-1000	227.2 ± 8.9	139.6 ± 14.9	0.145
AuB(10)@NU-1000	198.0 ± 5.0	104.8 ± 6.8	0.164
AuR(10)@NU-1000	198.4 ± 5.9	142.6 ± 8.7	0.152
AuR(20)@NU-1000	178.5 ± 3.8	131.9 ± 3.1	0.132
AuR(50nM)@NU-1000	144.0 ± 4.8	85.7 ± 2.1	0.150

The UV-Vis spectra shown in Figures 7-6b and 7-7b display the absorption profiles of both types of nanocomposites. Bands at 250, 320, and 410 nm are associated with the π-π* transitions of the H_4TBAPy linker.[366] In the NIR region, the LSPR of AuBipy and AuNRs is observed. A notable blue shift in the LSPR is evident when the concentration of plasmonic nanoparticles is lower. In previous chapters (5 and 6), this blue shift was attributed to the MOF shell thickness; however, in this case, the impact of shell thickness is more pronounced, shifting the LSPR by several hundred nanometers in the case of AuBipy, which is more affected than AuNRs. This shift is not solely attributed to shell thickness but also to the reshaping of the plasmonic nanoparticles when exposed to the MOF synthesis conditions (90 ºC for 30 minutes), as discussed in Chapter 5 (Figures 5-6b and 5-7b).

To further investigate this, SEM images at higher magnifications using both secondary and backscattered electrons were obtained, as shown in Figure 7-8. These images reveal that at the lowest concentration of PEGylated AuBipy (2 nM), significant reshaping occurs, with the bipyramidal particles transforming into an ovoid morphology, causing the LSPR to shift from 800 nm to 650 nm. At a concentration of 5 nM, the particles show a loss of tip sharpness, resulting in an LSPR shift to 700 nm. In contrast, at the highest concentration (10 nM), the particle morphology remains largely intact, demonstrating that the concentration of seeds used during the synthesis of the plasmonic nanocomposites not only affects the shell thickness but also influences the degree of morphological reshaping of the core particles.

To corroborate the reshaping of AuBipy, 3D tomography with *in situ* heating at 90 ºC was performed.[367] At 90 ºC, deformations occur relatively slowly, and changes in the internal nanoparticle morphology are subtle. Additionally, the plasmonic response becomes noticeable after only 10 minutes, which is attributed to the fact that, during conventional heating, the nanoparticles are surrounded by solvent that transfers heat through conduction and convection, whereas in the *in situ* experiment, heat transfer occurs exclusively through radiation. Figure 7-9 shows the tomography of the same AuBipy nanoparticle at different time points, highlighting in red the regions where volume was lost and in blue where volume was gained, confirming the reshaping even in vacuum. While this reshaping is significantly less pronounced than in solution-based heating, it provides insights into the impact of nanoparticle concentration on the final plasmonic response of the nanocomposite.

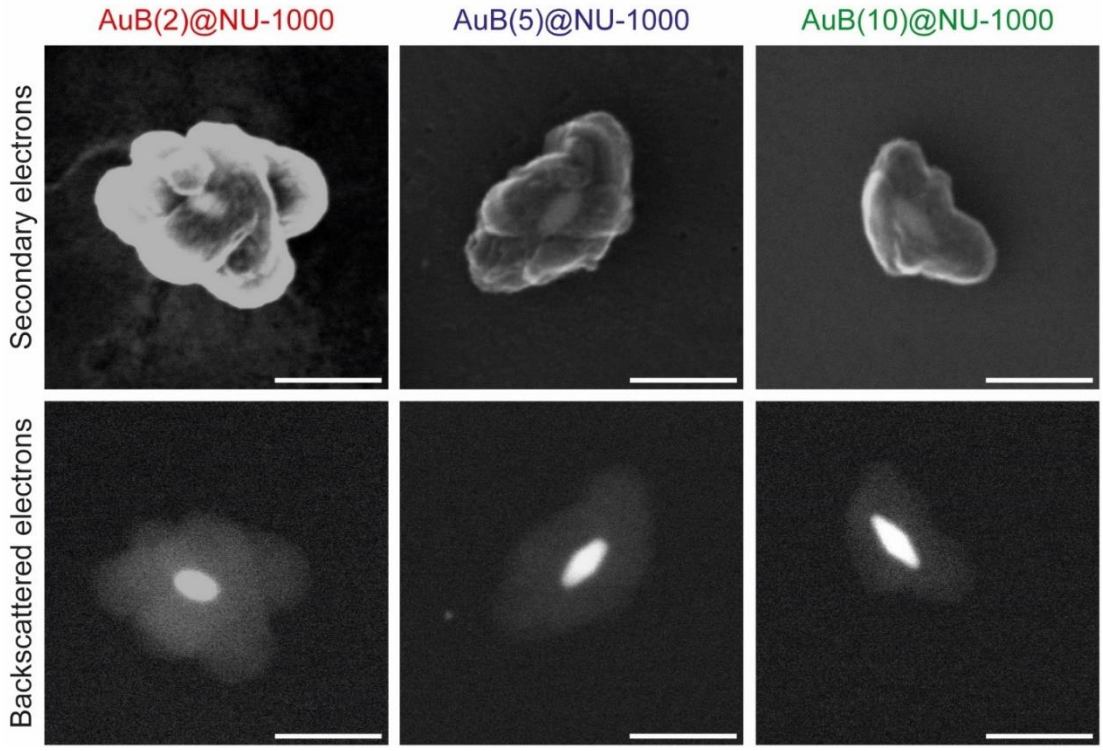

Figure 7-8. SEM images of AuBipy@NU-1000 nanocomposites synthesized with three different concentrations of PEGylated AuBipy (2, 5, and 10 nM) and analyzed using both secondary and backscattered electron imaging at 600k X magnifications. Scale bars are 100 nm.

USC UNIVERSIDADE DE SANTIAGO DE COMPOSTELA

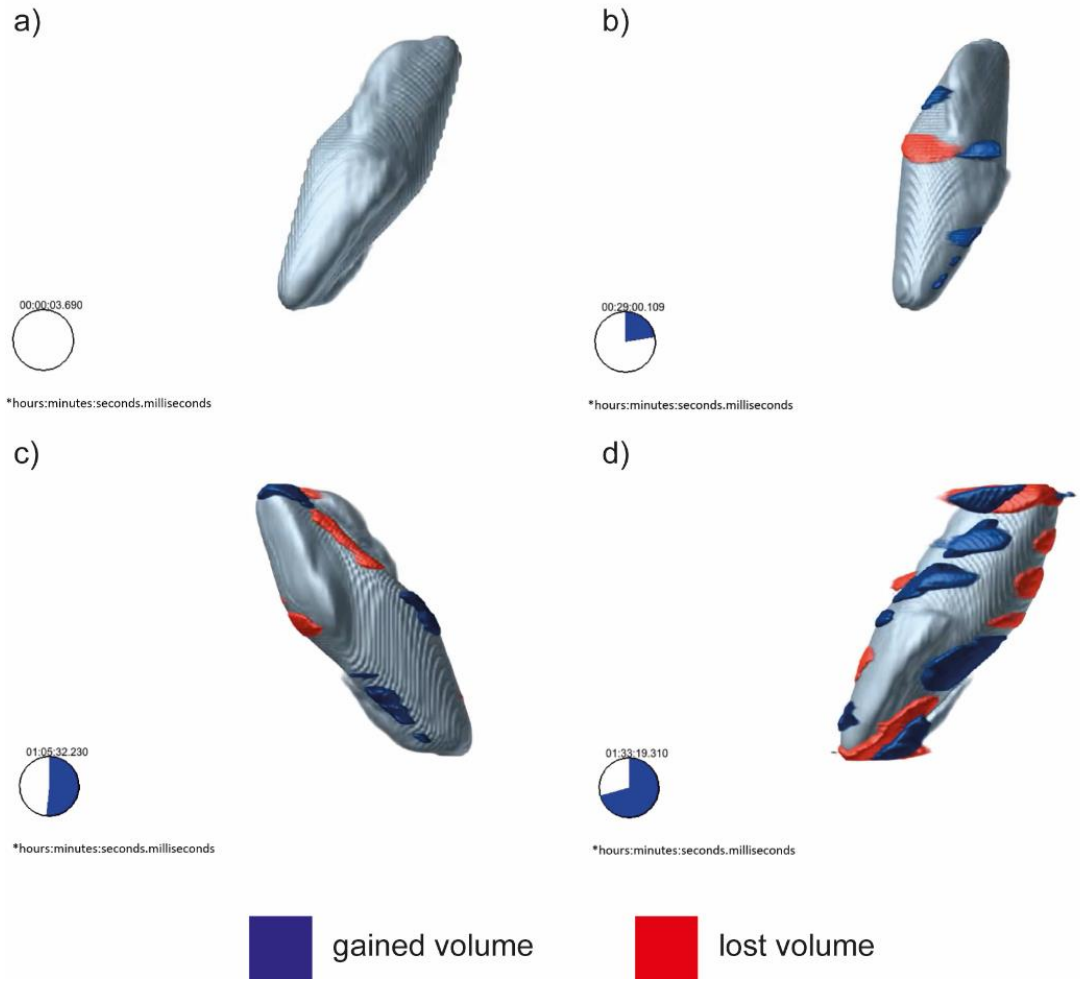

Figure 7-9. 3D tomography with *in situ* heating at 90 ºC at time intervals of a) 0 min, b) 30 min, c) 60 min, and d) 90 min.

The PXRD diffractograms for both systems (Figures 7-6c and 7-7c) align with the simulated pattern of NU-1000 in a hexagonal system. Additionally, an increase in the intensity of the first two Au reflections is observed with increasing nanoparticle concentration at 38.2º and 44.4º two theta, corresponding to the (111) and (200) crystallographic planes, respectively. Figure 7-10 presents the Pawley refinement of NU-1000, confirming its crystal structure with space group P6/mmm and unit cell parameters a = 39.5486 Å and c = 16.3391 Å, without evidence of its polymorph NU-901.[368] The crystalline structure was further confirmed by HRTEM analysis of AuB(10)@NU-1000 and AuR(50)@NU-1000, where the MOF channels were clearly visible. Additionally, FFT analysis allowed for the indexing of the (111) and (200) crystallographic planes.

The TGA analysis (Figures 7-6d and 7-7d) demonstrated thermal stability up to 400 ºC for all the NU-1000 nanocomposites as well as the pristine material. The amount of Au was quantified by subtracting the inorganic residue (ZrO_2) of pristine NU-1000 from that of the composites. This Au content directly affects the adsorption measurements, showing a reduction in N_2 uptake compared to the Type IV isotherm of pristine NU-1000 (Figures 7-6e and 7-7e). The decrease is attributed to the increased mass of Au in the composites, which, being non-porous, does not contribute to the BET surface area (Table 7-2).

USC UNIVERSIDADE DE SANTIAGO DE COMPOSTELA

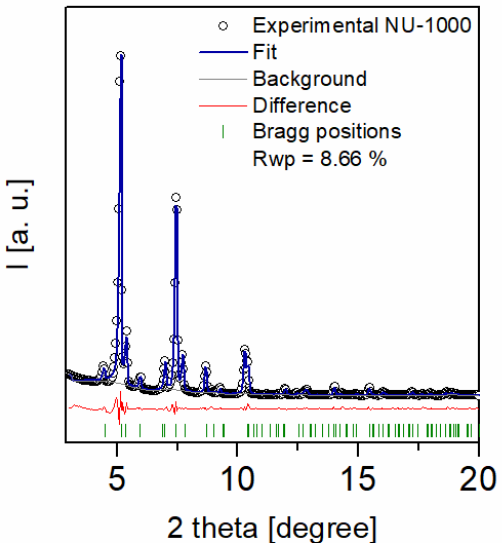

Figure 7-10. Pawley's refinement of pristine NU-1000.

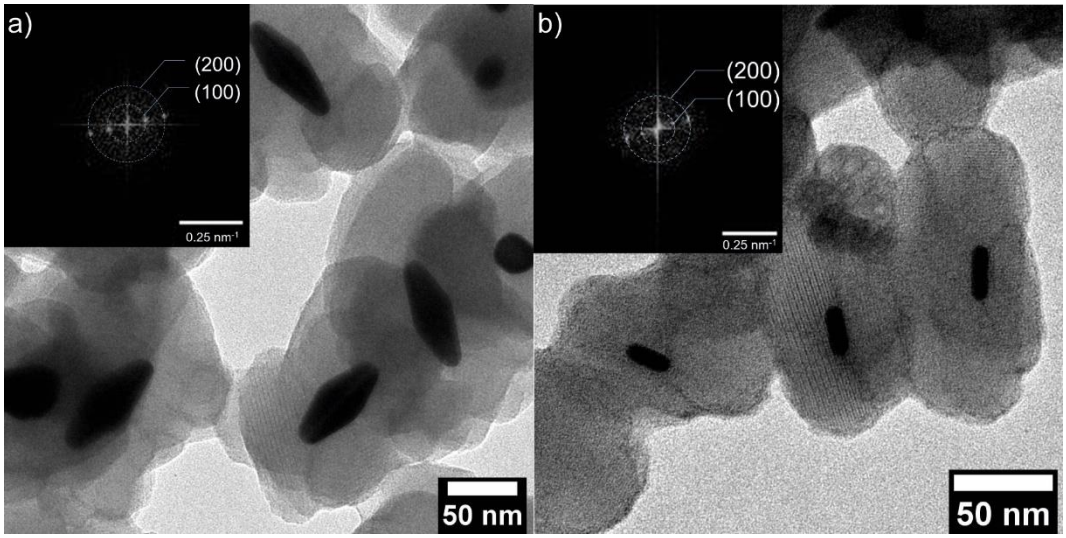

Figure 7-11. HRTEM images with FFT of a) AuB(10)@NU-1000 and b) AuR(50)@NU-1000

Table 7-2. Amount of Au content determined by TGA and BET surface area of the nanocomposites.

Sample	Au (%)	BET surface area (m^2/g)	Corrected BET surface area (m^2/g)
NU-1000	-	2168	-
AuB (2)@NU-1000	6.7	1824	1955
AuB(5)@NU-1000	12.9	1704	1956
AuB(10)@NU-1000	26.3	1424	1932
AuR(10)@NU-1000	1.8	1820	1853
AuR(20)@NU-1000	5.3	1514	1599
AuR(50)@NU-1000	15.0	1211	1425

USC UNIVERSIDADE DE SANTIAGO DE COMPOSTELA

The pore size distribution of NU-1000 and its nanocomposites (Figure 7-12a-b) was determined using the NLDFT model for cylindrical pores. This analysis identified three distinct pore sizes corresponding to the cavities in NU-1000: a micropore approximately 11.9 Å and two mesopores measuring 23.6 Å and 31.3 Å, as shown in Figure 7-12c.

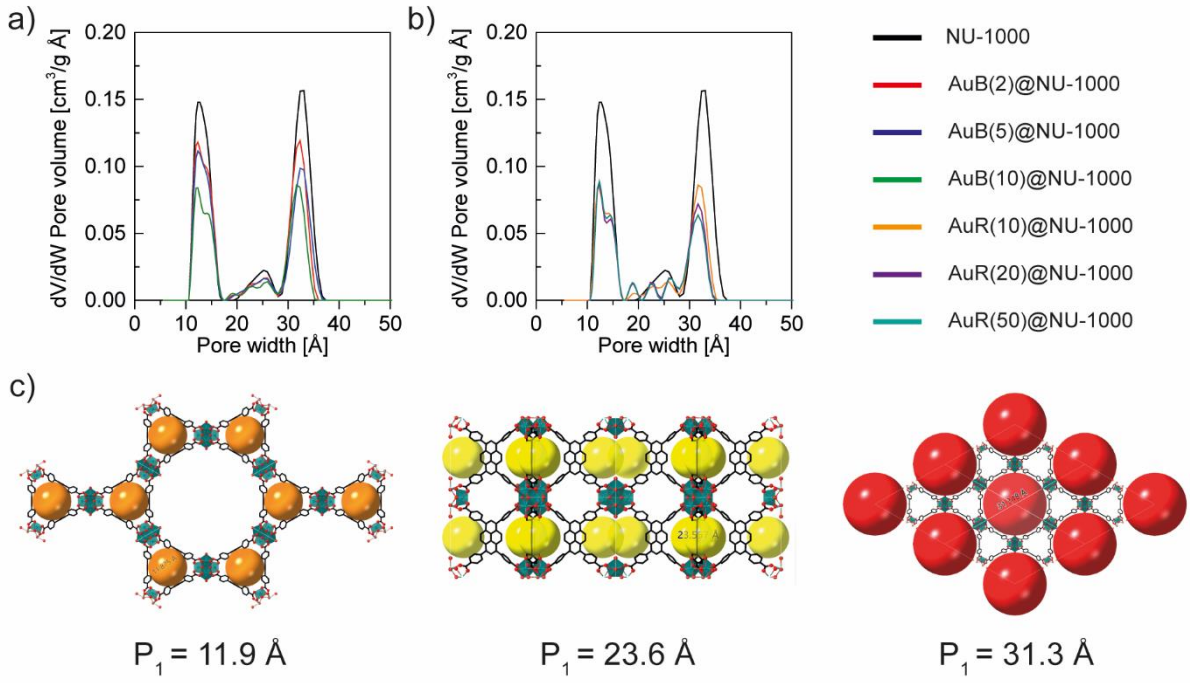

Figure 7-12. Pore size distribution of NU-1000 and its nanocomposites a) AuBipy@NU-1000, b) AuNRs@NU-1000 and c) schematic representation of NU-1000 cavities.

7.2.2. Effect of shell thickness and particle shape in photoluminescence properties.

The impact of particle shape and concentration on the photoluminescence properties of NU-1000 was evaluated (Figure 7-13). NU-1000 exhibited an emission spectrum centered at 450 nm, consisting of two components: one at shorter wavelengths corresponding to $S_1 \rightarrow S_0$ transitions, and the other at longer wavelengths attributed to excimer transitions.[369,370]

The incorporation of plasmonic nanoparticles as the core in the composites had a similar impact as observed in the PCN-224 composites (Chapter 6), leading to PL quenching due to various energy transfer mechanisms such as FRET and NSET.[351,352]

Table 7-3 summarizes the percentage of PL quenching in each sample, which correlates with the amount of Au in each sample, quantified by ICP-OES (Figure 7-14). The amount of Au is evident for each type of nanoparticle (Figure 7-14a). In the case of AuBipy, which displays a purple hue, the intensity of the coloration darkened as the seed concentration increased. Similarly, for AuNRs, which exhibit a brown coloration, the samples with higher concentrations showed a darker tone, irrespective of the yellowish coloration of pristine NU-1000. The PL quenching attributed to energy transfer exhibited a notable difference depending on the plasmonic core nanoparticles. In the case of AuBipy (Figure 7-13a), a gradual quenching of both the $S_1 \rightarrow S_0$ and excimer transitions was observed. However, with AuNRs (Figure 7-13b), the $S_1 \rightarrow S_0$ transitions were completely quenched, while the excimer transitions showed

USC UNIVERSIDADE DE SANTIAGO DE COMPOSTELA

a gradual quenching as the concentration of Au increased. The complete quenching of the $S_1 \rightarrow S_0$ band with the nanorods is likely due to their ability to generate more localized and efficient electric fields, facilitating a stronger energy transfer to the singlet excited states, with less impact on the excimer emission.

The TCSPC analysis for both systems did not reveal significant differences in the emission lifetimes compared to pristine NU-1000 (Figure 7-13c-d), which has an average lifetime of 0.40 ns (Table 7-4). This is attributed to the presence of static quenching, where fluorophores form a non-emissive complex with the energy acceptor (such as gold nanoparticles) before excitation. In this case, the emission lifetime remains unchanged because the fluorophores that are not bound to the acceptor retain the same lifetime as they would in the absence of quenching. Only the fluorophores not involved in the complex are able to emit, resulting in a reduction in intensity without affecting the lifetime.[371]

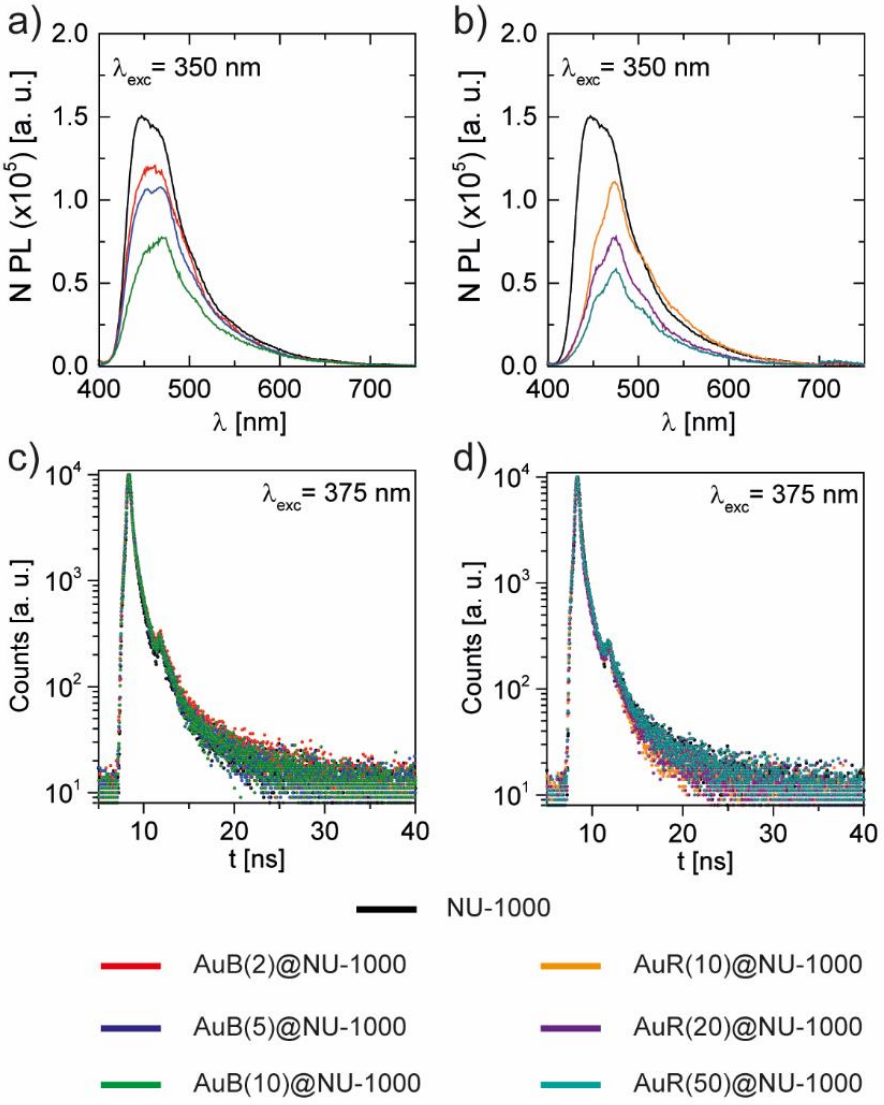

Figure 7-13. a-b) Photoluminescence spectra with an excitation wavelength of 350 nm and c-d) time-correlated single photon counting decay kinetics with an excitation wavelength of 375 nm for AuBipy@NU-1000 and AuNRs@NU-1000 nanocomposites.

Table 7-3. Quantification of photoluminescent quenching for NU-1000 nanocomposites.

Sample	PL quenching (%)
NU-1000	-
AuB (2)@NU-1000	34.37
AuB(5)@NU-1000	37.89
AuB(10)@NU-1000	58.19
AuR(10)@NU-1000	42.04
AuR(20)@NU-1000	65.88
AuR(50)@NU-1000	70.36

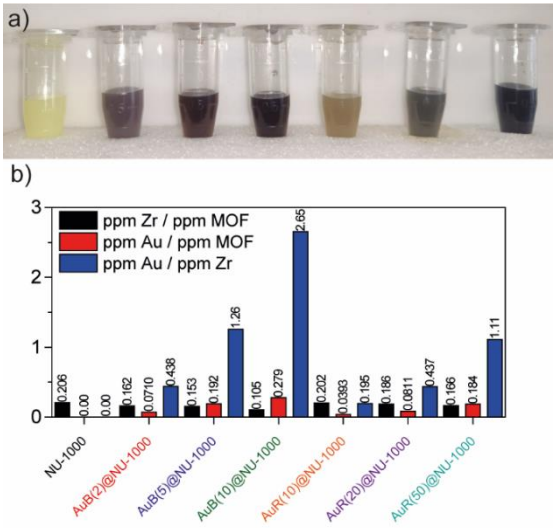

Figure 7-14. a) Digital photography and b) ICP-OES analysis of NU-1000 and its nanocomposites with AuBipy and Au NRs.

Table 7-4. Decay times values of NU-1000 and its nanocomposites with AuBipy and Au NRs and coefficients values for multiexponential function (Eq. 13).

Sample	A	B_1	%	τ_1 (s)	B_2	%	τ_2 (s)	B_3	%	τ_3 (s)	χ^2	Average τ (ns)
NU-1000	9.4767	0.1820	48.7800	1.15E-10	0.0252	39.9700	6.78E-10	0.0013	11.2500	3.83E-09	1.1101	0.43
AuB(2)@NU-1000	11.4849	0.1622	46.6400	1.28E-10	0.0227	41.3700	8.10E-10	0.0013	11.9900	4.05E-09	1.1692	0.49
AuB(5)@NU-1000	9.7724	0.1555	41.6400	1.20E-10	0.0294	47.3300	7.21E-10	0.0014	11.0200	3.65E-09	1.1669	0.40
AuB(10)@NU-1000	10.1136	0.1946	45.9600	1.05E-10	0.0244	43.3400	7.85E-10	0.0012	10.7000	3.81E-09	1.1966	0.41
AuR(10)@NU-1000	8.9226	0.2008	49.2400	1.02E-10	0.0241	40.8500	7.06E-10	0.0013	9.9100	3.19E-09	1.1995	0.32
AuR(20)@NU-1000	9.3561	0.2182	55.3700	9.97E-11	0.0177	32.9900	7.31E-10	0.0013	11.6400	3.43E-09	1.2431	0.40
AuR(50)@NU-1000	9.9248	0.2058	49.5400	1.02E-10	0.0216	38.2300	7.51E-10	0.0014	12.2300	3.78E-09	1.2378	0.46

7.2.3. Effect of particle shape in heating properties.

To investigate the effect of particle shape on the heating properties of the MOF, the nanocomposites were functionalized with MeO-PEG-PO_3 (5 kDa),[170] similar to the functionalization of PCN-224 nanocomposites (chapter 6), with the goal of imparting colloidal stability. This is necessary because, as the particles heat the medium, they move more rapidly, leading to increased collisions, the promotion of agglomeration, and eventual precipitation. Figure 7-15 shows changes in the ζ-potential, shifting from positive values in NU-1000 and unfunctionalized nanocomposites to negative values after MeO-PEG-PO_3 functionalization, attributed to the deprotonation of phosphate groups.[169,170]

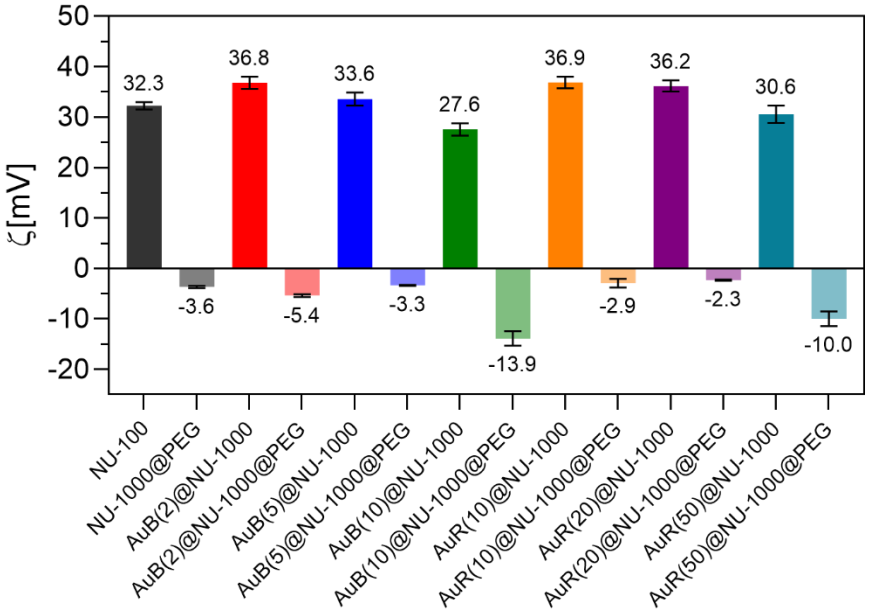

Figure 7-15. ζ- potential measurements of NU-1000 and its nanocomposites with and without PEGylation.

In these nanocomposites, the shell-thickness effect is difficult to assess due to the twinned MOF crystals on the plasmonic nanoparticles, as well as the anisotropic (rice-shaped) morphology, which may result in varying shell thicknesses along the length or at the tips of the plasmonic nanoparticle. In this study, the influence of particle shape and their heat generation capacity were evaluated.

Figure 7-16 shows the heating curves of NU-1000 nanocomposites under 808 nm laser irradiation at an irradiance of 10 W/cm². Figure 7-16a compares AuB(10)@NU-1000 and AuR(50)@NU-1000 nanocomposites, each at a particle concentration of 200 pM, under continuous wave irradiation across three cycles. These two nanocomposites were selected because it was demonstrated that higher seed concentrations during synthesis resulted in less pronounced morphological changes in the cores, minimizing shifts in the position of the LSPR. This allowed the LSPR to remain close to 808 nm, which corresponds to the wavelength of the laser used for the irradiation experiments (Figures 7-6b and 7-7b).

While the AuR(50)@NU-1000 needed 20 s to reach the boiling point of water (ΔT ≈ 70-75 ºC) the AuB(10)@NU-1000 needed 3 times more time (60s), because the energy absorbed

by a nanoparticle is divided between absorption and scattering processes and the nanoparticles with higher scattering (AuBipy) tend to disperse part of the incident energy rather than fully absorbing it and where the absorption is the main mechanism responsible for converting energy into heat. Therefore, in the case of AuBipy with higher scattering, a smaller fraction of energy is converted into heat, whereas the AuNRs, with a higher aspect ratio and less scattering, can absorb more energy and generate more heat.

While the AuR(50)@NU-1000 nanocomposite required only 20 s to reach the boiling point of water ($\Delta T \approx 70\text{-}75$ ºC), the AuB(10)@NU-1000 took three times longer (60 s). This difference arises from the distribution of absorbed energy between absorption and scattering processes. Nanoparticles with higher scattering, such as AuBipy, tend to disperse part of the incident energy rather than fully absorb it. Since absorption is the primary mechanism for converting energy into heat, the higher scattering in AuBipy results in a smaller fraction of energy being converted into heat. In contrast, AuNRs, with a higher aspect ratio and lower scattering, are more efficient at absorbing energy, leading to greater heat generation,[372] as is shown in the simulated extinction spectra of each morphology with their specific dimensions used (Figure 7-17).[199]

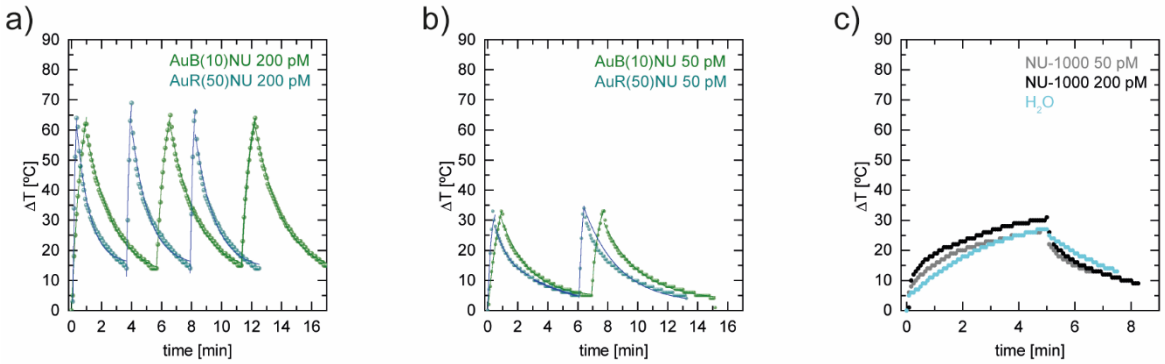

Figure 7-16. Heating curves of AuB(10)@NU-1000 and AuR(50)@NU-1000 at a) 200 pM, b) 50 pM, and c) NU-1000 at both concentrations with water as a blank, all measured under an irradiance of 10 W/cm^2.

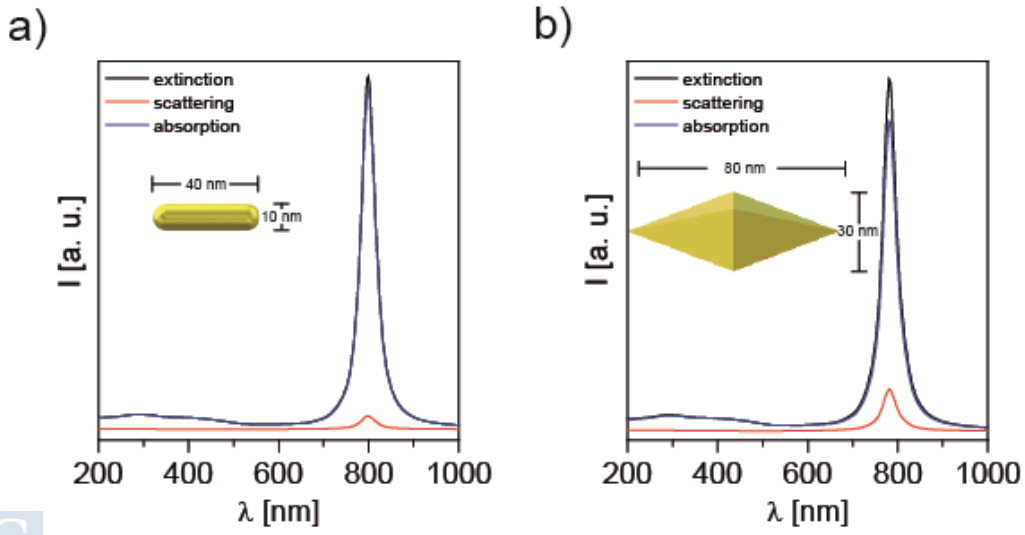

Figure 7-17. Simulated extinction spectra of AuNRs and AuBipy, illustrating the contributions from both scattering and absorption components.

Figure 7-16b shows the heating curves for the nanocomposites at a reduced concentration of 50 pM, where, as observed at 200 pM, both AuNRs and AuBipy reached a $\Delta T \approx 35$ ºC in the same time intervals (20 s for AuNRs and 60 s for AuBipy). To rule out the effects of NU-1000 and water heating under 808 nm laser irradiation, blank tests were conducted with water and NU-1000 irradiated for 5 minutes (Figure 7-16c), resulting in a maximum ΔT of 30 ºC. This confirms that the observed heating was primarily due to the plasmonic material in the core of the nanocomposites.

7.2.4. AuBipy@NU-1000 nanocomposites as SERS substrate in colloidal dispersion

As a proof of concept, the AuB(10)@NU-1000 nanocomposite was tested as a SERS substrate in colloidal dispersion. This was chosen due to its LSPR localized at 775 nm, which is slightly blue-shifted relative to the 785 nm Raman laser. It has been previously reported by Murphy *et al.* that being off-resonance in SERS experiments yields the highest Raman signal from nanorod suspensions with a plasmon resonance blue-shifted from the laser excitation wavelength.[373] This contrasts with SERS measurements from molecules dried onto roughened or patterned metal substrates, where the maximum signal is typically observed near or red-shifted from the laser excitation wavelength. These results can be explained by a competition between SERS enhancement and extinction at the excitation and scattered wavelengths.

The Raman probe molecule used with the AuB(10)@NU-1000 nanocomposite was 4-mercaptobenzonitrile(MBN) (Figure 7-18). This choice was made due to the mercapto group, which allows for covalent attachment to the gold surface, and the nitrile group, which exhibits a band in the silent region at 2232 cm^{-1} that minimizes interference with most organic molecules.[374]

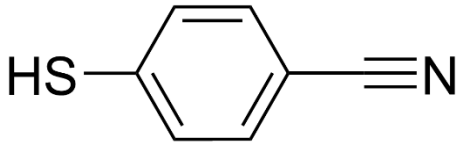

Figure 7-18. Chemical structure of 4-mercaptobenzonitrile.

The PEG chains covalently attached to the surface of AuBipy do not interfere with the Raman signal enhancement, as their low polarizability does not significantly contribute to the amplification of Raman signals.

The analyte MBN in methanolic solution with a final concentration of 5 µM was exposed to the AuB(10)@NU-1000 as synthesized in water overnight, in order to favorize the diffusion of the analyte inside the MOF porosity and attach chemically to the surface of AuBipy. Figure 7-19a shows the Raman spectra of the composite as synthesized in order to identify the signals from the MOF (black line) and the with the methanolic solution 5 µM of MBN where the signal form the analyte (Table 7-5) were not distinguish jut the C-S mode at 1074 cm^{-1}.

The same concentration of analyte was exposed to varying dilutions of AuB(10)@NU-1000. Remarkably, the Raman signal of MBN increased by four orders of magnitude with a 1:10 dilution, and by five orders of magnitude with a 1:50 dilution, with some variations in signal ratios attributed to different adsorption modes (Figure 7-19b). However, at a 1:100 dilution, the signal enhancement decreased nearly to the level observed at the original

(undiluted) concentration. The increase in Raman signal with decreasing nanoparticle concentration is attributed to signal attenuation at higher concentrations. At elevated nanoparticle concentrations, several factors contribute to the reduction in signal, including excessive aggregation, optical saturation, reabsorption, and scattering losses. Reducing the nanoparticle concentration mitigates these negative effects, resulting in more efficient Raman signal enhancement due to improved particle separation, reduced aggregation, and minimized signal attenuation.[375]

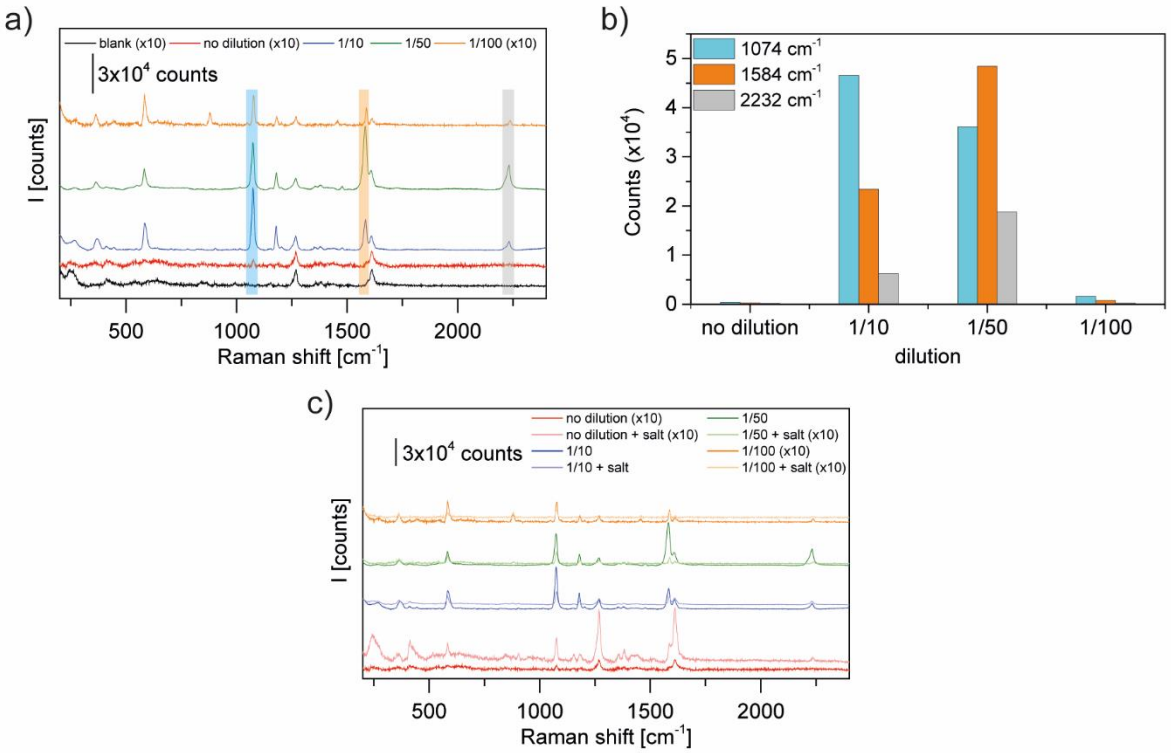

Figure 7-19. a) Raman spectra of 5 µM 4-mercaptobenzonitrile using AuB(10)@NU-1000 in colloidal dispersion, measured with a 785 nm laser at various dilutions; b) Raman intensities of the vibrational modes at different composite dilutions; and c) the effect of saturated NaCl solution on the SERS spectra.

Table 7-5. Raman modes of 4-mercaptobenzonitrile (MBN).

Raman shift (cm^{-1})	**Assignment**
1074	C-C stretching, breathing mode ν_{CC} and C-S ν_{CS}
1584	C-C stretching, ν_{CC}
2232	C N stretching, ν_{CN}

Saturated NaCl solution was added to the previously diluted nanocomposites with MBN to promote nanoparticle aggregation, potentially enhancing the Raman signals through hot-spot formation (Figure 7-19c). However, this resulted in near-complete attenuation of the Raman signal. This attenuation is likely due to the displacement of MBN molecules from the MOF's porosity to the external environment, caused by the high ionic strength of the saturated NaCl solution.[376]

USC UNIVERSIDADE DE SANTIAGO DE COMPOSTELA

7.3. Summary and Conclusions of Chapter 7

In this chapter, the impact of core shape on heating and photoluminescence properties was evaluated. The concentration of PEGylated plasmonic nanoparticle seeds is crucial in the reshaping process that occurs during heating under the synthetic conditions of the MOF NU-1000. This was corroborated by electron microscopy and 3D tomography with *in situ* heating. Higher seed concentrations result in less pronounced reshaping, which directly affects the absorption wavelength of the LSPR.

The shape of the nanoparticles, specifically nanorods and bipyramids, influences their photoluminescent properties differently. Both shapes cause gradual quenching of photoluminescence as the amount of gold in the nanocomposite increases. However, the AuBipy nanocomposites induce gradual quenching in both electronic transitions of the MOF ligand ($S_1 \rightarrow S_0$ and excimer transitions). In contrast, the AuNRs nanocomposites completely quench the $S_1 \rightarrow S_0$ transitions at any concentration. This is attributed to the AuNRs ability to generate more localized and efficient electric fields compared to the AuBipy, which produces more scattering due to its aspect ratio.

The heating properties of the nanocomposites also differ. The AuNRs nanocomposite is more efficient at generating heat compared to the AuBipy nanocomposites. This is attributed to the aspect ratio of the AuNRs (aspect ratio 4), which prevents light scattering and enables complete absorption and conversion of energy into heat more efficiently than the AuBipy nanocomposites, which have an aspect ratio of 2.67.

The AuBipy nanocomposites with a NU-1000 shell were utilized as SERS substrates in colloidal dispersion, enabling the detection of 4-mercaptobenzonitrile at a concentration of 5 µM. SERS enhancement was more effective when the nanocomposites were diluted, due to competition between extinction and enhancement. Additionally, this SERS effect was quenched upon the addition of a saturated NaCl solution, due to analyte displacement from the MOF pores resulting from increased ionic strength.

USC UNIVERSIDADE DE SANTIAGO DE COMPOSTELA

8. Conclusions

USC
UNIVERSIDADE
DE SANTIAGO
DE COMPOSTELA

USC
UNIVERSIDADE
DE SANTIAGO
DE COMPOSTELA

8.1 General conclusions

This chapter presents the key conclusions drawn from this Ph.D. thesis. The primary objective of this work was the synthesis of novel core-shell systems utilizing plasmonic nanoparticles with NIR absorption as the core and Zr-based MOFs as the shell. These core-shell systems are designed to combine optical absorption capabilities that generate heat within the MOF and the ability to load molecules of interest for use in light-triggered drug delivery systems.

While similar systems have been extensively studied in the scientific community, most existing research focuses on ZIFs, which suffer from poor stability in aqueous media. Consequently, Zr-based MOFs were selected for the shell material due to their high chemical, thermal, and structural stability, resistance to a broad range of pH levels, and low cytotoxicity.

This thesis investigated the limited number of reports on Zr-based MOFs, which are primarily attributed to the use of halogenated zirconium precursors, where halogen ions can oxidize gold, and the synthetic conditions required for Zr-based MOFs, which typically involve solvothermal conditions with high temperatures (>100°C) and extended reaction times (~24 hours). These conditions can compromise the morphology of the plasmonic nanoparticles, adversely affecting their optical properties and heat generation capabilities.

Three synthetic approaches were developed in this thesis to produce highly stable, reproducible, and robust plasmonic nanoMOFs based on zirconium. These methods include: (i) reactions with short times to minimize effects on the plasmonic cores, (ii) the use of Zr-alkoxides as precursors to reduce reaction times, even to room temperature, and (iii) the use of preformed Zr_6-oxo clusters, which facilitate MOF formation at room temperature.

Chapter 3 reveals that halides in the reaction medium, derived from the precursors, play a crucial role in controlling the shape, size, colloidal stability, and adsorption properties of the resulting nanoMOFs in UiO-66 systems. The effects of different halides were studied, with most halides (except fluoride) exhibiting similar impacts on particle size and monodispersity. The study also explored the influence of pendant groups, showing that halides do not react with them. The size of the resultant nanoMOFs was suitable for drug delivery applications in living cells, as demonstrated with rhodamine 6G tracking.

Chapter 4 demonstrated that Zr-alkoxides enable the synthesis of pure phases of porphyrinic Zr-based MOFs (PCN-224, PCN-222, and MOF-525) under mild conditions, such as room temperature or up to 75°C, with reaction times of 1 hour. These conditions provided excellent control over particle size (on the nanoscale) and resulted in exceptional optical, structural, and thermal properties. The rapid reaction with alkoxides allowed for the synthesis of pure phase PCN-224 in a flow system with a residence time of only 25 seconds.

Chapter 5 combined the use of Zr-alkoxides for the synthesis of UiO-family MOFs at reduced temperatures, including room temperature, with the incorporation of inorganic nanoparticles. The kinetics of reshaping AuBipy, AuNRs, and AuNSs were studied, concluding that the synthesis temperatures for Zr-based MOFs negatively impact the morphology of the plasmonic cores. By leveraging the reactivity of Zr-alkoxides at low temperatures, plasmonic nanoMOFs were successfully synthesized at temperatures as low as room temperature. The

shell thickness of the MOF acted as an insulating medium, requiring longer excitation times of the core to heat the surrounding media as shell thickness increased.

Chapter 6 explored the use of preformed Zr_6-oxo clusters for the formation of plasmonic nanoMOFs. It was found that the presence of 1-propanol, a byproduct from the synthesis of Zr_6-oxo clusters, was essential for the formation of core-shell systems. Its presence in the synthesis of PCN-224 without cores negatively affected the reaction yield and increased polydispersity. The plasmonic nanoMOFs exhibited varying shell thicknesses depending on seed concentration, which influenced their photoluminescence properties and heat generation capabilities. These systems were tested as light-triggered nanocarriers for drug release inside living cells under 808 nm laser illumination and were also capable of generating ROS with visible light, leading to cell death.

Chapter 7 examined the impact of seed concentration on the synthesis of plasmonic nanoMOFs with NU-1000. It was observed that lower concentrations of plasmonic nanoparticles led to greater damage and a pronounced blue shift in the LSPR. Additionally, the effect of morphology was evaluated using AuBipy and AuNRs as seeds, both with the same LSPR absorption. Significant differences were found in their heat generation efficiency, with AuNRs demonstrating superior performance due to their larger aspect ratio, which contributes to absorption without scattering. The plasmonic nanoMOFs with AuBipy were also tested as SERS substrates in colloidal dispersion, revealing that diluted nanoparticles achieved a five-order magnitude increase in enhancement compared to undiluted nanocomposites, attributed to the balance between enhancement and extinction effects.

USC
UNIVERSIDADE DE SANTIAGO DE COMPOSTELA

References

1. Yaghi, O. M. *et al.* Reticular synthesis and the design of new materials. *Nature* **423**, 705–714 (2003).
2. Freund, R. *et al.* 25 Years of Reticular Chemistry. *Angew. Chemie - Int. Ed.* **60**, 23946–23974 (2021).
3. Yaghi, O. M., Li, G., and L. H. Selective binding and removal of guests in a microporous metal-organic framework. *Nature* **378**, 703–706 (1995).
4. Moghadam, P. Z. *et al.* Development of a Cambridge Structural Database Subset: A Collection of Metal-Organic Frameworks for Past, Present, and Future. *Chem. Mater.* **29**, 2618–2625 (2017).
5. Furukawa, H., Cordova, K. E., O'Keeffe, M. & Yaghi, O. M. The chemistry and applications of metal-organic frameworks. *Science* **341**, 1230444 (2013).
6. Holst, J. R. & Cooper, A. I. Ultrahigh surface area in porous solids. *Adv. Mater.* **22**, 5212–5216 (2010).
7. Furukawa, H. *et al.* Ultrahigh porosity in metal-organic frameworks. *Science* **329**, 424–428 (2010).
8. Farha, O. K. *et al.* Metal-organic framework materials with ultrahigh surface areas: Is the sky the limit? *J. Am. Chem. Soc.* **134**, 15016–15021 (2012).
9. Hönicke, I. M. *et al.* Balancing Mechanical Stability and Ultrahigh Porosity in Crystalline Framework Materials. *Angew. Chemie - Int. Ed.* **57**, 13780–13783 (2018).
10. Yin, X., Alsuwaidi, A. & Zhang, X. Hierarchical metal-organic framework (MOF) pore engineering. *Microporous Mesoporous Mater.* **330**, 111633 (2022).
11. Kalaj, M. & Cohen, S. M. Postsynthetic Modification: An Enabling Technology for the Advancement of Metal-Organic Frameworks. *ACS Cent. Sci.* **6**, 1046–1057 (2020).
12. Dai, S. *et al.* Monodispersed MOF-808 Nanocrystals Synthesized via a Scalable Room-Temperature Approach for Efficient Heterogeneous Peptide Bond Hydrolysis. *Chem. Mater.* **33**, 7057–7066 (2021).
13. Decker, G. E., Stillman, Z., Attia, L., Fromen, C. A. & Bloch, E. D. Controlling Size, Defectiveness, and Fluorescence in Nanoparticle UiO-66 through Water and Ligand Modulation. *Chem. Mater.* **31**, 4831–4839 (2019).
14. Li, H., Eddaoudi, M., O'Keeffe, M. & Yaghi, O. M. Desing and synthesis of an exceptionally stable and highly porous metal-organic framework. *Nature* **402**, 276–279 (1999).
15. Chui, S. S. Y., Lo, S. M. F., Charmant, J. P. H., Orpen, A. G. & Williams, I. D. A chemically functionalizable nanoporous material [Cu3(TMA)2 (H2O)3](n). *Science* **283**, 1148–1150 (1999).
16. Férey, G. *et al.* A hybrid solid with giant pores prepared by a combination of targeted

USC UNIDADE SANTIAGO POSTELA

chemistry, simulation, and powder diffraction. *Angew. Chemie - Int. Ed.* **43**, 6296–6301 (2004).

17. Cavka, J. H. *et al.* A new zirconium inorganic building brick forming metal organic frameworks with exceptional stability. *J. Am. Chem. Soc.* **130**, 13850–13851 (2008).

18. Van Niekerk, J. N. & Schoenin, F. R. L. X-ray evidence for metal-to-metal bonds in cupric and chromous acetate. *Nature* **171**, 36–37 (1953).

19. Koyama, H. & Saito, Y. The Crystal Structure of Zinc Oxyacetate, Zn4O(CH3COO)6. *Bull. Chem. Soc. Jpn.* **27**, 112–114 (1954).

20. Figgis, B. N. & Robertson, G. B. Crystal-molecular structure and magnetic properties of Cr3 (CH3.COO)6O Cl.5H2O. *Nature* **205**, 694–695 (1965).

21. Kickelbick, G. & Schubert, U. Oxozirconium Methacrylate Clusters: Zr6(OH)4O4(OMc)12 and Zr4O2(OMc)12 (OMc = Methacrylate). *Chem. Berichte-Recueil* **130**, 473–477 (1997).

22. Jiang, H., Alezi, D. & Eddaoudi, M. A reticular chemistry guide for the design of periodic solids. *Nat. Rev. Mater.* **6**, 466–487 (2021).

23. Gagnon, K. J., Perry, H. P. & Clearfield, A. Conventional and unconventional metal-organic frameworks based on phosphonate ligands: MOFs and UMOFs. *Chem. Rev.* **112**, 1034–1054 (2012).

24. Banerjee, R. *et al.* High-Throughput Synthesis of Zeolitic Imidazolate Frameworks and Application to CO2 Capture. *Science* **319**, 939–943 (2008).

25. Padial, N. M. *et al.* Hydroxamate Titanium-Organic Frameworks and the Effect of Siderophore-Type Linkers over Their Photocatalytic Activity. *J. Am. Chem. Soc.* **141**, 13124–13133 (2019).

26. Furukawa, H. *et al.* Water adsorption in porous metal-organic frameworks and related materials. *J. Am. Chem. Soc.* **136**, 4369–4381 (2014).

27. Bon, V., Senkovska, I., Weiss, M. S. & Kaskel, S. Tailoring of network dimensionality and porosity adjustment in Zr- and Hf-based MOFs. *CrystEngComm* **15**, 9572–9577 (2013).

28. Øien, S. *et al.* Detailed structure analysis of atomic positions and defects in zirconium metal-organic frameworks. *Cryst. Growth Des.* **14**, 5370–5372 (2014).

29. Manna, K. *et al.* Chemoselective single-site Earth-abundant metal catalysts at metal-organic framework nodes. *Nat. Commun.* **7**, 1–11 (2016).

30. Ma, C. *et al.* Phase engineering of metal-organic frameworks. *Aggregate* **3**, e145 (2022).

31. Feng, D. *et al.* Zirconium-metalloporphyrin PCN-222: Mesoporous metal-organic frameworks with ultrahigh stability as biomimetic catalysts. *Angew. Chemie - Int. Ed.* **51**, 10307–10310 (2012).

32. Morris, W. *et al.* Synthesis, structure, and metalation of two new highly porous zirconium metal-organic frameworks. *Inorg. Chem.* **51**, 6443–6445 (2012).

USC UNIVERSIDADE DE SANTIAGO DE COMPOSTELA

33. Chen, Y., Hoang, T. & Ma, S. Biomimetic catalysis of a porous iron-based metal-metalloporphyrin framework. *Inorg. Chem.* **51**, 12600–12602 (2012).

34. Feng, D. *et al.* A highly stable porphyrinic zirconium metal-organic framework with shp-a topology. *J. Am. Chem. Soc.* **136**, 17714–17717 (2014).

35. Feng, D. *et al.* Construction of ultrastable porphyrin Zr metal-organic frameworks through linker elimination. *J. Am. Chem. Soc.* **135**, 17105–17110 (2013).

36. Jiang, H. L. *et al.* An exceptionally stable, porphyrinic Zr metal-organic framework exhibiting pH-dependent fluorescence. *J. Am. Chem. Soc.* **135**, 13934–13938 (2013).

37. Deria, P. *et al.* Framework-Topology-Dependent Catalytic Activity of Zirconium-Based (Porphinato)zinc(II) MOFs. *J. Am. Chem. Soc.* **138**, 14449–14457 (2016).

38. Mondloch, J. E. *et al.* Vapor-phase metalation by atomic layer deposition in a metal-organic framework. *J. Am. Chem. Soc.* **135**, 10294–10297 (2013).

39. Kung, C. W. *et al.* Metal-organic framework thin films composed of free-standing acicular nanorods exhibiting reversible electrochromism. *Chem. Mater.* **25**, 5012–5017 (2013).

40. Wei, Z. *et al.* Rigidifying fluorescent linkers by metal-organic framework formation for fluorescence blue shift and quantum yield enhancement. *J. Am. Chem. Soc.* **136**, 8269–8276 (2014).

41. Zhang, Q. *et al.* Piezofluorochromic metal-organic framework: A microscissor lift. *J. Am. Chem. Soc.* **137**, 10064–10067 (2015).

42. Schnobrich, J. K. *et al.* Linker-directed vertex desymmetrization for the production of coordination polymers with high porosity. *J. Am. Chem. Soc.* **132**, 13941–13948 (2010).

43. Qin, J. S. *et al.* Creating Well-Defined Hexabenzocoronene in Zirconium Metal-Organic Framework by Postsynthetic Annulation. *J. Am. Chem. Soc.* **141**, 2054–2060 (2019).

44. Chen, Z. *et al.* Reticular Access to Highly Porous acs-MOFs with Rigid Trigonal Prismatic Linkers for Water Sorption. *J. Am. Chem. Soc.* **141**, 2900–2905 (2019).

45. Tu, B. *et al.* Reversible Redox Activity in Multicomponent Metal-Organic Frameworks Constructed from Trinuclear Copper Pyrazolate Building Blocks. *J. Am. Chem. Soc.* **139**, 7998–8007 (2017).

46. Luo, T. Y. *et al.* Rare Earth pcu Metal-Organic Framework Platform Based on RE4(μ3-OH)4(COO)62+ Clusters: Rational Design, Directed Synthesis, and Deliberate Tuning of Excitation Wavelengths. *J. Am. Chem. Soc.* **139**, 9333–9340 (2017).

47. Chen, D. M., Shi, W. & Cheng, P. A cage-based cationic body-centered tetragonal metal-organic framework: Single-crystal to single-crystal transformation and selective uptake of organic dyes. *Chem. Commun.* **51**, 370–372 (2015).

48. Masciocchi, N. *et al.* Cubic octanuclear Ni(II) clusters in highly porous polypyrazolyl-based materials. *J. Am. Chem. Soc.* **132**, 7902–7904 (2010).

49. Kapustin, E. A., Lee, S., Alshammari, A. S. & Yaghi, O. M. Molecular Retrofitting Adapts a Metal-Organic Framework to Extreme Pressure. *ACS Cent. Sci.* **3**, 662–667

USC UNIVERSIDADE DE SANTIAGO DE COMPOSTELA

(2017).

50. Alezi, D. *et al.* Quest for highly connected metal-organic framework platforms: Rare-earth polynuclear clusters versatility meets net topology needs. *J. Am. Chem. Soc.* **137**, 5421–5430 (2015).

51. Kim, D., Liu, X. & Lah, M. S. Topology analysis of metal-organic frameworks based on metal-organic polyhedra as secondary or tertiary building units. *Inorg. Chem. Front.* **2**, 336–360 (2015).

52. Kalmutzki, M. J., Hanikel, N. & Yaghi, O. M. Secondary building units as the turning point in the development of the reticular chemistry of MOFs. *Sci. Adv.* **4**, eaat9180 (2018).

53. Yaghi, O. M., Davis, C. E., Li, G. & Li, H. Selective guest binding by tailored channels in a 3-D porous zinc(II)-benzenetricarboxylate network. *J. Am. Chem. Soc.* **119**, 2861–2868 (1997).

54. Lu, J., Mondal, A., Moulton, B. & Zaworotko, M. J. Polygons and Faceted Polyhedra and Nanoporous Networks. *Angew. Chemie - Int. Ed.* **40**, 2113–2116 (2001).

55. Feldblyum, J. I., Liu, M., Gidley, D. W. & Matzger, A. J. Reconciling the discrepancies between crystallographic porosity and guest access as exemplified by Zn-HKUST-1. *J. Am. Chem. Soc.* **133**, 18257–18263 (2011).

56. Hao, X. R. *et al.* Remarkable solvent-size effects in constructing novel porous 1,3,5-benzenetricarboxylate metal-organic frameworks. *CrystEngComm* **14**, 5596–5603 (2012).

57. Keeffe, M. O., Peskov, M. a, Ramsden, S. J. & Yaghi, O. M. The Reticular Chemistry Structure Resource (RCSR) Database of, and Symbols for, Crystal Nets. *Acc. Chem. Res.* **41**, 1782–1789 (2008).

58. Bhatt, P. M., Guillerm, V., Datta, S. J., Shkurenko, A. & Eddaoudi, M. Topology Meets Reticular Chemistry for Chemical Separations: MOFs as a Case Study. *Chem* **6**, 1613–1633 (2020).

59. Bueken, B. *et al.* Tackling the Defect Conundrum in UiO-66: A Mixed-Linker Approach to Engineering Missing Linker Defects. *Chem. Mater.* **29**, 10478–10486 (2017).

60. Tatay, S. *et al.* Synthetic control of correlated disorder in UiO-66 frameworks. *Nat. Commun.* **14**, 1–12 (2023).

61. Castells-Gil, J., Almora-Barrios, N., Lerma-Berlanga, B., Padial, N. M. & Martí-Gastaldo, C. Chemical complexity for targeted function in heterometallic titanium-organic frameworks. *Chem. Sci.* **14**, 6826–6840 (2023).

62. He, T. *et al.* Kinetically Controlled Reticular Assembly of a Chemically Stable Mesoporous Ni(II)-Pyrazolate Metal-Organic Framework. *J. Am. Chem. Soc.* **142**, 13491–13499 (2020).

63. Padial, N. M. *et al.* Isoreticular Expansion and Linker-Enabled Control of Interpenetration in Titanium-Organic Frameworks. *J. Am. Chem. Soc.* **145**, 21397–21407 (2023).

64. Liu, Y. *et al.* Molecular Weaving of Covalent Organic Frameworks for Adaptive Guest Inclusion. *J. Am. Chem. Soc.* **140**, 16015–16019 (2018).

65. Lin, W. *et al.* Snapshots of Postsynthetic Modification in a Layered Metal-Organic Framework: Isometric Linker Exchange and Adaptive Linker Installation. *Inorg. Chem.* **60**, 11756–11763 (2021).

66. Eddaoudi, M. *et al.* Systematic design of pore size and functionality in isoreticular MOFs and their application in methane storage. *Science* **295**, 469–472 (2002).

67. Gupta, M. & Vittal, J. J. Control of interpenetration and structural transformations in the interpenetrated MOFs. *Coord. Chem. Rev.* **435**, 213789 (2021).

68. O'Nolan, D. *et al.* Impact of partial interpenetration in a hybrid ultramicroporous material on C2H2/C2H4 separation performance. *Chem. Commun.* **54**, 3488–3491 (2018).

69. Tan, J. *et al.* Control over interpenetration for boosting methane storage capacity in metal-organic frameworks. *J. Mater. Chem. A* **9**, 24857–24862 (2021).

70. Ferguson, A. *et al.* Controlled partial interpenetration in metal-organic frameworks. *Nat. Chem.* **8**, 250–257 (2016).

71. Li, S. *et al.* A 2D metal-organic framework interpenetrated by a 2D supramolecular framework assembled by CH/π interactions. *Inorg. Chem. Commun.* **130**, 108705 (2021).

72. Ajoyan, Z. *et al.* A Simple Method for Teaching Bragg's Law in an Undergraduate Teaching Laboratory with the Use of Metal-Organic Frameworks. *J. Chem. Educ.* **100**, 1990–1996 (2023).

73. Seth, S. & Matzger, A. J. Metal-Organic Frameworks: Examples, Counterexamples, and an Actionable Definition. *Cryst. Growth Des.* **17**, 4043–4048 (2017).

74. Jiang, J., Zhao, Y. & Yaghi, O. M. Covalent Chemistry beyond Molecules. *J. Am. Chem. Soc.* **138**, 3255–3265 (2016).

75. Dickerson, P. N., Hibberd, A. M., Oncel, N. & Bernasek, S. L. Hydrogen-bonding versus van der Waals interactions in self-assembled monolayers of substituted isophthalic acids. *Langmuir* **26**, 18155–18161 (2010).

76. Zhang, Y., Jianmin, L., Nishiura, M. & Imamoto, T. Spectral and structural properties of 2D network complex [Ni(4,4'- bipyridine)2(NCS)2](n). *J. Mol. Struct.* **519**, 219–224 (2000).

77. Pauling, L. THE NATURE OF THE CHEMICAL BOND. APPLICATION OF RESULTS OBTAINED FROM THE QUANTUM MECHANICS AND FROM A THEORY OF PARAMAGNETIC SUSCEPTIBILITY TO THE STRUCTURE OF MOLECULES. *J. Am. Chem. Soc.* **53**, 1367–1400 (1931).

78. Shan, B. *et al.* Influences of Deprotonation and Modulation on Nucleation and Growth of UiO-66: Intergrowth and Orientation. *J. Phys. Chem. C* **122**, 2200–2206 (2018).

79. Du Bois, D. R., Wright, K. R., Bellas, M. K., Wiesner, N. & Matzger, A. J. Linker Deprotonation and Structural Evolution on the Pathway to MOF-74. *Inorg. Chem.* **61**,

UNIVERSIDADE DE SANTIAGO DE COMPOSTELA

4550–4554 (2022).

80. Tian, X. R. *et al.* A Strong-Acid-Resistant [Th6] Cluster-Based Framework for Effectively and Size-Selectively Catalyzing Reductive Amination of Aldehydes with N,N-Dimethylformamide. *Angew. Chemie - Int. Ed.* **62**, e202301764 (2023).

81. Liu, G. X., Xu, H., Zhou, H., Nishihara, S. & Ren, X. M. Temperature-induced assembly of MOF polymorphs: Syntheses, structures and physical properties. *CrystEngComm* **14**, 1856–1864 (2012).

82. He, X. & Wang, W. N. Pressure-regulated synthesis of Cu(TPA)·(DMF) in microdroplets for selective CO 2 adsorption. *Dalt. Trans.* **48**, 1006–1016 (2019).

83. Richardson, J. J. *et al.* Controlling the Growth of Metal-Organic Frameworks Using Different Gravitational forces. *Eur. J. Inorg. Chem.* **2016**, 4499–4504 (2016).

84. Ardila-Suárez, C., Rodríguez-Pereira, J., Baldovino-Medrano, V. G. & Ramírez-Caballero, G. E. An analysis of the effect of zirconium precursors of MOF-808 on its thermal stability, and structural and surface properties. *CrystEngComm* **21**, 1407–1415 (2019).

85. McKinstry, C., Cussen, E. J., Fletcher, A. J., Patwardhan, S. V. & Sefcik, J. Effect of synthesis conditions on formation pathways of metal organic framework (MOF-5) crystals. *Cryst. Growth Des.* **13**, 5481–5486 (2013).

86. Bustamante, E. L., Fernández, J. L. & Zamaro, J. M. Influence of the solvent in the synthesis of zeolitic imidazolate framework-8 (ZIF-8) nanocrystals at room temperature. *J. Colloid Interface Sci.* **424**, 37–43 (2014).

87. Schaate, A. *et al.* Modulated synthesis of Zr-based metal-organic frameworks: From nano to single crystals. *Chem. - A Eur. J.* **17**, 6643–6651 (2011).

88. Bauer, S. *et al.* High-throughput assisted rationalization of the formation of metal organic frameworks in the iron(III) aminoterephthalate solvothermal system. *Inorg. Chem.* **47**, 7568–7576 (2008).

89. Zhong, L., Ding, J., Qian, J. & Hong, M. Unconventional inorganic precursors determine the growth of metal-organic frameworks. *Coord. Chem. Rev.* **434**, 213804 (2021).

90. Li, Z. *et al.* A Metal-Organic Framework Incorporating Eight Different Size Rare-Earth Metal Elements: Toward Multifunctionality À La Carte. *Adv. Funct. Mater.* **33**, 2307369 (2023).

91. Park, J., Jiang, Q., Feng, D., Mao, L. & Zhou, H. C. Size-Controlled Synthesis of Porphyrinic Metal-Organic Framework and Functionalization for Targeted Photodynamic Therapy. *J. Am. Chem. Soc.* **138**, 3518–3525 (2016).

92. Taddei, M., Van Bokhoven, J. A. & Ranocchiari, M. Influence of Water in the Synthesis of the Zirconium-Based Metal-Organic Framework UiO-66: Isolation and Reactivity of [ZrCl(OH)2(DMF)2]Cl. *Inorg. Chem.* **59**, 7860–7868 (2020).

93. Hu, Z. *et al.* Modulator Effects on the Water-Based Synthesis of Zr/Hf Metal-Organic Frameworks: Quantitative Relationship Studies between Modulator, Synthetic Condition, and Performance. *Cryst. Growth Des.* **16**, 2295–2301 (2016).

94. Devic, T. & Serre, C. High valence 3p and transition metal based MOFs. *Chem. Soc. Rev.* **43**, 6097–6115 (2014).

95. Paseta, L. *et al.* Accelerating the controlled synthesis of metal-organic frameworks by a microfluidic approach: A nanoliter continuous reactor. *ACS Appl. Mater. Interfaces* **5**, 9405–9410 (2013).

96. Sorrenti, A. *et al.* Growing and Shaping Metal-Organic Framework Single Crystals at the Millimeter Scale. *J. Am. Chem. Soc.* **142**, 9372–9381 (2020).

97. Ren, H. & Wei, T. Electrochemical Synthesis Methods of Metal-Organic Frameworks and Their Environmental Analysis Applications: A Review. *ChemElectroChem* **9**, e202200196 (2022).

98. Khan, N. A. & Jhung, S. H. Synthesis of metal-organic frameworks (MOFs) with microwave or ultrasound: Rapid reaction, phase-selectivity, and size reduction. *Coord. Chem. Rev.* **285**, 11–23 (2015).

99. Thomas-Hillman, I., Laybourn, A., Dodds, C. & Kingman, S. W. Realising the environmental benefits of metal-organic frameworks: Recent advances in microwave synthesis. *J. Mater. Chem. A* **6**, 11564–11581 (2018).

100. Prochowicz, D., Nawrocki, J., Terlecki, M., Marynowski, W. & Lewiński, J. Facile Mechanosynthesis of the Archetypal Zn-Based Metal-Organic Frameworks. *Inorg. Chem.* **57**, 13437–13442 (2018).

101. Głowniak, S., Szczęśniak, B., Choma, J. & Jaroniec, M. Mechanochemistry: Toward green synthesis of metal–organic frameworks. *Mater. Today* **46**, 109–124 (2021).

102. Vaitsis, C., Sourkouni, G. & Argirusis, C. Metal Organic Frameworks (MOFs) and ultrasound: A review. *Ultrason. Sonochem.* **52**, 106–119 (2019).

103. Freund, R. *et al.* The Current Status of MOF and COF Applications. *Angew. Chemie - Int. Ed.* **60**, 23975–24001 (2021).

104. Rowsell, J. L. C., Spencer, E. C., Eckert, J., Howard, J. A. K. & Yaghi, O. M. Gas Adsorption Sites in a Large-Pore Metal-Organic Framework. *Science* **309**, 1350–1354 (2005).

105. Trickett, C. A. *et al.* The chemistry of metal-organic frameworks for CO2 capture, regeneration and conversion. *Nat. Rev. Mater.* **2**, 1–16 (2017).

106. Altintas, C. & Keskin, S. On the shoulders of high-throughput computational screening and machine learning: Design and discovery of MOFs for H2 storage and purification. *Mater. Today Energy* **38**, 101426 (2023).

107. Bondorf, L. *et al.* Isotope-selective pore opening in a flexible metal-organic framework. *Sci. Adv.* **8**, eabn7035 (2022).

108. Wang, G. D. *et al.* Rational Construction of Ultrahigh Thermal Stable MOF for Efficient Separation of MTO Products and Natural Gas. *ACS Mater. Lett.* **5**, 1091–1099 (2023).

109. Olorunyomi, J. F., Geh, S. T., Caruso, R. A. & Doherty, C. M. Metal-organic frameworks for chemical sensing devices. *Mater. Horizons* **8**, 2387–2419 (2021).

USC UNIVERSIDADE DE SANTIAGO DE COMPOSTELA

110. Zhao, R., Liang, Z., Zou, R. & Xu, Q. Metal-Organic Frameworks for Batteries. *Joule* **2**, 2235–2259 (2018).

111. Shen, M. & Ma, H. Metal-organic frameworks (MOFs) and their derivative as electrode materials for lithium-ion batteries. *Coord. Chem. Rev.* **470**, 214715 (2022).

112. Rojas, S. & Horcajada, P. Metal-Organic Frameworks for the Removal of Emerging Organic Contaminants in Water. *Chem. Rev.* **120**, 8378–8415 (2020).

113. Zhang, J. *et al.* Recent advances in performance improvement of Metal-organic Frameworks to remove antibiotics: Mechanism and evaluation. *Sci. Total Environ.* **811**, 152351 (2022).

114. Sriram, G. *et al.* Recent trends in the application of metal-organic frameworks (MOFs) for the removal of toxic dyes and their removal mechanism-a review. *Sustain. Mater. Technol.* **31**, e00378 (2022).

115. Kobielska, P. A., Howarth, A. J., Farha, O. K. & Nayak, S. Metal–organic frameworks for heavy metal removal from water. *Coord. Chem. Rev.* **358**, 92–107 (2018).

116. Mondol, M. M. H. & Jhung, S. H. Adsorptive removal of pesticides from water with metal–organic framework-based materials. *Chem. Eng. J.* **421**, 129688 (2021).

117. Shearer, G. C. *et al.* Tuned to perfection: Ironing out the defects in metal-organic framework UiO-66. *Chem. Mater.* **26**, 4068–4071 (2014).

118. Ding, S. shuai, He, L., Bian, X. wu & Tian, G. Metal-organic frameworks-based nanozymes for combined cancer therapy. *Nano Today* **35**, 100920 (2020).

119. Lan, G. *et al.* Nanoscale Metal–Organic Layers for Deeply Penetrating X-ray-Induced Photodynamic Therapy. *Angew. Chemie* **129**, 12270–12274 (2017).

120. Xu, Z. *et al.* Nanoscale Metal-Organic Framework with an X-ray Triggerable Prodrug for Synergistic Radiotherapy and Chemotherapy. *J. Am. Chem. Soc.* **145**, 18698–18704 (2023).

121. Wang, Z. *et al.* Recent advances in porphyrin-based MOFs for cancer therapy and diagnosis therapy. *Coord. Chem. Rev.* **439**, 213945 (2021).

122. Cedrún-Morales, M., Ceballos, M., Polo, E., del Pino, P. & Pelaz, B. Nanosized metal-organic frameworks as unique platforms for bioapplications. *Chem. Commun.* **59**, 2869–2887 (2023).

123. Horcajada, P. *et al.* Metal-organic frameworks as efficient materials for drug delivery. *Angew. Chemie - Int. Ed.* **45**, 5974–5978 (2006).

124. Nguyen, H. T. T. *et al.* Combining Linker Design and Linker-Exchange Strategies for the Synthesis of a Stable Large-Pore Zr-Based Metal-Organic Framework. *ACS Appl. Mater. Interfaces* **10**, 35462–35468 (2018).

125. Valenzano, L. *et al.* Disclosing the complex structure of UiO-66 metal organic framework: A synergic combination of experiment and theory. *Chem. Mater.* **23**, 1700–1718 (2011).

126. Sannes, D. K., Øien-ØDegaard, S., Aunan, E., Nova, A. & Olsbye, U. Quantification of

Linker Defects in UiO-Type Metal-Organic Frameworks. *Chem. Mater.* **35**, 3793–3800 (2023).

127. Zhang, J. *et al.* Neighboring Zn-Zr Sites in a Metal-Organic Framework for CO2Hydrogenation. *J. Am. Chem. Soc.* **143**, 8829–8837 (2021).

128. Kim, J. Y. *et al.* Stability of Zr-Based UiO-66 Metal–Organic Frameworks in Basic Solutions. *Nanomaterials* **14**, 110 (2024).

129. Chu, J. *et al.* Facile and reversible digestion and regeneration of zirconium-based metal-organic frameworks. *Commun. Chem.* **3**, 5 (2020).

130. Dissegna, S., Epp, K., Heinz, W. R., Kieslich, G. & Fischer, R. A. Defective Metal-Organic Frameworks. *Adv. Mater.* **30**, 1704501 (2018).

131. Ma, X., Wang, L., Zhang, Q. & Jiang, H. L. Switching on the Photocatalysis of Metal–Organic Frameworks by Engineering Structural Defects. *Angew. Chemie - Int. Ed.* **58**, 12175–12179 (2019).

132. Li, S., Han, W., An, Q. F., Yong, K. T. & Yin, M. J. Defect Engineering of MOF-Based Membrane for Gas Separation. *Adv. Funct. Mater.* **33**, 2303447 (2023).

133. Fang, Z., Bueken, B., De Vos, D. E. & Fischer, R. A. Defect-Engineered Metal-Organic Frameworks. *Angew. Chemie - Int. Ed.* **54**, 7234–7254 (2015).

134. Zhou, S. *et al.* Elastic Aerogels of Cellulose Nanofibers@Metal–Organic Frameworks for Thermal Insulation and Fire Retardancy. *Nano-Micro Lett.* **12**, 1–13 (2020).

135. Hu, T., Chang, S., Wu, H., Li, L. & Yuan, W. Construction of high thermal conductivity MOFs composite phase change materials with reinforced light-to-thermal conversion. *Sol. Energy Mater. Sol. Cells* **232**, 111339 (2021).

136. Zhu, S. Q., Shu, J. C. & Cao, M. S. Novel MOF-derived 3D hierarchical needlelike array architecture with excellent EMI shielding, thermal insulation and supercapacitor performance. *Nanoscale* **14**, 7322–7331 (2022).

137. Islamov, M., Boone, P., Babaei, H., McGaughey, A. J. H. & Wilmer, C. E. Correlated missing linker defects increase thermal conductivity in metal-organic framework UiO-66†. *AIChE Annu. Meet. Conf. Proc.* **2023-Novem**, 6592–6600 (2023).

138. Shearer, G. C. *et al.* Defect Engineering: Tuning the Porosity and Composition of the Metal-Organic Framework UiO-66 via Modulated Synthesis. *Chem. Mater.* **28**, 3749–3761 (2016).

139. Cliffe, M. J. *et al.* Correlated defect nanoregions in a metal-organic framework. *Nat. Commun.* **5**, 4176 (2014).

140. Bennett, T. D., Cheetham, A. K., Fuchs, A. H. & Coudert, F. X. Interplay between defects, disorder and flexibility in metal-organic frameworks. *Nat. Chem.* **9**, 11–16 (2016).

141. Simonov, A. & Goodwin, A. L. Designing disorder into crystalline materials. *Nat. Rev. Chem.* **4**, 657–673 (2020).

142. Meekel, E. G. & Goodwin, A. L. Correlated disorder in metal-organic frameworks.

CrystEngComm **23**, 2915–2922 (2021).

143. Feng, X. *et al.* Generating Catalytic Sites in UiO-66 through Defect Engineering. *ACS Appl. Mater. Interfaces* **13**, 60715–60735 (2021).

144. Nam, D., Kim, J. & Choe, W. Evolution of Zr nodes in metal–organic frameworks. *Trends Chem.* **5**, 339–352 (2023).

145. Zhang, Y. *et al.* A Flexible Metal-Organic Framework with 4-Connected Zr6 Nodes. *J. Am. Chem. Soc.* **140**, 11179–11183 (2018).

146. Wang, X. N., Zhao, Y. M., Kirchon, A., Li, B. & Zhou, H. C. Regulating the Topologies of Zirconium-Organic Frameworks for a Crystal Sponge Applicable to Inorganic Matter. *Inorg. Chem.* **59**, 11940–11944 (2020).

147. Chen, Y. *et al.* Structural Diversity of Zirconium Metal-Organic Frameworks and Effect on Adsorption of Toxic Chemicals. *J. Am. Chem. Soc.* **142**, 21428–21438 (2020).

148. Nguyen, P. T. K. *et al.* New Metal-Organic Frameworks for Chemical Fixation of CO2. *ACS Appl. Mater. Interfaces* **10**, 733–744 (2018).

149. Gong, W., Liu, Y. & Cui, Y. Chiral and robust Zr(iv)-based metal-organic frameworks built from spiro skeletons. *Faraday Discuss.* **231**, 168–180 (2021).

150. He, T. *et al.* Zr(IV)-Based Metal-Organic Framework with T-Shaped Ligand: Unique Structure, High Stability, Selective Detection, and Rapid Adsorption of Cr2O72- in Water. *ACS Appl. Mater. Interfaces* **10**, 16650–16659 (2018).

151. Zhang, Y. Z. *et al.* Tuning Water Sorption in Highly Stable Zr(IV)-Metal-Organic Frameworks through Local Functionalization of Metal Clusters. *ACS Appl. Mater. Interfaces* **10**, 27868–27874 (2018).

152. Bon, V., Senkovska, I., Baburin, I. A. & Kaskel, S. Zr- and Hf-based metal-organic frameworks: Tracking down the polymorphism. *Cryst. Growth Des.* **13**, 1231–1237 (2013).

153. Zhang, X., Frey, B. L., Chen, Y. S. & Zhang, J. Topology-Guided Stepwise Insertion of Three Secondary Linkers in Zirconium Metal-Organic Frameworks. *J. Am. Chem. Soc.* **140**, 7710–7715 (2018).

154. Hurlock, M. J. *et al.* Evolution of 14-Connected Zr6Secondary Building Units through Postsynthetic Linker Incorporation. *ACS Appl. Mater. Interfaces* **13**, 51945–51953 (2021).

155. Gong, W. *et al.* Highly Specific Coordination-Driven Self-Assembly of 2D Heterometallic Metal-Organic Frameworks with Unprecedented Johnson-type (J51) Nonanuclear Zr-Oxocarboxylate Clusters. *J. Am. Chem. Soc.* **143**, 657–663 (2021).

156. Jiang, H. *et al.* Topology-Based Functionalization of Robust Chiral Zr-Based Metal-Organic Frameworks for Catalytic Enantioselective Hydrogenation. *J. Am. Chem. Soc.* **142**, 9642–9652 (2020).

157. Bezrukov, A. A., Törnroos, K. W., Le Roux, E. & Dietzel, P. D. C. Incorporation of an intact dimeric Zr12 oxo cluster from a molecular precursor in a new zirconium metal-

USC UNIVERSIDADE DE SANTIAGO DE COMPOSTELA

organic framework. *Chem. Commun.* **54**, 2735–2738 (2018).

158. Gong, W. *et al.* Topological Strain-Induced Regioselective Linker Elimination in a Chiral Zr(IV)-Based Metal-Organic Framework. *Chem* **7**, 190–201 (2021).

159. Leubner, S. *et al.* Synthesis and Exfoliation of a New Layered Mesoporous Zr-MOF Comprising Hexa- A nd Dodecanuclear Clusters as Well as a Small Organic Linker Molecule. *J. Am. Chem. Soc.* **142**, 15995–16000 (2020).

160. Dai, R. *et al.* Electron Crystallography Reveals Atomic Structures of Metal-Organic Nanoplates with M12(μ3-O)8(μ3-OH)8(μ2-OH)6 (M = Zr, Hf) Secondary Building Units. *Inorg. Chem.* **56**, 8128–8134 (2017).

161. Hou, B., Qin, C., Sun, C., Wang, X. & Su, Z. Stepwise Construction of Multivariate Metal–Organic Frameworks from a Predesigned Zr16 Cluster. *CCS Chem.* **3**, 287–293 (2021).

162. Zhang, X. *et al.* A historical perspective on porphyrin-based metal–organic frameworks and their applications. *Coord. Chem. Rev.* **429**, 213615 (2021).

163. Chen, J., Zhu, Y. & Kaskel, S. Porphyrin-Based Metal–Organic Frameworks for Biomedical Applications. *Angew. Chemie - Int. Ed.* **60**, 5010–5035 (2021).

164. Feng, L., Wang, K. Y., Joseph, E. & Zhou, H. C. Catalytic Porphyrin Framework Compounds. *Trends Chem.* **2**, 555–568 (2020).

165. Cichocka, M. O. *et al.* A Porphyrinic Zirconium Metal-Organic Framework for Oxygen Reduction Reaction: Tailoring the Spacing between Active-Sites through Chain-Based Inorganic Building Units. *J. Am. Chem. Soc.* **142**, 15386–15395 (2020).

166. Liu, T. F. *et al.* Topology-guided design and syntheses of highly stable mesoporous porphyrinic zirconium metal-organic frameworks with high surface area. *J. Am. Chem. Soc.* **137**, 413–419 (2015).

167. Feng, D. *et al.* Metal-organic frameworks based on previously unknown Zr8/Hf 8 cubic clusters. *Inorg. Chem.* **52**, 12661–12667 (2013).

168. Koschnick, C. *et al.* Understanding disorder and linker deficiency in porphyrinic zirconium-based metal–organic frameworks by resolving the Zr8O6 cluster conundrum in PCN-221. *Nat. Commun.* **12**, 3099 (2021).

169. Ceballos, M. *et al.* Seeded-Growth of PCN-224 onto Plasmonic Nanoparticles: Photoactive Microporous Nanocarriers. *Small Struct.* **5**, 2300464 (2024).

170. Chen, X. *et al.* Formulation of Metal-Organic Framework-Based Drug Carriers by Controlled Coordination of Methoxy PEG Phosphate: Boosting Colloidal Stability and Redispersibility. *J. Am. Chem. Soc.* **143**, 13557–13572 (2021).

171. Gong, X., Noh, H., Gianneschi, N. C. & Farha, O. K. Interrogating Kinetic versus Thermodynamic Topologies of Metal-Organic Frameworks via Combined Transmission Electron Microscopy and X-ray Diffraction Analysis. *J. Am. Chem. Soc.* **141**, 6146–6151 (2019).

172. Koschnick, C. *et al.* Influence of Water Content on Speciation and Phase Formation in

USC UNIVERSIDADE DE SANTIAGO DE COMPOSTELA

Zr–Porphyrin-Based MOFs. *Adv. Mater.* **36**, 2210613 (2024).

173. Boström, H. L. B. *et al.* How Reproducible is the Synthesis of Zr–Porphyrin Metal–Organic Frameworks? An Interlaboratory Study. *Adv. Mater.* **36**, 102304832 (2024).

174. McGuire, C. V. & Forgan, R. S. The surface chemistry of metal-organic frameworks. *Chem. Commun.* **51**, 5199–5217 (2015).

175. Wang, J. *et al.* Covalently connected core–shell NH2-UiO-66@Br-COFs hybrid materials for CO2 capture and I2 vapor adsorption. *Chem. Eng. J.* **438**, 135555 (2022).

176. Chun, J. *et al.* Metal−Organic Framework@Microporous Organic Network: Hydrophobic Adsorbents with a Crystalline Inner Porosity. *J. Am. Chem. Soc.* **136**, 6786–6789 (2014).

177. Kolb, H. C., Finn, M. G. & Sharpless, K. B. Click Chemistry: Diverse Chemical Function from a Few Good Reactions. *Angew. Chemie - Int. Ed.* **40**, 2004–2021 (2001).

178. Morris, W., Briley, W. E., Auyeung, E., Cabezas, M. D. & Mirkin, C. A. Nucleic Acid − Metal Organic Framework (MOF) Nanoparticle Conjugates. *J. Am. Chem. Soc.* **136**, 7261–7264 (2014).

179. Fernández-Morales, J. M. *et al.* Direct sulfation of a Zr-based metal-organic framework to attain strong acid catalysts. *Microporous Mesoporous Mater.* **290**, 109686 (2019).

180. Liu, B., Baumann, A. E., Butala, M. M. & Thoi, V. S. Phosphate-functionalized Zirconium Metal–Organic Frameworks for Enhancing Lithium–Sulfur Battery Cycling. *Chem. - A Eur. J.* **29**, e202300821 (2023).

181. Syed, Z. H. *et al.* Sulfated Zirconium Metal-Organic Frameworks as Well-Defined Supports for Enhancing Organometallic Catalysis. *J. Am. Chem. Soc.* **144**, 16883–16897 (2022).

182. Wang, S. *et al.* Surface-specific functionalization of nanoscale metal-organic frameworks. *Angew. Chemie - Int. Ed.* **54**, 14738–14742 (2015).

183. Yang, X. *et al.* Metal-Organic Framework Nanoparticles with Universal Dispersibility through Crown Ether Surface Coordination for Phase-Transfer Catalysis and Separation Membranes. *Angew. Chemie* **135**, e202303280 (2023).

184. Wang, A., Barcus, K. & Cohen, S. M. Quantifying Ligand Binding to the Surface of Metal-Organic Frameworks. *J. Am. Chem. Soc.* **145**, 16821–16827 (2023).

185. Barcus, K. & Cohen, S. M. Free-standing metal-organic framework (MOF) monolayers by self-assembly of polymer-grafted nanoparticles. *Chem. Sci.* **11**, 8433–8437 (2020).

186. Barcus, K., Lin, P. A., Zhou, Y., Arya, G. & Cohen, S. M. Influence of Polymer Characteristics on the Self-Assembly of Polymer-Grafted Metal-Organic Framework Particles. *ACS Nano* **16**, 18168–18177 (2022).

187. Hang, Y., Wang, A. & Wu, N. Plasmonic silver and gold nanoparticles: shape- and structure-modulated plasmonic functionality for point-of-caring sensing, bio-imaging and medical therapy. *Chem. Soc. Rev.* **53**, 2932–2971 (2024).

188. Langer, J. *et al.* Present and Future of Surface-Enhanced Raman Scattering. *ACS Nano*

14, 28–117 (2020).

189. Deng, M. *et al.* Plasmonic Modulation of Valleytronic Emission in Two-Dimensional Transition Metal Dichalcogenides. *Adv. Funct. Mater.* **31**, 2010234 (2021).

190. Mishra, R. *et al.* Optimized Titanium Nitride Epitaxial Film for Refractory Plasmonics and Solar Energy Harvesting. *J. Phys. Chem. C* **125**, 13658–13665 (2021).

191. Jain, V., Kashyap, R. K. & Pillai, P. P. Plasmonic Photocatalysis: Activating Chemical Bonds through Light and Plasmon. *Adv. Opt. Mater.* **10**, 2200463 (2022).

192. Reguera, J. *et al.* Anisotropic metal nanoparticles for surface enhanced Raman scattering. *Chem. Soc. Rev.* **46**, 3866–3885 (2017).

193. Palik, E. *Handbook of Optical Constants of Solids*. (Academic Press, New York, United States, 1985).

194. Schlücker, S. *Surface Enhanced Raman Spectroscopy Analytical, Biophysical Ans Life Science Applications*. (Wiley-VCH, Weinheim, Germany, 2011).

195. Wiederrecht, G. *Handbook of Nannoscale Optics and Electronics*. (Elsevier B.V, Amsterdam, Nederlands, 2010).

196. Walker, C. T. & Slack, G. A. Who Named the -ON's? *Am. J. Phys.* **38**, 1380–1389 (1970).

197. Piel, A. *Plasma Physics – An Introduction to Laboratory, Space, and Fusion Plasmas*. *Contemporary Physics* (Springer-Verlag, Berlin, Germany, 2010).

198. Kittel, C. *Introduction to Solid State Physics*. (John Wiley & Sons, California, United States, 2005).

199. Yu, R., Liz-Marzán, L. M. & García De Abajo, F. J. Universal analytical modeling of plasmonic nanoparticles. *Chem. Soc. Rev.* **46**, 6710–6724 (2017).

200. Mie, G. Beiträge zur Optik trüber Medien, speziell kolloidaler Metallösungen. *Ann. Phys.* **330**, 377–445 (1908).

201. Bastús, N. G., Piella, J. & Puntes, V. Quantifying the Sensitivity of Multipolar (Dipolar, Quadrupolar, and Octapolar) Surface Plasmon Resonances in Silver Nanoparticles: The Effect of Size, Composition, and Surface Coating. *Langmuir* **32**, 290–300 (2016).

202. Lalisse, A., Tessier, G., Plain, J. & Baffou, G. Quantifying the Efficiency of Plasmonic Materials for Near-Field Enhancement and Photothermal Conversion. *J. Phys. Chem. C* **119**, 25518–25528 (2015).

203. Jain, P. K. Taking the Heat off of Plasmonic Chemistry. *J. Phys. Chem. C* **123**, 24347–24351 (2019).

204. Rahman, M. A. & Saghir, M. Z. Thermodiffusion or Soret effect: Historical review. *Int. J. Heat Mass Transf.* **73**, 693–705 (2014).

205. Biswas, A. *et al.* Advances in top-down and bottom-up surface nanofabrication: Techniques, applications & future prospects. *Adv. Colloid Interface Sci.* **170**, 2–27 (2012).

USC UNIVERSIDADE DE SANTIAGO DE COMPOSTELA

206. Grzelczak, M., Pérez-Juste, J., Mulvaney, P. & Liz-Marzán, L. M. Shape control in gold nanoparticle synthesis. *Chem. Soc. Rev.* **37**, 1783–1791 (2008).

207. Turkevich, J., Stevenson, P. C. & Hillier, J. A study of the nucleation and growth processes in the synthesis of colloidal gold. *Discuss. Faraday Soc.* **11**, 55–75 (1951).

208. Schulz, F. *et al.* Little adjustments significantly improve the Turkevich synthesis of gold nanoparticles. *Langmuir* **30**, 10779–10784 (2014).

209. Edwards, P. P. & Thomas, J. M. Gold in a metallic divided state - From Faraday to present-day nanoscience. *Angew. Chemie - Int. Ed.* **46**, 5480–5486 (2007).

210. Jin, R. *et al.* Photoinduced conversion of silver nanospheres to nanoprisms. *Science* **294**, 1901–1903 (2001).

211. Xue, C., Métraux, G. S., Millstone, J. E. & Mirkin, C. A. Mechanistic study of photomediated triangular silver nanoprism growth. *J. Am. Chem. Soc.* **130**, 8337–8344 (2008).

212. Zhang, Q., Li, N., Goebl, J., Lu, Z. & Yin, Y. A systematic study of the synthesis of silver nanoplates: is citrate a 'magic' reagent? *J. Am. Chem. Soc.* **133**, 18931–18939 (2011).

213. Mittal, A. K., Chisti, Y. & Banerjee, U. C. Synthesis of metallic nanoparticles using plant extracts. *Biotechnol. Adv.* **31**, 346–356 (2013).

214. Cobley, C. M. & Xia, Y. Engineering the properties of metal nanostructures via galvanic replacement reactions. *Mater. Sci. Eng. R Reports* **70**, 44–62 (2010).

215. Xia, X., Wang, Y., Ruditskiy, A. & Xia, Y. 25th anniversary article: Galvanic replacement: A simple and versatile route to hollow nanostructures with tunable and well-controlled properties. *Adv. Mater.* **25**, 6313–6333 (2013).

216. Cheng, H., Wang, C., Qin, D. & Xia, Y. Galvanic Replacement Synthesis of Metal Nanostructures: Bridging the Gap between Chemical and Electrochemical Approaches. *Acc. Chem. Res.* **56**, 900–909 (2023).

217. Nikoobakht, B. & El-Sayed, M. A. Preparation and growth mechanism of gold nanorods (NRs) using seed-mediated growth method. *Chem. Mater.* **15**, 1957–1962 (2003).

218. Pérez-Juste, J., Pastoriza-Santos, I., Liz-Marzán, L. M. & Mulvaney, P. Gold nanorods: Synthesis, characterization and applications. *Coord. Chem. Rev.* **249**, 1870–1901 (2005).

219. Walsh, M. J. *et al.* A Mechanism for Symmetry Breaking and Shape Control in Single-Crystal Gold Nanorods. *Acc. Chem. Res.* **50**, 2925–2935 (2017).

220. Walsh, M. J., Barrow, S. J., Tong, W., Funston, A. M. & Etheridge, J. Symmetry breaking and silver in gold nanorod growth. *ACS Nano* **9**, 715–724 (2015).

221. Guerrero-Martínez, A., Barbosa, S., Pastoriza-Santos, I. & Liz-Marzán, L. M. Nanostars shine bright for you. Colloidal synthesis, properties and applications of branched metallic nanoparticles. *Curr. Opin. Colloid Interface Sci.* **16**, 118–127 (2011).

222. Sánchez-Iglesias, A. *et al.* High-Yield Seeded Growth of Monodisperse Pentatwinned Gold Nanoparticles through Thermally Induced Seed Twinning. *J. Am. Chem. Soc.* **139**,

107–110 (2017).

223. Sato, Y. & Mizutani, F. Formation and characterization of aromatic selenol and thiol monolayers on gold: in-situ IR studies and electrochemical measurements. *Phys. Chem. Chem. Phys.* **6**, 1328–1331 (2004).

224. Hühn, J. *et al.* Selected standard protocols for the synthesis, phase transfer, and characterization of inorganic colloidal nanoparticles. *Chem. Mater.* **29**, 399–461 (2017).

225. Liu, B. & Liu, J. Methods for preparing DNA-functionalized gold nanoparticles, a key reagent of bioanalytical chemistry. *Anal. Methods* **9**, 2633–2643 (2017).

226. Pelaz, B. *et al.* Surface Functionalization of Nanoparticles with Polyethylene Glycol: Effects on Protein Adsorption and Cellular Uptake. *ACS Nano* **9**, 6996–7008 (2015).

227. del Pino, P. *et al.* Basic Physicochemical Properties of Polyethylene Glycol Coated Gold Nanoparticles that Determine Their Interaction with Cells. *Angew. Chemie* **128**, 5573–5577 (2016).

228. Malikova, N., Pastoriza-Santos, I., Schierhorn, M., Kotov, N. A. & Liz-Marzán, L. M. Layer-by-layer assembled mixed spherical and planar gold nanoparticles: Control of interparticle interactions. *Langmuir* **18**, 3694–3697 (2002).

229. Correa-Duarte, M. A., Kosiorek, A., Kandulski, W., Giersig, M. & Liz-Marzán, L. M. Layer-by-layer assembly of multiwall carbon nanotubes on spherical colloids. *Chem. Mater.* **17**, 3268–3272 (2005).

230. Osterrieth, J. W. M. & Fairen-Jimenez, D. Metal–Organic Framework Composites for Theragnostics and Drug Delivery Applications. *Biotechnol. J.* **16**, 2000005 (2021).

231. Zheng, G., Pastoriza-Santos, I., Pérez-Juste, J. & Liz-Marzán, L. M. Plasmonic metal-organic frameworks. *SmartMat* **2**, 446–465 (2021).

232. Dai, S., Tissot, A. & Serre, C. Recent Progresses in Metal–Organic Frameworks Based Core–shell Composites. *Adv. Energy Mater.* **12**, 2100061 (2022).

233. Zhang, W., Bojdys, M. J. & Pinna, N. A Universal Synthesis Strategy for Tunable Metal-Organic Framework Nanohybrids. *Angew. Chemie - Int. Ed.* **62**, e202301021 (2023).

234. Jiang, Y. *et al.* N-Heterocyclic Carbene-Stabilized Ultrasmall Gold Nanoclusters in a Metal-Organic Framework for Photocatalytic CO2 Reduction. *Angew. Chemie - Int. Ed.* **60**, 17388–17393 (2021).

235. Cao, J. *et al.* Tailoring the Asymmetric Structure of NH 2 -UiO-66 Metal-Organic Frameworks for Light-promoted Selective and Efficient Gold Extraction and Separation. *Angew. Chemie* **135**, e202302202 (2023).

236. Volosskiy, B. *et al.* Metal-organic framework templated synthesis of ultrathin, well-Aligned metallic nanowires. *ACS Nano* **9**, 3044–3049 (2015).

237. Carrillo-Carrión, C. *et al.* Plasmonic-Assisted Thermocyclizations in Living Cells Using Metal-Organic Framework Based Nanoreactors. *ACS Nano* **15**, 16924–16933 (2021).

238. Carrillo-Carrión, C. *et al.* Aqueous Stable Gold Nanostar/ZIF-8 Nanocomposites for Light-Triggered Release of Active Cargo Inside Living Cells. *Angew. Chemie* **131**,

USC UNIVERSIDADE DE SANTIAGO DE COMPOSTELA

7152–7156 (2019).

239. Martínez, R. *et al.* Core-Shell Palladium/MOF Platforms as Diffusion-Controlled Nanoreactors in Living Cells and Tissue Models. *Cell Reports Phys. Sci.* **1**, 100076 (2020).

240. Li, Y. Y. H. *et al.* Creating an Aligned Interface between Nanoparticles and MOFs by Concurrent Replacement of Capping Agents. *J. Am. Chem. Soc.* **143**, 5182–5190 (2021).

241. Zhao, L. *et al.* Gold Nanorods (AuNRs) and Zeolitic Imidazolate Framework-8 (ZIF-8) Core-Shell Nanostructure-Based Electrochemical Sensor for Detecting Neurotransmitters. *ACS Omega* **6**, 33149–33158 (2021).

242. Zheng, G. *et al.* Shape control in ZIF-8 nanocrystals and metal nanoparticles@ZIF-8 heterostructures. *Nanoscale* **9**, 16645–16651 (2017).

243. Yang, X. *et al.* Site-Selective Deposition of Metal-Organic Frameworks on Gold Nanobipyramids for Surface-Enhanced Raman Scattering. *Nano Lett.* **21**, 8205–8212 (2021).

244. Li, Y., Guo, H., Yin, Z., Lyle, K. & Tian, L. Metal-Organic Frameworks for Preserving the Functionality of Plasmonic Nanosensors. *ACS Appl. Mater. Interfaces* **13**, 5564–5573 (2021).

245. Zorlu, T. *et al.* Optical Quantification of Metal Ions Using Plasmonic Nanostructured Microbeads Coated with Metal-Organic Frameworks and Ion-Selective Dyes. *ACS Nanosci. Au* **3**, 222–229 (2023).

246. De Marchi, S. *et al.* Programmable Modular Assembly of Functional Proteins on Raman-Encoded Zeolitic Imidazolate Framework-8 (ZIF-8) Nanoparticles as SERS Tags. *Chem. Mater.* **32**, 5739–5749 (2020).

247. Cedrún-Morales, M. *et al.* Light-Responsive Nanoantennas Integrated into Nanoscale Metal–Organic Frameworks for Photothermal Drug Delivery. *Small Sci.* **4**, 2400088 (2024).

248. Osterrieth, J. W. M. *et al.* Core-Shell Gold Nanorod@Zirconium-Based Metal-Organic Framework Composites as in Situ Size-Selective Raman Probes. *J. Am. Chem. Soc.* **141**, 3893–3900 (2019).

249. Khaletskaya, K. *et al.* Integration of porous coordination polymers and gold nanorods into core-shell mesoscopic composites toward light-induced molecular release. *J. Am. Chem. Soc.* **135**, 10998–11005 (2013).

250. Li, J. *et al.* Assembly of gold nanorods functionalized by zirconium-based metal-organic frameworks for surface enhanced Raman scattering. *Nanoscale* **14**, 5561–5568 (2022).

251. Rungtaweevoranit, B. *et al.* Copper Nanocrystals Encapsulated in Zr-based Metal-Organic Frameworks for Highly Selective CO2 Hydrogenation to Methanol. *Nano Lett.* **16**, 7645–7649 (2016).

252. Zheng, Z., Xu, H., Xu, Z. & Ge, J. A Monodispersed Spherical Zr-Based Metal–Organic Framework Catalyst, Pt/Au@Pd@UIO-66, Comprising an Au@Pd Core–Shell Encapsulated in a UIO-66 Center and Its Highly Selective CO2 Hydrogenation to

Produce CO. *Small* **14**, 1702812 (2018).

253. Zhao, M. *et al.* Core−Shell Palladium Nanoparticle@Metal−Organic Frameworks as Multifunctional Catalysts for Cascade Reactions. *J. Am. Chem. Soc.* **136**, 1738–1741 (2014).

254. He, L. *et al.* Core-Shell Noble-Metal@Metal-Organic-Framework Nanoparticles with Highly Selective Sensing Property. *Angew. Chemie* **125**, 3829–3833 (2013).

255. Yang, Y. *et al.* Litchi-like Fe3O4@Fe-MOF capped with HAp gatekeepers for pH-triggered drug release and anticancer effect. *J. Mater. Chem. B* **5**, 8600–8606 (2017).

256. Li, Y. *et al.* Core-Shell Upconversion Nanoparticle@Metal-Organic Framework Nanoprobes for Luminescent/Magnetic Dual-Mode Targeted Imaging. *Adv. Mater.* **27**, 4075–4080 (2015).

257. Deng, K. *et al.* Aptamer-mediated up-conversion core/MOF shell nanocomposites for targeted drug delivery and cell imaging. *Sci. Rep.* **5**, 7851 (2015).

258. Chowdhuri, A. R., Laha, D., Pal, S., Karmakar, P. & Sahu, S. K. One-pot synthesis of folic acid encapsulated upconversion nanoscale metal organic frameworks for targeting, imaging and pH responsive drug release. *Dalt. Trans.* **45**, 18120–18132 (2016).

259. Liu, Y. *et al.* Core-shell metal-organic frameworks with fluorescence switch to trigger an enhanced photodynamic therapy. *Theranostics* **9**, 2791–2799 (2019).

260. Xu, H., Sommer, S., Broge, N. L. N., Gao, J. & Iversen, B. B. The Chemistry of Nucleation: In Situ Pair Distribution Function Analysis of Secondary Building Units During UiO-66 MOF Formation. *Chem. - A Eur. J.* **25**, 2051–2058 (2019).

261. Chen, Z. *et al.* Scalable, room temperature, and water-based synthesis of functionalized zirconium-based metal-organic frameworks for toxic chemical removal. *CrystEngComm* **21**, 2409–2415 (2019).

262. Chen, Z., Wang, X., Islamoglu, T. & Farha, O. K. Green synthesis of a functionalized zirconium-based metal-organic framework for water and ethanol adsorption. *Inorganics* **7**, 56 (2019).

263. Katz, M. J. *et al.* A facile synthesis of UiO-66, UiO-67 and their derivatives. *Chem. Commun.* **49**, 9449–9451 (2013).

264. Goesten, M. G. *et al.* Evidence for a chemical clock in oscillatory formation of UiO-66. *Nat. Commun.* **7**, 11832 (2016).

265. Yee, K. K., Wong, Y. L. & Xu, Z. Bio-inspired stabilization of sulfenyl iodide RS-I in a Zr(IV)-based metal-organic framework. *Dalt. Trans.* **45**, 5334–5338 (2016).

266. Lin, K. Y. A., Liu, Y. T. & Chen, S. Y. Adsorption of fluoride to UiO-66-NH2 in water: Stability, kinetic, isotherm and thermodynamic studies. *J. Colloid Interface Sci.* **461**, 79–87 (2016).

267. Reinsch, H. *et al.* First examples of aliphatic zirconium MOFs and the influence of inorganic anions on their crystal structures. *CrystEngComm* **17**, 331–337 (2015).

268. Zeng, H. *et al.* A novel strategy for enhancing the performance of membranes for dyes

separation: Embedding PAA@UiO-66-NH2 between graphene oxide sheets. *Chem. Eng. J.* **403**, 126281 (2021).

269. Ma, Y. *et al.* Atomically Dispersed Copper Sites in a Metal-Organic Framework for Reduction of Nitrogen Dioxide. *J. Am. Chem. Soc.* **143**, 10977–10985 (2021).

270. Pintado-Sierra, M., Rasero-Almansa, A. M., Corma, A., Iglesias, M. & Sánchez, F. Bifunctional iridium-(2-aminoterephthalate)-Zr-MOF chemoselective catalyst for the synthesis of secondary amines by one-pot three-step cascade reaction. *J. Catal.* **299**, 137–145 (2013).

271. Du, Y., Li, X., Lv, X. & Jia, Q. Highly Sensitive and Selective Sensing of Free Bilirubin Using Metal-Organic Frameworks-Based Energy Transfer Process. *ACS Appl. Mater. Interfaces* **9**, 30925–30932 (2017).

272. Hou, J. *et al.* Synthesis of UiO-66-NH2 derived heterogeneous copper (II) catalyst and study of its application in the selective aerobic oxidation of alcohols. *J. Mol. Catal. A Chem.* **407**, 53–59 (2015).

273. Jiang, Y., Liu, C., Caro, J. & Huang, A. A new UiO-66-NH2 based mixed-matrix membranes with high CO2/CH4 separation performance. *Microporous Mesoporous Mater.* **274**, 203–211 (2019).

274. Feng, Y., Chen, Q., Cao, M., Ling, N. & Yao, J. Defect-Tailoring and Titanium Substitution in Metal-Organic Framework UiO-66-NH2 for the Photocatalytic Degradation of Cr(VI) to Cr(III). *ACS Appl. Nano Mater.* **2**, 5973–5980 (2019).

275. Subudhi, S., Swain, G., Tripathy, S. P. & Parida, K. UiO-66-NH2 Metal-Organic Frameworks with Embedded MoS2 Nanoflakes for Visible-Light-Mediated H2 and O2 Evolution. *Inorg. Chem.* **59**, 9824–9837 (2020).

276. Dwyer, D. B. *et al.* Toxic Organophosphate Hydrolysis Using Nanofiber-Templated UiO-66-NH2 Metal-Organic Framework Polycrystalline Cylinders. *ACS Appl. Mater. Interfaces* **10**, 25794–25803 (2018).

277. Safa, S., Khajeh, M., Reza Oveisi, A. & Azimirad, R. Graphene quantum dots incorporated UiO-66-NH2 as a promising photocatalyst for degradation of long-chain oleic acid. *Chem. Phys. Lett.* **762**, 138129 (2021).

278. Molavi, H., Eskandari, A., Shojaei, A. & Mousavi, S. A. Enhancing CO2/N2 adsorption selectivity via post-synthetic modification of NH2-UiO-66(Zr). *Microporous Mesoporous Mater.* **257**, 193–201 (2018).

279. Užarević, K. *et al.* Mechanochemical and solvent-free assembly of zirconium-based metal-organic frameworks. *Chem. Commun.* **52**, 2133–2136 (2016).

280. Morris, W. *et al.* Role of modulators in controlling the colloidal stability and polydispersity of the UiO-66 metal-organic framework. *ACS Appl. Mater. Interfaces* **9**, 33413–33418 (2017).

281. Haddad, S. *et al.* Design of a Functionalized Metal-Organic Framework System for Enhanced Targeted Delivery to Mitochondria. *J. Am. Chem. Soc.* **142**, 6661–6674 (2020).

USC UNIVERSIDADE DE SANTIAGO DE COMPOSTELA

282. Orellana-Tavra, C. *et al.* Amorphous metal-organic frameworks for drug delivery. *Chem. Commun.* **51**, 13878–13881 (2015).

283. Abánades Lázaro, I., Abánades Lázaro, S. & Forgan, R. S. Enhancing anticancer cytotoxicity through bimodal drug delivery from ultrasmall Zr MOF nanoparticles. *Chem. Commun.* **54**, 2792–2795 (2018).

284. Abánades Lázaro, I. *et al.* Mechanistic Investigation into the Selective Anticancer Cytotoxicity and Immune System Response of Surface-Functionalized, Dichloroacetate-Loaded, UiO-66 Nanoparticles. *ACS Appl. Mater. Interfaces* **10**, 5255–5268 (2018).

285. Hashemzadeh, A. *et al.* When metal-organic framework mediated smart drug delivery meets gastrointestinal cancers. *J. Mater. Chem. B* **9**, 3967–3982 (2021).

286. Chen, D. *et al.* In Vivo Targeting and Positron Emission Tomography Imaging of Tumor with Intrinsically Radioactive Metal-Organic Frameworks Nanomaterials. *ACS Nano* **11**, 4315–4327 (2017).

287. Pan, Y. *et al.* A versatile and multifunctional metal-organic framework nanocomposite toward chemo-photodynamic therapy. *Dalt. Trans.* **49**, 5291–5301 (2020).

288. Abánades Lázaro, I., Wells, C. J. R. & Forgan, R. S. Multivariate Modulation of the Zr MOF UiO-66 for Defect-Controlled Combination Anticancer Drug Delivery. *Angew. Chemie* **132**, 5249–5255 (2020).

289. Polo, E., Collado, M., Pelaz, B. & Del Pino, P. Advances toward More Efficient Targeted Delivery of Nanoparticles in Vivo: Understanding Interactions between Nanoparticles and Cells. *ACS Nano* **11**, 2397–2402 (2017).

290. Pelaz, B. *et al.* Diverse Applications of Nanomedicine. *ACS Nano* **11**, 2313–2381 (2017).

291. Orellana-Tavra, C., Mercado, S. A. & Fairen-Jimenez, D. Endocytosis Mechanism of Nano Metal-Organic Frameworks for Drug Delivery. *Adv. Healthc. Mater.* **5**, 2261–2270 (2016).

292. Samanta, S. *et al.* Fluorescent Probes for Nanoscopic Imaging of Mitochondria. *Chem* **5**, 1697–1726 (2019).

293. Ma, C., Xia, F. & Kelley, S. O. Mitochondrial Targeting of Probes and Therapeutics to the Powerhouse of the Cell. *Bioconjug. Chem.* **31**, 2650–2667 (2020).

294. Xu, M. *et al.* How entanglement of different physicochemical properties complicates the prediction of in vitro and in vivo interactions of gold nanoparticles. *ACS Nano* **12**, 10104–10113 (2018).

295. Feliu, N. *et al.* Nanoparticle dosage-a nontrivial task of utmost importance for quantitative nanosafety research. *Wiley Interdiscip. Rev. Nanomedicine Nanobiotechnology* **8**, 479–492 (2016).

296. Schubert, U. En route from metal alkoxides to metal oxides: metal oxo/alkoxo clusters. *J. Sol-Gel Sci. Technol.* **105**, 587–595 (2023).

297. Piszczek, P., Radtke, A., Grodzicki, A., Wojtczak, A. & Chojnacki, J. The new type of [Zr6(μ3-O)4(μ3-OH)4] cluster core: Crystal structure and spectral characterization of

USC UNIVERSIDADE DE SANTIAGO DE COMPOSTELA

[Zr6O4(OH)4(OOCR)12] (R = But, C(CH3)2Et). *Polyhedron* **26**, 679–685 (2007).

298. Kickelbick, G., Wiede, P. & Schubert, U. Variations in capping the Zr6O4(OH)4 cluster core: X-ray structure analyses of [Zr6(OH)4O4(OOC-CH=CH2) 10]2(μ-OOC-CH=CH2)4 and Zr6(OH)4O4(OOCR)12(PrOH) (R = Ph, CMe = CH2). *Inorganica Chim. Acta* **284**, 1–7 (1999).

299. Kickelbick, G. & Schubert, U. Oxozirconium Methacrylate Clusters: Zr6(OH)404(OMc)12 and Zr402(OMc)12 (OMc = Methacrylate). *Chem. Berichte-Recueil* **130**, 473–477 (1997).

300. Guillerm, V. *et al.* A zirconium methacrylate oxocluster as precursor for the low-temperature synthesis of porous zirconium(iv) dicarboxylates. *Chem. Commun.* **46**, 767–769 (2010).

301. Jerozal, R. T., Pitt, T. A., MacMillan, S. N. & Milner, P. J. High-Concentration Self-Assembly of Zirconium- and Hafnium-Based Metal-Organic Materials. *J. Am. Chem. Soc.* **145**, 13273–13283 (2023).

302. Semivrazhskaya, O. O. *et al.* Deciphering the Mechanism of Crystallization of UiO-66 Metal-Organic Framework. *Small* **19**, 2305771 (2023).

303. Kubo, M., Miyoshi, Y., Uchitomi, Y. & Shimada, M. Insights into the Spray Synthesis of UiO-66 and UiO-66-NH2 Metal–Organic Frameworks: Effect of Zirconium Precursors and Process Parameters. *Crystals* **14**, 116 (2024).

304. DeStefano, M. R., Islamoglu, T., Garibay, S. J., Hupp, J. T. & Farha, O. K. Room-Temperature Synthesis of UiO-66 and Thermal Modulation of Densities of Defect Sites. *Chem. Mater.* **29**, 1357–1361 (2017).

305. Dai, S., Nouar, F., Zhang, S., Tissot, A. & Serre, C. One-Step Room-Temperature Synthesis of Metal(IV) Carboxylate Metal—Organic Frameworks. *Angew. Chemie - Int. Ed.* **60**, 4282–4288 (2021).

306. Tulig, K. & Walton, K. S. An alternative UiO-66 synthesis for HCl-sensitive nanoparticle encapsulation. *RSC Adv.* **4**, 51080–51083 (2014).

307. Wang, J., Imaz, I. & Maspoch, D. Metal−Organic Frameworks: Why Make Them Small? *Small Struct.* **3**, 2100126 (2022).

308. Willems, T. F., Rycroft, C. H., Kazi, M., Meza, J. C. & Haranczyk, M. Algorithms and tools for high-throughput geometry-based analysis of crystalline porous materials. *Microporous Mesoporous Mater.* **149**, 134–141 (2012).

309. Verma, P. K. *et al.* Solution Shearing of Zirconium (Zr)-Based Metal-Organic Frameworks NU-901 and MOF-525 Thin Films for Electrocatalytic Reduction Applications. *ACS Appl. Mater. Interfaces* **15**, 53913–53923 (2023).

310. G, E., K, V. & Nudelman, A. NRM Chemicals Shifts of common laboratory solvents as traces imputities. *J. org. Chem* **3263**, 7512–7515 (1997).

311. Osterrieth, J. W. M. *et al.* How Reproducible are Surface Areas Calculated from the BET Equation? *Adv. Mater.* **34**, 2201502 (2022).

USC UNIVERSIDADE DE SANTIAGO DE COMPOSTELA

312. Ma, C., Wolterbeek, H. T., Denkova, A. G. & Serra Crespo, P. Porphyrinic metal-organic frameworks as molybdenum adsorbents for the 99Mo/99mTc generator. *Inorg. Chem. Front.* **10**, 2239–2249 (2022).

313. Polyzoidis, A., Etter, M., Herrmann, M., Loebbecke, S. & Dinnebier, R. E. Revealing the Initial Reaction Behavior in the Continuous Synthesis of Metal-Organic Frameworks Using Real-Time Synchrotron X-ray Analysis. *Inorg. Chem.* **56**, 5489–5492 (2017).

314. Shukre, R. *et al.* Batch-screening guided continuous flow synthesis of the metal-organic framework HKUST-1 in a millifluidic droplet reactor. *Microporous Mesoporous Mater.* **339**, 112005 (2022).

315. Rasmussen, E. G., Kramlich, J. & Novosselov, I. V. Synthesis of metal-organic framework HKUST-1 via tunable continuous flow supercritical carbon dioxide reactor. *Chem. Eng. J.* **450**, 138053 (2022).

316. Ma, D., Huang, X., Zhang, Y., Wang, L. & Wang, B. Metal-organic frameworks: Synthetic methods for industrial production. *Nano Res.* **16**, 7906–7925 (2023).

317. Chen, Y. & Wu, T. Sustainable and scalable continuous synthesis of metal-organic frameworks for CO2 capture. *Greenh. Gases Sci. Technol.* **13**, 409–420 (2023).

318. Bailey, T., Pinto, M., Hondow, N. & Wu, K. J. Continuous microfluidic synthesis of zirconium-based UiO-67 using a coiled flow invertor reactor. *MethodsX* **8**, 101246 (2021).

319. Ren, J. *et al.* Review on the current practices and efforts towards pilot-scale production of metal-organic frameworks (MOFs). *Coord. Chem. Rev.* **352**, 187–219 (2017).

320. Dunne, P. W., Lester, E. & Walton, R. I. Towards scalable and controlled synthesis of metal-organic framework materials using continuous flow reactors. *React. Chem. Eng.* **1**, 352–360 (2016).

321. McKinstry, C., Cussen, E. J., Fletcher, A. J., Patwardhan, S. V. & Sefcik, J. Scalable continuous production of high quality HKUST-1 via conventional and microwave heating. *Chem. Eng. J.* **326**, 570–577 (2017).

322. Chang, M. *et al.* Discovery of a Scalable Metal-Organic Framework with a Switchable Structure for Efficient CH4/N2 Separation. *Chem. Mater.* **35**, 4286–4296 (2023).

323. Carné-Sánchez, A., Imaz, I., Cano-Sarabia, M. & Maspoch, D. A spray-drying strategy for synthesis of nanoscale metal-organic frameworks and their assembly into hollow superstructures. *Nat. Chem.* **5**, 203–211 (2013).

324. Carné-Sánchez, A. *et al.* Protecting metal-organic framework crystals from hydrolytic degradation by spray-dry encapsulating them into polystyrene microspheres. *Adv. Mater.* **27**, 869–873 (2015).

325. Garzón-Tovar, L. *et al.* A spray-drying continuous-flow method for simultaneous synthesis and shaping of microspherical high nuclearity MOF beads. *React. Chem. Eng.* **1**, 533–539 (2016).

326. Crawford, D. *et al.* Synthesis by extrusion: Continuous, large-scale preparation of MOFs using little or no solvent. *Chem. Sci.* **6**, 1645–1649 (2015).

USC UNIVERSIDADE DE SANTIAGO DE COMPOSTELA

327. Zhao, J. & Peng, R. Gas-Solid Two-Phase Flow Synthesis Equipment: A New Method for Continuous, Large-Scale Preparation of Metal-Organic Frameworks with No Solvent. *Ind. Eng. Chem. Res.* **59**, 15791–15795 (2020).

328. Zhang, M. *et al.* Continuous synthesis of ZIF-67 by a microchannel mixer: A recyclable approach. *Microporous Mesoporous Mater.* **327**, 111423 (2021).

329. Wang, Y. *et al.* Continuous synthesis for zirconium metal-organic frameworks with high quality and productivity via microdroplet flow reaction. *Chinese Chem. Lett.* **29**, 849–853 (2018).

330. Sun, C. *et al.* Droplet-based millifluidic synthesis of a proton-conducting sulfonate metal–organic framework. *Chem. Eng. J.* **474**, 145892 (2023).

331. Fu, Q. *et al.* A versatile microfluidic strategy using air–liquid segmented flow for continuous and efficient synthesis of metal–organic frameworks. *Mater. Lett.* **343**, 134344 (2023).

332. Wu, H. Y. *et al.* Continuous and ultrafast MOF synthesis using droplet microfluidic nanoarchitectonics. *J. Mater. Chem. A* **11**, 9427–9435 (2023).

333. Kevat, S., Sutariya, B. & Lad, V. N. Microfluidics-assisted, time-effective and continuous synthesis of bimetallic ZIF-8/67 under different synthesis conditions. *J. Mater. Sci.* **58**, 5219–5233 (2023).

334. Rasmussen, E. G., Kramlich, J. & Novosselov, I. V. Scalable Continuous Flow Metal-Organic Framework (MOF) Synthesis Using Supercritical CO2. *ACS Sustain. Chem. Eng.* **8**, 9680–9689 (2020).

335. Taddei, M., Steitz, D. A., Van Bokhoven, J. A. & Ranocchiari, M. Continuous-Flow Microwave Synthesis of Metal-Organic Frameworks: A Highly Efficient Method for Large-Scale Production. *Chem. - A Eur. J.* **22**, 3245–3249 (2016).

336. Waitschat, S., Wharmby, M. T. & Stock, N. Flow-synthesis of carboxylate and phosphonate based metal-organic frameworks under non-solvothermal reaction conditions. *Dalt. Trans.* **44**, 11235–11240 (2015).

337. Chang, M., Wei, Y., Liu, D., Wang, J. X. & Chen, J. F. A General Strategy for Instantaneous and Continuous Synthesis of Ultrasmall Metal–Organic Framework Nanoparticles. *Angew. Chemie - Int. Ed.* **60**, 26390–26396 (2021).

338. Rubio-Martinez, M. *et al.* New synthetic routes towards MOF production at scale. *Chem. Soc. Rev.* **46**, 3453–3480 (2017).

339. Carraro, F. *et al.* Continuous-Flow Synthesis of ZIF-8 Biocomposites with Tunable Particle Size. *Angew. Chemie - Int. Ed.* **59**, 8123–8127 (2020).

340. Liu, Z., Zhu, J., Peng, C., Wakihara, T. & Okubo, T. Continuous flow synthesis of ordered porous materials: from zeolites to metal–organic frameworks and mesoporous silica. *React. Chem. Eng.* **4**, 1699–1720 (2019).

341. Zuliani, A., Carmen Castillejos, M. & Khiar, N. Continuous flow synthesis of PCN-222 (MOF-545) with controlled size and morphology: a sustainable approach for efficient production. *Green Chem.* **25**, 10596–10610 (2023).

342. Polyzoidis, A. *et al.* Improved continuous synthesis of UiO-66 enabling outstanding production rates. *React. Chem. Eng.* **6**, 679–684 (2021).

343. Alizar, Y. Y., Ramasamy, M., Kim, G. W. & Ha, J. W. Tuning Chemical Interface Damping: Competition between Surface Damping Pathways in Amalgamated Gold Nanorods Coated with Mesoporous Silica Shells. *JACS Au* **3**, 3247–3258 (2023).

344. Ryu, K. R. & Ha, J. W. Influence of shell thickness on the refractive index sensitivity of localized surface plasmon resonance inflection points in silver-coated gold nanorods. *RSC Adv.* **10**, 16827–16831 (2020).

345. He, M. Q. *et al.* Capping Ligand Size-Dependent LSPR Property Based on DNA Nanostructure-Mediated Morphological Evolution of Gold Nanorods for Ultrasensitive Visualization of Target DNA. *Anal. Chem.* **92**, 7054–7061 (2020).

346. Chowdhury, A. D. *et al.* Controlling distance, size and concentration of nanoconjugates for optimized LSPR based biosensors. *Biosens. Bioelectron.* **170**, 112657 (2020).

347. Nyamekye, C. K. A., Weibel, S. C. & Smith, E. A. Directional Raman scattering spectra of metal–sulfur bonds at smooth gold and silver substrates. *J. Raman Spectrosc.* **52**, 1246–1255 (2021).

348. Trickett, C. A. *et al.* Definitive Molecular Level Characterization of Defects in UiO-66 Crystals. *Angew. Chemie - Int. Ed.* **54**, 11162–11167 (2015).

349. Nickerl, G. *et al.* Integration of accessible secondary metal sites into MOFs for H2S removal. *Inorg. Chem. Front.* **1**, 325–330 (2014).

350. Gonzalez, M. I., Bloch, E. D., Mason, J. A., Teat, S. J. & Long, J. R. Single-crystal-to-single-crystal metalation of a metal-organic framework: A route toward structurally well-defined catalysts. *Inorg. Chem.* **54**, 2995–3005 (2015).

351. Chen, C. & Hildebrandt, N. Resonance energy transfer to gold nanoparticles: NSET defeats FRET. *TrAC - Trends Anal. Chem.* **123**, 115748 (2020).

352. Yun, C. S. *et al.* Nanometal surface energy transfer in optical rulers, breaking the FRET barrier. *J. Am. Chem. Soc.* **127**, 3115–3119 (2005).

353. Nwahara, N., Achadu, O. J. & Nyokong, T. In-situ synthesis of gold nanoparticles on graphene quantum dots-phthalocyanine nanoplatforms: First description of the photophysical and surface enhanced Raman scattering behaviour. *J. Photochem. Photobiol. A Chem.* **359**, 131–144 (2018).

354. Cao, X., Hu, B., Ding, R. & Zhang, P. Plasmon-enhanced homogeneous and heterogeneous triplet-triplet annihilation by gold nanoparticles. *Phys. Chem. Chem. Phys.* **17**, 14479–14483 (2015).

355. Zampini, G. *et al.* Effects of Gold Colloids on the Photosensitization Efficiency of Silica Particles Doped with Protoporphyrin IX. *ChemPhotoChem* **1**, 553–561 (2017).

356. Shi, L. *et al.* Implantation of Iron(III) in porphyrinic metal organic frameworks for highly improved photocatalytic performance. *Appl. Catal. B Environ.* **224**, 60–68 (2018).

357. Burger, T., Winkler, C., Dalfen, I., Slugovc, C. & Borisov, S. M. Porphyrin based metal-

USC UNIVERSIDADE DE SANTIAGO DE COMPOSTELA

organic frameworks: Highly sensitive materials for optical sensing of oxygen in gas phase. *J. Mater. Chem. C* **9**, 17099–17112 (2021).

358. Peng, M. *et al.* PCN-224/rGO nanocomposite based photoelectrochemical sensor with intrinsic recognition ability for efficient p-arsanilic acid detection. *Environ. Sci. Nano* **6**, 207–215 (2019).

359. Ceballos, M. *et al.* High-yield halide-assisted synthesis of metal-organic framework UiO-based nanocarriers. *Nanoscale* **14**, 6789–6801 (2022).

360. Yang, F. *et al.* Mitochondria-Targeted Nanosystem with Reactive Oxygen Species-Controlled Release of CO to Enhance Photodynamic Therapy of PCN-224 by Sensitizing Ferroptosis. *Small* **19**, 2206124 (2023).

361. Schlachter, A., Asselin, P. & Harvey, P. D. Porphyrin-Containing MOFs and COFs as Heterogeneous Photosensitizers for Singlet Oxygen-Based Antimicrobial Nanodevices. *ACS Appl. Mater. Interfaces* **13**, 26651–26672 (2021).

362. Demel, J. *et al.* Lanthanide-porphyrin hybrids: From layered structures to metal-organic frameworks with photophysical properties. *Inorg. Chem.* **52**, 2779–2786 (2013).

363. Park, K. C., Seo, C., Gupta, G., Kim, J. & Lee, C. Y. Efficient Energy Transfer (EnT) in Pyrene- and Porphyrin-Based Mixed-Ligand Metal-Organic Frameworks. *ACS Appl. Mater. Interfaces* **9**, 38670–38677 (2017).

364. Estévez-Varela, C. *et al.* Plexcitonic Nanorattles as Highly Efficient SERS-Encoded Tags. *Small* 2306045 (2023).

365. Wang, S. *et al.* DNA-Functionalized Metal-Organic Framework Nanoparticles for Intracellular Delivery of Proteins. *J. Am. Chem. Soc.* **141**, 2215–2219 (2019).

366. Shao, M. *et al.* High-Efficiency Electrogenerated Chemiluminescence of Novel Zr-Based Metal–Organic Frameworks through Organic Linkers Regulation. *ChemElectroChem* **9**, e202200866 (2022).

367. Craig, T. M., Kadu, A. A., Batenburg, K. J. & Bals, S. Real-time tilt undersampling optimization during electron tomography of beam sensitive samples using golden ratio scanning and RECAST3D. *Nanoscale* **15**, 5391–5402 (2023).

368. Verma, P. K. *et al.* Controlling Polymorphism and Orientation of NU-901/NU-1000 Metal-Organic Framework Thin Films. *Chemis* **32**, 10556–10565 (2020).

369. Deria, P., Yu, J., Smith, T. & Balaraman, R. P. Ground-State versus Excited-State Interchromophoric Interaction: Topology Dependent Excimer Contribution in Metal-Organic Framework Photophysics. *J. Am. Chem. Soc.* **139**, 5973–5983 (2017).

370. Gabriel, F., Roussey, A., Nobre, S. S. & Carella, A. Pesticide luminescent detection and degradation using NU-1000 MOF. *J. Mater. Chem. C* **12**, 11378–11385 (2024).

371. Hao, W., Huang, G., Jiang, G., Dauda, S. adu A. & Pi, F. Direct phoxim sensing based on fluorescent metal-organic framework of Nu-1000 induced FRET. *Food Biosci.* **55**, 102967 (2023).

372. Manrique-Bedoya, S. *et al.* Multiphysics Modeling of Plasmonic Photothermal Heating

USC UNIVERSIDADE DE SANTIAGO DE COMPOSTELA

Effects in Gold Nanoparticles and Nanoparticle Arrays. *J. Phys. Chem. C* **124**, 17172–17182 (2020).

373. Sivapalan, S. T. *et al.* Off-resonance surface-enhanced raman spectroscopy from gold nanorod suspensions as a function of aspect ratio: Not what we thought. *ACS Nano* **7**, 2099–2105 (2013).

374. Gao, X. *et al.* Integrated SERS platform for reliable detection and photothermal elimination of bacteria in whole blood samples. *Anal. Chem.* **93**, 1569–1577 (2021).

375. Van Dijk, T. *et al.* Competition between extinction and enhancement in surface-enhanced raman spectroscopy. *J. Phys. Chem. Lett.* **4**, 1193–1196 (2013).

376. Xue, W., Sewell, C. D., Zhou, Q. & Lin, Z. Metal–Organic Frameworks for Ion Conduction. *Angew. Chemie - Int. Ed.* **61**, e202206512 (2022).

USC UNIVERSIDADE DE SANTIAGO DE COMPOSTELA

USC
UNIVERSIDADE
DE SANTIAGO
DE COMPOSTELA

Appendices – Rights & Permissions

Appendix I: Conflict of interest

Juan Manuel Ceballos Guzmán, the doctoral candidate, declares that there is no conflict of interest associated with this Doctoral Thesis.

Santiago de Compostela, November 8th, 2024

USC
UNIVERSIDADE DE SANTIAGO DE COMPOSTELA

Appendix II: PhD publications and permissions

The results presented in chapter 3 are published in:

"High-yield halide-assisted synthesis of metal–organic framework UiO-based nanocarriers". (**2022**). *Nanoscale, 14*(18), 6789-6801.

Manuel Ceballos[1], Manuela Cedrún-Morales[1], Manuel Rodríguez-Pérez[1], Samuel Funes-Hernando[1], José Manuel Vila-Fungueiriño[1], Giulia Zampini[1], Maria F. Navarro Poupard[1], Ester Polo[1], Pablo del Pino*[1] and Beatriz Pelaz *[1]

[1]*Center for Research in Biological Chemistry and Molecular Materials (CiQUS), University of Santiago de Compostela, 15705 Santiago de Compostela, Spain.*

Contributions: Preparation, optimization, and characterization of the materials; writing – original draft.

Impact Factor: 6.7 in 2022. Q1 in Nanoscience & Nanotechnology.

High-yield halide-assisted synthesis of metal–organic framework UiO-based nanocarriers

M. Ceballos, M. Cedrún-Morales, M. Rodríguez-Pérez, S. Funes-Hernando, J. M. Vila-Fungueiriño, G. Zampini, M. F. Navarro Poupard, E. Polo, P. del Pino and B. Pelaz, *Nanoscale*, 2022, **14**, 6789 **DOI:** 10.1039/D1NR08305H

This article is licensed under a Creative Commons Attribution-NonCommercial 3.0 Unported Licence. **You can use material from this article in other publications, without requesting further permission** from the RSC, provided that the correct acknowledgement is given and it is not used for commercial purposes.

To request permission **to reproduce material from this article in a commercial publication**, please go to the Copyright Clearance Center request page.

If you are **an author contributing to an RSC publication, you do not need to request permission** provided correct acknowledgement is given.

If you are **the author of this article, you do not need to request permission to reproduce figures and diagrams** provided correct acknowledgement is given. If you want to reproduce the whole article in a third-party commercial publication (excluding your thesis/dissertation for which permission is not required) please go to the Copyright Clearance Center request page.

Read more about how to correctly acknowledge RSC content.

USC UNIVERSIDADE DE SANTIAGO DE COMPOSTELA

The results presented in chapter 6 are published in:

"Seeded-Growth of PCN-224 onto Plasmonic Nanoparticles: Photoactive Microporous Nanocarriers". (2024). *Small Structures, 5*(5), 2300464.

Manuel Ceballos[1], Samuel Funes-Hernando[1], Giulia Zampini[1], Manuela Cedrún-Morales[1], José Manuel Vila-Fungueiriño[1], Beatriz Pelaz *[1] and Pablo del Pino*[1]

[1]Center for Research in Biological Chemistry and Molecular Materials (CiQUS), University of Santiago de Compostela, 15705 Santiago de Compostela, Spain.

Contributions: Preparation, optimization, and characterization of the materials; writing – original draft.

Impact Factor: 13.9. Q1 in Nanoscience & Nanotechnology.

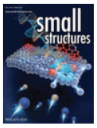

Seeded-Growth of PCN-224 onto Plasmonic Nanoparticles: Photoactive Microporous Nanocarriers

Author: Manuel Ceballos, Samuel Funes-Hernando, José Manuel Vila-Fungueiriño, et al
Publication: SMALL STRUCTURES
Publisher: John Wiley and Sons
Date: Feb 9, 2024

© 2024 The Authors. Small Structures published by Wiley-VCH GmbH

Open Access Article

This is an open access article distributed under the terms of the Creative Commons CC BY license, which permits unrestricted use, distribution, and reproduction in any medium, provided the original work is properly cited.

You are not required to obtain permission to reuse this article.

For an understanding of what is meant by the terms of the Creative Commons License, please refer to Wiley's Open Access Terms and Conditions.

Permission is not required for this type of reuse.

Wiley offers a professional reprint service for high quality reproduction of articles from over 1400 scientific and medical journals. Wiley's reprint service offers:

- Peer reviewed research or reviews
- Tailored collections of articles
- A professional high quality finish
- Glossy journal style color covers
- Company or brand customisation
- Language translations
- Prompt turnaround times and delivery directly to your office, warehouse or congress.

Please contact our Reprints department for a quotation. Email corporatesaleseurope@wiley.com or corporatesalesusa@wiley.com or corporatesalesDE@wiley.com.

USC UNIVERSIDADE DE SANTIAGO DE COMPOSTELA

Appendix III: All the other images, tables, and figures

Juan Manuel Ceballos Guzmán, the doctoral candidate, declares that all the other images, tables and figures shown in this Doctoral Thesis have been personally elaborated.

USC
UNIVERSIDADE DE SANTIAGO DE COMPOSTELA

This thesis focuses on the development of new synthetic strategies for core-shell plasmonic-nanoMOF systems. The research investigates the factors that influence the synthesis of plasmonic nanoparticles and their role as seeds in the nucleation process of the metal-organic framework (MOF) shell. These nanocomposites are designed to facilitate light-triggered release from within the MOF's porous structure into the surrounding medium, driven by the thermodiffusion effect. The efficiency of this release is directly influenced by the thickness of the MOF shell and the shape of the plasmonic core.